Experimental Study of Localised Deformation in Porous Sandstones

Elli-Maria Charalampidou

Submitted for the degree of Doctor of Philosophy

Heriot Watt University

Institute of Petroleum Engineering

April 2011

Co-supervision agreement between
Heriot Watt University
and
Université de Grenoble

Abstract

This PhD thesis presents a laboratory study aiming at a better understanding of the stress-strain response of the Vosges sandstone (porous rock) tested at a range of confining pressures (*i.e.,* 20-190 MPa) and different axial strain levels. Localised deformation was captured at different scales by a combination of full-field experimental methods, including Ultrasonic Tomography (2D), Acoustic Emissions (3D), X-ray Tomography (3D), and 3D volumetric Digital Image Correlation, plus thin section and Scanning Electron Microscope observations (2D). These experimental methods were performed before, during and after a number of triaxial compression tests. The combined use of the experimental techniques, which have different sensitivity and resolution, described the processes of shear band and shear-enhanced compaction band generation, which formed at low to intermediate and relatively high confining pressures, respectively. Pure compaction bands were not identified. The deformation bands were characterised as zones of localised shear and/or volumetric strain and were captured by the experimental methods as features of low ultrasonic velocities, places of inter- and intra-granular cracking and structures of higher density material. The two main grain-scale mechanisms: grain breakage (damage) and porosity reduction (compaction) were identified in both shear band and shear-enhanced compaction band formation, which presented differences in the proportions of the mechanism and their order of occurrence in time.

Key words: sandstones, triaxial compression, shear bands, compaction bands, ultrasonic tomography, acoustic emissions, x-ray tomography, 3D digital image correlation, thin sections, strain, damage, geomechanics

Résumé

Cette étude expérimentale traite la localisation des déformations sur un grès poreux: le grès de Vosges. Un nombre des essais triaxiaux sont effectués sous des pressions de confinement (i.e., 20 MPa - 190 MPa) et des déformations axiales différentes pour mieux comprendre la réponse mécanique de ce grès. La localisation des déformations a été étudiée dans des ***différentes échelles*** en appliquant une variation de mesures de champs (full-field methods) comme la Tomographie Ultrasonore (en 2D), les Emissions Acoustiques (en 3D), les Rayons X (en 3D), et la Corrélation des Images (en 3D). Les méthodes expérimentales ont été appliquées avant, pendant et après les essais triaxiaux. Des coupes fine ont été observées sous le ***microscope*** optique et électronique (SEM). La combinaison des multiples techniques expérimentales, qui ont des différentes sensitivités et résolutions, a décrit la procédure de la formation et l'évolution des bands de déformation observées sur le grès de Vosges. Des bandes de cisaillement ont été formées sous des pressions intermédiaires et des bandes de compaction sous des pressions élevées. Des bandes de compactions pure n'ont pas été observées.

Les bandes de déformations observées se sont caractérisées comme des zones de déformation de cisaillement localisée et/ou de compaction. En plus, elles se sont caractérisées comme des structures de fable vitesse ultrasonore, des places d'origine des fissures inter- ou intra- granulaires, et des places des densités de matériel élevées.

Deux mécanismes principales ont été observées au niveau de grain dans les bandes de cisaillement et de bandes de compaction (shear-enhanced compaction bands): d'un cote c'est la fissuration des grains (endommagement) et de l'autre cote c'est la réduction de porosité (sur la forme de compaction). Les deux mécanismes i présent différences sur leurs proportions et leur ordre d'occurrence dans le temps.

Mots clés: grès, essais triaxiaux, bands de cisaillement, bands de compaction, tomographie ultrasonore, émissions acoustiques, tomographie de rayons X, Corrélation des images en 3D, coupes fine, déformation de localisations, endommagement, géotechnique.

To my parents

Acknowledgements

At the first page of this manuscript, I would like to acknowledge all these people who contributed in various ways to this study. Their presence has been a key aspect of this PhD thesis and I am really grateful for that.

The biggest vote of thanks must go to my advisors who helped me accomplish this work: Steve Hall, Cino Viggiani, Helen Lewis and Gary Couples; different people, different backgrounds, 'beautiful' collaboration. Their contribution from both scientific and personal point of view has been very important to me. I feel really lucky having met these people and really happy having worked with them during these years. It was not an easy period, but finally, it seems like time lapsed fast. I thank them all for having trusted me during all these years.

I would like to thank Professor Teng Fong Wong, Professor René Chambon and Professor Ken Sorbie, for accepting to act as my examiners.

Thanks to Niko for his daily support and understanding, especially during these last years. His presence is of a great significance to me. Thanks also to Lena, Costa, Giorgi and my parents Fotoula and Laki for all the daily support and all their love. Thanks to Koula and Yianni for their presence and love. You are all very important to me!

I would also like to gratefully acknowledge Institute of Petroleum Engineering, Heriot Watt University, University of Grenoble and INPG Enterprise and thank for the financial support during these years.

A very warm thanks to Sergei Stanchits for all this nice and fruitful collaboration, and to Georg Dresen for the financial support of the experiments carried out at the German Research Centre for Geosciences (GFZ, Potsdam) and also for his understanding during the last months while I'm working at GFZ. Many thanks to Stefan Gehrmann (GFZ, Potsdam) for the preparation of the thin sections. Thanks also to Philippe Roux (LGIT, Grenoble) for all the help and discussions on the barrettes. Anne-Marie Boullier (LGIT, Grenoble) is gratefully acknowledged for all her assistance and remarks concerning the thin section observations. I would especially like to thank Carlos Santamarina (GT, Georgia) for all his help and contribution (I will always remember all these fruitful endless discussions we had during his stay at 3SR) and Pierre Besuelle (3SR, Grenoble) for all his presence and contribution. I particularly like to thank Gaël Combe (3SR, Grenoble), for all his friendly support from the first moment of our collaboration and later on during the writing-up of the thesis, for his

encouraging mails and his scientific feed-back on the statistical interpretation. Many thanks also to Kostas Zachariadis (AUTH, Thessaloniki), for all these discussions on statistics during the last summer. Thanks also to Jim Buckman (Institute of Petroleum Engineering, Edinburgh) for the SEM collaboration and to Sally Hamilton and Roger Hutchison (Institute of Petroleum Engineering, Edinburgh) for all their assistance during the first year of my thesis. Many thanks to Pascal Charrier, Christophe Rousseau and Alexandre Martin (3SR, Grenoble) for all their help and technical assistance. Nicolas Charalampakis (AUTH, Thessaloniki) is gratefully acknowledged since he is my first 'great' teacher who inspired me to start working on this field. Many thanks also to Euripides Papamichos (AUTH, Thessaloniki) for all these discussions and help during the last years.

Finally, I would like to thank all my friends and colleagues who have been there during these years. Thanks much to Sophia, Ifigeneia, Kaiti and Kevin, Simona and Elina who have supported me a lot during these years. A special thank to Eddy, Erika, Laura and Nando for their help on this work and their support. I would like to thank Marcos, Lam, Daiki, Brunella, Nico, Shara, Christina, Fab, Rena, Pano, and Maria. Many thanks also to Xiangwei, who was just a hero bearing me at the office, and the rest of the 3SR post-graduate team: Anca, Gabriela, Hana, Krzysztof, Ola, Michal, Jeremy… I would also like to thank my Heriot Watt mates Aisha and Amran, Zeyun, Greg, Margarita, Arnold, Simon, Claudia, Marta, Karen and Mateo. Thanks to Grzegorz for all fruitful discussions. Thanks also to all my rest Greek friends for being there for me.

DECLARATION STATEMENT

(Research Thesis Submission Form should be placed here)

List of contents

Chapter 6: Compaction band characterisation

Chapter 7: Discussion and conclusions

List of Tables

List of Figures

Πάντες ἄνθρωποι τοῦ εἰδέναι ὀρέγονται φύσει.

ΑΡΙΣΤΟΤΕΛΟΥΣ , ΤΩΝ ΜΕΤΑ ΤΑ ΦΥΣΙΚΑ Α , [980a.21]

During the years, people tried, keep trying, and will possibly continue to try to better understand Nature. The more they learn about it, the more interesting and seductive Nature becomes. Because the Natural World, as Aristotle described 2500 years ago: *«ἔτι δὲ φύσις λέγεται ἐξ οὗ πρώτου ἢ ἔστιν ἢ γίγνεταί τι τῶν φύσει ὄντων, ἀρρυθμίστου ὄντος καὶ ἀμεταβλήτου ἐκ τῆς δυνάμεως τῆς αὐτοῦ»* [*Αριστοτέλης «τά μετά τά φυσικά*[1]*»*], which is to say that *«'NATURE' means the primary material of which any natural object consists or out of which it is made, which is relatively unshaped and cannot be changed from its own potency»*,[*Aristotle's Metaphysics*, 1014b.26-1015a19, translated by *W. D. Ross*]. People could never be able to understand the 'Nature' of Human Beings and deal with Noble Ideas, if they do not primarily understand how Nature functions, because Human Beings are part of Nature (Aristotle, 345 BC).

[1] ***«τά μετά τά φυσικά»*** is translated as ''all those things that cannot be explained by the human senses''.

Chapter 1 - Introduction

1.1 Background

This work was motivated by the need for a good understanding of the deformation processes in the Earth's crust. Such knowledge is needed, particularly in engineering, as these processes could have an impact on structures and be integral to their viability. This could have implications to both surface and subsurface engineering projects. The main focus of this thesis, localised deformation in the form of shear and compaction bands in sandstones, concerns mainly the latter. In the subsurface high stresses can exist that may vary with space and time leading to different deformation processes.

In natural sandstone outcrops [e.g., *Antonellini et al.,* 1994], large scale faults are usually expressed as finite-thickness shear zones consisting of closely spaced, smaller scale *shear bands*. Such shear zones define regions of material that have been permanently altered due to deformation. Faults, and by implication shear bands, are inclined with respect to the direction of the major principal stress. On the other hand, *compaction bands* are described as narrow, roughly planar zones of localised porosity loss and reduced permeability [e.g., *Mollema & Antonellini*, 1996; *Sternlof et al.*, 2005]. These bands develop perpendicular to the direction of major principal stress (unlike shear bands). Additionally, they are inferred to have formed under relatively higher mean effective field stresses than the shear zones or faults.

Knowledge of the mechanisms of shear band and shear zone formation and evolution is a key aspect in understanding fault sealing and fault leakage. What is of a great importance is how the permeability of a damaged rock has changed and if (and where) permeability reduction is enough to significantly influence (increase or decrease) fluid flow under the current fluid saturation and stress field conditions. Surface observation of uplifted fault rocks strongly suggests complex deformation fabrics. Micro-processes taking place in compaction bands have also attracted great scientific interest, since it was observed that these deformation structures have important sealing potential and thus may constitute fluid flow barriers. Their presence in the subsurface can, thus, have practical implications for subsurface fluid injection or withdrawal (*i.e.*, oil and gas production, CO_2 storage and waste disposal). However, surface analogues of compaction bands are quite rare.

1.2 Challenge

A major objective of this work was to advance the understanding of the behaviour of porous sandstone in triaxial compression experiments at the laboratory scale. Experiments have been carried out for a range of confining pressures and axial strains. The particular sandstone studied is a Vosges sandstone from the Vosges Mountains in northern France. The mechanical behaviour of this sandstone under confining pressures up to 60 MPa has already been investigated by *Besuelle* [1999]. In this work confining pressures in the range of 120 to 190 MPa were investigated as well as the range 20 to 50MPa.
The questions that this thesis addresses are:

- What deformation features develop in this Vosges sandstone under triaxial compression and how do they vary with the main experimental parameters?
- Do these deformation features depend on the mean normal stress, and if yes how?
- How do these features initiate and evolve inside a laboratory-deformed specimen?
- What is the role of an induced structural heterogeneity (*e.g.*, a notch) on the formation and evolution of these deformation features?
- What are the mechanisms occurring (at different scales) in these deformation features?
- What features are common to the different deformation bands that have been produced in this study and how do they differ?

To answer these questions, a methodological strategy was designed: to apply a number of experimental methods (geophysical, geological and material science fields), both singly and, where appropriate, in combination that could potentially capture the onset and propagation of the observed deformation features and also provide further insights into the deformation mechanisms. A good understanding of the deformation processes at the scale of a laboratory specimen seems to be a first necessary step in view of expanding our knowledge of the larger scale natural systems.

1.3 Outline of the thesis

This thesis is organized into six further chapters. The present Chapter (Chapter 1) is the introduction to this work.

- Chapter 2 provides a literature review of previous studies focusing on the mechanisms and factors that control localised deformation in sandstones. The majority of the review focuses on laboratory experimental studies, with a few field studies included.

- Chapter 3 describes the different experimental techniques applied during this experimental programme. Non-destructive full-field techniques such as Ultrasonic Tomography, Acoustic Emission location and source mechanism analysis, x-ray Computed Tomography and 3D-volumetric Digital Image Correlation have been used. In some cases, they have been used in conjunction with destructive methods such as post-test thin section observations.

- Chapter 4 provides details on the Vosges sandstone studied in this work then goes on to describe the experimental equipment used before discussing the overall mechanical behaviour of the rock.

- Chapter 5 presents results from experiments at relatively low to intermediate confining pressures using the experimental methods presented in Chapter 3. The deformation features observed in these experiments are termed *shear bands* (which is also the title of this Chapter).

- Chapter 6 presents results from experiments at higher confining pressure using the experimental methods presented in Chapter 3. The deformation features observed in these experiments are termed *compaction bands* (which is also the title of this Chapter). However, this term is later reconsidered in Chapter 7.

- In Chapter 7 a summary of the work carried out in this study is presented. The key observations are discussed in light of the questions listed in the introduction (Chapter 1) and conclusions are drawn. Finally, a few recommendations for further research are suggested.

Chapter 2 - Mechanisms and factors that control the localised deformation in sandstones: literature review on previous studies

2.1 Introduction

This Chapter provides a summary of some of the previous field and laboratory studies on localised deformation bands of different sandstones presented in the literature. A brief introduction to the origin of sedimentary rocks is presented at the beginning. A literature review on shear and compaction bands developed in sandstones with different characteristics (*e.g.*, grain size and shape, type and degree of cement, mineralogical composition), aims at a summary of the state-of-the-art of knowledge related to factors affecting the onset, development and evolution of deformation bands.

2.2 Short overview on the origin and the characteristics of sandstones

Sedimentary rocks, which constitute about 70% of the earth's surface, are the main rocks of water aquifers and petroleum reservoirs. They consist of deposited sediments that have undergone burial and diagenesis (a set of physical, chemical and, potentially, biological processes that modify the original sediment and turn it into the sedimentary rock). All these processes may alter the petrophysical characteristics of sedimentary rocks (predominately porosity, fluid saturation and permeability). Tectonic activity adds an extra deformation in addition to that from simple burial.

This work focuses on sandstones (clastic, sedimentary rocks), which were formed by the deposition and lithification of quartz-rich sediments produced by weathering (chemical or physical breakdown of minerals) or erosion (transport by wind, water, or ice) of pre-existing rocks. The characteristics of sandstone fabrics are discussed below: note that much of the terminology applies to all sedimentary rocks.

Sandstones are mainly composed of sand-size quartz grains. Mineralogically, the main constituents of sandstones are quartz, with feldspars, micas and general rock particles being common subsidiary components, although the proportions of these elements may vary widely due to the different depositional environments and sediment sources.

Focusing on the scale of individual grains, an important feature of sedimentary rocks is their texture characterised by the grain size, the grain morphology, and the sedimentary fabric [*Tucker*, 2001]. In particular, in sandstones, the grain-size, which is defined as ranging from 63 μm (very fine) to 1000 μm (coarse), depends on the source material and the depositional processes. The range of grain-sizes usually alters during any subsequent deformation processes. Moreover, the shape, the sphericity and the roundness of the grains are described by the grain morphology, which is highly linked to the transport and reworking of the grains. Finally, the sedimentary fabric refers to the orientation (with respect to depositional horizontal) and packing as well as the nature of the grain contacts. Sandstone grains can bind together by a silt or mud matrix and also by mineral cement formed during burial diagenesis.

Sandstone cements are typically quartz or calcite cements. Quartz cement can appear as obvious intra-granular cements but also as quartz overgrowths. In some situations, it can be difficult to distinguish the grain from its overgrown cement, which normally takes the same crystallographic orientation as its grain and so is in optical continuity; thus, the quartz grains appear angular, showing crystal faces, and tightly interlocking. Calcite cement, which is also quite common in these sedimentary rocks, may both fill the pores and replace some grains, *i.e.*, feldspar grains may be altered along twin and cleavage planes and finally be replaced; while quartz grains cemented by calcite are corroded and etched at their boundaries [*Tucker*, 2001]. Cement is of great importance in sandstones, since it strengthens the material and, therefore, stabilise the grain framework and may also inhibit grain fracturing. It is also one of the principal porosity loss and permeability reduction processes, the second being burial-induced compaction in which the granular materials are rearranged so as to occupy a smaller volume.

The values of porosity (a scalar) and permeability (a tensor) play a crucial role in the mechanical behaviour of sandstones. Primary porosity is that porosity which is present when the sandstone is deposited. The value of primary porosity is typically smaller in a sandstone with fine grains, poor sorting and more densely packed sediments, grains that are more angular and/or sediment with clay content. Secondary porosity is alteration of primary porosity as the rock is buried, altered diagenetically and subjected to structural deformation. Classically, secondary porosity is taken to as an increase due to removal into solution of either previously deposited cements or the original grain framework. But the term secondary porosity can also be used for the deformation processes and the form of

resulting micro-cracks and fractures on the grains or the grain bonds. Porosity values are affected by grain shape and packing. Permeability values are affected by the packing, but also by the grain shape and grain assembly sorting: for instance, sandstones with very good sorting and well-rounded grains have looser packing, thus higher porosity and permeability. Note that permeability is affected by grain-size but porosity does not vary with grain-size. In addition, both the geometry and size of the pore network and micro-fractures that develop in the rock affect both porosity and permeability values. However, the relation of these two parameters is not always positively dependant [*Fredrich et al.*, 1993; *Vajdova et al.*, 2004; *Sulem et al.*, 2006].

2.3 Deformation bands classification and a hint of deformation processes in sandstones

Geological investigations on the Earth, from the near-surface down to some kilometres or even tens of kilometres depth, indicate that failure in sandstones is not homogeneously distributed; instead, they are focused faults and shear zones, regions of intense compaction or distinct dilation or possibly both, and joints or pressure solution steams. Most of outcrop deformation is quite typical of water or reservoir aquifers.

Aydin et al. [2006] presented a broad classification of failure modes in granular rocks, based on their kinematic attributes. The first category has to do with sharp discontinuities, which include fractures with predominantly shear slip, and discontinuities with predominantly volumetric deformation, *e.g.*, joints (dilatant /opening fractures), pressure solution surfaces (material removal by dissolution). This kind of failure modes is not within the scope of the present work. Deformation bands, which are structures formed by localisation of strain in narrow zones, belong to the second category suggested by *Aydin et al.* [2006]. When shear is the prevailing mechanism, these bands are called shear deformation bands; they include the isochoric shear bands, in which pure shear is present and no volumetric change occurs (Fig. 2.1a), and the dilatant or compactant shear bands, which are accompanied by volume increase (Fig. 2.1c) or volume decrease (Fig. 2.1b), respectively.

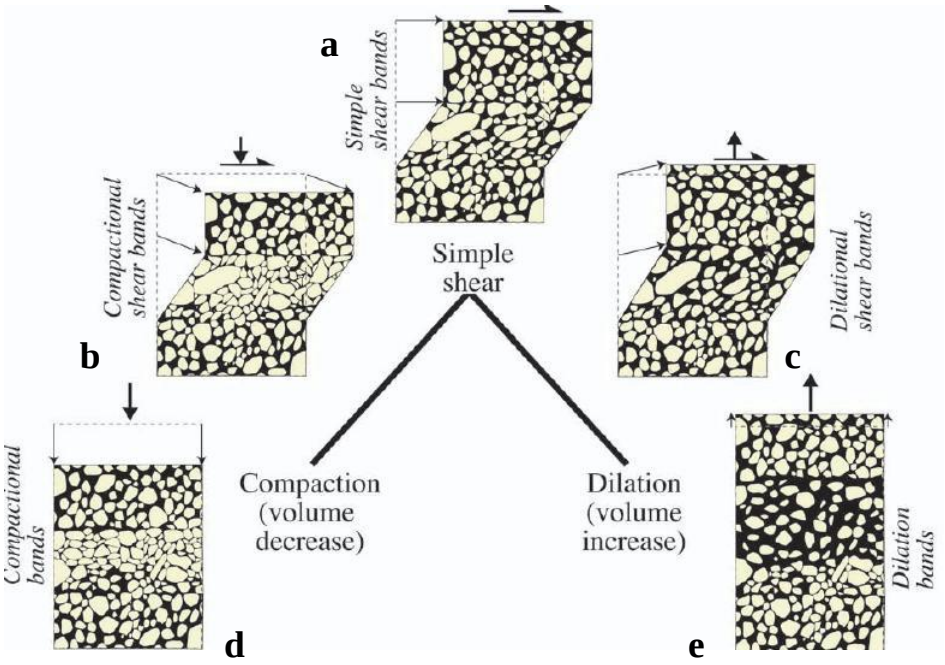

Fig. 2.1: Kinematic classification of deformation bands [*Fossen et al.,* 2007]. (a) Simple shear bands; (b) Compactant shear bands; (c) Dilatant shear bands; (d) Compaction bands; (e) Dilation bands.

When volumetric deformation is predominant, the bands are called volumetric deformation bands and are subdivided into dilation bands, characterised by volume increase (Fig. 2.1e), and compaction bands, characterised by volume decrease with respect to the host rock (Fig. 2.1d). Dilation bands are presented in detail by *Du Bernard et al.* [2002].

An in-depth understanding of deformation bands in sandstones requires a good track of the processes occurring during deformation. The focus on the scale of individual grains appears to be a key step, since deformation involves always changes in the texture of grains. At low temperatures (upper crust) or high strain rates brittle deformation occurs at grains, causing fracture formations [*Passchier & Trouw,* 2005]. When fracture affects a single grain, then it is called intra-granular, while fractures that transverse several grains are known as inter-granular. In porous sandstones, fractures tend to initiate from grain contacts due to the rearrangement of stresses at the grain-scale and have straight and diagonal trajectories or occur in a cone-shape pattern known as Hertzian fractures (Fig. 2.2).

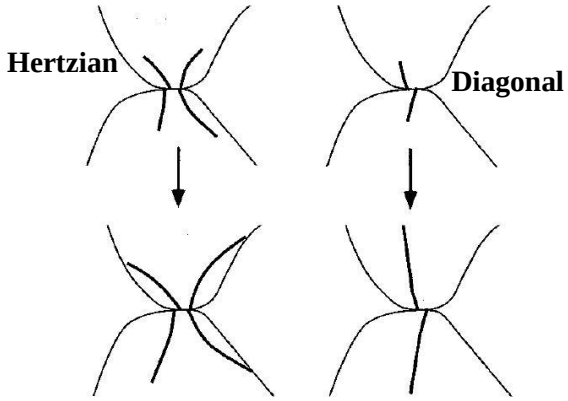

Fig. 2.2: In porous rocks, impingement micro-cracks form at contact points: examples of Hertzian and diagonal intra-granular micro-cracks [*Passchier & Trouw*, 2005].

When the sandstone is poorly lithified (typically but not exclusively at shallow depths), fractures are likely to initiate by rupture at the grain-cement contact formations [*Passchier & Trouw,* 2005]. Moreover, intense fracturing leads usually to grain disaggregation. In such case, finer particles with angular boundaries and a range of grain sizes are formed from the fractured grains. Rotation and sliding of the fragments may result in further fragmentation and local porosity reduction or in local porosity enhancement depending on whether the surrounding grains move close together or further apart.

However, intra-granular fractures in quartz grains may also be healed by optically continuous quartz cement, which, in turn, makes difficult the detection of such fractures [*Passchier & Trouw,* 2005]. Therefore, cementation is likely to mislead the interpretation of deformation mechanisms. This is why the history and physical properties of cement are also an important parameter to take into consideration for the understanding of deformation processes in shear and compaction bands.

2.4 Deformation failure modes

The link between the physical characteristics of a sandstone and the observed deformation bands is not straightforward. A large number of processes on the grain-scale (micro-scale) are responsible for the deformation in sandstones. The actual mechanisms depend on

factors such as mineralogy, grain-size and shape, packing, nature of the bonds between the grains, and degree and distribution of cement. They are also affected by external controls such as temperature, pore fluid composition, shear and normal tractions on the boundary of the volume of interest and kinematics constrains, which govern the type of the formed deformation [*Wong et al.*, 1997; *Mair et al.*, 2002; *Baud et al.*, 2004; *Haimson et al.*, 2004; *Passchier & Trouw*, 2005; *Aydin et al.*, 2006; *Fossen et al.*, 2007]. Multiple experimental laboratory campaigns were carried out in order to identify the impact of all these internal and external controls on the observed failure features (see sections 2.5-2.6).

In porous sandstones, different failure modes occur at the brittle regime, the cataclastic flow regime, and the transitional regime from brittle faulting to cataclastic flow. These different failure regimes are characterised by a critical stress state, which introduces changes in porosity values [*Wong et al.*, 1990, cited in *Wong et al.*, 1997]. Triaxial compression experiments involve both hydrostatic and deviatoric compression stress states, during which the sandstone's porosity values alter. In laboratory experiments, the application of the hydrostatic stress state results in porosity decrease (compaction), after a critical effective pressure denoted as P* [*Zhang et al.*, 1990, cited in *Wong et al.*, 1997, Fig. 2.3b]. The value of P* is partially dependant on the mineralogical composition, the grain-size, and the initial porosity of the sandstone; its value is reduced in the presence of water [*Guéguen et al.*, 2009]. If porosity values due to deviatoric stress state were controlled solely by the hydrostatic stress state (and were independent of the former), then the stress-strain curves would coincide with the relevant curves of the hydrostatic stress state. However, deviations from the hydrostat imply that the deviatoric stress state induces additional porosity change [*Wong et al.*, 1997], which results in the occurrence of different failure modes.

In the brittle regime, the deviatoric stress state results in a change of porosity decrease (compaction) to porosity increase (dilation) after a critical stress marked as C'(Fig. 2.3a). This phenomenon is coined as 'shear-induced dilation' [*Wong et al.*, 1997]. In the cataclastic flow regime, the deviatoric stress state provides considerable contribution to the compactant strain, since compaction accelerates, compares to that of the hydrostatic stress state, after the critical stress marked as C* (Fig. 2.3b). This phenomenon is named 'shear-enhanced compaction' [*Wong et al.*, 1992, cited in *Wong et al.*, 1997]. The transitional regime between the brittle and cataclastic regime is characterised by porosity

increase relative to the hydrostat during the pre-peak stress state and porosity decrease in the post-peak stress state.

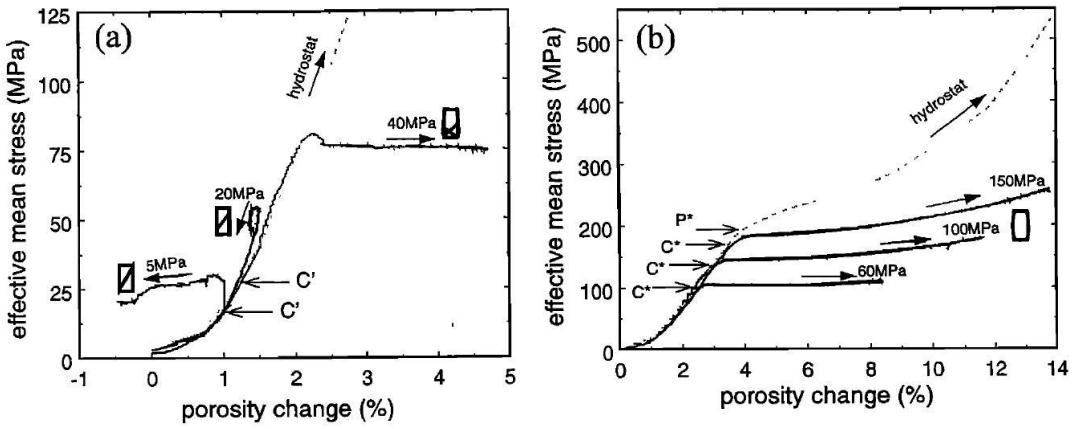

Fig. 2.3: (a) Shear-induced dilation and (b) compaction in Adamswiller sandstone. Solid curves present the effective mean stress at fixed confining pressures as a function of porosity, together with the failure modes. The hydrostat is shown as dashed curves. The critical stress states C', C*, and P* are indicated by the arrows [*Wong et al,* 1997].

Different deformation modes develop in each of these regimes (see sections 2.5 and 2.6). This work focuses solely on shear and compaction bands. Shear bands, being zones of intense damage, appear either weaker than the host rock [*El Bied et al.*, 2002] or stronger than the host rock [*Gibson*, 1998; *Wibberley et al.*, 2007]. Shearing enhances sliding of the material inside the band, and therefore further rearrangement of the grains results in porosity changes. Compaction bands, which were identified twice in the outcrops, suggest that the material inside them is much stronger than the parent rock [*Sternlof et al.*, 2005]. The sandstones selected to be discussed in the following sections, in which shear and compaction bands were developed during laboratory experiments, have different porosities, grain sizes and shapes, and different mineralogical compositions (see Table 2.1 and 2.3, section 2.8).

2.5 Shear deformation bands

Many geological field studies have been carried out in order to track the fault zone architectures, make a link between the damaged zone and the surrounding host rock, and further understand the occurred macroscopic processes [*e.g.*, *Antonellini et al.*, 1994; *Myers & Aydin*, 2004; *Wibberley et al.*, 2008]. Faults and shear zones consist of several closely-spaced bands. *Schultz et al.* [2005 and references therein] argued that faulting of band zones occurs during two stages: slip-surfaces nucleate on the formed band zone, which later on are linked producing a through-going fault inside the damage zone. The slip surface(s) and their identification, in the field, usually, appear to be conceptually straightforward, because of adjacent markers, *i.e.*, offset of layers or bedding or localised adjacent bands (Fig. 2.4). However, neither faults nor deformation bands constitute a single slip surface. *Fossen et al.* [2007] argued that slip surfaces could form within the bands or at the edges of zones of deformation bands.

Fig. 2.4: Old Red sandstone of Scotland: offset of beddings due to shearing.

A shear offset along their width, which is relatively small compared to the other two dimensions, is macroscopically apparent also in shear bands. Consequently, from a macroscopic point of view, the mechanism responsible for the onset and propagation of shear bands seems to be the shearing. However, note that faults represent a displacement

discontinuity, unlike shear bands, which are characterised by a deformation discontinuity. Microstructural observations on laboratory produced shear bands have documented more complex on going processes [among others, *Aydin*, 1978; *Menéndez et al.*, 1996; *Mair et al.*, 2000; *Du Bernard et al.*, 2002].

In the sections below, published experimental studies on eight different sandstones, starting from those of lower initial porosity (porosity before the laboratory induced deformation), and ending to those of higher initial porosity, are presented. Porosity, which is an inherent characteristic of the sedimentary rock, appears to be of a great importance.

2.5.1 The Gosford sandstone

Ord et al. [1991] performed biaxial compression experiments (unconfined and from 5 to 20 MPa confining pressures) on the Gosford sandstone, which is a poorly cemented, immature sandstone with a low porosity (~ 5%) containing minor quartz overgrowths and iron-staining, 20-30% feldspar minerals and clay minerals.

Rectangular sandstone specimens (see Table 2.1) were used. After *Ord et al.* [1991], shear band formation under plane-strain conditions occurred in the hardening regime (of the axial stress-strain curve) and it was the result of gradual alteration of the microstructure (*i.e.*, grain rearrangement followed by grain fracturing through a discrete zone). These authors suggested that the dip of the shear band was stress dependant. They also observed that the region of failure was characterised by a white, chalky appearance. Two slightly different cases of shear bands are described below.

After *Ord et al.* [1991], at relatively low confining pressures (*i.e.*, 15 MPa), rigid body movements, rotation and displacement of quartz grains and feldspars within the clay matrix took place during the initial localised deformation - before the peak stress, but still in the hardening regime. Close to the peak stress, inter- and intra-granular cracking, covering a region of one to two grain-sizes, developed along the centre of the shear zone, separated by zones of less grain cracking. Discontinuous inter-granular cracking was also observed outside the shear zone.

A discrete fracture formed after the failure, at 20 MPa confining pressure. *Ord et al.* [1991] highlighted that well defined sections having the same orientation, highly cracked grains and a width of one to two mm were separated by more diffuse and shorter shear zones, in which deformation was not accompanied by grain cracking but by rigid body

displacements and rotation of quartz grains and feldspars. The visible irregularity of the orientation of the shear zone was attributed to the different position of the shear band along its length, which was caused due to the characteristics of its different components.

2.5.2 The Darley Dale sandstone

The micromechanics of compressive failure and spatial evolution of damage in the Darley Dale sandstone were presented by *Wu et al.* [2000]. This sedimentary rock has a porosity of 13%. The grains are sub-angular and poorly sorted with an average grain-size of 220 μm. The mineralogical composition yields 67% quartz, 14% feldspar, 2% micas and 6% clays.

Cylindrical specimens were subjected to triaxial compression under different effective pressures (*i.e.*, 20 and 210 MPa confining pressure and a back-pressure of 10 MPa), and at different axial strain values. Brittle faulting was developed under a relatively low mean effective stress (*i.e.*, 10 MPa), while a higher mean effective stress (*i.e.*, 200 MPa) resulted in shear-enhance compaction and cataclastic flow (see section 2.6.1.1).

Wu et al. [2000] demonstrated that shear localisation and dilatancy occurred under relatively low mean effective stresses. The laboratory undeformed rock presented partially cracked grain boundaries, short intra-granular cracks along the feldspar cleavages and heterogeneously distributed clay and cement. After *Wu et al.* [2000], the spatial evolution of laboratory induced damage increased with increasing axial strain values (quantitative microstructural analysis). From the onset of dilatancy and in the half-way to peak stress, cracks in feldspars became longer and few inter-granular cracks, having a preferential orientation sub-parallel to the major imposed principal stress direction, developed. Close to the peak stress, *Wu et al.* [2000] commented that the number of inter- and intra-granular cracks, between quartz grains, feldspars and their grain contacts, increased in population, while few intra-granular cracks traversed two to three grains. Finally, after the failure, a curved shear band, in which intense grain cracking was apparent, was observed having an orientation varying from 25° to 38° towards the major imposed principal stress direction (dip from 65° to 52°). *Wu et al.* [2000] illustrated that over 70% of the shear band's discontinuity ran along the grain boundaries, whereas the rest was formed by the coalescence of intra-granular cracks in feldspars and quartz grains and grain crushing.

2.5.3 The Fontainebleau sandstone

The studies of *Haied et al.* [1997], *El Bied et al.* [2002], and *Sulem et al.* [2006] on the Fontainebleau sandstone are discussed in this section. This rock has several porosities due to the varied cementations and is widely characterised as well-sorted sandstone with constant grain-size. Moreover, it is a very homogeneous rock containing 98% quartz.

Cylindrical and prismatic specimens, loaded under triaxial compression at a range of confining pressures (from 10 to 40 MPa), were used in the study of *Haied et al.* [1997]. This quartz rich sandstone has 250 μm average grain-size and relatively low porosity (~ 10%). The detection of localisation was not systematically in the cylindrical specimens; therefore, prismatic specimens were used instead. The latter showed a lower strength and a transition from axial splitting to shear banding occurred at 10 MPa confining pressure. Increased confining pressure resulted in an earlier onset of localisation (*i.e.*, smaller peak-stress value), and a decrease in the dip and the width of the band (from two mm to one mm for a confining pressure varying from 10 to 40MPa). However, since it was difficult to control the spatial onset of the shear band, these authors used another sample configuration: a cylindrical hole had been drilled in the prismatic specimens to facilitate the initiation of the shear band formation. Tests stopped before the peak stress and at different axial strain values. Microstructural observations showed micro-cracks close to the peak stress, whereas, these authors commented that, in earlier stages, the loss of cohesion was mainly due to cracking of grain boundaries. Inside the shear band, cracks were preferentially oriented parallel to the loading axis.

El Bied et al. [2002] conducted triaxial compression test in a high porosity Fontainebleau sandstone (~ 21%), which is poorly cemented and has 230 μm grain-size. The behaviour of this rock, under low to middle confining pressures (form 0 to 42 MPa), was brittle.

In both dry and saturated cylindrical specimens, only one shear band developed due to the small post-peak axial strain (experiments were stopped just after the peak stress). The shear band could be easily identified because of the colour change, which corresponded to crushed quartz grains (naked eye observations). *El Bied et al.* [2002] observed that with increasing confining pressure the orientation of the shear band towards the major imposed principal stress direction increased (pressure-dependence), whereas, the thickness of the

band decreased, for both dry and saturated specimens. Two different types of shear band were identified in dry specimens.

A dilatant shear band of 1.17 mm thickness formed under relatively low confining pressures (7 MPa). Higher porosity values were measured inside it compared to those of the host rock (*i.e.*, 31.7 % versus 21%). Two distinct regions were identified: the central part of the band, which had 0.3 mm thickness and in which highly cracked grains were observed, and the surrounding zones, which had 0.43 mm thickness and in which slightly cracked grains were observed (Fig. 2.5a).

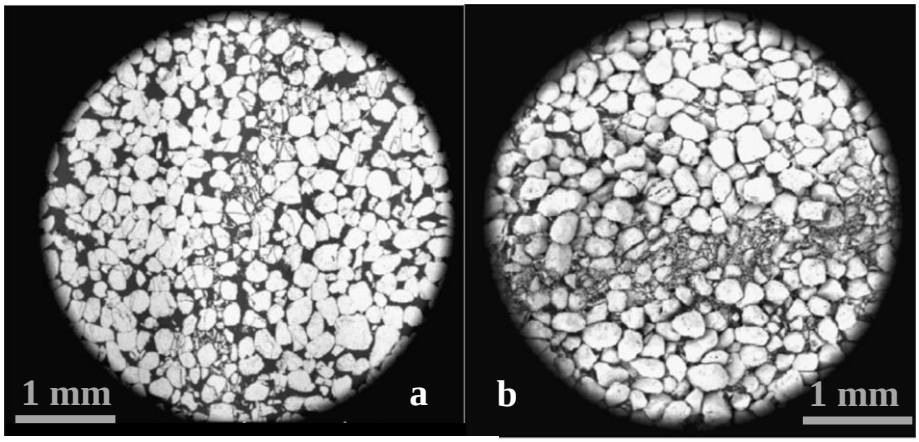

Fig. 2.5: Shear zone observed with Electron Scanning Microscope. Dry specimen tested under: (a) 7 MPa, (b) 28 MPa [*El Bied et al.,* 2002].

At a higher confining pressure (28 MPa) the structure of the shear band was more complex and somehow different. The central part of the band had the same thickness (0.3 mm) but the grains were crushed, the size of the particles was smaller, and the measured porosity values were reduced from 19% to 2%, whereas, the surrounding zones, containing broken or strongly cracked grains, had higher porosity values (36.4%) but smaller thickness (0.18 mm) (Fig. 2.5b). Therefore, the total thickness of the shear band was 0.66 mm (smaller than that measured at 7 MPa). *El Bied et al.* [2002] summarised that the dilating shear bands, observed at low confining pressures, altered to shear bands that had a compacting zone in the centre and dilating zones surrounding the central part of the band at higher confining pressures (transitional regime at 28 MPa). The material outside the band, in both cases, was undamaged and had the same porosity as the host rock.

Sulem et al. [2006] presented the role of the fluid and the drainage conditions on the shear band formation in a Fontainebleau sandstone that has a porosity of 21% and a grain-size of 250 μm. Cylindrical specimens were loaded under triaxial compression at various confining pressures (from 7 to 50 MPa) under drained and undrained conditions. All experiments were stopped soon after the peak stress had been reached in order to focus on the shear band onset. The behaviour of this sandstone was brittle. Experimental results for both drained and undrained experiments were similar to these observed by *El Bied et al.* [2002].

Microstructural analysis carried out by *Sulem et al.* [2006] revealed similar patterns at low confining pressures (from 7 to 14 MPa) for both drained and undrained conditions; grains were broken and little localised grain crushing was observed. The thickness of the shear band was ranging from 200 μm to 500 μm (*i.e.*, one to two intact grain-sizes). Even so, the structure did alter for higher confining pressures (from 28 to 50 MPa). As far as the drained experiments are concerned, the shear band was characterised by intense grain crushing, very small particle production, and pulverisation; thus, considerable change in the grain-size distribution. Moreover, the grain fabric did change, *i.e.*, the fragments were densely packed. The presence of heterogeneous pore pressure during the undrained experiments affected the microstructure of the shear band in this range of confining pressures. Therefore, a more heterogeneous shear band, with zones of compaction (as in drained conditions) and zones of dilation, developed. *Sulem et al.* [2006] argued that since no fluid exchange was allowed between the specimen and the exterior system, the pore pressure inside the shear band resulted in local fluidisation of the crushed grains. Consequently, the formation of connected channels was observed in the central part of the band, which encouraged local fluid migration inside the band, *i.e.*, the compacting zones were expelling fluid whereas the dilating zones were absorbing it. In all the above cases, the grains were slightly damaged (cracked but not crushed) close to the band, whereas the cracking was fading outward the band (Fig. 2.6).

Sulem et al. [2006] suggested that, despite the microstructural differences, porosity changes inside the band were almost similar for both conditions. At low confining pressures (from 7 to 14 MPa) an increase in porosity values (~30%) was observed, compared to the initial porosity values, and a pronounced decrease occurred after a confining pressure of 20 MPa (*e.g.*, at 50 MPa the porosity reached a value of 10% inside the shear band). *Sulem et al.* [2006] demonstrated that permeability values showed a

drastic reduction (1-2 orders of magnitude) inside the dilating shear bands, for both conditions. Furthermore, these authors showed that at higher confining pressures, the porosity decrease inside the band was accompanied by a more intense permeability decrease (3 orders of magnitude). Such remarks highlight that the porosity-permeability relation is not always linear and is closely affected by the microstructure inside the localised bands.

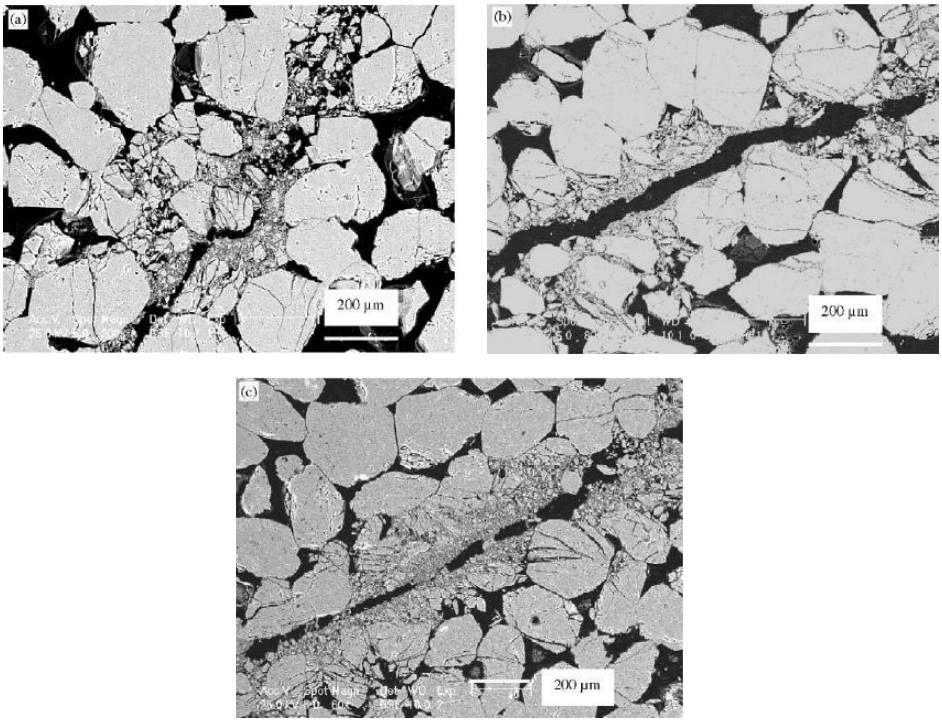

Fig. 2.6: Connected channels formed in undrained tests: (a) 28 MPa; (b) 40 MPa, and (c) 50 MPa [*Sulem et al.,* 2006].

2.5.4 The Berea sandstone

The works of *Menéndez et al.* [1996] and *Riedel et al.* [2007] are reviewed in this section.

Menéndez et al. [1996] investigated the behaviour of Berea sandstone in brittle regime focusing on the failure evolution. Berea sandstone has 173 μm average grain-size, sub-angular well sorted quartz grains, and dolomite (carbonate) cement. The mineralogical composition yields 83% quartz, 7% potassium feldspar, 2% dolomite, 7% kaolinite and 1% accessory mineral. The porosity of this particular sandstone is 21%.

These authors conducted several hydrostatic and triaxial compression experiments, under different confining pressures and at various axial strain values. Brittle faulting occurred for 20 and 50 MPa confining pressures and 10 MPa back-pressures; shear localisation developed in the post-failure stage. Under lower effective mean stress (10 MPa), shear bands were characterised by very high density of micro-cracking and stress-induced anisotropy, however, very little intra-granular cracking was observed after the onset of dilatancy (C', see also section 2.4), whereas many isolated clusters of Hertzian fractures initiated from the grain contacts just beyond the peak stress. The shear band had a width of 450 μm and an inclination angle of 30° (dip of 60°). Conjugate shear bands, which had a width of 1 mm and an inclination angle of 40° towards the major imposed principal stress direction (dip of 50°), were observed at middle mean effective stress (40 MPa). Intense grain crushing and intra-granular cracks, initiating at grain contacts, were apparent inside the conjugate shear bands. Relative undeveloped micro-cracking related to the pre-existing micro-cracks was indentified outside the bands.

Menéndez et al. [1996], in order to describe the brittle deformation mechanisms in Berea sandstone, suggested that local shear stress concentration, at a stress level corresponding to C', resulted in translation and rotation of grains and hence, promoted an overall volume increase. For such grain movement, grain bonds needed to be ruptured. Near the peak- stress, Hertzian fractures developed in isolated clusters, which coalesced in the post-failure region and resulted in the formation of the shear bands (Fig. 2.7).

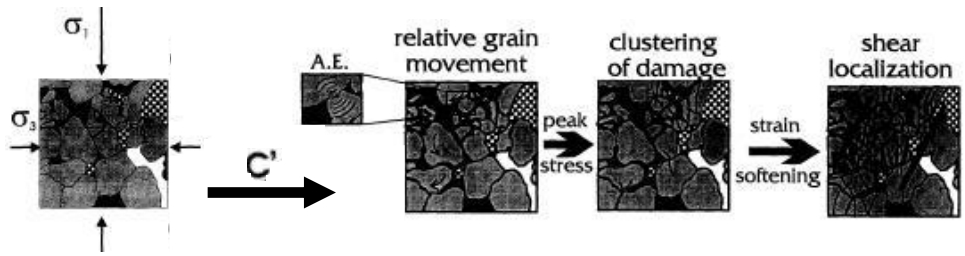

Fig. 2.7: Synopsis of the key micromechanical processes involved in the development of shear-induced dilatancy and shear localisation at the brittle regime [*Menéndez et al.,* 2006].

Riedel et al. [2007] performed biaxial compression experiments on a Berea sandstone of a porosity ranging from 15% to 18%, using prismatic specimens (see Table 2.1), cored

perpendicular to bedding. Specimens without and with a circular imperfection (on the 28x75 mm surface) were loaded under a confining pressure of 5 MPa. Both experiments were stopped before the complete rupture of the samples and shear bands, which initiated at the corner of the specimen (sample with no imperfection) or at the circular imperfection, developed. Based on microstructural observations, *Riedel et al.* [2007] indicated that micro-cracking among individual grains was the dominant failure mechanism in both specimens. Rupture of grain contacts and re-orientation of grains resulted in dilatancy prior to the peak stress and before the shear bands formation. Intra-granular cracking, which was directly linked to the localised deformation, took place inside the shear band only during the post-peak region while the region around the band remained relatively undamaged.

2.5.5 The Rothbach sandstone

The evolution of localised deformation in the Rothbach sandstone and the spatial complexity of damage were studied by *Bésuelle et al.* [2003] for the transitional regime from brittle faulting to cataclastic flow. Rothbach sandstone has a porosity of 20%, consists of 68% quartz, 16% feldspar, 12% clay and 3% micas and oxides, and has an obvious bedding heterogeneity.

The study of *Bésuelle et al.* [2003], which was guided by the mechanical data presented by *Wong et al.* [1997], included triaxial compression experiments under a range of effective mean pressures (*i.e.*, 15 to 140 MPa confining pressures and 10 MPa back-pressures).

After *Bésuelle et al.* [2003] brittle faulting occurred under low effective mean pressures (5 MPa). Strain softening and dilatancy took place in the post-peak region. Dilating shear bands developed (see more in section 3.4.2), with an orientation angle of about 30° towards the major imposed principal stress direction (dip of 60°).

Shear enhanced compaction, according to *Bésuelle et al.* [2003] occurred at higher effective mean pressures (up to 40MPa). A small amount of strain softening followed the peak-stress. Microscopic observations on a specimen, which failed in the brittle regime (loaded at 20 MPa effective mean pressure and undergone 3% of axial strain), showed a planar shear band of an inclination angle about 40° (dip of 50°). Intense grain crushing took place in the central part of the band, while inter- and intra-granular cracking was

apparent also at the periphery of the band (Fig. 2.8). The grain damage fainted when moving away from the band (four to five grains).

A transitional regime, which inhibited dilatancy, was observed from 45 to 130 MPa effective mean pressures, according to *Bésuelle et al.* [2003]. These authors attributed the variability of peak-stress values to the local variations of bedding that characterised this sandstone. *Wong et al.* [1997, cited in *Bésuelle et al.*, 2003] also suggested a sensitivity of strength and yield stress to the bedding (*e.g.*, specimens cored parallel to bedding presented lower strengths and yield stresses).

Microstructural observations on the conjugate bands, which developed in a specimen that failed in the transitional regime (55 MPa effective mean pressure and 3% of axial strain), indicated pore collapse and Hertzian fractures, which resulted in further grain crushing [*Bésuelle et al.*, 2003]. The comminuted particles filled the pores and, thus, the porosity values inside these bands decreased. *Bésuelle et al.* [2003] observed no bedding layers inside the damaged zone as opposed to the intact rock. Therefore, these authors suggested that either the grain crushing inside the bands 'homogenised' the material or the bedding inhibited the damage localisation, thus, the latter developed in regions outside the bedding heterogeneity. At higher effective mean pressures (90 MPa), *Bésuelle et al.* [2003] observed grain crushing and pore collapse and intense cracking spread in a larger surface of the specimen.

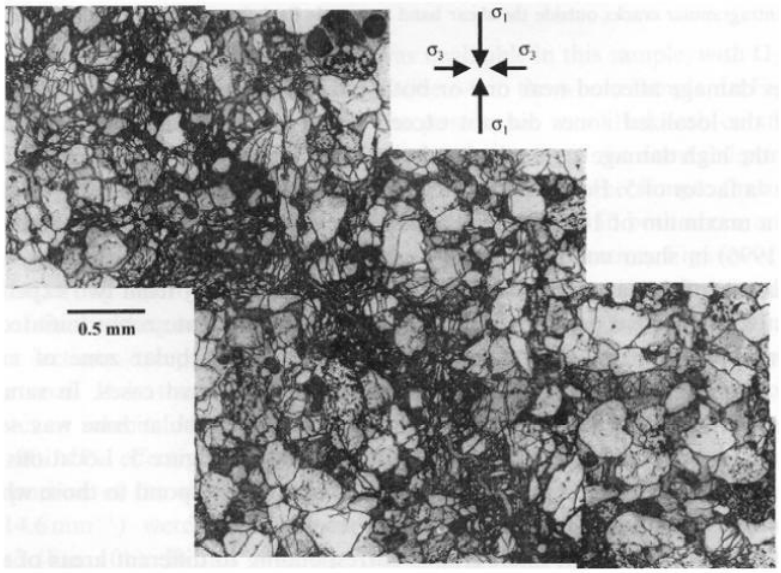

Fig. 2.8: Mosaic of optical (reflexion) micrographs showing part of the shear band that developed in a Rothbach sandstone specimen deformed in the brittle regime – 20 MPa of effective mean pressure [*Bésuelle et al.*, 2003].

2.5.6 The Vosges sandstone

Triaxial compression tests, conducted under a variety of confining pressures (from 0 to 60 MPa), on dry Vosges sandstone cylindrical specimens are presented by *Bésuelle et al.* [2000; 2001]. The Vosges sandstone, which is poorly cemented and has a porosity of 22%, is a quartz rich sandstone (93%) with a few percentage of feldspars and micas, and has 300 μm grain dimension.

Specimens with slenderness ratio H/L=1 and H/L=2 (H being the diameter and L being the length) were used. *Bésuelle et al.* [2000; 2001] commented that the onset of localised deformation was detected before the peak stress. The orientation and the complexity of the bands depended on the applied confining pressure. *Bésuelle et al.* [2000; 2001] indicated that from 0 to 10 MPa confining pressures, axial splitting took place, for 10 and 30 MPa one or two parallel shear bands developed in specimens, and from 40 to 60 MPa conjugate shear bands were formed. These authors suggested that the confining pressure increase resulted in an increase in the inclination angle of the band towards the major imposed principal stress direction, an increase in the number of shear bands, and a decrease in the distance between them (Fig. 2.9).

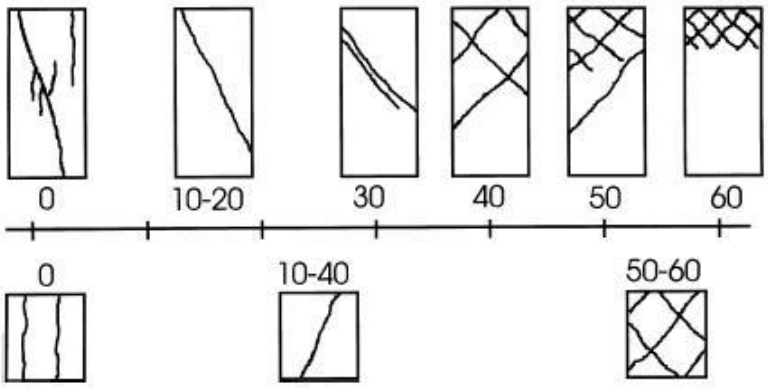

Fig. 2.9: Schematic view of the observed shear band patterns as a function of the confining pressure for triaxial compression experiments with H/D=2 and 1 [*Bésuelle et al.*, 2000].

Both low and high slenderness ration specimens showed the same localised features, according to *Bésuelle et al.* [2000; 2001], however, the former had a smaller number of lower angle shear bands than the latter did for the same confining pressure. Moreover, the shorter specimens presented 10% greater strength than the longer ones (Fig. 2.9).

Microstructural observations on specimens loaded up to the peak-stress (of the stress-strain curve) indicated a more complex internal structure of the bands than that revealed by the x-rays tomography (see section 3.4.2). *Bésuelle et al.* [2000; 2001] suggested the formation of two different bands. The centre of the band, at both 30 and 50 MPa confining pressures, showed a dilatant cataclastic deformation, similar to a gouge layer (grain crushing, mean grain-size reduction and porosity increase). As the applied confining pressure was increased, the boundaries of the band indicated a particular volumetric behaviour being either dilatant (at 30MPa, Fig. 2.10) or compactant (at 50MPa).

The thickness of the dilating shear band (30 MPa), according to these authors, was ranging from 360 µm to 1200 µm (*i*.e., one to four intact grain-sizes), while the region around the band (damage zone) had a width of 300 µm to 600 µm (*i.e.*, one to two intact grain-sizes). Grain cracks were either oriented towards the loading axis (at 30 MPa) or had no particular orientation (at 50 MPa). According to *Bésuelle et al.* [2000; 2001], the compacting shear band was considered to be the transition mechanism between the brittle and semi-brittle regimes.

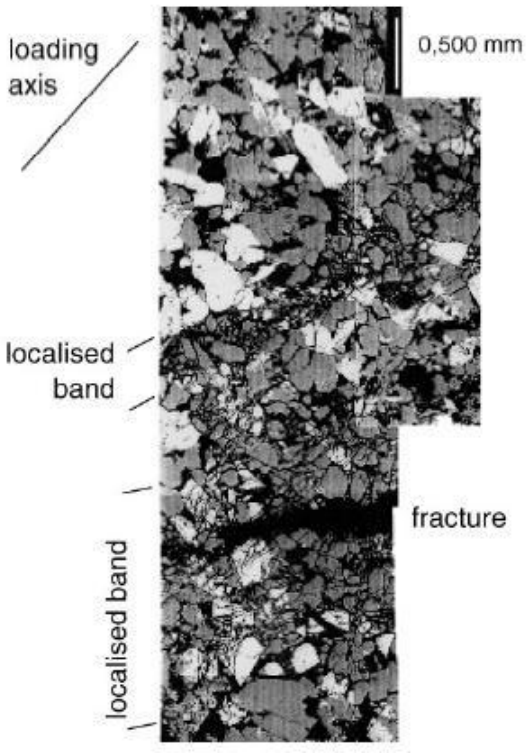

Fig. 2.10: Scanning electron micrograph of shear zone of specimens tested at a confining pressure of 30MPa. The bands are characterised by cataclastic deformation. [*Bésuelle et al.*, 2000].

2.5.7 The Locharbriggs sandstone

The studies of *Mair et al.* [2000; 2002] on the Locharbriggs sandstone are reported here.

Mair et al. [2000] studied the effect of increasing amount of post-failure axial strain in Locharbriggs sandstone specimens, which were loaded under triaxial compression at 34 MPa confining pressure. Locharbriggs sandstone is a highly porous hematite and silica cemented sandstone (22.2% of porosity), containing 88.1% quartz, 5.9% k-feldspars, and 5% major element (clay components were absent; for more details, see *Mair et al.*, 2000). The grains are well rounded with a mean grain diameter equal to 200 μm [*Mair et al.*, 2002]. Specimens cored parallel and perpendicular to bedding showed similar characteristics, however the latters were stronger (~ 20MPa) than the formers; all specimens deformed by shear localisation (cataclastic bands).

Mair et al. [2000] distinguished three different parts in the deformed specimens: the undeformed host rock (~ 12 mm far from the fault zone), the wall rock (a region of five to ten grain diameter width adjacent to the fault zone), and the fault zone itself. The wall rock that had lower porosity than the host rock - despite some cases of local dilation - was characterised by an enhanced micro-fracture density. The main fault zone presented features that were more complex. Longitudinally continuous regions of the host rock (pods) lay in between distinct fault strands, which interacted with each other forming a macroscopic zone of damage (Fig. 2.11). Grains inside the pods were characterised by the largest ratio of micro-cracks that were oriented sub-parallel to the major imposed principal stress direction. Although luck of micro-fractures was observed inside the fault strands, which were formed in the post-failure region according to *Mair et al.* [2000], the observed significant grain-size reduction resulting in a wider grain-size range with increased angularity (compared to the host rock) indicating that brittle cataclastic mechanisms (*i.e.*, grain crushing) should have taken place inside these structures. For such reason, these structures were named after *Mair et al.* [2000] 'gouge' strands. The gouge strands had a width almost three times smaller than that of the pods (300 μm compared to 800 μm). Both the number of discrete strands and the width of the fault zone increased with increasing post-failure axial strain values.

Mair et al. [2000] further suggested that grain-size decrease accompanied by changes in sorting and packing of grains might have led to reduction in porosity and permeability values. Thin section observations indicated much smaller porosity and permeability

values of the fault strands compared to those of the fault zone pods and the host rock. Therefore, these authors speculated that the gouge strands might constitute barriers to fluid migration.

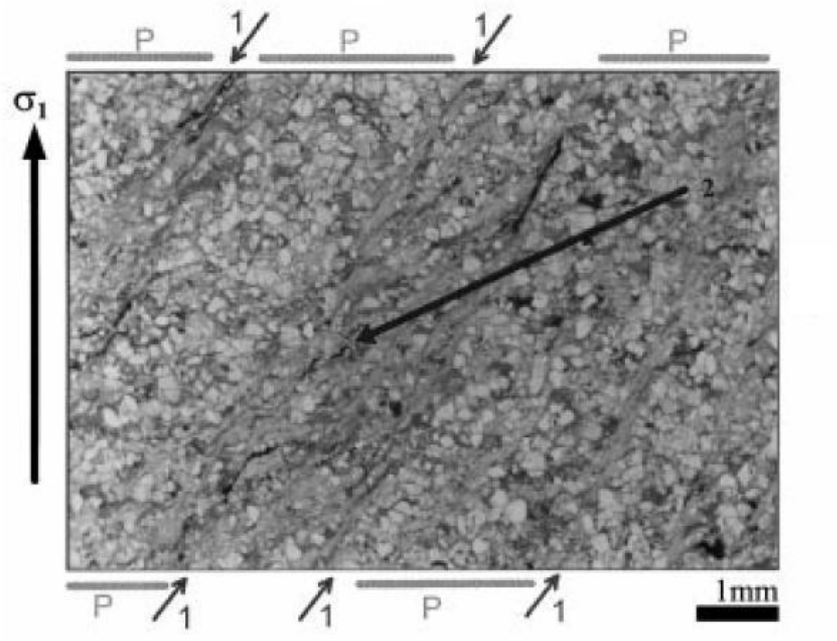

Fig. 2.11: Image of a thin section cut parallel to the major imposed principal stress direction (plane polarised light): several fine grained gouge strands (arrow 1) with internal structures (arrow 2) separated by pods of host rock [*Mair et al.*, 2000].

Mair et al. [2002] expanding the experimental study by *Mair et al.* [2000], came up with the conclusion that deformation band formation in Locharbriggs sandstone was highly confining pressure-sensitive. These authors carried out triaxial compression experiments, for a variety of confining pressures (from 13.5 to 54.8 MPa), and observed that the increase in the confining pressure resulted in a decrease in the stress deviator drop (at the peak stress), which affected the signature of the macroscopic damage. Despite the resembling microstructural characteristics, the deformation bands had different spatial distributions (*e.g.*, orientation and number of bands). *Mair et al.* [2002] demonstrated that in Locharbriggs sandstone, the transition from brittle (from 13.5 to 41.4 MPa confining pressures) to semi-brittle regime (54.8 MPa confining pressure), was manifested by an increasing number of distinct shear bands, and, thus, a wider distributed deformation, an increasing inclination angle towards the major imposed principal stress direction, and a macroscopic suppression of dilatancy.

2.5.8 The Bleurswiller sandstone

Fortin et al. [2005] studied the mechanical behaviour of the Bleurswiller sandstone under a range of confining pressures (from 12 to 110 MPa) and 10 MPa back-pressure, focusing on the relation among the volumetric strains, the elastic wave velocities and the permeability values. The particularity of this rock, which has 110 μm average mean grain diameter (personal communication) and 25% porosity, is its mineral composition. It is not a quartz rich sandstone (50 % quartz) and it consists of a considerable amount of feldspar (30 %) and micas and oxides (20%).

Cylindrical specimens, deformed under triaxial compression in the brittle regime (from 2 to 20 MPa effective confining pressure), developed dilating shear bands (single discrete fracture plane), which had 400 μm to 1000 μm width. Moreover, the dipping angle of the shear band decreased with increasing confining pressure, similarly, to what it was observed by *Bésuelle et al*. [2001]. *Fortin et al*. [2005] mentioned no visible change in permeability, but the dilating shear bands had higher porosity than the material outside them (x-ray medical scanner). The onset of cataclastic dilatancy (at the inflection point C') was associated with a drastic drop in elastic wave velocities. *Fortin et al.* [2005] justified the decrease in velocities by the seemingly competing effects of dilatant (grain crushing and crack formation) and compactant micro-mechanisms (pore collapse) that took place at this level of confining pressure (Fig. 2.12).

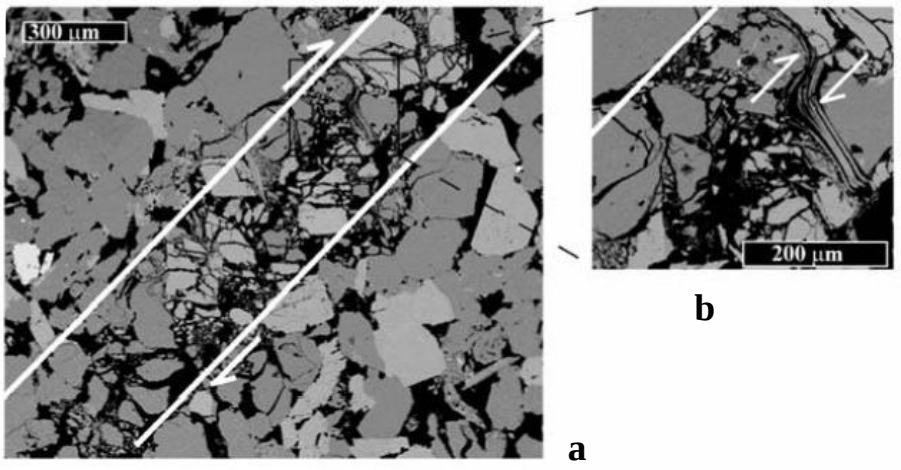

Fig. 2.12: SEM micrographs of deformed Bleurswiller specimen loaded under 20 MPa confining pressure and 10 MPa back-pressures: pervasive grain crushing. [*Fortin et al.,* 2009].

Fortin et al. [2009] presented the Acoustic Emission event locations for the three modes of failure (brittle faulting, cataclastic compaction and compacting localisation), which developed in Bleurswilles sandstone (also in section 3.3.2), expanding the results presented by *Fortin et al.* [2005]. Brittle faulting was expressed via dilatant fracture and shear localisation at 20 MPa confining pressure and 10 MPa back-pressure in deformed Bleurswilles sandstone specimens, which were cored normal to bedding and had larger dimensions than those used by *Fortin et al.* [2005]. The developed shear bands had ~45° orientation towards the major imposed principal stress direction and 300 μm width. Intense grain crushing took place in the center of the band, while very little damage occurred outside it (Fig. 2.12). According to *Fortin et al.* [2009] micas accommodated easily deformation and facilitated the displacement of adjutant quartz grains and feldspars.

2.6 Compaction bands

Compaction bands, which form tabular zones of localised deformation that accommodated pure compaction, with no macroscopic evidence of shear, have been recorded at different outcrops of two Aeolian sandstones: the East Kaibab monocline, Utah and the Valley of Fire, Nevada [see *Mollema & Antonellini*, 1996; *Sternlof et al.*, 2004; *Holcomb et al.*, 2007; *Eichhubl et al.*, 2010]. This is the main reason, why in this section a description of these two field observations is made briefly.

Compaction bands at the Jurassic Navajo sandstone (Kaibab monocline, Utah) formed at the higher porosity (20-25%) and bigger grain-size sediments (unlike shear bands) either in particular dunes far from any close-by faults or in the compressional quadrant tip of deformation band faults [*Mollema & Antonellini*, 1996]. These bands were either straight, thick (4-5 mm) and in many cases oriented parallel to the cross-bed lamina or crooked, thinner (~ 1mm in thickness) and more irregular in shape (wavy). Micro-fracturing, reduced grain size, drastic porosity reduction to a few percentages (~5%) and lack of any shear offset across their plane were the main characteristics of compaction bands. Furthermore, these deformation bands had a shorter length (1-4 m) compared to the adjusting shear bands (length up to 10 m). They were spaced in a wider and more discontinuous zone (single compaction bands were separated by 4 to 50 cm), resulting to

a very thick and continuous (well interconnected) structure, compared to single shear bands, which were very closed spaced (less than 1 mm).

Compaction bands at the Jurassic Aztec sandstone (Valley of Fire State Park, southeaster Nevada) had been formed due to regional compression, associated to tectonic shortening [*Hill*, 1989, cited in *Sternlof et al.*, 2005]. The low-angle shear bands, which formed later on at the Aztec sandstone and extended to the near deposits, resulted in a strong constrain on the upper limit of burial [*Sternlof et al*., 2005]. Compaction bands, seen in the weakly lithified outcrops (Fig. 2.13), were tabular, bounded, and penny-shape structures with distinctive weathered out fines. They had a thickness from one to two cm (in the middle of the band), a trace length from tens to more than one hundred meters, and spacing from centimetres to more than a meter [*Sternolf et al*., 2004; 2005]. *Sternlof et al*. [2005] commented that pervasive quartz cracking at grain bonds and grain micro-cracks could justify the porosity loss inside the compaction bands (10% compared to 20% porosity of the parent rock). Since no granular disaggregation could be identified inside these bands, they were characterised as nearly pure compaction bands with no or little shear.

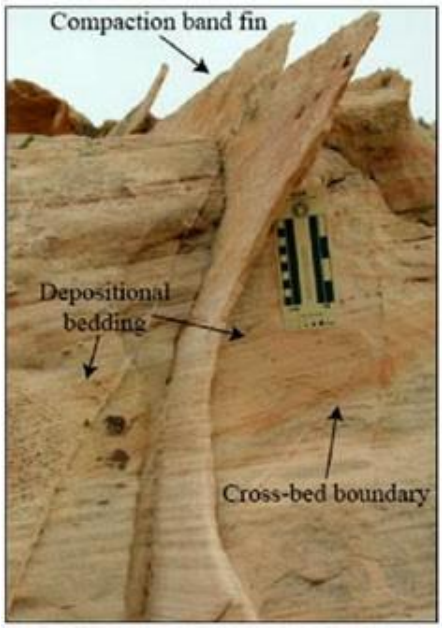

Fig. 2.13: Well developed compaction band fin in outcrop [*Sternlof et al.,* 2005].

Few isolated regions of grain damage and grain collapse outside the bands potentially indicated according to *Sternlof et al*. [2005] prominent places of compaction band nucleation (*i.e.*, material heterogeneity), which for any reason did not develop further. At

the tip of the band or around it, no damaged grain was observed; therefore, *Sternlof et al*. [2005] suggested that no process zone develops around the compaction, unlike what is observed around faults or opening modes fractures.

Bed-parallel compaction bands, which have been recently identified in the Jurassic Aztec sandstone (Valley of Fire State Park, northeast of Las Vegas, Nevada) and had been formed sub-parallel to flat-lying and shallowly inclined beds, were attributed to the vertical component of stress due to overburden [*Aydin and Ahmadov*, 2009]. These deformation bands had dipping angles ranging from sub-horizontal to moderate incline (lower than 20°). Their highly inclined segments were characterised by a high percentage of fractured grains with increased intra-granular fractures. Although no macroscopic shearing was identified in the field, a microscopic shear offset was detectable in thin sections as the dipping angle of the band was increased. Both porosity and permeability values were decreased compared to those of the host rock.

Geological observations were followed by many experimental laboratory investigations in different sandstones (see section 2.6.1). The keen scientific interest in compaction bands (see section 2.6.1) was motivated by open issues such as under which conditions compaction bands occur, which are their main characteristics and their impact on fluid flow, and to what extent compaction bands differ from other localised features (*i.e.*, shear or dilation bands).

2.6.1 Laboratory observations

This section summarises some of the important findings of different published laboratory works concerning compaction band formation and evolution in several porous sandstones, which may constitute analogues to the reservoir sandstones. Seven different sandstones are presented below, starting from the Darley Dale, with a porosity of 13%, moving to the Castlegate, with a porosity of 28%.

2.6.1.1 The Darley Dale sandstone

Results on the brittle regime presented by *Wu et al.* [2000] in the Darley Dale sandstone (13% porosity), were shown in section 2.5.2. Herein, results by these authors on the shear enhanced compaction and cataclastic flow are presented.

Wu et al. [2000] commented that the onset of shear enhanced compaction in this sandstone was manifested by inter-granular cracks, which were absent in the laboratory undeformed rock. Intra-granular cracks along the cleavage of feldspars were observed. Furthermore, isolated clusters of intra-granular cracks, which nucleated at the grain contacts, indicated the onset of grain crushing.

Wu et al. [2000] observed that as the level of axial strain increased (~4% of axial strain), the population of crushed grains increased. Intense grain crushing initiated as cleavage crack arrays in feldspars and later as Hertzian fractures at grain contacts. These authors argued that for more than the double axial strain value (~9.5% of axial strain), intense grain crushing, pore collapse, and comminuted particles, which filled the pore space, appeared in the deformed sandstone. *Wu et al.* [2000] suggested that the crack density at this axial strain was almost the double of that observed in the brittle regime for the same strain level. Furthermore, these authors demonstrated that crack density increased with increasing axial strain (similarly to the brittle faulting); however, the stress-induced cracking was relatively isotropic during the cataclastic flow, and therefore, the stress-induced anisotropy was rather small.

2.6.1.2 The Rothbach sandstone

The studies by *Bésuelle et al.* [2003], and *Louis et al.* [2007a] on the Rothbach sandstone are discussed in this section.

Part of the work presented by *Bésuelle et al.* [2003] associated with shear bands, was discussed in section 2.5.5. Here, the compaction band part is discussed. Microstructural observations on Rothbach sandstone specimens (20% porosity) deformed under 130 MPa effective mean pressure (transitional regime), revealed intense cracking in a wider part of the specimen (*e.g.*, 2/3 of the specimen compared to 1/2 observed at 90 MPa, see also 2.5.5). Intense grain crushing, located in elongated, planar clusters almost parallel to the bedding (sub-horizontal to the major imposed principal stress direction) and pore collapse were observed at this pressure level. These authors interpreted the observed localised features as compaction bands or compacting shear bands at relative low dip of around 10°. The observed grain damage outside these deformation bands was less.

Triaxial compression tests on Rothbach sandstone (20% porosity), under 140 MPa confining pressure and 10 MPa back-pressures, were presented by *Louis et al.* [2007a].

The aim of these experiments was to investigate the impact of the bedding on the development of the strain localisation associated with compactive failure. Recall that the Rothbach sandstone presents a strong bedding heterogeneity. All specimens, taken to ~3% axial strain, showed strain hardening (shear-enhanced compaction, after the C*). The strain field was measured using 2D Digital Image Correlation (see section 3.5.2).

According to *Louis et al.* [2007a] diffuse compaction bands developed in the more porous regions of specimens that were cored normal to bedding. These bands were sub-parallel to the bedding (sub-normal to the major imposed principal stress direction) and had widths of the order of several grains. Compactive shear bands, inclined towards the major imposed principal stress direction, developed in specimens, cored oblique (45°) to the bedding. These bands were parallel to the bedding intersecting with several shorter deformation bands along conjugate directions. Further observations on the damage index in these regions indicated that the grain fractures were oriented ~45° to the major imposed principal. Finally, specimens cored parallel to the bedding deformed by relative homogeneous compaction. The damage in this case was lower compared to that observed in the two previous cases.

Note that in all cases, no localised or diffuse deformation was observed inside the relative low porosity bedding laminations, which possibly halted the propagation of the bands. Therefore, according to *Louis et al*. [2007a], bedding laminations controlled the location of strain localisation and compactive failure, since both failure modes developed primarily in regions outside the dense laminations. Moreover, these authors suggested that the laminations acted, possibly, as stress-supporting framework shifting strain localisation in the more porous zones.

2.6.1.3 The Berea sandstone

Results from the Berea sandstone on the brittle regime presented by *Menéndez et al.* [1996] were discussed in section 2.5.4. Herein, results by these authors are presented on the transitional and cataclastic flow regimes.

Menéndez et al. [1996] investigated also the behaviour of Berea sandstone under relatively high mean effective stresses (*e.g.*, 250 MPa), where shear enhanced compaction and cataclastic flow took place. These authors focusing on microstructural observations, indicated the presence of increased cracking, grain crushing and pore collapse, especially

in weakly cemented regions, after the C*. *Menéndez et al.* [1996] highlighted two distinctive microstructural prcesses, which were characteristic of the deviatoric compression. The wide grain-size range of comminuted particles, which collapsed and filled the pore space and the stress-induced cracking, which had a preferential orientation sub-parallel to the major imposed principal stress direction (resulting in highly heterogeneous spatial distribution of damage).

Menéndez et al. [1996] suggested that since the grain movement was restrained by the increased stress state C*, Hertzian fractures at the grain contacts, grain crushing and pore collapse were promoted, instead, during the shear enhanced compaction (Fig. 2.14). Comminuted particles of different grain-sizes filled the pore space and resulted in a decrease in porosity values. Moreover, the micro-cracking was highly anisotropic.

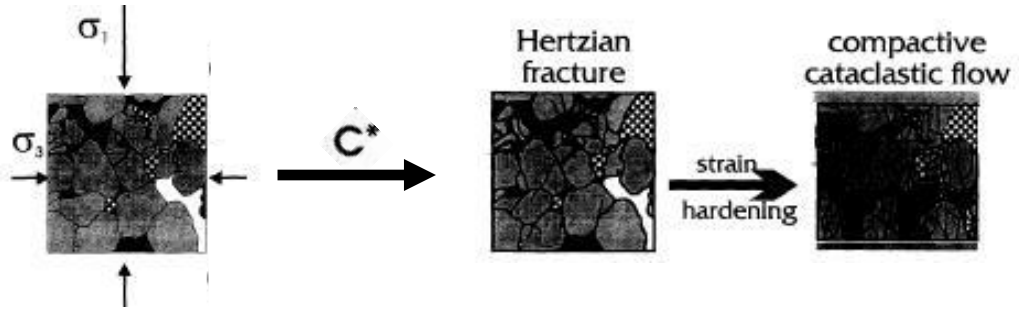

Fig. 2.14: Synopsis of the key micromechanical processes involved in the development of shear-enhanced compaction and cataclastic flow in the ductile regime [*Menéndez et al.*, 2006].

2.6.1.4 The Bentheim sandstone

In this section, laboratory works presented by *Klein et al.* [2001], *Vajdova et al.* [2003a; 2003b], *Stanchits et al.* [2009] are discussed.

Klein et al. [2001] performed hydrostatic and triaxial compression tests on dry cylindrical specimens. The Bentheim sandstone used in this study is a quartz rich homogeneous sandstone with a composition of 95% quartz, 3% kaolinite and 2% orthoclase and a porosity of 22.8%. The quartz grains are round to sub-round, with grain-size from 200 μm to 400 μm. These authors performed a series of experiments under a wide range of confining pressures (from 10 to 300 MPa), to study the transitional from brittle faulting to cataclastic flow.

Microstructural observation on deformed specimens loaded under isotropic compression revealed that the onset of grain crushing and pore collapse occurred in this sandstone beyond a critical pressure P* of 390 MPa, while deformed specimens under 375 MPa appeared relatively undamaged.

Under triaxial compression, brittle deformation was observed in specimens loaded up to 60 MPa confining pressure, which failed by shear localisation along a single shear band, while a 'quasi-brittle' transitional failure mode (strain-softening with negligible dilatacy) was observed in specimens loaded under 90 MPa confining pressure. However, specimens loaded from 120 to 300 MPa confining pressure developed compaction bands, which nucleated at the top and bottom edges of the specimen and were sub-normal to the major imposed principal stress direction (Fig. 2.15).

These bands were characterised by porosity decrease, which was reduced to few percentages compared to 16%-23% porosity of the less damaged zones in between the bands. *Klein et al.* [2001] highlighted that episodic strain softening, which resulted in the formation of compaction bands, accompanied the overall strain hardening behaviour during the ductile failure of Bentheim sandstone. Therefore, these authors characterised this failure mode as 'quasi-ductile'. The stress drops coincided with the number of compaction bands. Moreover, these authors observed that increasing axial strain values resulted in increasing number of bands, which propagated from the boundaries towards the centre of the specimen. *Klein et al.* [2001], speculated that compaction bands were the innate failure mode in the quasi-ductile regime, since similar features developed in both dry and saturated specimens, with or without lubrication at their boundaries, loaded at slower strain rates and in different triaxial cells.

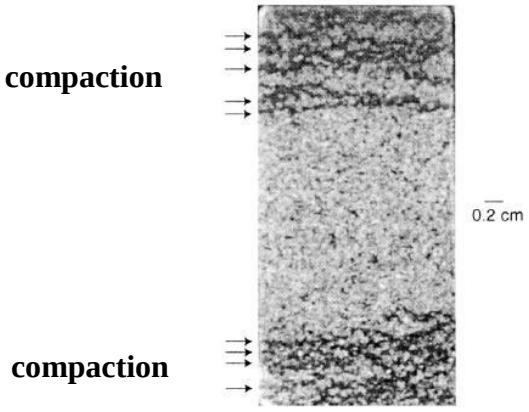

Fig. 2.15: View of a thin section from a specimen deformed at 300 MPa confining pressure [*Klein et al.,* 2001].

Vajdova et al. [2003a, 2003b] aiming at simulating the way compaction localisation develops from structural and stress field heterogeneities, carried out triaxial compression tests under 300 MPa confining pressure, on Bentheim sandstone specimens having a V-shape circumferential notch. These experiments were taken to different axial strain values in order to focus on the micromechanics of compaction band formation. Acoustic Emissions were recoded during the experiments (for this method, see section 3.3). The notch, acting as stress concentrator, forced inelastic damage to initiate at a relative low stress level. *Vajdova et al*. [2003a,b] commented that compaction bands nucleated at the notch tips and propagated by sequential increments as 'anti-cracks'. Moreover, these authors suggested that episodic stress drops and peaks in the Acoustic Emission activity punctuated the overall strain hardening behaviour (likely what it was observed by [*Klein et al*., 2001], for unnotched specimens).

An intense grain crushing (from two to three grains) was identified inside compaction bands of both notched and unnotched specimens (microstructural observations, *Vajdova et al.*, 2003). In unnotched specimens, discrete compaction bands (sub-normal to the major imposed principal stress direction) initiated as two clusters at both ends of the specimen; the number of bands increased with increasing cumulative strain [*Baud et al.*, 2004]. In notched specimens, compaction bands initiated from the notches and propagated toward the centre (*Vajdova et al.*, 2003b). Significant grain cracking and moderate grain crushing were observed close to the peak stress. Compaction bands were sub-parallel but not coplanar, after the peak- stress. *Vajdova et al.* [2003] commented that the initiation and propagation of compaction bands were not exactly axisymmetric, regardless the loading axisymmetry and the geometry of the specimens, which might be attributed to a slight geometric imperfection of the notch.

Stanchits et al. [2009] studied the onset and propagation of compaction bands in dry and wet cylindrical Benthiem specimens, which had a circumferential notch machined on their mid-height, keeping a constant effective stress. These authors observed discrete compaction bands, slightly inclined to the notch plane, which nucleated from there and propagated inwards (Fig. 2.16).

A decrease in the P-wave velocities was observed with the formation of the bands, which had a thickness close to the thickness of the notch. Microstructural observations indicated grain crushing and reduced porosity (10-15%). *Stanchits et al.* [2009] suggested that the propagation of the bands occurred due to the coalescence of individual defect

clusters. The lateral propagation of the band was almost 100 times faster than its axial shortening.

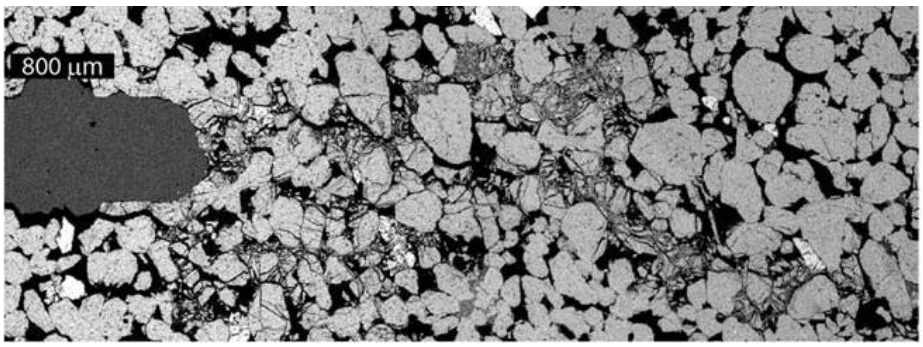

Fig. 2.16: Microscopic image of the compaction band developed in a notched specimen, which was loaded under 185 MPa constant effective pressures [*Stanchits et al.*, 2009].

2.6.1.5 The Diemelstadt sandstone

Louis et al. [2006] presented triaxial compression experiments on the Diemelstadt sandstone over a wide range of effective pressures (*e.g.*, from 10 to 165 MPa) to investigate the failure mode and brittle to ductile transition. Diemelstadt sandstone is a porous rock (24.3%) with 80 µm average grain-radius and yields 68% quartz, 26% feldspar, 2% micas and 4% other minerals (mostly oxides).

These authors showed that from 60 to 165 MPa confining pressure Diemelstadt sandstone deformed by compactant failure. Results from experiments performed at 150 MPa effective mean stresses for different axial strain values were presented. The stress-strain curves presented strain hardening punctuated by small stress drops in Acoustic Emission rate (episodic surges). According to *Louis et al.* [2006] increasing axial strain values resulted in an increase number of bands, which developed sub-normal to the major imposed principal stress direction and had a dip of 7°. These authors also observed intense grain crushing and Hertzian fracturing inside the bands, while regions outside the bands were relative undamaged.

Statistical analysis on x-ray images presented by *Louis et al.* [2006] showed compaction bands as tortuous discrete zones (see also section 3.4.2) with 490-540 µm width (*i.e.*, three to four grains). The porosity reduction in these compaction bands was estimated to be around 13.8%, which, according to these authors, was consistent with

values inside discrete compaction bands from the Bentheim sandstone, suggested by *Baud et al.* [2004] and *Vadjova et al.* [2004] (*e.g.*, 14-15%).

2.6.1.6 The Bleurswiller sandstone

The Bleurswiller sandstone was widely studied by *Fortin et al.* [2005; 2006; 2007; 2009]. It is a porous sandstone (25% porosity), with 110 µm grain-radius (personal communication), containing 50 % quartz, 30% feldspars, and 20 % oxides and micas. These authors commented that the mineral composition of the rock affected significantly the effective pressure at which pore collapse took place, but it did not bother the development and evolution of compaction band (when the rock was loaded under high confining pressures).

Fortin et al. [2005] studied the evolution of elastic wave velocities, permeability and volumetric strain values in specimens deformed under triaxial hydrostatic and deviatoric compression from 12 to 110 MPa confining pressure and a back-pressure of 10 MPa. Experiments stopped at relative small axial strain values (~3%). Results from the brittle regime were presented in section 2.5.8. Hereby, the isotropic compression and the shear-enhanced compaction will be discussed.

Distributed cataclastic flow developed during the isotropic compression. Different distinct domains of the isotropic compression were described to make a link among the measured elastic wave velocities, the permeability, the porosity and the mechanical data [*Fortin et al.*, 2005]. These authors attributed the non-linear increase in elastic wave velocities to the closure of pre-existing cracks of the rock. During that phase, the permeability remained constant; but it decreased slightly when the elastic velocities reached a plateau. The moment of the accelerated inelastic compaction (P*), pore collapse and grain crushing started occurring; the latter resulted in a drastic decrease in velocities. A drastic drop in permeability values (1 order of magnitude) was also indicated. These authors identified the occurrence of two competitive mechanisms occurring during the compactive cataclastic flow (beyond P*). One the one hand, grain crushing, which was associated with large velocity decrease, and on the other hand, pore collapse and porosity reduction, which were linked to an increase in elastic velocities (Fig. 2.17).

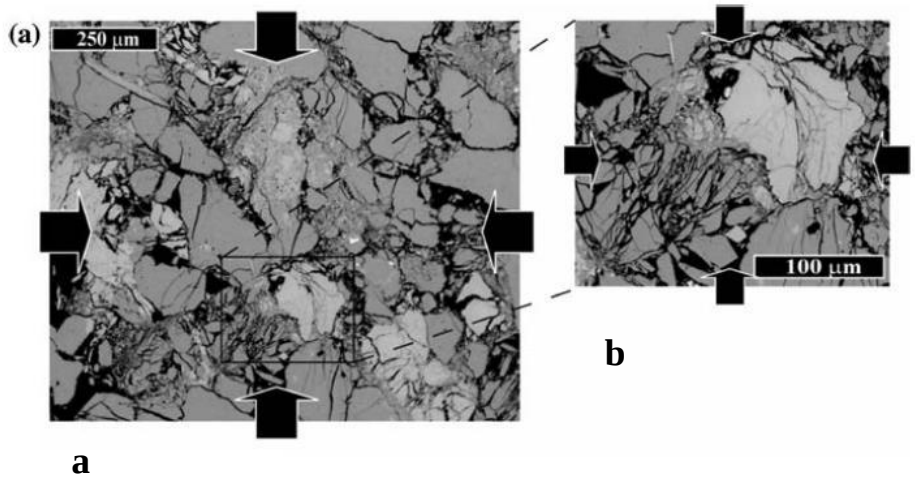

Fig. 2.17: SEM micrographs from a deformed Bleurswiller specimen loaded under hydrostatic pressure: pervasive grain crushing [*Fortin et al.,* 2009].

During unloading, the elastic velocities decreased, while the permeability increased due to opening of cracks (created during pore collapse and grain crushing). *Fortin et al.* [2005] suggested a certain interplay between the opening/closure of cracks and the pore collapse during the isotropic compression and underlined a non straightforward relation among the macroscopic strains, the permeability and the elastic velocities.

Shear-enhanced compaction took place during triaxial loading for confining pressures ranging from 50 to 110 MPa [*Fortin et al.,* 2005]. Localisation took place through slightly oblique bands (developed from 50 to 70 MPa confining pressure) or bands oriented normal to the major imposed principal stress direction (under higher confining pressures), which were inferred to be compaction bands.

The rock showed a pure plastic behaviour (at 50 MPa confining pressure), and the material continued to harden with an increasing in confining pressure values [*Fortin et al.,* 2005]. These authors attributed the initial increase in elastic velocities (beginning of loading) to the crack closure. When velocities reached a plateau (after which they remained constant), a decrease in permeability values was observed. Porosity and permeability values and elastic velocities decreased rapidly at the onset of shear enhanced compaction (C*). *Fortin et al*. [2005], therefore, demonstrated that compaction was always associated with decreased elastic velocities, and porosity and permeability reduction, which strongly recommend the nucleation of micro-cracks and the reduction of the pore-space.

Microstructural observations of a specimen loaded under 110 MPa confining pressure revealed intense grain crushing inside the compaction bands [*Fortin et al.*, 2005], which propagated incrementally from the top and bottom boundaries to mid-height of the specimen (observing their morphology). These authors suggested less than 5% porosity values inside the compaction bands, while 18-23% porosity values characterised the less damaged zones outside the band.

Acoustic Emission analysis was used by *Fortin et al.* [2006] to delve into development of compaction bands in Bleurswiller sandstone. Triaxial compression experiments under 60, 80, and 100 MPa confining pressures, 10 MPa back-pressure and approximately 3% of axial strain values were presented. A considerable reduction in elastic wave velocities was attributed to grain-cracking during the formation of compaction bands [like in *Fortin et al.*, 2005]. In addition, these authors speculated that the formation of compaction bands was related to a small anisotropy observed at the elastic properties (also verified by microstructural observations).

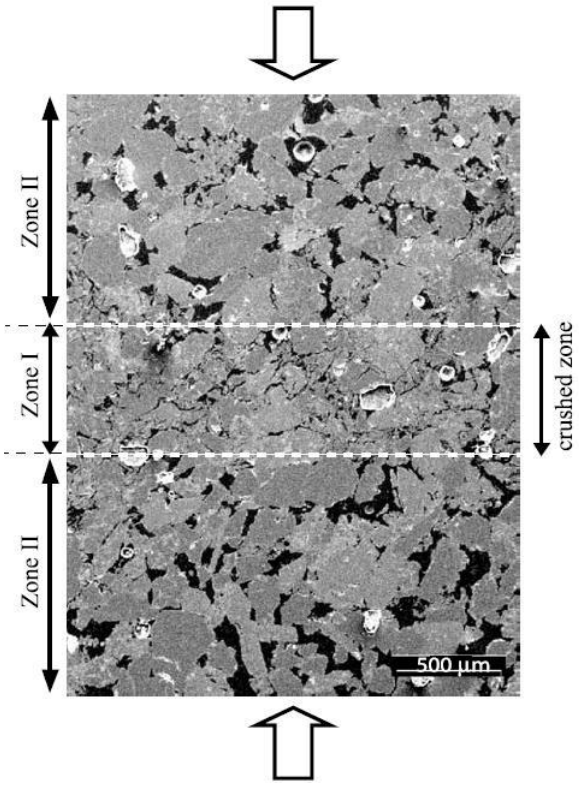

Fig. 2.18: SEM micrograph of deformed Bleurswiller specimen loaded under triaxial compression. Zone I is a compaction band with a thickness of 0.6 mm and porosity of less than 5%, due to grain crushing and pore collapse. In zone II, the porosity is close to the initial porosity of the rock, *i.e.*, ~ 25% [*Fortin et al.*, 2006].

Specimen deformed at 60 MPa confining pressure developed discrete conjugate bands (captured by Acoustic Emission locations), oriented at an angle of 60° to the major imposed principal stress direction (dip of 30°). Cracks at the grain boundaries, crushed grains and grain fragments filling the collapsed pore space took place inside the conjugate compaction bands (Fig. 2.18). Porosity reduction (values less than 5%) was observed inside them, while regions of around 25% porosity values (porosity of the host rock) were observed far from it. The thickness of the compaction band was 600 μm.

At 80 MPa confining pressure, Acoustic Emission locations revealed non-planar discrete compaction bands, normal to the major imposed principal stress direction, with a width ranging from 500 μm to 2000 μm. These authors suggested that new bands created above and below the older ones once the latter were fully developed.

Fortin et al. [2007] extending the research on Bleurswiller sandstone, investigated the evolution of elastic wave velocities (both compressional and shear) in dry and wet samples under isotropic compression at 208 MPa confining pressure. Pore collapse and grain crushing resulted in a decrease in elastic velocities. The saturated samples were much weaker than the dry ones.

In a more recent paper by *Fortin et al.* [2009] the Acoustic Emission locations of shear localisation, compaction localisation and cataclastic compaction is presented; similar micromechanical processes seemed to take place in these failure modes despite their differences at the macroscopic scale. Specimens in *Fortin et al.* [2009] had bigger dimensions than those from previous works [*Fortin et al.*, 2005; 2006]. Brittle faulting was discussed in section 2.5.8; cataclastic compaction and compacting localisation are presented here.

During isotropic compression, the sandstone failed by cataclastic compaction. The damage distribution was quite homogeneous. According to these authors, extensive grain crushing, initiating at the grain bonds due to stress concentration took place in the deformed specimens. The grain fragments filled the pore space and resulted in considerable reduction in porosity. During compaction localisation, intense cracking, grain crushing, and overall porosity reduction (due to compaction and movement of the grain fragments in the pore space) took place inside compaction bands. Outside the bands the microstructure was largely undeformed and the porosity was around 25%.

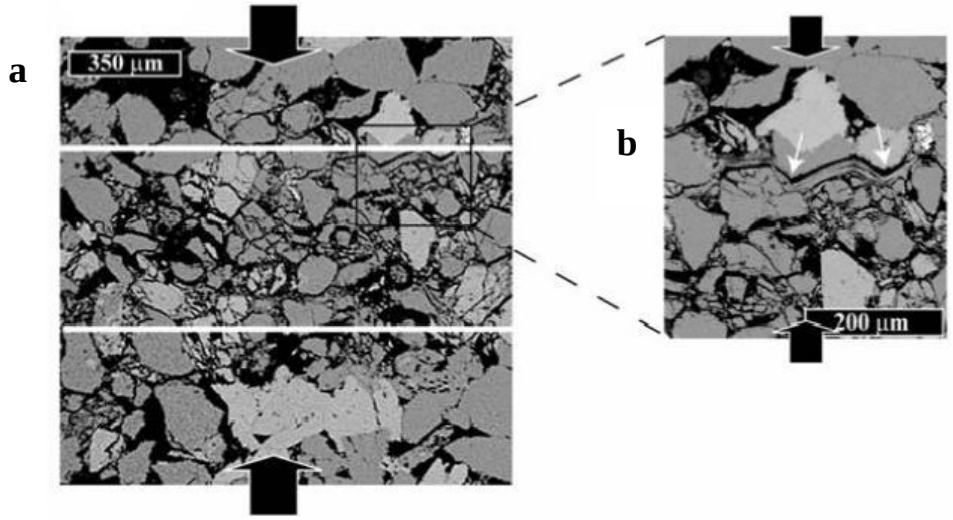

Fig. 2.19: SEM micrographs of deformed Bleurswiller specimen loaded in triaxial compression at 70 MPa effective pressures. (a) Compaction band; (b) Zoom in a deformed mica [*Fortin et al.*, 2009].

These micro-mechanisms are similar to those observed during pure isotropic compression, although differences in the macroscopic characteristics were observed here: the bands formed normal to the major imposed principal stress direction and had a thickness of 600 μm. Furthermore, these authors demonstrated through microstructural observations, that much of the deformation was accommodated by micas (Fig. 2.19).

2.6.1.7 The Castlegate sandstone

In this section the works by *DiGiovanni et al.* [2000], *Olsson & Holborn* [2000], *Olsson* [2001] and *Olsson et al.* [2002] on an analogue reservoir sandstone are reviewed.

The Castlegate sandstone is a highly porous (28%), weakly cemented sandstone, with 200 μm grain-size. The main minerals of this sandstone are quartz (80%), clays (5-10%) and feldspars [*DiGiovanni et al.*, 2000].

Olsson and Holcomb [2000] performed triaxial compression experiments from 3.5 to 250 MPa confining pressure on cylindrical specimens. Compaction localisation was observed from 45 to 100 MPa confining pressure, while generalised compaction occurred from higher than 150 MPa confining pressure. Localised compaction concentrated in bands perpendicular to the major imposed principal stress direction was observed at 45 MPa confining pressure and for high axial strainvalues (10% of total axial strain) [*Olsson*

and Holcomb, 2000]. A drop in the stress deviator was recorded after the peak-stress and the material started to harden above 6.5% of axial strain. Acoustic Emissions demonstrated that these zones nucleated near the ends of the specimen during the pre-peak region and increased in thickness growing towards the centre of the specimen. The planar boundary, separating the compacted from uncompacted material, was named compaction front [*Olsson and Holcomb*, 2000].

DiGiovanni et al. [2000] presented results on cylindrical specimens, subjected to triaxial compression under 80 MPa confining pressure and at high axial strain values (5% of total axial strain). A small drop in stress (after the peak-stress) was distinguished. Microstructural observations on regions of little Acoustic Emission activity revealed almost unfractured grains but they suggested a reduction in porosity. In regions of intense Acoustic Emission activity, the original fabric of the grains was altered; many grains were highly fractured and crushed, grain fragmentation was obvious and the porosity was reduced. Moreover, clay minerals were remarkably deformed. These authors suggested that compaction, in this weakly cemented sandstone, emanated in two phases. An initial porosity reduction due to grain bonds breakage and a consequent grain rotation was marked by limited diffuse Acoustic Emission activity. Later, a more pronounced volume decrease due to intense grain breakage and further rotation of the grain fragments was associated with intense Acoustic Emission activity. The transitional region (compaction front) had a thickness of one to two cm. The porosity changed from 28% to approximately 20%.

Olsson [2001] focused on the behaviour of the compaction front analysing the propagation of the front as a shock phenomenon.

Olsson et al., [2002], continued further research on the same rock speculating that the occurrence and propagation of compaction fronts affected significantly the permeability of the host rock. In fact, a reduction in permeability (from 2 to 3 orders of magnitude) was measured after the propagation of the compaction front.

1.6.1.8 Comparative studies

In this section comparative published studies on different sandstones are summarised [*Wong et al.*, 1997; *Wong et al.*, 2001; *Zhu et al.*, 1997; *Baud et al.*, 2004; *Temble et al.*, 2006]. The Adamswiller, the Berea, the Boise, the Darley Dale, the Keyenta, the

Rothbach, the Bentheim, and the Diemelstadt sandstones were studied in these comparative works.

Wong et al. [1997] presented a comparative study on the mechanical deformation of sandstones with different porosities (ranging from 15% to 35%), grain-sizes and mineralogical compositions, shedding light on the transitional mode from brittle faulting to cataclastic flow. The Adamswiller, the Berea, the Boise, the Darley Dale, the Kayenta, and the Rothbach sandstones, with porosities of 22.6%, 21%, 35%, 14.5%, 21%, and 19.9%, respectively, were studied.

These authors speculated that the differences in the mechanical behaviour and the observed failure modes could be explained by variations on the inherent sandstone characteristics. *Wong et al.* [1997] based on the fact that Berea sandstone (21% porosity, 0.13 grain radius) showed much higher values of the compactive yield-envelope compared to the Boise (35% porosity, 0.28 grain radius), claimed that the different porosity and grain size played a considerable role on the compactive yield behaviour. Furthermore, these authors suggested that the mineralogy of the sandstone is also of a great importance, since Berea and Kayenta sandstone (same porosity, slightly different grain size and different mineral compositions) presented discrepancies in the yield envelopes. Additionally, *Wong et al.* [1997] speculated that heterogeneities, such as the lamination, may also have an impact on the localised deformation, since Rothbach sandstone specimens, cored normal to bedding presented a higher compactive yield stress than those cored parallel.

In *Zhu et al.* [1997] the effect of water on shear enhanced compaction and cataclastic flow was investigated. Berea and Darley Dale sandstones (21% and 13% porosities, respectively), were deformed under hydrostatic and triaxial compression from 100 to 360 MPa effective pressures, under both dry and water saturated conditions, and failed by catclastic flow with shear-enhanced compaction. These authors suggested that, although the inelastic behaviour and failure mode were qualitatively similar for both dry and wet specimens, water enhanced compaction and affected the yield strengths in both hydrostatic and triaxial compression experiments. Furthermore, *Zhu et al.* [1997] demonstrated that in Berea sandstone the observed water weakening effect was much smaller than in the Darley Dale. Therefore, these authors, after the observation of intra-granular cracking in the deformed specimens (thin sections), attributed the intense weakening effect of water in the latter sandstone to its mineralogy, and particularly to the

feldspars content (21% feldspars compared to 10% in the Berea). They speculated that feldspars, which possibly had an increased density of pre-existing micro-cracks along their cleavage, could have been places of crack nucleation and propagation, and thus, they could have much attributed to the intense weakening effect observed in Darley Dale sandstone with the presence of water.

Wong et al. [2001] presented different localised features, which were observed in sandstone specimens of different porosities, and which were linked to the different stress states within the brittle to ductile transitional regime. Dry Bentheim sandstone specimens (23% porosity), and two saturated Berea and Darley Dale specimens (21% and 13% porosity, respectively) were subjected to triaxial compression. High-angle conjugate shear bands and sub-parallel arrays of compaction bands, associated to intensive comminution, developed in Bentheim sandstone, at 90MPa and from 120 to 300 MPa effective pressures, respectively. A combination of high-angle conjugate shear bands and compaction bands developed in Berea sandstone, from 40 to 150 MPa effective pressures. Finally, shear bands with 45° orientation angle towards the major imposed principal stress direction and higher-angle shear bands together with compaction bands (near the ends of the specimen) developed in the less porous Darley Dale sandstone, at 80 MPa and from 90 to 95 MPa effective pressure, respectively. The work presented by *Wong et al.* [2001] was a short introduction on the work by *Baud et al.* [2004].

Baud et al. [2004] presented a very interesting comparative work on five different sandstones, with porosities ranging from 13% to 24%, aiming at characterise the observed failure modes and shed further light into the brittle to ductile transitional regime. The Darley Dale, the Rothbach, the Berea, the Bentheim and the Diemelstand sandstones (13%, 20%, 21%, 23%, and 24% porosities respectively) were subjected to triaxial compression. The less porous sandstone developed relatively high-angle shear bands, the more porous sandstones formed arrays of discrete compaction bands sub-normal to the major imposed principal stress direction, and hybrid localisation bands, including high-angle shear bands and diffuse compaction, were developed in sandstones with intermediate porosities.

Darley Dale sandstone, which is the less porous sandstone as described by *Baud et al.* [2004] deformed by high angle shear bands, which formed from 80 to 95 MPa effective pressures (narrowest observed range). In particular, at 95 MPa conjugate high angle shear bands developed, in which intense grain crushing and axial cracking was observed, while

outside them, some axial cracks and little grain crushing were apparent only in isolated clusters. During the formation of these shear bands, no stress drops were recorded.

Rothbach sandstone deformed by conjugate shear bands, when loaded from 40 to 90 MPa effective pressure (wider range), while at 130 MPa diffuse compaction bands formed punctuated by small stress drops.

Berea sandstone showed a hybrid localisation, like the Rothbach, when loaded from 90 to 200 MPa effective pressures. High-angle conjugate shear bands developed close to the boundaries of the specimen at 90 MPa effective pressures. With increasing bulk shortening, these bands widened and became diffused bands. Intense grain crushing was observed in the heart of the shear bands accompanied by considerable intra-granular cracking in their periphery (*i.e.*, six to eight grains laterally). At 150 MPa effective pressures, diffuse compaction bands formed at both boundaries of the specimens, which, however, did not spread to the middle part (even at higher axial strain values, ~ 3.2%). However, at 200 MPa effective pressures diffuse compaction bands formed at both boundaries and discrete compaction bands developed in the middle part. The latter had a width of two grains and were tortuous. Furthermore, these discrete compaction bands where characterised by crushed grains, while micro-cracks were absent beyond a distance of around two grains.

Discrete compaction bands were observed also in Bentheim sandstone, in which compaction localisation took place from 90 to 395 MPa effective pressures (widest range) and was accompanied by episodic stress drops. *Baud et al.* [2004] demonstrated that the number of the well-developed discrete compaction bands increased with increasing axial strain values. These discrete compaction bands, which were tortuous and some of them were intersected each other, constituted two sub-parallel arrays moving towards the middle part of the specimens (Fig. 2.20). No stress drops were observed after the moment these bands covered the whole height of the specimen (6% of axial strain). Crushed grains and smaller grain fragments were observed in a width of around 500 μm inside these compaction bands, while few cracks and negligible damage was observed beyond a lateral distance of around two to three grains (outside the bands). Finally, *Baud et al.* [2004] showed that Dimelstadt sandstone deformed in a similar way to Bentheim. Discrete compaction bands, accompanied by small stress drops in the stress-strain curve developed at 160 MPa effective pressures and at 3.9% axial strain.

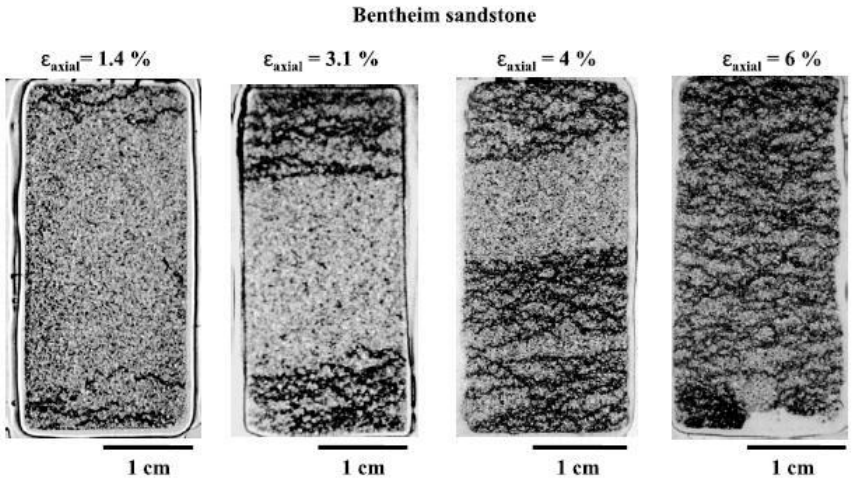

Fig. 2.20: Optical micrographs of Bentheim sandstone specimens deformed at 300 MPa confining pressure at different axial strain levels [*Baud et al.*, 2004].

Tembe et al. [2006] studied the influence of an analogue structural heterogeneity on the initiation and propagation of deformation bands, developed in Bentheim and Berea sandstones (porous rocks) in the compactive failure (from 250 to 350 MPa confining pressure for the former and from 150 to 250 MPa for the latter). Dry specimens with a V-shape circumferential notch in their mid-high were used. These authors claimed that the presence of the notch, which also represented a stress heterogeneity, enhanced the local mean stresses and activated a series of failure modes. Furthermore, notched specimens failed in lower stress states. *Tembe et al.* [2006] argued that the onset of deformation bands at the notch tip presented similar characteristics for both sandstones (*i.e.*, comminution and intense Hertzian fracturing, process zone of three to four grains from the notch tip); however, the subsequent growth of the localised bands showed fundamental differences. According to these authors, the Bentheim notched specimens developed discrete compaction bands (punctuated by episodic force drops), similarly to unnotched specimen [*Wong et al*., 2001]. However, the Berea notched specimens developed conjugate diffuse bands (accompanied by strain hardening), since a transition from conjugate shear bands to diffuse compaction bands occurred in the unnotched specimens [*Baud et al*., 2004]. *Tembe et al.* [2006] suggested that around the notch a wide range of mean stresses developed, therefore various localisation modes might be activated around its tip. These failure modes, however, were not much different from those observed in the unnotched specimens.

2.7 General remarks

Based on the literature review presented in this Chapter, some general remarks on shear and compaction bands are made in this section. A series of Tables was edited to summarise the literature review's key points concerning shear and compaction deformation bands. Table 2.1 refers to shear bands and collects information such as the grain-size and shape, the porosity and permeability, the mineralogy and the type and degree of cementation for each of the sandstones presented in section 2.5. In fact, the grain-size measurement is complicated, since grains are cut randomly in thin sections and the 3D grain-size is not constant in the sectioning plane. For such reason a range of grain-sizes is observed in cross section (none of them larger than the maximum grain sampled in the thin section). Grain shape also varies, particularly as a function of grain-size. In the literature, grain-size is not cited precisely all the times. Grain diameter, mean grain-size, grain radius, sizes of grains is some the terminology used. In works by *Wong and co-authors*, the mean intercept length, $\boldsymbol{L_3}$, is introduced instead. In stereology, the mean intercept length is defined as the average length of the line along the chord that passes through the outline of the feature on the section (Fig. 2.21). When grains are assumed to be spherical, the mean intercept length, $\boldsymbol{L_3}$, is related to the grain radius, $\boldsymbol{R_g}$, by: $R_g = ¾\ L_3$ [*Wong et al.*, 1997; *Russ & Dehoff*, 2000].

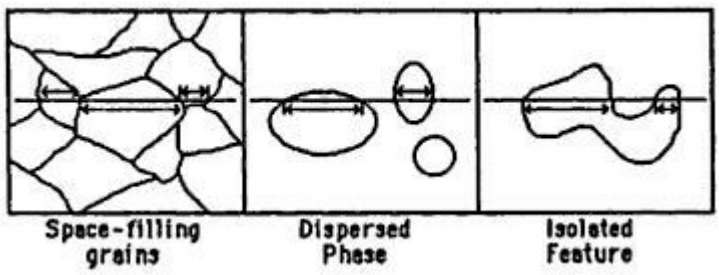

Fig. 2.21: Intercept lengths (marked with arrows) of a test line with different types of features [*Russ*].

In this Chapter, the grain-size or any equivalent unit to that is cited as used in the literature. In Table 2.1, the mean grain diameter is cited instead, assuming that this is equivalent to the mean intercept length. Moreover, Table 2.1 includes information concerning the core orientation towards the bedding direction of the rock, the sample configuration, the drained or un-drained conditions and the saturation liquid, as well as

the displacement/strain rate of each performed experiment. The basic points/remarks from each of the reviewed papers are presented in Table 2.2. The same implies to Tables 2.3 and 2.4, for the case of compaction bands (see section 2.6). Shear and compaction bands deserve extra attention, from an academic point of view, since their understanding provides helpful insights into the way that deformation in geomaterials occurs, and particularly for this PhD work, in porous sandstones.

Table 2.1: Summary of information concerning specimens which failed by shear bands (from the literature review).

sand-stone	mean grain D	shape	porosity	perme-ability	mineralogy	cement	core orientation to bedding	sample	saturation liquid	rate	Reference
Berea	173 µm	sub-angular well-sorted quartz	21%	$5x10^{-14}$ m^2 @ p_{eff} = 3MPa	83% quartz 7% kaolinite 7% potassium feldspar 2% dolomite 1% accessory minerals	dolomite cement	------	cylindrical D=18.4 mm H=38.1 mm	distilled water	$5x10^{-1}$ s^{-1} strain rate	***Menéndez et al., 1996***
Berea	------	------	15%-18%	------	------	------	perpendi-cular	100x28x75mm	no pore fluid	10^{-4} mm s^{-1} displace-ment rate	***Riedel et al, 2007***
Bleurs-willer	110 µm	------	25%	during the test	50% quartz, 30% feldspar, 20% oxides-micas	------	parallel	cylindrical D=40 mm H=80 mm	tap water, fully drained conditions	$1.0x10^{-5}$ s^{-1} strain rate	***Fortin et al., 2005***
Bleurs-willer	110 µm	------	25%	------	50% quartz, 30% feldspars, 20% oxides-micas	------	perpendi-cular	cylindrical D=50 mm H=100 mm	distilled water Fully drained conditions	$1.0x10^{-5}$ s^{-1} strain rate	***Fortin et al., 2009***
Darley Dale[1]	220 µm	sub-angular poorly sorted	13%[2]	------	67% quartz, 14% feldspar, 2% micas 6% clays	heteroge-neously distributed cement	------	cylindrical D=18.4 mm H=38.1 mm	distilled water, drained conditions	$1.3x10^{-5}$ s^{-1} strain rate	***Wu et al., 2000***

[1] The specimens were coming from the same block as in *Read et al.*, [1995] and *Wong et al.*, [1997].
[2] The specimens in *Wu et al.*, [2000] had initial porosities ranging from 13.1% to 13.6%, with a mean of 13.4%.

Table 2.1: Summary of information concerning specimens which failed by shear bands (from the literature review).

Fontai-nebleau	250 µm	------	10%	------	98% quartz 2% clay minerals	------	------	cylindrical & prismatic (with and without circular hole	no pore fluid	5×10^{-6} s^{-1} strain rate	***Haied et al., 1997***
Fontai-nebleau	230 µm	------	21%	------	------	poorly cemented quartz interlo-cking	------	cylindrical D=40 mm H=60 mm	both dry & saturated	5×10^{-6} s^{-1} strain rate	***El Bied et al., 2002***
Fontai-nebleau	250 µm	------	21%	------	98% quartz	------	------	cylindrical D= 37.5 mm H= 77 mm	saturated, drained & undrained conditions	10^{-5} s^{-1} strain rate	***Sulem et al., 2005***
Gosford	200 µm - 300 µm	immature sandstone	5%, poorly connecte d porosity	------	minor quartz overgrowths, some iron-staining, 20-30% feldspars, clay mineral	poorly cemented	------	80x40x80 mm	------	2.78×10^{-6} s^{-1} strain rate	***Ord et al. , 1991***
Lochar-briggs	200 µm	rounded-well rounded	22.2%	------	88.8% quartz 5.9% k-feldspar 5% major elements	hematite and some silica	perpendi-cular and parallel	cylindrical D=100mm	no pore fluid	5×10^{-6} s^{-1} strain rate	***Mair et al., 2000***
Lochar-briggs	200 µm	rounded-well rounded	22.2%	------	88.8% quartz 5.9% k-feldspar 5% major elements	hematite and some silica	perpendi-cular	cylindrical D=100mm H=230mm	no pore fluid	5×10^{-6} s^{-1} strain rate	***Mair et al., 2002***

Table 2.1: Summary of information concerning specimens which failed by shear bands (from the literature review).

Roth-bach[3]	------	------	20%	------	68% quartz, 16% feldspar, 12% clay, 3% micas and oxides	-----	perpendi-cular	cylindrical D=18.1 mm H=38.1 mm	distilled water, drained conditions	$1.3x10^{-5}$ s^{-1} strain rate	***Bésuelle et al., 2003***
Vosges	300 µm	------	22%	------	93% quartz, few % of feldspars and micas	poorly cemented; interlocking of grains	------	cylindrical H/D=1 D= 40mm H=40mm, H/D=2 D= 40mm H=80mm	dry	10^{-5} s^{-1} strain rate	***Bésuelle et al., 2000/ Bésuelle, 2001***

[3] *Bésuelle et al.*, [2003], mention that the specimens were cored from the same block as in *Davis et al.*, [1994], and *Wong et al.*, [1997]. The petrophysical description can be met there.

Table 2.2: Comments on the presented works from different sandstones focusing on shear bands (from the literature review).

sandstone	Reference	comments
Berea	*Menendez et al., 1996*	Deformation band mechanisms (shear localisation in the post-failure stage).
Berea	*Riedel et al, 2007*	Damage zone, role of imperfection; biaxial compression test
Bleurswiller	*Fortin et al., 2005*	Correlation of the evolution of elastic wave velocities, permeability, and volumetric strains.
Bleurswiller	*Fortin et al., 2009*	Acoustic emission signatures of three modes of failure: cataclastic compaction, shear localisation, compaction localisation.
Darley Dale	*Wu et al., 2000*	Micromechanics of compressive failure and characterisation of the spatial evolution of anisotropic damage (quantitative micro-structural analysis).
Gosford	*Ord et al., 1991*	Plain strain conditions; Stress dependence of the orientation of the shear band; Fracture is a result of gradual alteration of the micro-structure.
Fontainebleau	*Haied et al., 1997*	Influence of increasing pc: increase in band orientation, decrease in the band width.
Fontainebleau	*El Bied et al., 2002*	Tests stopped just after the peak stress; Influence of confining pressure; Orientation, thickness, porosity and grain size distribution; Both dry and saturated drained tests.
Fontainebleau	*Sulem et al., 2005*	Role of fluid and drainage conditions; Change in the structure of the band; Microstructural differences; Porosity and permeability changes.
Locharbriggs	*Mair et al., 2000*	Increasing amount of post-failure deformation/ strain effect; Fault strands and fault pods; Microstructure; Increasing number of strands with increasing axial deformation.
Locharbriggs	*Mair et al., 2002*	Range of confining pressures; Pressure sensitive deformation bands.
Rothbach	*Bésuelle et al., 2003*	Spatial complexity of damage and evolution of localised failure in the transitional regime from brittle faulting to cataclastic flow, x-rays, microstructural observations, damage maps.
Vosges	*Bésuelle et al., 2000*	Different slenderness rations; Stress dependent shear bands: dilating and compacting; Onset, orientation, patterning of the bands.

Table 2.3: Summary of information concerning specimens which failed by compaction bands (from the literature review).

sandstone	mean grain D	shape	porosity	perme-ability	mineralogy	cement	core orientation to bedding	sample	saturation liquid	rate	Reference
Bentheim	50 µm – 500 µm [4]	round to sub-round	22.8%	------	95% quartz, 3% kaolinite, 2% orthoclase	------	------	cylindrical D=20 mm H=40mm	dry	2.5×10^{-5} s^{-1} strain rate	***Klein et al., 2001***
Bentheim[5]	200 µm	------	23%	------	------	------	perpendi-cular	cylindrical D=18.4mm H=38.1mm V-shape notch[6]	dry	1.0×10^{-5} s^{-1} strain rate	***Vajdova et al., 2003***
Bentheim	300 µm	------	22%	------	95% quartz, 3% feldspar, 2% kaolinite	------	------	cylindrical D=50 mm H=105 mm U-shape notch[7]	dry & distilled water	3.2×10^{-8} - 3.2×10^{-4} s^{-1} strain rate	***Stanchits et al., 2009***

[4] 200-400 µm being most of grain sizes.
[5] Same Sandstone used in Baud et al. [2004].
[6] V-shape notch, 2 mm in width and 2 mm in height, was machined along the circumference of the mid-section of the sample.
[7] U-shape notch, 0.8 mm wide and 5 mm depth, circumferential notch at the mid-high of the specimen.

Table 2.3: Summary of information concerning specimens which failed by compaction bands (from the literature review).

Berea	173 µm	sub-angular well-sorted quartz	21%	$5x10^{-14}$ m^2 @ p_{eff}=3MPa	83% quartz 7% kaolinite 7% potassium feldspar 2% dolomite 1% accessory minerals	dolomite cement	------	cylindrical D=18.4 mm H=38.1 mm	distilled water	$5x10^{-1}$ s^{-1} strain rate	***Menéndez et al., 1996***
Bleurswiller	110 µm[8]	------	25%	measure-ments during the test	50% quartz, 30% feldspars, 20% oxides-micas	------	parallel	cylindrical D=40 mm H=80 mm	tap water fully drained conditions	$1.0x10^{-5}$ s^{-1} strain rate	***Fortin et al., 2005***
Bleurswiller	110 µm[9]	sub-angular to sub-rounded	25%	------	50% quartz, 30% feldspars, 20% oxides-micas	------	------	cylindrical[10] D=50 mm H=100 mm	distilled water fully drained conditions	$1.0x10^{-5}$ s^{-1} strain rate	***Fortin et al., 2006***
Bleurswiller	110 µm	sub-angular to sub-rounded	25%	200×10^{-16} m^2	[11]50% quartz, 30% feldspars, 20% oxides-micas	------	------	cylindrical D=40 mm H=80 mm	dry & wet (tap water) fully drained conditions	------	***Fortin et al., 2007***

[8] Personal communication.
[9] Grain sizes range from 80-150 µm with a mean value of approximately 110 µm.
[10] The specimens were cored from the same block as in *Fortin et al.*, 2005.
[11] Clay is often located within the pores, or between two grains.

Table 2.3: Summary of information concerning specimens which failed by compaction bands (from the literature review).

Bleurswiller	110 µm	------	25%	------	50% quartz, 30% feldspars, 20% oxides-micas	------	perpendi-cular	cylindrical D=50 mm H=100 mm	distilled water Fully drained conditions	1.0×10^{-5} s^{-1} strain rate	***Fortin et al., 2009***
Castlegate	200 µm	------	28%	$0.2\text{-}0.4 \times 10^{-12}$ m^2 intact rock	70-80% quartz, 5-10% clay feldspar, siderite, lithics, including chert	weakly-cemented	parallel	cylindrical D=50.8 mm H=127 mm	------	10^{-5} s^{-1} strain rate	***DiGiovanni et al., 2000***
Castlegate	------	------	28%	------	------	------	parallel	cylindrical D=50.8 mm H=127 mm	drained test	5.8×10^{-4} mm s^{-1} displace-ment rate	***Olsson and Holcomb, 2000***
Castlegate[12]	------	------	28%	2-3 orders lower than the uncompre ssed rock	------	------	------	------	------	------	***Olsson et al., 2002***
Darley Dale[13]	220 µm	sub-angular poorly sorted	13%[14]	------	67% quartz, 14% feldspar, 2% micas 6% clays	heteroge-neously distributed cement	------	cylindrical D=18.4 mm H=38.1 mm	distilled water, drained conditions	1.3×10^{-5} s^{-1} strain rate	***Wu et al., 2000***

[12] Same rock as in DiGiovanni et al., 2000, Olsson and Holcomb, 2000, Olsson, 2001
[13] The specimens were coming from the same block as in *Read et al.*, [1995] and *Wong et al.*, [1997].
[14] The specimens in *Wu et al.*, [2000] had initial porosities ranging from 13.1% to 13.6%, with a mean of 13.4%.

Table 2.3: Summary of information concerning specimens which failed by compaction bands (from the literature review).

Diemelstadt	107 μm[15]	fluvial sand-stone	24.3%	------	[16]68% quartz, 26% feldspar, 2% micas 4% other minerals-mostly oxides	------	perpendi-cular[17]	[18]cylindrica l D=18.4 mm H=38.1 mm	distilled water, drained conditions	$1.3x10^{-5}$ s^{-1} strain rate	***Louis et al., 2006***
Rothbach[19]	------	------	20%	------	68% quartz, 16% feldspar, 12% clay, 3% micas and oxides	------	perpendi-cular	cylindrical D=18.1 mm H=38.1 mm	distilled water, drained conditions	$1.3x10^{-5}$ s^{-1} strain rate	***Bésuelle et al., 2003***
Rothbach[20]	147 μm/ 300 μm[20]	------	20%	------	68% quartz, 16% feldspar, 6% clay, 3% micas and oxides	------	parallel, oblique (45°), perpendi-cular	cylindrical D=18.4 mm H=38.1 mm	distilled water, drained conditions	$1.3x10^{-5}$ s^{-1} strain rate	***Louis et al., 2007***

[15] The average grain Radius is equal to 80 μm.
[16] *Klein and Reuschlé*, 2004, cited in *Louis et al.*, 2006
[17] Specimens cored from the same block as the studied by *Baud et al.*, 2004.
[18] In this study, only macroscopically homogeneous specimens were used. The subset of specimens showing bedding laminations were excluded.
[19] *Bésuelle et al.*, [2003], mention that the samples were cored from the same block as in *Davis et al.*, [1994], and *Wong et al.*, [1997]. The petrophysical description can be met there.
[20] *Louis et al.*, [2007], mention that the specimens were cored from the same block as in *Baud et al.*, [2004]. The average grain Radius is equal to 110 μm; however, the average grain Radius in *Baud et al.*, [2004] is 230 μm.

Table 2.3: Summary of information concerning specimens which failed by compaction bands (from the literature review).

Adamswiller [a],	120 μm[21]	-----	22.6% [a]	-----	71% quartz, 9% feldspar 5% oxides and micas ~11% clay	------	parallel [a]	cylindrical D=18.4 mm H=38.1mm	wet, distilled water	$5x10^{-5}$ s^{-1} strain rate	***Wong et al., 1997***
Berea [b],	170 μm		21% [b]		71% quartz, 10% feldspar, 5% carbonate, ~10% clay		perpendi-cular [b]	for all samples			
Boise II [c],	370 μm		35% [c]		67% quartz, 14% feldspar, 2% micas, 13% clay		perpendi-cular [b]	apart from Darley Dale			
Darley Dale [d],	220 μm		14.5% [d]		66% quartz, 21% feldspar, 3% micas, 6% clay		perpendi-cular [b]	cylindrical D=20 mm H=40.6 mm			
Kayenta [e]	200 μm		21% [e]		81% quartz, 16% feldspar, 1% carbonate		perpendi-cular [b]				
Rothbach [f]	300 μm		19.9% [f]		68% quartz, 16% feldspar, 3% oxides and micas ~12% clay		parallel & perpendi-cular [b]				

Table 2.3: Summary of information concerning specimens which failed by compaction bands (from the literature review).

Berea **Darley Dale**	170 μm[22] 220 μm[23]	------	21% 13%	------	[24] 71% quartz, 10% feldspar, 5% carbonate, ~10% clay 66% quartz, 21% feldspar, 3% micas, 6% clay	------	perpendi-cular	cylindrical D=18.4 mm H=38.1mm	[a] dry [b] wet, distilled water, drained conditions	[a] 10^{-5} s^{-1} strain rate [b] 1-2 x 10^{-5} s^{-1} strain rate	***Zhu et al., 1997***
[25] **Bentheim [a],** **Berea [b],** **Darley Dale [c],** **Diemelstadt [d],**	140 μm 170 μm 220 μm 107 μm	------	23% [a] 21% [b] 13% [c] 24% [d] 20% [e]	------	95% quartz, 3% kaolinite 3% orthoclase 71% quartz, 10% feldspar, 5% carbonate, ~10% clay 66% quartz, 21% feldspar, 3% micas,	------	perpendi-cular	cylindrical D=18.4 mm H=38.1mm	[a] dry [b] wet, distilled water, [a,b] fully drained conditions	$1.3x10^{-5}$ s^{-1} strain rate	***Baud et al., 2004***

[21] Intercept Length for all sandstones.
[22] The intercept Length is cited in *Wong et al.*, [1997].
[23] The intercept Length is cited in *Wong et al.*, [1997].
[24] The Berea was from the same block as in *Wong et al.*, [1997]. Both Berea and Darley Dale have the petrophysical description as in *Wong et al.*, [1997].
[25] The Berea, the Darley Dale and the Rothbach were cored from the same block as in *Wong et al.*, [1997]. The Bentheim was from the same block studied in *Wong et al.*, [2001].

Table 2.3: Summary of information concerning specimens which failed by compaction bands (from the literature review).

Rothbach [e]	300 μm				~6% clay 68% quartz, 26% feldspar, 4% oxides, 2% micas 68% quartz, 16% feldspar, 3% oxides & micas ~6% clay						
Bentheim [a] **Berea** [b] **Darley Dale** [c]	-----	-----	23%[a] 21%[b] 13%[c]	-----	-----	-----	-----	-----	dry [a], saturated [b,c] in distilled water	-----	***Wong et al., 2001***
[26]**Berea**[a]	260 μm	-----	21%[a]	-----	75% quartz, 10% feldspar, 5% carbonates, 10% clays	-----	perpendi-cular	cylindrical D=18.4mm H=38.1mm V-shape notch[28]	dry	1×10^{-5} s^{-1} strain rate	***Tembe et al., 2006***
[27]**Bentheim**[b]	200 μm		22.8%[b]		95% quartz, 5% kaolinite						

[26]The specimens were cored from the same block as *Wong et al.*, [1997] and *Baud et al.*, [2004].
[27]The specimens were cored from the same block as *Wong et al.*, [2001] and *Vadjova and Wong*, [2003].
[28]The V-shape notch was machined along the circumference of the mid-section, to give a minimum diameter of d=14.4 mm (Fig. 1 from *Tembe et al.*, 2006].

Table 2.4: Comments on the presented works from different sandstones focusing on compaction bands (from the literature review).

sandstone	Reference	comments
Adamswiller, Berea, Boise, Darley Dale, Kayenta, Rothbach	*Wong et al., 1997*	Mechanical deformation of sandstones with different porosities (ranging from 15% to 35%), grain-sizes and mineralogical compositions in the transitional mode from brittle faulting to cataclastic flow.
Berea, Darley Dale	*Zhu et al.,1997*	How shear-enhanced compaction and cataclastic flow are influenced by the presence of water – effect of water on the porosity change.
Berea, Bentheim, Darley Dale, Dimelstand, Rothbach	*Baud et al., 2004*	Investigation of failure modes in the brittle to ductile transitional regime in five sandstone with porosities from 13% to 24%; shear bands at relative high-angles plus continuous accumulation of AEs for 13% porosity sandstones, arrays of discrete compaction bands normal to the major principal stress for 24% porosity sandstones punctuated by episodic stress drop in the stress-strain curve; hybridic localisation including high-angle shear bands and diffuse compaction bands for porosities in between; classification of deformation bands.
Berea, Bentheim	*Tembe et al., 2006*	'V-shape' circumferential notch; Initiation (similar) and propagation (different) of strain localisation in the Bentheim and the Berea sandstones.
Bentheim	*Klein et al., 2001*	Investigation of the mechanical behaviour and failure mode in the Bentheim Sandstone; Overall hardening trend 'punctuated by episodic strain softening'-quasi-ductile failure mode; Different axial strain levels.
Bentheim, Berea, Darley Dale	*Wong et al., 2001*	Failure modes in different porosity Sandstones (Bentheim, Berea and Darley Dale) in the brittle to ductile transitional regime.
Bentheim	*Vadjova et al., 2003*	'V-shape' circumferential notch; Comparison between notched and unnotches specimens; Different strain levels.
Bentheim	*Stanchits et al., 2009*	Initiation and propagation of compaction bands in dry and wet notched Bentheim specimens; 'U-shape' circumferential notch.
Berea	*Menendez et al., 1996*	Deformation mechanisms (shear enhanced compaction and cataclastic flow at high mean effective stresses).
Bleurswiller	*Fortin et al., 2005*	Evolution of elastic wave velocities, permeability and volumetric strain.
Bleurswiller	*Fortin et al., 2006*	Investigation of the formation (nucleation and growth) of compaction bands in the Bleurswiller Sandstone by means of Acoustic Emissions.

Table 2.4: Comments on the presented works from different sandstones focusing on compaction bands (from the literature review).

Bleurswiller	*Fortin et al., 2007*	Evolution of elastic wave velocities (*VP/VS*) during hydrostatic loading in dry and wet samples; Effects of pore collapse and grain crushing.
Bleurswiller	*Fortin et al., 2009*	Acoustic emission signatures of three modes of failure: cataclastic compaction, shear localisation, compaction localisation.
Castlegate	*DiGiovanni et al., ,2000*	Compaction occurring due to breakage of the grain contacts and rotation, and later grain crushing and rotation of the fragments.
Castlegate	*Olson and Holcomb, 2000*	Compaction zones nucleation and propagation.
Castlegate	*Olsson, 2001*	Analysis of the propagation of compaction fronts as a shock phenomenon.
Castlegate	*Olsson et al., 2002*	Permeability reduction inside the compaction fronts.
Darley Dale	*Wu et al., 2000*	Micromechanics of compressive failure and characterisation of the spatial evolution of anisotropic damage; isotropic stress induced cracking; increased number of crack density with increasing bulk shortening (similarly to the brittle faulting); higher AE activity compared to that of the brittle faulting.
Diemelstadt	*Louis et al., 2006*	Investigation of failure modes on the Diemlstand Sandstone; focus on CBs (for different stain levels); AE activity, thin sections, X-ray tomography, development of statistical analysis for the CT-images; comparison with the Rothbach Sandstone; width, orientation and tortuosity of the discrete compaction bands.
Rothbach	*Bésuelle et al., 2003*	Spatial complexity of damage and evolution of localised failure in the transitional regime from brittle faulting to cataclastic flow, x-rays, microstructural observations, damage maps.
Rothbach	*Louis et al., 2007*	X-rays, AE, 2D DIC-strain pattern, influence of bedding heterogeneity on the failure mode.

2.7.1 Nature-Laboratory: different scales

Both shear and compaction bands have already been identified in Nature (macro-scale)[*e.g., Antonellini et al.,* 1994; *Mollema and Antinellini,* 1996; *Sternlof et al.,* 2005; *Eichhub et al.,* 2010]. The need to better understand the conditions for their occurrence and the micro-mechanisms that govern their formation and evolution has motivated multiple experimental laboratory programs (meso- and micro-scale). The first important step was, therefore, to reproduce these deformation bands in different scales (moving from macro- to micro-scale). According to the presented literature review, shear bands were reproduced in sandstone specimens subjected to both biaxial compression [see *Ord et al.*, 1991; *Riedel et al.*, 2006] and triaxial compression [see *Menéndez et al.*, 1996; *Haied et al.*, 1997; *Wu et al.*, 2000; *Mair et al.*, 2000, 2002; *El Bied et al.*, 2002; *Bésuelle et al.*, 2000, 2001, 2003; *Sulem et al.*, 2006; *Fortin et al.*, 2005], while compaction bands were reproduced in sandstone specimens subjected to triaxial compression [see *Wong et al.*, 1997, 2001; *Zhu et al.*, 1997; *Wu et al.*, 2000; *DiGiovanni et al.*, 2000; *Olsson & Holcomb*, 2000; *Olsson*, 2001; *Klein et al.*, 2001; *Olsson et al.*, 2002; *Bésuelle et al.*, 2003; *Vajdova et al.*, 2003a; *Baud et al.*, 2004; *Haimson et al.*, 2004; *Fortin et al.*, 2005, 2006, 2007, 2009; *Temble et al.*, 2006; *Louis et al.*, 2006, 2007a; *Stanchits et al.*, 2009].

2.7.2 Geometry of specimens

Cylindrical and prismatic specimens of different dimensions (Table 2.1, Table 2.3), were used in the experimental studies reviewed. The most probable is that the dimensions of these specimens were chosen so as they fit in the available experimental apparatus. Note that the role of the different specimens' slenderness ratio was investigated only for the Vosges sandstone [*Bésuelle et al.*, 2000, 2001]. These authors commented that similar shear band patterns developed in both shorter and longer specimens, but the former developed a smaller number of lower inclination angle shear bands. Note also that shorter specimens were characterised by stronger strengths.

Additionally to the geometry (cylindrical and prismatic) of the tested specimens, the role of an inserted imperfection on the observed failure modes was investigated by *Haied et al.* [1997] for the case of shear bands. These authors moved from cylindrical to prismatic specimens in an attempt to systematically detect localised deformation. A hole

drilled on specimens (induced imperfection) facilitated the initiation of shear bands from its tip (acting as a stress concentrator).

Cylindrical specimens were used in all reviewed studies for the case of compaction bands. The concept of circumferential V-shape notch was introduced by *Vadjova et al.* [2003a] and was also used by *Tembe et al.* [2006]. A U-shape circumferential notch was used by both *Stanchits et al.* [2009] and the present work (section 4.3). The notch introduced stress heterogeneity and forced the onset of compaction bands from its tip (like in the case of shear bands). It also resulted to lower yield stresses. However, possible imperfections on the geometry of notches can result in non-symmetric initiation and propagation of deformation bands [*Vajdova et al.*, 2003a, *Tembe et al*., 2006].

2.7.3 Confining pressures and regimes

Confining pressure is an important factor that controls the type of failure modes (*i.e.*, shear or compaction bands). When relatively low confining pressures are applied (*e.g.*, brittle faulting regime), the material fails by axial splitting or shear localisation (*i.e.*, shear-induced dilation) through dilating shear bands [*e.g.*, *Menéndez et al.*, 1996; *Bésuelle et al.*, 2000; *El Bied et al.*, 2002; *Fortin et al.*, 2005; 2009)], while under relatively higher confining pressures (*e.g.*, ductile or cataclastic regime), compaction bands or diffuse compaction occur [*Mollema & Antonellini*, 1996; *Menéndez et al.*, 1996; *Wong et al.*, 1997; *Olsson & Holcomb*, 2000; *DiGiovanni et al.*, 2000; *Vadjova et al.*, 2003a; *Sternolf et al.*, 2005; *Fortin et al.*, 2005; 2006; 2009; *Baud et al.*, 2004]. Under middle to high confining pressures (*e.g.*, brittle to ductile transitional regime), shear enhanced compaction takes place and hybrid deformation occurs expressed through conjugate compacting shear bands- sometimes together with compaction bands [*Mair et al.*, 2000; 2002; *Wong et al.*, 2001; *Klein et al.*, 2001; *Bésuelle et al.*, 2001; 2003; *Baud et al.*, 2004; *Fortin et al.*, 2005; 2006; *Sulem et al.*, 2006; *Louis et al.*, 2006; 2007]. The latter regime is also referred to as semi-brittle regime for the Vosges and the Lochabriggs sandstones [*Bésuelle et al.*, 2001; 2002; *Mair et al.*, 2000; 2002], since compacting shear bands were formed or semi-ductile regime for the Bentheim sandstone [*Klein et al.*, 2001] since compaction bands were formed with an overall hardening trend punctuated by episodic stress drops.

In general, the higher the confining pressure is, the more the rock is prone to ductile deformation and the less is prone to brittle deformation. The brittle to ductile

transitional regime is associated with compaction localisation [*Wong et al.*, 2001; *Baud et al.*, 2004]. Compaction bands form in higher confining pressures than those responsible for shear band formation.

The pressure-dependant behaviour of sandstones does not result only in different failure modes, but influences also the characteristics of the deformation bands [*El Bied et al.*, 2002; *Mair et al.*, 2002]. For instance, an increase in the confining pressure results in an increase in the number of shear bands, an increase in their inclination angle towards the major imposed principal stress direction, and a decrease in the distance between them [*Bésuelle*, 2001; *Mair et al.*, 2002; *Fortin et al.*, 2005].

2.7.4 Mechanisms

Although shear and compaction bands appear to constitute different failure modes (*i.e.*, dipping angles, width, yield stress and macroscopic behaviour) their formation involves similar micromechanical processes. Both failure modes are characterised by fracturing of the grain bonds (intense) and inter- and intra-granular cracking, which indicated brittle mechanisms that dissipate a significant amount of inelastic energy (*e.g.*, recorded through Acoustic Emissions). With increasing axial strain values (in shear bands) or increasing stress level (in compaction bands), intense grain fracturing and grain-crushing leads to fragmentation, grain-size reduction, and comminution of the fragments, which are characteristics of cataclastic deformation (see for instance Chapter 5 and 6).

Mollema and Antonellini, [1996], argued that although the regions of cataclasis and compaction in shear bands (at the field) consisted of a random juxtaposition of larger and smaller grains, it was impossible to recognise the original grains due to grain breakage and redistribution of the smaller grain fragments inside the shear deformation bands. These authors commented that for the case of compaction bands (at the field), the original grain or its original location could be easier identified (in other words, there was no shear offset) despite the intense grain crushing.

For the case of the laboratory reproduced shear bands the following comments on the microstructural evolution were cited. *Ord et al.* [1991] underlined a gradual alteration of the microstructure of the Gosford sandstone. *Haied et al.* [1997] suggested that the loss of cohesion in Fontainebleau sandstone was due to grain boundary cracking (prior to peak-stress) and micro-cracking (at the peak-stress). Broken and localised grains were observed by *Sulem et al.* [2006] in the same rock under relatively low confining

pressures for both drained and undrained conditions, while grain crushing was observed at higher confining pressures. *Menéndez et al.* [1996] speculated that the grain bonds were ruptured due to grain movements; this translation and rotation of grains leaded to volume increase. *Reidel et al*. [2006] highlighted that micro-cracking was the dominant failure mechanism in Berea sandstone and attributed the observed dilation prior to peak-stress to rupture and re-orientation of grains and not to intra-granular cracking, which developed only after the peak-stress. Intense grain crushing was also observed in Vosges and Rothbach sandstones [*Bésuelle et al.*, 2000; 2003]. *Fortin et al.* [2006] argued that the primarily consequence of shear localisation was the very high density of intra-granular micro-cracking and the pronounced stress induced anisotropy (post-failure regime).

Volume changes inside shear bands were the outcome of all these observed grain deformations. Furthermore, apart from grain breakage, shearing was also another mechanism, which was present in shear bands (rotation and sliding of the grains, or the grain fragments).

For the case of laboratory produced compaction bands, the micro-mechanisms of failure were similar. *Wu et al.* [2000] observed intra-granular cracks and grain crushing inside the compaction bands of the Darley Dale sandstone. Intense grain cracking (Hertzian-like fractures), pore collapse and grain crushing (starting at grain contacts due to stress concentration) were identified in Rothbach, Diemelstand, Bleurswiller, and Castlegate sandstones [*Bésuelle et al.*, 2003; *Louis et al.*, 2006; *Fortin et al.*, 2005; 2009; *DiGiovanni et al.*, 2000]. In the latter sandstone, *DiGiovanni et al.* [2000] suggested two phase of compaction: initial porosity reduction due to grain bond breakage and grain rotation, followed by higher volume decrease due to intense grain breakage and further grain rotation (but lack of grain fragmentation). Recall that the Castlegate sandstone was poorly cemented; thus, grain rotation in higher pressure level was not inhibited. *Menéndez et al.* [1996] suggested that in Berea sandstone, compaction was associated with the onset of brittle micro-cracking at the grain contacts. Hertzian fractures at grain bonds resulted in grain crushing and pore collapse; the grain movement, however, was limited in these high stresses, due to the cementation of this sandstone. The comminuted particles filled the pore space and resulted in porosity reduction. Significant cracking and moderate grain crushing were observed in notched Bentheim specimens [*Vajdova et al.*, 2003a].

In all cases, inter- and intra-granular cracks were created due to local stress concentration. Grain crushing leaded to average grain-size reduction, changes the

packing geometry and increases grain angularity. Pore collapse was a consequent of rearrangement of the grain packing (since part of the cement (or other kind of grain bonds) and grains need to be broken in order to collapse a pore. The microstructure of the rock outside the deformation band remained, in all cases, relatively unchanged.

2.7.5 Deformation band patterns: shear bands, conjugate shear bands, discrete and diffuse compaction bands

Different deformation patterns characterise the different failure regimes. Dilating shear bands were observed at the brittle faulting regime [*e.g.*, *Menéndez et al.*, 1996; *Bésuelle et al.*, 2000; *El Bied et al.*, 2002; *Fortin et al.*, 2005; 2009)], while compaction bands or diffuse compaction characterised the ductile regime [*Mollema & Antonellini*, 1996; *Menéndez et al.*, 1996; *Olsson & Holcomb*, 2000; *DiGiovanni et al.*, 2000; *Vadjova et al.*, 2003a; *Sternolf et al.*, 2005; *Fortin et al.*, 2005; 2006; 2009; *Baud et al.*, 2004]. In the brittle to ductile regime, high angle compacting shear bands, compaction bands or a combination of both of them were observed [*Mair et al.*, 2000; 2002; *Wong et al.*, 2001; *Klein et al.*, 2001; *Bésuelle et al.*, 2001; 2003; *Baud et al.*, 2004; *Fortin et al.*, 2005; 2006; *Sulem et al.*, 2006; *Louis et al.*, 2006; 2007a; 2007b, *Tembe et al.*, 2006].

Baud et al., [2004], based on the width and the orientation of the localised features, introduced a classification of the deformation bands developed in the brittle to ductile transitional regime. According to these authors, tabular features of a few grains thickness (*e.g.*, one to three grains) are termed discrete bands, whereas features with a thickness of many grains are called diffuse bands. Moreover, deformation bands oriented at relatively high angles towards the major imposed principal stress direction (*e.g.*, 45°-80°) are named high-angled shear bands and usually appear as conjugate sets of bands, whereas deformation bands oriented sub-normal to the major imposed principal stress direction are named compaction bands. *Baud et al.* [2004] further distinguished compaction bands in two groups: the discrete bands, which develop in sub-parallel arrays with cumulative strain (accommodated by the formation of extra discrete bands), and the diffuse bands, which accommodate the cumulative strain by the lateral propagation of damage.

Diffuse compaction bands developed in Castlegate sandstone [*DiGiovanni et al.*, 2000; *Olsson and Holcomb*, 2000; *Olsson*, 2001; *Olsson et al.*, 2002] accompanied by strain hardening. Discrete compaction bands were observed in Bentheim sandstone [*Klein et al.*, 2001; *Wong et al.*, 2001; *Vajdova et al.*, 2003; *Tembe et al.*, 2006;

Stanchits et al., 2009] accompanied by local strain softening (stress-drops) linked to an increase in Acoustic Emission number. These bands were numerous, thin, somewhat wavy and were clustered near the end one-third regions. *Olsson et al.* [2002] suggested that differences in the mechanical behaviour of Castlegate and Bentheim sandstones might provide useful insights into the factors that governed the origin of compaction bands, speculating, for instance, that the different orientation of specimens might be important for the different kind of observed compaction bands. Note that Bentheim specimens were cored normal to bedding, whereas Castlegate specimens were parallel to bedding.

In Bentheim sandstone, tortuous discrete compaction bands developed [*Baud et al.*, 2004] in unnotched specimens, while in notched specimens parallel but not coplanar compaction bands initiated from the notches [*Vadjova et al.*, 2003a]. Tortuous discrete compaction bands formed in Diemelstand sandstone [*Louis et al.*, 2006]. Non planar discrete compaction bands occurred in Bleurswiller sandstone [*Fortin et al.*, 2006]. In Castlegate sandstone, the observed compaction fronts were planar after the peak stress and moved towards the middle part of the specimen [*Olsson & Holcomb*, 2000].

Shear bands in Gosford sandstone changed position along their length due to grain rearrangements [*Ord et al.*, 1991]. In Darley Dale sandstone, shear bands were curved and their bigger part ran across the grain boundaries [*Wu et al.*, 2000]. In Rothbach sandstone, planar shear bands developed under relative low confining pressures.

2.7.6 Material properties

Sandstone properties have a crucial impact on the failure mechanisms and control the failure patterns. The role of porosity, mineralogy, grain-size and morphology, cementation and bedding are summarised in this section.

2.7.6.1 Porosity values

Deformation bands are strongly dependent on the initial composition and porosity values of the host rock in addition to the imposed stress state [*Mair et al.*, 2000]. Porosity is a crucial factor for the formation and propagation of deformation bands, since grain rotation and displacement needs a high amount of pore space to take place. When compaction occurs, the packing of the grains change; thus compaction alters the porosity values of the sandstone. Further compaction results in local grain deformation

and pore collapse. Compaction localisation is more likely to occur in rocks with initial porosity values higher than 16% [*Holcomb et al*., 2007].

Sandstones of different porosities (from 5% in [*Ord et al.*, 1991] to 25% in [*Fortin et al.,* 2005]) developed shear deformation bands, when subjected to low to middle confining pressures. Laboratory experimental studies proved that shear –enhanced compaction bands and pure compaction bands develop in sandstones, with porosity values ranging from 13% (*i.e.,* Darley Dale sandstone in *Wong et al.*, 2001) to 28% (*i.e.,* Castlegate sandstone in *DiGiovanni et al.*, 2000; *Olsson and Holcomb*, 2000; *Olsson*, 2001; *Olsson et al.*, 2002).

Local changes in porosity (*e.g.,* local inherent heterogeneities) may also control the local strength of the sandstone and, thus, the sites of local brittle nucleation. In particular, in Rothbach sandstone, pre-existing micro-cracks and high porosity regions governed the onset of deformation bands [*Louis et al.*, 2007]. In Bleurswiller sandstone, the local high porosity regions acted as zones of stress concentration; compaction bands nucleated from these places during the deviatoric compression. *Fortin et al.* [2009] suggested that this process was similar to the effect of a notch (which induces stress concentration and facilitates the nucleation of compaction band, [*Stanchits et al.,* 2009]). However, in Bleurswiller sandstone, local heterogeneities induced several bands, which merged while propagating, while the notch in the Bentheim specimens introduced only one compaction band that initiated from its tip [*Fortin et al.,* 2009]. Based on such observation, these authors explained why compaction bands in Bleurswiller sandstone were not perfectly planar (formation of hybrid patterns of pure compaction localisation, normal to the major imposed principal stress direction, connected with small shear bands).

2.7.6.2 Mineralogy

The mineralogy of the pattern rock plays a considerable role on the deformation process. The Fontainebleau and Bleurswiller sandstone were the two end-members sandstones discussed in this Chapter, concerning their mineralogical composition, since the former was rather homogeneous (containing 98% quartz), while the latter was rather heterogeneous (containing 50% quartz, 30% feldspar, and 20% micas). However, the mineralogical composition of the Bleurswiller affected only the effective pressure at which pore collapse took place (P*), since it did not limited the onset and evolution of compaction bands [*Fortin et al.*, 2005]. Similar remarks were made by *Wong et al.*

[1997] concerning Berea and Kayenta sandstones; the differences in the yield surfaces of these sandstones were attributed to their different mineralogical composition (both rocks had the same porosities).

Microstructural observation on Darley Dale sandstone specimens [*Zhu et al.,* 1997; *Wu et al.,* 2000] indicated intra-granular cracks and grain crushing. Given that this particular sandstone contained a big amount of feldspars (14%), these authors suggested that the pre-existing cracks along the cleavage of feldspars possibly constituted sites of further crack nucleation. Hertzian fractures in quartz grains were suggested to be the primary mechanisms for the initiation of grain crushing in Berea sandstone [*Zhu et al.,* 1997].

2.7.6.3 Grain size and morphology

In the literature, the grain-size is defined by the average grain diameter, or the grain radius, which is equal to 0.75 times the intercept length of solid grain under an optical microscope [*Wong et al.,* 1997, see also at the beginning of section 2.7]. *Wong et al.,* [1997] emphasised that the grain size is as important as porosity. Both the initial size and morphology of grains may control (facilitate or not) the developed deformation bands.

In an analogue material (Schneebeli material), it was shown that rectangular shape particles could facilitate or halt the propagation of shear localisation, according to their orientation inside the matrix and toward the propagation of the shear band [*Charalampidou et al.,* 2009]. In natural sandstones, the shape and orientation of grains could affect the onset and propagation of deformation bands, in a similar way, but this is not easily identified in the field scale, since the dimensions of the grains are too small compared to the larger scale deformation. Laboratory studies demonstrated, however, that both micas and clays (which have elongated shapes) usually accommodated most of the deformations [*e.g., Fortin et al.,* 2005; 2009 and *DiGiovanni et al.,* 2000, respectively].

The original size and the morphology of the grains are usually altered due to the deformation. Grain cracking and grain crushing result in a smaller grain-size, and usually, in angular and heterogeneously distributed grain fragments. Therefore, it is very likely that initially rounded to sub-rounded grains become sub-angular to angular after deformation. Grain fragments can fill the pores and, thus, reduce the porosity values of the sandstone [*Menéndez et al.,* 1996; *Baud et al.,* 2004, *Fortin et al.,* 2006].

Note that also the pore space and pore-networks might considerably change during the deformation processes.

2.7.6.4 Cementation

Sandstone grains can be connected with cement bonds. Cementation might lead to a porosity reduction and strengthening the sandstone. In poorly cemented regions, the rupture of lithified and cemented grain contacts may occur easier than in cemented regions. Note that not many information on type and the degree of cementation is available in the literature. Castlegate, Fontanebleau, Gosford and Vosges sandstones were referred to as poorly cemented sandstones; Locharbriggs sandstone was silica cemented, while Berea sandstone was carbonate cemented; and Darley Dale sandstone had a heterogeneous distributed cement.

Menéndez et al. [1996] argued that the dolomite (carbonate) cement in Berea sandstone halted the onset and development of micro-cracking at the grain contacts. Both isotropic and deviatoric compression induced Hertzian fractures in the quartz and feldspar grains, while dolomite cemented regions remained relatively intact. These authors suggested that the high intensity of grain crushing and pore collapse was associated with weakly cemented regions.

Sternolf et al. [2004], argued that compaction bands in the field developed in essentially uncemented sandstones at middle mean compressive stresses, while at the laboratory, compaction bands formed in moderate to well cemented sandstones (*i.e.*, Berea, Bentheim, Castlegate) subjected to higher confining pressures (reaching even 300 MPa). The different confining pressure levels can be attributed to the fact that cemented sandstones have a higher strength. In particular, *Wong & Wu* [1995, cited in *Wong et al.*, 2004] showed that the development of cracking at cemented contacts would require at least one order of magnitude higher normal stress that those of uncemented contacts. However, it remains unclear why no evidence of compaction bands have been observed in cemented sandstones at the field.

2.7.6.5 Bedding heterogeneity

Bedding and layering may increase the anisotropy of rock mass [*e.g., Louis et al.*, 2003]. Rothbach Sandstone is the more heterogeneous of the sandstones reviewed in this Chapter due to its relative low porosity and high density lamination. Experimental

studies on Rothbach sandstone specimens cored normal to the bedding presented higher yield stresses compared to those cored parallel to it [*Wong et al.*, 1997; *Baud et al.*, 2005, cited in *Louis et al.*, 2007]. Strain localisation and compactive failure in Rothbach sandstone developed in regions outside the bedding heterogeneity, which indicates an inhibiting effect of bedding on strain localisation. Deformation bands were oriented sub-parallel to the bedding [*Bésuelle et al.*, 2003; *Louis et al.*, 2007a]. Additionally, the orientation of the bedding controlled the failure mode, since specimens cored normal, in 45°, and parallel to bedding developed diffuse compaction bands, compactant shear bands and rather relative homogeneous compaction (no continuous deformation bands), respectively [*Louis et al.*, 2007a].

Aydin and Ahmadov [2009], based on the geometrical characteristics of bed-parallel compaction bands (*e.g.*, interacting echelon geometries, bridge and eye structures or zonal pattern of observed structures), suggested that the bed interfaces should play an important role on the propagation paths of compaction bands and their final geometry with respect to the bedding.

2.7.7 Axial strain

The increasing amount of post-failure axial strain results in a further development of the localised bands and enhances the degree of damage inside them [*Wu et al.*, 2000; *Mair et al.*, 2000; *Klein et al.*, 2001; *Vadjova et al.*, 2003a; *Louis et al.*, 2006]. However, the damage is not the same at different regimes, when specimens are taken to the same axial strain values. In particular, for Darley Dale sandstone the crack density recorded at the ductile regime was twice the one observed at the brittle regime, for the same strain level [*Wu et al.*, 2000]. Increasing axial strain level might also result in an increase in the number of compaction bands [*Klein et al.*, 2001; *Baud et al.*, 2004; *Louis et al.*, 2006; *Fortin et al.*, 2006]. For the case of shear bands, the increased strain level resulted to an increase in the width of the fault zone [*Mair et al.*, 2000].

2.7.8 Orientation and thickness of the deformation bands

Laboratory experimental studies have also focused on the geometric complexity associated with the development of strain localisation. Table 2.5 summarises the available in the reviewed literature information on the thickness and orientation of the observed shear and compaction bands referring also to the grain-size of each sandstone,

the conditions of the experiment, and the method used for the detection these characteristics. In general, at low confining pressures low angle shear bands develop, while at middle confining pressures conjugate higher angle shear bands occur. Finally, under relatively higher confining pressures, compaction bands form normal to the major imposed principal stress direction. Therefore, the inclination of the deformation bands is pressure sensitive, *i.e.*, the orientation of the band increases with respect to the major imposed principal stress direction as the confining pressure increases [*Ord et al.*, 1991; *Haied et al.*, 1997; *El Bied et al.*, 2002; *Bésuelle et al.*, 2001; *Mair et al.*, 2002; *Fortin et al.*, 2005; *Vadjova et al.*, 2003a]. The thickness of the shear band sometimes decreases [*Haied et al.*, 1997; *El Bied et al.*, 2002], while other times increases [*Ord et al.*, 1991; *Menéndez et al.*, 1996; *Sulem et al.*, 2006; *Fortin et al.*, 2006] with increasing confining pressure. It should be underlined, however, that the estimation/measurement of both the thickness and the inclination of the deformation bands is related to the resolution of the experimental method used (for more, see Chapter 7). Furthermore, each method applied to measure the orientation and thickness of the deformation features is sensitive to different parameters (see Chapter 3). Therefore, differences in the measured values of the thickness and orientation should not only be linked to different characteristics (*e.g.*, grain size, mineralogy, porosity, etc.) of the sandstone, but should also be related to the different sensitivity of the applied experimental method.

Table 2.5: Summary of the thickness of the deformation bands (shear and compaction bands), measured by different experimental methods (literature review).

Reference	Sandstone	Mean grain size	Conditions[1]	Deformation	Thickness	Dip[2]	Characteristics/ Remarks/ Methods
Bésuelle et al., 2000	Vosges	300 μm	Triaxial compression p_c =0-60 MPa	Shear bands	at pc=30 MPa: 360 μm-1200μm (dilatant shear band), 300μm-600μm (damage zone)	Increases with increasing confining pressure Fig. 6 on the paper	Thin sections
Bésuelle et al., 2003	Rothbach	-----	Triaxial compression	Shear bands	--------- equal to 0.5 mm [b]	at p_{eff} =5 MPa 60° at p_{eff} =20 MPa [b] 50°	Thin sections
El Bied et al., 2002	Fontainebleau	230 μm	Triaxial compression, p_c =7 MPa and p_c =28 MPa	Shear bands	1.17 mm (7 MPa) 0.66 mm (28 MPa) Table 2 in the paper for a wider range	decreasing with increasing confining pressure Table 1 in the paper	Thin sections
Fortin et al., 2005	Bleurswiller	110 μm	Triaxial compression, p_c =12[a]-30[b] MPa u=10 MPa	Dilatant shear bands	400-1000 μm	decreases with increasing confining pressure, 75° [a] - 30° [b]	X-rays
Fortin et al., 2009	Bleurswiller	110 μm	Triaxial compression p_c =20 Mpa u=10 MPa	Dilatant shear bands	300 μm	45°	Thin sections (SEM)
Haied et al., 1997	Fontainebleau	250 μm	Triaxial compression, p_c =10[a] –40 [b] MPa	Shear bands	2 mm [a] - 1 mm [b]	61° [a] -58° [b]	Visual observations on the surface of the specimens

[1] The applied confining pressure is p_c, the back-pressure is u, and the effective pressure is p_{eff}.
[2] In most papers the inclination angle towards the major imposed principal stress is cited (a); however, here is mentioned the dip angle (90-a).

Table 2.5: Summary of the thickness of the deformation bands (shear and compaction bands), measured by different experimental methods (literature review).

Menendez et al., 1996	Berea	173 µm	Triaxial compression, p_c =10 MPa and p_c =40 MPa	Shear bands and conjugate shear bands	450 µm (SB) 1mm (conjugate SB)	60° (SB) 50° (conjugate SB)	Thin sections
Ord et al., 1991	Gosford	200-300 µm	Plain strain p_c = 15 MPa, p_c = 20 MPa	Shear bands	1 to 2 grains (15 MPa), 1-2 mm (20 MPa)	Table 1 on the paper	Thin sections
Sulem et al., 2006	Fontainebleau	250 µm	Triaxial compression	Shear bands	From 200 µm to 500 µm (7-14 MPa)	decreases with increasing confining pressure Fig. 12 in the paper	Thin sections
Wu et al., 2000	Darley Dale	220 µm	Triaxial compression p_{eff}=10 MPa	Shear bands	max width equal to 2-3 grains, *i.e.*, 440-660 µm	curved band, 65° to 52°	Thin sections

Table 2.5: Summary of the thickness of the deformation bands (shear and compaction bands), measured by different experimental methods (literature review).

Reference	Sandstone	Mean grain size	Conditions	Deformation[3]	Thickness	Dip	Characteristics/ Remarks/ Methods
Baud et al., 2004	Bentheim	210 μm	Triaxial compression p_{eff}=90-395 MPa	tortous and some intersecting CBs	500 μm	sub-normal to the major imposed principal stress	Microstructural observations (thin sections and distribution of damage)
	Berea	260 μm	p_{eff}=90 Mpa	high angle conjugate SBs	----------		
			p_{eff}=150 MPa	diffuse CBs	----------	----------	
			p_{eff}=200 MPa	diffuse and discrete (tortuous) CBs	[4]2 grains		
	Darley Dale	340 μm	p_{eff}=10 MPa	SBs	----------	60°	
			p_{eff}=80 MPa	high angle SBs	----------	45°	
			p_{eff}=95 MPa	conjugate SBs	----------	----------	
			p_{eff}=110 MPa	distributed cataclastic flow	----------	----------	
	Diemelstand	160 μm	p_{eff}=160 MPa	discrete CBs	----------	----------	
	Rothbach	460 μm	p_{eff}=40-90 MPa	conjugate high-angle SBs	----------	----------	
			p_{eff}=130 MPa	diffuse CBs	----------		
Bésuelle et al., 2003	Rothbach	----------	Triaxial compression	CBs		10°	Thin sections

[3] From now on, CBs is the abbreviation for the compaction bands and SBs is the abbreviation for the shear bands.
[4] At p_{eff}=150 MPa, diffuse bands were developed at the specimens edges, without spreading to the mid-high of the specimen. At p_{eff}=200 MPa diffuse bands were developed at the specimen edges and discrete tortuous bands were formed in the mid-high of the specimen.

Table 2.5: Summary of the thickness of the deformation bands (shear and compaction bands), measured by different experimental methods (literature review).

DiGiovanni et al., 2000	Castlegate	200 μm	Triaxial compression, p_c =80 MPa	Compaction fronts	1-2 cm thickness[5]	-------	Cited in Olsson , 2001
Fortin et al., 2005	Bleurswiller	220 μm	Triaxial compression, p_c =110 MPa	discrete CBs	Average width of band ~800 μm	Quite tortuous	Thin sections
Fortin et al., 2006	Bleurswiller	220 μm	Triaxial compression, [a] p_c =60 MPa [b] p_c =80 MPa	[a] discrete conjugate CBs [b] discrete CBs	[a] 600 μm [b] 500-2000 μm	[a] 30° [b] not perfectly planar	[a] Thin sections [b] (SEM) AEs[6]
Fortin et al., 2009	Bleurswiller	220 μm	Triaxial compression, p_c'=70 MPa	CBs	600 μm	normal to major imposed principal stress	Thin sections (SEM)
Louis et al., 2006	Diemelstadt	160 μm	Triaxial compression p_{eff}=150 MPa	discrete CBs	490-540 μm, *i.e.*, 3-4 grains	7° , sub-normal to the major principal stress	X-ray tomography
Louis et al., 2007	Rothbach	220 μm	Triaxial compression p_{eff} =130 MPa	[1]diffuse CBs[7] [2]compacting SBs [3]no continuous deformation bands	[1] width on the order of several grain diameter	[1,2]parallel to bedding, but outside it	2D-DIC, damage maps-thin sections
Olsson and Holcomb, 2000	Castlegate	-----	Triaxial compression tests, p_c=45 MPa	compaction fronts		25°	AE recordings

[5] Cited in Olsson, 2001.
[6] AE hypocenter location error is estimated to be approximately 2.5 mm.
[7] Diffuse CBs for specimens perpendicular to bedding, compacting SBs for specimens oblique (45°) to bedding, no continuous deformation bands foe specimens parallel to bedding.

Table 2.5: Summary of the thickness of the deformation bands (shear and compaction bands), measured by different experimental methods (literature review).

Stanchits et al., 2009	Bentheim	300 μm	Triaxial compression p_{eff}=185 MPa circumferential (mid-high) notched specimens 0.8 mm width 5 mm depth	discrete CBs	~ 0.8 mm (width of the notch)	slightly inclined to the plane of the notch	Thin sections, AEs
Tembe et al., 2006	Bentheim[8]	200 μm	Triaxial compression p_c=250-350 MPa	discrete CBs	process zone (initial stage) 2-3 grains from the notch tip	------	Thin sections
	Berea[9]	260 μm	p_c=150-250 MPa circumferential (mid-high) notched specimens 2 mm width 5 mm depth	conjugate diffuse CBs			
Vajdova et al., 2003	Bentheim	200 μm.	Triaxial compression, p_c =300 MPa, circumferential (mid-high) notched specimens 2 mm width 5 mm depth	CBs	process zone: 2-3 grains (both notched after the peak, and unnotched specimens)	------	Thin sections

[8] The specimens were coming from the same block as the one used by *Wong et al.*, [2001], *Vajdova et al.*, [2003].
[9] The specimens were coming from the same block as the one used by *Wong et al.*, [1997], *Baud et al.*, [2004].

Table 2.5: Summary of the thickness of the deformation bands (shear and compaction bands), measured by different experimental methods (literature review).

Wong et al., 2001	Berea,	------	Triaxial compression p_{eff} =40-150 Mpa	high-angle conjugate SBs and CBs	------	------	
	Bentheim,		p_{eff}=90 MPa	high-angle conjugate SBs		------	
			p_{eff}=120-300	sub-parallel arrays of CBs			
	Darely Dale		p_{eff}=80 Mpa	SBs		45°	
			p_{eff}=90-95 MPa	high angle SBs and CBs			

2.7.9 The role of water

It was shown that water influences the mechanical behaviour of the sandstone during shear enhanced compaction and cataclastic flow, since it enhances compaction and lowers the yield strengths for both isotropic and deviatoric compression [*Zhu et al.*, 1997; *Fortin et al.*, 2007]. Saturated Berea and Darley Dale sandstone specimens showed similarities in the general trend of the post-failure behaviour and the failure modes with the equivalent dry specimens [*Zhu et al.*, 1997]. In addition, dry and saturated Fontainebleau specimens showed similar characteristics on the evolution of the orientation and the width of the shear bands with increasing confining pressure.

Different features were observed in Fontainebleau sandstone under drained and undrained conditions [*Sulem et al.*, 2006]. In the latter case, the back-pressure resulted in a local fluidization of the crushed grains inside the shear band. Therefore, heterogeneous shear bands, characterised by zones of compaction and dilation, were formed under undrained conditions, while shear bands characterised by zones of compaction were developed under drained conditions, for the same range of confining pressures (*e.g.*, middle).

2.7.10 Permeability and Porosity

The deformation processes, the grain geometry and grain size and the pore-size and pore networks highly influence the transport properties (*i.e.*, permeability) of the sandstone. Granular flow (*e.g.*, grain boundary sliding and grain rotation, grain contact cement breakage) accompanied by both brittle (*e.g.*, grain cracking and Hertzian fractures) and cataclastic (*e.g.*, pore collapse, grain crushing, changes in the grain distribution and size) mechanisms resulted in a porosity reduction. Although the link between porosity and permeability is not always linearly related, changes in porosity, pore topology and grain arrangement (*e.g.*, structures) inside shear and compaction bands have an impact on the permeability of the rock.

Complex structures were detected inside the deformation bands of the sandstones discussed in this Chapter [*El Bied et al.*, 2002; *Sulem et al*., 2006; *Bésuelle et al*., 2001; *Mair et al*., 2000]. Usually, the central part of these deformation bands is characterised by crushed, densely packed grains, which form a gouge layer, while the grain structure

outside the heart of the band define the dilatant or compactant character of the deformation feature. Changes in the structure of the gouge material, such as grain crushing and porosity reduction, could affect the fluid migration along the band as well as the global permeability of the sandstone.

Sulem et al. [2006] showed that the permeability reduces from 1-2 orders of magnitude inside dilatant shear bands and 2-3 orders of magnitude inside compactant shear bands, which formed in Fontainebleau sandstone. *Fortin et al.* [2005] observed that in Bleurswiller sandstone (at 30 MPa confining pressure) dilatant shear bands did not show any change in permeability despite the increased porosity values in these regions. Under isotropic compression (where distributed cataclastic flow developed) the permeability decreased by 1 order of magnitude in places where pore collapse and grain crushing occurred (P*). Beyond that P*, further reduction in permeability was recorded (~1order of magnitude). *Olsson et al.* [2002] recorded a drop in permeability from 2-3 orders of magnitude after the propagation of the compaction front in Castlegate sandstone.

Deformation features such as compaction bands induce changes in porosity and pore topology [*Fortin et al.*, 2006]. *Fredrich et al.* [1993] investigated the relationship between permeability and pore structure in Fontainebleau specimens of varied porosities. Differences in the geometry and topology of the pore space were observed: pores in the lower porosity specimens were larger than those in the higher porosity specimens. These authors, thus, suggested that porosity decrease might not necessarily be linked to reduced pore connectivity.

The orientation of the deformation bands may also have an impact on the permeability [*Louis et al.***,** 2006]. Indeed, the inclination of the band and its internal structure may facilitate or halt the fluid flow through or along the band. Sealing deformation patterns constitute barriers to fluid migration, whereas highly fractured zones may enhance/facilitate the fluid flow. Both shear and compaction bands may act as seals, and thus, retard significantly the movement of fluids inside porous sandstones.

2.8 Theoretical studies

Different theoretical frameworks, based on both field and experimental observations, were developed to gain further insights into the development of compaction band in porous rocks. The conditions of the compaction band formation and evolution were analysed by many theoretical frameworks. A short overview is presented here.

Experimental compaction bands were predicted theoretically in the frame of the continuous mechanics. These bands were treated as a problem of instability of the constitutive description of the inelastic deformation of a porous medium via the bifurcation theory [*Olsson* 1999; *Issen and Rudnicki,* 2000, 2001; *Bésuelle,* 2001; *Bésuelle and Rudnicki,* 2004]. The critical conditions for the onset of localised deformation as a bifurcation of the homogeneous solution and the prediction of the orientation of these deformation features derived as a function of the constitutive parameters [*e.g., Rudnicki,* 2004; *Challa and Issen,* 2004]. *Olsson* [1999] proposed a single yield surface to be suitable for compaction band prediction in high porous sandstones, similarly to what was suggested by *Rudnicki and Rice* [1975] for the prediction of shear band development in low porosity rocks. However, *Issen* [2002] suggested that a two-yield surface was proper for the description of both shear and compaction bands in the transitional regime.

Although the bifurcation analysis appears to be a good theoretical framework to better understand compaction bands mechanisms, it is limited in a sense that the continuum analysis deals solely with the onset of constitutive instability in an initially homogeneous material. However, it is unable to explain compaction band propagation and geometrical complexities, plus the microscopic description of deformation bands cannot be ignored. As already discussed in sections 2.6, the material becomes strongly damaged, which rapidly degrades its mechanical characteristics. Insight into such parameters can be gained by taking into account the grain-scale heterogeneities, which are difficult to be captured by a continuum model [*Katsman & Aharonov.,* 2006].

Field observations of long linear natural compaction bands demonstrated that compaction bands were characterised by a significant damage (at the micro-scale) and a thickness that was reducing from the central band's segments towards its tips [*Sternolf et al.,* 2005]. Such idealised penny shape geometry of compaction bands motivated different models (anti-crack and inclusion models) analysed in the framework of linear elastic fracture mechanics [*Sternolf et al.,* 2005; *Rudnicki,* 2007; *Tembe et al.,* 2008]. The compressive anti-crack/ inclusion mechanisms, which were different from the bifurcation theory, implied the existence of weak initiation zones (*e.g.,* inclusions) that due to the stress concentration at band's extremities played an important role on the propagation of compaction band. The stress state was calculated in these cases in the inclusion and adjacent to its tips. Such micromechanical models accounting for heterogeneities were

developed in order to clarify how the microstructural heterogeneities affected the evolution of compaction band formation and propagation.

A combination of both mechanisms described by the bifurcation theory and an anti-crack model was applied by *Chemenda* [2011] to reproduce tabular compaction bands using finite-difference simulations. Compaction bands initiated as constitutive instabilities and propagated in a similar way to that of an anti-crack. In particular, *Chemenda* [2011] suggested that during an initial stage of propagation, the band retained its thickness while its material was affected by the inelastic deformation. During a later stage though, the bands became thicker and the inelastic deformation concentrated to its perimeter, while the response of the compacted central part of the band became mostly elastic.

Discrete element approaches were developed in order to highlight the way of compaction band propagation taking into account the micromechanical parameters that influence the formation of such deformation features (*e.g*., porosity, crushing strength, variability of grains). *Wang et al*., [2008] presented a 2D discrete element model to simulate compaction band micro-mechanisms, such as grain crushing and pore collapse, using an intra-granular damage mechanism. Such model could capture the damage evolution of failure modes that developped in the brittle-ductile transition. *Wang et al.*, [2008] showed that in a relatively homogeneous granular aggregate, discrete compaction bands developed, while in more heterogeneous systems diffuse compaction bands and distributed cataclastic flow were predominant. *Marketos and Bolton* [2005, 2009] presented 3D discrete element models shedding light onto the conditions for compaction band initiation and propagation. The role of the cementation bond strength and the post fragmentation behaviour of the grains on the observed behaviour were investigated. These authors suggested that localised discrete compaction bands were observed when both the bond strengths were high and the grains lost their load-currying capacity after being broken, while diffuse compaction bands (represented by advanced crushing front) were observed in cases where the broken grains could still curry force.

The literature review, presented in this Chapter reflects what the author considers as important issues regarding localised deformation in porous sandstones.

Chapter 3 - Experimental methods

3.1 Introduction

A wide range of experimental laboratory studies presented in Chapter 2 aimed at the better description of the localised deformation in sandstones and the physical mechanisms lying behind them. However, it is not always straightforward to determine, at the laboratory-scale, the onset and evolution of localised deformation using solely conventional measurements, which are typically taken at the boundaries of a specimen - even when multiple local measurements are available (*i.e.*, measurements from local strain gauges or LVDTs). As a consequence, the application of full-field measurements, as opposed to point-wise measurements, has become more and more common [see *Viggiani & Hall*, 2008, *Charalampidou et al*., 2010a; 2010b; *Dautriat et al.*, 2010; *Nguyen et al.*, 2010]. Many experimental full-field methods have been developed and are beginning to be applied in experimental geomechanics: ultrasonic tomography, acoustic emissions monitoring and source analysis, x-ray radiography and computed tomography, neutron tomography, digital image correlation, optical and electron microscopy are just some of them.

Both full-field and point-wise measurements might be destructive or non-destructive. Obviously, in laboratory work, non-destructive methods have an important advantage: a number of measurements can be made using the same or different methods on the same specimen, since the tested material remains essentially unaffected after the application of a method (*i.e.*, it is not mechanically strained or chemically altered).

This Chapter describes the experimental methods used during this work in the study of localised deformation in sandstones. Ultrasonic transmission measurements and tomography (UT), acoustic emissions (AE) analysis, x-ray computed tomography, 3D-volumetric Digital Image Correlation (DIC), and thin section observations are all described in detail.

3.2 Ultrasonic Tomography

3.2.1 Introduction

Ultrasonic testing is a non-destructive method, which can be used to investigate different velocity features inside a material. Ultrasonic velocity, which is the speed at which ultrasound propagates inside a material, changes when the material properties change. Thus material flaws might be detected with ultrasonic testing.

The sectional imaging of the velocity field in a material is called velocity tomography. Seismic travel-time tomography has been widely applied in geophysics through determination of the seismic velocity field inside areas of interest. The source of the seismic waves can be "passive" (e.g., earthquakes) or "active" (e.g., man-made explosions). For instance, seismic tomography has been used at the global scale for mapping the earth's internal structure (*e.g.,* active faults in *Peng et al*., 2003, heterogeneity of sedimentary structures or mantle in *Zhao*, 2009), in the hydrocarbon industry (e.g., *Pratt & Chapman*, 1992), and contaminated site investigations (e.g., *Yordkayhun et al.,* 2007).

The principles of travel-time tomography have also been applied at the laboratory scale for the study of velocity variations in geomaterials (but the number of these studies is relevantly small compared to the Acoustic Emission methods, section 2.3). For instance, *Daigle et al.* [2005] presented mapping of low and high velocity inclusions in cylindrical specimens of concrete, using ultrasonic sensors surrounding specimen's surface (the mapping plane was normal to the long axis of the specimen). *Scott et al.* [2002] used two horizontal arrays of sensors, placed at different elevations, to image velocity fields from two circular cross-sectional planes through specimens of sandstone and limestone, together with a third array of sensors, vertically oriented, to show the velocity field in a vertical cross-section of the specimens. *Johnson* [2004] presented sequential velocity fields from sandstone specimens, during indentation experiments. The sensors surrounded the specimens (horizontal cross-section). *Martins et al*. [2007] showed ultrasonic velocity tomograms from core plugs using ultrasonic sensors surrounded the surface of the core plugs.

Furthermore, ultrasound is used extensively, but not often through tomography, in medical applications. An example of ultrasonic tomography in this field can be found in [*Hormati et al*., 2010].

3.2.2 Ultrasonic sensors and experimental set-up: present study

In this study, ultrasonic velocity measurements for UT were taken before and after the deformation of the specimens. Initially, six small sensors were manufactured (see Appendix A) to measure the velocity fields inside rock specimens. However, the velocity variations were not captured in detail by such number of sensors because the actual ray coverage was relatively sparse (Appendix A). Denser ray coverage could be achieved by shifting the sensors on the surface of the specimen and getting multiple measurements, but this was very time consuming.

A pair of industrial multi-element ultrasonic transducer arrays ("barrettes") was used in combination with a rapid multi-channel emitter-receiver system (facility at LGIT in Grenoble, collaboration *P. Roux*). These ultrasonic transducers replaced the small sensors. The barrettes consisted of 64 piezoelectric elements, placed at a spacing of 0.75 mm (P-wave sensors, Fig. 3.1). The barrettes, which were manufactured to transmit and receive waves through water, had 1 MHz resonant frequency (which means that they were more sensitive to frequencies of 1 MHz).

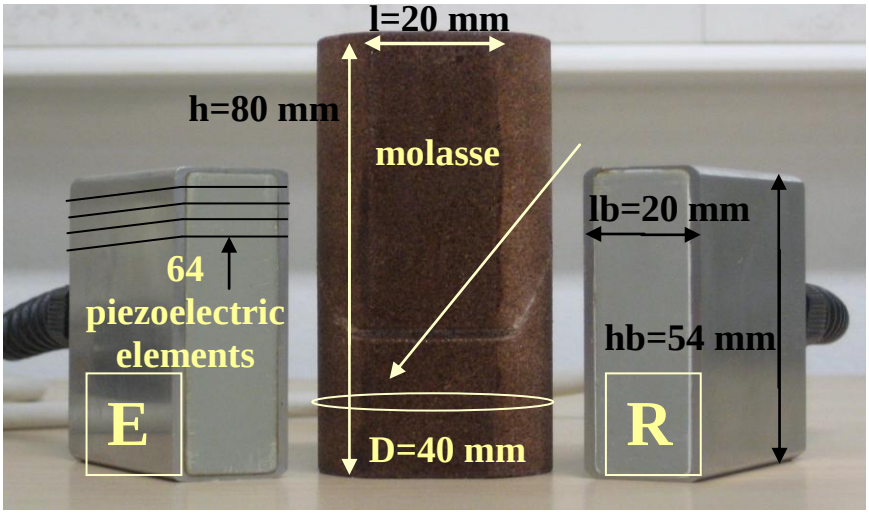

Fig. 3.1: Geometric characteristics of the 'barrettes' (ultrasonic multi-array sensors), which were used for the ultrasonic velocity measurements and a specimen of the Vosges sandstone. To improve the quality of the contact between the barrettes and the rock specimen, molasse was used as a couplant.

P-wave velocity measurements on the Vosges sandstone specimens were made, without any confining pressure, using the system at LGIT. A Matlab code (developed by *P. Roux* at LGIT) was used to control the 64 channel emitter-receiver recording system (*Lecoeur*

Electroniques) and the storage of the ultrasonic signals. The input signal (square pulse of 80 Volts) was generated activating each piezoelectric crystal of the emitter in turn. The signal transmitted through the rock was received by the 64 piezoelectric crystals of the receiver. A total number of 64x64 recorded signals were acquired (for both zero-offset and angular-coverage transmissions).

During the measurements, the barrettes were pushed by hands on the flattened surfaces (see Fig. 4.5 and Fig. 6.3) of the specimens. A thin layer of molasse was used as a couplant between the surface of the barrette and the flattened surface of the rock (Fig. 3.1). Molasse, which was applied by hand on the flattened surfaces of the specimen, was proven to be the best couplant (in terms of magnitude of the signal's amplitude) for the Vosges sandstone compared to other couplants such as washing liquid, grease, and vaseline. Figures 3.2 illustrate the positioning of the barrettes during the ultrasonic wave measurements. In order to image the whole height of the specimen (80 mm), an offset on the positioning of the barrettes was made thanks to two metallic spacers (30 mm high, Fig. 3.2b). The 'zero-offset' measurements correspond to the positions of the emitting and receiving transducers, placed at the same elevation on the two opposing flattened sides, while the 'angular coverage' measurements correspond to the positions of the emitting and receiving transducers, placed at a different elevation on the two opposing flattened sides (Fig. 6.3a).

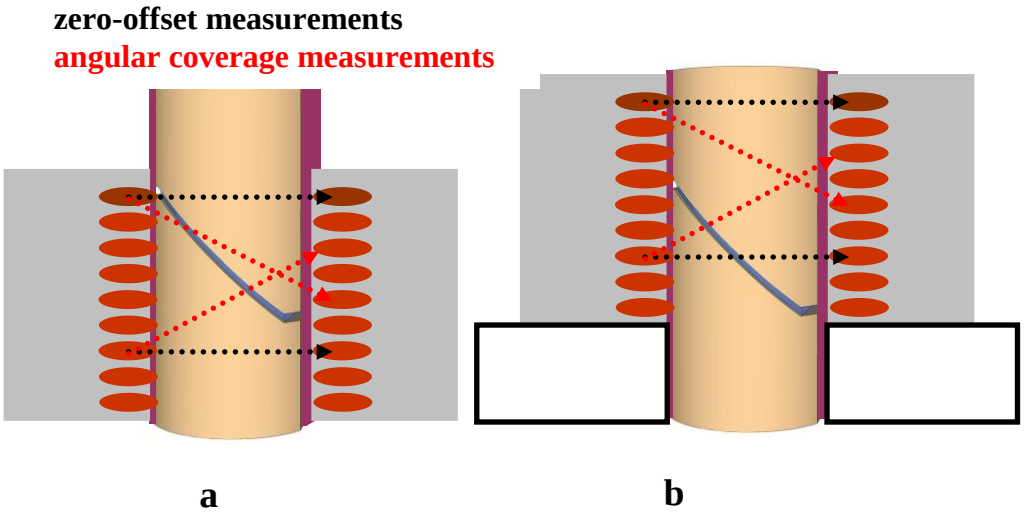

Fig. 3.2: Schematic representation of the velocity measurement configurations. (a), (b) Specimen traversed by a shear band (in blue). Different positioning of the barrettes (in grey). The red circles represent an exaggerated illustration of the piezoelectric crystals. The dashed fleshes are the potential ray-paths (assumption: straight rays).

It should be noted that the procedure followed during the ultrasonic measurements (barrettes) had some drawbacks:

- Slightly different amounts of molasse, applied on the flattened surface of the specimen by the same or different users, might have resulted in different transmissions of the signals (in terms of amplitude's magnitude).
- The polishing of the flattened surfaces during the specimen's preparation had produced micro-damage to the grains of this region (observed in the microscope, but not shown here). Multiple subsequent applications of the molasse to the flattened surfaces (*i.e.*, during multiple measurements) resulted in the penetration of the molasse in the rock volume, adjacent to the boundaries of flattened surfaces. Multiple applications of molasses, thus, resulted into increased velocities (not presented here).
- Manual forces had been applied on the barrettes during the ultrasonic signal transmission. Since no mechanical fixed support was used, it is likely that different applied forces will have had an influence on the quality of the transmitted/received ultrasonic signals.

3.2.3 Ultrasonic travel-time tomography: present study

In inverse problems, like UT, a set of model parameters (here the velocity field) is obtained from a set of observed data (here the travel-times) using the interaction of a physical system (here the ray-paths describing the trajectory of propagation of the waves). The forward and the inverse problems are described in indicial notation by the following Equations:

$$M_{ij} s_j = t_i \qquad \textbf{[1]}$$

$$s_j = (M_{ij}^T M_{ij})^{-1} M_{ij}^T t_i \qquad \textbf{[2]}$$

where $\boldsymbol{M_{ij}}$ is the ray-path matrix, $\boldsymbol{M_{ij}^T}$ is the transpose of matrix $\boldsymbol{M_{ij}}$, $\boldsymbol{M_{ij}^{-1}}$ is the inverse of matrix $\boldsymbol{M_{ij}}$, $\boldsymbol{s_j}$ is the slowness (velocity^{-1}) and $\boldsymbol{t_i}$ is the time vectors. The slowness matrix can be solved analytically if the $(\boldsymbol{M_{ij}^T M_{ij}})^{-1}$ matrix exist, which implies that matrix $\boldsymbol{M_{ij}}$ is square. Given the density of rays-paths inside a single cell (Fig. 3.5), the inverse problem, in this case, is over-determined (*i.e.*, bigger number of equations compared to the

unknowns, which is the slowness in each cell). Since $\boldsymbol{M_{ij}}$ matrix is not square, its inverse $\boldsymbol{M_{ij}^{-1}}$ does not exist and the solution is defined by optimisation methods applied to the linear equations (shown in matrix form by Equations [1] and [2]).

Matlab scripts, which were initially written by *S. Hall* and elaborated later by *L. Restaino*, *E.-M. Charalampidou* and *E. Tudisco*, were used for the velocity field calculation based on [*Chapman and Pratt*, 1992; *Pratt and Chapman*, 1992; *Pratt et al*., 1993]. Further information on the UT can be found in [*Berryman et al.*, 1990; *Gubbins*, 2004, *Santamarina and Fratta*, 2005]. A description of the basic steps of the UT follows.

- Measured arrival-time

The recorded wave-forms (64 sources by 64 receivers by two positions, see Fig. 2.2) were used to define the measured arrival times, which are the times taken by a transmitted signal to reach the receiver. The picking of the arrival-time was not trivial given the big number of measurements; thus, an automatic picking routine was necessary. In addition, the latter provides usually more robust results than the hand-picking and eliminates possible picking errors made by the user. Several algorithms [see *Oye et al.*, 2003; *Lokajicek and Klima*, 2006; *Kurz et al.*, 2005 and references therein] are usually applied for such reason.

In this study, the Akaike Information Criterion (AIC) was chosen as the automatic picking routine. AIC algorithm is suggested particularly for cases of noisy data (low signal-to-noise ratio). The idea behind this algorithm lies in the separation of the whole time-series into two segments, the second being the one containing the signal of the transmitted wave. The separation point of the two time series is determined by minimising the AIC. The minimisation of the variance inside the time-sequence segments defines the arrival time.

Figure 3.3 illustrates the transmitted waveforms of the zero-offset measurements from the specimen VEC5 before triaxial loading (see Table 4.2) together with the arrival time profile (as a function of the source/receiver height on the specimen). As an example, a zoom in the region from the 67^{th} to the 71^{st} receiving piezoelectric crystals is shown on the right to highlight the accuracy on the arrival time picking.

To increase the quality and quantity of the picked arrival times, especially in cases where the ray coverage was relatively poor due to the high attenuation of the signals (*e.g.*,

inside the damaged zone), arrival times were picked by hand. It is, however, underlined that an automatic time-picker is more reliable than hand-picking methods, even when it inserts errors into the picked travel times, since it always introduces similar kind of errors in the data-set.

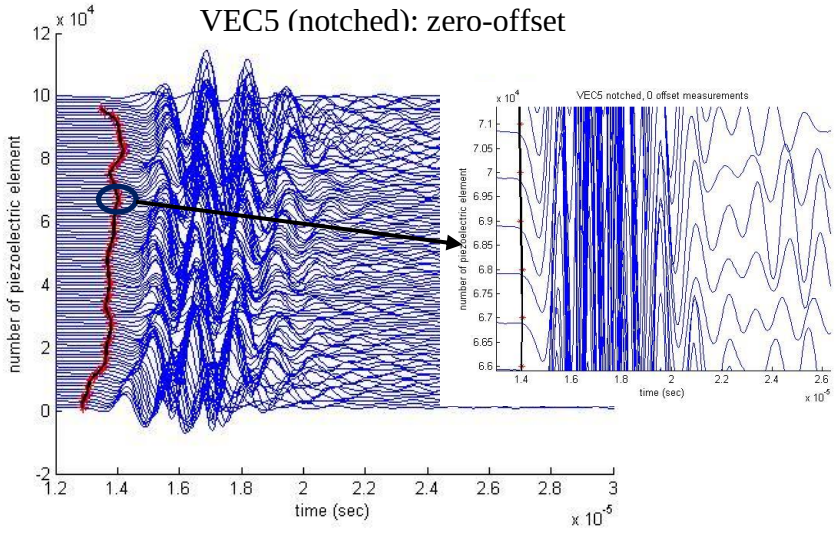

Fig. 3.3: Waveforms from specimen VEC5 (intact). The red spots represent the arrival time and the black line is a running average of the arrival times. On the right a zoom in a region highlights the quality of the picked arrival-time points.

- Ray-path tracing

For the ray-tracing algorithm, to describe the trajectory of the wave propagation from each source to each receiver, straight ray-paths were assumed as a first approximation. According to *Debski* [2002] and *Martin et al.* [2007], this approach is acceptable assuming low to moderate velocity variations, because the dependence of the ray-path on the velocity can be neglected (with a loss of sharpness of the tomograms, *Maxwell & Young*, 1993, cited in *Debski* 2002). Figure 3.5 illustrates an example of the considered ray-paths inside the velocity model.

The calculated travel-times, $\boldsymbol{t_i}$, of the i^{th} ray-path - Equation [3] - can be considered to be described by the summation of the ray-path times the slowness along the ray-path, where $\boldsymbol{s_j}$ is the slowness of the j^{th} cell, along the straight ray-paths, $\boldsymbol{l_{ij}}$ (the length of the i^{th} ray-path along the j^{th} cell) and n the total number of the cells (see also Fig. 3.4).

$$t_i = \sum_{j=1}^{n} s_j l_{ij} \qquad \textbf{[3]}$$

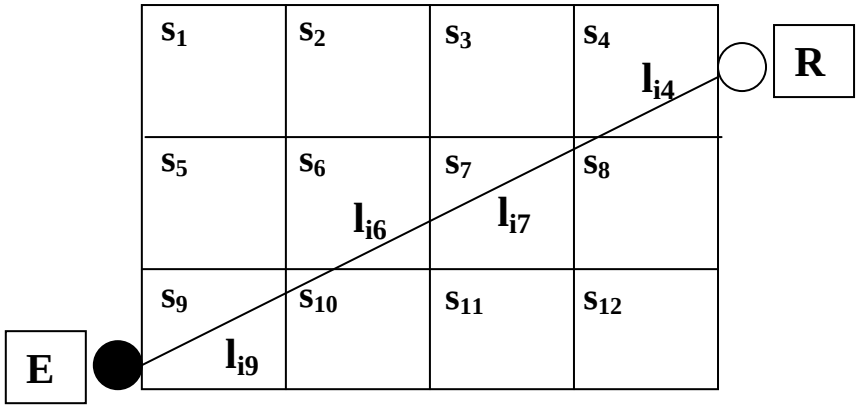

Fig.3.4: Schematic illustration of the ray-paths through a cell slowness model. S_j (j=1-12) is the slowness of the jth cell, l_{ij} is the length of the ith ray-path along the jth cell, and t_i is the travel-time of the ith ray-path.

Figure 3.5a illustrates the ray-coverage (straight rays) for position I (Fig. 3.2a) and Figure 3.5b is a detail of the image on the left. Note that this was relatively dense, since the piezoelectric crystals were closely spaced.

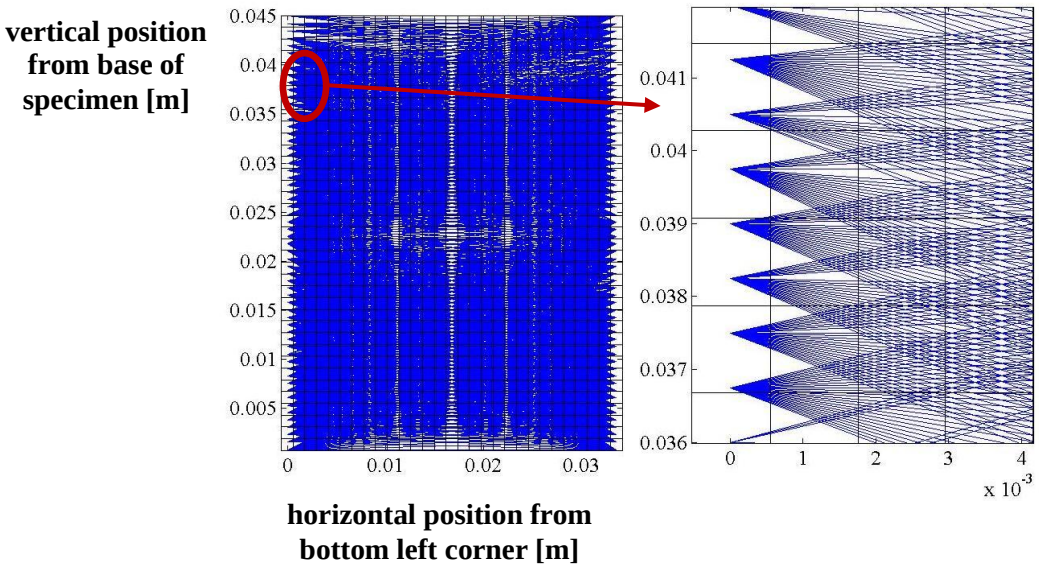

Fig.3.5: Ray-coverage, highlighting the dense ray network obtained by the use of the barrettes: (a) Position I (Fig. 3.2a); (b) Zoom in (a). The grid used for the UT is also plotted.

- Velocity field calculation

The outcome of the UT, as already mentioned, is the velocity (or slowness) value at each square cell/pixel (Fig. 3.4). To solve the inversion numerically, velocity (or slowness) values inside the region of interest (vertical section) were discretised into a regular grid of square cells (Fig. 3.5). The dimensions of the square cells were chosen to be relatively not far from the dimensions of the wavelength, which is defined as the average velocity over the dominant frequency. *Martins* [2007] suggested that the maximum cell dimensions should be equal to half the wavelength. Given that, the measured wavelength in this study was equal to 3 mm (average velocities from 1800-2100 m/s had a dominant frequency of 0.6-0.7 MHz, see also section 6.2), the cell dimensions were chosen to be equal to 1.5 mm.

To run the inversion algorithm, an initial velocity model was required. Two different initial velocity models were tested. The first model used the mean velocity of the zero-offset measurements as the initial velocity (homogeneous assumption), while the second model applied the zero-offset velocity profile, assigning a different mean velocity to each cell (heterogeneous assumption). *Tudisco* [2009] showed that the heterogeneous assumption of the velocity model produced lower quality topographic images compared to the homogeneous assumption. Therefore, in this work the mean zero-offset velocity was used as initial velocity model.

When the measured travel-times of the ultrasonic waves, the emitter-receiver geometry (coordinates of the stations), the ray-path algorithm, the sizes of the cells, and the initial slowness model were defined, the travel-time UT problem was solved by calculating the slowness field. The Least Squares Solution (LSS) can be used to solve over-determined inverse problems like the present one. In this case, the optimum slowness solution can be obtained by minimising the sum of squared time residuals. The (time) residuals- or error- are defined as the difference between the actual data (measured travel-times) and the predicted by the model data (predicted travel-times by the slowness model). However, the model must be constrained to avoid unrealistic velocities and velocity gradients. For such reason, the Regularised Least Squares Solution (RLSS) was applied instead, which is essentially the LSS coupled with a regularisation parameter $\boldsymbol{\varepsilon}$ (roughness penalty, dimensionless) applied to the slowness model. In such case, the velocity field was calculated for a range of regularisation parameters. RLSS leads to adequate estimates even in the presence of data or model errors, *e.g.*, travel-time picking errors, or ray-

assumption in places of complex velocity structures [*Pratt and Chapman, 1992; Santamarina and Fratta, 2005*]. Figure 3.6 shows the flow chart of the ultrasonic travel-time tomography method described above.

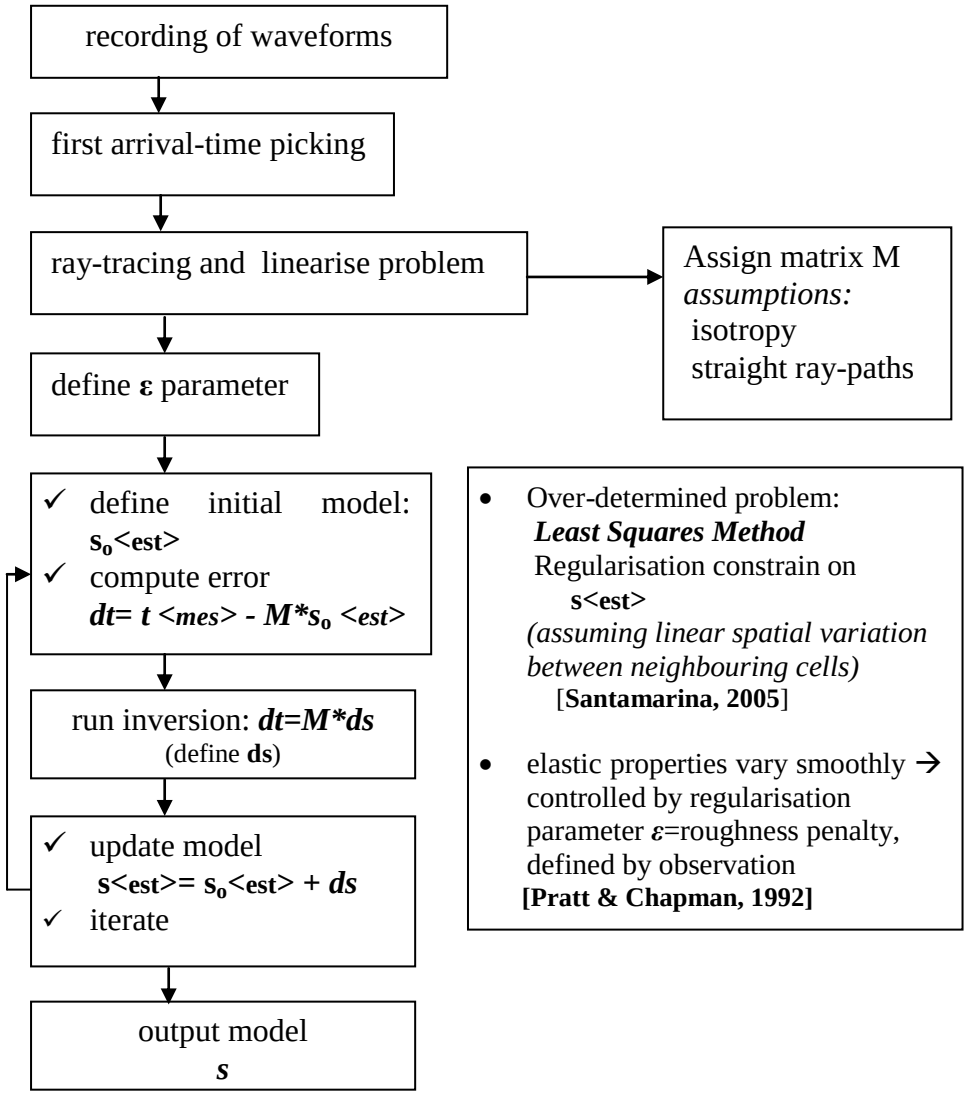

Fig. 3.6: Flow-chart of the ultrasonic travel-time tomography.

The effects of the regularisation parameter cannot be evaluated by solving a single velocity model. A series of solutions are required in order to construct the 'trade-off' curve [*Pratt and Chapman*, 1992; *Gubbins*, 2004*; Santamarina and Fratta*, 2005].

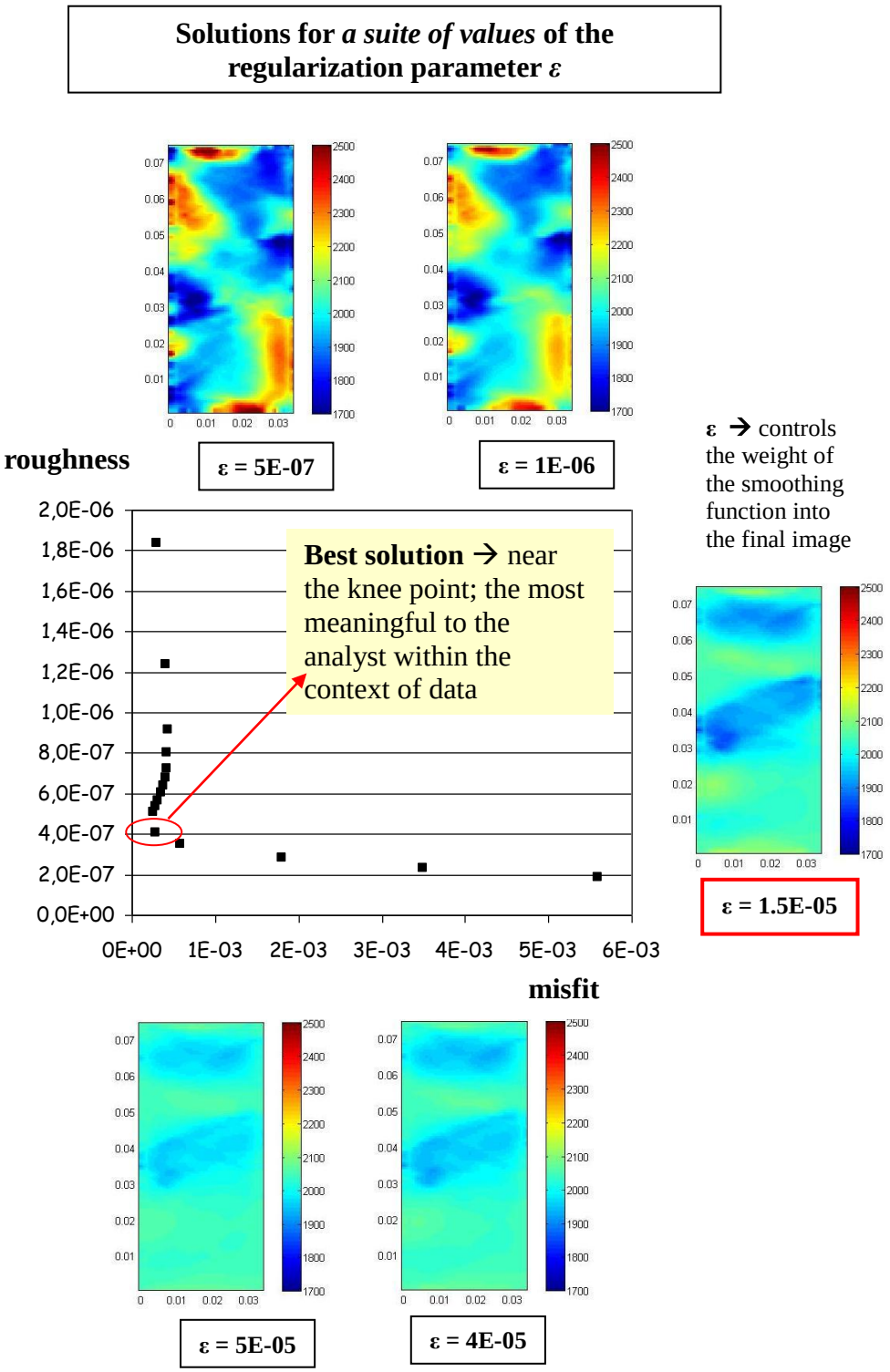

Fig. 3.7: Solutions of velocity fields from specimen VEC1, using different ε parameters (in terms of the misfit-roughness curve). The best solution is the one for ε=1.5E-05.

Figure 3.7 presents the trade-off curve of the misfit of the time residuals and the roughness of the slowness, from the VEC1 specimen with a shear band (Table 4.2), together with different ultrasonic velocity field solutions. The discretisation was made on square cells of 1.5^2 mm^2 size. By zooming in different parts of the trade-off curve, different optimal solutions are presented.

Figure 3.7 illustrates that the solutions are rougher and the misfit in time-residuals smaller, as $\boldsymbol{\varepsilon}$ decreased (the roughness constrains are relaxed, *Pratt et al.,* 1993). Therefore, the solutions with a lower misfit resulted in less smooth velocity fields. The best solution is a compromise between the misfit and the roughness and is found in the region around the 'knee-point' of the misfit-roughness curve [*Pratt et al.,* 1993]. The determination of the "best" solution should have an appropriate physical explanation considering also the resolution of the method. In this method, there is no unique solution; the best suggested velocity field depends on the user's critical choice and subjectivity.

The best suggested solution, in Figure 3.7, was that for ε=1.5E-05. In this case, where the specimen was deformed under 50 MPa confining pressure, a zone (band) of low-velocities can be seen to traverse the sample diagonally in the region where the deformation is expected to have localised. A layer of lower velocity, observed on the top part of the image, is likely due to a higher porosity sedimentary layer.

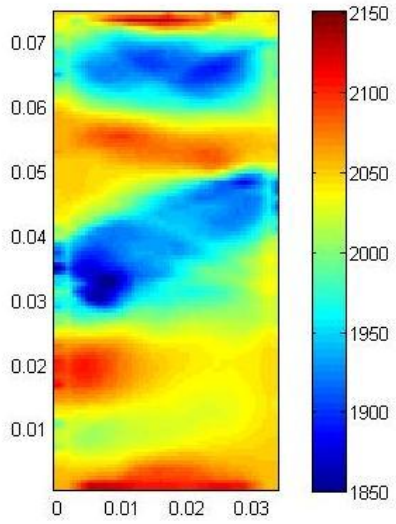

Fig. 3.8: Best-fit solution from specimen VEC1 (restricted colour-bar).

Note that the width of the shear band is larger in the UT images than observed using other experimental methods (see Chapter 5). This might be attributed to smearing effects (errors in the AIC picking and ray-tracing errors) inside this region. On the other hand, the wider shear band might also be attributed to a wider damage zone (note that loading stopped after the peak stress, Table 4.2).

3.2.4 General remarks

Opilinski and Gurda [1998] summarised the main source of error in the ultrasonic transmission tomography method. These authors suggested that changes of the measurement conditions, the measurement method, possible movements and vibrations of the pair of sensors, and possible changes of the received pulse front shapes could lead to further data errors, which would be reflected in the UT images. In the present study, the molasse quantity, the positioning of the barrettes (recall there was no mechanical support), the applied force on the barrette during the ultrasonic measurements, and also the offset of the barrettes in order to cover the whole height of the specimens (see Fig. 3.2) could have been possible sources of error in the data set. It is also speculated that possible artefacts on the velocity fields (sections 5.4.1, 6.2) might be attributed to the poor ray-path coverage (*e.g.,* the coverage at the ends of the vertical cross-sections is extremely limited). Furthermore, possible errors in the picking of the arrival time (especially in regions of increased damage) and possible interaction of the closely-spaced piezoelectric crystals (barrettes) should be also considered as potential sources of error.

Furthermore, *Opilinski and Gudra* [1998] suggested that the image reconstruction algorithm, the ray-tracing algorithm and possible refraction of the transmitted ultrasonic waves (*e.g.,* on the borders of the specimen) might additionally blur the velocity field; thus, these issues should be taken into consideration. To focus on the present study, as described before, straight ray-paths were used and an isotropic initial velocity model was applied (without taking into account any anisotropy). The application of bent ray-paths might improve the quality of the ultrasonic travel-time UT fields. Another suggestion might be the use of a heterogeneous velocity model consisting, for instance, of three layers of different velocity-the one being that of the localised zone and the other two being the mean velocities of the regions above and below. Recall that the velocity profile was proven to be less appropriate compared to the mean velocity model [*Tudisco*, 2009]. In addition, the application of an anisotropic velocity algorithm might also ameliorate the

UT results. Note that the thin section analysis (sections 3.6, 5.6, and 6.9) demonstrated the existence of both inter- and intra-granular cracks and micro-fractures (close to the notches-possibly attributed also to the unloading of the specimens), which might suggest an anisotropic velocity field.

A drawback of the measurements performed by the barrettes in this study is that the ultrasonic system was not specifically calibrated for the sandstone measurements. Therefore before any further elaboration of the tomographic algorithm, it would be necessary to pay further attention on issues such as the calibration of the barrettes for different rocks, the role of noise or the source response, which was not fully carried out during this thesis due to time restrictions. Although the calculated velocity fields make qualitatively sense (see Chapters 5 and 6), a note of caution is in order as for the absolute velocity values. For such reason, only qualitative interpretation of the UT results is presented in the following chapters.

3.3 Acoustic Emissions

3.3.1 Introduction

During rock deformation, energy may be released in the form of propagating waves, which are commonly referred to as acoustic emissions (AE) in the laboratory studies

Ouyang et al. [1991] underlined that AE method differentiates from other non-destructive methods in two significant aspects. On the one hand the energy is not supplied by en external source (*i.e.,* ultrasonic tomography), but generated from the specimen itself. AE techniques are capable of detecting the dynamic processes associated with the degradation of structural integrity. Another major advantage of this non-destructive method is that it can be performed during the loading of the material (*in situ*). Therefore, the time-dependent damage process can be recorded during the whole loading history.

Laboratory studies on AEs consist of the following categories:

- Analysis of AE rates together with mechanical data (by counting the cumulative number of AE events during loading).
- Localisation of hypocentres of AE events and depiction of the topography of the fracture plane (temporal and spatial analysis). The precise arrival time of waves,

recorded over an array of ultrasonic sensors, and the velocities of these waves are required for the AE source location.

- Source-mechanisms which describe the possible type of AE events (further details are given in section 3.3.3.4).
- Elastic wave velocities and attenuation analysis.

In the following, some background to AE methods and applications in laboratory rock mechanics is provided, which is followed by specifics on the application in this work.

3.3.2 Acoustic emission studies

AE analysis has been widely used in rock mechanics (more commonly than UT) and a variety of laboratory studies on different rocks exist. The temporal and spatial distribution of the AE locations (the so-called hypocentres) can shed light on the progression of micro-crack growth and clustering leading to rock failure, *e.g., Lockner & Byerlee*, 1978; *Lockner et al.*, 1991; 1992, *Lockner*,1993 in granite, *Lei et al.*, 2000 in schist, *Ouyang et al.*, 1991; *Labuz et al.*, 2003; *Katsaga et al.*, 2008 in concrete.

Zietlow & Labuz [1998] used AE hypocenter locations to characterise the dimensions of the intrinsic process zone (i.e., region of localised micro-cracking) of different rocks, among which the Berea sandstone. AE locations demonstrated that the size of this zone varied between rocks of different type, since it was related to the grain-size of each rock, however it did not vary much for specimens of different size from the same material.

Lockner et al. [1992] presented the nucleation and growth of fractures in the Berea sandstone, based on AE hypocentre locations. AE events were relatively distributed (diffuse) in the early stages of loading and they started to localise in a roughly planar fault zone before the peak-stress. During the propagation of the fault AE activity was more intense.

Reches and Lockner [1994] based on AE hypocentre locations from granite specimens, argued that in brittle homogeneous rocks, the nucleation of a fault occurred at a point without apparent precursors while the subsequent fault propagation in the faults plane, occurred via a leading process zone. According to these authors, such remark was in contradiction with previous notions that faulting resulted from the coalescence of micro-cracks, which had been formed before it.

Baud et al. [2004] linked the observed peaks in the cumulative number of AEs to the stress drops and the number of discrete bands that developed in sandstones. An unstable propagation of a discrete compaction band resulted in individual stress drops, while the intense grain cracking inside the bands induced the surge of AE activity. A similar unstable propagation was also indicated by *Vajdova and Wong* [2003a] implying almost two orders of magnitude faster transverse propagation of the compaction band - corresponding to a 'dynamic runaway' - than the axial displacement rate.

Fortin et al. [2006] presenting the AE hypocentre location from experiments on Bleurswiller sandstone showed that the nucleation and propagation of compaction bands was a result of continuous strain hardening. Similar observations were made by the AE locations from the Berea sandstone [*Menendez et al.*, 1996; *Baud et al*., 2004] and the Rothbach sandstone [*Baud et al.*, 2004]. However, the AE locations from the Bentheim sandstone indicated that local AE surges were accompanied by episodic drops in the stress-strain curves [*Wong et al.*, 2001; *Klein et al.*, 2001; *Vajdova et al.*, 2003a; *Baud et al.*, 2004; *Tembe et al*., 2006].

3.3.3 AE sensors and experimental set-up: present study

Elastic wave measurements (ultrasonic transmission) and AE activity were monitored during the triaxial compression experiments (those performed at GFZ) by eight pairs of P-wave and two pairs of S-wave polarised piezoelectric sensors (in situ). The P-wave sensors were composed by piezoelectric disks of 5 mm diameter and 1 mm thickness and the S-wave sensors had square shape piezoelectric plates of 5x5x1 mm. The resonant frequency of the P-wave sensors was of 1 MHz. All sensors, apart from two P-wave sensors, which were embedded in the top and bottom end-caps (see Fig. 4.9, section 4.4.2), were glued to the surface of the specimen and sealed in a Neoprene jacket (Fig. 3.9a) using a two-component epoxy. These sensors were manufactured at GFZ by *S. Stanchits*.

Figure 3.9 illustrates the position of the sensors. It is recommended that the sensors should surround the prominent AE sources, in order to ameliorate the spatial resolution of the AE method in all directions. However, the location of the sensors (Fig. 3.9) was restricted by the geometrical characteristics of the specimens (see Chapter 4), the positions and the lengths of the external local LVDTs (attached on the caps of the sensors for the local strain measurements), and the anticipated location of failure. The notches,

which were machined on the surface of the specimens, encouraged localisation to occur in the region in between them (see also Chapter 4).

During the loading of the specimens, acoustic emissions were recorded by all connected sensors (Fig. 3.9), which were used as receivers. During the ultrasonic transmission, which was scheduled periodically, the P-sensors of the pink group (Fig. 3.9) were also used as emitters, while those of the yellow group (Fig. 3.9) were continuously receiving. Sensors of the pink group were switched from the AE recordings to ultrasonic transmission every 300 seconds and P-wave velocities were measured normal, parallel and in an angular directions to the specimen axis. S-wave signals, which were recorded for further velocity analysis, were not elaborated during this study. The two P-sensors-mounted on the end-caps (16-15 in Fig. 3.9) - were only used for axial wave transmission (no AE recording). All the rest of the P-sensors were used for both the velocity measurements (independent from the AE locations) and the AE recording. Only velocities from five traces (1-3, 4-2, 9-10, 8-6, 5,-7, Fig. 3.9) were also applied to the velocity model used for the location of the AE events (see section 3.3.4).

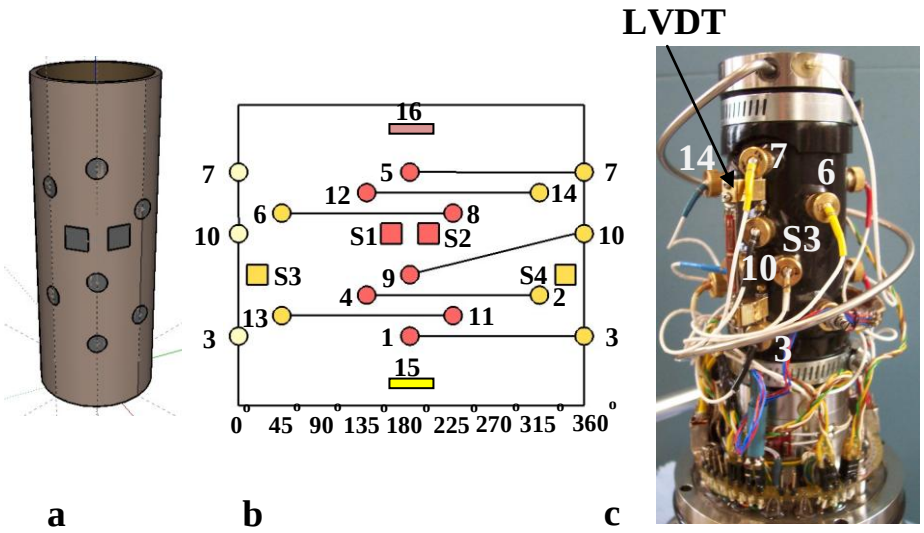

Fig. 3.9: (a) Schematic representation of the pierced Neoprene membrane placed on the specimen, on which the P- and S-wave sensors were glued; (b) 2D map of the position of the sensors. For the velocity measurements, the group of senders is shown in pink and the group of receivers in yellow. Black lines illustrate the pairs of sensors for the 'zero-offset' measurements; (c) Photograph of a specimen illustrating the sensors and their connections.

Ultrasonic signals were amplified by Physical Acoustic Corporation (PAC) preamplifiers equipped with 100 kHz high-pass filters [*Stanchits et al.*, 2009]. The gain was set to 40

dB for the P-sensors (and to 60 dB for the S-sensors). Preamplifiers were connected to all sensors during the AE monitoring and to the group of receivers (yellow group, Fig. 3.9) during the ultrasonic transmission. Each of the sensors belonging to the group of emitters (pink group, Fig. 3.9) sent a square pulse of 100 Volts when connected to a pulse generator (HP 214B), during the ultrasonic transmission. Full waveforms of AE data and ultrasonic signals from the P-wave velocity measurements were stored in a 14 channel transient recording system (PRÖKEL, Germany) with an amplitude resolution of 16 bit at 10 MHz sampling rate [*Stanchits et al.,* 2009]. The AE recording system was equipped with a 6 Gb memory buffer for temporary storage during the experiments that allowed recording of digitised waveforms of 256 thousand AE signals with a length of about 100 μs. All waveforms were recorded in the transient memory with no dead time between consecutive signals [*Stanchits et al.,* 2009].

3.3.4 AE hypocentre location

Recorded ultrasonic transmission and AE waveforms were separated automatically after the experiment. C++ codes were used for the separation of the signals, the ultrasonic transmission velocity analysis and the location of the AE events [written by *S. Stanchits,* GFZ]. The maps of AE presented in Chapters 5 and 6 were produced by *S. Stanchits,* while those presented in Chapter 4 were by the author of this thesis.

As mentioned, the ultrasonic P-wave transmission velocities measured during the triaxial experiments were used to determine the anisotropic velocity model, used for the AE locations. This was a five layer anisotropic velocity model, incorporating the P-wave velocities from five pairs of sensors and those from the vertical sensors (note that sensors 16-15 were not registering any AE activity).

The Akaike information criterion [*Leonard and Kennett*, 1999, in *Stanchits et al.*, 2009] was applied as an automatic picker for the P-wave arrival times from the recorded AEs. An automatic minimisation of time residuals, using the downhill simplex algorithm [*Nelder and Mead*, 1965, in *Stanchits et al.*, 2009] was performed during the AE hypocentre locations. Note that in this case, the unknown parameters are the coordinates of the events, instead of the slowness. Noisy channels were excluded. The ray-tracing algorithm considered that AE waves propagated along straight ray paths. The AE hypocentre location accuracy was almost 2mm (keeping time-residuals lower to 0.5 μsec).

The key aspects of the AE hypocentre locations are summarised in the following:

- Anisotropic velocity model applied to the location algorithm
- Coordinates of the sensors (which recorded AEs)
- Definition of the arrival times picked from the AE signals
- Estimation of the three spatial coordinates of each AE event
- Minimisation of the travel time residuals and adjustments of the initial estimated coordinates
- Updated coordinates and recalculation of the adjustments
- The procedure was repeated until all parameters converged on the best estimate.

3.3.5 Focal mechanisms

Focal mechanisms analysis is presented for specimen Ve2 (Fig. 5.2) and Ve4, and Ve6 (Fig. 6.2, 6.10). The analysis was carried out by *S. Stanchits* and a short overview of the method is presented here. There are two main categories for the analysis of the focal mechanisms, which are widely used in seismological studies: first motion (or polarity) analysis and moment tensor analysis [*e.g.*, *Stein and Wysession*, 2003]. The former was applied to the present study.

First motion analysis is grounded on the fact that the polarity (direction) of the radiated waves (AEs at the laboratory-scale) is related to the geometry (orientation) of the "fault" plane and the sense of movement on this plane. In this analysis, the focus is on the P-wave first motion at different sensors at different positions relative to the source. In theory, for an AE event in a homogeneous, isotropic medium, the first motions of the P-wave arrivals at sensors positioned in a sphere all around the AE source can be divided into four groups corresponding to their positions relative to four quadrants of the sphere. In two of these quadrants the first arrivals of the P-waves will be compressional and in the other two dilational. The planes separating these quadrants will be parallel and perpendicular to the plane of the "fault" or slip-surface. The convention made here is that compression occurs when the localised structure ‘moves’ towards the sensors and dilation when it ‘moves’ away from them. In the first-arrival method, the fracture type is determined by ratio between the compressional and dilational first motions of a certain event. If most of the recorded waveforms had compressional first motions, then the events are named T-type (tensile), if most of them have dilational first-motions the events are

called C-type (pore collapse), otherwise, they are S-type (shear) events [*Zang et al*., 1998]. Equation [5] presents the different type of source-mechanisms depending of polarities, shown in Equation [4], of the events according to [*Zang et al*., 1998]:

$$pol = \frac{1}{k}\sum_{i=1}^{k} sign(A_i) \qquad \textbf{[4]}$$

where $\boldsymbol{A_i}$ is the amplitude of the $\boldsymbol{i^{th}}$ channel and $\boldsymbol{k}$ is the number of the channels used for the AE event location (hypocentre determination).

$$\begin{array}{rl} -1 \le polarity < -0.25 & \textbf{\textit{T-type events: tensile}} \\ -0.25 \le polarity < +0.25 & \textbf{\textit{S-type events: shear}} \\ +0.25 \le polarity \le +1 & \textbf{\textit{C-type events: pore collapse}} \end{array} \qquad \textbf{[5]}$$

Note that the number of the AE events and the precision of the first arrival times are crucial for the accuracy of the determination of the type of AE events. In the present study, first motion amplitudes were picked automatically and first motion polarities were used to discriminate AE source types in tensile, shear and pore collapse [*Zang et al.*, 1998].

The moment tensor analysis is a more sophisticated approach, which combines force couples of different orientations acting on the slip plane along distances of different direction and it may represent various seismic sources (*e.g.*, not only tensile, shear and pore collapse) [*Stein and Wysession*, 2003]. This method is based on the inversion of the first motion amplitudes of the AE signals. The obtained tensor can be decomposed in isotropic, double-couple (DC) and compensated linear vector dipoles (CLVD) components, which provide information on the source mechanisms of an event [*Stein and Wysession*, 2003]. *Graham et al.* [2010] distinguished the focal mechanisms (moment tensor components) in purely shear, entirely tensile, and in more complex mechanisms that are characterised by predominately shear, tensile and mixed-mode with significant shear and tensile components. *Graham et al.* [2010] argued that the moment tensor inversion provides more informative results compared to the polarity method. However, the author believes that one should be sceptical about the moment tensor method, applied at the laboratory-scale, since the inversion of amplitudes might lead to erroneous

conclusions when errors are involved in the measurements (due to calibration of the sensors and coupling issues). The magnitude of amplitudes might be degraded due to high degree of attenuation and the relation of amplitudes in different frequencies should also be taken into account.

Fortin et al. [2009], expanding the work presented by *Fortin et al.* [2005], presented the source-mechanisms from three different failure modes (brittle faulting, cataclastic compaction and compacting localisation), which developed in deformed Bleurswilles sandstone specimens (larger than those used in *Fortin et al.,* 2005). In the brittle regime (shear localisation), these authors commented that the observed increase in the *S*-type events (from ~20% to 50% from the onset to the post-failure) and decrease in the *C*-type events (from ~80% to 40% from the onset to the post-failure) indicated an increase in the shear cracks and a decrease in pore collapse activity, respectively. During the cataclastic compaction (hydrostatic loading), the source-mechanisms analysis demonstrated around 28% of *S*-type events and 67% of *C*-type events, representative of shear cracks and pore collapse, respectively. During compaction localisation, the source-mechanisms demonstrated that the *S*-type events ranged from 12% to 20%, while the *C*-type events from 84% to 70% (shear enhanced compaction). *Fortin et al.* [2009] speculated that similar micro-mechanisms took place in both cataclastic compaction and compacting localisation, unlike shear localisation.

3.4 X-ray Computed Tomography

3.4.1 Introduction

X-ray Computed Tomography (x-ray CT) provides a full-field measurement for mapping the x-ray attenuation. Equation [6] presents the linear attenuation coefficient ($\boldsymbol{\mu}$), which is related to the density of the material ($\boldsymbol{\rho}$) and its atomic number ($\boldsymbol{Z}$) and to the photon energy $\boldsymbol{E}$ [*J. Baruchel et al.,* 2000]. The ratio ($\boldsymbol{\mu/\rho}$) is the mass attenuation coefficient and ($\boldsymbol{K}$) is a constant. The x-ray attenuation increases with increasing atomic number and density of the material.

$$\frac{\mu}{\rho} = K\frac{Z^4}{E^3} \qquad \textbf{[6]}$$

The obtained spatial resolution, which might be adjusted from some mm to one or two nm, varies according to the specimen size, the energy of the x-ray source and the quality of the detector. Medical scanners of different generations (usually conventional CT with a resolution of few μm, *i.e.,* 300-700), industrial systems adapted to material research (non-conventional CT with a resolution of 100 μm voxel size or less) and synchrotron radiation facilities (micro- or nano-tomography with a resolution of some μm or nano voxel-size) can be used. The possible resolution is determined by the size of the details to be viewed. In general, the best quality images, in terms of signal-to-noise ratio and spatial resolution, are obtained when Synchrotron Radiation facilities are used; the parallel monochromatic beam delivers a huge photon flux that allows very short exposure time. Furthermore, high signal to noise ratio is obtained. However, a drawback of such high resolution systems is that high resolution can be obtained only for rather small specimen's dimensions.

Although x-ray CT was initially used in medical imaging applications, this method also expanded to the fields of geology and engineering over the past few years (for further applications on Geoscience see *Ketcham & Carlson* [2001], *Mees et al.*, [2003] and references therein).

Experimental studies, conducted in geomaterials (*i.e.*, soil, rocks, concrete), used x-ray CT to characterise the localised deformation. With x-ray CT it is possible to extract qualitative information such as the visualisation of localised patterns and textural heterogeneities and quantitative data such as the spatial distribution of features (*e.g.*, orientation and thickness of fractures or bands) [*e.g., Desrues et al.*, 1996]. Moreover, the porosity evolution (see section 6.7) or the evolution of grain contacts [*Fonseca et al.*, 2010; *Hall et al.*, 2010c; *Ando et al.*, 2010] are feasible using techniques such binarisation and segmentation on the x-ray tomography images. In cases of resolution of some microns, x-ray CT might be comparable in resolution with optical microscope, since information on the grain shape and grains contacts can be acquired. Therefore, x-ray CT could be a competitive complementary method to thin section petrography [*Remeysen & Swennen*, 2008].

It should be underlined, however, that x-ray CT is sensitive solely to density variations (when the photon energy and the atomic number are constant). In the absence of volumetric strain, for instance, in the region of localised deformation, x-ray CT will fail to detect the phenomenon, particularly in its early stages [*Bésuelle*, 2004; *Lenoir*, 2007]. In such cases, it is essential either to apply statistical approaches to the grey-scale values

of the x-ray CT images or to combine x-ray CT with Digital Image Correlation (DIC, see section 3.5).

3.4.2 X-ray studies in sandstones

Herein, studies performed on different sandstones (*e.g.*, the Vosges, the Rothbach, the Diemelstadt, and the Fontainebleau sandstones) are discussed. The main characteristics of these rocks, such as the porosity, the mean grain-size and the mineralogy, were presented in Chapter 2. These studies on sandstones, as discussed below, have shown that conventional medical or industrial x-ray scanners can capture the pore and grain structure and the deformation features of scanned sandstone specimens.

Bésuelle et al. [2004] presented x-ray CT analysis of laboratory deformed Vosges and Rothbach sandstone specimens, using a medical scanner, to characterise the damage evolution related to shear localisation. For the Vosges specimens, x-ray tomography provided information not only on the localised patterns, but also on the inherent structural heterogeneities of this rock. A slightly darker colour region (more porous), which was not obvious by naked eye and possibly had been created due to sedimentation, was the place where localisation took place. Two vertical projections of the x-ray tomography images from the Vosges sandstone specimens, which were subjected to triaxial compression under 30 and 50 MPa confining pressure, are illustrated in Figure 3.10.

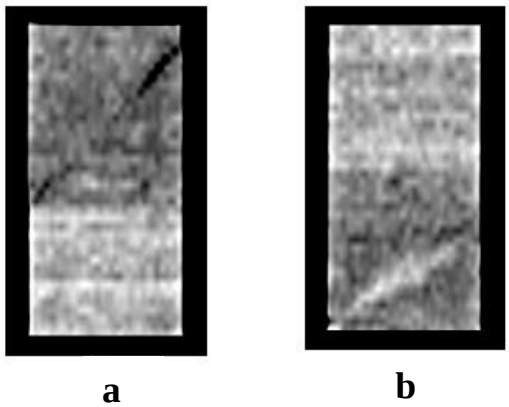

Fig. 3.10: X-ray tomography images from deformed Vosges sandstone specimens tested at 30 Mpa (a) and 50 Mpa (b) confining pressure [*Bésuelle et al.*, 2004].

The resolution of these images was 700 μm voxel size [*Bésuelle et al.*, 2004]. The darker colour bands (indicating less dense material), which developed at 30 MPa confining

pressure, were characterised as dilatant shear bands, while the lighter colour bands (indicating more dense material), which developed at 50 Mpa confining pressure, were characterised as compactant shear bands [*Bésuelle et al.*, 2004]. The latter shear bands appeared to be conjugated in reconstructed planes normal to the axis of the specimen, did not propagate to the core of the specimen and were relatively large and not so well defined. Both dilatant and compactant shear bands were not perfectly planar and presented a non-uniform porosity evolution [*Bésuelle et al.*, 2004], see also section 2.5.6].

Although porosity observations in terms of density contrast were feasible for the Vosges sandstone, based on x-ray tomography images, this was not the case for the Rothbach sandstone, which had a strong bedding heterogeneity (see sections 2.5.5, 2.6.1.2). X-ray medical CT images, with a spatial resolution of 200 μm voxel-size, captured less clearly the localised features inside the Rothbach sandstone [*Bésuelle et al.*, 2004]. Figure 3.11 shows x-ray CT imaging from projections parallel to the axis of the specimen. The sub-horizontal bright layers were related to the initial bedding. The localised patterns were easy to identify in specimens that had been loaded under lower confining pressures.

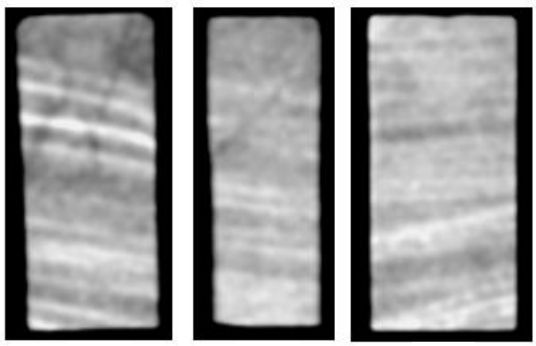

Fig. 3.11: X-ray tomography images from Rothbach sandstone specimens tested at 5 Mpa (a), 20 Mpa (b) and 55 Mpa (c) confining pressure [*Bésuelle et al.*, 2004].

X-ray CT imaging, with a resolution of 49 μm was used by *Louis et al.* [2006] to visualise compaction bands in the Diemelstadt sandstone. These authors commented that CT imaging of such structures was not a straightforward procedure. Processes such as pore collapse and grain crushing, which are common in compaction bands, resulted, according to these authors, in a homogeneous spatial distribution of the x-ray attenuation values between neighbouring voxels (see also *Otani et al.*, 2005, cited in *Louis et al.*, 2007b). A statistical technique based on the dispersion coefficient (the standard deviation

normalised by the mean x-ray attenuation), was developed by *Louis et al.* [2006] based on the analysis presented by *Otani et al.* [2005]. The measurement of the local damage intensity was described by the dispersion coefficient of the CT values calculated in an elementary volume of voxels. In such way, compaction bands were visualised as zones of relatively low dispersion coefficient.

A 3D reconstructed image of a deformed Diemlstand sandstone specimen is shown in Figure 3.12. Compaction bands, which were visualised in darker colours (black), had a mean dip of 7° and a thickness of 10 to 11 voxels (between three and four intact grain-size). *Louis et al.* [2006] commented that both thickness and orientation of the compaction bands were in good agreement with the microstructural observations carried out in the same specimens.

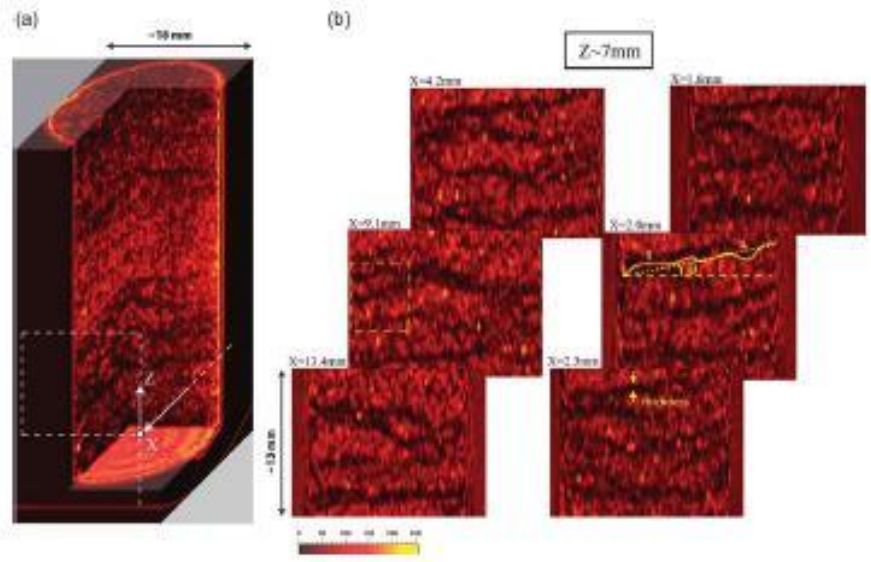

Fig. 3.12: 3D x-ray CT reconstructed volume from the Diemelstand sandstone specimens in terms of the dispersion coefficient. Compaction bands appear as black narrow zones. Calculations were performed on a subset of 3x3x3 voxels^3. The specimen was loaded in triaxial compression at 160 MPa confining pressure and 10 MPa back-pressure [*Louis et al.*, 2006].

Louis et al. [2007a] applied x-ray CT to investigate both the compaction bands and the impact of structural heterogeneity on the failure mode developed in the Rothbach sandstone. The spatial resolution (voxel size) of these x-ray tomography images was of 21 μm, which is almost 10 times higher than the resolution used by *Bésuelle et al.* [2004]. However, these authors argued that compaction bands were not visible from the density variations, since the bedding blurred their effect. Recall that the Rothbach sandstone

presented a strong inherent heterogeneity, due to the bedding. 2D DIC, which was performed on x-ray images, did reveal the compaction bands and resulted in less evident visualisation of bedding [Louis et al., 2007a]. Radiographs and pre- and post-mortem x-ray tomography images from the Rothbach sandstone specimens are shown in Figure 3.13.

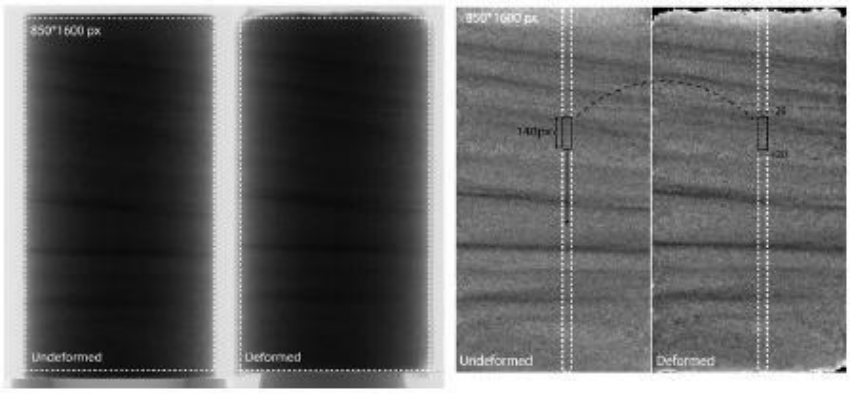

Fig. 3.13: Radiographs and pre- and post-mortem x-ray tomography images from the Rothbach sandstone specimens, which were loaded at 140 MPa confining pressure, and were cored perpendicular to the bedding [*Louis et al.*, 2007a].

High resolution synchrotron x-ray images from the Fontainebleau sandstones of different porosities, having a spatial resolution of 5.6 μm, were used to estimate single-phase and multi-phase transport properties [*Arns et al.*, 2003]. Permeability values calculated from the x-ray tomography images and single-phase calculations on network models were in good agreement with the experimentally measured values.

X-ray imaging, with a resolution of 2.8 μm, was used to study the pore and grain structure of a clean reservoir sandstone by *Knackstedt et al.* [2009]. The high resolution of these images allowed the sandstone fabric and texture, as well as the pore scale structure and networks to be identified.

3.4.3 X-ray CT to study localisation on the Vosges sandstone: present study

X-ray computed tomography was applied in the present PhD thesis to study the localised deformation patterns of laboratory deformed specimens in Vosges sandstone. Different analysis of the x-ray tomography images from specimens loaded in triaxial compression under a range of confining pressures (from 20 to 190 MPa) allowed for the 3D visualisation of the deformation bands and the measurement of bands' orientation angle

and width (see Chapter 5 and 6). Moreover, porosity field calculations, based on x-ray tomography images from deformed specimens, were conducted for some of the specimens (see section 4.5 and 6.7). The focus of this section is on the characteristics of the x-ray scanner used in this work and the experimental procedure that was followed.

3.4.3.1 Tools

The x-ray scanning facility of Laboratoire 3SR, at Grenoble (built by RX-solutions) was used for all x-ray scans carried out in this work. The general scanning set-up consists of three elements: the x-ray source, the specimen to be imaged and the 2D detector (Fig. 3.14). The specimen sits on a rotation platen that can move horizontally along the source-detector axis. The source and the detector, which can be shifted vertically and horizontally, are placed in a fixed distance (768 mm). The obtained spatial resolution of the x-ray image (voxel-size) is related (partially) to the position of the specimen. The closer to the source the specimen is, the higher the obtained resolution is.

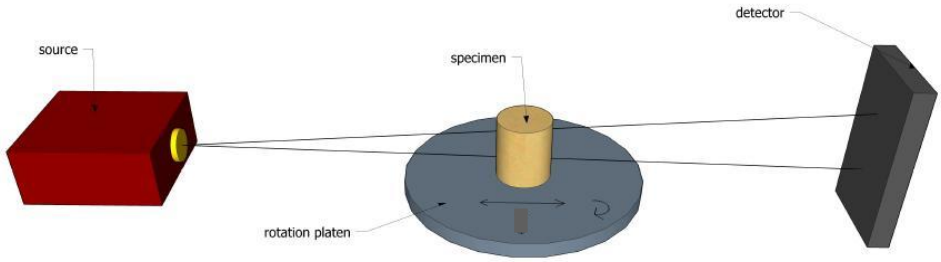

Fig. 3.14: Schematic representation of the RX resolution scanning configuration at Laboratoire 3SR.

The system uses a cone polychromatic beam, which traverses the specimen and the associated x-ray attenuation map is captured on the surface of the detector (x-ray radiography). Multiple radiographies are acquired over a range of angular orientations as the specimen rotates over 360^{o}. The number of the acquired radiographies defines the rotation angle of the platen. Using a reconstruction algorithm implemented in the software provided by RX-solutions, 2D horizontal slices, which represent maps of the x-ray attenuation across a specimen, are reconstructed from a set of radiographies.

An x-ray *micro-focus* tube is used, which allows high resolution images to be obtained. The micro-focus technology allows a high magnification image acquisition on a

small dimension object. The x-ray beam generates in a shape of cone and the focal spot-size can be varied according to the required resolution. Three focal spot-sizes are available in this scanner: 50 μm (Large) supports a maximum power of 75 W (*i.e.*, 500 μA at 150 kV); 20 μm (Middle) supports a maximum power of 30 W; 5 μm (Small) supports 10 W.

Apart from the beam focal spot-size, two more variables should be defined: the x-ray energy and the x-ray intensity. The x-ray energy defines the energy of the x photons. The higher the x-ray energy is, the higher the mean energy of the photons is, and the easier the photons travel through the material. It is highly recommended to use high voltage (higher than 100 kV) when scanning dense material or large specimens. The maximum voltage of the scanner is up to 150 kV. The x-ray intensity defines the number of the electrons produced each time. Hence, the higher the x-ray intensity is, the more electrons (and the more x-ray photons) are produced, so the brighter the image becomes. The maximum current flux is 500 μA.

The detector converts the x-ray photons, which go through the scanned specimen, to a digital image. The detector consists of a Csl scintillator screen. This type of detector has excellent qualities concerning the contrast (16384 grey-scale range), the acquisition speed (up to 30 images/s), the signal-to-noise ratio and the definition (up to 1536 x 1920 pixels).

Further details on the scanner facility at Laboratoire 3SR can be found at http://www.3s-r.hmg.inpg.fr/3sr/spip.php?article363 .

3.4.3.2 Procedure

The main objective of x-ray scanning, in this experimental program, was to capture features induced by the localised deformation. Therefore, for comparison, most of the specimens were scanned before (pre-deformation) and after (post-deformation) the triaxial compression experiments. The pre-deformation x-rays scans shed light on the inner structure of the sandstone before deformation in the laboratory. The pre- and post-deformation x-ray tomography images constituted the input images for the 3D-volumetric DIC (see section 3.5).

The sections below present the details of the scanning conditions (*i.e.*, specimen's position and parameters of acquisition). Further elaboration of the x-ray images acquired in this work is also discussed.

3.4.3.2.1 Scanning conditions

The spatial resolution of the x-ray images from the present study was limited by the dimensions of the specimens (diameter of 40 mm and height of 80 mm). Three different resolutions scans were performed: the low resolution (LR) scans throughout the whole height of the sample, which had a resolution of about 90 μm, the high resolution (HR) scans focusing only on the region of the localised deformation, which had a resolution of 30 μm, and the very high resolution (VHR) scans on small cores (of 10 mm diameter) coming from localised regions of the laboratory deformed samples, which had a resolution of about 5-7 μm. The regions of interest, from which the small specimens came from, were defined after the visualisation of the localised patterns by means of other methods (*i.e.*, UT, AE, x-ray CT, 3D-DIC). Figure 3.15 illustrates the time sequence of the x-ray scans and gives an image of the resolution from the Vosges sandstone x-ray images, acquired in this work.

Table 4.1 presents more information on the pre- and post-mortem x-ray measurements for each specimen used in this work. Obviously, the higher the resolution is, the more details are imaged. It is worth to mention that the x-ray CT is a very powerful tool; it may be compared to images acquired by the optical or scanning electron microscope. For instance, in this study, the x-ray scans of ~7 μm resolution resolved information comparable to those from the thin section observations on the optical microscope (see section 3.6), or at least in the similar order of magnitude. Moreover, the great advantage of x-ray CT is its non-destructive nature.

An important artefact related to x-ray CT is beam-hardening, which refers to the preferential attenuation of low energy x-rays when a polychromatic x-ray beam passes through a material. This effect can be reduced to some extent by using a hardware filter, which involves a loss in intensity of the x-ray beam and a lowering of contrast in the radiographs. In this work, to minimise possible beam-hardening artefacts, a filter was placed directly on the x-ray tube. For the case of LR scans, an inox and a copper foil (of 1 mm and 0.5 mm, respectively) were used to filter the x-ray beam, while, for the case of HR and very HR (e.g., small cores) scans only an inox filter was used. Ring artefacts could not be avoided in all experiments.

A Large focal spot size was used for the scans of ~ 90 μm voxel-size, a Middle focal spot size was used for the scans of ~ 30 μm voxel-size, and a Small focal spot size was used for the scans of ~ 5-7 μm voxel-size. The x-ray beam energy was 150 kV, 117 kV,

and 80 kV, while the x-ray intensity was 500 μA, 255 μA, and 125 μA, for the LR, HR, and very HR scans, respectively.

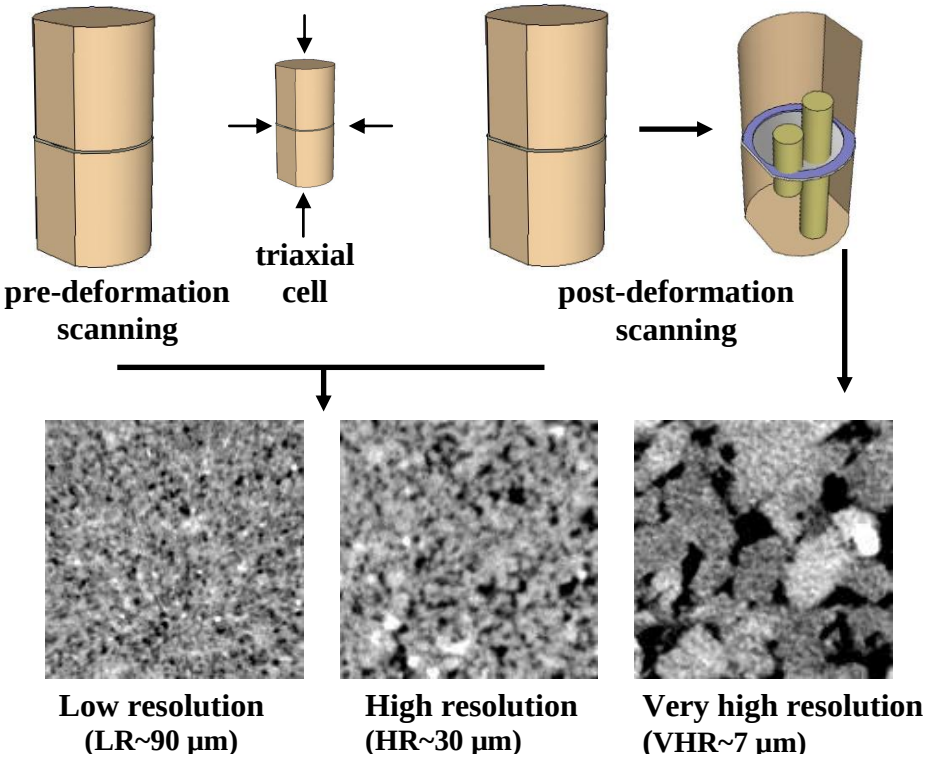

Fig. 3.15: Procedure: pre- and post-mortem deformation LR and HR x-ray tomography scans and post-deformation very HR x-ray tomography scans on small cores coming from the localised regions of the deformed Vosges specimens. Examples of LR, HR, and very HR x-ray images are shown.

Since pre- and post-deformation x-ray images were used also for the 3D-volumetric DIC, the specimens were placed at the same position every time they were scanned (*i.e.*, before and after the test). In order to reassure the exact position, the specimen was placed on a pvc base (Fig. 3.16). The need for this support was revealed during the course of the experimental program; therefore, not all specimens were placed on this pvc base.

A complete LR tomographic scan (over 360 degrees) was obtained by taking 700 radiographs (approximately 20 minutes). For the HR scans, 1000 radiographs were made for the shear bands and 1200 radiographs for the compaction bands (acquired within almost 90 minutes). The VHR scans involved the acquisition of 1200 radiographs (in 150 minutes). The sets of radiographs were processed with a reconstruction software (either RX reconstruction or Octopus, both available at Laboratoire 3SR) in order to generate the

tomograms of the specimen. Additional corrections on the beam-hardening were carried out by the reconstruction software.

Fig. 3.16: Specimen of sandstone placed on the pvc-base: set-up [Figure produced by *P. Charrier*, 3SR].

Table 3.1 summarises the characteristics of the x-ray tomography experiments on the Vosges sandstone performed in this study. The images were encoded in 16-bits (0-65535). The power parameters (x-ray energy and x-ray intensity, Table 3.1) were chosen so as to have the wider possible spread in grey-scale range.

Table 3.1: Characteristics of x-ray tomography experiments performed on Vosges sandstone specimens.

voxel resolution	**LR scans (~90 µm)**	**HR scans (~30 µm)**	**VHR scans (~6 µm)**
filters	Inox & brass foil	Inox foil	Inox foil
spot size	Large	Middle	Small
x-ray energy	150 kV	117 kV	80 kV
x-ray intensity	500 µA	255 µA	125 µV
radiographs/projections	700	1000/1200[1]	1200
acquisition time	20 min	1 hr 20 min	2 hrs 30 min
scanned region of interest	the whole height	focus on the localised region	focus on the localised region of the cored sample

1. 1000 radiographs were taken for the case of the shear bands (see Chapter 5) and 1200 radiographs for the case of compaction bands (see Chapter 6).

3.4.3.2.2 X-ray tomography image elaboration

The x-ray tomography images can be elaborated in different ways in order to visualise better (qualitatively) the patterns of interest (*i.e.*, sedimentary structures, localised bands, fractures, pore networks) and/or quantify parameters such as the orientation and width of the bands, the porosity variations etc. In this work, the x-ray images were elaborated by two different approaches.

The first refers to the visualisation of LR and HR x-ray tomography images. In general, the features of interest could be visualised by adjusting the histogram of the grey-scale range to values corresponding to the grey-scale values of the features to be imaged. For the case of shear bands, such procedure appeared to be quite promising. However, direct observations on the x-ray tomography images did not allow compaction band features to be well resolved in the Vosges sandstone. *Louis et al.* [2006] used local statistical measurements of grey-scale values, such as skewness and standard deviation to visualise the localised patterns in the Diemelstand sandstone. For the case of the Vosges sandstone (present study), compaction bands were viewed as zones of decreased standard deviation values. Calculations were made over representative elementary volumes, for different spacing sizes. It is worth to note, that the standard deviation analysis was also applied for the shear bands, however, the shear bands were visible even without the implementation of such statistical method. This observation is likely to provide some information on the microstructure of compaction bands. Low values of standard deviation indicate homogeneous regions, which could be explained because of the grain cracking and crushing and, therefore smaller size distribution.

Figure 3.17 presents x-ray images of the same vertical projection from the Ve6 Vosges specimen (Table 4.2). The raw x-ray data, the x-ray data after the calculation of the standard deviation, the mean, and the median of the grey-scale value are illustrated. Calculations were performed over sub-volumes of 300x300x300 μm^3 at a spacing of 300 μm in each direction. Calculations of the mean and median of the grey-scale values did not resolve the deformation features. On the other hand, it appears that calculations of the standard deviation of the grey-scale values did visualise compaction bands from specimen Ve6 as zones of lower standard deviation values (*i.e.*, more homogeneous regions from an image processing point of view).

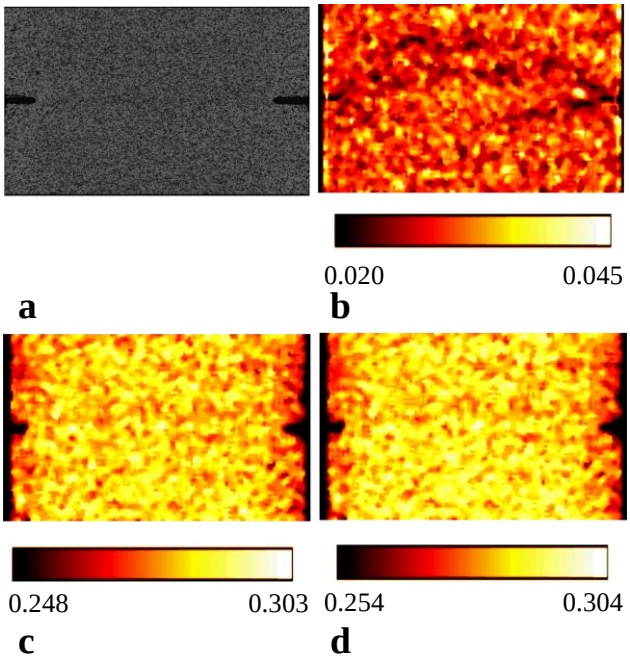

Fig. 3.17: Specimen Ve6 (triaxial compressions under 180 MPa confining pressure): (a) Raw x-ray tomography image; (b) Calculation of the standard deviation of the grey-scale values; (c) Calculation of the mean; (d) Calculation of the median. Calculations were made over sub-volumes of 10x10x10 voxels^3 at a spacing of 10 voxels in each direction (30 μm resolution).

Note that the raw x-ray data were visualised in this work in two different techniques: (i) isocontouring and (ii) volume rendering. The former consists of defining one or more surfaces (isosurfaces) that mark the boundaries of the specimen, which correspond to particular CT values. The latter assigns a red-green-blue colour to each voxel and opacity. By setting the opacity of some pixels to zero, the non-transparent voxels are visualised. Details on both techniques can be found at *Ketcham & Carlson*, [2001].

The second approach focuses on the very HR x-ray tomography images from small specimens (10 mm in diameter) coming from deformed and undeformed Vosges sandstone specimens. These images have a resolution very close to that of the thin sections. Calculations of porosity fields were performed and pore networks were visualised from these x-ray images. Figure 3.18 illustrates the 3D pore network of the host material, using the vg-max-studio software (1.24 x 1.26 x 0.25 mm). The pore space was isolated by a segmentation of the solid and void fractions (thresholding of the histogram of the grey-scale).

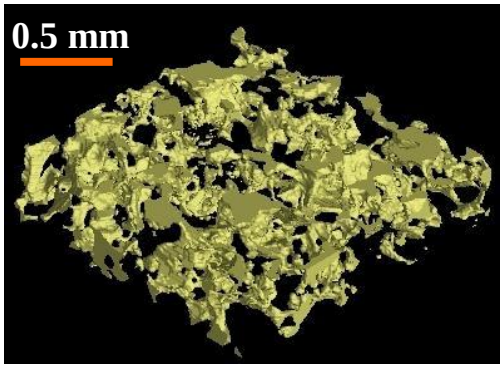

Fig. 3.18: 3D pore-network from a region of a laboratory undeformed small core (1.24 x 1.26 x 0.25 mm). Very HR x-ray tomography images (~ 6 μm voxel size): *vg-studio.*

3.5 Digital Image Correlation

3.5.1 Introduction

Passing from the analysis of a one digital image (see x-ray images, section 3.4.3.2.2) to the comparison of two digital images, this section describes digital image correlation (DIC), which is a full-field technique used primarily for mapping the deformation (displacement field) in a specimen. The main idea of this non-destructive method is grounded on the comparison of two digital images, the reference image (undeformed) and the deformed one. This mathematical tool is based on the assumption that if the intensity of some pixels (voxels in 3D) from the reference image correlates with those from a region of the deformed one, it is likely that they both represent the same region [*Quinta Da Fonseca et al.*, 2005]. The whole DIC idea is based on the finding of displacement between two similar (in terms of grey-scale values) regions: the reference and the target one assuming a one-to-one correspondence of their grey-scale range. The applied images might be taken during the experiment (in situ) or can be pre-deformation and post-deformation (pre- and post-mortem) images. Additionally, these images might come either from an optical imaging devise (*i.e.*, digital camera) or from x-ray CT. DIC has been used the last few years for a wide range of materials [*e.g., Pan et al.,* 2009; *Dautriat et al*., 2010, and reference therein].

3.5.2 Application of DIC at the laboratory scale

DIC was initially developed for tracking deformation in 2D (in-plane displacement and strain measurements). A fundamental description of the method in 2D, reviewing its basic principles and concepts can be found in *Pan et al.* [2009], while 3D DIC was first presented in *Bay et al*. [1999].

Louis et al. [2007a] used 2D DIC to investigate the localised structures that developed in specimens of the Rothbach sandstone. Recall that this particular sandstone had a strong bedding heterogeneity (Chapter 2), which was proven to play a key role on the developed deformation features. The 2D DIC analysis revealed diffuse compaction bands sub-parallel to bedding, in specimens cored normal to it, compactive shear bands (dip of 45°), in specimens cored 45° to bedding, and distributed and smaller strains than those of the previous cases, in specimens cored parallel to bedding. These authors demonstrated via DIC that the bedding controlled the location of strain localisation in regions outside it and guided the development of the localised features.

Nguyen et al. [2010] presented fracture evolution from artificially pre-cut inclined flaws (slits) under plane strain conditions in a soft rock (Neapolitan Tuff) using 2D DIC. Fractures represent displacement discontinuities; DIC, using in situ high resolution images taken by a digital camera, allowed the tracking of these discontinuities and their quantification in terms of displacement jumps along their length. Although shearing was identified in the meso-scale (specimen-scale), the DIC analysis demonstrated also local-scale opening linked to tensile micro-cracks.

Dautriat et al. [2010] applied optical monitoring (camera) and Scanning Electron Microscope (SEM) imaging to obtain 2D-DIC strain fields. These authors, using a multi-scale approach argued that local deformation in carbonate rocks (limestone) was induced by local heterogeneities. 2D-DIC appeared to be a powerful tool to resolve the strain fields, in the case of very small global measured strain levels (lower to 0.2%).

Lenoir et al. [2007] demonstrated that the use of 3D-DIC (volumetric DIC), applied to HR synchrotron x-ray CT images, visualised localised deformation in an argillaceous rock (Callovo-Oxfordian argillite). The HR x-ray images (14 μm spatial resolution) alone failed to reveal the deformation, since this was essentially shear strain and fractures in shear, thus it did not involve changes in bulk density. These authors therefore encouraged the combined use of x-ray tomography and DIC.

Hall et al. [2010b] used a continuum and a discrete 3D volumetric DIC to investigate localised deformation in sand at the grain-scale. Continuum DIC adopted a continuum hypothesis (continuity between adjacent sub-volumes, see also section 2.5.3), while discrete DIC focused on individual grains (sub-volumes centred on each individual grain). The procedure for the continuum DIC analysis is same as that presented in section 2.5.3 (present work), while more details on the discrete DIC analysis can be found in *Hall et al.* [2010b].

3.5.3 3D-DIC to study localisation on the Vosges sandstone: present study

3D-volumetric DIC was carried out during this work to obtain the shear and volumetric strain fields from deformed Vosges sandstone specimens. The analysis was performed using the code *TomoWarp* (*S. Hall*, Laboratoire 3SR)-a C code based on the work of [*Hall*, 2006], which was initially developed for time-lapse analysis of hydrocarbon reservoirs under production, based on 3D seismic images. Results on a granular analogue material (the so-called Schneebeli material) using the *PhotoWarp* code, which is a 2D application of the code, were presented in [*Hall et al.*, 2010a]. Results from the 3D application of the *TomoWarp* code on sands are presented in [*Hall et al*., 2009; *Hall et al.*, 2010b] and on sandstones in the present thesis [also in *Charalampidou et al*., 2010a,b,c].

Pre- and post-mortem High- and Low-resolution x-ray tomography images (~30 μm and ~90 μm voxel resolution, respectively) were used as input image sets to the 3D-DIC. The 3D displacement and strain fields as well as the Cross Correlation (CC) values (see description of the DIC principles) were the outputs of the 3D-DIC code. Recall that the experimental procedure for the acquisition of the x-ray tomography images demands the very same positioning of the specimen every time it is scanned, in order to avoid any erroneous displacements resulting from displacements, which do not come from the deformation.

The principles of the code *TomoWarp* are discussed below:

- Definition of the set of images to be correlated: the reference image (pre-mortem) and the deformed image (post-mortem). Note that the input sets of images should have the same size and the same coordinates.
- Definition of the volume of the two sets of images over which the DIC was performed. This parameter gives the option to run the code in different volume

sizes, which contained either a region of interest (*i.e.*, the deformation bands) or the whole scanned x-ray image.

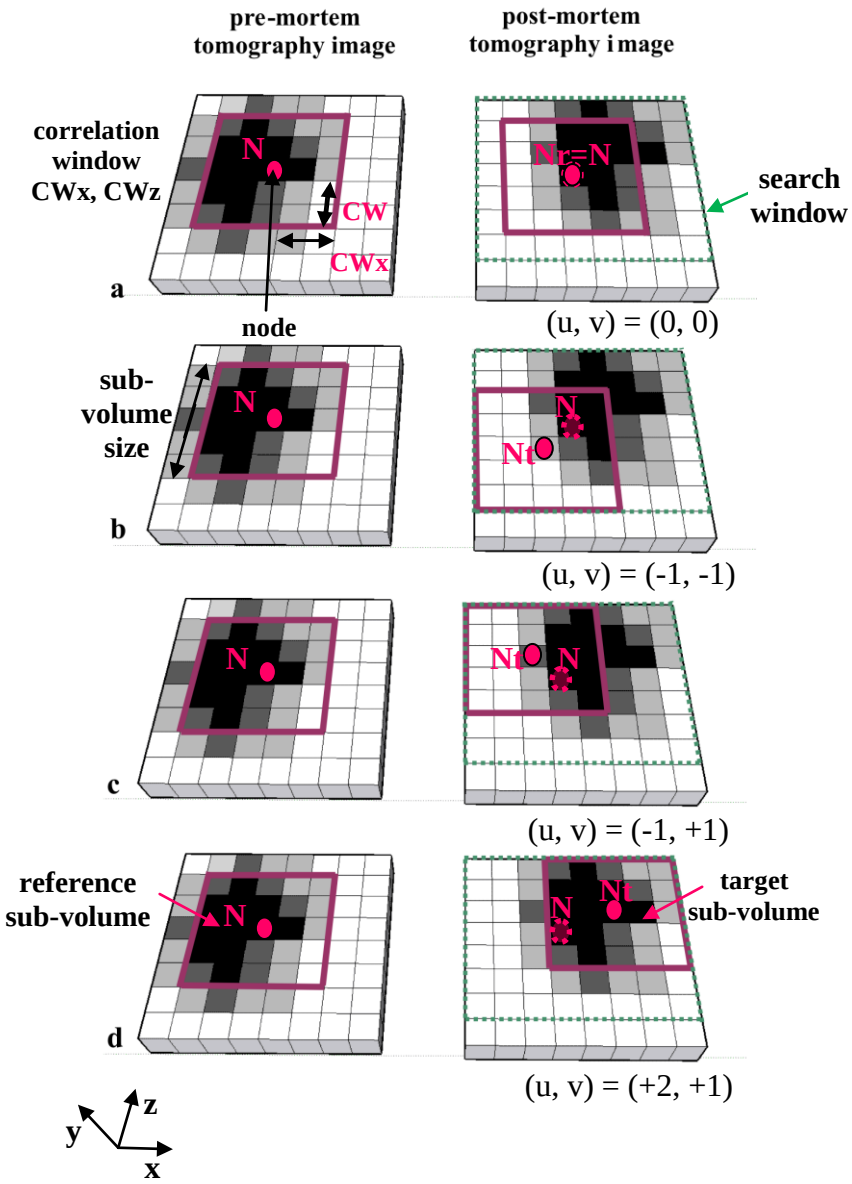

Fig. 3.19: Schematic representation of a region from the pre- (on the left) and post-mortem (on the right) x-ray tomography images (8x8x1 voxels). The sub-volume size is equal to twice the correlation window size plus one voxel. A node Nr, which is placed on the centre of the reference sub-volume is shown on the left (in pink colour, a-d). The search window on the right images (deformed images, a-d) is shown in green. The target sub-volume translates in different places over the search window (a-d). The nodes of the reference and target sub-volumes are also illustrated. The aim is to define the optimum integer displacement between the two sub-volumes (d).

- Definition of a regular grid of nodes, *i.e.*, the DIC analysis points, over the reference image (pre-mortem)(Fig. 3.19) based on the distance between the calculation nodes (*spacing* or *step*). During the first stage analysis, in which an initial rough estimation of the displacement field is acquired, a coarse mesh (bigger spacing) was used. An investigation of the impact of spacing on the resolution of the deformation features is presented in Chapters 5 and 6. The spacing is a key parameter for the spatial resolution of the method.
- Definition of a region centred on each node (the so-called *correlation window*). Strain fields were calculated on the sub-volumes defined by the correlation window (2xcorrelation window +1). Furthermore, a small sub-volume turns the DIC calculations faster but can reduce the signal to noise and lead to noisier results. An investigation of the impact of sub-volume size on the resolution of the deformation features is also presented in Chapters 5 and 6.
- An assumption is made that the grey-scale distribution in the two images was preserved after deformation and that only rigid body translation (characterised by only its three components) occurred between the reference and homologous target sub-volumes (pre- and pot-mortem images, respectively). No rotation on the correlation window was taken into account.
- Definition of the *search window* for the search of the target sub-volume (post-mortem image). This parameter defined the region of search in which the target sub-volume would be identified (Fig. 3.19). During the first stage analysis, a big search window is recommended (together with a bigger spacing). The initial maximum estimated displacement values (***u*** (x-axis), ***v*** (z-axis), and ***w*** (y-axis)) for any point within the specimen define a new, usually smaller search window size. During the second stage, analysis a smaller search window defined from the first analysis reduces the calculation time, although a finer mesh was used instead.
- Calculation of a correlation coefficient for each displacement of the sub-volume within the defined search window of the post-mortem image (see Fig. 3.19). The correlation coefficient, which was applied to evaluate the similarity degree (in terms of the grey-scale values) between the reference and the target sub-volumes, was the Semblance CC parameter,

$$SEMB = \frac{\Sigma_{x,y,z}(I_1(x,y,z) + I_2(x+u, y+v, z+w))^2}{\Sigma_{x,y,z} I_1(x,y,z)^2 + I_2(x+u, y+v, z+w)^2} \quad \textbf{[7]}$$

where $\boldsymbol{I_1}$ and $\boldsymbol{I_2}$ are the images before and after deformation, (***x, y, z***) are the local spatial coordinates and (***u, v, w***) are the local displacement coordinates (see Fig. 3.19). A review on other correlation criteria can be found in [*Pan et al*., 2009].

- Definition of the discrete displacements, as integer number of voxels, given by the displacement with the best SEMB cross-correlation (maximum).
- Sub-voxel refinement, since the displacements are rarely integer numbers of voxels. This is an essential step in the DIC, especially when strains are calculated from displacements. Actually, without the sub-voxel refinement, only integer values of voxel displacements are resolved, and this has as a consequence of 'stepped' displacement fields, strain fields with very high values corresponding to these steps and no strains between [*Viggiani*, 2009]. The role of the sub-pixel refinement was proven in [*Hall et al*., 2010b], where an example of DIC analysis with and without sub-pixel refinement is presented. The sub-voxel refinement method involved an interpolation function of the local 3D correlation surface that describes the variation in the SEMB CC over each voxel of the sub-volume. The Newton-Raphson method was used to find the maximum of the interpolation function.
- Definition of the vector-displacement field with sub-voxel accuracy.
- Computing of the local strain tensor components based on the derived displacement field with sub-voxel accuracy. A regular Finite Element (FE) mesh was constructed by eight-node trilinear elements, which coincided with the node mesh of the reference image. In particular, strains are calculated as described in *Hall* [2006]. This involves an eight-node (cubic) element and the strain is derived from the displacements at each of the nodes making up the element and assigned to the central point of the element. So the gauge-length is the spacing between nodes. Continuity is only assumed within each of these elements. The strain tensor is given, in indicial notation, by:

$$\varepsilon_{ij} = \frac{1}{2}\left(\frac{\partial u_i}{\partial x_j} + \frac{\partial u_j}{\partial x_i}\right) \quad \textbf{[8]}$$

where $\boldsymbol{u_i}$ is the displacement vector and $\boldsymbol{x_i}$ the coordinate vector. This second order tensor has nine components in 3D. Note that the absolute values of the strains are size dependent (i.e., they change when smaller sub-volumes are taken into account, see Chapters 5 and 6). However, although the strain calculation was principally used to indicate the presence of localisation (and not the precise values of strains) a comparison of the strain fields for the case of shear and compaction bands as well as the different sub-volume and spacing sizes was made in Chapters 5 and 6, considering a kind of relative change of the strain fields in an attempt to comment not only on the qualitative but also on the quantitative aspects of the resolved strain fields.

- Calculation of the deviator (shear) strain, shown in Equation [9] and the volumetric strain, shown in in Equation [10], based on the principal strains of the strain tensor,

$$\varepsilon_s = \sqrt{\frac{2}{3}}[(\varepsilon_1 - \varepsilon_2)^2 + (\varepsilon_2 - \varepsilon_3)^2 + (\varepsilon_3 - \varepsilon_1)^2]^{\frac{1}{2}} \quad \textbf{[9]}$$

$$\varepsilon_v = \varepsilon_1 + \varepsilon_2 + \varepsilon_3 \quad \textbf{[10]}$$

with ε_1, ε_2 and ε_3 the major, intermediate and minor imposed principal strains, respectively. Compactant volumetric strains are considered to be positive and dilatant volumetric strains are considered to be negative.

Results of the 3D-DIC on shear and compaction bands are discussed in Chapter 5 and 6, respectively.

3.6 Thin sections

Microstructural observations on thin sections from undeformed and laboratory deformed Vosges sandstone specimens provided useful insights into the mechanisms involved in shear and compaction bands. A number of experimental studies (see Chapter 2) demonstrated that both pore network and grain matrix evolve during deformation. Mechanisms such as rotation of grains, pore collapse, cracking of grain bonds, grain fragmentation, and grain crushing were widely observed in the microscope. Different

types of microscopes (*e.g.*, optical or scanning electron) provide the possibility to describe in more detail observed features by using different magnifications. Nevertheless, the great disadvantage of this method is its destructive character. Another shortcoming of this method is that the information gained from the thin sections is only two-dimensional.

A good grasp of knowledge in mineralogy is required in order to delve into the microstructure of the studied rock. However, it is not always trivial to identify the different minerals that appear in a thin section; a geological background is also required to understand how and why the grain network was built up. Therefore, to get a better conception of the laboratory induced damage, it is highly recommended before carrying out any microstructural analysis on a laboratory deformed sample, to observe a part of the intact rock.

In this section, some general information on sandstone minerals is given first, with particular attention to quartz, feldspar, micas and clay, which constitute the basic minerals of the studied material (in more details in section 4.2). A description of the thin section preparation, carried out at GFZ, follows. Thin section observations took place mainly at HW and partially at LGIT.

3.6.1 Mineral characteristics

In this section, the basic characteristics of quartz, feldspars, micas and clays, are given. The identification of such characteristics is important in the observed thin sections because they may indicate specific deformation mechanisms and processes. More details on these minerals can be found in *Kerr* [1959]; *Tucker* [2001]; *Passchier & Trouw* [2005]; *Wenk & Bulakh* [2008]; *Vernon* [2008]; *MacKenzie & Adams* [2009].

- Quartz is the most common mineral in sandstones. In thin sections, it appears to be a clear and clean-looking grain. Cleavage is usually absent. Twining is common, but rarely seen in thin sections. Quartz is usually easy to determine due to its lack of alteration (is the less affected mineral).
- Feldspars have a strong cleavage (usually in two directions), which turns to be a distinctive characteristic from the quartz grains. Additionally, these minerals have a lower mechanical stability and they are softer. Therefore, during deformation process, feldspars tend to be more deformed/damaged compared to quartz. Chemical alteration involves replacement of the feldspar by clay minerals. Moreover, the alteration gives

the feldspar a dusty appearance. These minerals are subjected to dissolution; therefore, partial or total loss of feldspars may occur during either diagenesis or burial uplift. Sandstones near the surface and those beneath unconformities may be characterised by grain-size pores, which might have been places that hosted feldspars, which were dissolved later through contact with meteoric water. Most of the feldspars exhibit twinning.

- Clay minerals present no twinning and have a perfect cleavage in one direction. These minerals do not preserve the shape of the grain they replaced (e.g., feldspar), since they become trapped in between other grains due to compaction.
- Micas are easily identified in thin sections on account of their elongated shape (flakes), their distinctive bright interference colours (in cross polars), and the perfect cleavage in one direction. Both biotite and muscovite may be concentrated along laminae and bedding planes.

One important characteristic to be taken seriously into account is the cleavage of the minerals. Apart from helping in distinguishing minerals, cleavage along with twinning may indicate prominent places where fracture planes may occur.

Figure 3.20 shows a region of a laboratory undeformed Vosges sandstone thin section and Figure 3.21 illustrates some of the minerals observed in this sandstone.

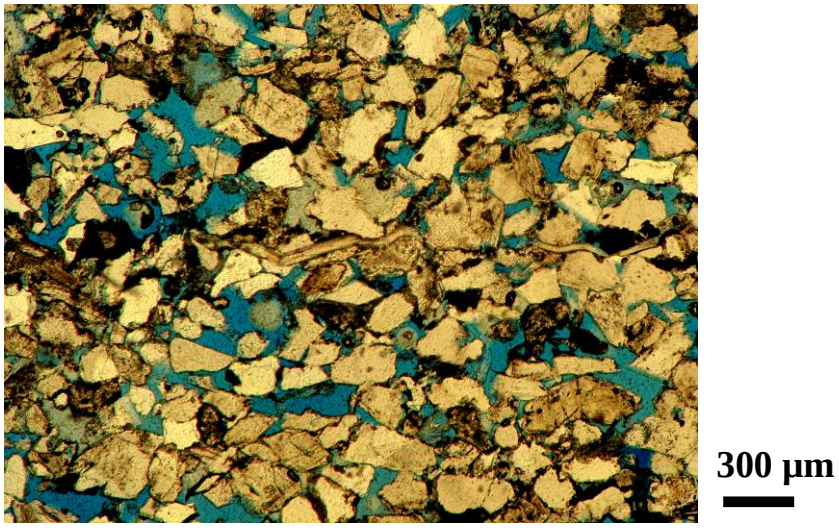

Fig. 3.20: Optical image of minerals from a thin section coming from the laboratory undamaged Vosges sandstone.

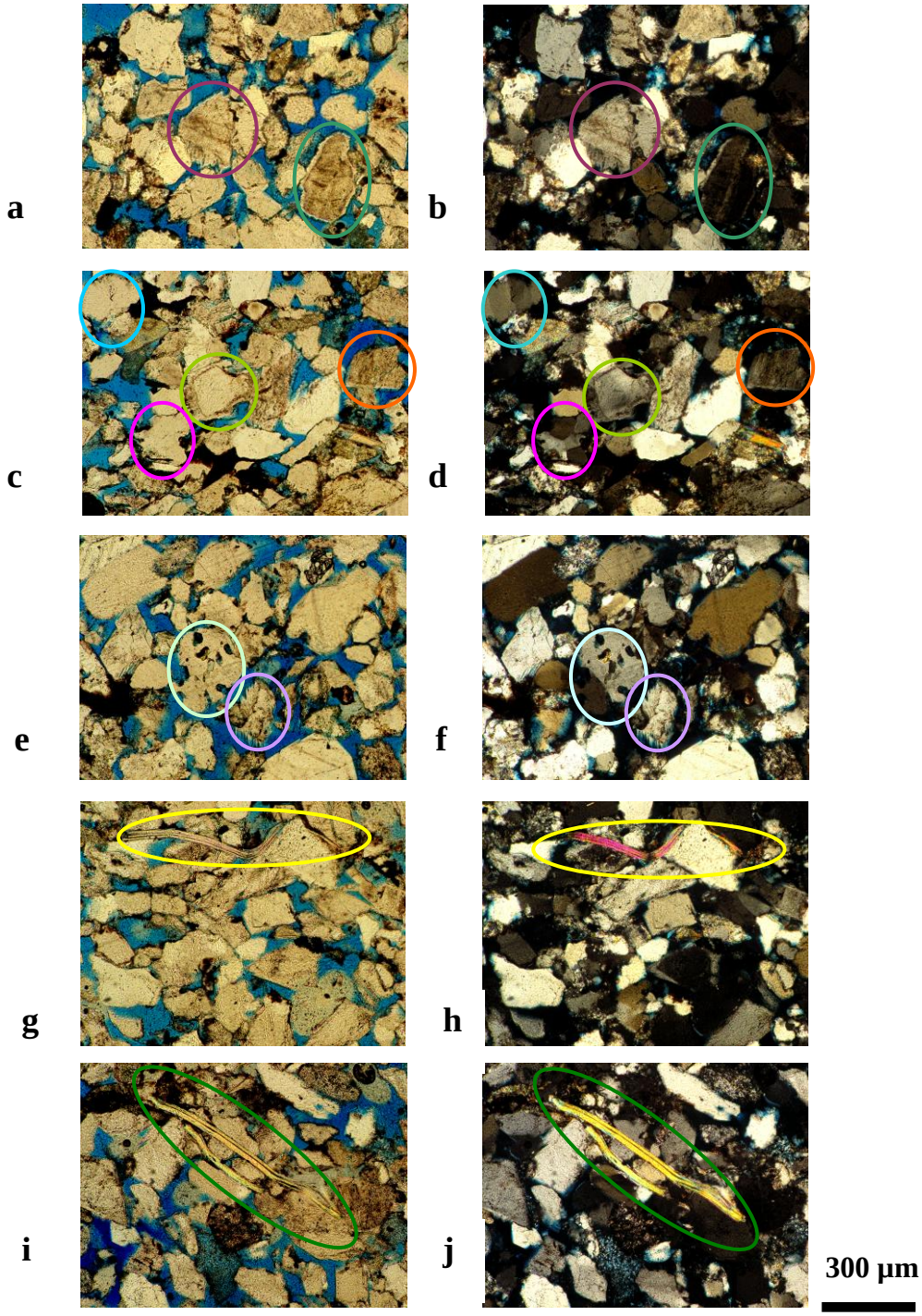

Fig. 3.21: Plane-polarised light optical images (a),(c),(e),(g),(i) from regions of the laboratory undeformed Vosges sandstone; Cross-polarised light optical images (b),(d),(f),(h),(j) from similar regions as those shown on the plane-polarised images. The basic minerals (quartz, feldspars-altered feldspars, and micas) are shown.

3.6.2 Thin section preparation

Thin section preparation was conducted at GFZ, Potsdam, with the help of *Stefan Gehrmann*. The specimens were impregnated in blue epoxy. Then they were sawn axially into two halves, after being cured from the impregnation. Thin sections were prepared from the part where the localised deformation took place. For specimens having experienced a shear band such place was in between the region of the notches, for specimens having experienced a compaction band, that was below and above the notches, and for specimen Ve1, which had no notches, that was on its top half (see also Chapter 4). Additionally to the thin section preparation, small specimens of a diameter of 10 mm were cored from the localised zones of the deformed specimens from the other half of the deformed specimen (see section 6.7). A schematic representation of the procedure is presented in Figure 3.22. The decision for the position of the thin sections was guided by the results obtained via the non-destructive methods (*e.g.*, x-ray images, 3D-volumetric DIC) used in this work.

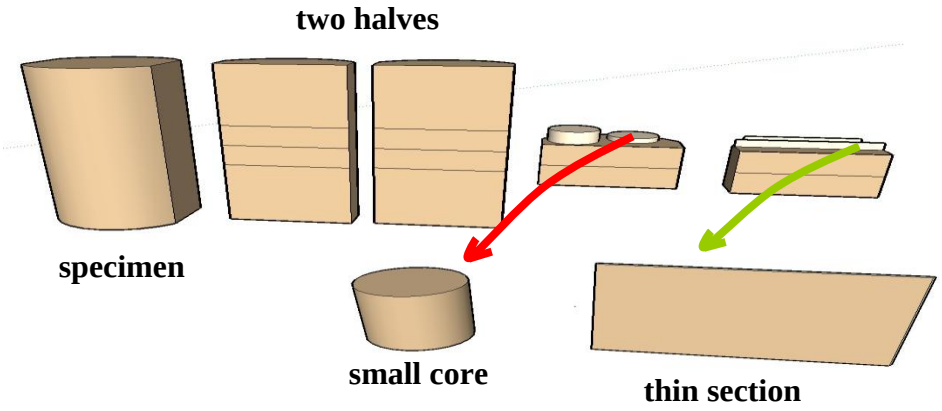

Fig. 3.22: Schematic representation of the small core and thin section preparation from the deformed Vosges sandstone specimens.

The outline of the thin section preparation is described in the following:

- Impregnation of the specimen with blue epoxy
- Cutting of the impregnated specimens
- Identification of the region of interest on the cut surface of the rock
- Cutting of the slabs
- Cleaning up of the slabs (wash the debris)

- Trimming of the slabs at the size of the thin section
- Gluing of the glass on the trimmed slab (attention should be paid on the constant thickness of the epoxy used)
- Cutting off the extra material (reduce the width of the material for the under-preparation thin section)
- Gridding of the slice to the correct thickness
- Polishing of the thin section

A schematic view of the indicative positions of the thin sections from two deformed specimens, containing shear and compaction bands, and the indicative position of the small cores are presented in Figure 3.23a. Figure 3.23b illustrates an exaggerated view of a thin section. Three parts can be seen: the glass slice, the epoxy/glue and the rock slice, which has a thickness of 30 μm.

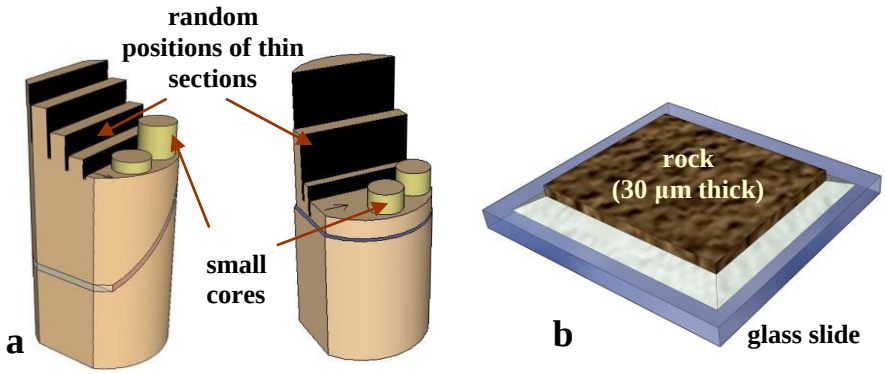

Fig. 3.23: (a) Schematic view of the position of thin sections and small cores on two deformed specimens; (b) exaggerated representation of a thin section.

3.6.3 Thin section observation

Thin section observations at HW were carried out using an Olympus BH-2 polarizing binocular microscope, equipped with an Olympus C50-60 Camedia camera, and a XL30 ESEM made by FEI. At LGIT, the microscope used was an Olympus BH2-Pol polarised binocular microscope was used equipped with an Olympus DP25 camera and the AnalySys software for the image analysis.

3.7 Conclusions

This Chapter presents and discusses the different experimental methods that were used to acquire the results presented in Chapters 5 and 6. Each method is sensitive to different parameters. Furthermore, most of the methods were used in different experimental times; for instance UT and X-ray CT was used before and after the deformation of the specimen, AEs were used during the deformation process, DIC measured the ``total`` deformation fields (comparing pre- and post-mortem X-ray images), and the thin section observations were carried out after the deformation of the specimens. Additionally, each method has a restricted resolution. For instance, UT cannot resolve features smaller than the wavelength. X-ray CT can have a wider range of resolution depending on the specimen dimensions, its distance from the source, the energy of photons and the quality of the detector. DIC has a resolution defined by the distance of the spacing parameter. Finally the resolution of the thin section images depends on the microscope used.

Chapter 4 - Material and Experiments

4.1 Introduction

The mechanical behaviour of a Vosges sandstone, loaded under triaxial compression at a range of confining pressures (20 - 190 MPa), was studied during this experimental program. The objective was to better understand the onset and the spatial and temporal propagation of the localised deformation features that develop under such loading conditions. A combination of non-conventional full-field experimental techniques were utilised in these investigations (see Chapter 3 for details on the different techniques).

In this Chapter, details on the experimental program are given. Section 4.2 is dedicated to the description of the material studied. Section 4.3 describes the specimen preparation. The two triaxial cells - used in the experimental campaign - are presented briefly in sections 4.4. Section 4.5 describes the experimental set-ups, and the testing program. The mechanical data, including 'meso-scale', conventional stress-strain curves and AE event analysis, are discussed in sections 4.6 (shear bands) and 4.7 (compaction bands). Finally, section 4.8 presents a summary of the key points from this Chapter.

4.2 Material

The material studied in this work was the same sandstone (coming from adjacent blocks) as that investigated by *Bésuelle* [1999; 2000; 2001]. This sandstone was chosen for this study as its mechanical behaviour and failure modes under triaxial compression up to 60 MPa confining pressure can be considered as relatively well known: they were characterised using standard methods by *Bésuelle* [*Bésuelle*, 1999; 2000; 2001]. The focus of this work, at this relatively low to middle confining pressure range (up to 60 MPa, for more details see section 4.6), was to use a combination of different experimental full-field techniques (see Chapter 5) to characterise the mechanisms and consequences of localised deformation evolution in more detail. Under relatively higher confining pressures, from 130 to 190 MPa, the objective of this work was to capture the mechanical

response of this sandstone and to investigate the developed failure modes using different experimental methods (see section 4.7 and Chapter 6).

The mineralogical composition, average grain-size, cement, and porosity of this sandstone are to be the same as those presented by *Bésuelle*. No further analysis of these properties was conducted during this thesis (apart from some grain-size observations). The 'Vosges' sandstone studied came from the Woustviller quarry in the Vosges Mountains, France [*Bésuelle et al.*, 2000]. The rock had a general pink colour and contained approximately 93% quartz, 5% microcline, 1% kaolinite and 1% micas, and average porosity of 22%. The mean grain diameter was of 300 μm in diameter [*Bésuelle*, 1999; 2001]. Figure 4.1 presents a very HR x-ray tomography image (6μm voxel-size) of the rock before any laboratory deformation (intact).

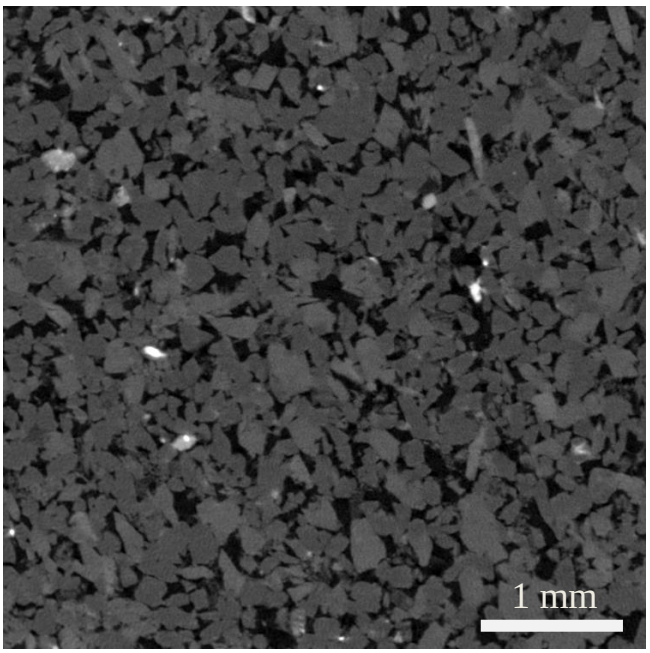

Fig. 4.1: Very HR x-ray image of the intact Vosges sandstone (~ 6 μm voxel size). The grains have sub-angular to rounded shape.

Note that both the shape and the size of this sandstone grains were identified, during the present study, via very HR x-ray tomography images and microstructural observations on thin section from the intact rock. Grains were moderately sorted. Quartz grains and feldspar minerals were sub-angular to round.

The micro-scale observations (*i.e.*, with µm resolution, either using optical or electron scanning microscope or very HR x-ray tomography images) provided a detailed picture of the sandstone in its natural state (*i.e.*, before any laboratory induced deformation).

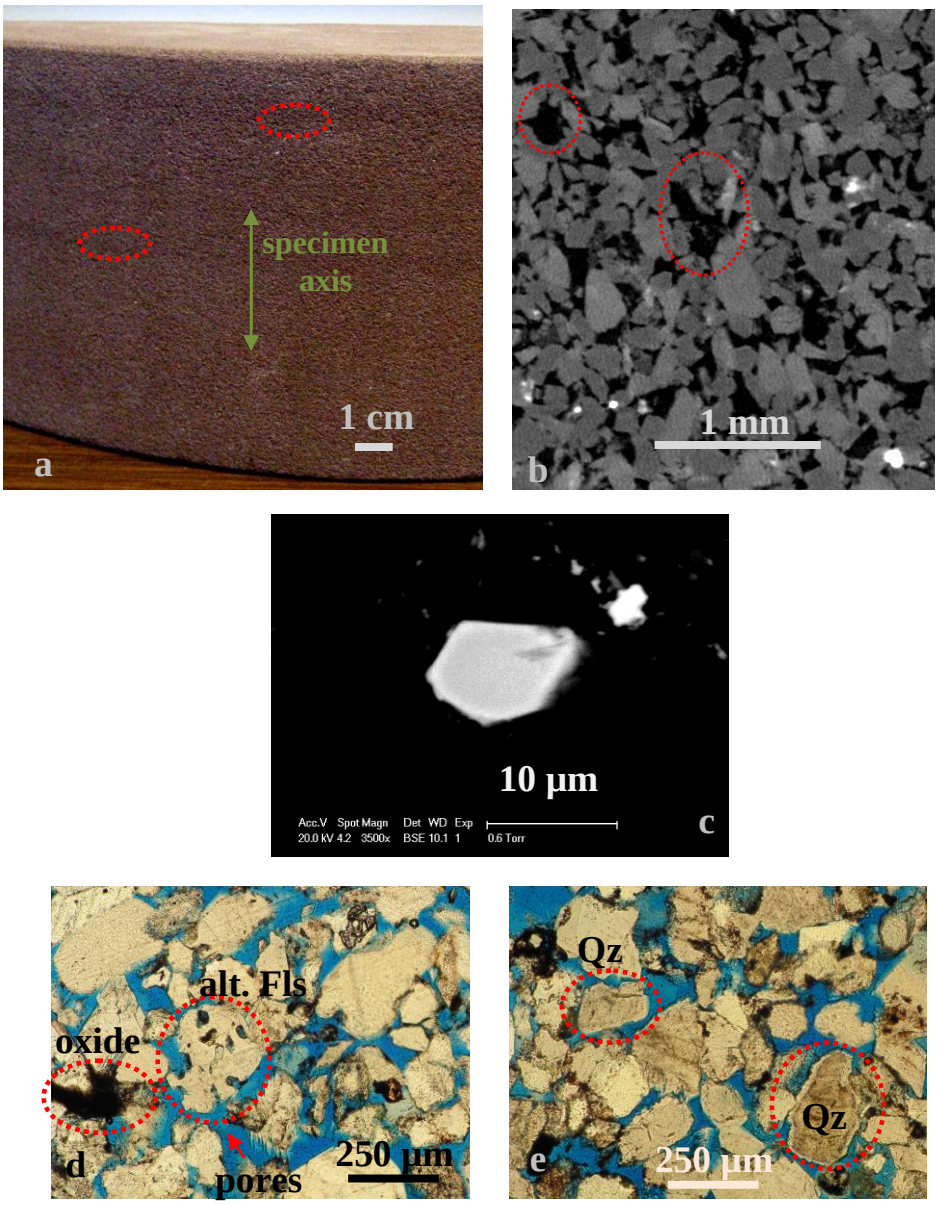

Fig. 4.2: (a) Photograph of the side of the intact rock block, showing darker layers on the top part; (b) Very HR x-ray image (~ 6 µm voxel-size) of the intact rock showing grains with sub-angular to rounded shape. The grain-sizes and pore-shapes, in some regions (circled), possibly correspond to a feldspar that had been removed; (c) SEM image of an oxide; (d,e) Optical microscope images illustrating several grains and their shape; examples of oxides, altered feldspar, quartz overgrowths (in red circle) and pore space (in blue, due to the blue epoxy impregnation) are shown.

The pore network of this sandstone tended to be rather inhomogeneous. For instance, in certain regions, some of the pores were rather small in size, while in other fewer regions the pores had a shape and a size resembling much to a grain (Fig. 4.2b). Observations of some grain-shaped pores suggested a weathering out of grains. Most probably some feldspar minerals, which could have been chemically altered to clays, had subsequently been transported out of the host rock. Such assumption is supported by observations of various chemically altered feldspar minerals, like those later presented in Figure 4.2d.

Mica flakes were aligned in layers with a dip of 7° to 8° degrees (Fig. 4.3). A similar dip was also identified in a couple of layers, visible to the naked eye, at the surface of the sandstone block (Fig. 4.2a). Some of the micas from the intact rock appeared slightly bent, probably due to rearrangement of the adjacent grains during the diagenetic processes (Fig. 4.3c). Although the percentage of micas in this rock was rather small (~1%), it is possible that micas would have played a role during the laboratory induced deformation. Furthermore, as micas deform rather easily, it is likely that they would have accommodated laboratory induced deformation in a similar way to during diagenesis (Fig. 4.3).

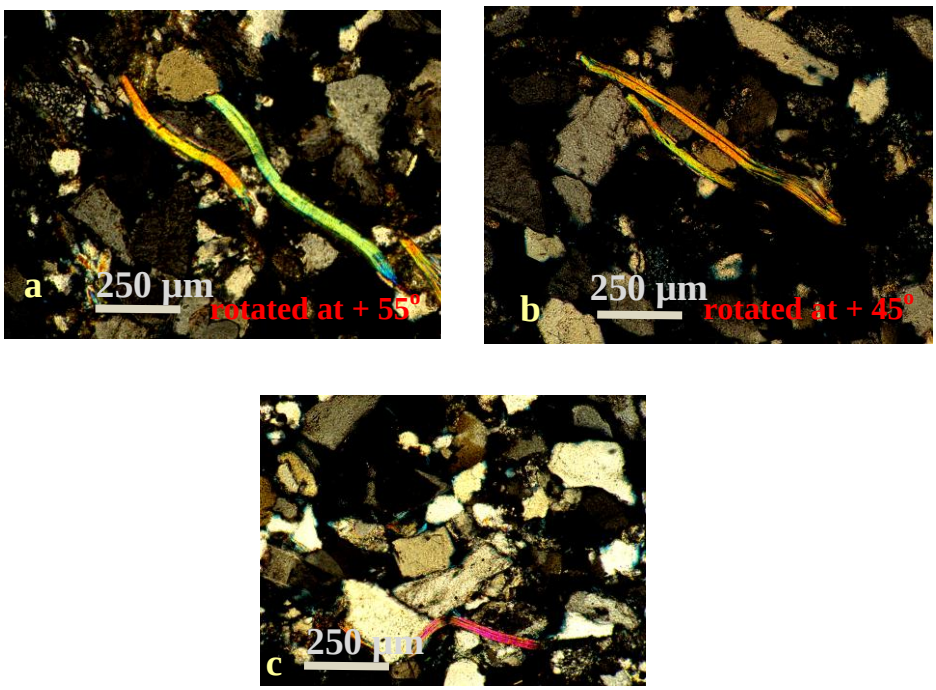

Fig. 4.3: Cross-polarised optical microscope images from the laboratory undeformed rock showing: (a), (b) Mica layers and near-by grains. These Figures are rotated at + 55^0 and + 45^0 to the vertical axis of the specimens; (c) Deformed mica due to diagenetic processes.

The cement, which binds together the grains, appeared mostly as quartz overgrowths (Fig. 4.2e). The presence of oxides was identified by both the x-ray tomography images (*i.e.*, oxides appeared as brighter grains, which indicated higher density, see Fig. 4.2b) and the SEM images (Fig. 4.2c). Figures 4.2a-4.2e illustrate the different observed aspects of the microstructure in this rock before laboratory deformation.

In addition, the Bentheim sandstone was partially used in this work for comparison. Bentheim sandstone is a more homogeneous sandstone of yellow colour containing 95% quartz, 3% feldspar and 2% kaolinite with a porosity value of about 22% and a mean grain-size of about 300 µm [*Stanchits et al.*, 2009]. No mechanical data of this sandstone are discussed here, since they have not been obtained within this work. The deformed specimen Be6 had been provided by *S.Stanchits* [*Stanchits*, 2010a] and only results on the post-deformation HR x-ray tomography images (resolution of ~ 30 µm voxel- size) are discussed in section 6.9.

Figure 4.4 presents x-ray tomography images (~30 µm voxel-size resolution) of both a Vosges specimen and a Bentheim specimen before any laboratory deformation. The scanning conditions, in terms of power (x-ray energy in kV and x-ray intensity in µA), were adapted for each of the materials to get the best possible image in each case.

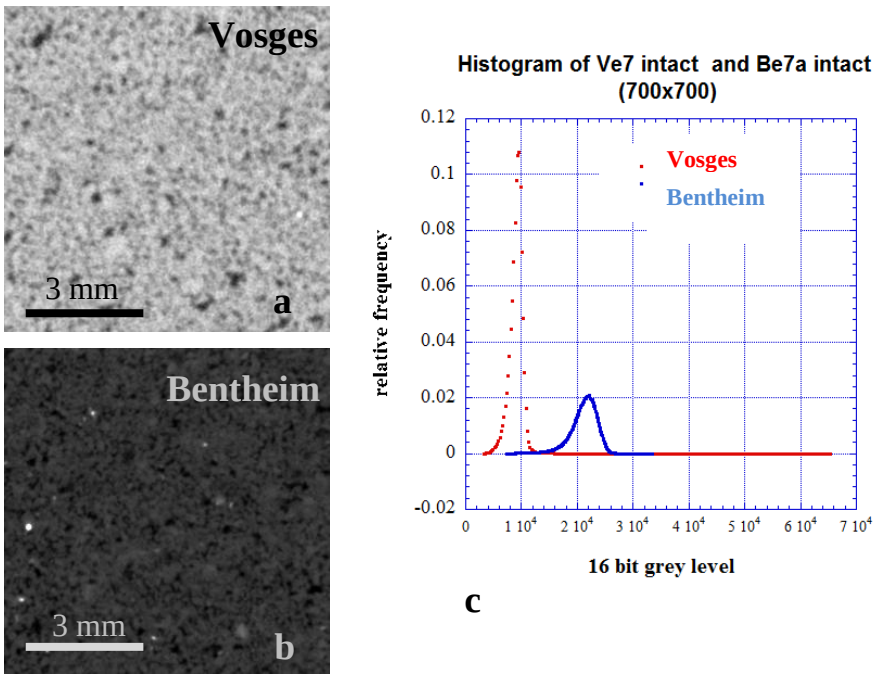

Fig. 4.4: (a), (b) Very HR x-ray tomography images (6 µm voxel-size) from the Vosges and the Bentheim intact sandstone specimens together with the histograms of the grey-scale from the x-ray images.

Although the thresholded grey level was set the same in both cases, considerable differences in the grey scale distribution occur possibly due to the different scanning conditions. Therefore, in Figure 4.4, the Bentheim sandstone shows a higher density compared to the Vosges sandstone, which is characterised by an overall lower density regardless the amount of oxides (higher density material). The calculated weighted standard deviation value of the grey scale for the Vosges sandstone is smaller compared to that of the Bentheim (*e.g.,* 2324 for the Bentheim, compared to 1176 for the Vosges), which implies that the Vosges has a more homogeneous density than the Bentheim. This might be attributed to the cementation of the former (a zoom in Fig. 4.4a,b shows more clear grain shapes in the Bentheim compared to the Vosges).

4.3 Preparation of the specimens

All specimens of Vosges sandstone presented were cored from the same block of material, perpendicular to the sedimentary bedding. Cylindrical specimens were made with diameters of 40 mm and a height of 80 mm (as in *Bésuelle's* work). However, one main difference in the geometry of the specimens, compared to *Bésuelle's* study, is that two opposite flattened surfaces were machined along their height. This particular geometry was necessary to facilitate the ultrasonic tomography measurements (section 3.2). Furthermore, notches were machined - for the majority of the specimens - as stress concentrators and encouraged the onset of localisation in the region between them. The role of notches is highlighted in Chapter 6. Figure 4.5 illustrates the different steps of the specimen preparation. Note that all surfaces (flattened and top and bottom surfaces) were polished to ensure perfect parallelism and minimum friction during testing.

The impact of a notch on the failure modes has already been studied for other sandstones [*Vajdova et al.*, 2003a; *Tembe et al.*, 2006; *Lin et al.*, 2009, *Stanchits et al.*, 2009]. The presence of a notch, usually, represents an induced structural heterogeneity. Different notch configurations, concerning the shape and position, have been used in order to observe the initiation and failure of the damage zone. A V-shape notch machined along the circumference of the mid-section of the specimen was used by *Vajdova et al.*

[2003a] and *Tembe et al.* [2006]. Similarly, a rounded shape notch was machined circumferentially, at the mid-height of the specimen by *Stanchits et al.* [2009].

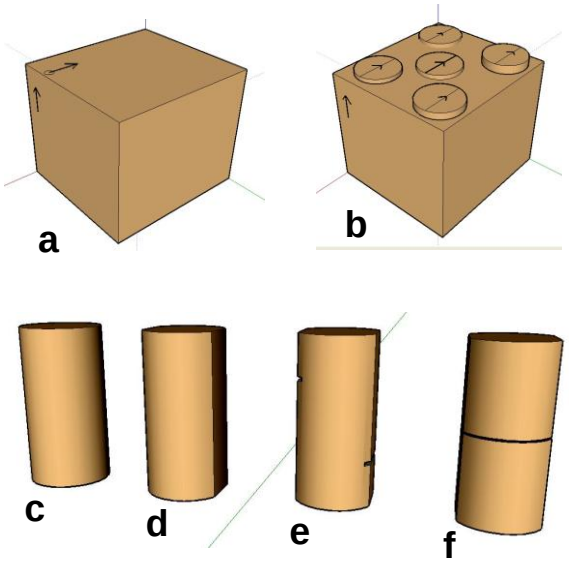

Fig. 4.5: Evolution of the specimen geometry: (a) Part of the block; (b) Cores normal to bedding with a specific orientation; (c) Cylindrical core; (d) Specimen with opposite flattened surfaces; (e-f) Specimens with two different notch shapes and positions.

Which could be the actual impact of the shape of the notch on the actual deformation processes? After *Lin et al.* [2009] the machined notch controls the onset of the damage zone as well the development and final position of the fracture. Characteristics of the notch, such as the size or the position, play an important role in the observed deformation, since the notch, being a stress concentrator, locally promotes higher deformation. Therefore, the size and the position of the notch determine the prevailing damage zone and thus, the position of failure, while, the final deformation characteristics (*e.g.,* length of damaged zone) are not much influenced [*Lin et al.*, 2009]. However, the size and shape of the notch may affect the number of deformation bands. In particular, a V-shape circumferential notch (about 5x5 mm) in Bentheim sandstone created the conditions for the formation of two compaction bands, above and below the notch [*Vajdova et al.*, 2003a, *Tembe et al.,* 2006], while a rounded shape notch (width of 4 mm and 0.8 mm height) facilitated the onset of a sole compaction band [*Stanchits & Fortin, 2010b*].

Two different notch configurations (Fig. 4.5e-f) were used in this work: (i) two notches on opposite flattened faces position with a vertical separation corresponding to a

pre-defined expected (shear) band angle for the relatively low confining pressures; (ii) a circumferential notch for the higher confining pressures when horizontal or sub-horizontal compaction bands were expected.

Bésuelle [2001] observed that for triaxial compression tests, at 50 MPa confining pressure, conjugate compactant shear bands developed in the upper part of cylindrical specimens (without any flattened surfaces). These bands had an orientation of about 50° towards the major imposed principal stress direction (dip of 40°). To encourage the occurrence of a shear band in the middle part of the specimen (where the observation techniques would be most effective), two offset round-ended notches (2.5 mm deep and 2.0 mm high) were machined on the flattened surfaces (Fig. 4.5e, 4.6b) for the case of the relatively low confining pressures. The position of the notches was determined according to the theoretical values of the deformation band angle as function of the confining pressure [*Bésuelle* 2001] (see Fig. 4.6a).

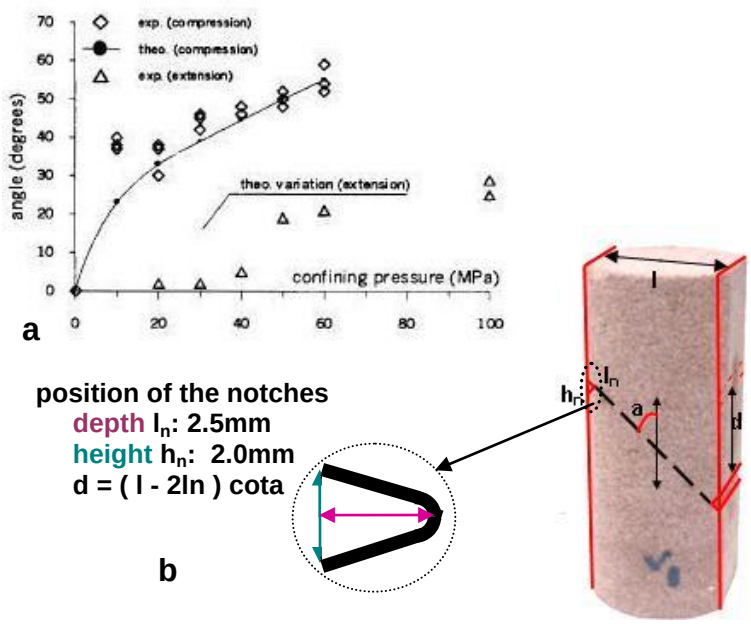

Fig. 4.6: (a) Theoretical and experimental values of the deformation band orientation as a function of the confining pressure values [*Bésuelle*, 2001]; (b) Picture of a Vosges sandstone notched specimen, and description of the notch characteristics.

For relatively higher confining pressures (*i.e.*, 130-190 MPa), a circumferential rounded notch of 4 mm depth and 0.8 mm height was machined at the specimens' mid-height (Fig.

4.7), to encourage and accelerate the onset of compaction band occurrence. *Stanchits et al.* [2009] showed previously that a similar notch geometry resulted into the onset of a single compaction band in Bentheim sandstone. Slight geometric imperfections of the notch could influence the propagation of the compaction bands [*Vajdova et al*., 2003a]. Figure 4.7 depicts the notch characteristics used for the higher-confining pressure experiments presented in Chapter 6.

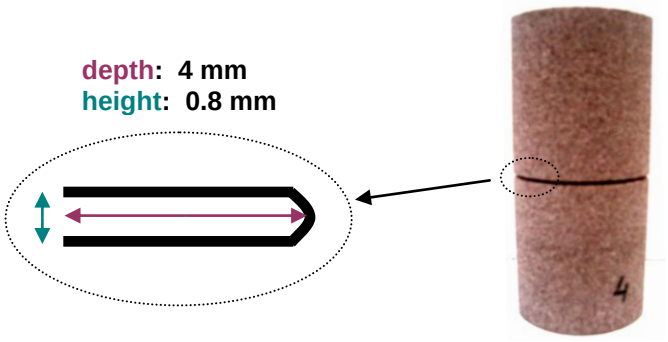

Fig. 4.7: Picture of a Vosges sandstone specimen having a circumferential notch and description of the notch characteristics.

4.4 Triaxial devices

Experiments were carried out at Laboratoire 3SR, in Grenoble, with the help of *P. Charrier*, and at German Research Centre for Geosciences (GFZ), in Potsdam, in collaboration with *S. Stanchits*. The triaxial cell at Laboratoire 3SR is able to sustain a confining pressure up to 60 MPa and a deviatoric stress up to 270 MPa. Therefore, the experiments from 20 to 50 MPa confining pressure were performed in Grenoble. To study the impact of higher confining pressures on the failure mode of Vosges sandstone specimens, the triaxial cell at GFZ was used. Moreover, since recording of AEs during an experiment is feasible at GFZ, an extra test at 50 MPa confining pressure was performed there, in addition to the experiments at relatively high confining pressure. This experiment served also as a comparative test, so as to infer whether similar localised

features are observed in specimens tested under the same confining pressure, in different triaxial cells. A brief description of the experimental devices used at both laboratories follows.

4.4.1 Experimental device at Laboratoire 3SR

The triaxial device at 3SR is a *Bishop & Wesley*-type stress path triaxial cell, which can be used for automated stress or strain control tests. As mentioned, the system sustains a confining pressure of 60 MPa and a deviatoric stress up to 270 MPa.

Figure 4.8 shows the triaxial apparatus at 3SR, which consists of two parts; the upper (1) and the lower (4). These two parts are joined by eight bolts (9). The upper part (1) hosts a self-compensating piston (‘balanced ram’ for the axial load) (2). The piston is pushed from the top chamber (3) by oil pressure. The lower part of the cell (4) allows application of a confining pressure and a back-pressure to the specimen (5), which is usually jacketed in a neoprene membrane of a thickness of 0.7 mm (6) so as to avoid a confining oil penetration. Local axial and radial strain can be measured using strain gauges glued directly onto the membrane that jackets the specimen. Both upper and lower load caps (7) are connected to drainage lines. Different pore pressures can, therefore, be imposed at the ends of the specimen, in order to allow fluid flow and measurement of the rock permeability under load. In this work, such measurements were not performed. Furthermore, two intermediate smooth enlarged plates (8), used to insure a frictionless interface and avoid edge effects, are attached at each end of the specimen to match its diameter to the somewhat larger diameter of the load caps. Four identical independent pressure-volume controllers supply four different pressures (*i.e.*, the deviatoric stress, the confining pressure, and the top and bottom pore pressures).

During these experiments, only the deviatoric stress and the confining pressure were recorded (dry samples). All triaxial compression tests were performed under strain control, at a constant rate of axial displacement. Such displacement control is necessary to experimentally follow the post-peak portion of the specimen response. Further information on the triaxial apparatus at 3SR can be found in *Bésuelle* [1999]; *Bésuelle et al.* [2001], and *Coll* [2005].

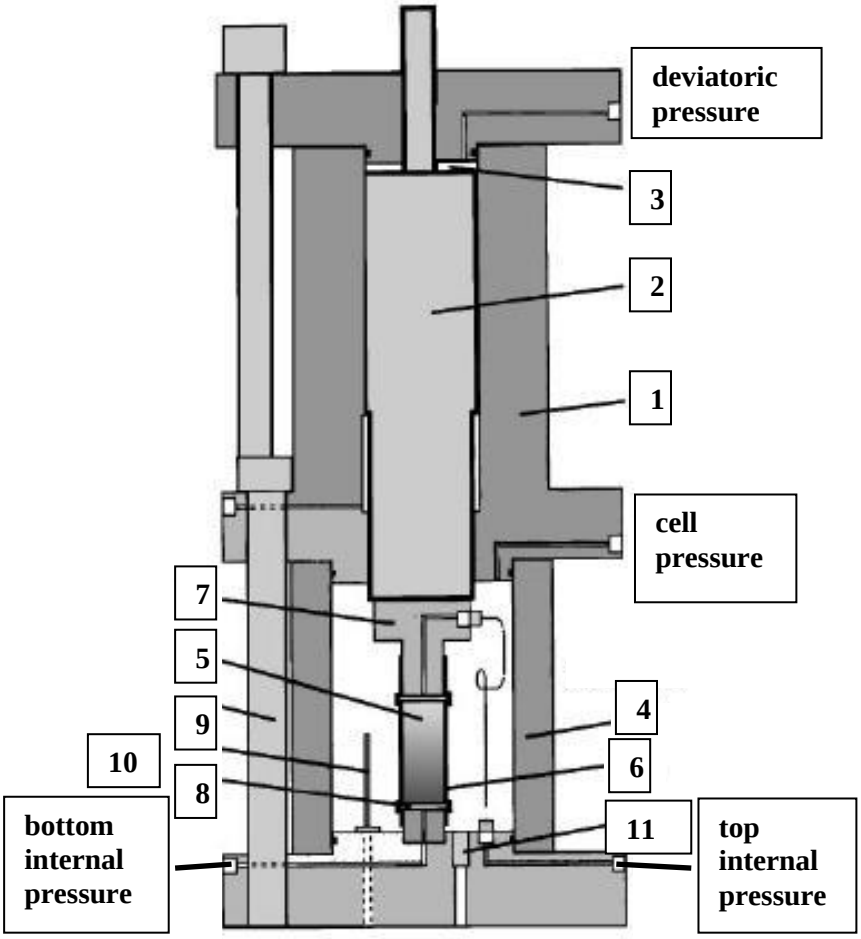

Fig. 4.8: Schematic representation of the triaxial cell at 3SR: (1) Upper part of the cell; (2) Self-compensated load piston; (3) Deviatoric pressure chamber; (4) Lower part of the cell; (5) Specimen; (6) Neoprene membrane; (7) Load caps; (9) Bolts; (10) Steel sheath; (11) Internal tight connectors.

4.4.2 Triaxial cell at GFZ

The apparatus at GFZ consists of a servo-hydraulic loading frame from Material Testing Systems (MTS) with a load capacity of 4600 kN and a triaxial cell sustaining a confining pressure up to 200 MPa. An important characteristic of this system is the ability to record AEs and ultrasonic transmission signals throughout the duration of the experiments.

Figure 4.9 shows a schematic representation of the apparatus, which consists mainly of the confining pressure chamber (1) and the MTS ram (2). The piston (3) on which the specimen sits (4) is placed on the MTS ram and is screwed on the confining pressure

chamber. A P-wave piezoelectric transducer is embedded in its top part, which is in contact to the specimen. The end-cap (5), placed on the top of the specimen, also incorporates a P-wave piezoelectric transducer. Therefore, P-wave measurements parallel to the specimen's loading axis are feasible during the experiments. P- and S-wave piezoelectric transducers (7) can be glued directly on the cylindrical surface of the specimen in order to make ultrasonic measurements at angles to the loading axis during the test.

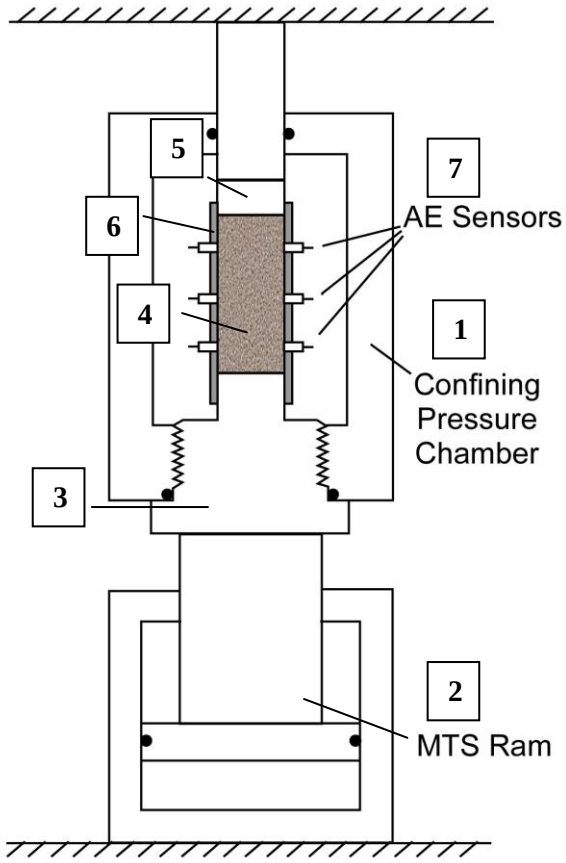

Fig. 4.9: Schematic representation of the triaxial cell at GFZ: (1) Confining pressure Chamber; (2) MTS Ram; (3) Piston, which embeds a P-wave piezoelectric transducer, and to which the cables of the AE sensors are connected; (4) Specimen; (5) Top end-cap, which embeds a P-wave piezoelectric sensor; (6) Neoprene membrane, which jackets the specimen and has been pierced so as the AE sensors could be directly glued on the surface of the specimen; (7) AE Sensors: P- and S-wave piezoelectric transducers.

These transducers are sealed to a Neoprene membrane (6) using two-component epoxy. The Neoprene membrane, which jackets the specimen, has been previously pierced in places where the sensors are later glued on. The positions of the sensors used during the

experiments carried out at GFZ, were illustrated in section 3.3. The sensors are connected with cables to the base of the piston.

4.5 Testing program and experimental set-up

The experimental program consisted of thirteen triaxial compression experiments on dry Vosges sandstone specimens. The tests involved an initial phase of isotropic compression, during which the confining pressure on the specimen was increased from zero to the largest pressure for the given experiment (between 20 to 190 MPa) at a constant rate of 1 MPa/min. The subsequent phase of deviatoric loading was performed under a displacement control at a rate of 20 μm/min (for both experiments carried out at 3SR and GFZ). The axial loading was stopped at different axial strain levels (see sections 4.6 and 4.7), after which the specimens were fully unloaded.

Different measurements were taken before, during, and after the triaxial experiments. In particular, before (pre-deformation) and after (post-deformation) the experiment, elastic wave measurements were carried out and LR and HR x-ray scans were performed. For some of the triaxial tests, ultrasonic transmission measurements were made and AEs were recorded during the experiment (syn-deformation). Thin sections were prepared for some of the deformed specimens. Additionally, small specimens were cored from the regions of localised deformation of some specimens and very HR x-ray scans were performed on such cores. Not all techniques were applied for every specimen, due to practical difficulties. Table 4.1 summarises the measurements taken for each experiment.

The set-up for each of these measurements was described in Chapter 3. Concerning the triaxial compression experiments the following points are highlighted. For all experiments carried out at 3SR, the interfaces between the metallic disks used as spacers and the specimen ends were lubricated with a mixture of stearic acid and vaseline [*Labuz and Bridel*, 1993]. However, this was not the case for the experiments carried out at GFZ. In particular, no extra interface was used for experiments on specimens Ve4, Ve5, and Ve1, while a Teflon interface was used on specimens Ve6, Ve7, and Ve2 acting as lubricant (Fig. 4.10c, 4.10d). Relatively increased AE activity was recorded at the specimen edges when no Teflon was used, which is assumed to be associated with the

friction with the end-caps. Note that metallic discs (platens) were placed at the top and bottom edges of the specimen, similarly to the experiments carried out at 3SR (Fig. 4.10c). Furthermore, both in the present study and the work by *Stanchits et al*. [2009], the circumferential notch was filled with a 0.7 mm thickness Teflon O-ring preventing the membrane from entering the notch and so reducing the risk of failure of the experiment due to an oil leakage through the membrane. In addition, two extra Teflon pieces, which were matched to the flattened surfaces of the specimen, were used during the triaxial experiments carried out at GFZ (Fig. 4.10a, 4.10b).

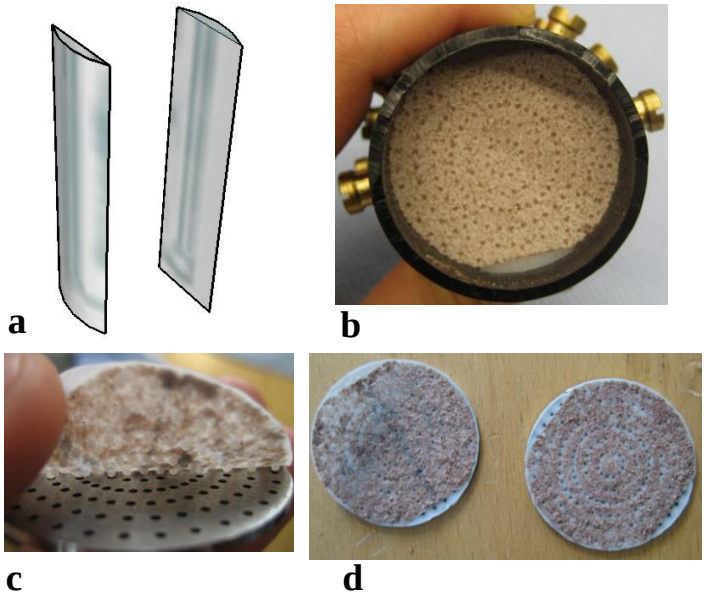

Fig. 4.10: (a) Teflon pieces matching the flattened surfaces; (b) Specimen's top edge; (c) Metallic disks and Teflon film; (d) Teflon films used at the top and bottom edges of the specimen as lubricants

Table 4.1: View of different measurements performed in every test of this experimental campaign. The triaxial compression experiments carried out at 3SR are highlighted in orange and those carried at GFZ are highlighted in blue. Photographs of the meso-scale failure (specimen-scale) from experiments subjected up to 50 MPa confining pressure can be seen in Figure 4.12. SB stands for shear bands and CB for compaction bands. Symbols 'v' and 'x' stand for 'yes' and 'no', respectively.

name of specimen	notches	confining pressure	deformation bands	measurements										
				UT		AEs	x-ray CT					3D DIC		thin sections
				pre-	post-	syn-	pre-		post-			pre-, post-		post-
							LR	HR	LR	HR	VHR	LR	HR	
VEC2	✓	20 MPa	fracture	✗	✗	✗	✗	✗	✗	✓	✗	✗	✗	✗
VLR00	✓	20 MPa	SB	✗	✓	✗	✗	✗	✗	✓	✗	✗	✗	✗
VET3	✓	30 MPa	SB	✓	✓	✗	✓	✗	✓	✓	✗	✓	✗	✓
VLR0	✓	50 MPa	SB	✗	✓	✗	✗	✗	✗	✓	✗	✗	✗	✗
VEC1	✓	50 MPa	SB	✓	✓	✗	✗	✗	✗	✓	✓	✗	✗	✓
VEC4	✓	50 MPa	SB	✓	✓	✗	✓	✗	✓	✓	✗	✓	✗	✓
VEC5	✓	50 MPa	SB	✓	✓	✗	✓	✗	✓	✓	✗	✓	✗	✗
Ve2	✓	50 MPa	SB	✓	✗	✓	✓	✓	✓	✓	✓	✓	✓	✓
Ve4	✓	130 MPa	CB	✗	✓	✓	✓	✓	✓	✓	✓	✓	✓	✓
Ve6	✓	130 MPa	CB	✓	✗	✓	✗	✓	✗	✓	✓	✗	✓	✓
Ve1	✗	160 MPa	CB	✗	✓	✓	✓	✗	✓	✓	✓	✓	✗	✓
Ve5	✓	160 MPa	CB	✗	✓	✓	✓	✓	✓	✓	✗	✓	✓	✗
Ve7	✓	190 MPa	CB	✓	✓	✓	✗	✓	✗	✓	✗	✗	✓	✗

Specimens VLR00 VLR0 were tested during L.Restaino's Master Thesis [2008].

Specimen VET3 was tested during E. Tudisco's Master Thesis [2009].

4.6 Low and intermediate confining pressure experiments (20-50 MPa): *shear bands*

Figure 4.11 presents a schematic representation of the localised bands developed in Vosges sandstone specimens loaded under triaxial compression and extension (for different slenderness ratios) for a range of confining pressures from 0 to 60 MPa [*Bésuelle*, 1999]. The angle of the shear bands with respect to the major imposed principal stress direction increases with the confining pressure. An increase in the confining pressure results also in more numerous and closely spaced bands.

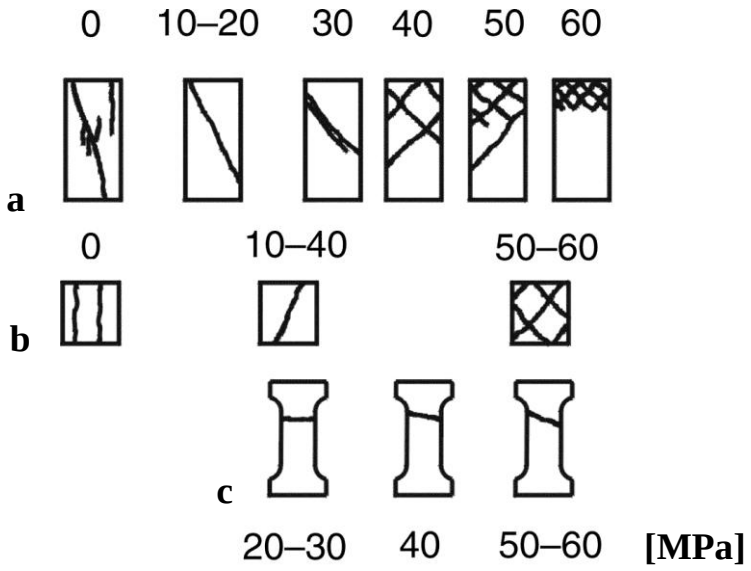

Fig. 4.11: Illustrations of observed shear band patterns with changing confining pressure for compression tests (a, b) with two slenderness ratio values H/D=2 and H/D=1, respectively, and for extension tests (c) [*Bésuelle*, 1999].

Figures 4.12 show images of the deformed Vosges sandstone specimens, loaded under 20, 30 and 50 MPa confining pressure. All specimens from this experimental campaign were tested dry and had notches machined at their flattened surfaces, as described earlier (section 4.3). In these experiments, either a single strain localisation feature developed between the notches (Fig. 4.12a, 4.12c), or more than one bands developed (Fig. 4.12e-4.12h). Note that specimens VLR0 and VLR00 were taken to a very small axial strain; therefore, although localisation was captured by the full-field methods (see Chapter 5), no visual signs of damage were identified on the surface of these specimens (Fig. 4.12b, 4.12d

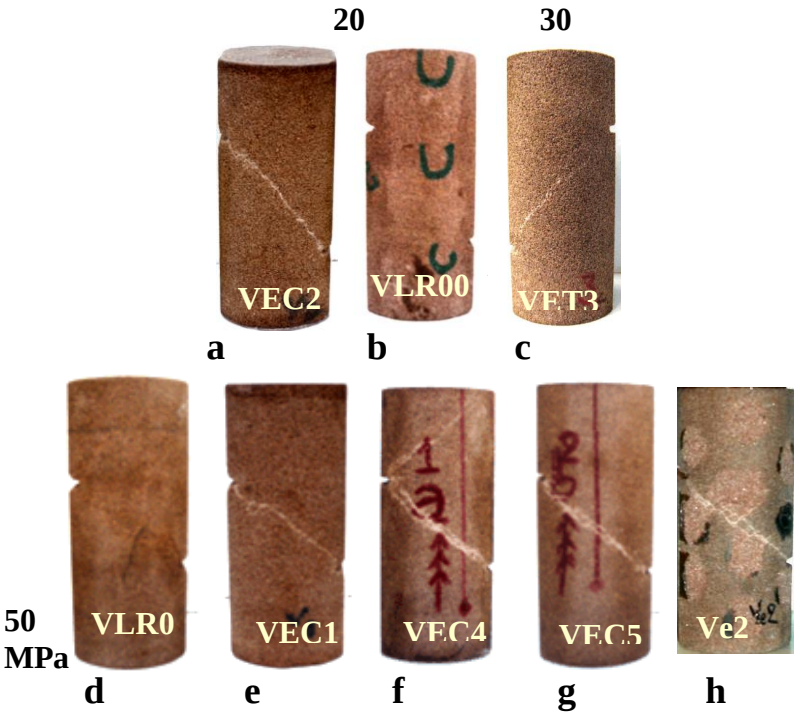

Fig. 4.12: Pictures of deformed Vosges specimens loaded under 20 MPa (a,b), 30 MPa (c), and 50 MPa (d-h). All specimens had notches machined at their flattened surfaces.

Recall that the aim of all experiments loaded under relatively low confining pressures was to investigate the onset and evolution of localised features using full-field methods. The mechanical response of this material had been well characterised over this pressure range by [*Bésuelle*, 1999; 2001; 2002]. For this reason no local LVDT measurements were taken during the triaxial compression experiments (with the only exception of specimen Ve2 tested at GFZ). Figures 4.13a, 4.13b and 4.13c present the mechanical response of experiments VEC2 and VLR00 (at 20 MPa), VET3 (at 30 MPa) and VLR0, VEC1, VEC5, and VEC4 (at 50 MPa), respectively. The stress deviator (which is the difference between the major and minor principal stress in a triaxial compression experiment) is plotted versus the axial strain from the piston displacement. All these experiments were carried out at 3SR. Specimens loaded at these different confining pressures were taken to different axial strain values. The loading and unloading curves are shown for all specimens (unloading is not fully shown for specimen VLR00 and VET3).

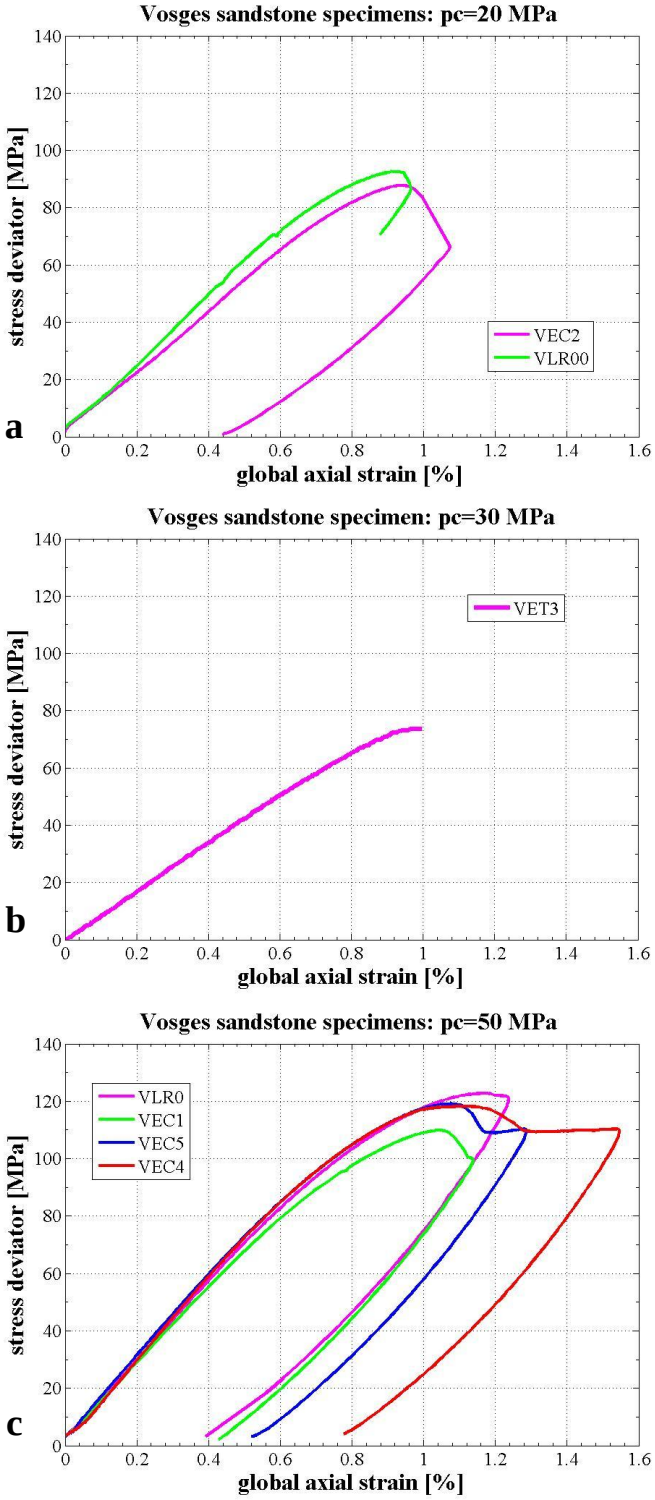

Fig. 4.13: Stress-strain response from specimens loaded under 20 MPa (a), under 30 MPa (b) and under 50 MPa (c) confining pressures. Stress deviator is plotted versus global axial strain. Specimens were taken to different axial strain values.

Axial strain, stress deviator, and confining pressure were monitored during the experiments. Axial strain was computed from the displacement of the cell piston (measured by an external transducer to the cell). The axial stress was calculated by the load value, measured by the internal load cell, divided by the initial cross-sectional area of the specimen, assuming that the cross-sectional area remained constant throughout the experiment, which is a reasonable approximation. Compaction is positive and dilation is negative, for both the mechanical data (present chapter) and the strain fields (Chapter 5 and 6).

Specimen VLR00 was unloaded soon after the peak-stress; no measurements of the full unloading were taken for this specimen. No visible signs of deformation were apparent at the surface of the VLR00 after unloading. Specimen VEC2 was taken to a higher axial strain (1.08% compared to 0.96% for the VLR00). Moreover, specimen VEC2 was characterised by slightly smaller stress deviator values for the same axial strain compared to the VLR00. At 20 MPa confining pressure, the formation of shear bands in Vosges sandstone was accompanied by strain softening, which lead to sudden fracturing with a small increase in the axial strain. In fact, specimen VEC2 was partially fractured after loading because it was unloaded relatively late. Therefore, apart from post-mortem HR x-ray scans, no other full-field measurements were taken for this specimen (see section 5.5).

Specimen VET3 (loaded under 30 MPa confining pressure) was unloaded soon after the peak-stress. No measurements of the full unloading were taken for this specimen (like for VLR00). A shear band was visible between the notches of specimen VET3 (Fig. 4.12). This specimen had a peak stress deviator value lower than those observed in specimens VLR00 and VEC2 (at 20 MPa confining pressures). This difference in the peak stress is attributed to the fact that no accurate load measurements could be made on this specimen (due to a problem with the internal load cell; thus stress deviator values were approximately corrected from the values of the internal pressure of the piston).

At 50 MPa confining pressure, the formation of shear bands in Vosges sandstone was also accompanied by strain softening (like at 20 MPa), however, the increasing axial strain resulted in strain hardening soon after the development of the shear band(s) (unlike at 20 MPa). Specimens VLR0, VEC1, VEC5, and VEC4 were taken to 0.03%, 0.09%, 0.205% and 0.425% of axial strain above the peak-stress deformation (which could be easily identified from the stress-strain curves). The slightly lower stress deviator values

observed in specimen VEC1 could be attributed to possible textural heterogeneities of the specimen. The number of the obvious by-naked-eye traces of deformation bands on surface of the specimen increased with increasing axial strain values (Fig. 4.12).

Specimens VLR00 and VLR0 were tested during *Restaino's* Master thesis [2008]. Note that further investigation of the failure mechanisms, which occurred in these two specimens, via the full-field methods was carried out during this thesis. Specimen VET3 was tested during *Tudisco's* Master thesis [2009]. Thin sections were prepared from this specimen during this thesis.

Specimen Ve2 is discussed separately, since it was tested at GFZ. Note that for this specimen internal local LVDTs (two vertical and one horizontal) were used to measure the axial and radial local strain. During the isotropic compression stage the readings of the LVDTs were influenced by the increasing confining pressure. Therefore, only the data from the deviatoric loading stage were analysed.

Figure 4.14a presents the stress deviator as a function of the axial strain (calculated by the displacement of the piston and corrected for the compliance of the apparatus, in black) and the local axial strain (calculated by the one of local LVDTs, in red). The axial strain measured by the LVDTs concerns the central part of the specimen, where the shear band formed. Note that the LVDTs were attached from +10 mm to +70 mm from the bottom of the specimen. The global axial strain measured by the displacement of the piston is sensitive to the strain in the whole specimen. The latter has a lower stiffness and also shows a greater decrease in the stiffness during loading. This is attributed to additional strain and damage at the ends of the specimen, where it contacted with loading platens. The calculated global and local displacements differ at about 7.5% (Fig. 4.14b). In Appendix B, the measured global and local displacements are compared to the equivalent displacements calculated by the 3D-DIC.

Figure 4.14b illustrates all axial strains (local from the LVDTs and global from the piston) versus the global axial strain. Although the axial strain measured by LVDT2 indicates strain softening, it is much smaller than that measured by LVDT1 or the piston. Furthermore, from Figure 4.14b is not straightforward to distinguish any initial sign of the localised deformation before the peak stress (maximum axial strain of 1.27%).

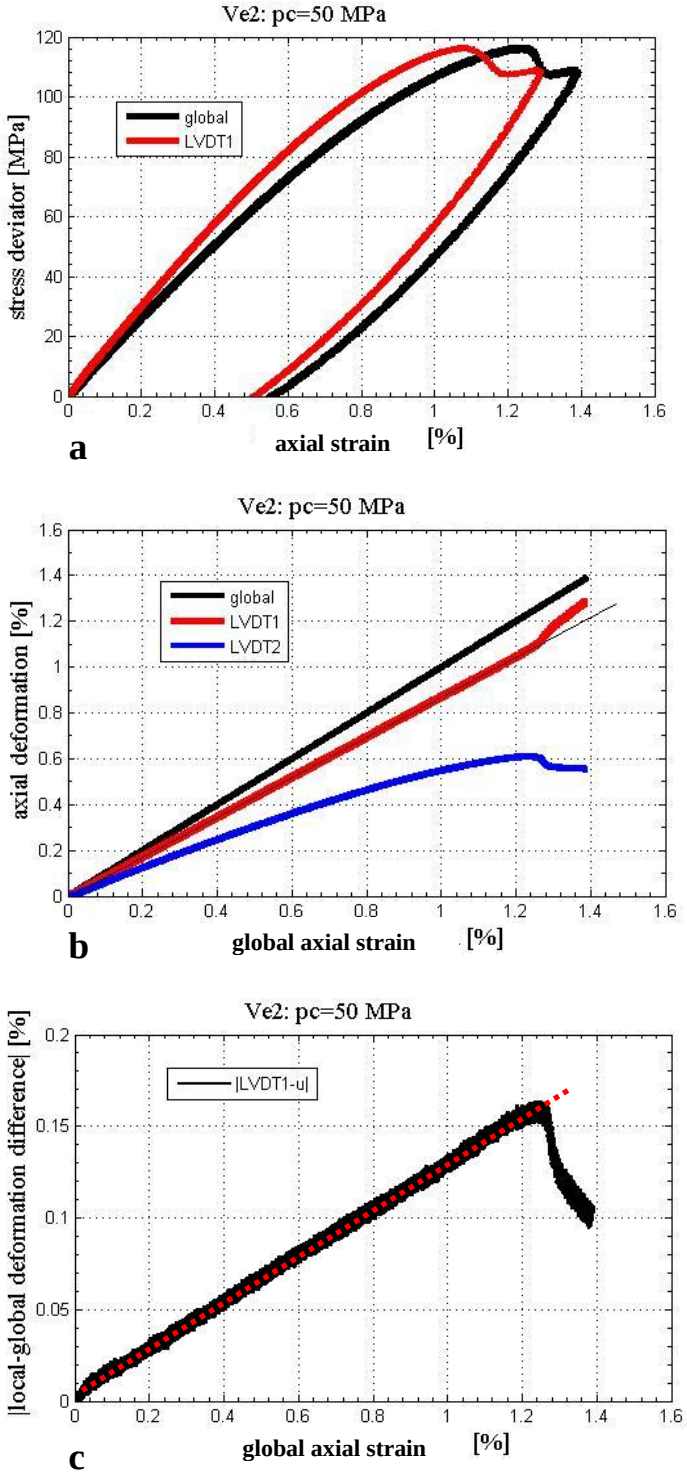

Fig. 4.14: Specimen Ve2: (a) Stress deviator versus axial strain; (b) Axial strain from the local LVDTs, and the displacement of the piston as a function of the axial strain of the latter; (c) Absolute difference of local and global axial strain versus global axial strain.

A slight deviation from the linear trend can be distinguished in Figure 4.14c, which presents the absolute difference of the local axial strain (LVDT1) and the global axial strain (piston) versus the global axial strain, for axial strain values higher than 1.2%.

Figure 4.15a presents the volumetric strain (calculated from the measured values of LVDT1 and the radial LVDT) as a function of the global axial strain and Figure 4.15c shows the stress deviator as a function of the axial strain. Seven segments of these loading curves have been identified in places where the gradient changes (see Fig. 4.15a and 4.15c), the last corresponding to the strain softening part (Fig. 4.15c). Note that changes in the gradient are more obvious in Figure 4.15c than in Figure 4.15a.

In order to visualise the 3D distribution of the AE events between the chosen axial strain values, the axial strain space was projected to the time space (the appropriate stress deviator values were initially identified in the axial strain space and then projected to the time space). Figure 4.15b illustrates the 2D y-z vertical projections of the 3D AE distributions for specimenVe2 (throughout the whole volume of the specimen), over the six first axial strain increments shown in Figures 4.15a and 4.15c. AE event amplitudes higher than 0.5 Volts were set for these 2D projections; the accuracy of the AE hypocentre locations is 2 mm (+/- 1 mm from the edges of the specimen). It could be argued that the choice of the strain segments shown in Figures 4.15a and 4.15c is quite subjective since changes in the gradient of the curves can also be observed inside some of the defined strain segments (*e.g.*, segment 2, in Fig. 4.15c). However, it should be noted that 2D AE projections produced for strain values inside the chosen strain increments (not shown here) did not show much different AE location maps from those presented in Figure 4.15b.

No AE activity was recorded (for the given amplitude threshold) for an axial strain lower than 0.4% (Fig. 4.15b, image 1). From 0.4% to 0.9% of axial strain, AE activity was located mainly at the notches, and only some diffuse AEs were located in the region between the notches (Fig. 4.15b, image 2). From 0.9% of axial strain a small number of AEs concentrated at the centre of the region between the notches (Fig. 4.15b, image 3), while from 1% of axial strain, some more AEs started locating in this (Fig. 4.15b, image 4). From 1.04% of axial strain a much greater number of AEs were located in the region of the subsequently determined zone of localised deformation (Fig. 4.15b, images 5, 6).

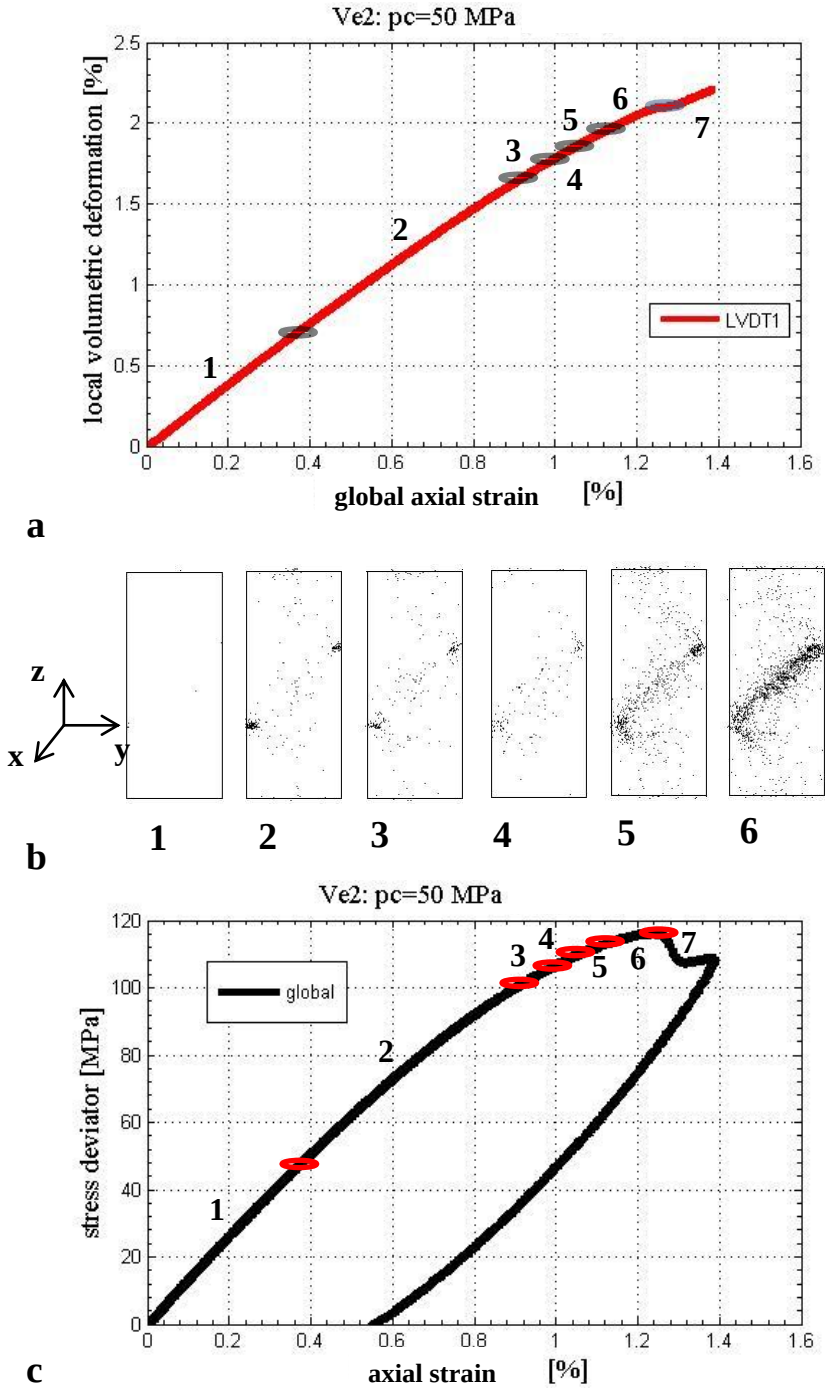

Fig. 4.15: Specimen Ve2: (a) Local volumetric strain versus axial strain; (b) Images from 1 to 6 illustrate the 2D vertical projections (y-z) of the 3D AE distributions throughout the volume of specimen Ve2. These projections correspond to the axial strain intervals highlighted in (a, c); (c) Stress deviator versus axial strain.

From the AE locations (Fig. 4.15b), it could be argued that the onset of the formation of strain localisation occurred at around 106-109 MPa of stress deviator (image 5), while the

peak stress deviator value is equal to 116 MPa (after image 6). Furthermore, it is interesting to mention that before image 5 a small AE activity was located initially at the notches and later in the central distance between the notches.

4.7 High confining pressure experiments (130-190 MPa): '*compaction bands*'

Figure 4.16 present the mechanical response of specimens Ve4, Ve6 (at 130 MPa), Ve5, Ve1 (at 160 MPa) and Ve7 (at 190 MPa). The stress deviator is plotted as a function of the axial strain from the piston displacement. Only the loading curves are shown. All these experiments were carried out at GFZ. Specimens loaded dry at these three different confining pressures were taken to different axial strain values (*e.g.*, Ve4, Ve6) and had or did not have a circumferential notch (*e.g.*, Ve5, Ve1). Local LVDTs were also used in all these experiments. After the loading stage, all specimens were fully unloaded.

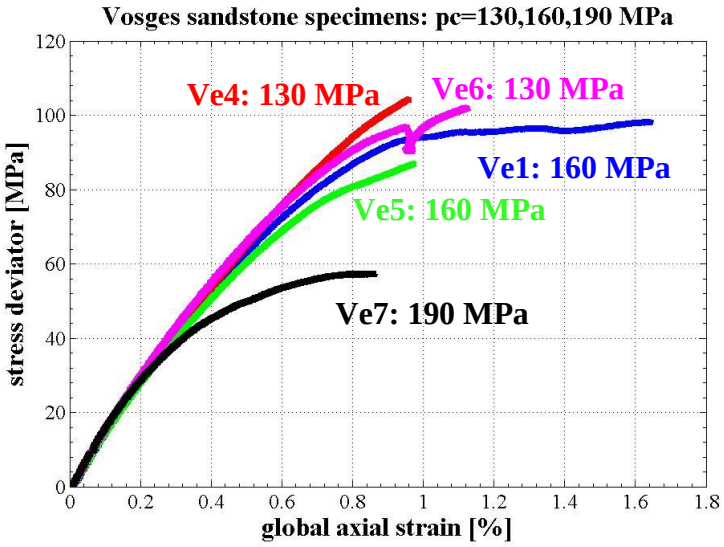

Fig. 4.16: Stress-strain response from specimens loaded under 130 MPa , 160 MPa, and 190 MPa confining pressure. Stress deviator is plotted versus global axial strain. Specimens were taken to different axial strain values and had or did not have a notch on their surface.

Strain hardening took place in all specimens deformed under confining pressures between 130 and 190 MPa. From Figure 4.16, it appears that the maximum stress deviator value decreases with increasing confining pressure, which indicates that the mean p-q values

from these experiments are placed on the cap of the yield surface at the p-q plane (for further details see Chapter 7). Furthermore, the role of the notch on the value of stress deviator is highlighted by the stress-strain curve of specimens Ve5 (with a notch) and Ve1 (without a notch).

It was not straightforward to determine the onset of localised deformation in these experiments due to the absence of a clear peak in the stress-strain responses obtained. Additionally, the readings of the LVDTs were not always reliable during the deviatoric compression part (*i.e.*, one of the LVDTs might have failed during the experiment), thus, it was not always easy to get a representative local volumetric strain measurement.
Note that the method suggested by *Wong et al.* [1997] (see Chapter 2) could not be applied to these experiments due to lack of volumetric strain data from the isotropic compression part of the experiments for a number of reasons (specimens were tested dry, no strain gauges were used and local LVDTs were not sensitive during that loading part). For such reasons, the identification of the onset of inelastic deformation was acquired by combining the reliable mechanical results (meso-scale) with the AE analysis (transitional measurements from meso- to micro-scale, *i.e.*, specimen- and grain-scale, respectively; see also Chapter 7). In this section, results from experiments Ve4, Ve6, Ve5, Ve1, and Ve7 are presented.

Experiment Ve4 was stopped soon after the initiation of the compaction bands, in order to focus on the early stage of their propagation. Note that for this specimen no lubricant was used on the top and bottom ends; therefore, the specimen was in direct contact with the metallic spacers (see Fig. 4.10).

Figure 4.17a presents the stress deviator as a function of the axial strain. The axial strain measured by the local LVDTs was calculated from the displacement of the LVDTs divided by their length (local axial strain). The global axial strain was calculated by the displacement of the piston, which was corrected for the loading system's compliance, divided by the initial length of the specimen. Probably as a result of the damage on the top and bottom boundaries of the specimen, the stiffness derived from the local LVDTs was higher than that from the global strain (piston). Note that already at the beginning of this experiment, the two Young moduli were not the same, which could be attributed to bad calibration of the LVDTs (see Appendix B for a further comparison of the LVDT displacements with the local DIC displacements). However, given that both LVDTs'

displacements had relatively close values during the loading history, they could still be used for the identification of the onset of localised deformation.

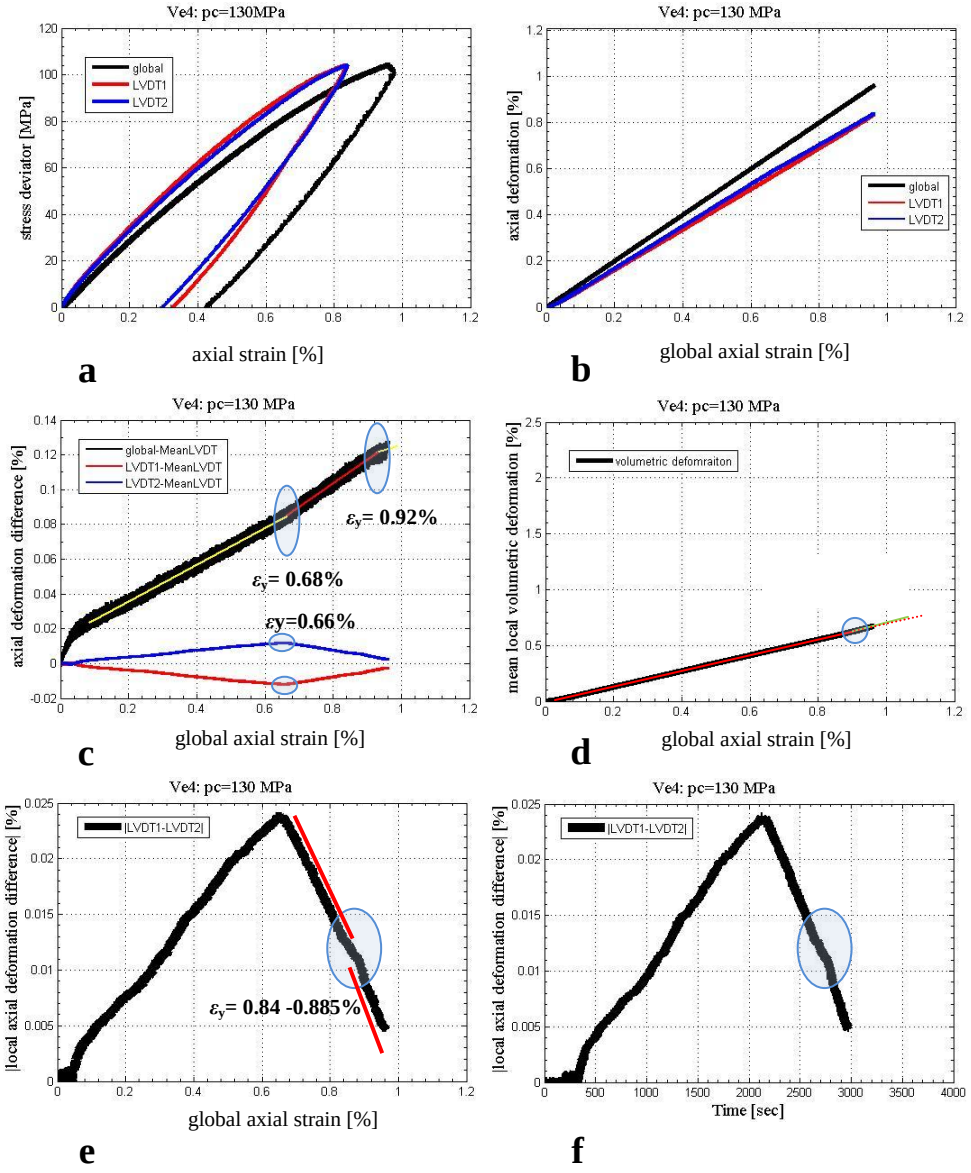

Fig. 4.17: Stress-strain responses from experiment Ve4: (a) Stress deviator versus axial strain; (b) Axial global and local strains versus axial global strain; (c) Axial global and local strain difference from the mean axial local strain versus axial global strain; (d) Volumetric strain, measured by the local LVDTs, versus axial global strain; (e) Absolute difference between the local axial strains versus axial global strain; (f) Absolute difference between the local axial strains versus deviatoric compression time.

Figure 4.17b presents the two local and global axial strains as a function of the global axial strain. From this plot, no particular signs of the onset of localised deformation could

be observed. Only slight differences in the two local LVDT measurements could be identified. To get a better understanding of the strain measurements, Figure 4.17c presents the difference between the local and global strains from the mean local strain as a function of the global axial strain. Three global strain values were identified from this plot (axial strain of 0.66% and, of 0.68% and 0.92%) in places of deviation from the linear trend.

Figure 4.17d plots the volumetric strain (calculated by the mean local axial (ε_l) and the local radial ($\varepsilon_r=\varepsilon_2=\varepsilon_3$) strains, $\varepsilon_v=\varepsilon_1+2\varepsilon_r$) as a function of global axial strain. The axial global and volumetric strains show a generally linear relationship, however, a slight deviation from this is observed around 0.88% of global axial strain.

Figure 4.17e presents the absolute difference of the local axial strains (from LVDT1 and LVDT2) as a function of the axial global strain. A distinctive difference was observed for axial strain of 0.66% (like in Fig. 4.17c) and from 0.84% to 0.885%. Figure 4.17f shows the absolute difference of the local strains as a function of the deviatoric compression time history.

Figure 4.18b shows the y-z vertical projections of the 3D distribution of the AE events, inside the specified strain intervals (Fig. 4.17, Fig. 4.18a). These 2D projections subplot AE events within x=+-2 mm from the centre of the specimen. Note that AE projections within the whole volume (like in Fig. 4.15b) gave denser AE maps, in which the onset of localised deformation could not be identified. This is linked to the use of the circumferential notch, which acted as stress concentrator. Recall that the specimens tested under lower confining pressures had notches only on their flattened surfaces.

AE events up to 0.66% of axial strain are illustrated in image 1 (Fig. 4.18b), from 0.66% to 0.68% in image 2, from 0.68% to 0.874% in image 3, from 0.874% to 0.92% in image 4, and from 0.92% up to the end of loading in image 5. Localisation of the AE events into a band is visible from image 3 and on, although, in image 1, some AE activity is observed close to the notches.

Figure 4.19 presents, in more details, the AE activity from 0.68% to 0.874% of axial strain, corresponding to image 3 (Fig. 4.18b). The total time of this particular axial strain range was divided in six equal AE number intervals (132 events per plot). The AE activity located at the left notch from 2220 to 2356 s (from the beginning of the experiment) is attributed to the local damage around this notch. However, these AE clusters have a length that is smaller than then the width of the notch (taking into account

also the accuracy of the method). AE activity appears to be rather distributed than localised, before the time interval from 2654 to 2715 s, in which propagation of a band of clustered AE events is seen starting from the right notch and advancing horizontally towards the centre. This is taken to indicate the onset of strain localisation and occurs at a stress deviator value of 97.6 MPa (2654 s).

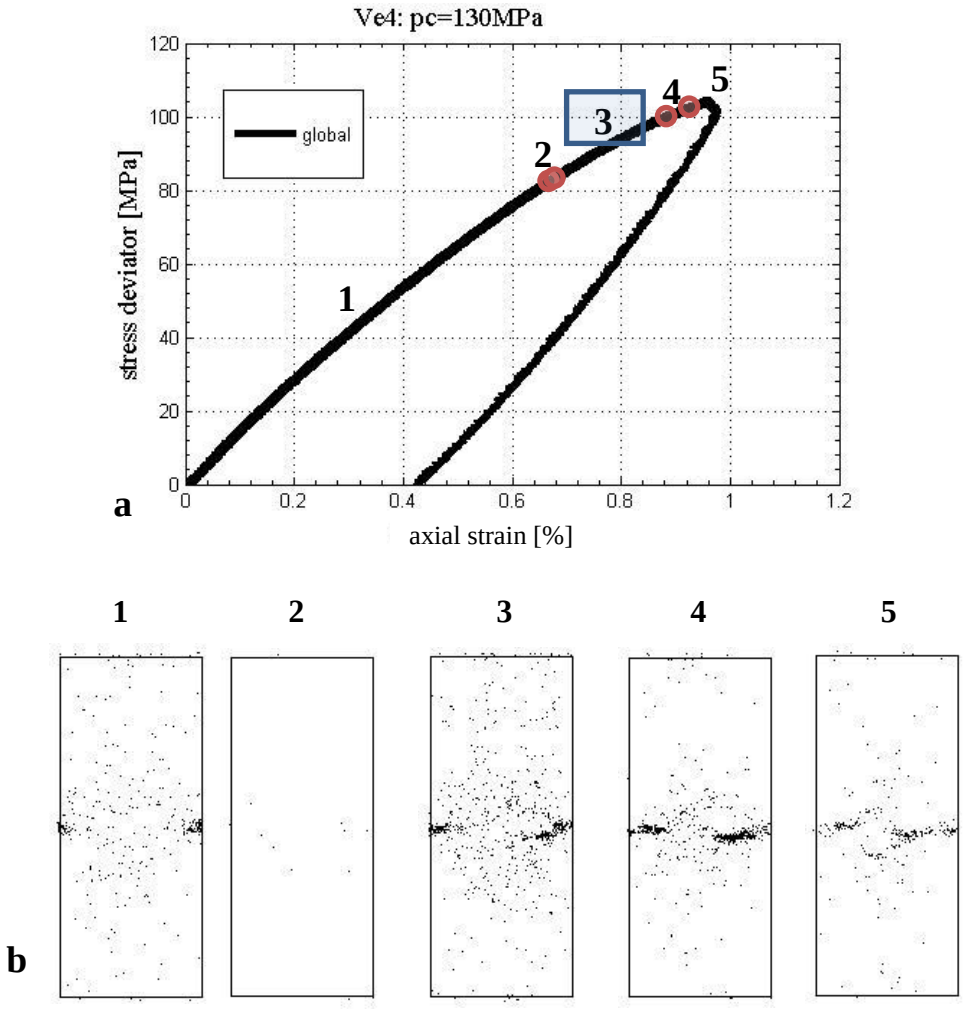

Fig. 4.18: Specimen Ve4: (a) Stress deviator versus axial strain; (b) Images from 1 to 5 visualise the 3D AE distribution in vertical projections of x=+-2 mm from the y-z vertical projection (middle of the specimen) for the axial strain intervals shown in (a).

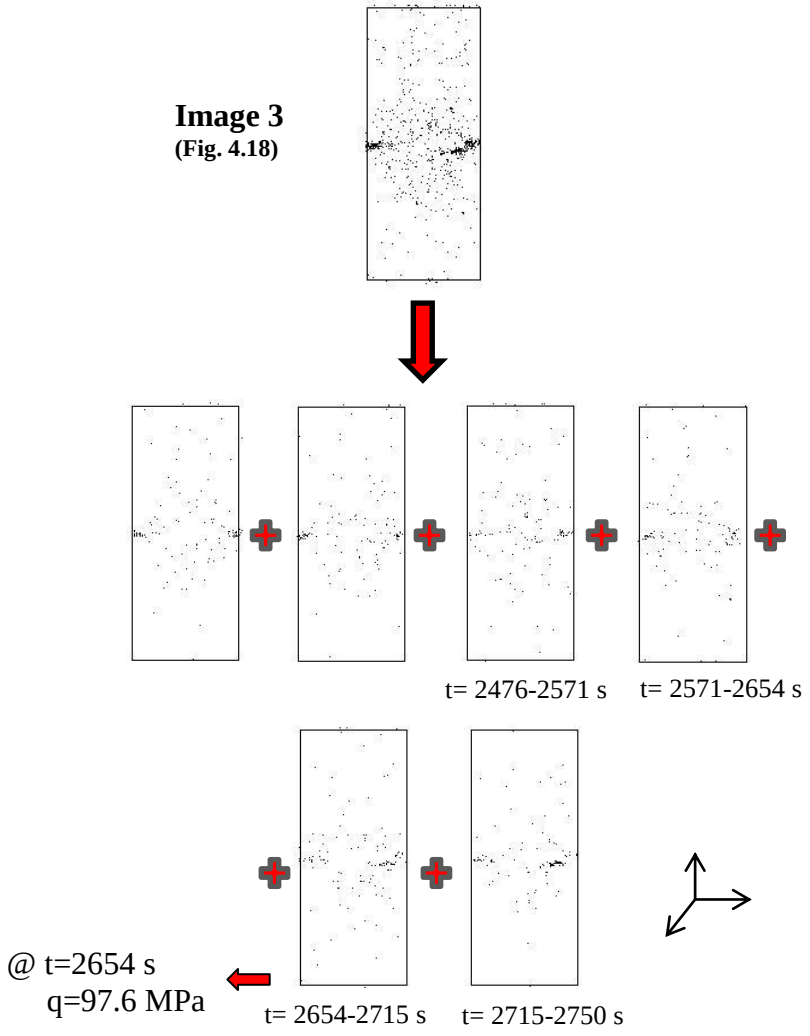

Fig. 4.19: Specimen Ve4: Vertical projections from the y-z plane, for x=+-2 mm from the middle of the specimen. A stress deviator value equal to 97.6 MPa, which corresponds to 2654 s, is suggested to correspond to the onset of stress localisation.

Specimen Ve6 was loaded under the same confining pressure as the Ve4, but it was taken to a higher axial strain (0.17% more). Figure 4.20a shows the stress deviator (like in Fig. 4.17a) as a function of the axial strain. Specimen Ve6 had a lower strength compared to specimen Ve4 (lower stress deviator value compared to that of the Ve4, for the same axial strain). Note that loading was stopped temporarily during this experiment (Fig. 4.20, in orange bar). Recall also that a Teflon film was placed at the bottom and top surfaces of the Ve6, as a lubricant.

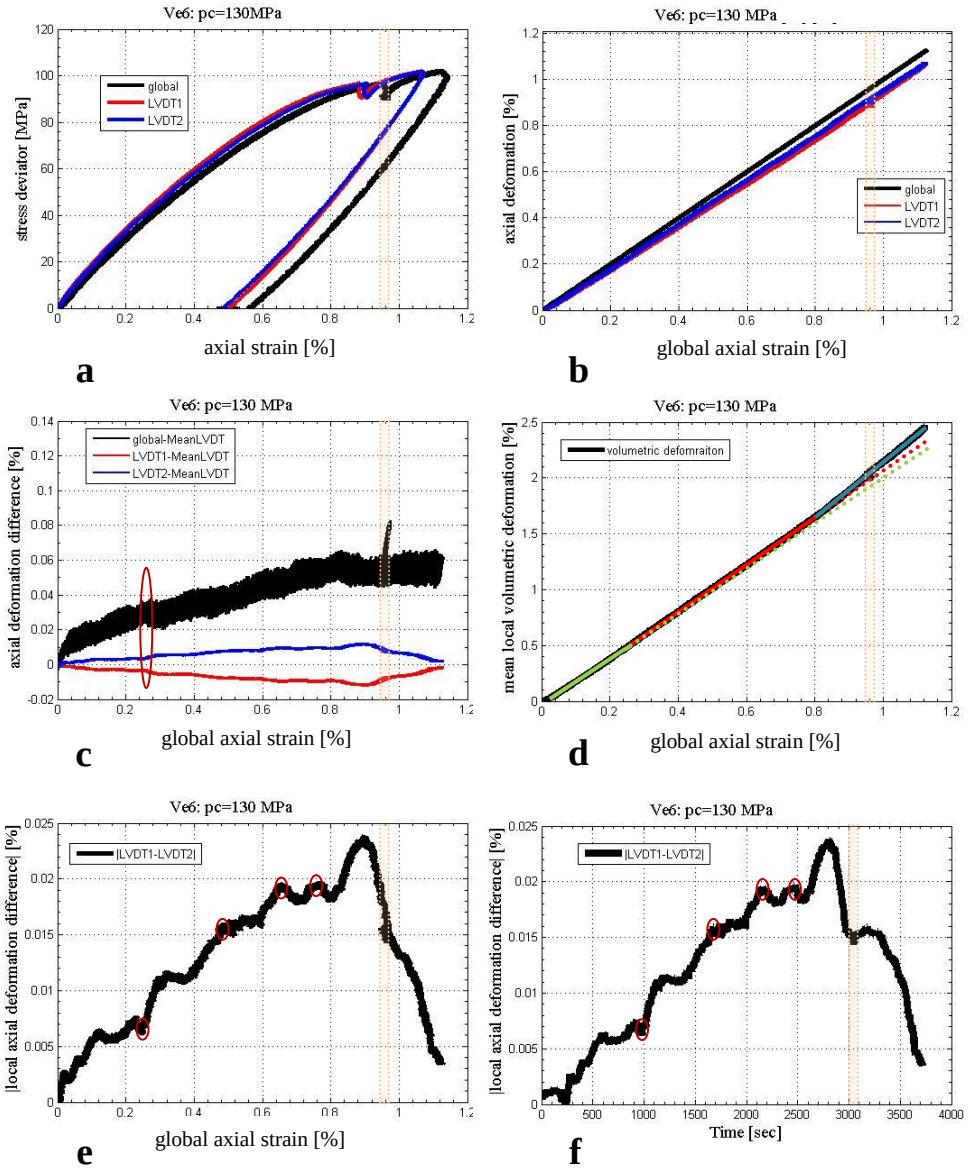

Fig. 4.20: Stress-strain responses from experiment Ve6: (a) Stress deviator versus axial strain; (b) Axial global and local strains versus axial global strain; (c) Axial global and local strain difference from the mean axial local strain versus axial global strain; (d) Volumetric strain, measured by the local LVDTs, versus axial global strain; (e) Absolute difference between the local axial strains versus axial global strain; (f) Absolute difference between the local axial strains versus deviatoric compression time.

The local and global axial strain curves versus the axial strain do not seem to deviate much from a linear trend (Fig. 4.20b). However, some more obvious deviations can be observed on Figure 4.20c, showing the difference between global and mean local strain, and the difference between the individual and mean local strain. Figures 4.20e and 4.20f present the absolute difference between the two local strains as a function of the axial

strain and the deviatoric compression time history. Four points, corresponding to axial strains equal to 0.26% (see also Fig. 4.20c), 0.48%, 0.65%, and 0.76%, were identified. Note that the volumetric strain as a function of the axial strain, shown in Figure 4.20d, presents also two deviations from the initial linearity, which were observed for axial strain equal to 0.26% and 0.8%. As already discussed, this kind of strain value identification has some degree of subjectivity (the author is aware of that, but there is nothing she can further do about it). However, defining such points (and thus intervals between them) provides a way to observe the evolution of strain localisation throughout the experiment.

An investigation of the 3D AE distributions within the strain increments, highlighted by the mechanical data, is presented in Figure 4.21a. Different y-z vertical slices, projecting AE hypocentre locations within a range of x=+-2 mm from the centre of the specimen were plotted for seven identified axial strain intervals.

Image 1 in Figure 4.21b corresponds to the increment of axial strain up to 0.48%. AE events appeared to be distributed, but no sign of localised deformation is seen. From 0.48% to 0.35% of axial strain, AE events appeared to be located at the right notch (image 2, Fig. 4.21b). The length of the band, measured from image 2, was equal to 4.3 mm. Given the accuracy of the method, which is 2 mm (see Chapter 6), and since the notch had a width of 1 mm, this length corresponds to a band, which started propagating inwards the specimen (note that the width of the notch was 4 mm in Fig. 4.7, but the y-z projections presented here were those normal to the flattened notches, therefore, the notch width in these projections was 3 mm smaller). Image 3 (Fig. 4.21b), corresponding to an axial strain from 0.65% to 0.76%, indicates the propagation of a second band, above the region of the first band, while image 4 (Fig. 4.21b), which corresponds to an axial strain from 0.76% up to the temporary pause in loading, shows the propagation of the previous band and the onset and propagation of a third band, this time close to the left notch. Image 5 in Figure 4.21b corresponds to the AE activity during the temporary pause in loading. It is interesting that AE activity is also observed when no load was applied. The propagation of a fourth band is observed on image 6 (Fig. 4.21b), which corresponds to the re-loading and up to 1.02% of axial strain. Finally, image 7 (Fig. 4.21b) shows further AE activity occurring from 1.02% of axial strain up to the end of loading. During this strain interval, the material continued to harden in less steep way. Note that AE event

amplitudes higher than 0.5 Volts were set in all AE projections from specimens Ve4 and Ve6.

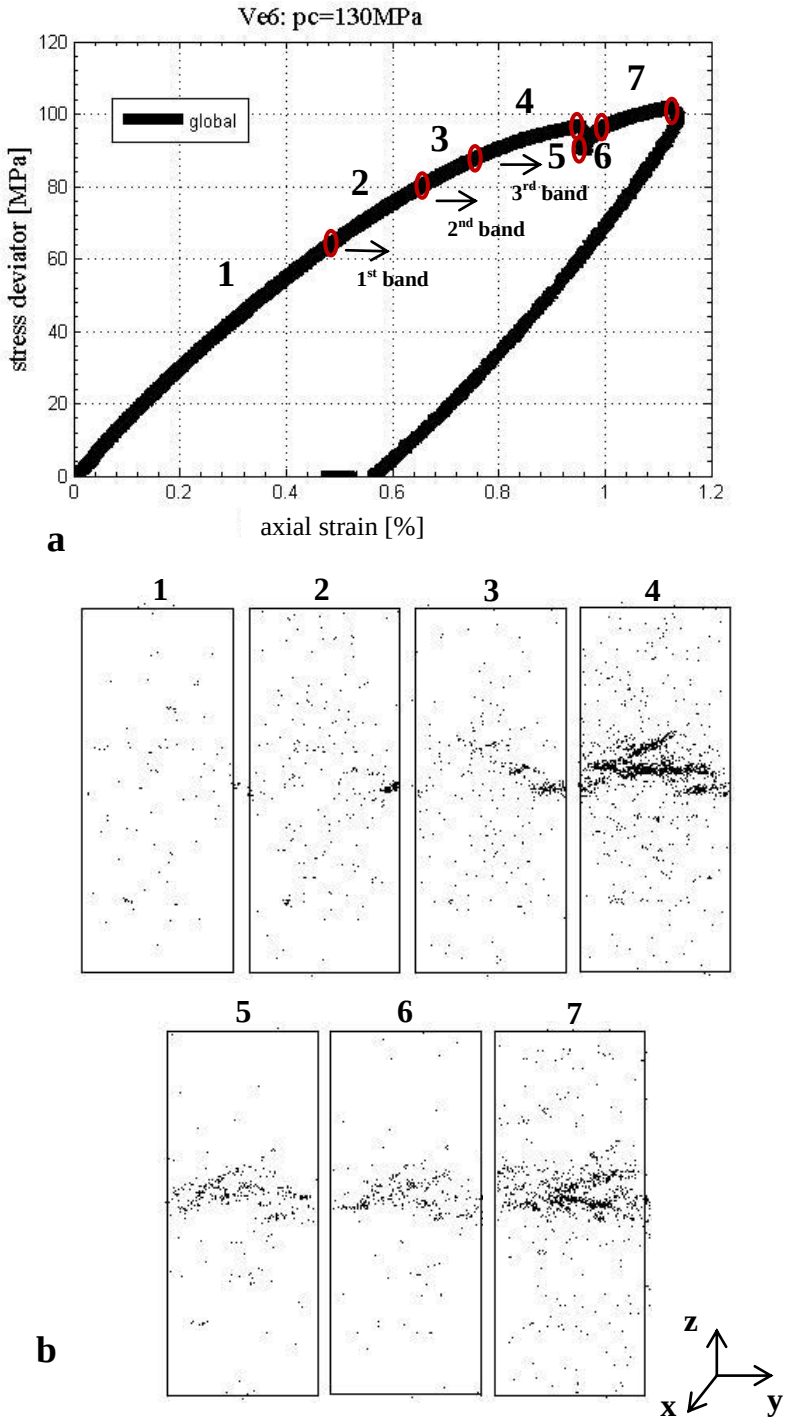

Fig. 4.21: Specimen Ve6: (a) Stress deviator versus axial strain; (b) Images from 1 to 7 visualise the 3D AE distribution in vertical projections of x=+-2 mm from the y-z vertical projection (middle of the specimen) for the axial strain intervals shown in (a).

To identify the onset of the compaction band, Figure 4.22 presents a detail of image 2 (Fig. 4.21b). Image 2 was divided in four equal AE event vertical projections (75 events per projection). The onset of the localisation of AE events, and thus of deformation observed close to the right notch was identified for a stress deviator of 70.5 MPa, since the band visualised in the time interval from 1854 to1972 s had a length of 4.8 mm (recall that the width of the notch in these vertical projections was 1 mm).

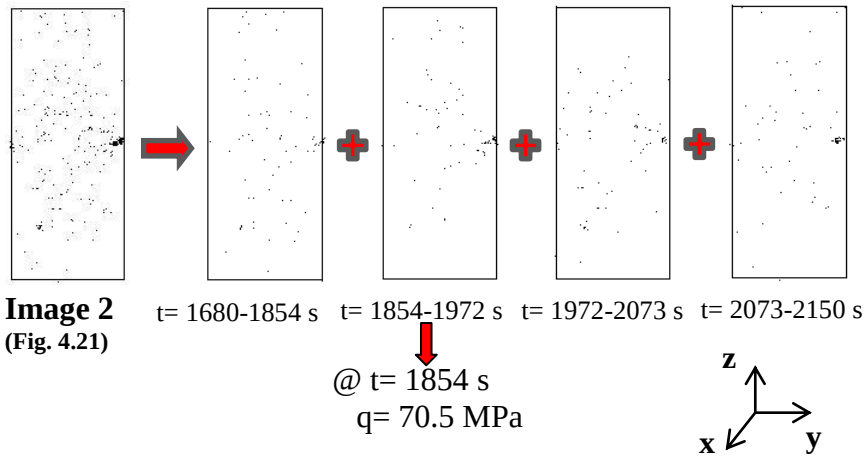

Fig. 4.22: Specimen Ve6: Vertical projections from the y-z plane, for x=+-2 mm from the middle of the specimen. A stress deviator value equal to 70.5 MPa, which corresponds to 1854 s, is suggested to correspond to the onset of stress localisation.

Specimen Ve5 was tested under 160 MPa confining pressure. Recall that no lubricant was used at the top and bottom edges of this specimen. Figure 4.23a presents the stress deviator as a function of the axial strain. The scale of axial strain for specimen Ve5 was adjusted to 1.8%, for comparing these results to those obtained on specimen Ve1, which was deformed under the same confining pressure but was taken to a higher axial strain. The latter specimen had no notches at the flattened surfaces. In specimen Ve5, most of the deformation occurred in between the region where the local LVDTs were attached. Note that the stress-strain curve from the LVDTs is steeper than that from the piston, probably due to damage occurring at the ends of the specimen, captured only by the global strain however, the difference in stiffness is small.

Figure 4.23b shows the global and local axial strains as a function of the axial global strain. Note that the readings of the LVDTs deviated at 0.76% of axial strain. To better visualise the deformation differences, Figure 4.23c presents the difference between the

global and local strains from the mean local strain as a function of the axial strain. Axial strain values of 0.44%, 0.75%, and 0.81% were identified from this plot in places of deviation from the linear trend (in circles). Additionally, the volumetric strain curve as a function of the axial strain deviated from the linear, for axial strain s of 0.44%, 0.68%, 0.81%, and 0.95% (Fig. 4.22d).

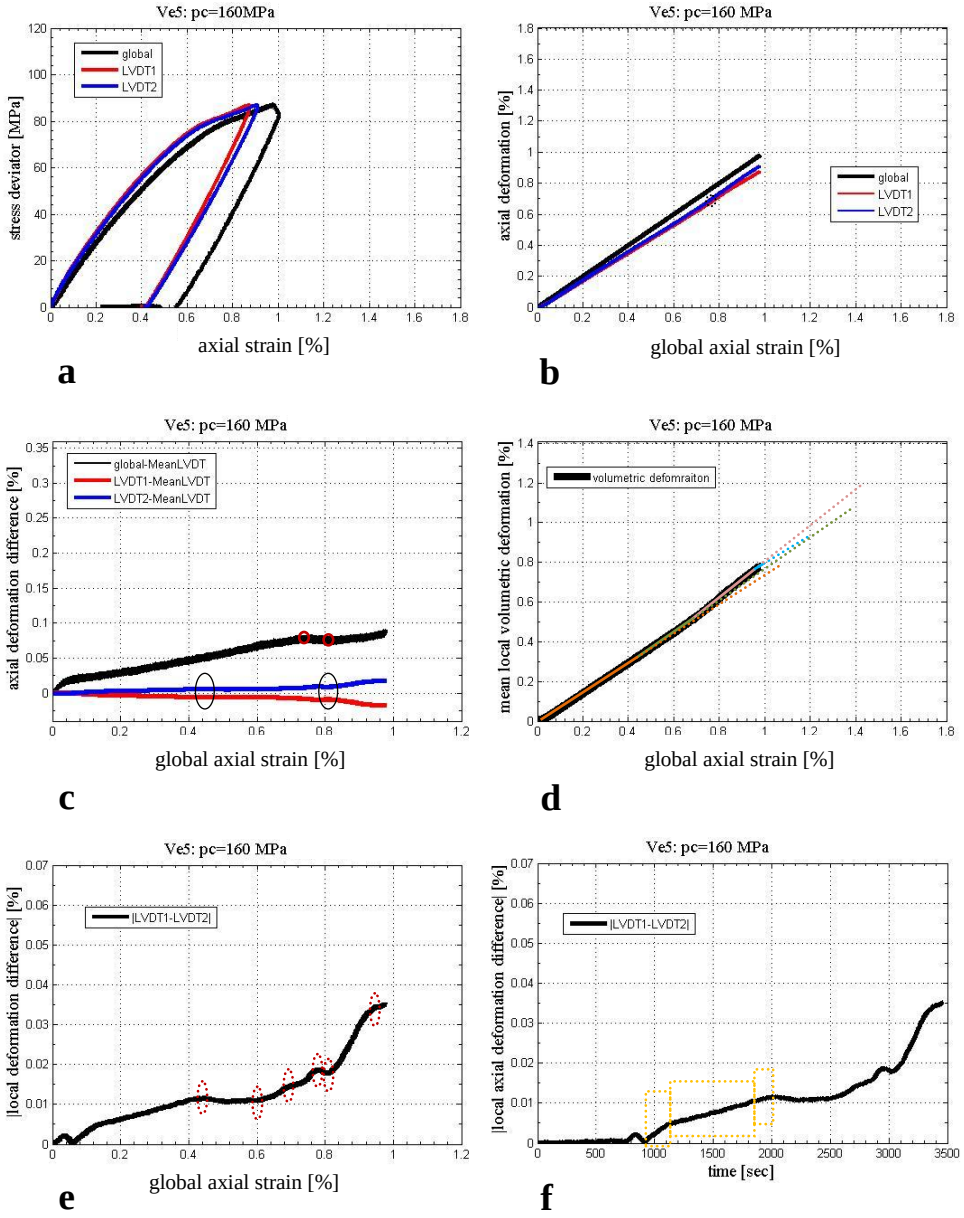

Fig. 4.23: Stress-strain responses from experiment Ve5: (a) Stress deviator versus axial strain; (b) Axial global and local strains versus axial global strain; (c) Axial global and local strain difference from the mean axial local strain versus axial global strain; (d) Volumetric strain, measured by the local LVDTs, versus axial global strain; (e) Absolute difference between the local axial strains versus axial global strain; (f) Absolute difference between the local axial strains versus deviatoric compression time.

Figure 4.23e shows the absolute difference between the local axial strains plotted as a function of axial strain (global). Deviations from the linear trend of this curve highlight some extra axial strain values from those of Figure 4.23c. Figure 4.23f shows the absolute difference between the local deformations as a function of the time history.

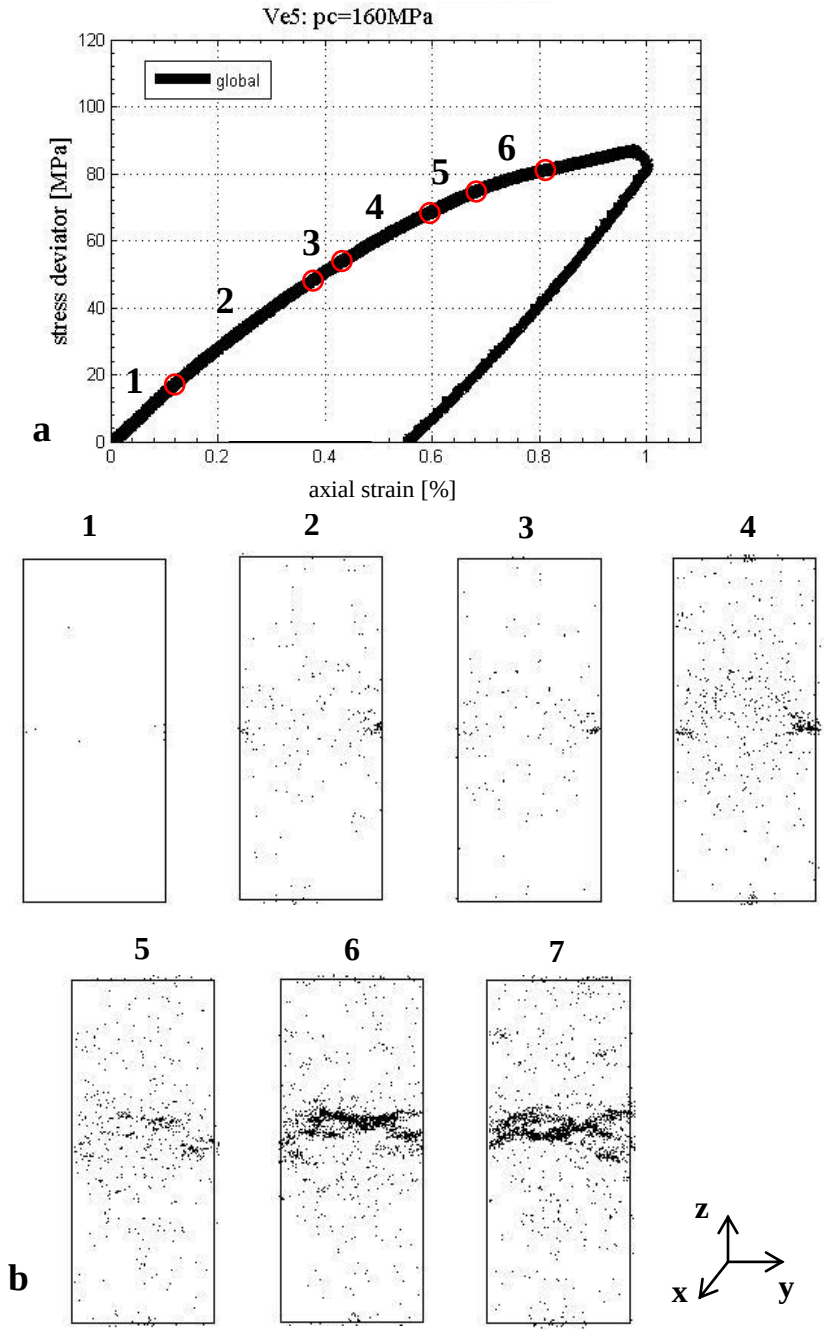

Fig. 4.24: Specimen Ve5: (a) Stress deviator versus axial strain; (b) Images from 1 to 7 visualise the 3D AE distribution in vertical projections of x=+-2 mm from the y-z vertical projection (middle of the specimen) for the axial strain intervals shown in (a).

Guided by the mechanical data, seven increments of axial strain have been identified, for which y-z vertical projections of the AE hypocentre distributions are presented in Figure 4.24b. These increments are 0.13%-0.38%, 0.38%-0.44%, 0.44%,-0.6% 0.6%-0.68%, 0.68%-0.81% of axial strain (Fig. 4.24a). Images 2 and 3 (Fig. 4.24b) show AE activity located close to the right notch. The width of these AE clusters was rather small. Recall that the notch in these projections was of 1 mm length and these clusters covered 2 mm length in total, and so, given the 2 mm accuracy of the AE locations it is not certain if localised deformation initiated before 0.44% of axial strain. Localised deformation expressed via AE events is more obvious in image 4 (Fig. 4.24b), in which bands appear to propagate inwards into the specimen. In image 5 (Fig. 4.24b), a second band closer to the centre of the core appeared. Further propagation of conjugate bands is depicted in images 6 and 7 (Fig. 4.24b). Note that AE event amplitudes higher than 0.5 Volts were used for the y-z vertical slices, which project AE events that occurred in a region of +/- 2 mm from the y-z central projection.

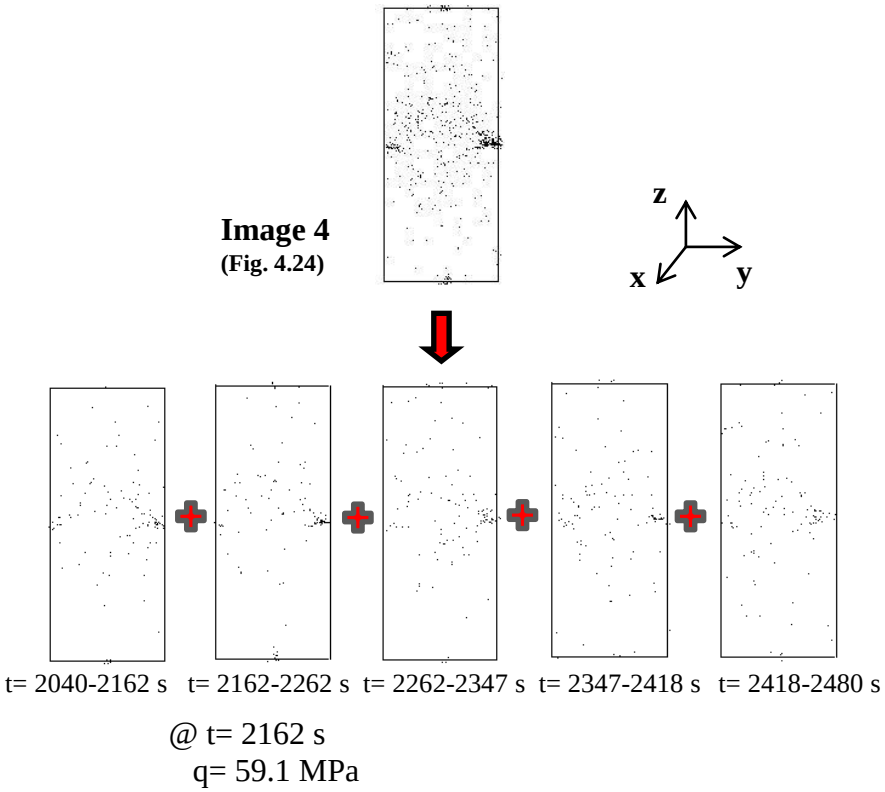

Fig. 4.25: Specimen Ve5: Vertical projections from the y-z plane, for x=+-2 mm from the middle of the specimen. A stress deviator value equal to 59.1 MPa, which corresponds to 2162 s, is suggested to correspond to the onset of stress localisation.

A detail of the 3D AE distributions during the strain increments of 0.44% to 0.6% of axial strain is presented in Figure 4.25, to provide more insights into the onset of the strain localisation. This axial strain range is divided into five time intervals of equal number of AE events (122 events per image). The onset of localisation and propagation can be identified from 2162 s to 2262 s (from the onset of the experiment), corresponding to a stress deviator value of 59.1 MPa.

The stress deviator for specimen Ve1 as a function of axial strain is presented in Figure 4.26a. Several bands could be visually observed on the surface of the Ve1 after the experiment because of (i) the absence of the circumferential notch on this specimen (recall that few or no signs of deformation bands could be seen on the surface of notched specimen, since these bands initiated at the notch tip and propagated towards the centre of the specimens) and (ii) the fact that many bands developed on the top part of the specimen (see Fig. 4.27). The effect of the increased number of bands was reflected to the stress-strain curve (Fig. 4.27a), which presents small fluctuations during the strain hardening (indication of new bands, Fig. 4.27b). Different axial strain values, corresponding to 0.62%, 0.89%, 0.96%, 1.08%, 1.12%, 1.145%, 1.22%, and 1.35% of axial strain, were identified from Figures 4.27b-4.27f in places of deviation from the linear trend.

Figure 4.27 presents nine y-z vertical projections of the AE hypocentre locations for the above mentioned axial strain intervals for the Ve1. Note that AE event amplitudes higher than 0.5 Volts were used. Intense acoustic emission activity was located at the top and bottom boundaries of the specimen (recall the absence of lubricant). The onset of three zones of localised deformation visualised via the AE event activity, one at the top, one in the middle and one at the bottom, can be observed in image 2 (Fig. 4.27). Later on, these deformation bands propagated together with the onset and propagation of more new bands.

To focus on the onset of localised deformation in specimen Ve1, Figure 4.28 presents three equal number AE sections (617 events in each plot) of Image 2 (Fig. 4.27). A concentration of AE events at the top and middle parts (in red) is observed for the time interval between 3699 s and 3929 s, which appears more pronounced in the later images (and also in Fig. 4.27). These clusters were interpreted as newly made compaction bands. For such reason, a stress deviator equal to 83.1 MPa, which corresponds to the onset of this time interval, is suggested as the stress value for the onset of localised deformation

(note that a concentration of AE events at the top and bottom boundaries of the Ve1 started at a lower stress deviator value, but is taken to be just associated with the boundary).

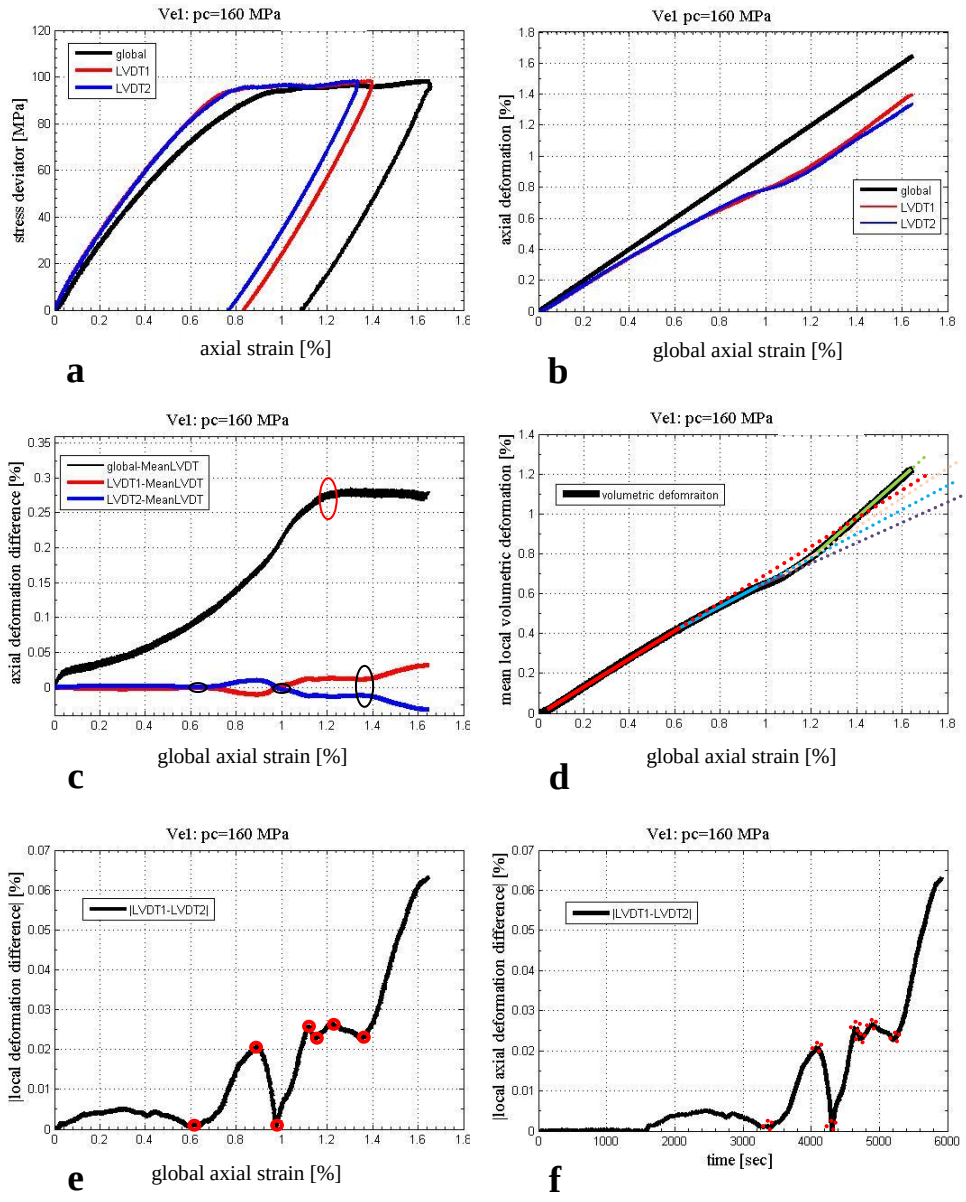

Fig. 4.26: Stress-strain responses from experiment Ve1: (a) Stress deviator versus axial strain; (b) Axial global and local strains versus axial global strain; (c) Axial global and local strain difference from the mean axial local strain versus axial global strain; (d) Volumetric strain, measured by the local LVDTs, versus axial global strain; (e) Absolute difference between the local axial strains versus axial global strain; (f) Absolute difference between the local axial strains versus deviatoric compression time.

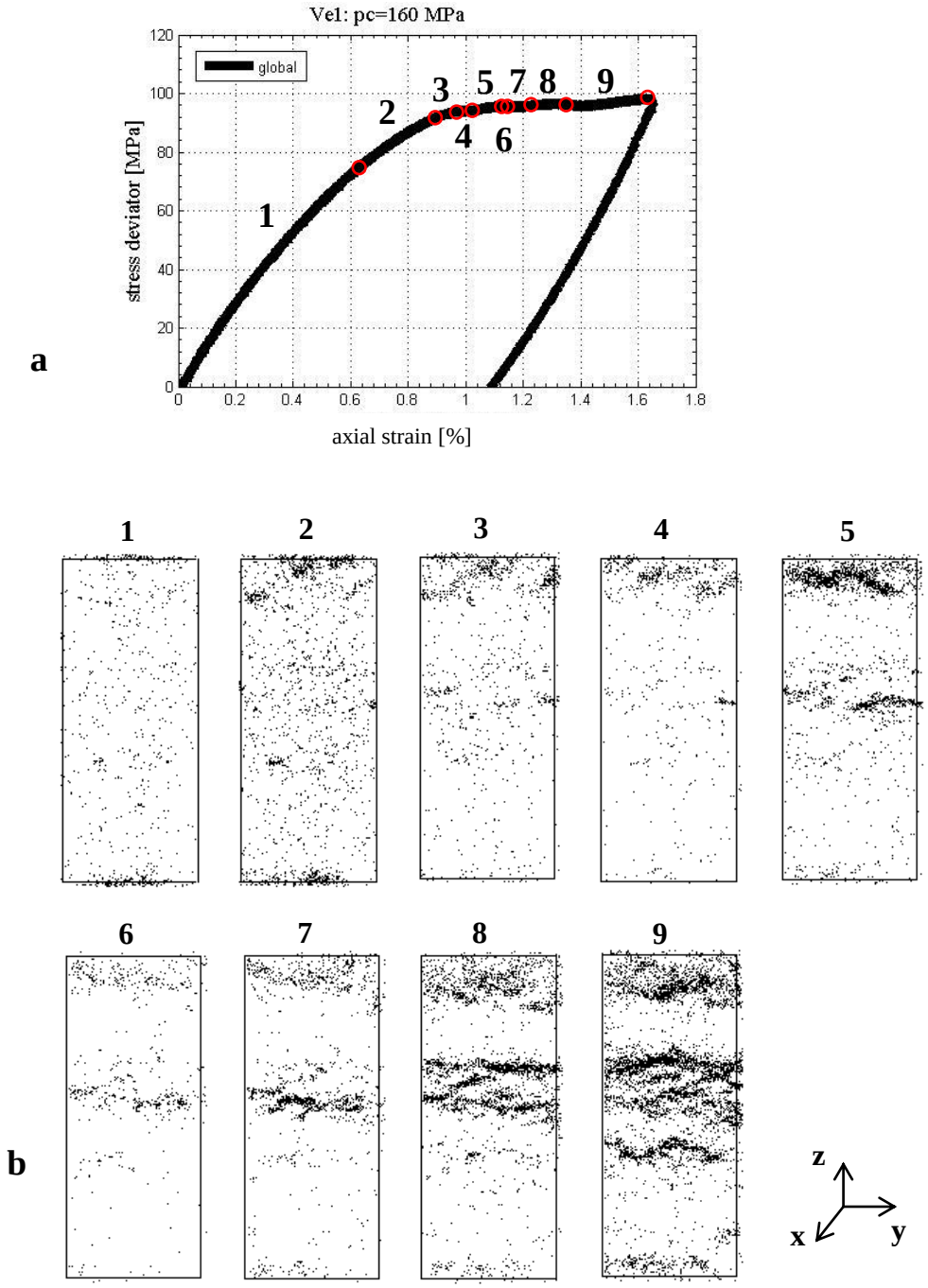

Fig. 4.27: Specimen Ve1: (a) Stress deviator versus axial strain; (b) Images from 1 to 9 visualise the 3D AE distribution in vertical projections of x=+-2 mm from the y-z vertical projection (middle of the specimen) for the axial strain intervals shown in (a).

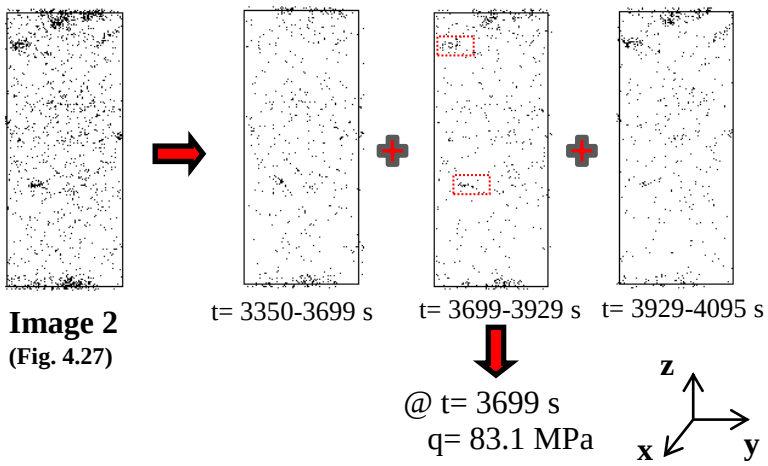

Fig. 4.28: Specimen Ve1: Vertical projections from the y-z plane, for x=+-2 mm from the middle of the specimen. A stress deviator value equal to 83.1 MPa, which corresponds at 3699 s, is suggested to correspond to the onset of stress localisation.

Specimen Ve7 was subjected to a confining pressure of 190 MPa. A Teflon film was used at the top and bottom of this specimen as lubricant. Figure 4.29a presents the stress deviator as a function of the axial strain (which indicates strain hardening). From images 4.29b-4.29f different values of axial strain were identified in places of deviation from the linear trend (axial strain of 0.245%, 0.46%, 0.65%, and 0.73%). Recall the already mentioned relative subjectivity of the choice of the strains.

Five y-z vertical projections of the AE distribution are illustrated in Figure 4.30 based on the above mentioned strain values (Fig. 4.29). AE event amplitudes higher than 0.5 Volts were used. Image 1 (Fig. 4.30) shows that the initial AE activity was located near the notches (from 0% to 0.245% of axial strain). Soon after, with increasing axial strain, a network of sub-horizontal and conjugated bands developed (Fig. 4.30 images 2-5). Note that the y-z projections concern a region of +/- 2 mm from the centre of the specimen (Fig. 4.30).

Figures 4.31b, 4.31c present the vertical projection shown in image 1 (Fig. 4.30, Fig. 4.31a), plotting the AE clusters over +/- 5 mm and 10 mm (width of the flattened surfaces) from the centre of the specimen. The wider the width of projection is, the more intense the number of the AE clusters is and the wider the image of the compaction bands appears to be. The choice of the width of projection for the visualisation of the onset of

localised deformation was important for the case of the higher confining pressure experiments compared to the low to intermediate confining pressure experiments.

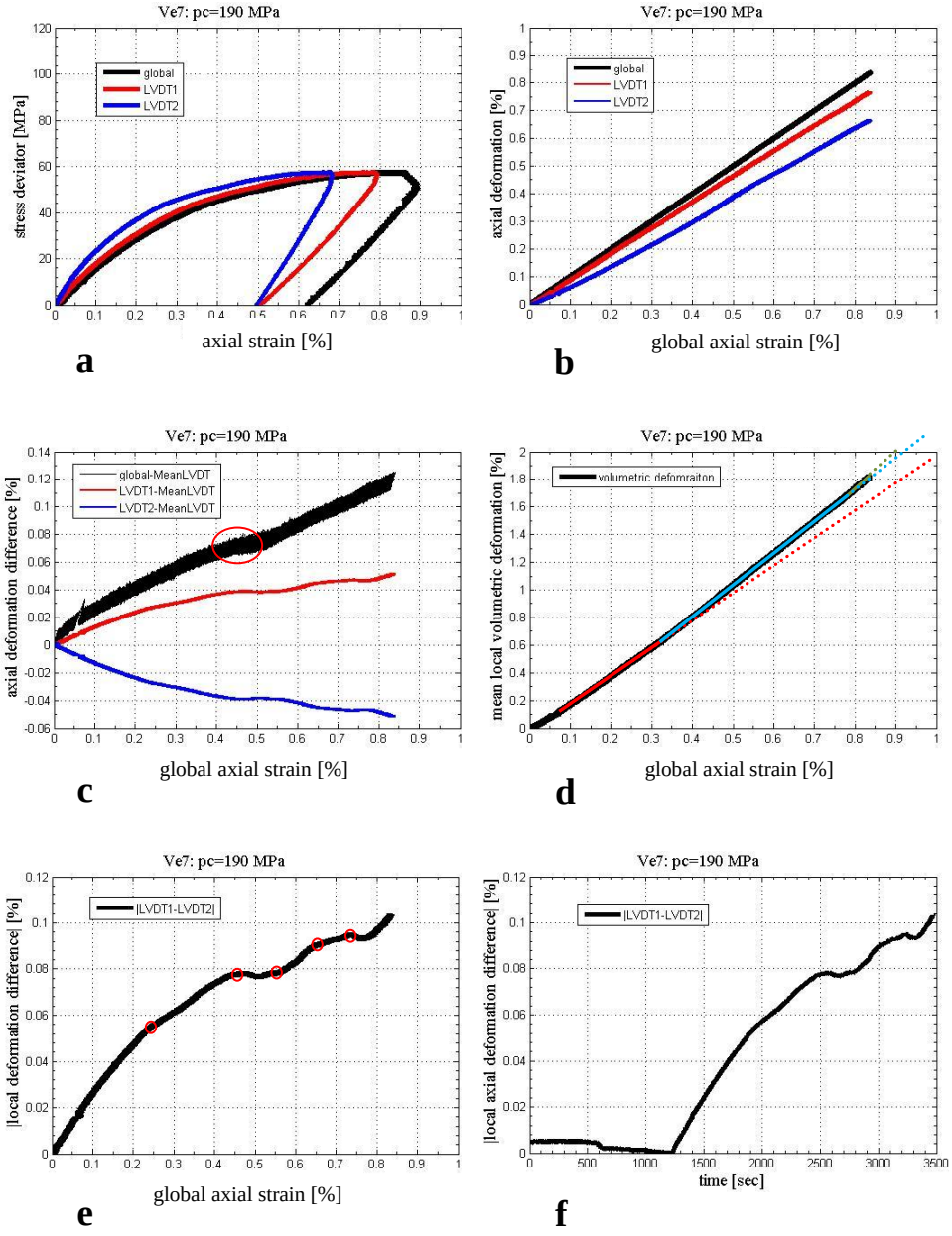

Fig. 4.29: Stress-strain responses from experiment Ve7: (a) Stress deviator versus axial strain; (b) Axial global and local strains versus axial global strain; (c) Axial global and local strain difference from the mean axial local strain versus axial global strain; (d) Volumetric strain, measured by the local LVDTs, versus axial global strain; (e) Absolute difference between the local axial strains versus axial global strain; (f) Absolute difference between the local axial strains versus deviatoric compression time.

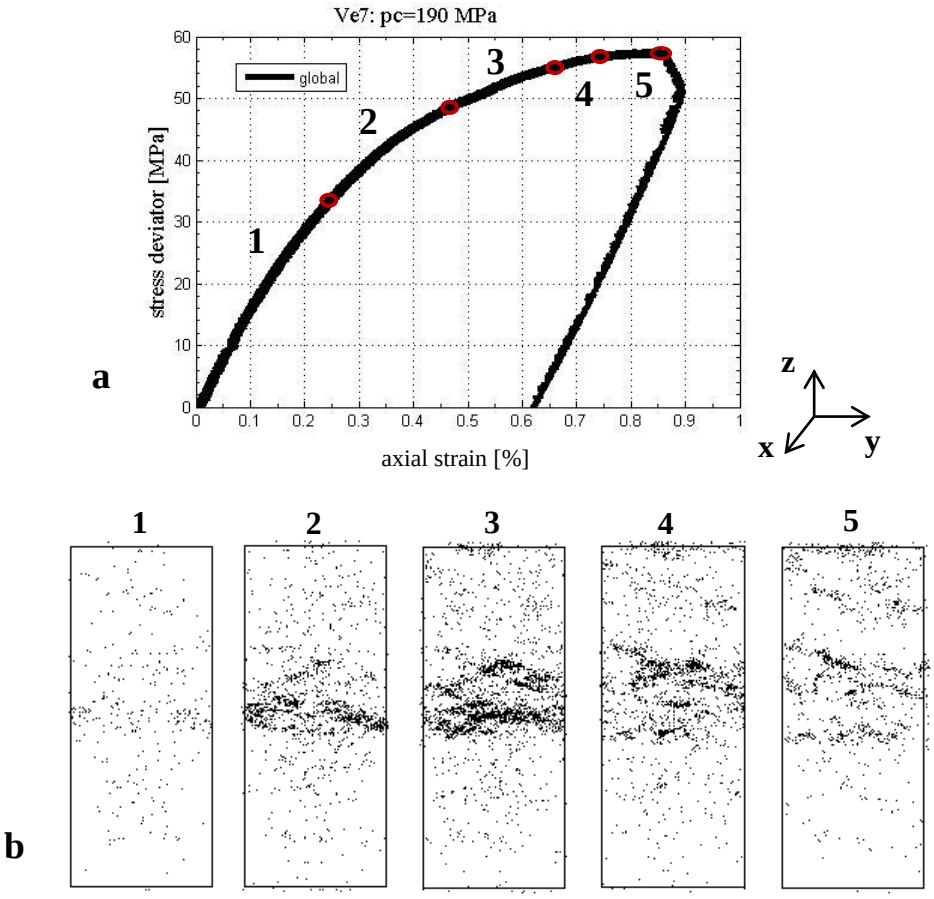

Fig. 4.30: Specimen Ve7: (a) Stress deviator versus axial strain; (b) Images from 1 to 5 visualise the 3D AE distribution in vertical projections of x=+-2 mm from the y-z projection (middle of the specimen) for the axial strain intervals shown in (a).

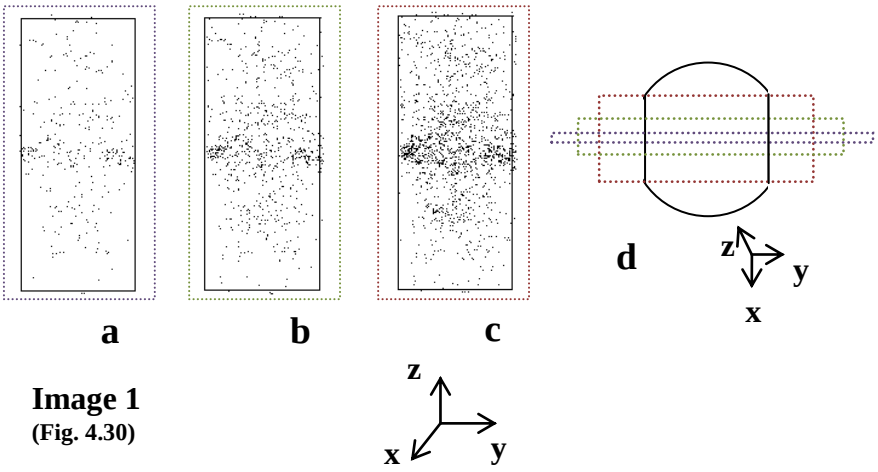

Fig. 4.31: Specimen Ve7: Vertical projections from the y-z plane, for x=+-2 mm (a), +/-5 mm (b), and +/-10 mm (c) from the middle of the specimen; (d) The cross-section normal to the long axis of the specimen, together with the width of the three projections.

In specimen Ve7 it was not straightforward to define the stress deviator value corresponding to the onset of localised deformation. To help determine the onset of localised deformation, Figure 4.32 shows two vertical projections (85 events in each plot) corresponding to the AE activity in the same time interval as in Image 1 of Figure 4.30. A small concentration of AE events near the notches is observed from the beginning of the experiment (Fig. 4.32, t=1250-1792 s). The length of the band (in red rectangle) was around 4 mm (recall that the notch had a length of 1 mm, in all these projections). However, the exact onset of the band could not be defined, since even in Figure 4.32 (t=1250-1792 s), the intensity of the plotted AE clusters was not so big. It is, thus, speculated that for specimen Ve7, a stress deviator value from 0 MPa (that indicates that strain localisation possibly have started during the isotropic compression) to 33.5 MPa (that corresponded to the time onset of image 2, Fig. 4.30) can be suggested as a stress range corresponding to the onset of localised deformation.

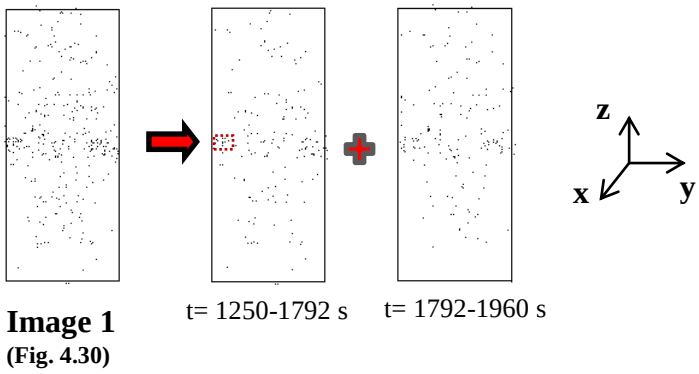

Fig. 4.32: Specimen Ve1: Vertical projections from the y-z plane, for x=+-2 mm from the middle of the specimen. A stress deviator value ranging from 0 MPa to 33.5 MPa, which corresponds from 1250 s to 1960 s, could be suggested as the onset time of stress localisation.

4.8 Conclusions

The mechanical data of all experiments discussed in this Chapter are summarised in Table 4.2, which is used as a reference Table in Chapters 5 and 6. In this Table, the confining pressure, the peak stress deviator identified from the stress-strain curves, the stress deviator value identified by the combination of the stress-strain curves (where possible) and the AE plots, and the maximum axial strain together with the maximum axial strain

after the peak stress and the plastic axial strain (unrecovered strain before unloading to an isotropic compression stage) are presented. Note that these values are mainly based on measurements referring to the meso- (specimen-) scale. Only the AE stress deviator values are defined by a combination of two different scales: (i) the meso- scale (mechanical data) and a scale between the meso- and micro-scale (AE hypocentre locations). Recall that the AE locations depict grain-scale activity and the accuracy of the method is 2 mm.

Table 4.2: Summary of the performed experiments together with values of the applied confining pressure, the peak stress deviator, the AE stress deviator, the maximum axial strain (total and after the peak stress) and the plastic strain.

specimen	confining pressure [MPa]	peak stress deviator [MPa]	AEs stress deviator [MPa]	maximum axial strain [%]	maximum axial strain (after peak) [%] [2]	plastic axial strain [%]
VLR00	20	92.6	---	0.944	0.034	---
VEC2	20	87.72	---	1.073	0.136	1.256
VLR0	50	122.8	---	1.230	0.054	0.392
VEC1	50	109.9	---	1.129	0.080	0.439
VEC5	50	119.1	---	1.281	0.205	0.529
VEC4	50	118.2	---	1.538	0.425	0.781
Ve2	50	116	106-109	1.390	0.155	0.539
Ve4	130	---	97.6	0.955	---	0.426
Ve6	130	---	70.5	1.125	---	0.564
Ve5	160	---	59.1	0.979	---	0.554
Ve1 [1]	160	93.8	83.1	1.644	0.676	1.086
Ve7	190	---	0-33.5	0.865	---	0.621

[1] Recall that specimen Ve1 had no circumferential notch machined at its surface.

[2] The maximum axial strain after the peak stress is the difference of the maximum axial strain (up to unloading) and the axial strain corresponding to the peak stress deviator.

The outcomes of this Chapter are summarised below:

- In the experiments carried out with confining pressures up to 50 MPa, strain softening was observed after the peak stress. For the case of 20 MPa confining pressure, the specimen was split in two parts (fracture) after 0.13% of post-peak axial strain. For 50 MPa confining pressure, strain hardening was observed after 0.08% of post-peak axial strain (and after the initial strain softening). Under higher confining pressures (from 130 MPa to 190 MPa) no peak was observed in the stress-strain response.

- The onset of localised deformation was identified before the peak stress deviator value. For specimens tested at the low to intermediate confining pressures, the peak stress was easily identified, unlike for the tests at relatively higher confining pressures, in which it was difficult to determine a peak stress.
- The increasing value of axial strain resulted in an increased number of localised bands that were obvious by naked eye on the surface of the specimens.
- Visual inspection of specimens from the low to intermediate confining pressure tests, which were taken to smaller values of the axial strain (VLR0, VLR00), and from the higher confining pressure test (apart from the Ve1), did not reveal any sign of localised deformation on the surface of the specimens. For the first case, this was because of the early stage of deformation; for the second case, this was mainly due to the presence of the circumferential notch, which obscured such visual observation. The (full-field) AE measurements allowed localised deformation features to be observed, even in cases of absence of deformation bands on the surface of the specimens (for further results see Chapter 5 and 6).

The suggested stress deviator values corresponding to the onset of localised deformation, which developed in specimens loaded under relative higher confining pressures (from 130 MPa to 190 MPa), were identified by a combination of the mechanical data (meso-scale) and the AE hypocentre locations (micro-scale). The multi-scale approaches presented in Chapters 5 and 6, are further discussed on Chapter 7

Chapter 5 - Shear Band characterisation

5.1 Introduction

Results on Vosges sandstone specimens that were loaded under triaxial compression at relatively low to middle confining pressures, *i.e.*, from 20 to 50 MPa (approximately equivalent to 2 km to 3 km burial depth) are presented in this Chapter. A range of experimental techniques, as described in Chapter 3, have been used. The experimental procedure for this series of triaxial compression tests and the mechanical results were both presented in Chapter 4. This particular Chapter is divided into six additional sections. A short description on the contents of each section follows.

Most of the triaxial tests were carried out at 50 MPa confining pressure. The results presented here will be used to show that deformation in these specimens localised in shear bands and to describe in detail the mechanisms of deformation inside these shear bands. Section 5.2 presents results from one of these experiments, focusing on the identification of shear band characteristics, using AE, HR x-ray images (~ 30 μm voxel resolution), and 3D-DIC applied to LR and HR x-ray images (~ 90 μm and 30 μm voxel resolution). Section 5.3 investigates the different parameters (*i.e.*, size of the sub-volume gauge and spacing size of the former in each direction) used for the HR and LR 3D-DIC and the role that these parameters play in the visualisation of the deformation features. Section 5.4 presents results on more specimens (deformed at 50 MPa confining pressure and stopped at different axial strain values), discussing the impact of the increased axial strain on the evolution of the shear bands. Note that different experimental methods were applied (*i.e.*, UT, HR x-ray tomography, and LR 3D-DIC); however, not all methods were used for each of these experiments. Section 5.5 shows results for specimens loaded under triaxial compression at lower confining pressures (20 MPa). Section 5.6 focuses on microstructural observations on thin sections from some of the specimens already presented in previous sections of this Chapter. These observations illustrate the grain-scale deformation and provide some extra

feed-back on the deformation features, which were identified by the non-destructive methods. Finally, section 5.7 summarises the main outcomes from this Chapter.

5.2 Shear band characterisation by a combination of AE, x-ray CT, and 3D-volumetric DIC

Experimental characterisation of shear bands that have developed under laboratory loading in a Vosges sandstone specimen (Ve2) are presented herein. AE hypocentre location during deformation and the calculated source-mechanisms are presented together with post-mortem HR x-ray tomography images (~30 μm voxel-size) and 3D-volumetric DIC based on pre- and post-mortem HR and LR x-ray tomography images (~ 30 μm and ~ 90 μm, respectively). The study focus is on the characteristics of the developed shear bands, as resolved by these methods. Some comments on the potential of each method are also provided in this section.

Mechanical results from specimen Ve2 were discussed in Chapter 4. The Ve2 was loaded under 50 MPa confining pressure. Two notches were machined on the flattened surfaces of the specimen (Fig. 4.6). The positions of the notches were chosen so as the notch to encourage the onset of the band in an angle similar to the values suggested by *Bésuelle* [2001] (see also section 4.3).

Some thousands of AE events were recorded during this triaxial compression experiment. The stress deviator and the cumulative number of AE events during the experiment (functions of time) are presented in Figure 5.1a for a series of increasing cumulative time windows. Note that the temporal evolution of the AE events aims at a better visualisation of the formation and propagation of the deformation band. Only AE events with amplitude greater to 2 Volts were selected for this analysis by the end of the experiment (Fig. 5.1a). Three 2D projections of the 3D distributions of AE event locations (one perpendicular and two parallel to the specimen axis) are shown in Figures 5.1b, 5.1c and 5.1d. No 3D view of the AE data is presented here. Such visualisations can be better supported by video files. The perpendicular projections of the 3D AE hypocentre distributions plot AE events over almost the whole height of the specimen (from 10 to 70 mm from the bottom edge of the specimen;

recall that the initial height of the specimen was 80 mm, Fig. 5.1b). The z-x parallel projection (Fig. 5.1d) plots AE events recorded from the volume parallel to the area of the flattened surfaces (+/- 10 mm from the centre). The z-y parallel projection (Fig. 5.1c) plots AE events recorded from a shorter volume, normal to the flattened surface (+/- 2 mm from the centre). Amplitudes greater than 0.5 Volts were selected for Figures 5.1b-5.1d. Colours change to highlight the latest AE events, with red indicating progressively most recent events as shown in Figure 5.1a. The accuracy of AE hypocentre location is 2 mm (+/- 1 mm each side from the true location).

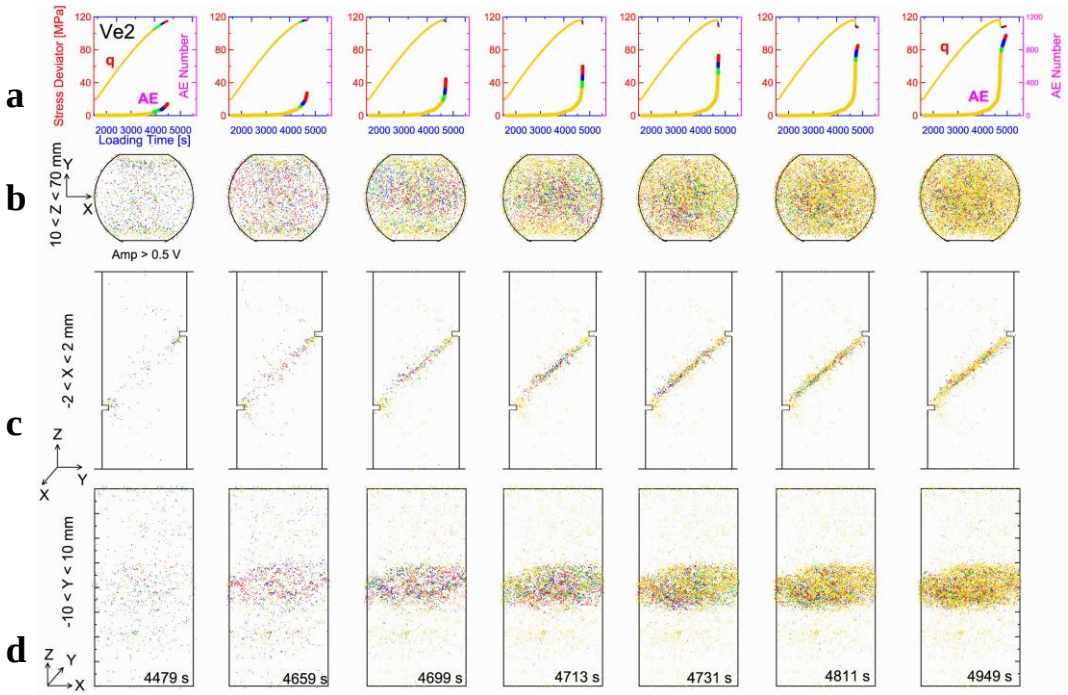

Fig. 5.1: AE results from specimen Ve2: (a) Stress deviator and number of AE events as functions of time over a series of cumulative time intervals of increasing time from left to right; colour changes to highlight most recent events; (b)-(d) Maps of AE event locations for the same time intervals viewed perpendicular to the specimen's height, parallel to the specimen's height in a projection perpendicular to the flattened surfaces projections and parallel to the specimen's height in a projection parallel to the flattened surfaces projections.

The earliest AE events were located near the notches, which fits the expectation that the notches act as stress concentrators. As loading progressed, the majority of the AE events

were located in a diagonal band, connecting the notches (Fig. 5.1c). AE events nucleated in different positions and were relatively spread inside this band during the early stages of deformation (Fig. 5.1c, at 4659 seconds). When strain softening occurred (at around 4699 seconds), the intensity of the AE events increased and covered almost the whole length of this band, which is likely to indicate that the bigger macroscopic single shear band was the result of the continuous coalescence of many AE clusters. However, still, the events were not equally distributed. New AE events were located closer to the top notch. At 4713 seconds, a kink at the tip of the band, which was developed close to the top notch, is observed. At 4731 seconds, new AE events started nucleating in two different, closely spaced places: the old tip of the top band and between the bottom notch and the kink near the old tip of the top shear band. At 4811 seconds, a change in the slope of the cumulative number of AE events (plotted against time) is observed (Fig. 5.1a), which possibly indicates that the top shear band was fully developed and the bottom band started developing, or they both started to further coalescence. The inclination angles of the bands towards the major imposed principal stress direction, during this time sequence, are 40^o and 50^o (bottom and top shear band, dip of 50^o and 40^o, respectively). However, from the AE hypocentre locations, it is not so easy to distinguish these two bands in Figure 5.1, because the bands were relatively closely spaced and the AE locations were relatively broadly spread inside the width of the band. Note also that any other activity outside the deformation bands was extremely reduced.

Figure 5.2 presents an initial AE source analysis, for this particular specimen, based on the polarity method (see section 3.3.5). Events from 0.5% axial strain to the maximum axial strain (end of the experiment) are plotted for the deviatoric loading. The majority of AE events were C-type (73% at 0.5% of axial strain, increasing to 93% before fully unloading, Fig. 5.2b, 5.2c). S-type events decreased by around 75% (*i.e.,* from 23% at 0.5% of axial strain to 6% when the test stopped, Fig. 5.2b, 5.2d). S-type events increased temporarily from 6.5% to 19% (Fig. 5.2d) during the strain softening (stress-strain curve, Fig. 5.2a) and after it they dropped rapidly to 6% and remained almost constant (Fig. 5.2d). Furthermore, a small, but not negligible amount of T-type events was detected (*i.e.*, from 5% at 0.5% of axial strain to 1% by the end of the experiment, Fig. 5.2d). Figure 5.2 shows the stress deviator, the type and the amount of AE source mechanisms as a function of the axial strain.

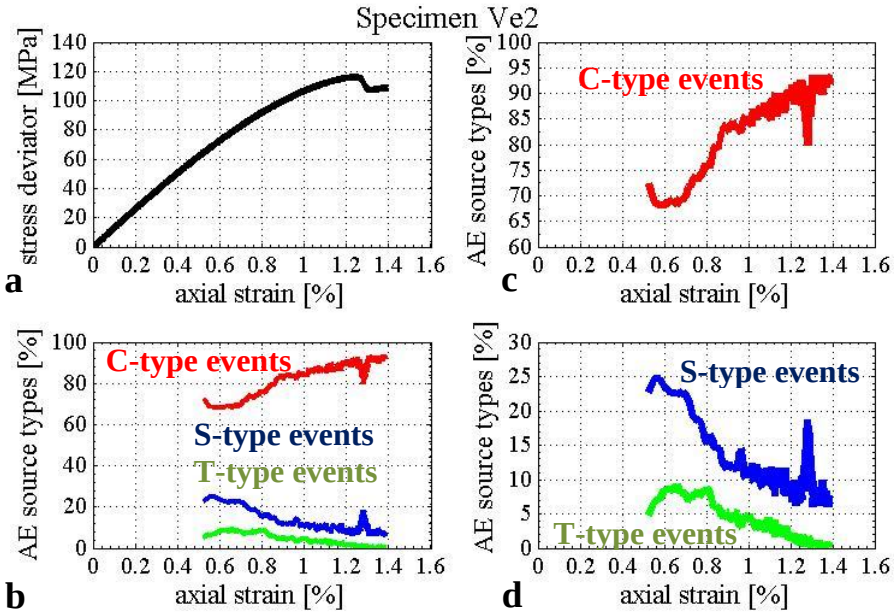

Fig. 5.2: Plots of stress deviator (a), the amount and type of AE source-mechanisms (b), and zooms in C-type events (c) and S- and T-type events (d) during the deviatoric compression of specimen Ve2, all as a function of the axial strain.

A set of vertical HR x-ray tomography slices (volume rendering) through the volume of specimen Ve2 is shown in Figure 5.3. The two bands of higher density (darker colours) were interpreted as compacting shear bands. The structure of these bands varied slightly in the third dimension. From these post-mortem HR x-ray tomography images, it is argued that the two shear bands initiated one from each notch and propagated inwards, to meet near the mid-way between the notches. However, the post-mortem HR x-ray images provide no direct information on the evolution of the shear bands, as the syn-deformation AE analysis did.

Band width ranges from 150 to 300 μm (*i.e.*, from half to one intact grain-size) and the damage zone, including the band, ranges from 360 to 600 μm (up to 2 intact grain-sizes). Near the notches open cracks were visible (lower density - light colours); these have a mean width of approximately 60 μm (note this is after isotropic compression unloading, see also section 5.6). Information on the width measurements can be found in Appendix B. The

inclination angle of the bands is from 40° to 55° (dip of 50° to 35°). Recall that similar inclination angles are identified in Figure 5.1 (AE analysis).

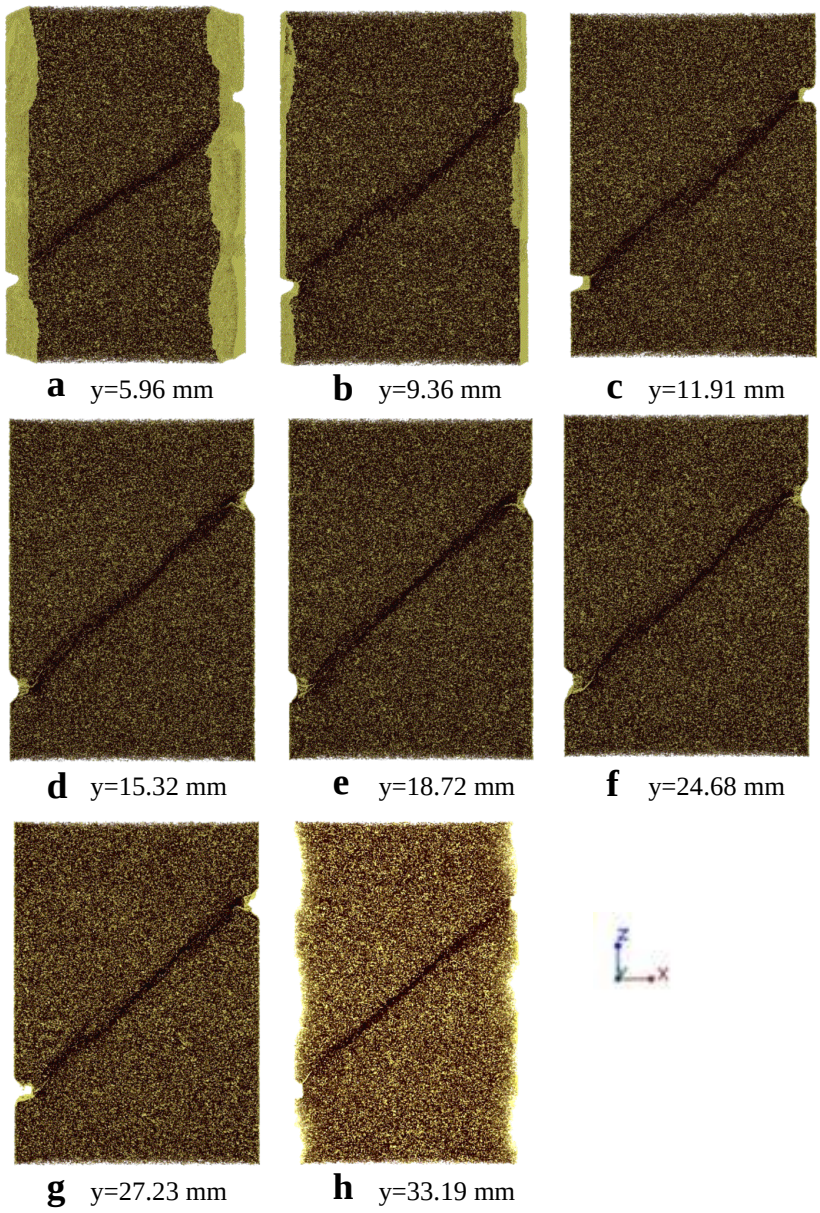

Fig. 5.3: Post-mortem X-ray tomography images (volume rendering): (a) - (h) Sequence of vertical slices of the x-z plane as the y-axis position changes inside specimen Ve2 (voxel size ~30 μm).

Figure 5.4 shows in 3D representation of the volume of the specimen at a place where the two shear bands meet. The shear band is non-planar also at the plane normal to the axial loading (x-y plane).

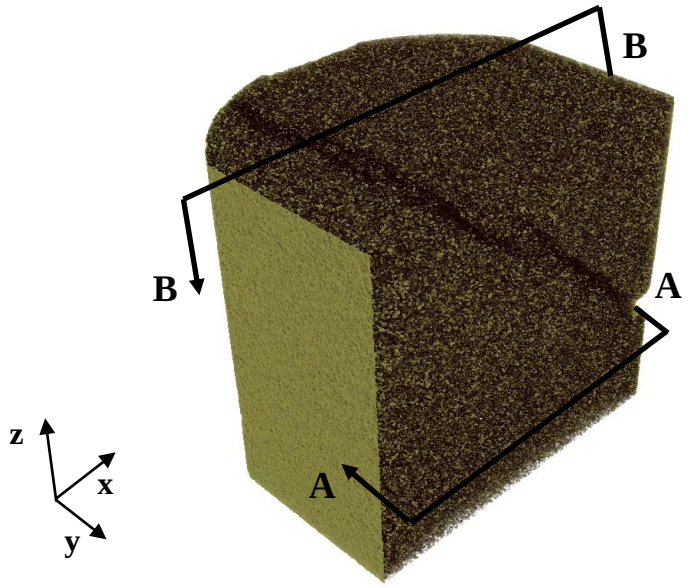

Fig. 5.4: 3D visualisations of specimen Ve2 in a region where the two shear bands meet (post-mortem HR x-ray tomography images volume rendering, ~30 μm resolution). Planes A-A, and B-B are parallel and normal to the loading axis.

In Figures 5.3 and 5.4 it was shown that it is possible to visualise shear bands when using the raw post-mortem HR x-ray tomography images. Additionally, the calculation of the standard deviation of the grey-scale values from the raw x-ray tomography images describes the degree of heterogeneity of the deformation bands, as this is revealed by an image analysis standpoint (for the given resolution of the x-ray image). Figure 5.5 presents projections of the standard deviation of the grey-scale values throughout the volume of specimen on two orthogonal vertical planes. Calculations were made throughout the image volume over sub-volumes of 600x600x600 μm^3 at a spacing of 150 μm in each direction.

Shear bands in specimen Ve2 were characterised by raw HR x-ray tomography images as higher density zones (raw data are linked to density variations, see Fig. 5.4). Calculations of the standard deviation fields, in Figure 5.5, visualise shear bands as homogeneous zones, of lower standard deviation values (darker colours). This suggests that inside the shear bands the grain size is much smaller than the voxel size of the tomography image, and thus, the

image becomes 'more homogeneous', as the different grains and porosity attenuations are averaged together over a voxel to give an average grey-scale, which can be similar over a region (as indicated by the standard deviation measure). In regions outside the shear bands, where higher values of standard deviation were measured, grains (and pores) are large enough to be imaged partially, if not completely, such that different voxels have different grey-scale values depending on the mineral or porosity imaged.

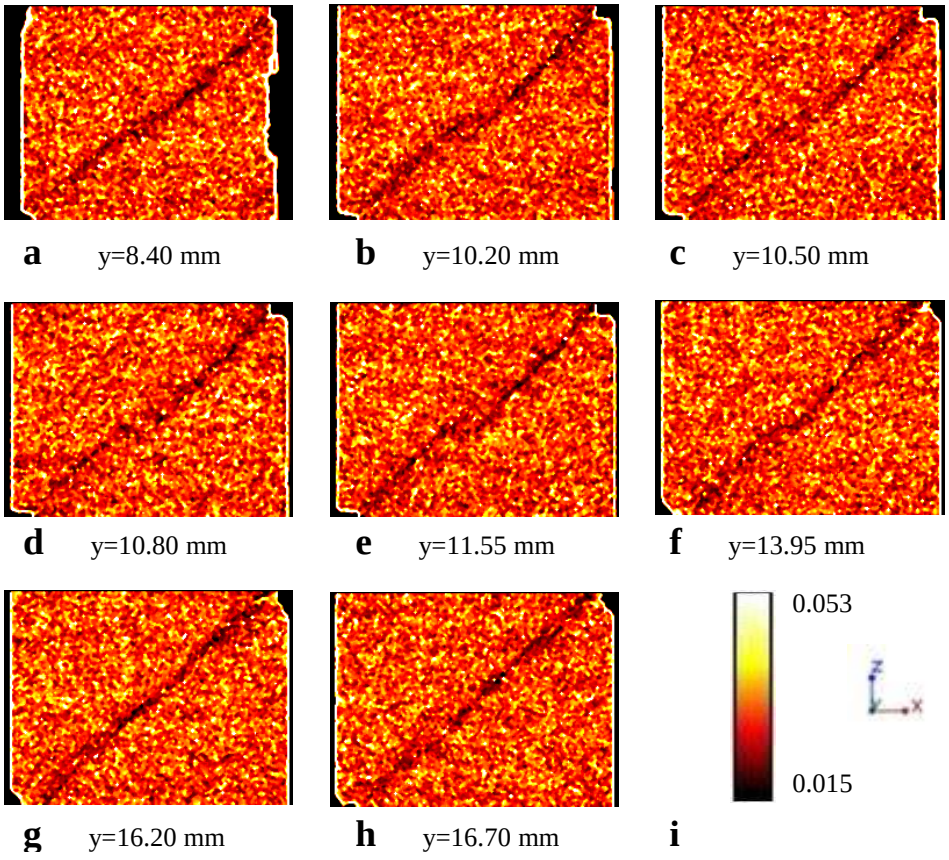

Fig. 5.5: Standard deviation maps, calculated on the grey-scale of the post-mortem HR x-ray images, from vertical projections of specimen Ve2 (a)-(h); (i) Colour map of the standard deviation range. The deformation band is visualised as a place of lower standard deviation values (black/darker colours; more homogeneous). Calculations were made over sub-volumes of 20x20x20 voxels^3 at a spacing of 5 voxels in each direction. The resolution of the x-ray images was of ~30 μm.

The geometrical representation of shear bands in Figure 5.5 appears to be similar to that shown in Figure 5.3. Figures 5.5b-5.5e show places where the two bands meet, while Figures

5.5a, 5.5f and 5.5g show a single non-planar shear band. The band width varies from one to four grains (*e.g.*, 300 µm -1200 µm).

By visualising different values of the standard deviation throughout the specimen further information on the geometric characteristics of the shear band linked to a possibly different degree of grain damage can be gained. Figures 5.6 present two 3D images of the shear band from specimen Ve2 for different calculated standard deviation values.

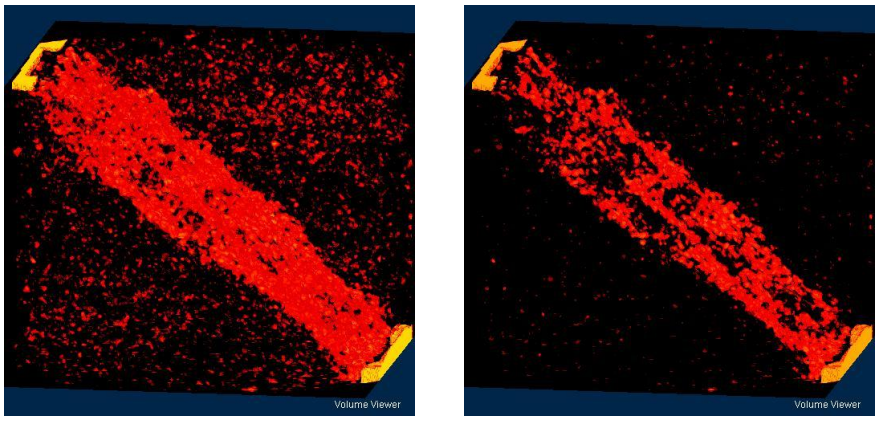

a STD values less than 0.022 **b** STD values less than 0.020

Fig. 5.6: 3D images visualising different standard deviation (STD) values from specimen Ve2: (a) for STD values less than 0.022; (b) for STD values less than 0.020. Red depicts the more homogeneous regions (lower values of standard deviation).

Full strain tensor fields, mapping the deformation between the pre- and post-mortem HR x-ray tomography images, were obtained by 3D-volumetric DIC using the code *TomoWarp* (see section 3.5.3). The results are presented using two invariants of the strain tensor, the deviatoric strain ($\varepsilon_s = \sqrt{2/3}\ [(\varepsilon_1 - \varepsilon_2)^2 + (\varepsilon_2 - \varepsilon_3)^2 + (\varepsilon_3 - \varepsilon_1)^2]^{1/2}$**,** with ε_1, ε_2 and ε_3 the major, intermediate and minor principal strains, respectively) and the volumetric strain ($\varepsilon_v = [\varepsilon_1 + \varepsilon_2 + \varepsilon_3]$).

Figures 5.7 illustrate strain fields, in places close to the core of the specimen, where the two bands meet (Fig. 5.7b -5.7i) and in places farther from the specimen's centre (Fig. 5.7a, 5.7j-5.7k). Deviatoric (shear) strains are presented in Figures 5.7ai-5.7ki, volumetric strains

are shown in Figures 5.7aii-5.7kii and an overlap of the two strain fields is illustrated in Figures 5.7aiii-5.7kiii. Strains were calculated on a regular grid with spacing equivalent to twice the average intact grain-size in each direction (i.e., 600 μm), over sub-volumes, which were also twice the average intact grain-size. Intense shear strain was identified inside the bands (bright colours); with deviatoric strain values ranging from 1.8% to 6.5%, whereas the shear strains in the rest of the specimen were rather negligible compared to those inside the shear band (less than 0.7%).

The volumetric strain fields indicated that the shear bands were compacting in particular regions while in others dilation is dominant. Note that lower density that might be expected to accompany the dilation in the shear bands was not apparent in the post-mortem HR x-ray images (Fig. 5.3). Compaction was identified mainly in regions where the two bands met (Fig. 5.7bii-5.7iii). The volumetric strain in these zones reached up to +4.5% (compaction). However, the shear strains showed lower values compared to those measured in other regions along the shear band (Fig. 5.7bi-5.7ii). Such observation suggests that compaction together with less pronounced shearing has occurred in place where the shear bands meet. For the same images, higher values of shear strains concurred with lower values of compactant or even dilatant strains (*i.e.*, up to -1.3% (dilation)). Therefore, it is argued that intense shear results in volumetric rearrangement (usually dilation) in these particular regions.

In other places (Fig. 5.7a, 5.7j, 5.7k), where one shear band was visualised, compaction was dominant mainly in the central part, with volumetric strain up to +4% (compaction). Dilation in regions near the notches, with volumetric strain up to -1.8% (dilation), likely reflected the initiation of cracks near the notches, where stress concentrations were expected. Lower volumetric strains characterised the rest of the specimen.

Shear and volumetric strain values varied also along the shear band (Fig 5.7). Since no x-ray scans were performed during the triaxial compression phase of the Ve2, it is not possible to determine the temporal variations of these strains. Furthermore, note that no thin sections were prepared for this particular specimen (see section 5.6).

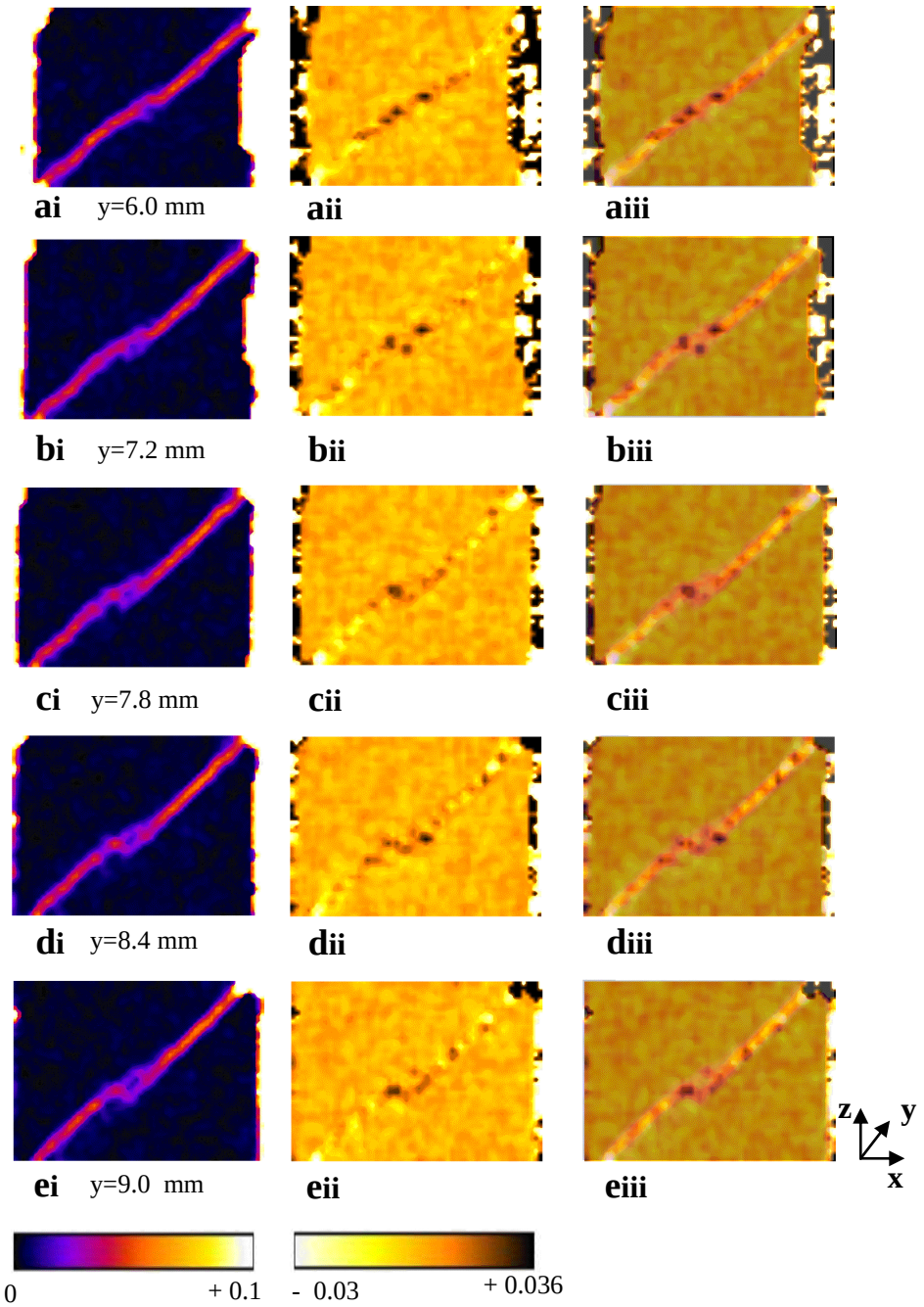

Fig. 5.7: Specimen Ve2: (ai)-(ki) Shear strain field derived from pre- and post-mortem HR x-ray tomography images (~ 30 μm); (aii)-(kii) Volumetric strain field derived from pre- and post-mortem HR x-ray tomography images; (aiii)-(kiii) Superposition of the volumetric and shear strain fields, for the same projections. Calculations were made over sub-volumes of 20x20x20 voxels^3 at a spacing of 20 voxels in each direction. The resolution of the x-ray images was of ~30 μm.

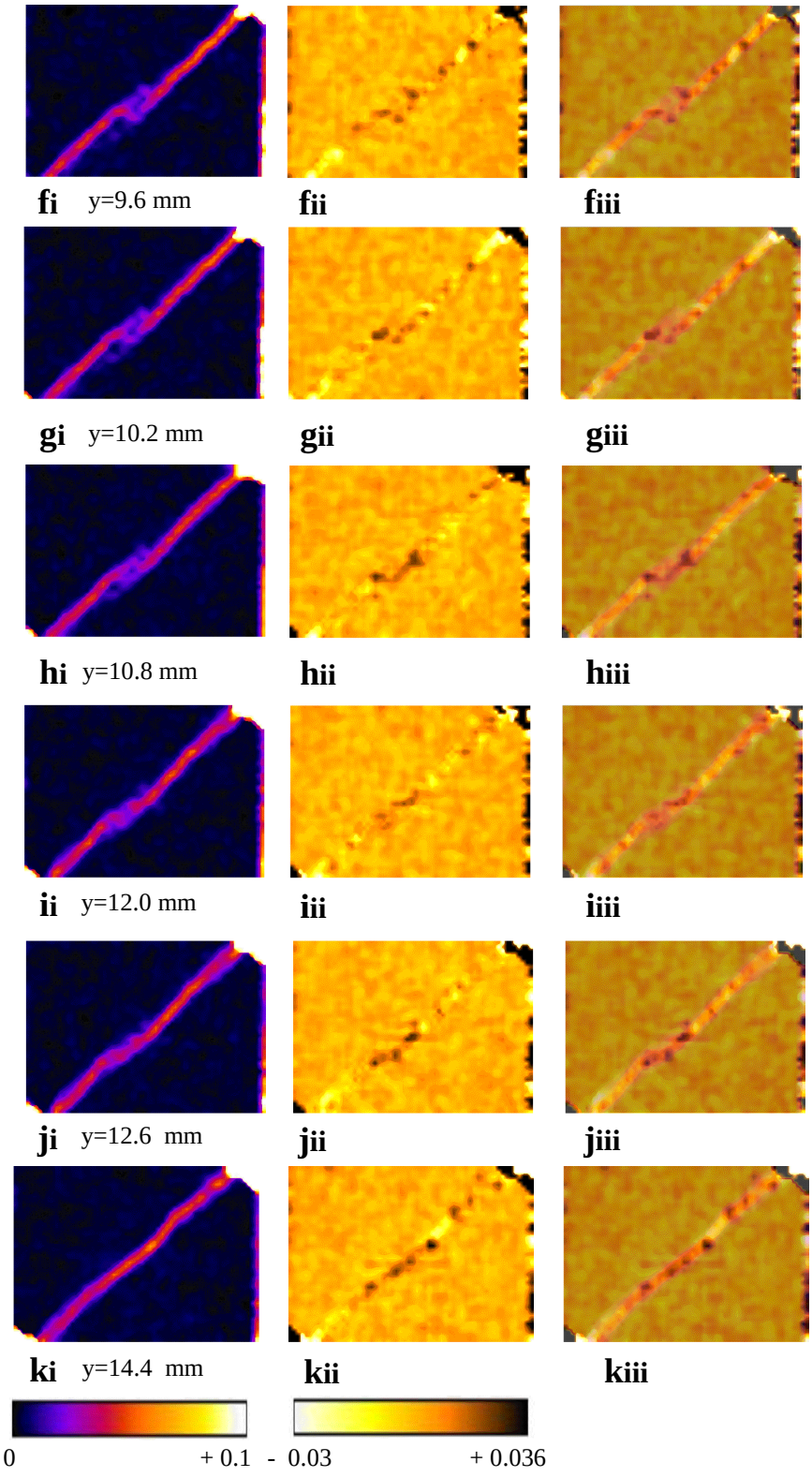

Fig. 5.7: Continued.

When strains were calculated at a smaller spacing than shown in Figure 5.7 and over smaller sub-volumes, some extra information was gained. In particular, Figures 5.8 illustrate shear strain fields calculated over sub-volumes of 600x600x600 μm^3 at a spacing of 600 μm in each direction (same calculations were shown in Fig. 5.7) and shear strain maps calculated over sub-volumes of 300x300x300 μm^3 at a spacing of 300 μm in each direction. DIC calculation with a larger spacing and a bigger sub-volume size resulted in a visualisation of smoother shear bands. Strain values appear to be higher when calculations were performed in smaller sub-volumes and at a smaller spacing (also see section 5.3). Note, however, that calculated strains might be overestimated at the latter case.

Figures 5.9 illustrate more shear strain vertical projections throughout the volume of specimen Ve2, in which regions of relatively higher shear strain values appeared to be much more obvious. Furthermore, the geometry of the shear band(s) in Figures 5.8_ii and 5.9, as this was visualised by the shear strain calculations, is much more complex (than this in Fig. 5.8_i), since it is resolved in more detail.

When shear strain calculations were performed on smaller sub-volume and spacing sizes (*e.g.*, Fig. 5.8_ii and Fig. 5.9), the width of the bands ranges from 1 to 2.7 intact grain-size (300-810 μm), which is close to the width of the band that was identified by the post-mortem HR x-ray tomography images. The width of the shear band identified by the strain calculations performed on larger sub-volume and spacing sizes (*e.g.*, Fig. 5.7 and Fig. 5.8_i) is from 1.5 to 2 times bigger than this from Figures 5.8_ii and 5.9. The different measured width of the shear bands (from the shear strains) is directly linked to the resolution of each calculation parameters (different spacing and sub-volume sizes). Nevertheless, it should be underlined that the width change is also linked to the parameters visualised- and the technique used in that visualisation (*i.e.*, density fields in the x-ray tomography images and strain fields in the DIC images).

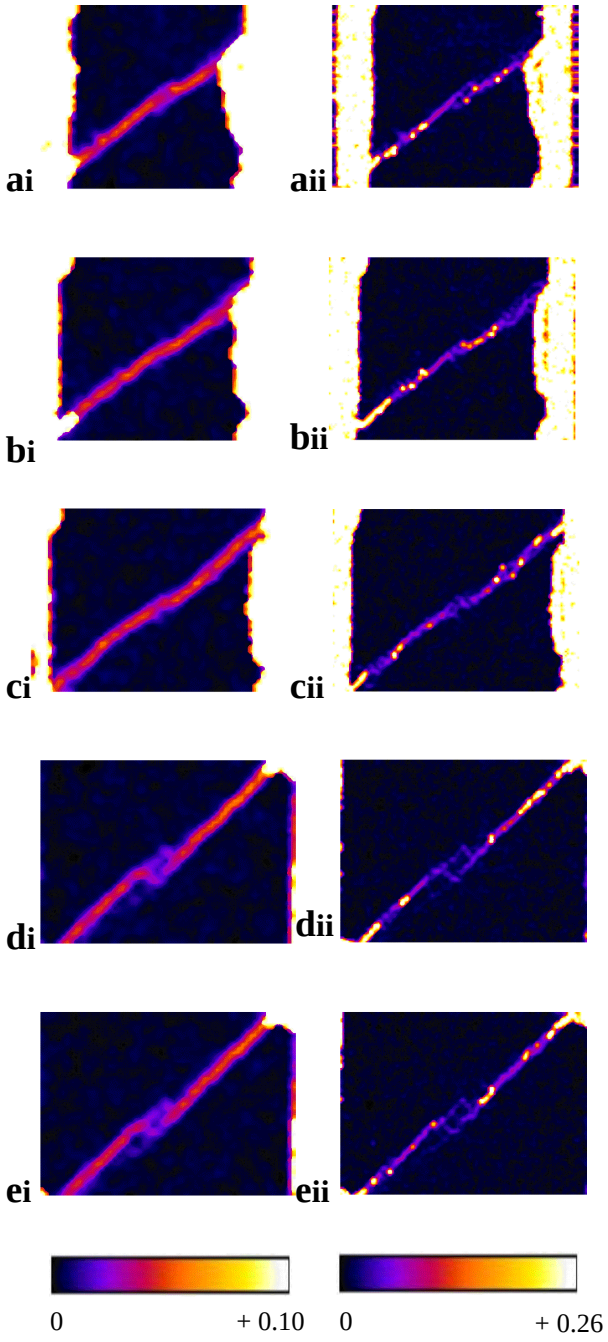

Fig. 5.8: Shear strain fields from specimen Ve2. (ai-ki) Calculations were made over sub-volumes of 20x20x20 voxels^3 at a spacing of 20 voxels in each direction; (aii-kii) Calculations were made over sub-volumes of 10x10x10 voxels^3 at a spacing of 10 voxels in each direction. HR x-ray tomography images were used in both cases (~30 μm).

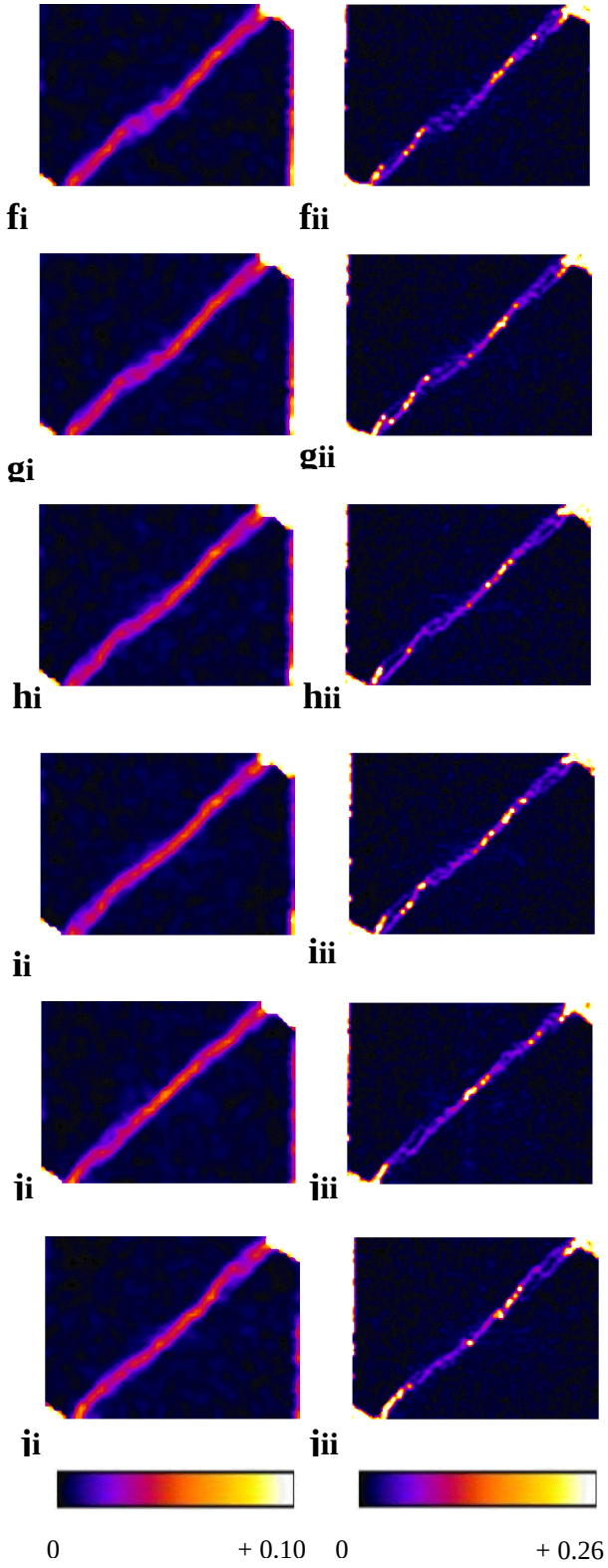

Fig. 5.8: Continued.

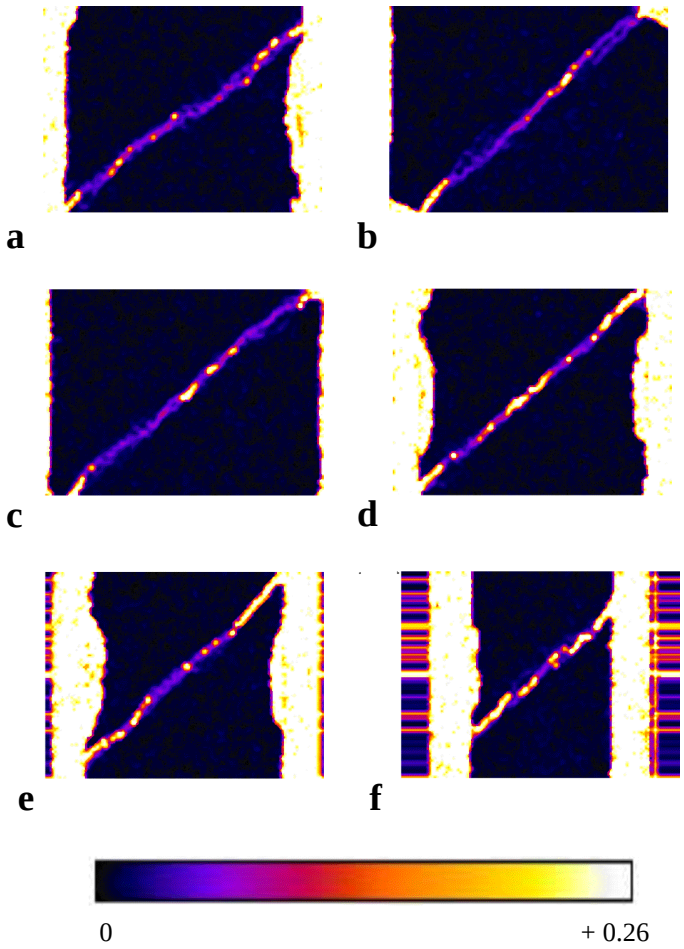

Fig. 5.9: Shear strain fields from vertical slices of specimen Ve2. (a)-(f) Calculations were performed over sub-volumes of 10x10x10 voxels^3 at a spacing of 10 voxels in each direction. The resolution of the x-ray images was of ~30 μm.

Volumetric strain fields from specimen Ve2 showed dilation near the notches and both dilation and compaction in the more central parts of the shear band (Fig. 5.7aii- 5.7kii). Dilation was usually observed in regions where high shear strains were measured. On the other hand, post mortem HR x-ray tomography images indicated higher density (compaction) inside the shear bands and captured some open fractures near the notches (Fig. 5.3). To reconcile this apparently inconsistent observation of compacted material in zones of dilative volumetric strains, one should take into account the resolution of the methods used. The x-rays images had a voxel size of 30x30x30 μm^3; therefore fractures having an opening greater

than 30 μm could be clearly identified. DIC strain field calculations were made over a cubic gauge volume of side 600 μm, therefore opening fractures were necessarily interpreted as high dilation and not resolved discretely (see also *Nguyen et al.*, 2010). Near the notches, in the x-ray images both fractures and compacting material close to the fracture boundary were seen, whilst DIC showed volumetric dilative strains. The maximum opening of the fractures were measured to be about 60 μm (from the x-rays images), which is much less than the DIC gauge volume-size. The DIC gauge volume therefore contained both the opening fracture and the compacting material around the fracture, and the net obtained dilation indicated that the compaction of the material around the fractures was less significant than the fracture opening. Far from the edge, further into the material, no open fractures were visible in the x-ray images but just bands of denser material. However, the DIC still indicated dilation, which might suggest that open fractures existed but with an opening less than the x-ray image resolution. In the central portion of the band, both x-rays and DIC indicated volumetric compaction.

Clearly the resolution of the x-ray tomography images and of the DIC analysis affects the interpretation of the visualised deformation features; therefore this is investigated further in the following section.

5.3 Different resolution 3D-volumetric DIC: investigation of parameters

Two different x-ray tomography resolutions were used for the 3D-volumetric DIC of specimen Ve2; the HR (~30 μm voxel-size) and the LR (~90 μm voxel-size). In this section, the impact of these two different resolutions on the visualisation of shear bands, in terms of their geometry and their strain values, is explored. In addition, the role of both sub-volume sizes (in which strains were calculated) and spacing size (of this cubic gauge in each direction) on the calculation of strain fields is discussed. Sub-volume size and spacing size are the two out of three parameters used in 3D-volumetric DIC, the other being the displacement range (see section 3.5.3). Recall that both parameters are related to the grain-size of the host rock (*i.e.*, a multiple of 300 μm). The optimal combination is not always

trivial; the choice here was guided by the combination that provided the best visualisation of the shear band. Examples of median vertical projections from specimen Ve2 are presented in this section. Note that these projections are 2D maps where the value of each pixel is the median value of all voxel values for the given x-y position through the width of the specimen. Moreover, the median projection reduces the influence of noise and provided a clearer picture of the band structure. Another objective of this section is to make a point of the potential of each combination, presenting a statistical analysis of the resolved strain fields.

Six and five different combinations were used for the HR and LR 3D-DIC, respectively; a 2D schematic view is presented in Figure 5.10, 5.11. For the HR 3D-DIC, calculations were made at a spacing of 900 μm in each direction over sub-volumes of 900x900x900 μm^3 (Fig. 5.10a), over sub-volumes of 600x600x600 μm^3 (Fig. 5.10b), and over sub-volumes of 300x300x300 μm^3 (Fig. 5.10c), at a spacing of 600 μm in each direction over sub-volumes of 600x600x600 μm^3 (Fig. 5.10d), and over sub-volumes of 300x300x300 μm^3 (Fig. 5.10e), and at a spacing of 300 μm in each direction over sub-volumes of 300x300x300 μm^3 (Fig. 5.10f).

For the LR strain values, calculations were made over sub-volumes of 1800x1800x1800 μm^3 at a spacing of 1800 μm in each direction (Fig. 5.11a) or of 900 μm in each direction (Fig. 5.11c), and over sub-volumes of 900x900x900 μm^3 at a spacing of 1800 μm in each direction (Fig. 5.11b), a spacing of 900 μm in each direction (Fig. 5.11d), and a spacing of 450 μm in each direction (Fig. 5.11e).

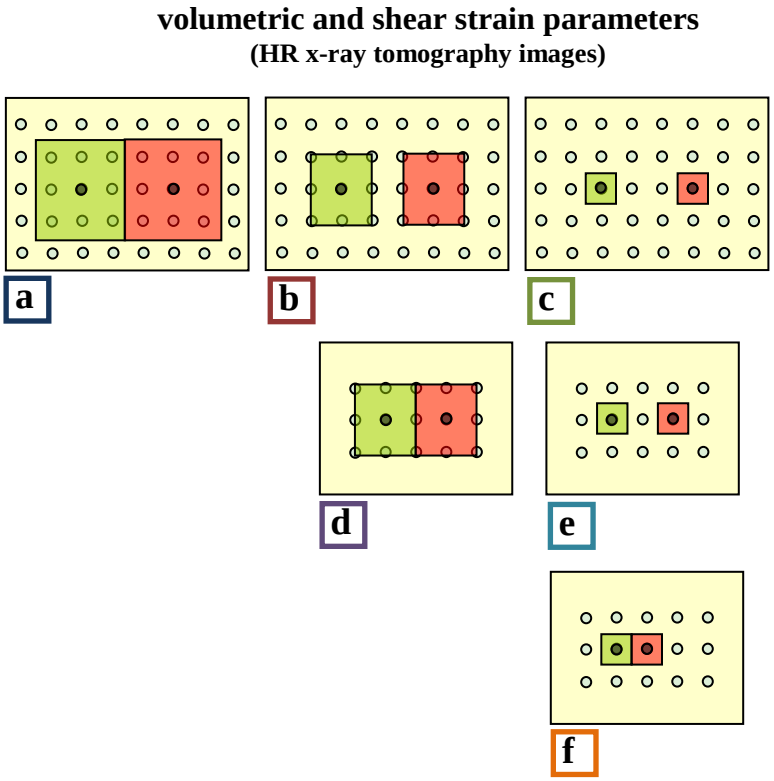

Fig. 5.10: 2D schematic representation of the spacing size and the sub-volume size combinations used for the calculation of the volumetric and shear strain values, using the pre-and post-mortem HR x-ray tomography images. Strains calculations were made: (a) Over sub-volumes of 30x30x30 voxels^3 at a spacing of 30 voxels in each direction (*i.e.*, sub-volumes equivalent to 3x3x3 intact grain-sizes, at a spacing equivalent to 3 intact grain-sizes); (b) Over sub-volumes of 20x20x20 voxels^3 at a spacing of 30 voxels in each direction (*i.e.*, sub-volumes equivalent to 2x2x2 intact grain-sizes, at a spacing equivalent to 3 intact grain-sizes); (c) Over sub-volumes of 10x10x10 voxels^3 at a spacing of 30 voxels in each direction (*i.e.*, sub-volumes equivalent to 1x1x1 intact grain-size, at a spacing equivalent to 3 intact grain-sizes); (d) Over sub-volumes of 20x20x20 voxels^3 at a spacing of 20 voxels in each direction (*i.e.*, sub-volumes equivalent to 2x2x2 intact grain-sizes, at a spacing equivalent to 2 intact grain-sizes); (e) Over sub-volumes of 10x10x10 voxels^3 at a spacing of 20 voxels in each direction (*i.e.*, sub-volumes equivalent to 1x1x1 intact grain-size, at a spacing equivalent to 2 intact grain-sizes); (f) Over sub-volumes of 10x10x10 voxels^3 at a spacing of 10 voxels in each direction (*i.e.*, sub-volumes equivalent to 1x1x1 intact grain-size, at a spacing equivalent to 1 intact grain-size). The resolution of the HR x-ray images was of ~30 µm.

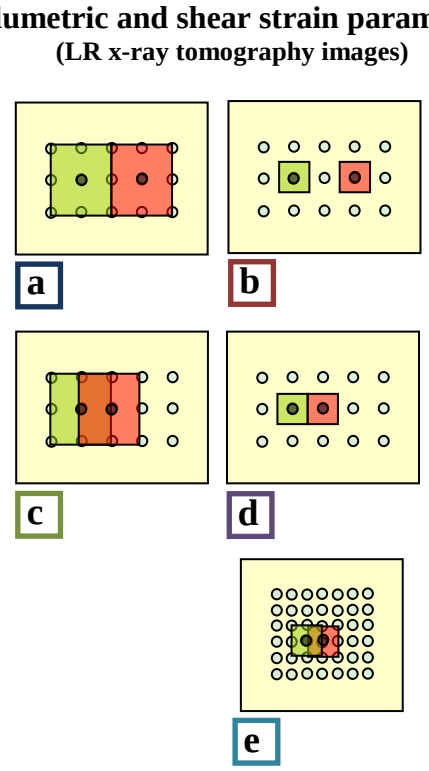

Fig. 5.11: 2D schematic representation of the spacing size and the sub-volume size combinations used for the calculation of the volumetric and shear strain values, using the LR pre-and post-mortem x-ray images. The strains calculations were made: (a) Over sub-volumes of 20x20x20 voxels^3 at a spacing of 20 voxels in each direction (*i.e.*, sub-volumes equivalent to 6x6x6 intact grain-sizes, at a spacing equivalent to 6 intact grain-sizes); (b) Over sub-volumes of 10x10x10 voxels ^{3} at a spacing of 20 voxels in each direction (*i.e.*, sub-volumes equivalent to 3x3x3 intact grain-sizes, at a spacing equivalent to 6 intact grain-sizes); (c) Over sub-volumes of 20x20x20 voxels ^{3} at a spacing of 10 voxels in each direction (*i.e.*, sub-volumes equivalent to 6x6x6 intact grain-sizes, at a spacing equivalent to 3 intact grain-sizes); (d) Over sub-volumes of 10x10x10 voxels ^{3} at a spacing of 10 voxels in each direction (*i.e.*, sub-volumes equivalent to 3x3x3 intact grain-sizes, at a spacing equivalent to 3 intact grain-sizes); (e) Over sub-volumes of 10x10x10 voxels ^{3} at a spacing of 0.5 voxels in each direction (*i.e.*, sub-volumes equivalent to 3x3x3 intact grain-sizes, at a spacing equivalent to 1.5 intact grain-sizes). The resolution of the LR x-ray images was of ~90 µm.

Figure 5.12 illustrates the median vertical projections of the shear strain fields; calculated using the different combinations of all these parameters discussed in Figure 5.10, together with their equivalent histograms and mean shear strain values.

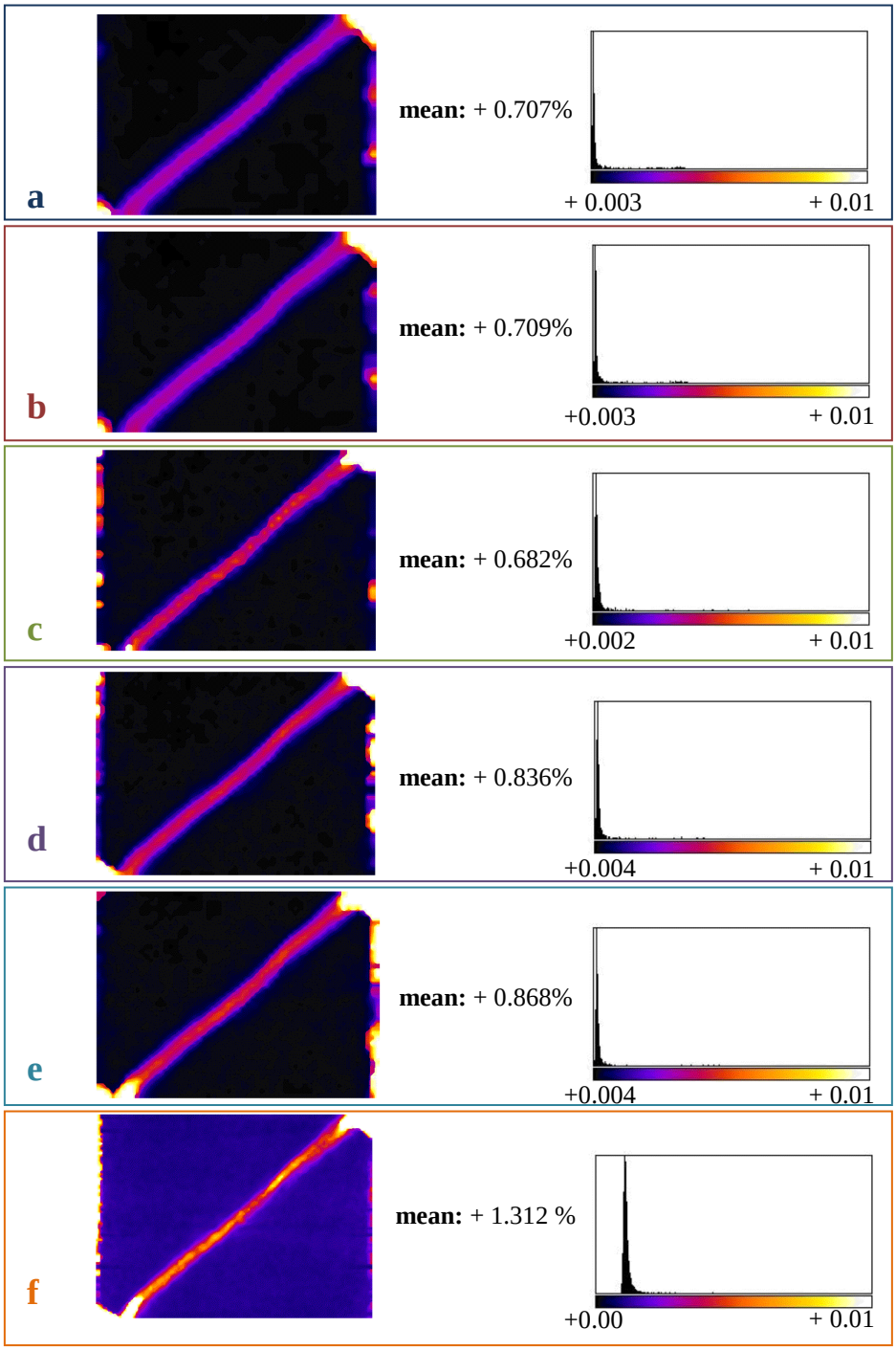

Fig. 5.12: 2D median vertical projections of shear strains from specimen Ve2 together with the equivalent histograms. Figures (a-f) illustrate the six different combinations that were presented in Figure 5.10. The combination of spacing size and sub-volume size and the shear strain fields in both Figures 4.10 and 4.12 are denoted by the same colours.

When the strain calculations were made over smaller sub-volume size and at smaller spacing in each direction, higher mean shear strains were calculated (Fig. 5.12a, 5.12d, 5.12f). Furthermore, the width of the shear band became smaller and the shear strain variations inside the band illustrated a more complex shear strain field structure. For constant gauge spacing, minor differences in the mean strain values were calculated for different sub-volume gauge sizes. The general trend of the decrease in the sub-volume gauge size was a slight increase in the mean shear strain values (Fig. 5.12a, 5.12b, 5.12d-5.12e, with an exception of Fig. 5.12c).

Apart from the mean strain values, other statistical parameters such as the standard deviation or the mode were calculated, however, no significant interpretation of such parameters could be achieved. *Sornette et al.*, [1993] introduced the participation ratio S_2 to express in a more quantitatively way the evolution of large-scale deformation during in-situ fault growth in brittle-ductile experiments. S_2 denotes the fraction of the system surface which has undergone a considerable deformation. The ´participation ratio` S_2 used in this approach is described by the following equation:

$$S_2 = \frac{1}{N_{tr}} \frac{[\sum \varepsilon]^2}{[\sum (\varepsilon)^2]} \qquad [1]$$

where ε is the appropriate strain value (volumetric or shear strain) of every voxel and N_{tr} is the total number of voxels. When S_2 has a large value (close to 1) then the deformation is rather homogeneous, while smaller values of S_2 correspond to a well localised deformation. Although in this particular case, the local deformation has been measured, a global approach such as that of the S_2 has been used in order to identify the impact of the localised band on the global deformation of the analysed volume.

Table 5.1 summarises the S_2 values, calculated from the median vertical projections of the shear strain field, for the six different spacing and sub-volumes combinations (Fig. 5.10). For the case of sub-volume gauge size equal to spacing size (Fig. 5.12a, 5.12d, 5.12e), S_2 increases when calculations were performed over a smaller sub-volume gauge, indicating a less heterogeneous strain field. Therefore, it could be argued that in such case, the

heterogeneity of the localised feature is not so strong compared to that of the overall volume, since the volume far from the band appears to be also locally heterogeneous due to the possibly overestimated calculation (over small sub-volume gauge). Another explanation might be the fact that the deformation structure is better resolved when calculations were performed over smaller sub-volume gauges, therefore it consists a smaller heterogeneity inside the shear strain field. When the spacing size remained constant and calculations were performed over smaller sub-volume sizes, ***S2*** decreases (Fig. 5.12a, 5.12c, 5.12d-5.12e, with an exception of Fig. 5.12b), indicating, in that case, that smaller gauge sizes resolve a more heterogeneous field inside the band.

Table 5.1: S2 parameter calculated from the median vertical projections of the shear strain field of specimen Ve2 for the different combination of spacing and sub-volume sizes.

Specimen	S2: values of the shear strains
900 μm spacing, 900x900x900 μm^3 sub-volume	0.3737
900 μm spacing, 600x600x600 μm^3 sub-volume	0.3754
900 μm spacing, 300x300x300 μm^3 sub-volume	0.3116
600 μm spacing, 600x600x600 μm^3 sub-volume	0.4279
600 μm spacing, 300x300x300 μm^3 sub-volume	0.3832
300 μm spacing, 300x300x300 μm^3 sub-volume	0.6438

The different spacing size and sub-volume gauges sizes affected not only the mean shear strain and the ***S2*** (global values) but they also had an impact on the shear strain values inside the shear band. Table 5.2 presents the minimum and the maximum calculated shear strains inside the shear band and the mean shear strain outside the band. Two different volumes were taken into account to group the appropriate voxels with strain values inside the width of the deformation band and outside it. The values of the latter (outside the band) increase with decreasing spacing, for different sub-volume gauge sizes. Inside the shear band the shear strain range increases with decreasing gauge size (for both the case of spacing-size equal to

gauge-size and that of same spacing-size but decreasing gauge-size), since a smaller gauge results in a less smooth shear strain field inside the band (see also Fig. 5.12).

Table 5.2: Minimum and maximum shear strain values measured inside the shear bands and an indicative value of the strains outside the bands for specimen Ve2 and different combination of spacing and sub-volume width (median vertical projections).

Different spacing and sub-volume length combination	Min shear strains inside the band [%]	Max shear strains inside the band [%]	Indicative shear strains outside the bands [%]
900 μm spacing, 900x900x900 μm^3 sub-volume	0.81	3.54	~0.36
900 μm spacing, 600x600x600 μm^3 sub-volume	0.85	3.60	~0.36
900 μm spacing, 300x300x300 μm^3 sub-volume	0.70	5.30	~0.36
600 μm spacing, 600x600x600 μm^3 sub-volume	0.60	4.66	~0.49
600 μm spacing, 300x300x300 μm^3 sub-volume	0.64	4.90	~0.49
300 μm spacing, 300x300x300 μm^3 sub-volume	1.51	8.60	~1.04

Figure 5.13 presents the normalised shear strain population inside the shear band as a function of the shear strain values, for the six different spacing- and gauge-size combinations. Note that these values belong to the 25% of the highest shear strain values calculated inside the specimen's volume (group analysis; strains were grouped in classes of 0.1 step, *i.e.*, groups of strain values from 0-0.1, 0.1-0.2 up to 8.5-8.6). The strain values presented in Fig. 5.13 were thresholded by the minimum and maximum shear strains of Table 5.2 (in such case a part of the 25% of the highest shear strain values is plotted in Fig. 5.13).

When shear strains were calculated at spacing equal to three intact grain-sizes (900 μm), the majority of their population is concentrated on the higher values of the shear band strain range, regardless of the sub-volume size (Fig. 5.13; blue, red, green surfaces). For a sub-volume equal to 300x300x300 μm^3, higher shear strains were calculated inside the band; however their population is less heterogeneously distributed. For smaller spacing-sizes, the shear range inside the band becomes wider, and the majority of the strain population is

concentrated on the lower shear strain values. This possibly indicates that in such cases, the higher strain values were better resolved (therefore the population of these strains is lower and its distribution wider, Fig. 5.13; purple, cyan, orange surfaces). Note that a sub-volume gauge equal to 300x300x300 μm^3 (*i.e.*, 1x1x1 intact grain-size) resulted always in a higher shear strain range and thus, in higher shear strain values (Fig. 5.13, see green and orange surfaces).

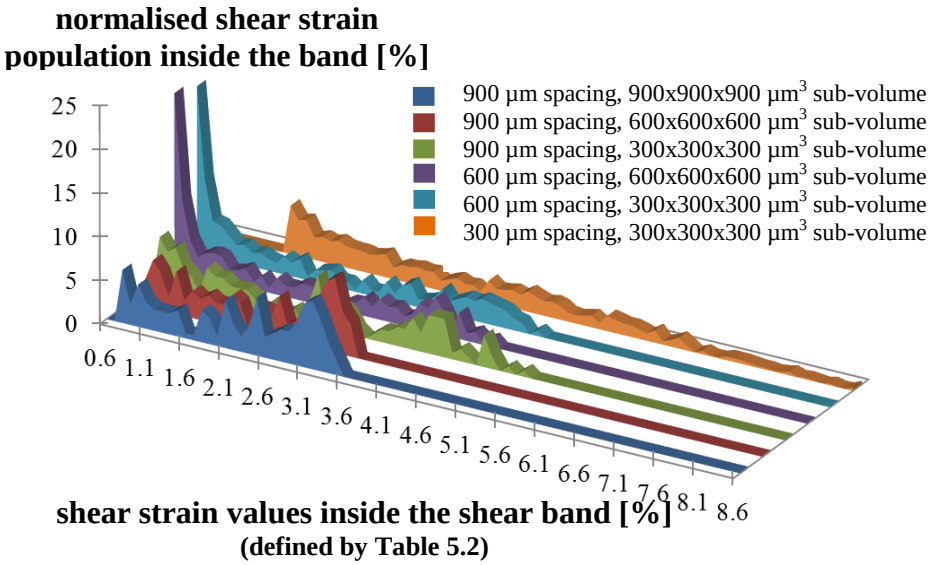

Fig. 5.13: Shear strain values distribution inside the shear band of specimen Ve2. Different colours correspond to different spacing-sub-volume combinations presented in Figure 5.10. HR x-ray tomography images were used for the DIC.

A similar analysis, performed on different spacing and sub-volume gauge combinations, applied to the LR DIC images. Figure 5.14 presents the median vertical projections of the shear strain fields from specimen Ve2 for the five different combinations discussed in Figure 5.11. Recall the LR x-ray tomography scans were performed throughout the whole height of specimen Ve2. The histograms of the shear strain values as well as the mean strain values are also shown.

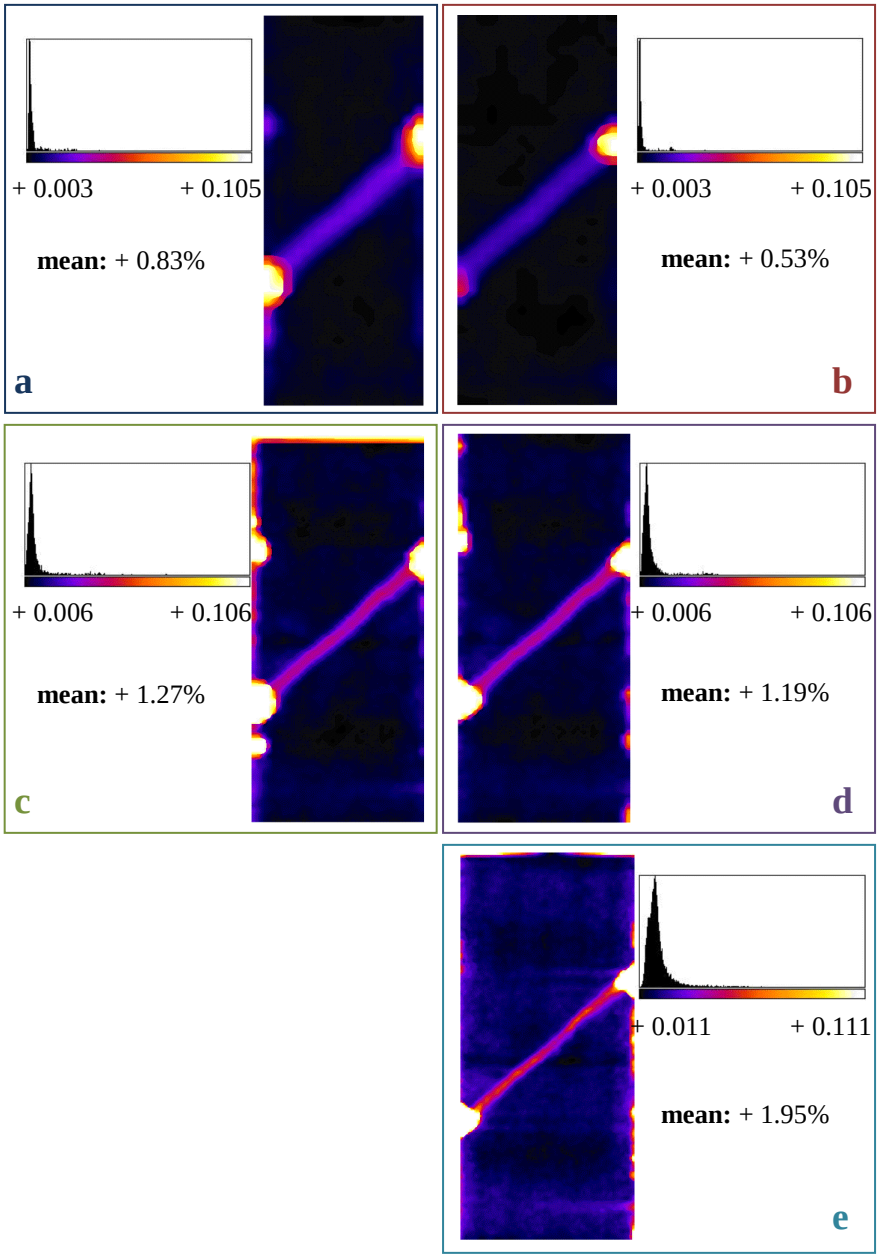

Fig. 5.14: 2D median vertical projections of shear strains from specimen Ve2 together with the equivalent histograms. Figures (a-e) illustrate the six different combinations of parameters that have been presented in Figure 5.10. The combination of parameters and the strains in both Figures are denoted by the same colours.

For spacing-size equal to six intact grains, the shear band appears rather smooth. As the sub-volume gauge decreases (from 1800x1800x1800 μm^3 to 900x900x900 μm^3) smaller mean

shear strains were calculated (Fig. 5.14a, 5.14b). However, the difference is not that much profound for a spacing-size equal to three intact grains (Fig. 5.14c, 5.14d). When the spacing is equal to the sub-volume size, a decrease in the latter resulted in an increase in the mean shear strain and a smaller width of the band (Fig. 5.14a, 5.14d, similarly to the HR DIC in Fig. 5.12a, 5.12d, 5.12f). When there is an overlapping in the sub-volume gauges (*i.e.*, the spacing is half the size of the gauge, Fig., 5.14c, 5.14e), then mean shear strain increases with decreasing gauge size and the shear band is better resolved.

Furthermore, for the LR DIC case, the shear strain fields, which were calculated throughout the whole height of the specimen, resolved, also, some horizontal layers of lower shear strain values, which possibly reflected the existence of bedding layers, obvious by naked eye, on the intact rock (see Fig. 4.2a). Due to the small dip of these structural heterogeneities and, possibly, the resolution of the LR x-ray images; it could not be identified whether or not there was an offset of the layer at the place of its intersection with the shear band.

Table 5.3 presents the S_2 parameter for the five different spacing and sub-volume combinations (Fig. 5.11). When the spacing-size is equal to or half of the sub-volume size, S_2 increases with decreasing gauge-size, and therefore, the global strain field appears to be more homogeneous (similarly to what is observed in Table 5.1). As already mentioned, higher mean shear strain values are resolved in these cases, the width of the band becomes smaller and possibly the strains distribution inside the band does not affect much the more homogeneous strain field. Therefore, a global statistical parameter such as the S_2 gets higher values and attributes a more homogeneous character to the whole strain field. However, when the spacing remains constant, a decrease in the size of the gauge results in a decrease in the S_2 (Fig. 5.14a, 5.14b), where a reduction of the mean shear strain results in a more localised shear strain field.

Table 5.4 shows the minimum and maximum shear strains values inside the shear band for the case of the LR DIC. For a spacing equal to or half of the sub-volume gauge size, the mean shear strain outside the band and the shear range inside it increase with decreasing gauge size. Higher shear strains are also better resolved inside the band. For the case of spacing equal to six intact grain-sizes, smaller mean shear strains outside the band and

smaller higher strains inside the band are resolved as the gauge size decreases, which was not the case for the HR DIC images (see Table 5.2). Such observation might indicate that these particular parameters should give underestimated calculations of the shear strains (since a downscale decrease the resolution instead of increasing it).

Table 5.3: S2 parameter calculated from the median vertical projections of the shear strain field of specimen Ve2 for the different combination of spacing and sub-volume width.

Specimen	**S2: values of the shear strains**
1800 µm spacing, 1800x1800x1800 µm^3 sub-volume	0.3419
1800 µm spacing, 900x900x900 µm^3 sub-volume	0.3291
900 µm spacing, 1800x1800x1800 µm^3 sub-volume	0.5411
900 µm spacing, 900x900x900 µm^3 sub-volume	0.6082
450 µm spacing, 900x900x900 µm^3 sub-volume	0.8804

Table 5.4: Minimum and maximum shear strain values measured inside the shear bands and an indicative value of the strains outside the bands for specimen Ve2 together with different combination of spacing and sub-volume width (median vertical projections).

Different spacing and sub-volume length combination	**Min shear strains inside the band [%]**	**Max shear strains inside the band [%]**	**Indicative value of shear strains outside the bands [%]**
1800 µm spacing, 1800x1800x1800 µm^3 sub-volume	1.02	2.58,	~0.49
1800 µm spacing, 900x900x900 µm^3 sub-volume	1.02	1.95	~0.34
900 µm spacing, 1800x1800x1800 µm^3 sub-volume	1.90	4.34	~0.89
900 µm spacing, 900x900x900 µm^3 sub-volume	1.90	4.20	~0.91
450 µm spacing, 900x900x900 µm^3 sub-volume	2.40	6.60	~1.75

Figure 5.15 presents the normalised strain population inside the shear band as a function of the shear strains, for the five different combinations discussed in Figure 5.11. Shear strain values defined by Table 5.4 are plotted (these values correspond to the 25% of highest shear strain values (group analysis, similarly to 5.13)). Note that the same gauge size but different spacing size results in different distribution of the resolved shear strains inside the band (blue-green and red-purple surfaces, Fig. 5.11).

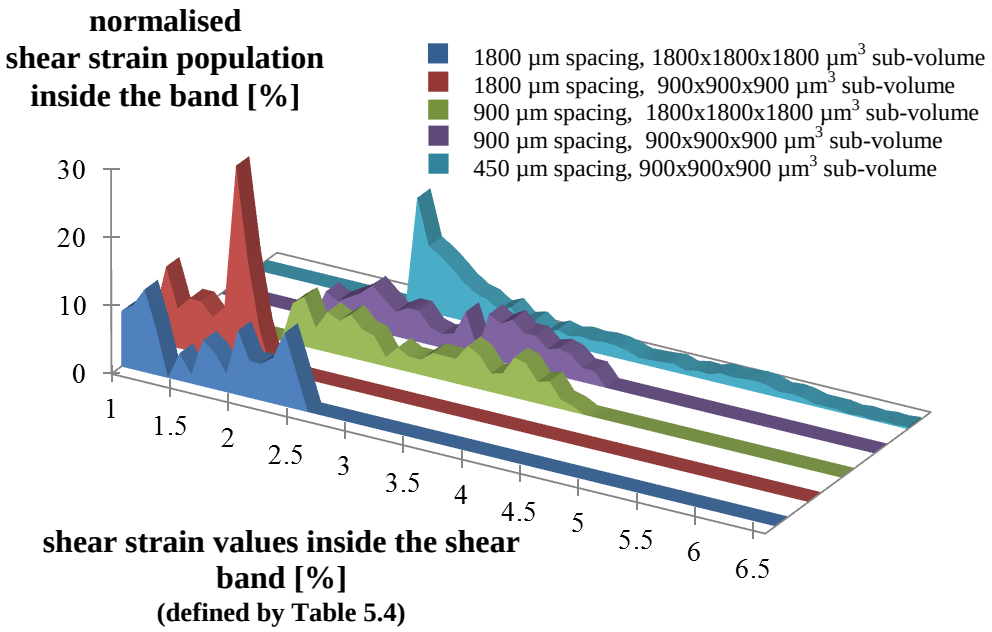

Fig. 5.15: Shear strain value distribution inside the shear band of specimen Ve2. Different colours correspond to different spacing-sub-volume combinations presented in Figure 5.11. LR x-ray tomography images were used for the DIC.

Figure 5.16 makes a comparison between the median vertical projections of the shear strain fields, calculated from the HR and LR x-ray tomography images, using the same spacing and sub-volume gauge size. Calculations were performed over sub-volume of 900x900x900 µm^3, at 900 µm spacing in each direction (equal to 3 intact grain-sizes). The LR-DIC shear strain field presented higher values inside the band (yellow colours, Fig. 5.16b). Some regions of relatively higher strains were resolved outside the band, which is not the case for the strain field derived from the HR-DIC. Note that the geometry of the shear band was similarly resolved for both HR-DIC and LR-DIC; however, the width of the band was somewhat

smaller in the former representation. Both strain fields resolved shear strains which faded in places far from the band (*e.g.*, intense shear in the heart of the band, smaller shear strains close to the borders of the band and relatively smaller strains far for the band).

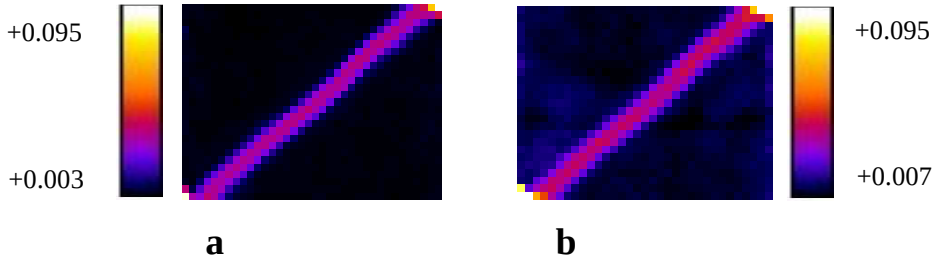

Fig. 5.16: Shear strain fields derived from HR x-ray tomography images (a) and LR x-ray tomography images (b). Calculations have been performed over sub-volumes of 900x900x900 μm^3 at 900 μm spacing in each direction.

Both dilation and compaction was observed inside the volumetric strain fields. For the time being, no similar statistical analysis was performed on the volumetric strain fields.

5.4 Different strain levels

In this section results from specimens, which were loaded under the same confining pressure but were taken to different strain values are presented, using some of the experimental methods presented in Chapter 3. Following the experimental methods' presentation order (Chapter 3), UT results are presented initially followed by X-ray tomography images.

5.4.1 Ultrasonic tomography

Ultrasonic transmission measurements, using the barrettes (section 3.2.2), were made for specimens VLR0, VEC1, VEC5, and VEC4, which were subjected to different axial strains (see Tables 4.1, 4.2). In this section results on the waveform and frequency measurements together with the resolved ultrasonic velocity fields (travel-time tomography) are presented.

Recall that all specimens had a notch machined on their flattened surfaces (Fig. 4.12). Results from specimen VEC1 are presented in *Tudisco*`s Master Thesis [2009] and were also shown in Figures 3.7 and 3.8. Herein, results for specimens VLR0, VEC5, and VEC4 are discussed.

Zero-offset and angular P-wave ultrasonic transmission measurements were made through the whole height of the deformed specimens (see section 3.2). Figures 5.17 present the amplitude spectrum of the zero-offset measurements together with the zero-offset P-wave velocity profiles and the velocity fields from specimens VLR0, VEC5, and VEC4. Visual inspections of the surface of the specimens revealed the existence of shear bands (based on their inclination angle, Fig. 4.12). In particular, two small traces of bands, initiating from the notches and propagating towards the boundaries, could be seen on the surface of the specimen VLR0, but only faintly. A shear band developed in between the notches of specimenVEC5 and in VEC4 a shear band developed in between the notches and another initiated at the top notch and propagated towards the top boundary.

Specimen VLR0 was taken to 0.054% axial strain beyond the peak-stress (Table 4.2). The amplitude of the transmitted signal is slightly reduced near the region of the notches (Figure 5.17a). Small P-wave velocity variations were also observed in the zero-offset velocity profile. In particular, the velocity field revealed regions of reduced velocity near the notches. Two zones of relatively higher (but still low) velocities were resolved above and below the notches and in the vicinity of the notches. These low velocity regions are inferred to correspond to the shear bands (hardy seen by naked eye on the surface of the VLR0). Low velocities are often linked to damage (*e.g.,* micro-cracks), so it is inferred that there is a damage associated with the localised deformation. Furthermore, an interesting low velocity feature was observed in between the notches. This low velocity either is linked to damage in a place far from the notches, or corresponds to a zone which appears to be dilating in the centre of the specimen, as dilation can also cause reduced velocities, *e.g.*, by opening up existing cracks.

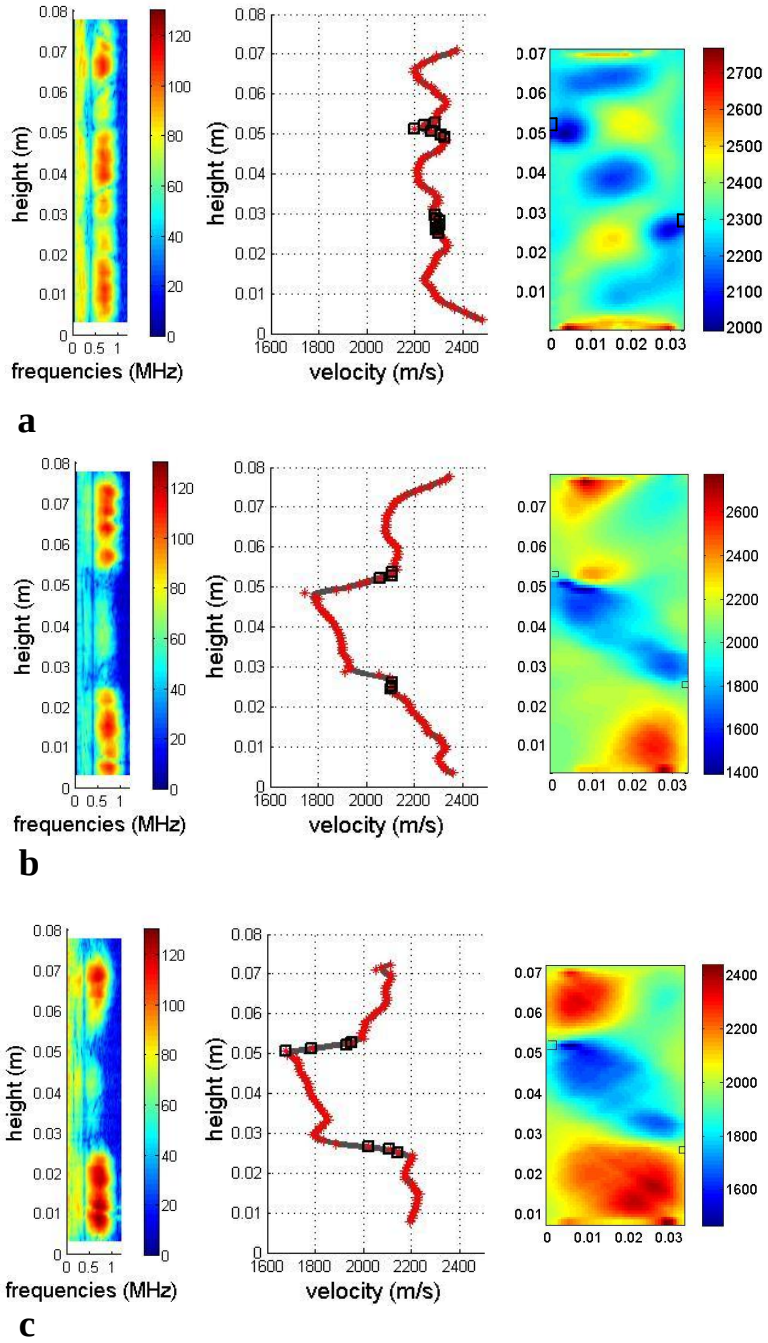

Fig. 5.17: Amplitude spectra from the zero-offset measurements, velocity profile of the zero-offset measurements, ultrasonic travel-time tomography velocity fields (zero-offset and angular coverage measurements) from specimens: (a) VLR0; (b) VEC5; (c) VEC4. The colour-bar in the velocity fields is adjusted to the minimum and maximum velocities inside each field.

Specimen VEC5, which was taken to 0.205% axial strain beyond the peak-stress (Table 4.2), showed a considerable reduction in the P-wave transmission amplitude near the region of the notches (Fig. 5.17b), which was accompanied by a decrease in the zero-offset velocity. The velocity field revealed a diagonal zone of lower velocity (reduction of almost 15%) in between the notches, which is related to the shear band formation. Note that lower velocities were measured at the regions close to the notches than far from them (and inside the shear band), which indicated that possibly more damage was accumulated close to the notches of the shear band.

Specimen VEC4, which was taken to 0.425% axial strain above the peak-stress (Table 4.2), showed a more pronounced amplitude reduction near the region of the notches and a frequency shift (Fig. 5.17c). The zero-offset velocity profile of this specimen showed lower velocity values in more regions along the shear band. Similarly, the velocity field resolved a much wider region of lower velocity in between the notches, which can be linked to a wider damage due to the increased axial strain value. A velocity reduction of 18% is measured inside the band. However, no lower velocity structure was resolved at the top notch and upwards, where a band was obvious on the surface of the specimen (Fig. 4.12). This is attributed to the fact that many of the ray-paths along this region were not used because of the big attenuation of the signals due to the damage.

In all cases presented in Figure 5.17, higher velocities are observed in the regions outside the shear band than those observed inside it.

Strong velocity variations were observed in specimens VEC5 and VEC4, close to the top notch. Figures 5.18 focusing on specimen VEC5 try to explain these velocity variations. Recall that the low velocities located in the region of the shear band were linked to a high degree of damage. Figure 5.18b shows the median projection of the HR x-ray tomography images from specimen VEC5 (resolution of ~30 μm). In this image, the region of the band is characterised by higher density material (light colours), while an open fracture was observed at the top notch. Figure 5.18a shows a poor ultrasonic ray-coverage of the region of the notch. P-waves were highly attenuated due to the open crack and there were difficulties in picking the arrival-time. The velocity variation in Figure 5.18c indicates that a high velocity layer possibly existed in the region above the top notch. However, it is likely that the

tomography algorithm overestimated the velocities due to the near-by shear band damage (roughness penalty in the tomography algorithm). Note that the higher velocity regions on the bottom and top of the specimen are attributed to artefacts due to the poor ray-coverage of the specimen's boundaries (recall that no velocity measurements were taken on the vertical direction, see also Fig. 3.2).

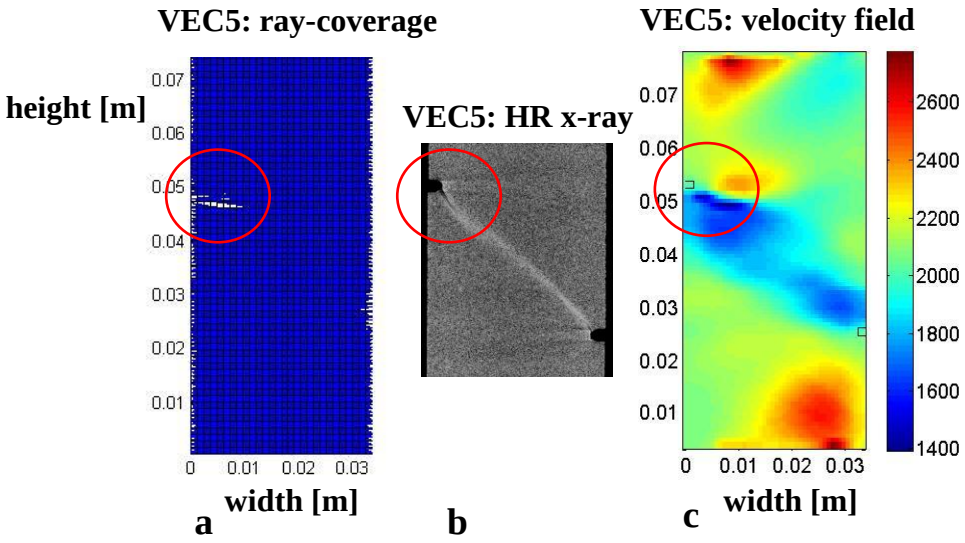

Fig. 5.18: Specimen VEC5 (after test): (a) ray-coverage, highlighting a region of poor coverage close to the top notch (in red); (b) Median projection of HR x-ray tomography images, highlighting an open crack located at the top notch; (c) Ultrasonic travel-time velocity field. The shear band is represented as a region of low velocities.

Figures 5.19 compare the velocity fields from specimen VEC5 before and after the deformation (pre- and post-mortem velocity fields). The colour-bar in both images is at the same scale. Higher velocities characterised the intact specimen (~2400 m/s), which decreased after the triaxial compression (~2200 m/s) while velocities reduced much more inside the shear band (~1800 m/s). However, similar geometry velocity structures were observed inside both velocity fields, which might be attributed either to inherent structural heterogeneities-which were not influenced equally by the damage process compared to the rest of the material, or to artefacts due to the ray-coverage and the tomography algorithm.

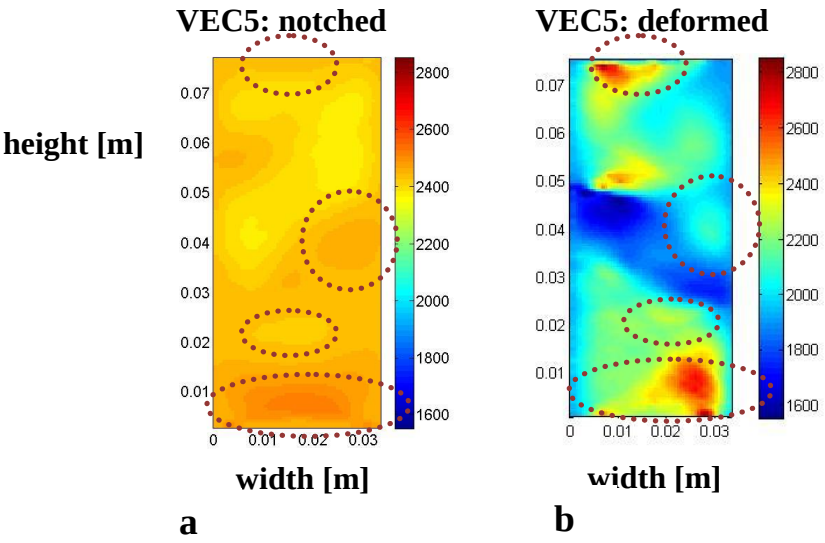

Fig. 5.19: Velocity fields from specimen VEC5 before (a) and after (b) the triaxial compression experiment.

Figures 5.20 present a comparison of the velocity field solutions from the three specimens (VLR0, VEC5, and VEC4). The increased axial strain values resulted in more spread and intense damage, which was expressed by a wider shear band (characterised by lower velocity values). However, the width of the band might be exaggerated due to the resolution of the ultrasonic tomography. The measured wavelength is of around 3 mm, which indicates that structures narrower than 3 mm could not be resolved. On the other hand, the damage zone increased with increasing axial strain values (see section 5.4.2); therefore it is suggested that despite the resolution of the method, the wider band width might also be assigned to the development of a wider damage zone. Note that the structure of the 'macroscopic' band, as this was resolved by the velocity fields from specimens VEC5 and VEC4, was non-planar (see also section 5.4.2). Furthermore, although the resolution of the method was not enough to measure the exact dip of these bands, the dipping angle was very close to that measured by the AE locations in specimen Ve2 (Fig. 5.1) and to the angle suggested by [*Bésuelle*, 2001] (40° for unnotched specimens deformed under 50 MPa confining pressure).

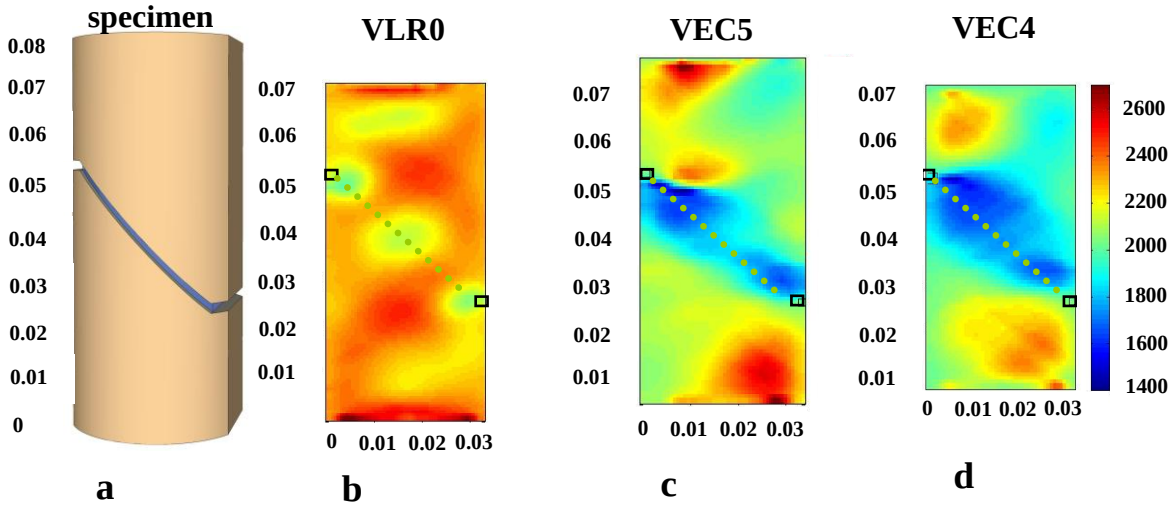

Fig. 5.20: (a) Schematic representation of the Vosges specimen; Ultrasonic velocity fields from deformed specimens (b) VLR0; (c) VEC5; (d) VEC4. The dashed line indicates the theoretical shear band dip.

5.4.2 X-ray CT

The shear bands that developed under 50 MPa confining pressure (triaxial compression) in Vosges sandstone were characterised by a compactant behaviour, as this was visualised by the higher grey-scale values of the HR x-ray tomography images (see section 5.2). This section presents HR x-ray tomography images throughout the volume of specimens VLR00, VEC1, VEC5, and VEC4, which were all tested at 50 MPa confining pressure but different axial strain values (see Table 4.2).

Different vertical projections throughout the volume of specimen VLR0 are illustrated in Figures 5.21. The shear bands in this specimen did not fully evolve, because the experiment was stopped shortly after the peak-stress (plus 0.054%, Table 4.2). The deformation bands, which initiated from both the top and bottom notches, developed mainly at the regions above and below the notch and propagated toward the top and bottom edges of the specimen. In addition, a single band appeared to have initiated from the bottom notch and propagated inwards (Fig. 5.21e-5.21g). Based solely on HR x-ray tomography images, it is rather

difficult to explain why the shear bands did not fully develop in the region between the notches. A possible explanation might be the notch geometry or local structural heterogeneities of the rock, which possibly facilitated the stress concentration in other regions. However, it is worth to mention that locally, some bands developed in places inside the volume of the flattened surfaces (in between the notches) but far from the cylindrical surface boundaries (Fig. 5.21e-5.21g).

The geometry and the length of propagation of the shear bands change throughout the volume of the specimen. Their inclination towards the major imposed principal stress direction varies from 36.5° to 51.5° (dip of 53.5° to 38.5°), which is somewhat lower than the theoretical and experimental values presented by *Bésuelle* [1999]. It could be argued that the (existence and) geometry of the notch could have slightly changed the inclination angle of the shear band.

Shear bands in specimen VEC1, which was taken to a higher axial strain above the peak-stress (plus 0.08%, see Table 4.2), developed and propagated further than those observed in specimen VLR0. Figure 5.21 presents different HR x-ray tomography images (vertical slices) through the volume of specimen VEC1. In this particular specimen, the shear bands were located only at the region between the notches. Two different bands initiated from both notches, and through the volume of the VEC1, either these bands were separated or they met and formed a single band. This illustrates the 3D structure of the band(s) (*i.e.*, the geometry of the bands was non-planar). The inclination angle of these bands towards the major imposed principle stress varies from 41° to 51° (dip of 49° to39°).

Specimen VEC5 was taken to 0.205% extra axial strain after the peaks stress. Figure 5.23 presents vertical projections of HR x-ray tomography images through the volume of specimen VEC5. The developed compactant shear bands (*i.e.*, higher density) had an orientation angle towards the major imposed principal stress direction from 37° to 50° (dip of 53° to 40°). Cracks of a width from 60 μm to 90 μm, initiating from the notches and propagating towards the centre of the specimen, are apparent.

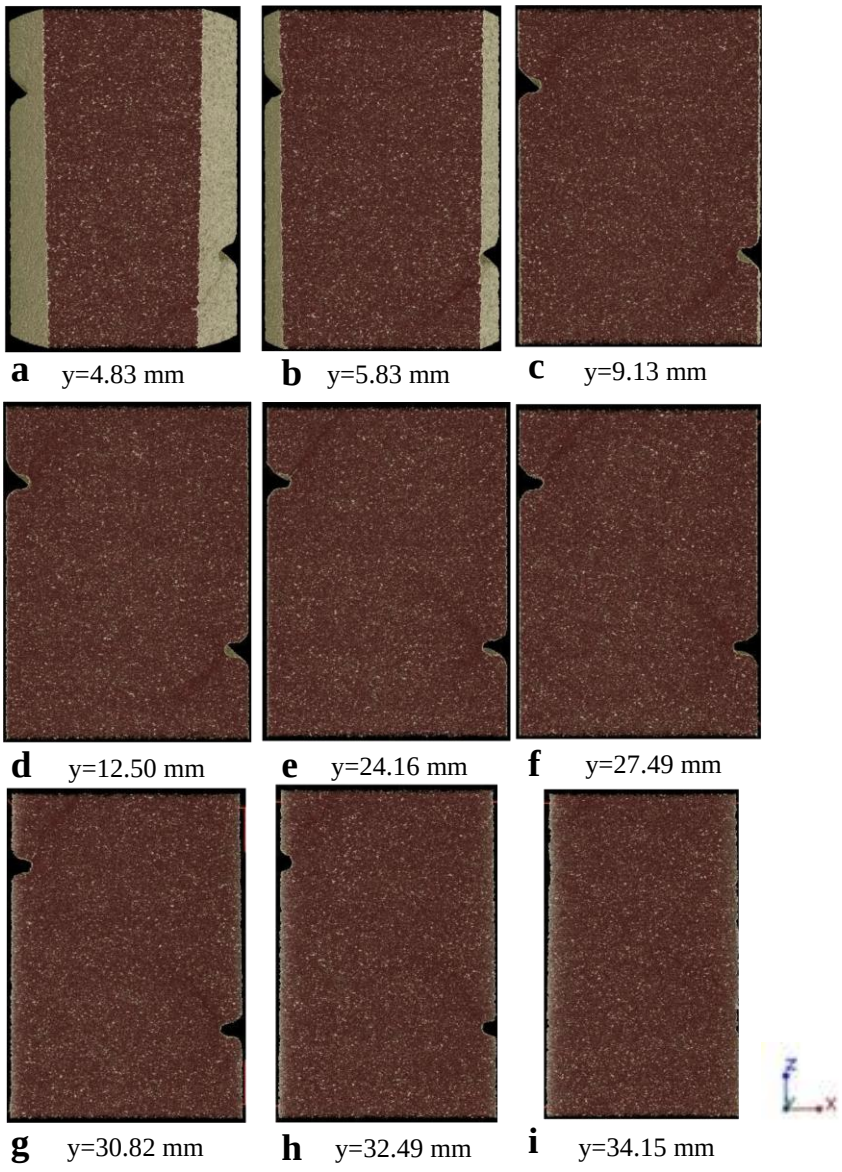

Fig. 5.21: Post-mortem HR x-ray tomography images (volume rendering) from (a) to (i) are a sequence of snapshots of the x-z plane as the y-axis position changes though specimen VLR0 (voxel-size ~30 μm).

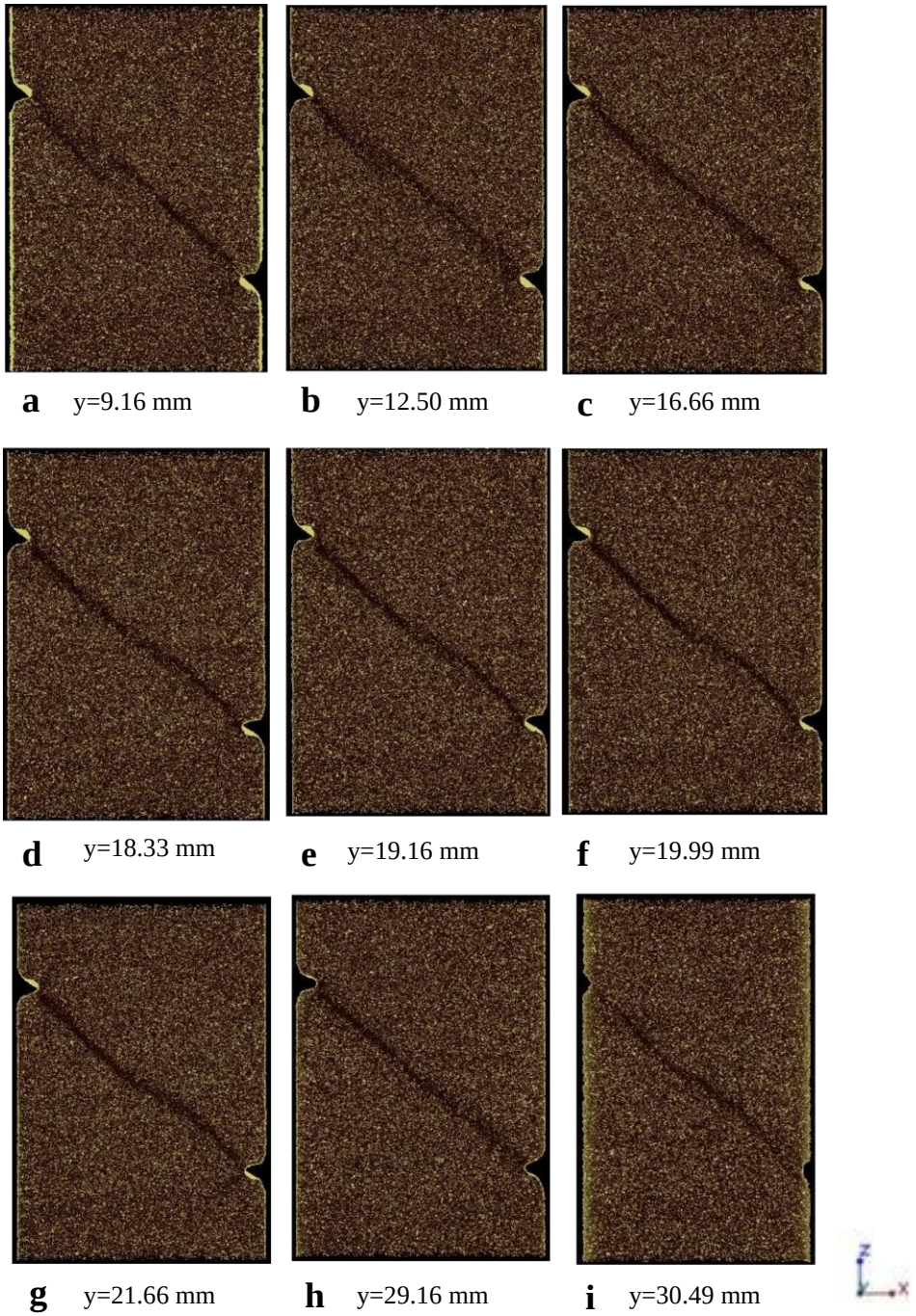

Fig. 5.22: Post-mortem HR x-ray tomography images (volume rendering) from (a) to (i) are a sequence of snapshots of the x-z plane as the y-axis position changes in specimen VEC1 (voxel-size ~30 μm).

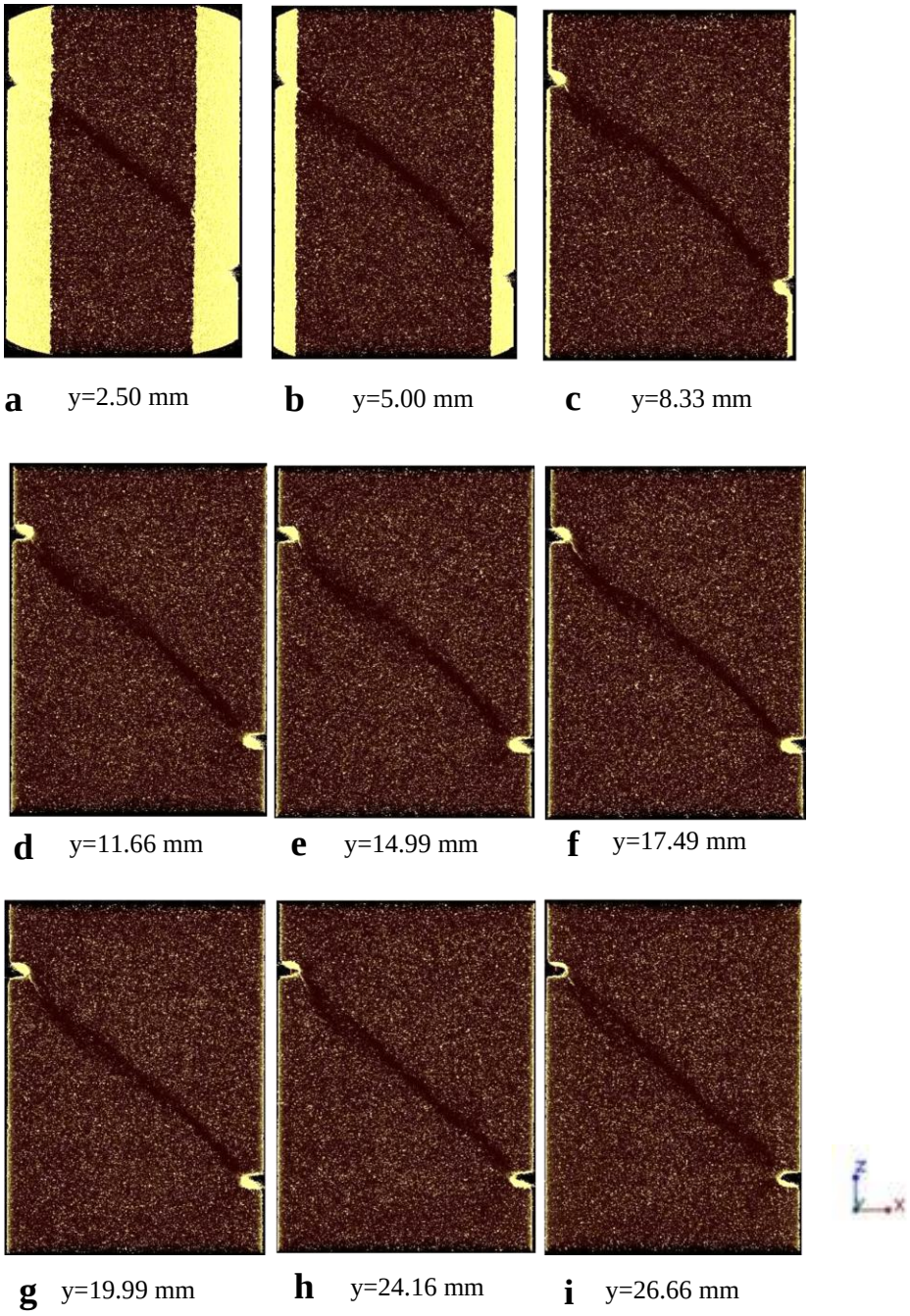

Fig. 5.23: Post-mortem HR x-ray tomography images (volume rendering) from (a) to (l) are a sequence of snapshots of the x-z plane as the y-axis position changes in specimen VEC5 (voxel-size ~30 μm).

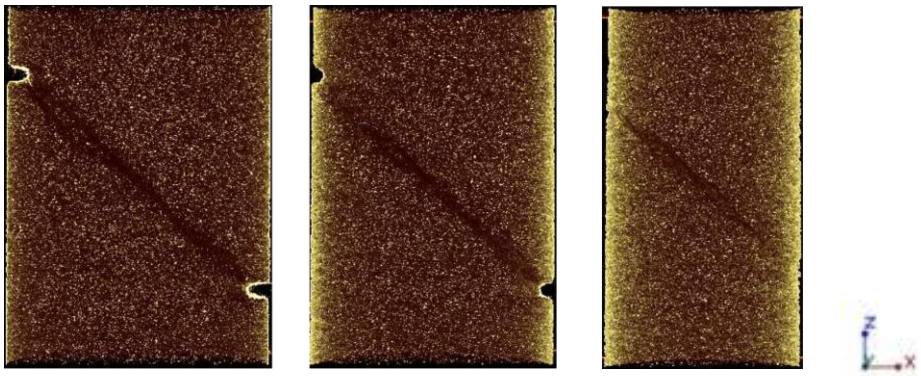

Fig. 5.23: Continued.

Figure 5.24 illustrates that the geometry of the band inside the volume of the specimen is non-planar. It shows the existence of two closely spaced bands (y-z plane) and a non-planar band (x-z plane). Shear bands are visualised as higher density zones (darker colours).

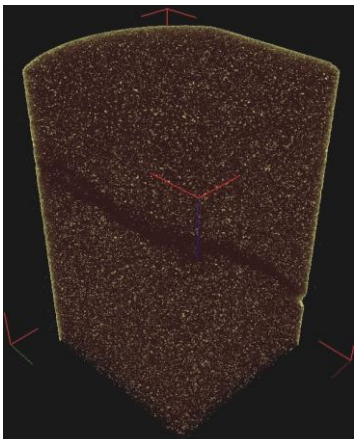

Fig. 5.24: 3D visualisations of specimen VEC5 in a region where the two shear bands meet (post-mortem HR x-ray tomography images ~30 µm, volume rendering).

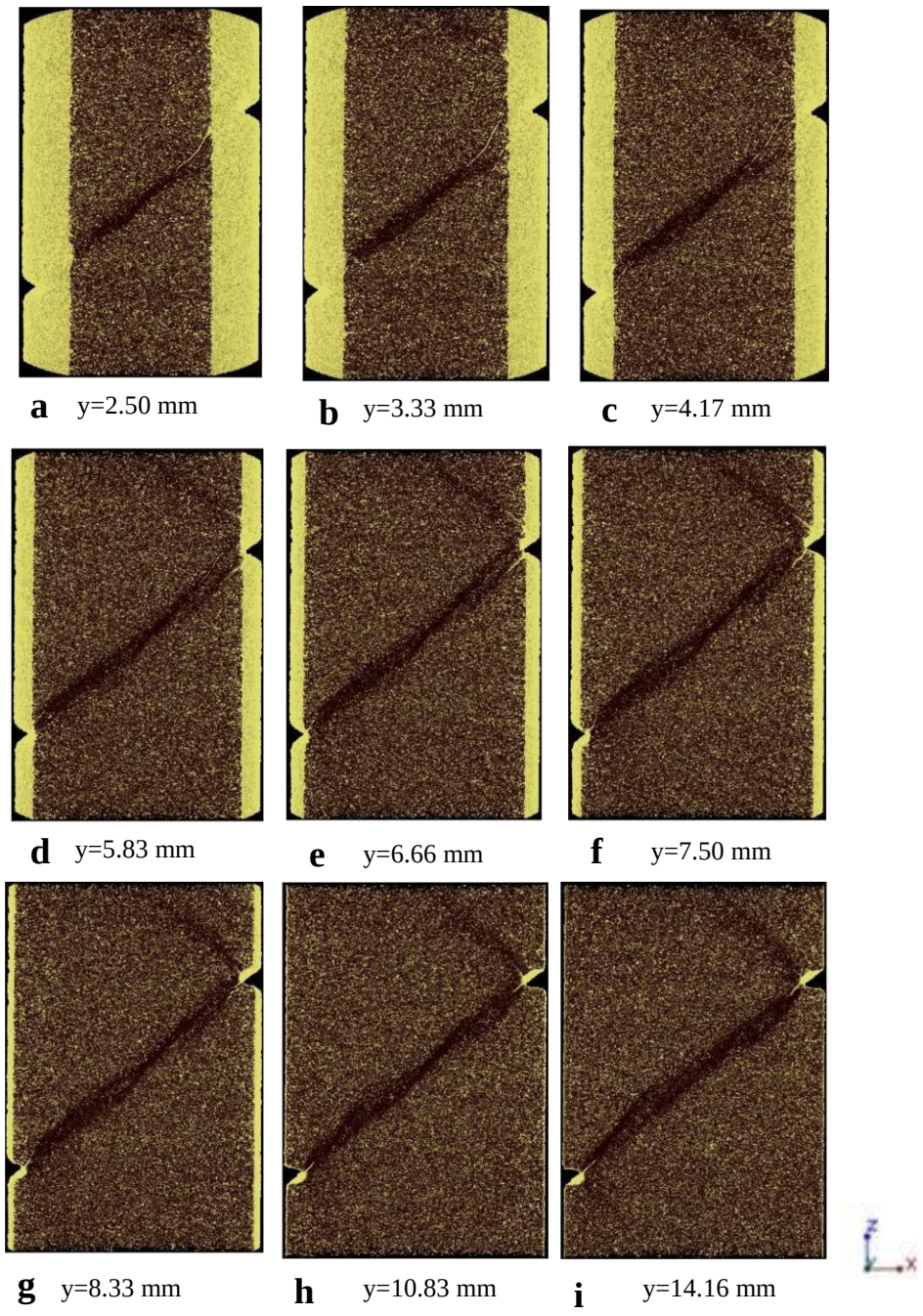

Fig. 5.25: Post-mortem HR x-ray tomography images (volume rendering) from (a) to (p) are a sequence of snapshots of the x-z plane as the y-axis position changes in specimen VEC4 (voxel-size ~30 μm).

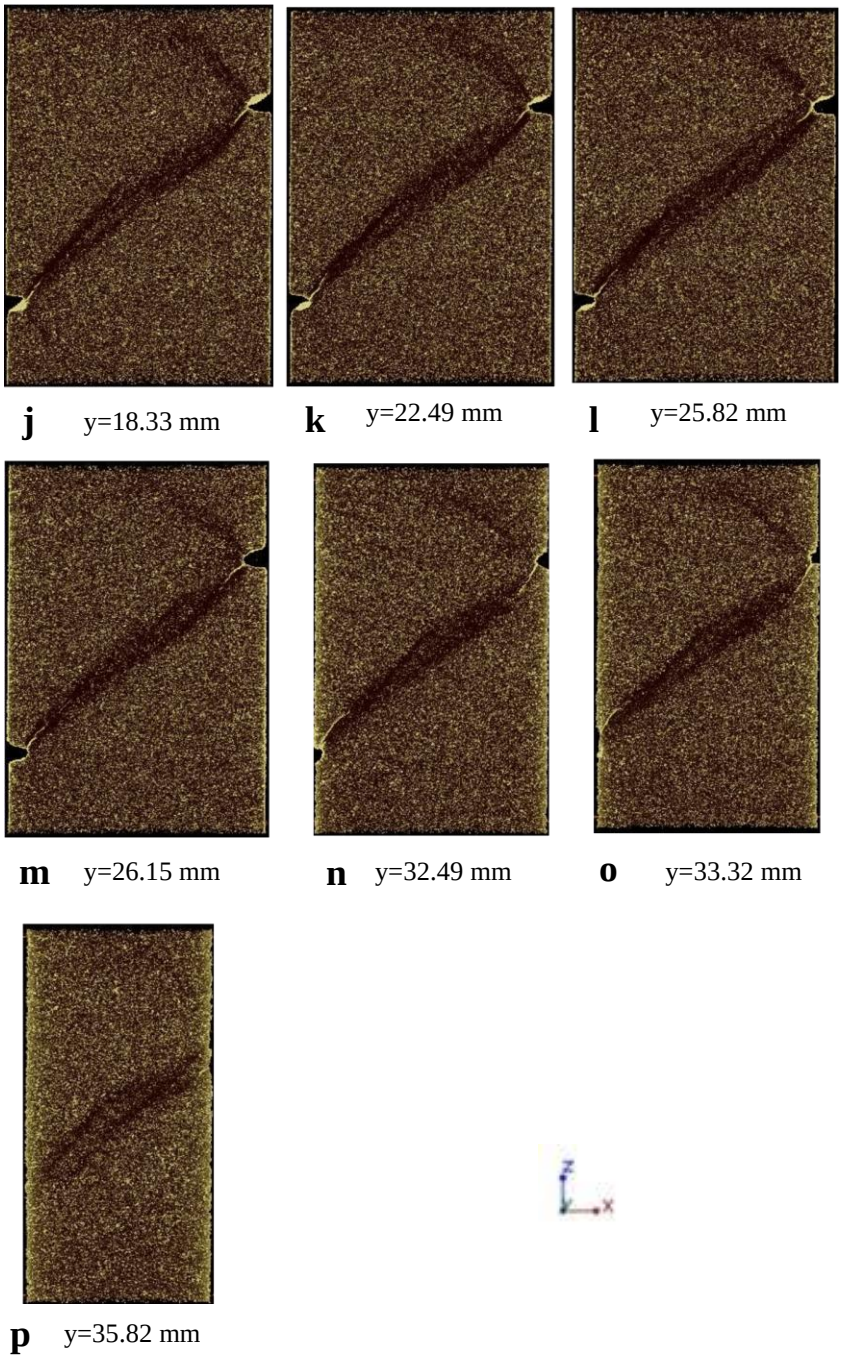

Fig. 5.25: Continued.

Specimen VEC4 was taken to 0.425% extra axial after the peak-stress (Table 4.2). This specimen is the one that had undergone the maximum axial strain out of the group of specimens loaded under 50 MPa confining pressure (Table 4.2). Compactant shear bands developed also in this specimen. Figure 5.25 presents vertical projections of HR x-ray tomography images through the volume of specimen VEC4. The orientation angle towards the major imposed principle stress ranged from 40° to 59° (dip of 50° to 31°). In the VEC4, compactant shear bands developed also towards the top boundaries of the specimen. These bands had an orientation of 47° to 48°. Longer cracks of a width of 60 μm to 105 μm were observed at the region of the notches. The population of the resolved cracks was higher than that of specimen VEC5.

Figure 5.26 presents the 3D geometry of the shear bands. More closely spaced higher density bands are visualised in both y-z and x-z planes.

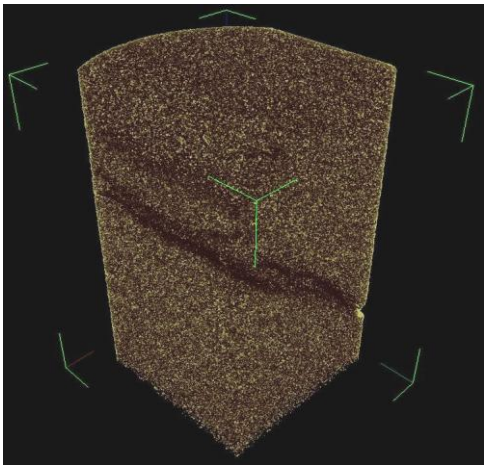

Fig. 5.26: 3D visualisations of specimen VEC4 in a region where the two shear bands meet (post-mortem HR x-ray tomography images ~30 μm, volume rendering).

5.5 Different strain level (than in 5.4)

In this section, HR x-ray tomography images (~30 μm voxel-size) from specimens loaded under 20 MPa confining pressure are discussed. Recall that the behaviour of the Vosges

Sandstone under this confining pressure level is very brittle. Specimen VLR00 was taken to lower axial strain values than specimen VEC2 (0.34% and 0.136% above the peak-stress, respectively). Recall that the latter specimen was fractured during loading due to the high axial strain (Tables 4.1 and 4.2).

Figure 5.27 presents different HR x-ray tomography vertical projections (x-z plane) through the volume of specimen VLR00 (~30 μm voxel-size). A high density band initiated at the top notch and propagated towards the centre of this specimen. Note that at this strain level, no signs of deformation were visible on the surface of the specimen (Fig. 4.12). The band is relatively narrow and is oriented at 32° to 35° towards the major imposed principal stress direction (dip of 58°-55°).

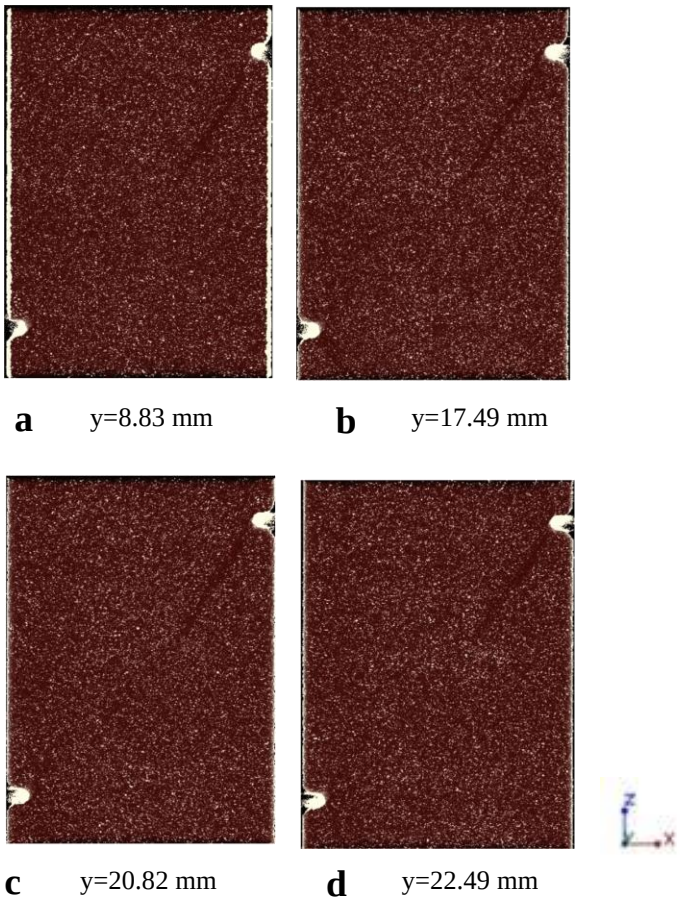

Fig. 5.27: Post-mortem HR x-ray tomography images (volume rendering) from (a) to (d) are a sequence of snapshots of the x-z plane as the y-axis position changes in specimen VLR00 (voxel-size ~30 μm).

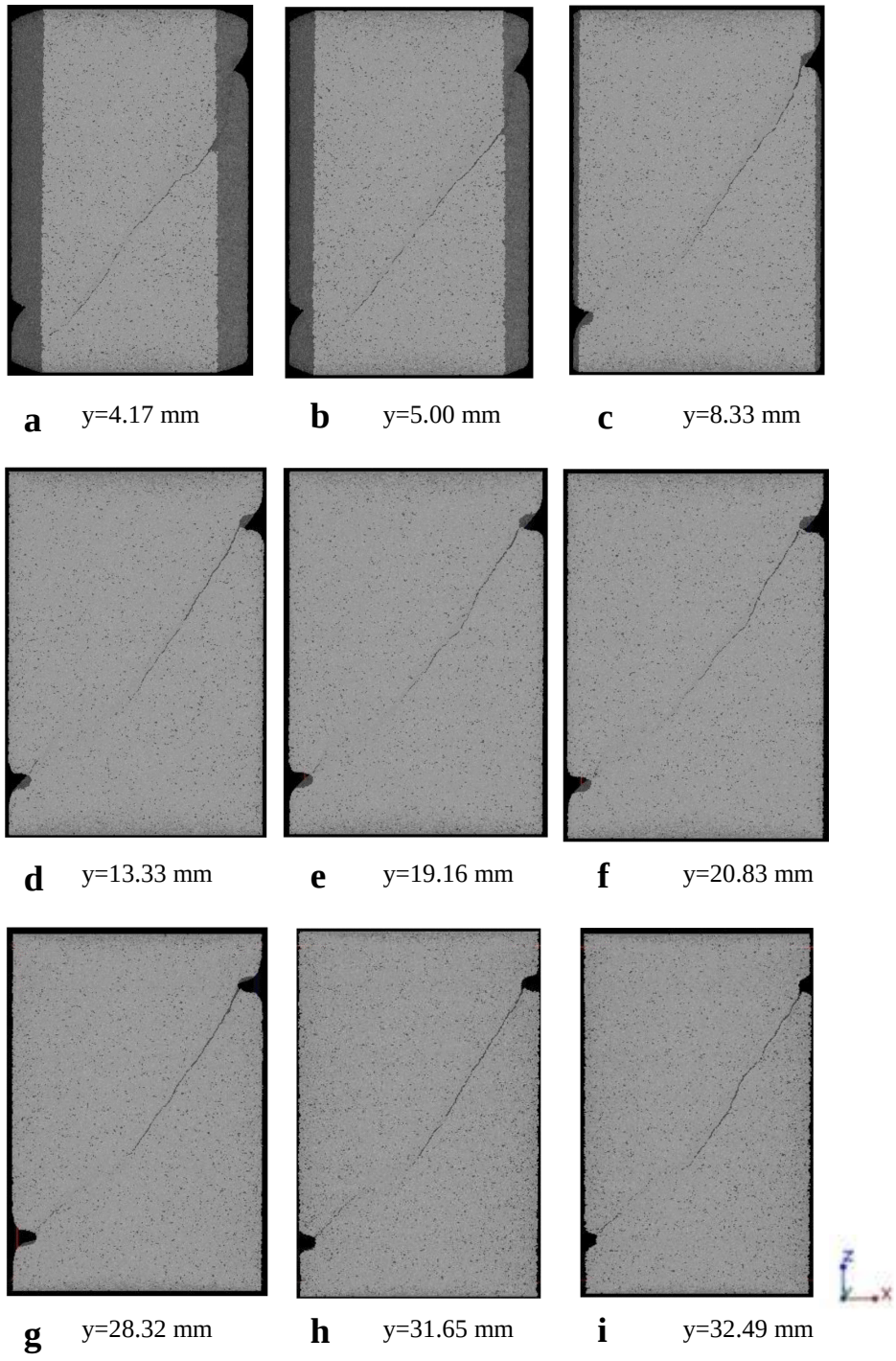

Fig. 5.28: Post-mortem HR x-ray images (isosurface) from (a) to (i) are a sequence of vertical slices of the x-z plane as the y-axis position changes in specimen VEC2 (voxel-size ~30 μm).

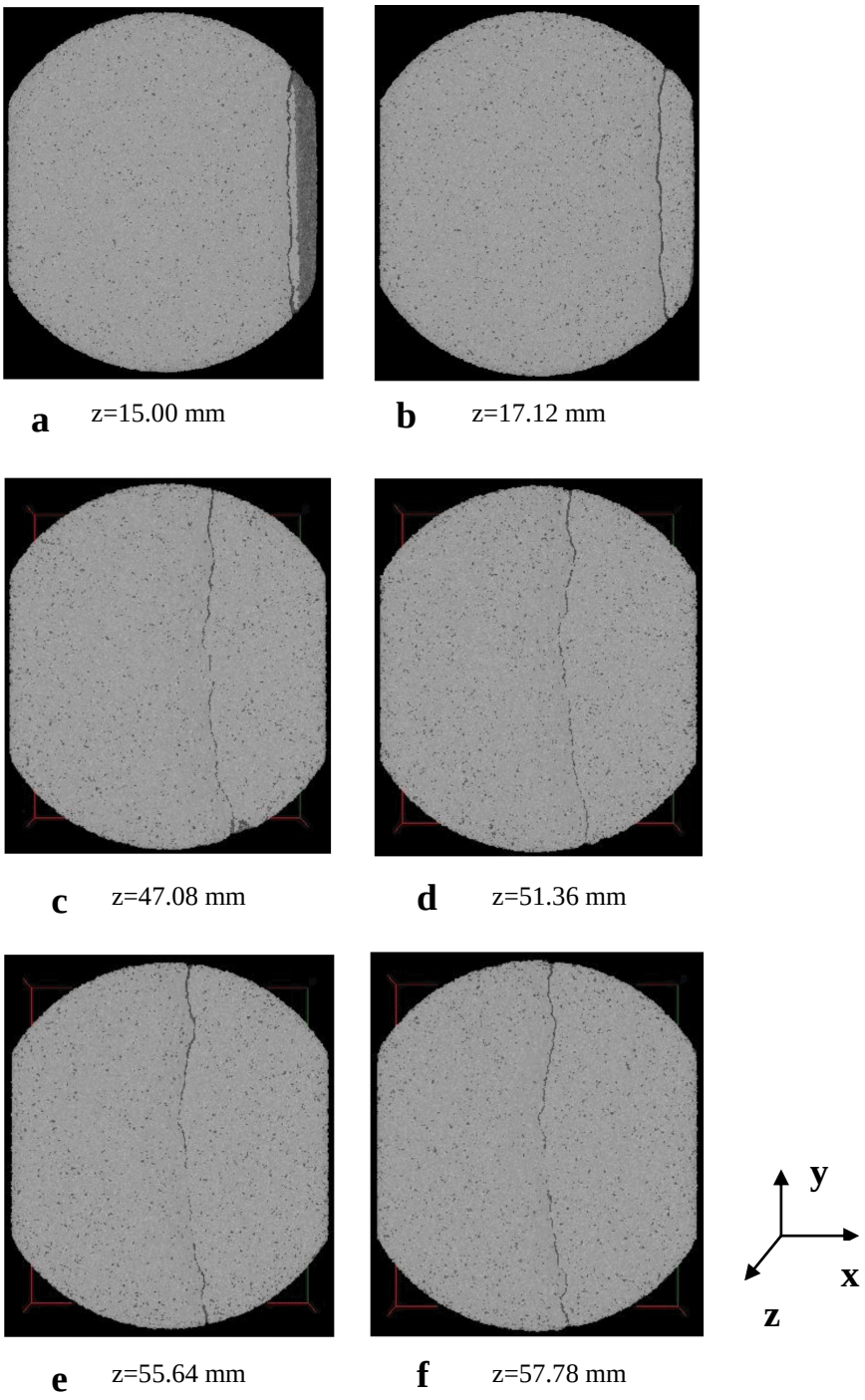

Fig. 5.29: Post-mortem HR x-ray images (isosurface) from (a) to (f) are a sequence of vertical slices of the x-y plane as the z-axis position changes in specimen VEC2 (voxel-size ~30 μm).

Figures 5.28 and 5.29 illustrate vertical and horizontal projections of HR x-ray tomography images (isosurfaces) from specimen VEC2. An open fracture, which initiated from the top notch and propagated through the specimen, is clearly seen in all images. The width of the fracture ranges from 100 μm to 300 μm (almost one intact grain size). Note that the maximum width of the fracture is greater in the x-z plane compared to in the x-y plane (360 μm and 300 μm, respectively). The fracture is non-planar. It appears to be curved; possibly because it followed some of the grain-boundaries (see also Fig. 5.31, section 5.6.1). Furthermore, it is argued that many smaller fractures developed in that specimen. In some places, these smaller fractures are individually visible, while in other places there is sufficient information to suggest that they linked and formed a long fracture. Where the continuity of the fracture is halted, these regions are characterised by a departure from the more typical texture, for example in the form of a more heavily cemented area. Note that these images come from post-mortem HR x-ray images; therefore it cannot be determined if these open fractures were created during the experiment or during unloading.

5.6 Microscopy

Microstructural observation, carried out on thin sections coming from some of the specimens, tested at relatively low confining pressures (30-50 MPa), are presented in this section. The goal of this section is to investigate the micromechanical processes that took place during the shear band formation. Light optical (planar light and cross-polarised) and scanning electron microscopy (SEM) were used for the microstructural observations.

Thin section preparation was described in section 3.6. The thin sections discussed in this section were taken along the region of the shear bands (see Fig. 5.30). Microstructural observations on three different specimens: VET3, VEC1 and VEC4, are presented here.

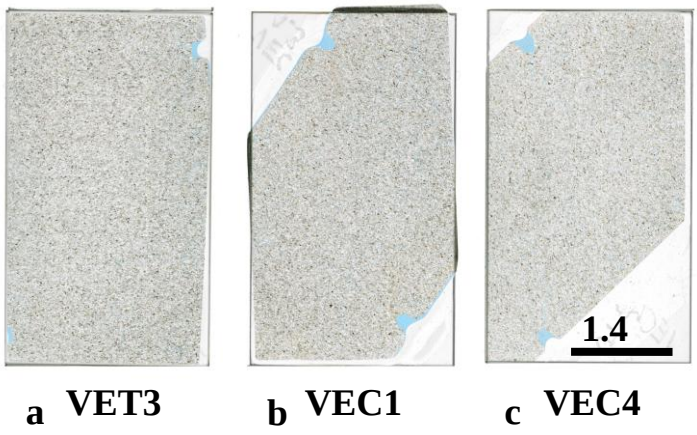

Fig. 5.30: Scanned thin sections. The notches were filled by the blue epoxy. (a) Thin section from specimen VET3 (tested at 30 MPa confining pressure); (b) Thin section from specimen VEC1 (tested at 50 MPa confining pressure); (c) Thin section from specimen VEC4 (tested at 30 MPa confining pressure).

5.6.1 SpecimenVET3

Specimen VET3 was subjected to triaxial compression at 30 MPa confining pressure. The experiment was stopped very close to the peak-stress [*Tudisco*, 2009], since under this confining pressure level the specimen risks to be totally fractured for a small amount of further axial strain value. Figure 5.31 presents a region near the notch.

An open fracture (~ 50 μm width, after unloading), which had initiated near the notch and propagated inwards, is illustrated. The fracture was non-planar; its trajectory changes along its length. It is inclined 12°-35° to the major imposed principal stress direction (vertical). Feldspars and quartz grains along the path of the fracture were highly damaged (Fig. 5.31a, 5.31b, 5.31e). Micas, trapped between quartz and feldspar grains, were also damaged (delaminated, Fig. 5.31c-5.31d, see also how micas look like in the undeformed specimens, section 3.6). Grain fragments moved (in green in Fig. 5.31a, 5.31c) and possibly rotated (Fig. 5.31a); however, not much detail concerning the movement of the grains could be identified in Figure 5.31. The adjacent regions along the open fracture walls appeared to be of a reduced porosity (in blue).

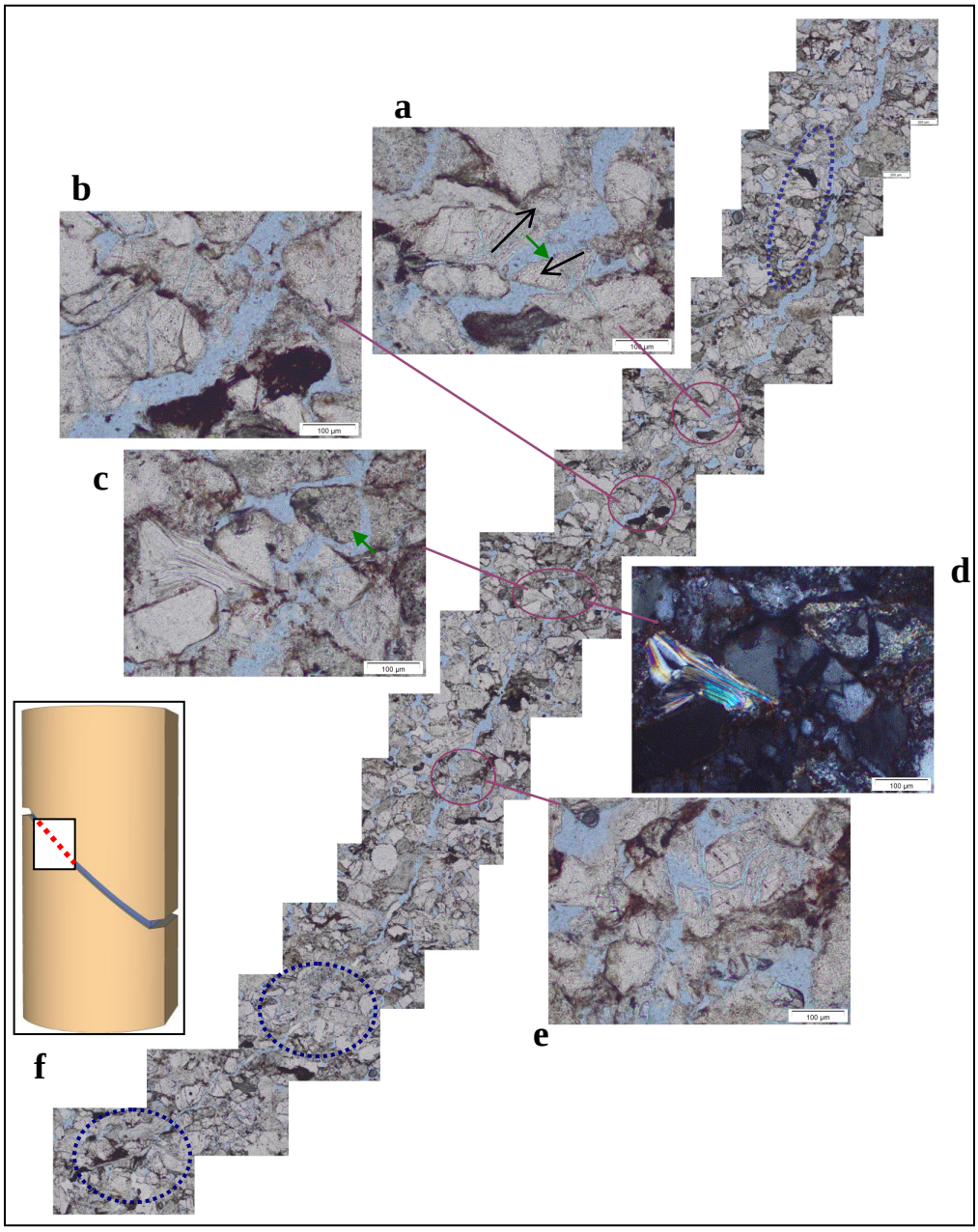

Fig. 5.31: Plane-polarised light optical images of a thin section from specimen VET3 (region around the top notch) illustrating an open fracture initiated at the notch and propagated from the upper right to lower left corner. Grain damage is observed along the tips of the fracture. The porosity of the adjacent regions along the fracture appears to be reduced (blue ellipse). The dimensions of the image collage are 7.6x10.3 mm; (a)-(e) Plane- and cross-polarised optical images of several regions along the open fracture. The maximum

compressive stress direction was vertical; (f) Schematic diagram of the specimen configuration together with the area covered by the image-collage (a)-(e).

In addition, porosity was also reduced at the end of the fracture tip (in blue). Beyond the open fracture tip (and further into the specimen body) deformation consistent with shear band development is observed.

5.6.2 Specimen VEC1

Specimen VEC1 was deformed under triaxial compression at a confining pressure of 50 MPa (see Table 4.2). The full-field methods revealed the occurrence of a compactant shear band (section 5.4.2), in which grain damage might have occurred (section 3.2.3). Two different thin sections are presented from this specimen.

Figure 5.32 illustrates open fractures, which started from the notches and propagated inwards, like in specimen VET3. The fractures were non-planar; its trajectory, at this region, can be seen in Figures 5.32c-5.32d (in red). The fracture either followed the grain boundaries or fractured the grains along its way (Fig. 5.32a). In addition, the grains on the wall rock were damaged. Hertzian-like fractures on quartz grains, with an orientation sub-parallel to the major imposed principal stress direction, were observed (Fig. 5.32b). Figures 5.32c-5.32f focus on a deformed muscovite, which was severely damaged. This mica was bent, twisted and split; therefore, it appears to have accommodated a big amount of deformation. The open fracture had split it in two parts (Fig. 5.32f). The boundaries of the muscovite layers revealed that shear possibly occurred also along the length of this mica in a direction almost sub-normal to the open fracture (at this region). The middle part of the muscovite (in green circle), which was sub-parallel to the open fracture, was slightly bent and twisted (Fig. 5.32c-5.32d) but it was not split. The left part of the muscovite was also damaged (Fig. 5.32c-5.32d, and 5.32e in more details). The interference colours changed along the length of this part. In addition, the crystal was split in two parts due to the open fracture and the adjacent grain movement (Fig. 5.32e).

The shear band developed beyond the tip of the open fracture. Regions inside the shear band are presented in Figures 5.33a-5.33d. The deformation band seems to have a lower porosity than that of the undeformed wall rock (visual inspection).

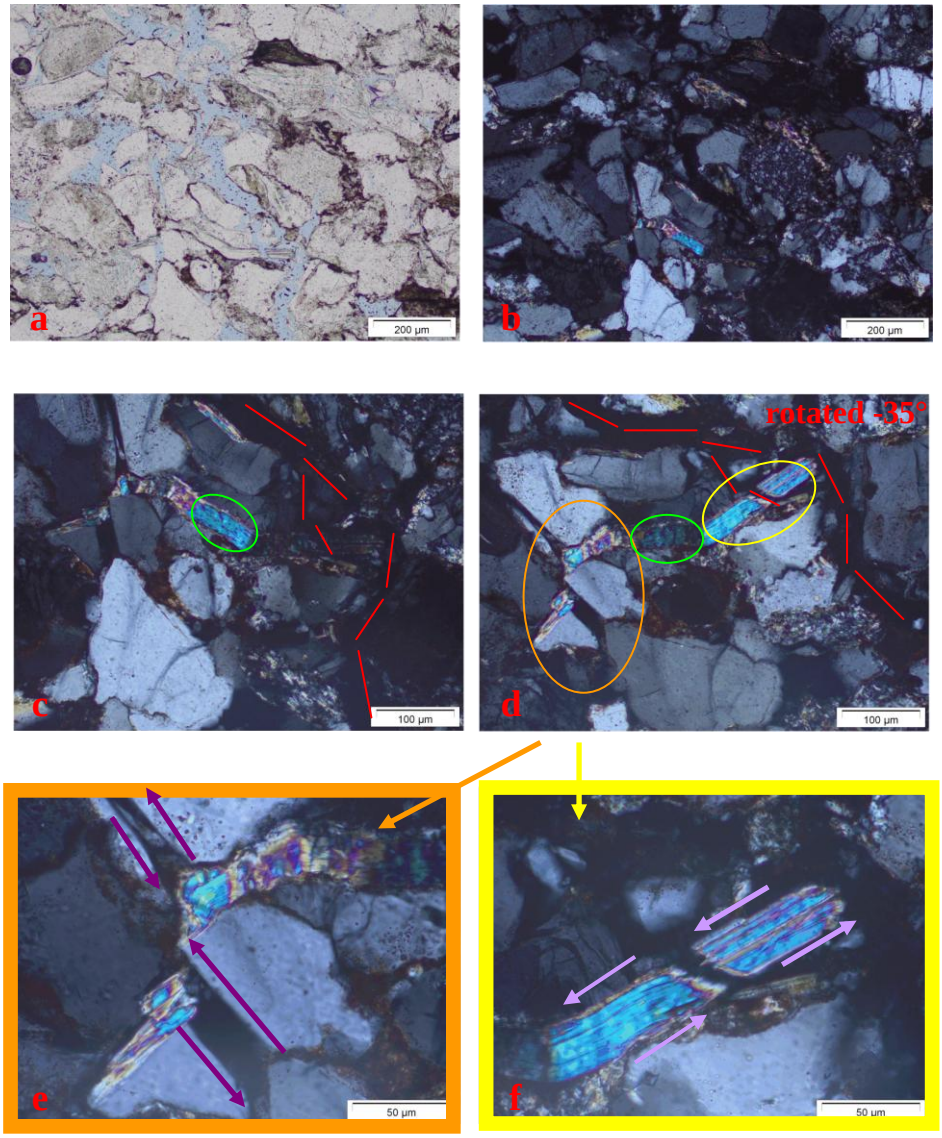

Fig. 5.32: (a) Plane-polarised light optical image from a region on the wall of the open fracture from specimen VEC1; (b) Cross-polarised light optical image of the same region. Inter- and intra-granular fractures are observed on the grains; (c) Zoom in (b); (d) Rotated cross-polarised light optical image (-35° to (c)). The trajectory of the open fracture appears in red lines (also in (c)). A part of the muscovite is oriented parallel to the fracture (in green, also in (c)). The fracture has split the muscovite (right part). The left part of the muscovite is also separated due to the adjacent grains movement; (e-f) Zoom in the muscovite. Arrows represent possible movement of adjacent grains. The maximum compressive stress direction was vertical (a-c).

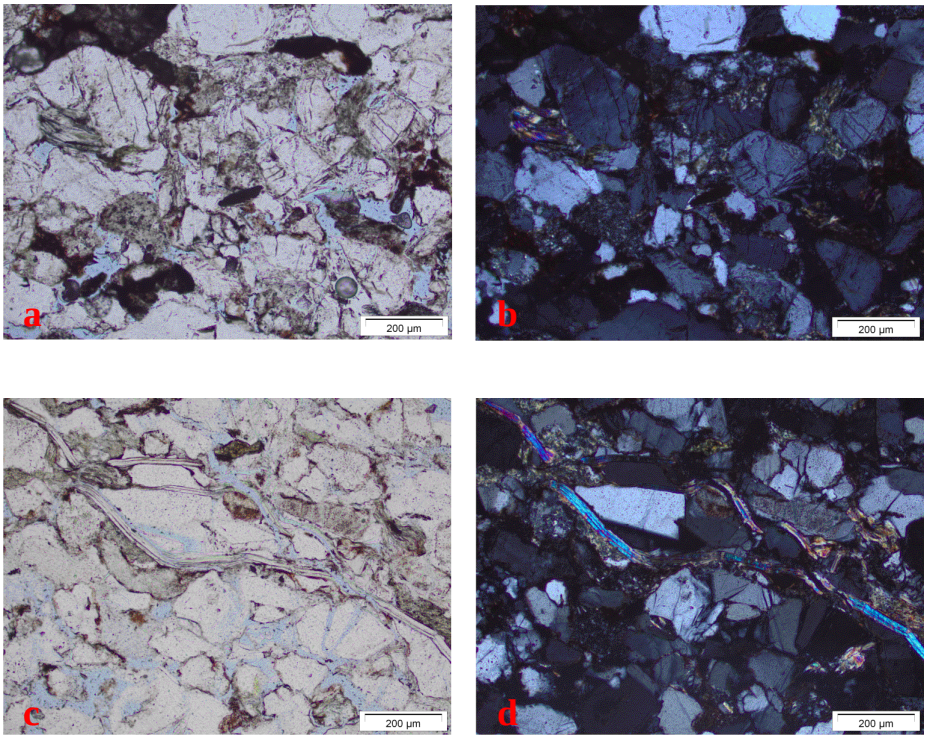

Fig. 5.33: (a) Plane-polarised light optical images from a region of the shear band from specimen VEC1. Intense grain damage is observed. Hertzian fractures on quartz grains are observed. The porosity of this region appears to be reduced; (b) Cross-polarised light optical image of the same region; (c) Plane-polarised light optical image of another region of the shear band focusing on micas layers. Micas appear bent and twisted. They are inclined from 35° to 40° towards the major imposed principal stress direction. Note that the micas layers of the undeformed rock were inclined at 80° to major imposed principal stress direction; (d) Cross-polarised light optical image of the same region. The maximum compressive stress was vertical.

The damage intensity was not equally distributed along the band. Quartz grains and feldspars were fractured (the latter, along their cleavage, Fig. 5.33a-5.33b). Mica layers were bent or twisted and they possibly accommodated the bigger amount of deformation. Note that the mica layers of the undeformed rock were dipping at around 10°**.** In Figures 5.33c-5.33d, micas were much more inclined (dip of ~ 45°to 50°).

Figure 5.34 presents a backscattered Electron Image (BSE) of a second thin section from the same specimen. The open fracture appeared wavy and non- planar, similarly to Figure 5.32. A shear band, with a width of 490 to 600 μm, evolved after the tip of the fracture.

Grains were highly fractured inside the shear band. Grain damage was also observed at the wall rock, close to the tip of the open fracture. Grains were relatively undamaged far from the band and the open fracture. Porosity was higher in these regions.

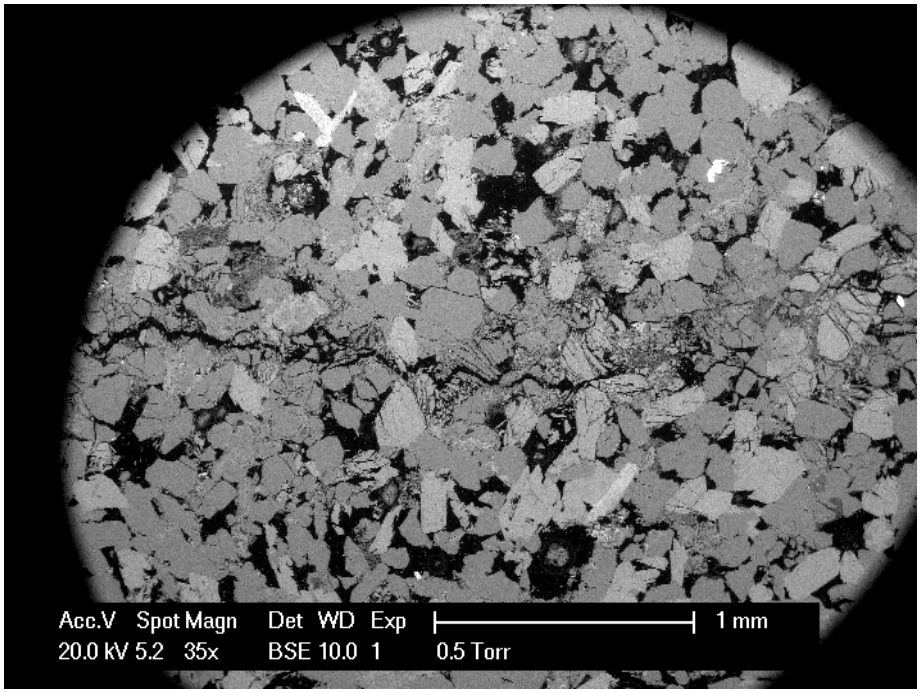

Fig. 5.34: Backscattered Electron Image (BSE) of a region from specimen VEC1. An open fracture is clearly seen in the central part of the image. A compactant shear band, with a width of 490-600 μm, was generated beyond the tip of the open fracture. Hertzian-fractures and severe grain fracture in some grains, as well as grain fragment rearrangement are observed in the region of shear band, while far from these places almost undeformed grains are observed. The porosity reduction is much more strongly developed inside the bands. The maximum compressive stress direction was 47° from the vertical.

Micro-fractures along the cleavage of feldspars are illustrated in Figure 5.35 (BSE image). Quartz grains and feldspars were crushed. The grain fragments started filling the pore space. In particular, quartz grains present sharp bounded micro-fractures at their surface. Some of these fractures separated quartz grains in two parts (on the right of Fig. 5.36). The right part of the quartz (on the left of the image) was slightly rotated and translated (slid on the left part quartz surface). Crushed fragments of the adjacent above feldspars moved to the pore space between the two separated quartz parts. Bent and twisted mica (on the right top of Fig. 5.35)

experienced intense damage on its right part. The layers of the mica were delaminated but no splitting had occurred.

a

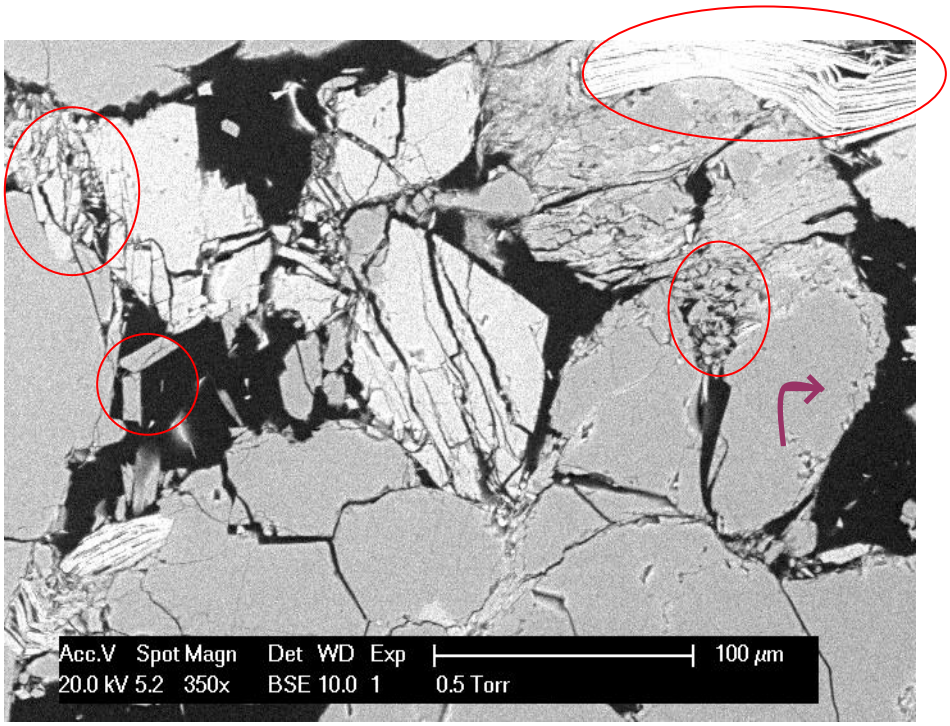

Fig. 5.35: Backscattered Electron Image (BSE) of heavily damaged feldspars (lighter grey), fractured quartz (medium grey) and severely deformed mica (top right) from specimen VEC1 (region inside the shear band). Micro-fractures along the cleavage of feldspars and sharp micro-fractures on quartz grains are observed. Some parts of feldspars and quartz are heavily crushed and the fragments have filled the pore space. A mica on the right of the image has also experienced intense damage. It appears bent and twisted, while in its right ending the layers appear to be delaminated.

Another region inside the shear band, where intense damage took place, is illustrated in Figures 5.36a-5.36c (BSE images). Hertzian-like fractures, micro-fractures and highly crushed grains, which filled the pore space, are distinguished. A relative movement of the fragments has occurred. The porosity in this region was reduced compared to that of regions far from the shear band (visual inspection, Fig. 5.36a). Figures 5.36b and 5.36c are BSE images of increased magnification focusing on the heavily fractured grain. The micro-fractures along their cleavage planes had a width of 1-4 μm.

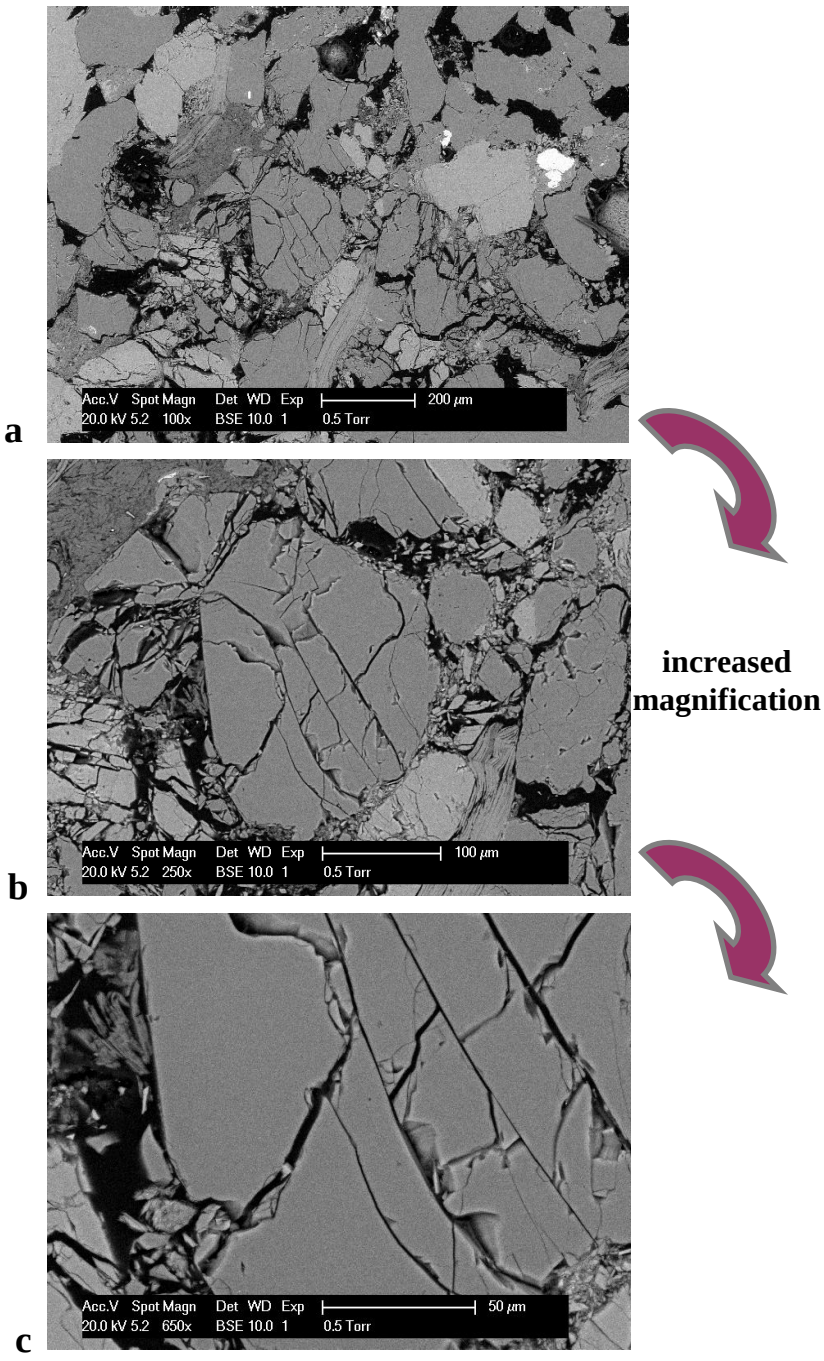

Fig. 5.36: Increasing magnification Backscattered Electron Images (BSE) of a heavily damaged grain from specimen VEC1. (a) BSE image of a wider region inside the shear band showing cataclastic deformation. Hertzian fractures and grain crushing are apparent, while far from the deformation band grains are relatively undamaged. Grains have heavily deformed. Micro-fractures along their cleavage are clearly seen. The bright grains on the right are oxides; (b) BSE image zooming in crushed grain; (c) BSE image showing further zoom in the fractured grain. The micro-fractures have a width of 1-4 μm.

5.6.3 SpecimenVEC4

Specimen VEC4 was loaded under triaxial compression at 50 MPa confining pressure and was taken to a higher axial strain value than specimen VEC1 (Table 4.2). Here, plane- and cross-polarised light optical microscope images of thin section are presented verifying what was observed through the full-field non-destructive methods (section 5.4): a compactant shear band developed in this specimen (higher density, HR x-ray images), inside of which grain damage occurred (low elastic velocities, UT).

Figure 5.37 shows a region of the shear band from specimen VEC4. Two regions inside the band are observed. The central part of the band, with a width of around 330 μm, included highly damaged grains. Hertzian fractures on quartz and intense fracturing on feldspars were observed inside this region. At the borders of the heart of the band, the damage intensity is lower, despite the existence of fractured grains. Relative movement of the grain fragments is illustrated with red arrows, which indicates that the grains inside the shear band experienced shear. The grains of the wall rock were less damaged. A mica (on the right bottom) was on the transitional region between the wall rock and the shear band. Its right part was relatively less deformed, having the same orientation as the micas layers of the undeformed rock. However, its central part was bent and twisted; this part was located at the borders of the shear band. Its left part, which was inside the band, experienced severe damage and delamination. The width of the band is around 1000 μm (*i.e.*, almost three intact grain-sizes). Recall that the shear bands from specimen VEC1, which was loaded to a lower axial strain value, had a smaller width (Fig 5.34).

Figures 5.38a and 5.38b show a region far from the shear band. Grains were locally compacted and, thus, local reduction in porosity was observed (visually) in some places. However, no considerable grain damage was observed.

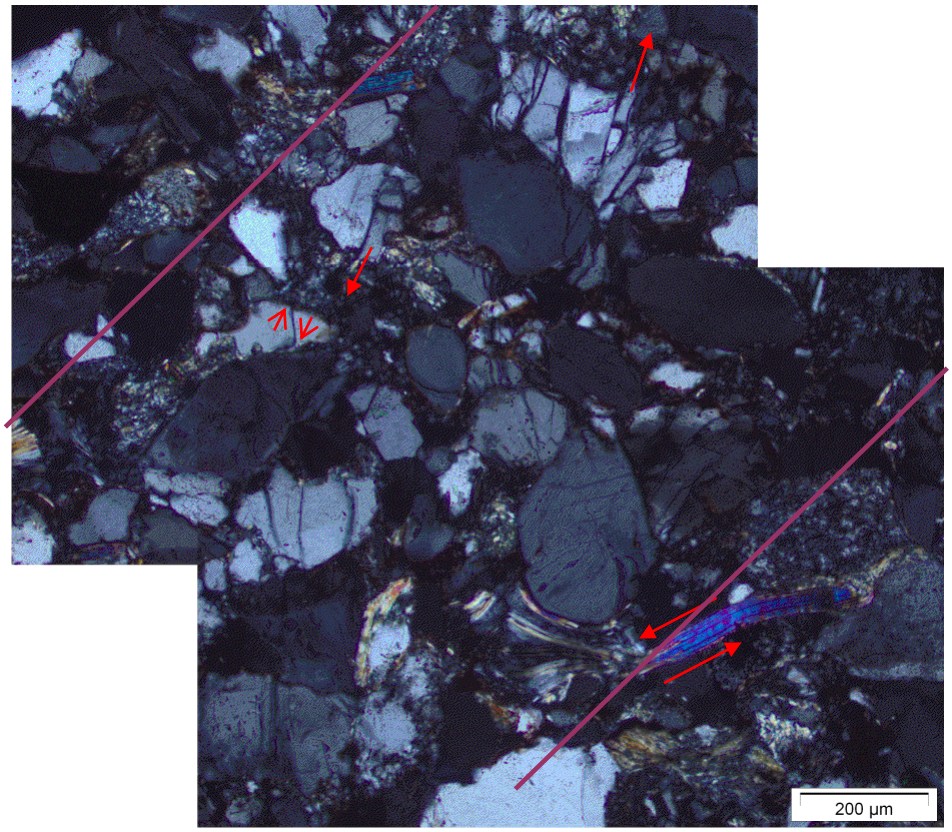

Fig. 5.37: Cross-polarised light optical images for a thin section of a region of the shear band from specimen VEC4. The width of the shear band is around 1000 µm and the thin section is vertically oriented. Purple lines indicate the approximate shear band boundaries. Grains in the centre of the band are severely damaged. Hertzian fractures on quartz and fracturing along the cleavage of feldspars are observed. Relative movement of some of the grain fragments can be observed (in red arrows). Most of the grains have experienced shear, which involved relative movements of parts of the grains. A mica (bottom right) appears to be between the border line of the shear band and the wall rock. Its part, inside the shear band, has experienced intense damage (layers are split). The inclination angle of the band in this region is around 45° towards the major imposed principal stress direction, which was vertical.

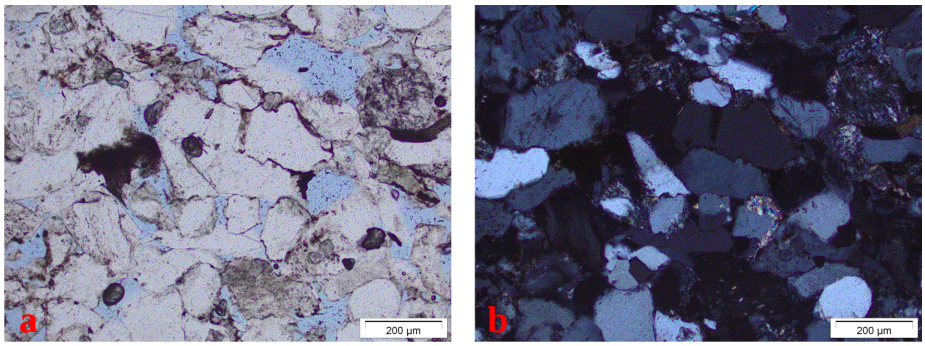

Fig. 5.38: (a) Plane-polarised light optical images of a relatively undamaged region (far from the shear band) from the VEC4; (b) Cross-polarised light optical images of the same region. Grains do not seem to be damaged. The maximum compressive stress was vertical.

5.7 Conclusions

In this section, the main results from the shear bands, which developed in Vosges Sandstone are summarised:

- The full-field methods allow to identify and characterise the shear bands, which developed in sandstone specimens loaded under triaxial compression at low to intermediate confining pressures (from 20 MPa to 50 MPa) and taken to different axial strain levels (Table 4.2). Thin section observations validated what was previously indicated by the full-field experimental methods.
- The AE hypocentre locations (during the triaxial experiment) illustrated the onset and evolution of shear bands, which initiated at the tips of the offset notches. Small clusters of AE events were identified also between the notches at the early stage of the experiment. The syn-deformation AE locations demonstrated that the final shear band was a result of en-echelon propagation of these AE clusters. X-ray images have also indicated local fractures along the shear band (Fig. 5.29).
- The cumulative number of AE events increased with increasing stress deviator values, which indicated an increase in grain-scale activity (also visualised in the hypocentre

locations). For specimen Ve2, the AE rate drastically changed at about 4000 seconds from the beginning of the experiment. The stress deviator value at that point was 100 MPa, which is very close to the stress deviator value defined in Chapter 4 for the onset of localised deformation (see Table 4.2).

- A preliminary source-mechanisms analysis for specimen Ve2 (Table 4.2), which showed strain localisation in the form of shear bands, indicated pore collapse to be the dominant mechanism, since the great majority of the AE events were C-type. The number of S-type events was almost 2 times smaller than the C-type events-initially, but it reduced significantly by the end of the experiment. A considerable increase in the S-type events was observed only during the strain softening. A very much smaller number of T-type events was also identified.
- Grain-scale damage at the region of the shear bands was also identified by the lower elastic wave velocities.
- Shear bands were resolved as features of higher density material. In addition, the decreased standard deviation values (calculated on the grey-scale of the HR raw x-ray tomography images) visualised images with homogeneous regions inside the shear bands (seen from an image analysis standpoint). This is linked to local grain-scale damage.
- Grain damage inside the regions of shear bands, in the form of grain fracturing, was observed in the thin section. When mica flakes were observed inside the deformation band, their orientation was close to the dip angle of the band, while outside the band, micas' orientation was similar to that of the observed sedimentary layers.
- Open fractures were identified at the notches by both x-rays and thin section observations. It is likely that these fractures opened during the unloading stage. The width of the fractures is relatively small compared to that of the shear band (thin sections and x-rays), and their length increases with increasing axial strain (thin sections).
- Higher values of shear strain were located inside the bands, which were characterised locally by either compactant or dilatant volumetric strain. Note that in places where two shear bands met, the compactant volumetric strains had higher values than the

shear strains. On the other hand, in places where the shear strains had the highest values, lower values of compactant or dilatant volumetric strain were identified. When a single shear band was resolved, the compactant strains were located in the middle part, while dilatant strains were located near the notches. The alteration of compactant and dilatant strains inside the shear band adds on the understanding of compactant shear bands at this confining pressure range [*Besuelle* et al., 2004, and also x-ray images of the present study]. The volumetric strains inside the band reveal a more complex structure than pure compaction.

- The inclination angle of the shear bands was consistent with the angles suggested by *Besuelle* [2001] for the same material. However, the 3D structure of the shear bands resulted in a wider inclination angle range, which changed with different axial strain (see also Chapter 7). Additionally, the shear bands were revealed as non-planar features.
- Increased axial strain resulted in a higher degree of damage, which was captured by lower values of ultrasonic velocities (UT maps), a shift in the dominant frequency, and lower amplitudes which were linked to higher attenuation. The width of the band increased with increasing axial strain. This was observed in the thin section, and was visually seen in the x-ray images.
- The number of shear bands was restricted by the existence of the notch and the geometry of the specimen. Note that usually two shear bands were resolved inside the flattened surface volume, while usually one band developed close to the surface of the specimen.

Chapter 6 - Compaction Band characterisation

6.1 Introduction

This Chapter presents experimental results on Vosges sandstone specimens that were loaded under triaxial compression at relatively high confining pressures, *i.e.*, from 130 MPa to 190 MPa (approximately equivalent to 8 km to 11.5 km burial depth). At these loading conditions, specimens showed strain localisation in the form of compaction bands. The term `compaction bands` is used in the present Chapter to describe deformation features that are characterised predominantly by compaction with a small component of shear (*i.e.*, not only pure compaction). A variety of experimental techniques (see Chapter 3) was applied. Both the experimental procedure for this series of triaxial compression tests and the mechanical results obtained were discussed in Chapter 4. This present Chapter is divided into nine further sections. A short description on what is presented in each of the sections is given below.

Section 6.2 presents results from a single Vosges sandstone specimen (Ve4) using all experimental non-destructive full-field methods applied to this work (*i.e.*, UT, AE, x-ray tomography, 3D-DIC), aiming at a more detailed characterisation of the compaction bands. Recall that each technique is sensitive to different parameters (Chapter 3). Information on the onset and evolution of compaction bands as well as several characteristics of these deformation features, which describe the occurred micro-mechanisms, are given. Section 6.3 focuses on the influence of increasing axial strain level on the evolution of compaction bands and on the alteration of their physical characteristics (*i.e.*, the orientation of the band, its width, and the strain inside the band); results are presented from two experiments (Ve4 and Ve6), carried out at the same confining pressure but taken to different axial strain levels, via different experimental full-field measurements (*i.e.*, AE, x-ray tomography, and 3D-DIC). Section 6.4 shows results for compaction bands that developed in specimens loaded under different confining pressures (Ve6, Ve5, and Ve7 loaded at 130 MPa, 160 MPa, and 190 MPa, respectively). The role of confining pressures on the characteristics of the developed

deformation features is highlighted. The influence of a circumferential notch on the formation and evolution of compaction bands is discussed then in section 6.5. Results from a specimen with a notch (Ve5) are compared to results from a specimen without a notch (Ve1). Both specimens were loaded under the same confining pressure, but were taken to different axial strain values. Section 6.5 also highlights the impact of different resolution of the x-ray tomograms analysed by 3D-DIC (*i.e.*, LR versus HR). Section 6.6 discusses how the different parameters used (size of the sub-volume in which the calculations were performed and spacing size in each direction) affect the visualisation of compaction bands. A preliminary statistical analysis on HR x-ray images and HR 3D-DIC is also presented herein. Section 6.7 presents porosity calculations on small cores taken from regions of strain localisation in the specimens. Section 6.8 illustrates microstructural observations of thin sections from some of the specimens already discussed in this Chapter. These observations illustrate the actual grain-scale deformation and validate what was previously shown by the non-destructive methods. Compaction bands characteristics from another sandstone specimen (the Bentheim sandstone) are presented in section 6.9; a preliminary comparison between the two different sandstones, the Vosges and the Bentheim, is made based on some post-mortem x-ray tomography images of the two rocks. Finally, section 6.10 summarises the main outcomes of this Chapter.

6.2 Compaction band characterisation by a combination of several experimental non-destructive techniques

The objective of this section is to characterise laboratory produced compaction bands on a Vosges sandstone specimen (Ve4) via full-field experimental techniques and comment on the potential of each method. AE event locations during triaxial compression (syn-deformation) and AE source analysis are shown together with ultrasonic velocity measurements and UT, which were carried out after the experiment (post-mortem). In addition, HR x-ray tomography images (with a resolution of ~30 μm, post-mortem) and 3D-volumetric DIC based on HR x-ray tomography images (pre- and post-mortem) are presented here.

The mechanical results from specimen Ve4, which was loaded under 130 MPa confining pressure, were discussed in Chapter 4 (Table 4.2). A circumferential notch was machined horizontally at the mid-height of the specimen to encourage localisation. AEs were recorded during triaxial compression. Figure 6.1a shows the time history (in seconds) of the stress deviator and the cumulative AE number, separated into increasing time intervals moving from left to right. Three 2D projections of the 3D distributions of AE event locations (one perpendicular and two parallel-one of which parallels the cutoff and one of which is normal to the cutoffs- to the specimen axis) are shown in Figure 6.1b, 6.1c and 6.1d. The perpendicular projection, from the 3D distribution of AE locations, overprints AE events from the middle portion of the specimen (*i.e.*, from 30 mm to 50 mm from the bottom of the specimen). Both parallel projections overprint AE events recorded in the central section of the specimen (*i.e.*, +/- 2 mm of the central plane that is parallel and normal to the cutoff plane).

By the end of the deviatoric compression, several thousand AE events nucleated. Approximately 3000 AE events are plotted on Figure 6.1a. Note that common lower amplitude values were set for all specimens to aid comparison. Only AE event amplitudes greater than 2 Volts were plotted for the cumulative number of AE events (Fig. 6.1a) and AE event amplitudes higher than 0.5 Volts were used for the 3D projections (Fig. 6.1b-6.1d). Colours in Figure 6.1 change to highlight most recent events. The cumulative AE number increases with increasing stress deviator.

An AE event concentration was observed near the circumferential notch (at mid-height of the specimen). Later AE events were located in an approximately horizontal band, which was inferred to be a compaction band, such that events apparently nucleated from the notch and propagated inwards. The experiment was stopped before the complete propagation of the band into the central section of the core. Diffuse and less intense AE activity was also recorded above and below the compaction band. The accuracy of AE hypocentre location is about 2 mm; therefore, AE events located within the error-bar distance outside of the specimen were interpreted as having nucleated from the specimen`s surface. The concentration of AE events close to the top and the bottom of the Ve4 was most likely due to the end-cap friction. Recall that no lubricant had been used at the two ends of this specimen

(section 4.5). AE events are associated with grain-scale micro-cracks of cement-grain contacts and grains.

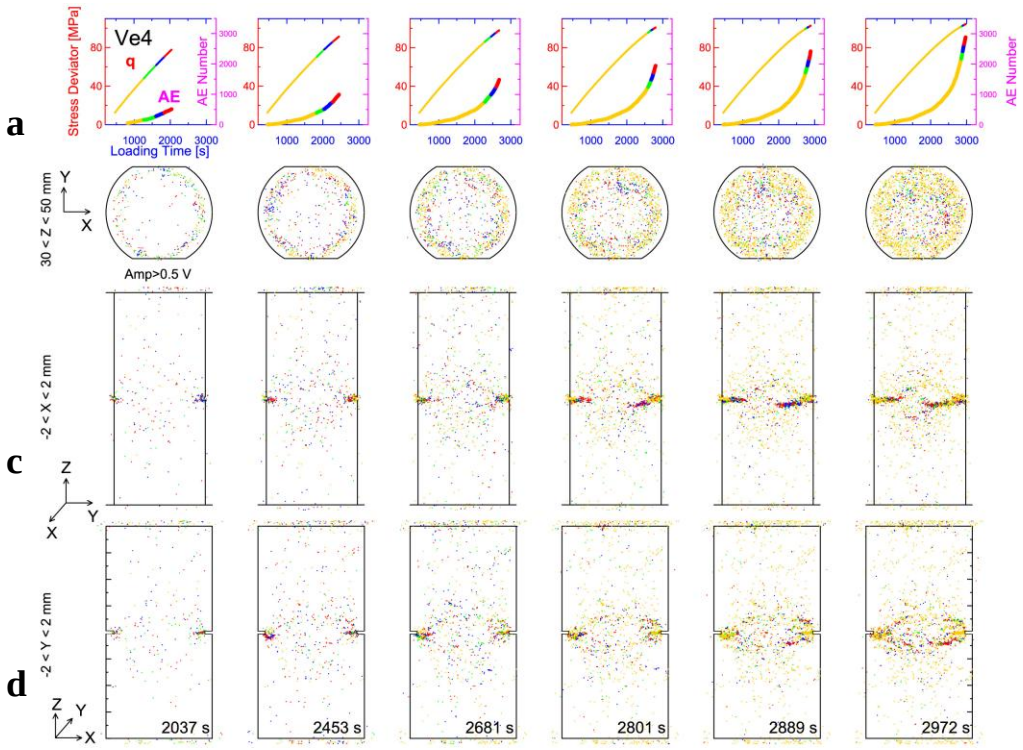

Fig. 6.1: AE results from specimen Ve4: (a) Axial load as a function of the number of AE events in different time intervals; colours change to highlight most recent events; (b)-(d) Maps of AE event locations for the same time intervals viewed perpendicular to the specimen's height, parallel to the specimen's height in a projection perpendicular to the flattened surfaces projections and parallel to the specimen's height in a projection parallel to the flattened surfaces projections.

Figure 6.2, which presents initial AE source-mechanisms analysis (see section 3.3.5) for specimen Ve4, shows that during the deviatoric compression the majority of AE events were C-type (98% at 0.15% of axial strain, reducing slightly to 96% when the loading was stopped, Fig. 6.2b, 6.2c). S-type events increased by 2% (the final number of S-type events was twice the amount of S-type events at 0.15% of axial strain, Fig. 6.2b, 6.2d); however, they were much less abundant to C-type events. A small, yet not negligible number of T-type events (around 0.4%, Fig. 6.2b, 6.2d) was identified in this experiment.

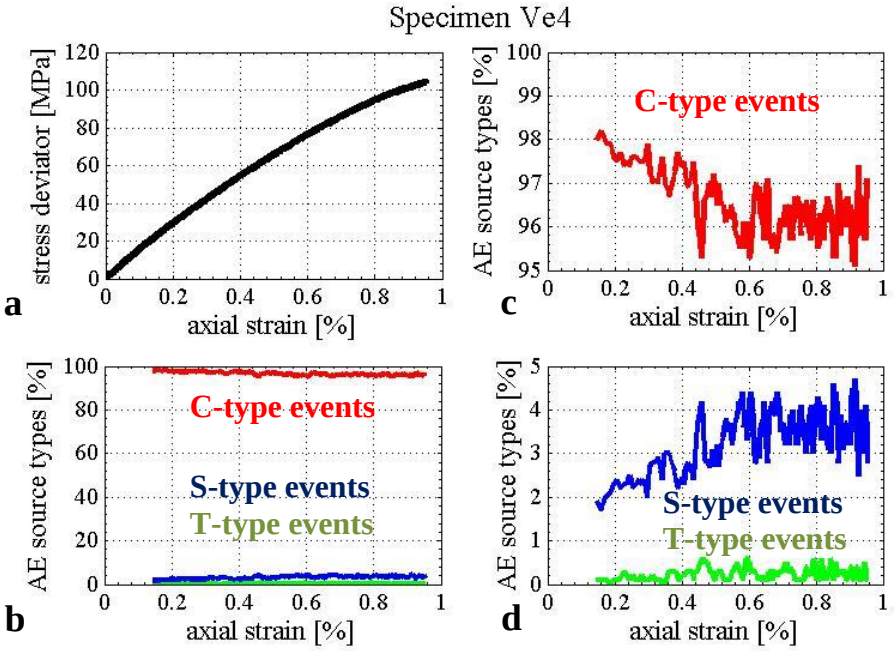

Fig. 6.2: Plots of stress deviator (a), the amount and type of AE source-mechanisms (b), and zooms in C-type events (c) and S- and T-type events (d) during the deviatoric compression of specimen Ve4, all as a function of the axial strain.

Post-mortem ultrasonic P-wave measurements are presented in Figure 6.3. Recall that the 'zero-offset' measurements correspond to emitting and receiving transducers at the same elevation on the two opposed flattened sides, while the 'angular coverage' measurements correspond to emitting and receiving transducers placed at a different elevation on the two opposed flattened sides (Fig. 6.3a).

During the measurements, the barrettes were offset (Fig. 3.2a and Fig. 3.2b) so as to cover the whole height of the specimen. Figure 6.3b shows the post-mortem zero-offset arrival time profile printed on the ultrasonic waveforms (zero-offset measurements). To highlight the details on both the waveforms and the arrival time, Figure 6.3c is a detail of Figure 6.3b. At the place where the circumferential notch was machined (from 39 to 64 piezoelectric elements, Fig. 6.3b), the zero-offset waveforms were highly attenuated and the arrival time profile shifted, indicating a decrease in velocities (see also Fig. 6.4) linked to local damage (section 6.8). A smaller shift in the arrival time profile was also observed close to the top and

bottom boundaries of the specimen. Much of this could be attributed to induced damage during specimen preparation (prior to testing damage).

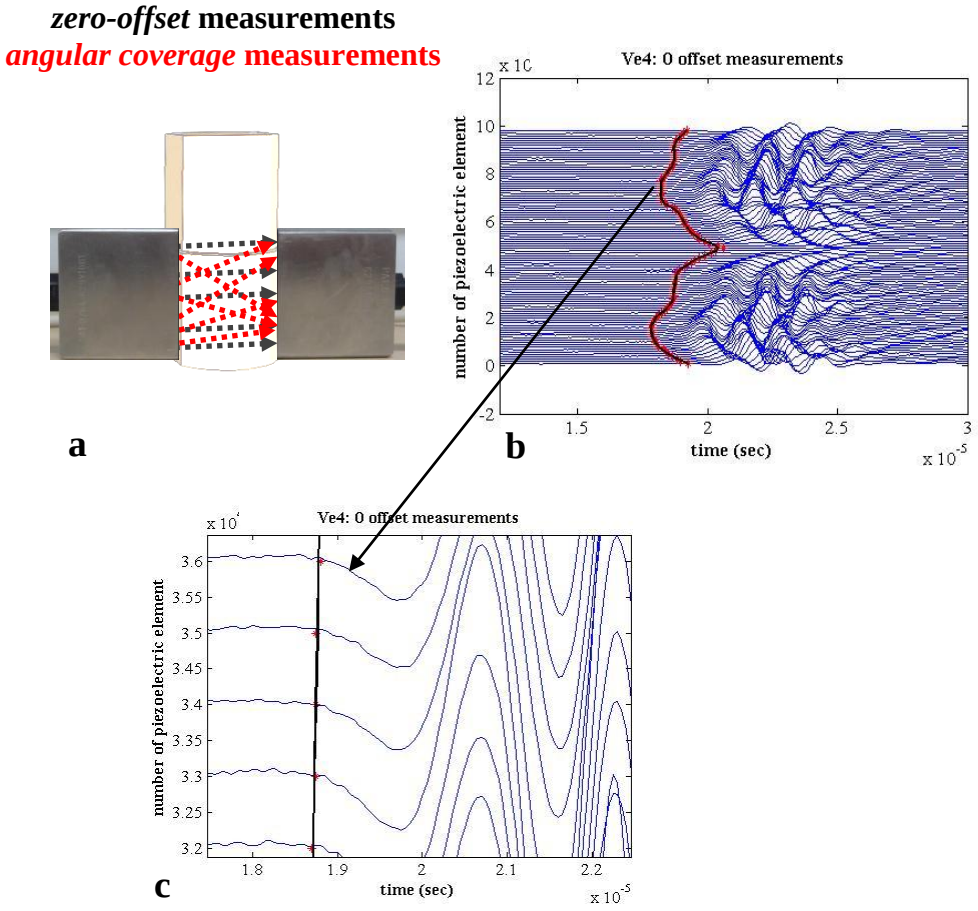

Fig. 6.3: Specimen Ve4: (a) Example of few 'zero-offset' measurements, in black, and 'angular coverage' measurements, in red; (b) Ultrasonic waveforms of the zero offset measurements plotted versus time. The arrival time profile (in red) is superimposed; (c) Zoomed part of figure (b) to highlight the picked arrival times and the waveforms.

Ultrasonic measurements from specimen Ve4 were grouped in three sections: the bottom (from 0.008625 m to 0.031125 m, corresponding to the position of the 8th to 38th piezoelectric element), the middle (from 0.031875 m to 0.050625 m, corresponding to the position of the 39th to 64th piezoelectric element), and the top (from 0.051375 m to 0.070125 m, corresponding to the position of the 65th to 90th piezoelectric element). Note that the piezoelectric elements at the very top and bottom edges were not taken into account since

these measurements are likely to be biased due to the polishing during the specimen preparation. Figure 6.4a shows the zero-offset velocity profile throughout the height of the specimen for these three sections, together with the average velocities (the bottom section is in red, the middle section is in green and the top section is in black). The velocity profile indicates that low velocities were measured at the region of the notch (and close to the notch; central section), where the localised deformation was identified by the AE locations (Fig. 6.1). Higher velocities characterised the regions above and below the notch; the slightly lower average velocity in the top section, compared to the bottom, is likely to be linked to textural heterogeneities reflecting the fine depositional layering (denser layer).

Figures 6.4b and 6.4c present the average unfiltered frequency-power spectra (amplitude) of the zero-offset measurements and the calculated wavelengths from these three sections of specimen Ve4. The dominant frequency and the wavelength were not the same in each of the three sections. The lowest frequency and the longest wavelength were observed in the middle section, where the lower velocities were measured (Fig. 6.4a). Figure 6.4c is a detail of the dominant frequencies.

Figure 6.5 presents the velocity profile of the 'zero-offset' measurements (Fig. 6.5a), the amplitudes and the frequency spectra of these measurements (Fig. 6.5b), the velocity field derived from the UT (Fig. 6.5c) and a picture of the AE hypocentres before unloading the specimen (Fig. 6.5d). All images, with an exemption of (6.5d), correspond to post-mortem measurements. The velocity field was derived from ultrasonic travel-time tomography using both zero-offset and angular measurements (Fig. 6.5c).

Overall, these results indicate that the compaction band appears as a zone of lower velocity (and lower amplitudes), while above and below the band the velocities were higher (and closer to the velocities measured in the undeformed material). The width of the compaction band in Fig. 6.5c was potentially exaggerated due to the resolution of travel-time tomography method, which is linked to the wavelength of the transmitted signal (in this case around 3 mm, corresponding to 600 kHz, see Fig. 6.4). However, it is also well possible that UT detects damage on a wider band than other full-field methods (see similar discussion on shear bands, section 5.4.1). AE clusters projected onto the same region as the velocity field presented a distribution similar to that of the low velocity anomaly (Fig. 6.5d).

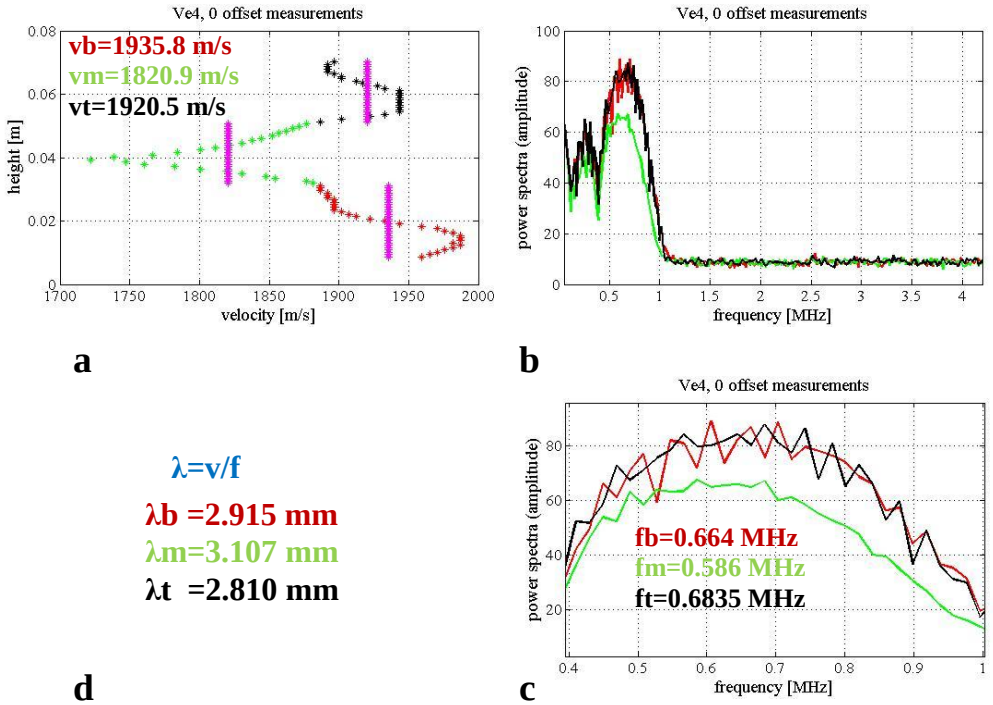

Fig. 6.4: Specimen Ve4: (a) 'Zero-offset' measurements' velocity profile: red refers to the bottom section of the specimen, green to the middle, and black to the top, together with the average velocity values of each section (magenta); (b) Unfiltered power spectra of the three sections versus frequencies; (c) Zoom in the dominant frequencies of each section; (d) Calculated wavelength values in each of the three sections.

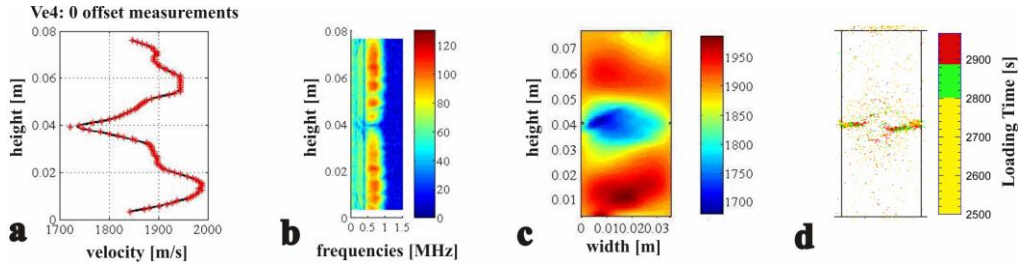

Fig. 6.5: Specimen Ve4: (a) Velocity profile of zero-offset measurements; (b) Amplitude spectrum of zero-offset measurements; (c) Velocity field using UT; (d) Map of AE for the same region as the velocity field.

Direct observation on x-ray tomography images does not typically allow compaction band features to be resolved. As described in section 3.4.2, *Louis et al.*, [2006; 2007a] used for this reason local statistical measurements of the grey-scale values, such as the skewness and the standard deviation. A similar approach was followed in the present study. Figure 6.6a illustrates an example of a raw x-ray tomography image from specimen Ve4 in which almost no trace of compaction could be observed in places where compaction bands were identified by the velocity methods (Fig. 6.5). However, the local standard deviation of the x-ray tomography image grey-scale values allowed the visualisation of the compaction bands (calculations were made over sub-volumes of 600x600x600 μm^3 at a spacing of 150 μm in each direction). Results from this analysis are shown in Figures 6.6b-6.6o, in which compaction bands appeared as zones of decreased standard deviation values, which from an image analysis standpoint (based on the x-ray tomography images at a given resolution) indicates more homogeneous regions (in red, standard deviation values higher than 0.03 are visualised in black). These regions are linked to broken material (smaller grain sizes).

From these images, it could be inferred that the deformation band initiated near the notches and propagated inwards (since the band appeared to be more developed at the edges), but did not reach the specimen's centre (likely what shown by the AE in Fig. 6.1). The bands (highlighted in the figure by light blue lines) were inclined at about 52°-84° towards the direction of the major imposed principal stress, with a mean value of approximately 62° (dip of 28°).

In addition, the band-width was between 300 and 900 μm, which corresponds to one to three mean undeformed grain-diameters. This latter observation is consistent with values reported in the literature [*Tembe et al*., 2006; *Louis et al*., 2006; *Stanchits et al*., 2009] for experimentally deformed sandstones. However, it should be noted that the width of the band varied through the volume of the specimen.

Figure 6.7a shows the standard deviation of the grey-scale values for a vertical projection (x=11.025 mm from the front boundary of specimen Ve4), and Figure 6.7d the 3D geometry of the standard deviation values. Figures 6.7b and 6.7c show the volumetric and shear strains, for the same vertical projections as those shown on Figure 6.7a. The calculations of the strain fields in Figures 6.7b, 6.7c were made throughout the image volume over sub-volumes of

600x600x600 μm^3 at a spacing of 600 μm in each direction. These dimensions correspond to sub-volumes and spacing sizes equivalent to two undeformed grain-sizes (*i.e.*, 600 μm).

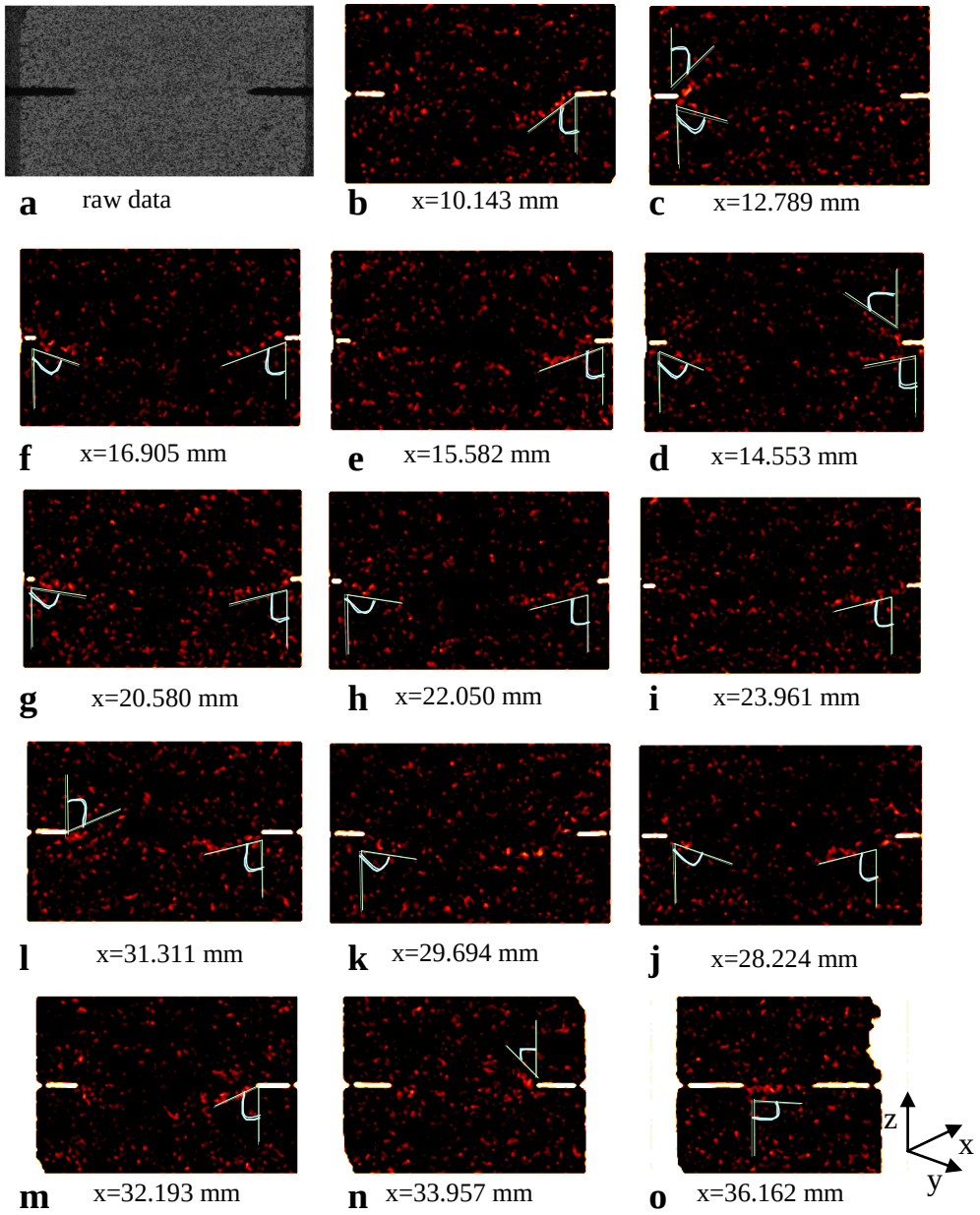

Fig. 6.6: (a) Raw x-ray tomography images; (b)-(o) Standard deviation images of x-ray tomography data, in different vertical slices throughout the volume of the Ve4. Calculations were performed over sub-volumes of 20x20x20 voxels^3 at a spacing of 5 voxels (*i.e.*, 150 μm) in each direction. The threshold level is from 0.01 to 0.03 (Values higher than 0.03 are visualised in black). The resolution of the HR x-ray image was of ~30 μm.

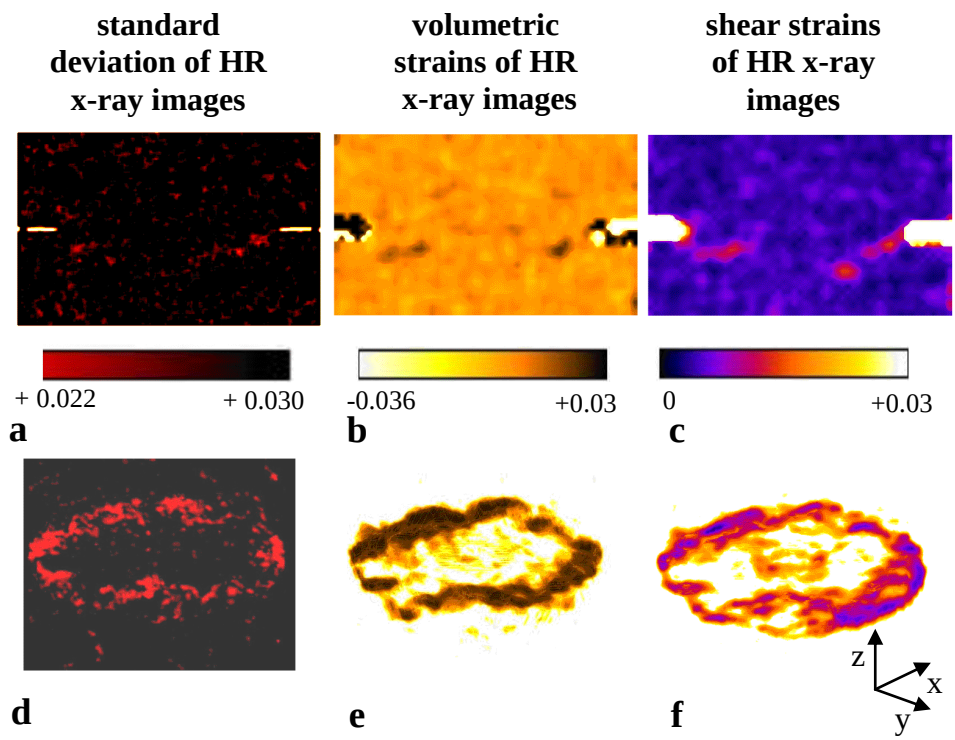

Fig. 6.7: Specimen Ve4: (a) Vertical slice of the local standard deviation from the post-mortem HR x-ray tomogram (red depicts low standard deviation (more homogeneous) and black high standard deviation (less homogeneous), at x=11.025 mm. Calculations were made over sub-volumes of 20x20x20 voxels^3 at a spacing of 5 voxels in each direction; (b)-(c) Equivalent position vertical slice through the shear and volumetric strain volumes, respectively. Calculations were made over sub-volumes of 20x20x20 voxels^3 at a spacing of 20 voxels; (d)-(f) 3D view of the standard deviation, the volumetric and the shear strain fields to highlight just the region of localized compaction.

The shear strain in the band ranged from 0.6 to 1.4% (recall that $\varepsilon_s = \sqrt{2/3}\,[(\varepsilon_1 - \varepsilon_2)^2 + (\varepsilon_2 - \varepsilon_3)^2 + (\varepsilon_3 - \varepsilon_1)^2]^{1/2}$ is the deviatoric strain, with ε_1, ε_2 and ε_3 the major, intermediate and minor principal strains, respectively). Inside compaction band the volumetric strain, ($\varepsilon_v = [\varepsilon_1 + \varepsilon_2 + \varepsilon_3]$), was always compactant with values of up to +1.9% (see sign convention in Chapter 4). Near the notches, some small dilation was measured, which is consistent with micro-crack opening (also in section 6.8). 3D views of the volumetric and shear strain fields, in Figure 6.7e and 6.7f, highlighted the 3D geometry of compaction bands.

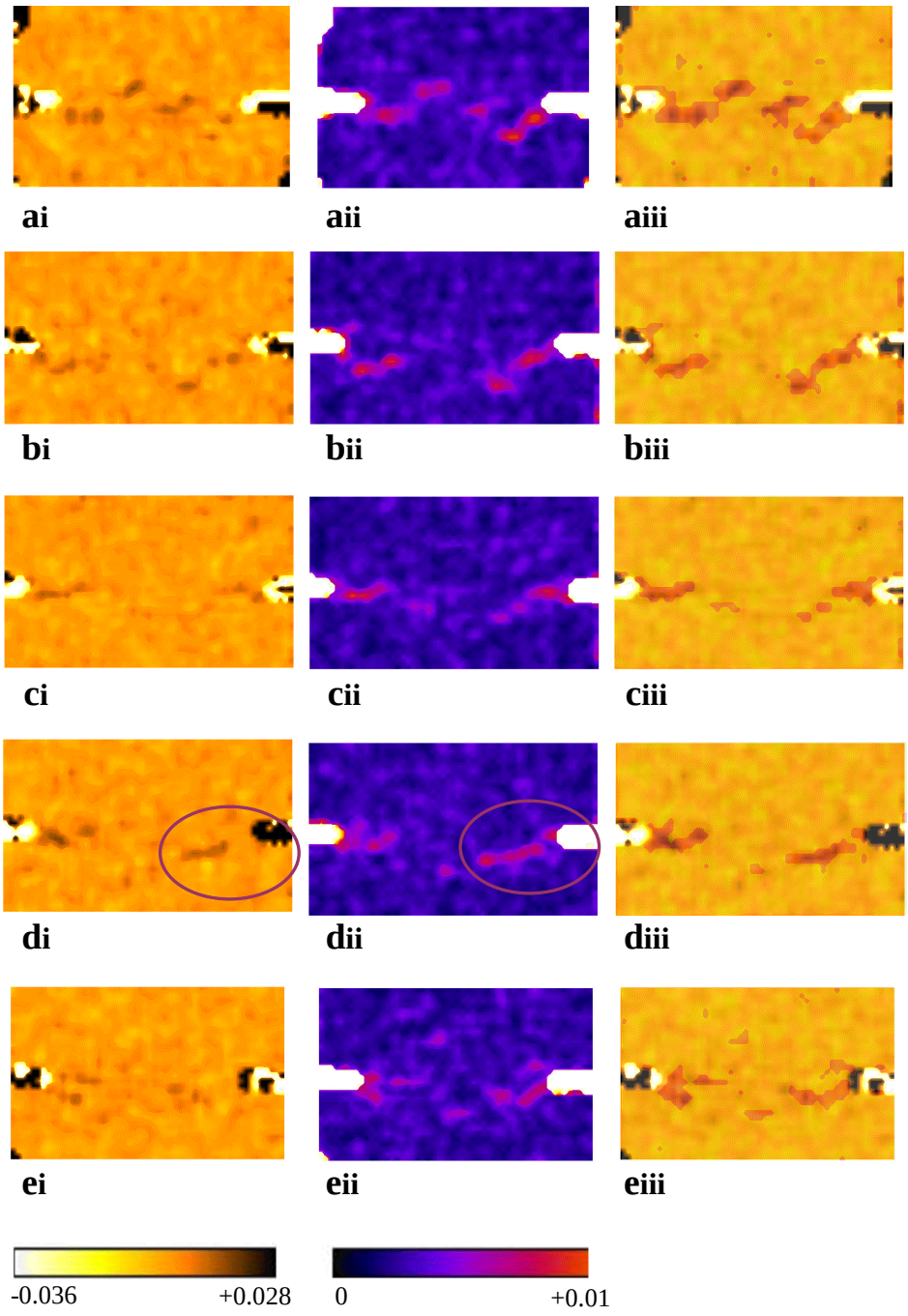

Fig. 6.8: Specimen Ve4: (ai), (bi), (ci), (di), (ei) volumetric strain fields; (aii), (bii), (cii), (dii), (eii) shear strain fields; (aiii), (biii), (ciii), (diii), (eiii) superposition of shear on volumetric strain fields for the same projections. Calculations were made over sub-volumes of 20x20x20 voxels^3 at a spacing of 5voxels in each direction. Pre- and post-mortem HR x-ray images had a resolution of ~30 µm.

Figure 6.8 presents some indicative vertical projections of the volumetric (Fig. 6.8ai, 6.8bi, 6.8ci, 6.8di, 6.8ei) and shear (Fig. 6.8aii, 6.8bii, 6.8cii, 6.8dii, and 6.8eii) strain fields from specimen Ve4. These projections correspond to different vertical positions throughout the volume of the Ve4. In order to visualise the geometry of both strain patterns together, the shear strain fields were superimposed on the volumetric strain fields (Fig. 6.8aiii, 6.8biii, 6.8ciii, 6.8diii, 6.8eiii). The shear strains show compaction bands as wider features as compared to the volumetric strains. Furthermore, smaller values of compactant volumetric strains inside the compaction band were usually located in regions near the circumferential notch (Fig. 6.8di). Shear strains in these regions were more pronounced (Fig. 6.8dii). The mean inclination angle of compaction bands in these near-notch regions measured from the volumetric and shear strain fields was about 66° to the major imposed principal stress (dip of 24°).

6.3 Different strain levels

In this section, results from specimen Ve6 are presented (see Chapter 4), which was loaded under triaxial compression at the same confining pressure as specimen Ve4 (130 MPa; Table 4.2); however, specimen Ve6 was taken to a greater axial strain value than specimen Ve4. Recall that specimen Ve6 had also a circumferential notch machined at its mid-height. In this section AEs, source-mechanism analysis, HR x-ray images, and 3D-DIC strain fields are discussed for a further comparison to the Ve4 results.

Figure 6.9 presents the AE signatures during the triaxial loading from specimen Ve6. The stress deviator-time history (in seconds) and the cumulative AE number, separated into increasing time intervals moving from left to right are presented in Figure 6.9a. Three 2D projections of the 3D distributions of AE event locations (one perpendicular and two parallel to the specimen's axis) are shown in Figure 6.9b, 6.9c and 6.9d. In particular, the perpendicular sections in Figure 6.9b show the overprint of the AE distribution from the middle height of the specimen (*i.e.*, from 30 mm to 50 mm from the bottom edge of the

specimen). Both parallel projections overprint AE event distributions recorded in the central section of the specimen (*i.e.*, +/- 2 mm or 4 mm thickness central vertical slice).

Approximately 5000 AE events were plotted on Figure 6.9a, by the end of loading (although several thousand of AE events were located). Note that only AE amplitudes higher than 2 Volts were set for the cumulative number of AE and amplitudes higher than 0.5 Volts were set for the 3D projections (Fig. 6.9b-6.9d), as done for specimen Ve4. Colours change to highlight most recent events (like in Fig. 6.1).

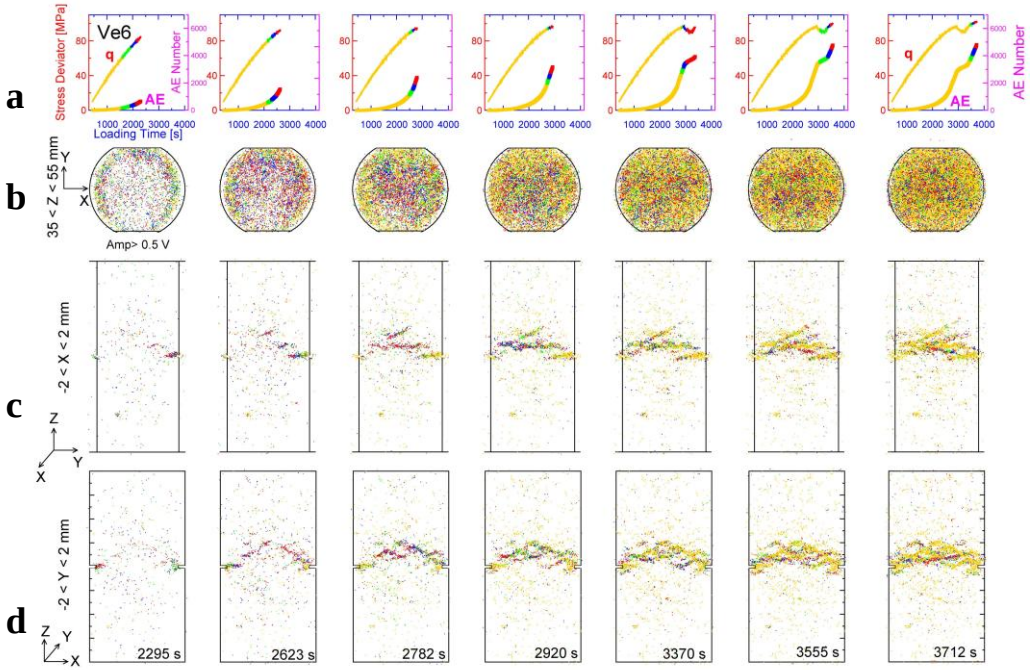

Fig. 6.9: AE results from specimen Ve6: (a) Axial load as a function of the number of AE events in different time intervals; colours change to highlight most recent events; (b)-(d) Maps of AE event locations for the same time intervals viewed perpendicular to the specimen's height, parallel to the specimen's height in a projection perpendicular to the flattened surfaces projections and parallel to the specimen's height in a projection parallel to the flattened surfaces projections.

For specimen Ve6, the majority of AE events were located at the middle and top region of the specimen. Notches acted as stress concentrators and encouraged the onset of compaction bands at the early stages of the experiment. These bands started propagating inward. However, soon after their propagation began, new compaction bands nucleated at the top part

close to the notch. Focusing on the AE signatures, it could be argued that compaction bands either developed further (inwards) or their propagation decelerated with increasing stress deviator values (see the initial compaction band at the right notch). Meanwhile, new bands initiated and started propagating. The cumulative AE number increased with increasing stress deviator, which indicates a grain-scale activity with increasing axial strain. Such activity corresponds to the further development of the existing bands as well as the nucleation of new bands. It should be noted that the number of AE events increased even when the loading was temporarily halted (at around 3000 seconds from the beginning of the experiment), which likely indicates further grain damage, possibly due to their rearrangement.

A distinctive difference between the AE signatures of specimens Ve4 and Ve6 is that multiple compaction bands developed in the latter, from the early stages of the experiment. A possible explanation is that these two specimens could have had some local textural differences, which in the case of specimen Ve6 encouraged the nucleation of more deformation bands. Moreover, the total number of AE events at the end of test Ve6 was higher than for test Ve4. Recall that for specimen Ve4 around 3000 AE events were plotted (Figure 6.1a); while for specimen Ve6 this number reached about 5000 AE events (for the same amplitude threshold, Figure 6.9a). At this stage of the analysis, the higher number of AE events (with amplitudes greater than 2 Volts) of specimen Ve6 cannot be justified based solely on the higher level of axial strain. It should be underlined, though, that the multiple compaction bands, which developed in specimen Ve6, should have increased considerably the total amount of AE events. However, with the present analysis, the number of AE events corresponding to a single compaction band of specimen Ve6 could not be compared to that of the Ve4 because of differences in compaction bands' development and evolution.

Figure 6.10 presents an initial AE source-mechanism analysis, for specimen Ve6. As already observed for specimen Ve4, during deviatoric loading the majority of events were C-type (97.4% at 0.3% of axial strain, reducing slightly to 97% when the loading was stopped, Fig. 6.10b, 6.10c). Ve6 S-type events increased by 0.4% (unlike what observed for specimen Ve4). A drop of S-type events and a local increase in C-type events occurred during the temporal stop of loading (Fig. 6.10d, 6.10c). Such observation possibly indicates that the axial loading encouraged the S-type events at this stress level. Furthermore, a small, but not

negligible amount of T-type events occurred during this experiment (0.2%, Fig. 6.10b, 6.10d). Figure 6.10 shows the stress deviator and the amount and type of AE source-mechanism as a function of axial strain.

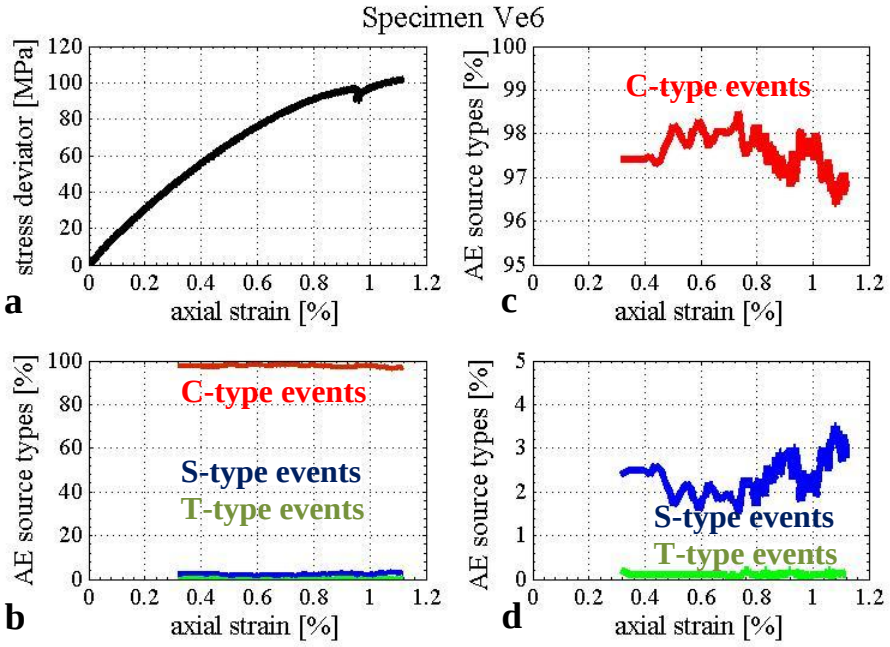

Fig. 6.10: Plots of stress deviator (a), the amount and type of AE source-mechanisms (b), and zooms in C-type events (c) and S- and T-type events (d) during the deviatoric compression of specimen Ve6, all as a function of the axial strain.

A standard deviation analysis of the grey-scale values was also applied to specimen Ve6. Figures 6.11a and 6.12a present the standard deviation of grey-scale values from HR x-ray tomography images at two different positions (x=15.676 mm, and x=20.364 mm from the front surface of the Ve6). The lower values of standard deviation (in red) were located inside structures that are inferred to represent compaction bands. Calculation of the standard deviation values was made over sub-volumes of 600x600x600 μm^3 at a spacing of 600 µm in each direction. Figures 6.11d and 6.12d show that compaction bands could be better resolved for a smaller spacing of the sub-volume gauge. When calculations of standard deviation were made over the same sub-volumes (*i.e.*, 600x600x600 μm^3), but at a spacing of 150 µm in each direction, much more details were retrieved.

Both volumetric and shear strains from specimen Ve6 unsurprisingly reached higher levels than those from specimen Ve4 (Fig. 6.11b, 6.11c, 6.12b, 6.12c). Calculations of the strain fields, presented in these Figures, were made throughout the image volume over sub-volumes of 600x600x600 μm^3 at a spacing of 600 µm in each direction, as for the standard deviation values (Fig. 6.11a, 6.12a). These dimensions correspond to a sub-volume and a spacing size equivalent to two undeformed grain-sizes (*i.e.*, 600 µm). Shear strain inside the compaction bands ranged from 0.9% to 2.3% and the volumetric strains were up to +3.3% and were always compactant. Outside the deformation bands, small volumetric strains were measured and the shear strains were almost negligible. Therefore, both compaction and shearing were mainly accommodated inside the compaction bands.

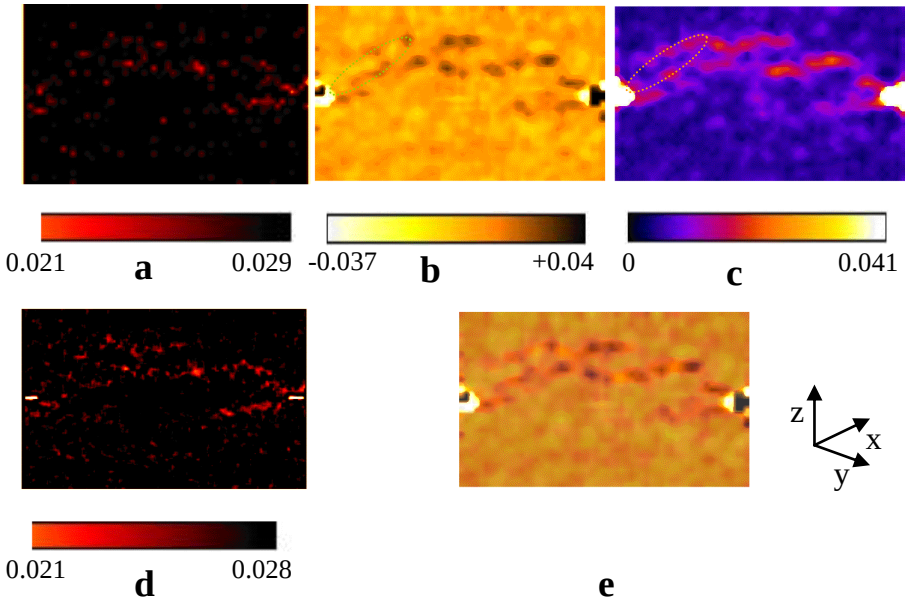

Fig. 6.11: Results from specimen Ve6: (a), (d) Vertical projections of the standard deviation values of HR x-ray images. Calculations were performed over sub-volumes of 20x20x20 $voxels^3$ at a step of 20 and 5 voxels in each direction, respectively. Lower values of standard deviation were located inside compaction bands. Standard deviation values higher than 0.029 are visualised in black; (b) Volumetric strain fields for the same position; (c) Shear strain fields for the same position; (e) Volumetric and shear strain fields superposition (x= 15.676 mm). Calculations of the strain fields were performed over sub-volumes of 20x20x20 $voxles^3$ at spacing of 20 voxels in each direction.

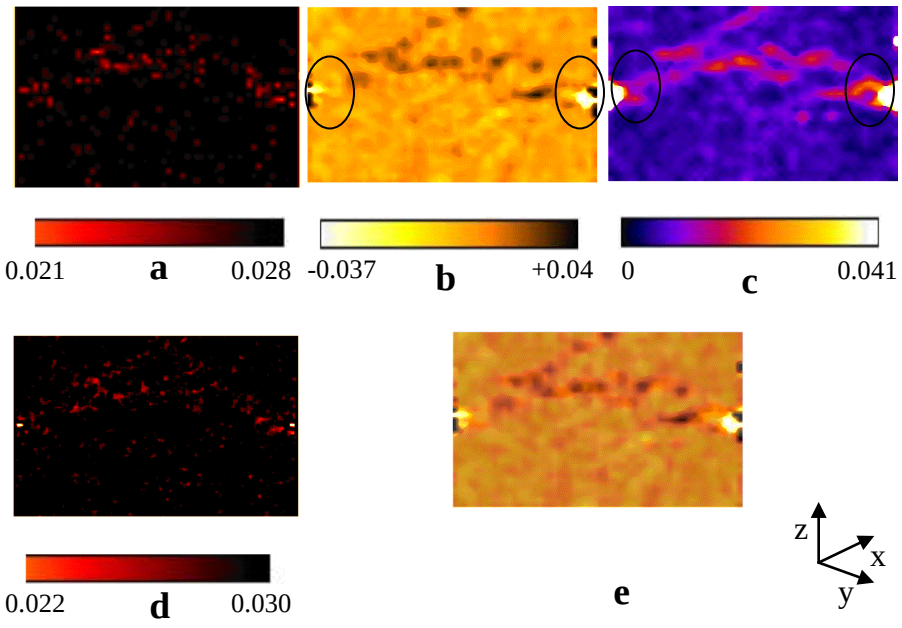

Fig. 6.12: Results from specimen Ve6: (a), (d) Vertical projections of standard deviation values from HR x-ray images. Calculations were performed over sub-volumes of 20x20x20 voxels^3 at a step of 20 and 5 voxels in each direction, respectively. Standard deviation values higher than 0.028 (a) and 0.030 (d) are visualised in black. Lower values of standard deviation were located inside compaction bands; (b) Volumetric strain fields for the same position; (c) Shear strain fields for the same position; (e) Volumetric and shear strain fields superposition (x= 20.364 mm). Calculations of strain fields were performed over sub-volumes of 20x20x20 voxles^3 at spacing of 20 voxels in each direction.

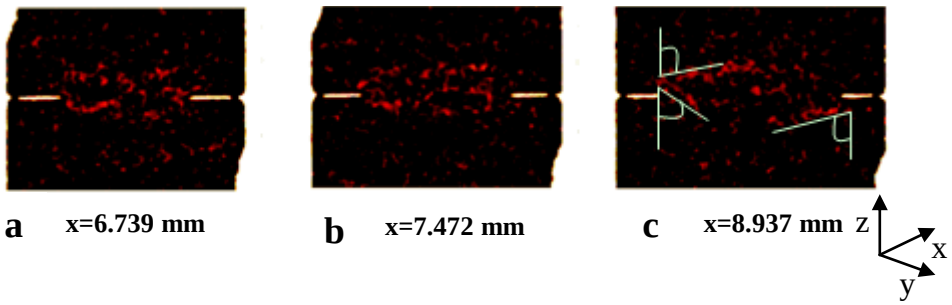

Fig. 6.13: Standard deviation of the grey-scale values from HR x-ray tomography images, in different vertical slices throughout the volume of specimen Ve6. Calculations were performed over sub-volumes of 20x20x20 voxels^3 at spacing of 5 voxels in each direction. The threshold level is from 0.01 to 0.03. Standard deviation values higher than 0.03 are visualised in black.

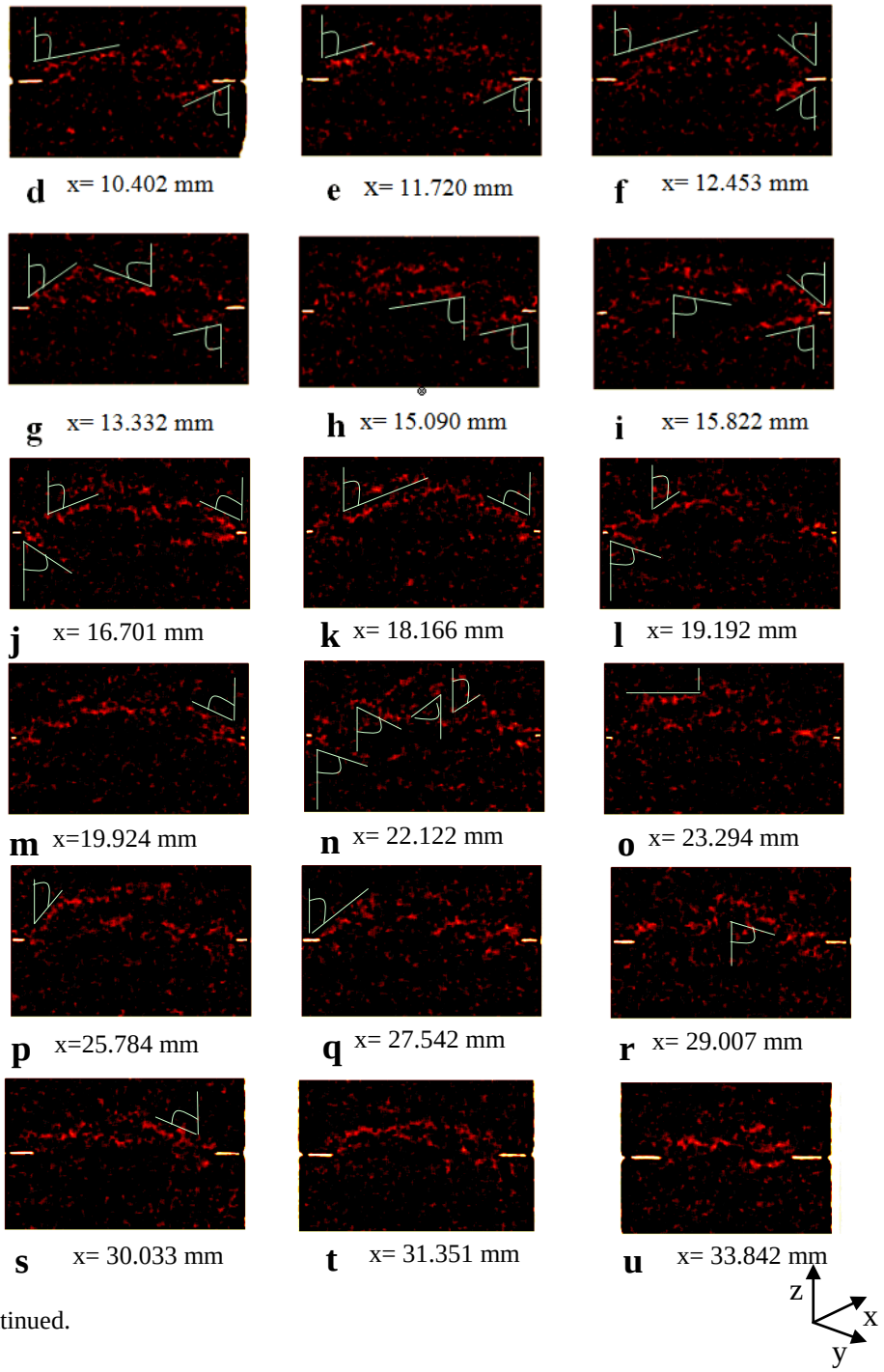

Fig. 6.13: Continued.

Figures 6.11e, 6.12e present the shear strain field superimposed on the volumetric strain field, for the same projections. Shear strain structures appeared more spread out compared to volumetric strain structures, similarly to what was also observed in Figure 6.8.Dilatant

volumetric strains were measured in a region between two compaction bands (in circle, Fig. 6.11b) and near the left notch. Relatively small shear strains were measured in this region (Fig. 6.11c). However, in some regions, dilation together with shearing was observed near the notches (Fig. 6.12b, 6.12c).

Since the geometry of the compaction bands became more complex (*i.e.*, a network of localised deformation bands was developed), it is more complicated to define the inclination angle of the compaction bands for this particular specimen. Figure 6.13 illustrates some of the inclination angles measured on HR x-ray images (using the standard deviation analysis). Compaction bands had inclination angles from about 53° to 90° towards the direction of the major imposed principal stress, with a mean value of around 67° (dip of 23°). The bands at the notches had a mean inclination angle of 63° (dip of 27°).

Compaction bands could not be distinguished by naked eye on the surface of the specimen due to the existence of the circumferential notch. The band-width was between 300 and 1500 μm, which corresponds to one to five mean intact grain-diameter. The grain damage was, thus, more spread out locally, compared to what was observed for specimen Ve4, which can be attributed to the higher axial strain level.

6.4 Different stress levels

The goal of this particular section is to highlight differences in compaction band characteristics at different confining pressure levels. Results from experiments carried out at 130 MPa confining pressure were discussed in sections 6.2 and 6.3. Herein, results of AEs, HR x-ray tomography images and 3D-DIC are presented for specimens loaded at 160 MPa (Ve5) and 190 MPa confining pressure (Ve7) (see Chapter 4, Table 4.2).

6.4.1 AE

Figures 6.14 and 6.15 show the location of AE events during the triaxial loading of specimen Ve5 (160 MPa confining pressure) and Ve7 (190 MPa confining pressure), respectively. Both

specimens had a circumferential notch machined at their mid-height. The differential load time history (in seconds) and the cumulative AE number, separated into increasing time intervals moving from left to right are presented in Figures 6.14a, 6.15a. Only AE event amplitudes higher than 2 Volts were set for the calculation of the cumulative number of AE events. Three 2D projections of the three dimensional distributions of AE event locations (one perpendicular and two parallel to the specimen axis) are shown in Figure 6.14b- 6.14d and 6.15b-6.15d. Colours change to highlight most recent events (as in Fig. 6.1).

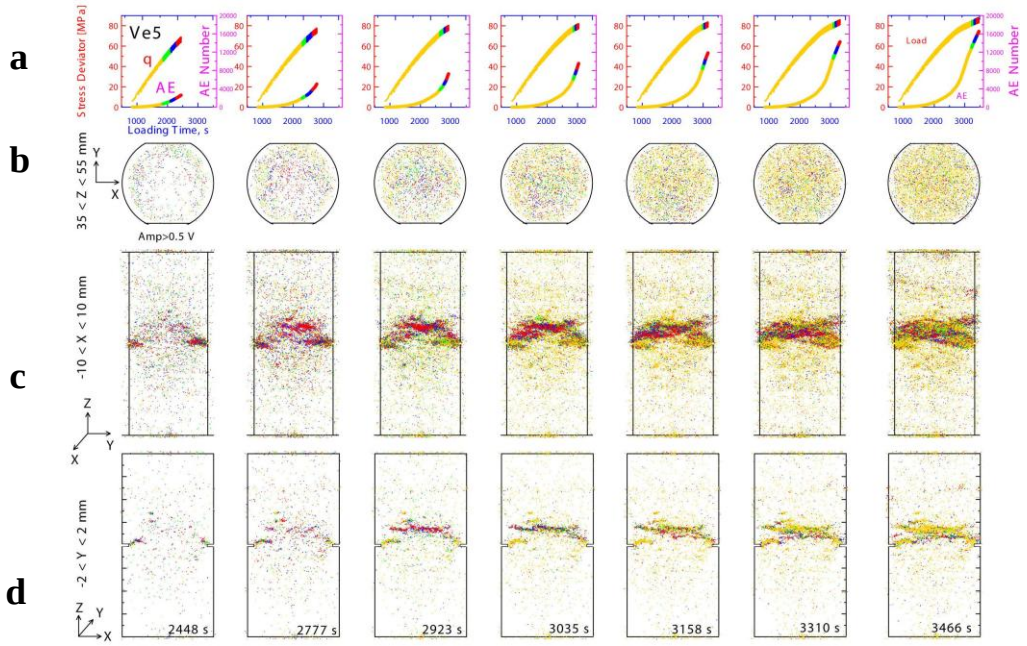

Fig. 6.14: AE results from specimen Ve5: (a) Axial load as a function of the number of AE events in different time intervals; colours change to highlight most recent events; (b)- (d) Maps of AE event locations for the same time intervals viewed perpendicular to the specimen's height, parallel to the specimen's height in a projection perpendicular to the flattened surfaces projections and parallel to the specimen's height in a projection parallel to the flattened surfaces projections.

Only AE event amplitudes higher than 0.5 Volts were set for the 2D projections in Figures 6.14b-6.14d, while amplitudes higher than 1 Volt were used in Figures 6.15b-6.15d. The perpendicular 2D projection of the 3D distribution of AE event locations overprint AE events of the middle height of the specimen (*i.e.*, from 35 mm to 55 mm from the bottom edge of

specimen Ve5 and from 25 mm to 55 mm from the bottom edge of specimen Ve7). The z-x perpendicular projection overprints AE events recorded in the central section of the specimen (i.e., +/- 2 mm), while the z-y perpendicular projection overprints AE events recorded in a wider section of the specimen (i.e., +/- 10 mm), for both specimens Ve5 and Ve7.

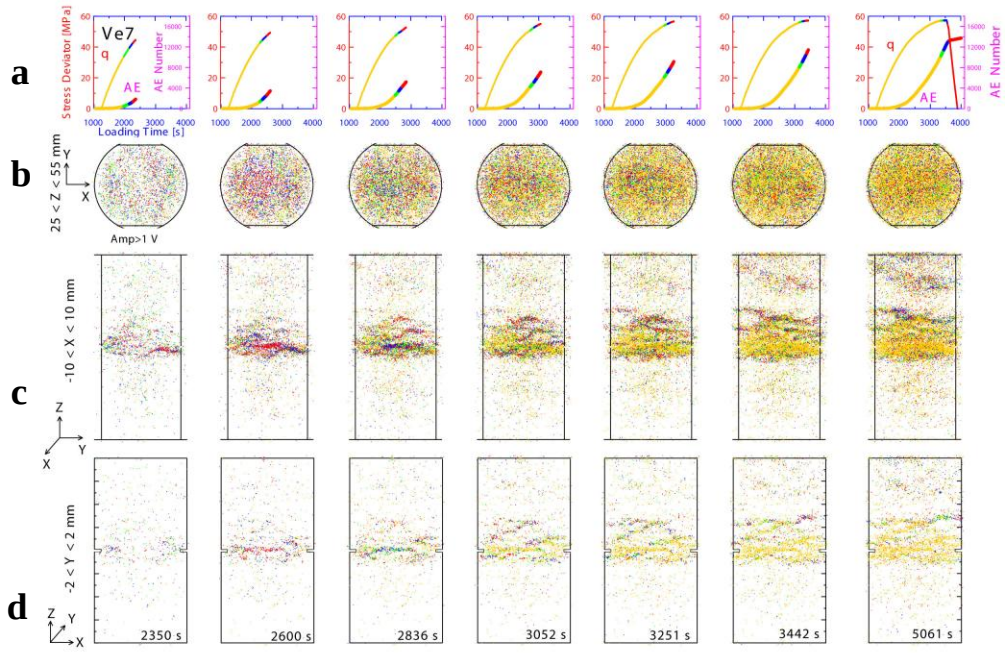

Fig. 6.15: AE results from specimen Ve7: (a) Axial load as a function of the number of AE events in different time intervals; colours change to highlight most recent events; (b)-(d) Maps of AE event locations for the same time intervals viewed perpendicular to the specimen's height, parallel to the specimen's height in a projection perpendicular to the flattened surfaces projections and parallel to the specimen's height in a projection parallel to the flattened surfaces projections.

All AE events were located in the middle and top section of the specimen. Since this was observed in all specimens (see also Fig. 6.1, 6.9), it could be argued that the top section of all specimens should have presented some textural heterogeneities that encouraged localisation to occur there. It is worth to note that *Bésuelle* [2004] observed via x-ray tomography that localisation in Vosges sandstone under relatively lower confining pressures (30 to 50 MPa) systematically took place in the more porous part of the specimens.

A rather complex network of compaction bands developed in both specimens. Deformation began at the notches, which acted as stress concentrators and facilitated the onset of compaction band formation. Soon after the onset of the initial compaction bands, other bands nucleated far from the notches accompanying the propagation of the former bands, as in Figure 6.10. These new bands developed in places where diffuse AEs had been mapped before. Note that the cumulative AE number increased with increasing stress deviator.

By the end of the loading phase, almost 16500 AE events were plotted for specimen Ve5 and almost 13500 AE events for specimen Ve7 (with amplitudes greater than 2 Volts; see Fig. 6.14a, 6.15a). Two possible explanations of this can be given. On the one hand, compaction bands in specimen Ve5 started to be well developed earlier than those in specimen Ve7, which might be linked to local textural heterogeneities. From the parallel to the specimen's axis projections it can be observed that multiple, rather distinct, compaction bands were developed in specimen Ve5, while more diffuse compaction bands occurred in specimen Ve7. Compaction bands in the Ve5 might be more developed, which could explain a higher number of AE events. On the other hand, since multiple bands developed in both specimens, it might be the case that more bands appeared in specimen Ve5 than in specimen Ve7. The link between the number of compaction bands and the number of AE events is not straightforward in the present analysis, since more than a band developed in both specimens.

Figure 6.15a shows that during unloading the number of AE events increased at a lower rate. Such remark, which applies to all specimens tested (although the number of AE event during unloading is shown only for specimen Ve7), indicates that further rearrangement of the grain fragments, and thus, further grain damage, might have occurred during unloading.

In specimen Ve7, a considerable AE activity was also recorded near the top edge boundary. This activity started to be apparent from 3442 seconds from the onset of the experiment and on (Fig. 6.15c). By the end of the experiment, AE events appeared to be located in two zones: on the top and the middle section of the specimen. It is interesting to note, though, that the region in between these two zones seems to have been relatively unaffected (less AE events were located there), which is likely to indicate that a textural heterogeneity (*e.g.*, bedding layer) was present in this region.

6.4.2 X-ray CT

Compaction bands in specimens Ve5 and Ve7 were visualised using the standard deviation of the HR x-ray grey-scale values, similarly to what was done for specimens Ve4 and Ve6 (130 MPa confining pressure, Fig. 6.6 -6.7, 6.11-6.13). Calculations were made throughout the image volume over sub-volumes of 600x600x600 μm^3 at a spacing of 150 mm in each direction. Figures 6.16 and 6.17 show the standard deviation of the x-ray grey-scale values (x-ray image with a resolution of ~ 30 μm) from specimens Ve5 and Ve7. These Figures show that the 3D structure of compaction bands became more complex due to the increased confining pressure and the increased number of bands. More closely spaced compaction bands developed in specimen Ve7 as compared to specimen Ve5. In addition, in specimen Ve7 the compaction bands appear to be longer, and thus, they go through a bigger surface of the specimen.

In specimen Ve5, a network of conjugate compaction bands developed. Inclination angles ranged from 55° to 83° towards the major imposed principal stress, with a mean value of around 68° (dip of 22°), although in some regions almost horizontal deformation bands developed. Usually, the lower inclination angles are shown by the deformation bands located close to the notches. In specimen Ve7, compaction bands appeared to be normal to the major imposed principal stress in many more places, while in places where conjugate deformation bands developed, the inclination angles ranged from 58° to 88° towards the major imposed principal stress, with a mean value of around 70° (dip of 20°). Recall that the mean inclination angle of compaction bands in specimens Ve4 and Ve6 was around 62° and 67° (dip of 28° and 23°), respectively. Since the geometry of the compaction band network is rather complicated for all specimens, except for the case of specimen Ve4, it is rather difficult to assign a single value to their inclination angles. However, it should be underlined that the results clearly indicate that the inclination angle depends on the mean normal stress (the confinement pressure). The higher the confining pressure is, the more the compaction bands tend to be horizontal, *i.e.*, inclined normal to the major imposed principal stress direction.

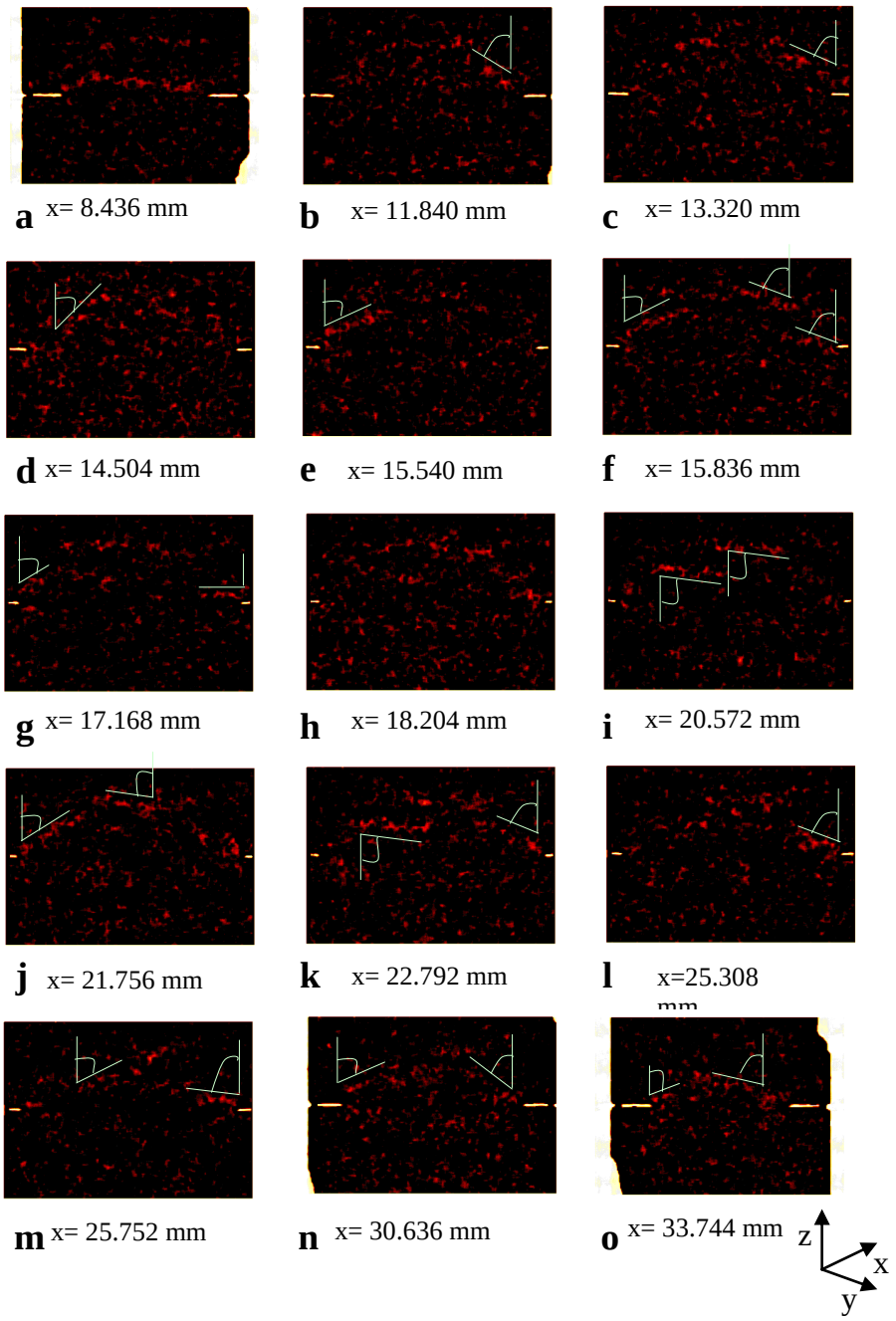

Fig. 6.16: Standard deviation of the grey-scale values from HR x-ray tomography images, in different vertical slices throughout the volume of specimen Ve5. Calculations were made over sub-volumes of 20x20x20 voxels^3 at spacing of 5 voxels in each direction. The threshold level is from 0.01 to 0.02. Standard deviation values higher than 0.02 are visualised in black.

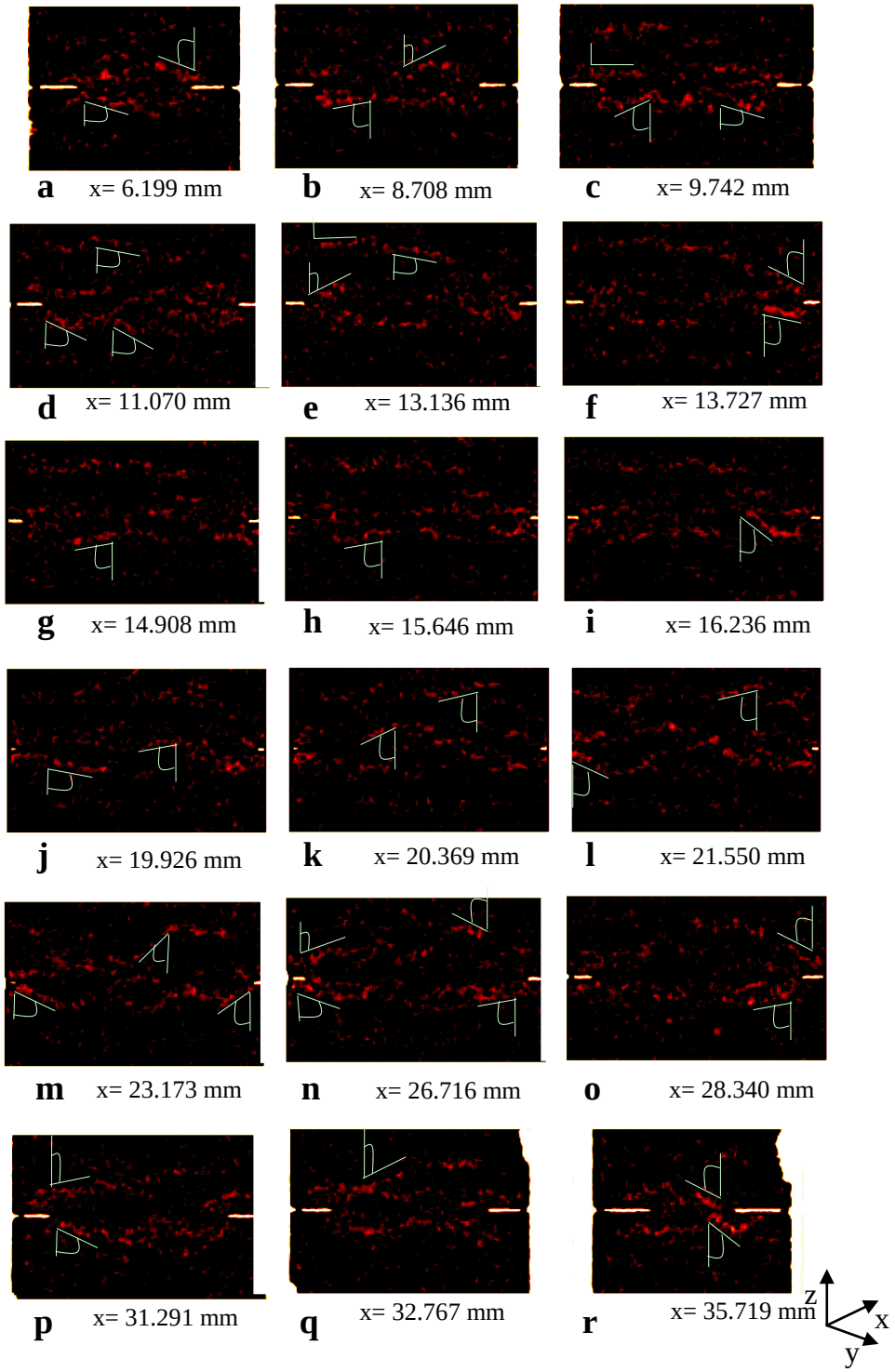

Fig. 6.17: Standard deviation of the grey-scale values from HR x-ray tomography images, in different vertical slices throughout the volume of specimen Ve7. Calculations were made over sub-volumes of 20x20x20voxels^3 at spacing of 5 voxels in each direction. The threshold level is from 0.01 to0.03.Standard deviation values higher than 0.03 are visualised in black.

6.4.3 3D-volumetric DIC

Volumetric and shear strain fields are presented in this section for both specimens Ve5 and Ve7. Calculations of the strain were made throughout the image volume over sub-volumes of 600x600x600 μm^3 at a spacing of 600 µm in each direction (*i.e.*, both sub-volumes and spacing were equivalent to two undeformed grain-diameters). Figures 6.18a and 6.18b present a vertical projection of shear and volumetric strain fields from specimen Ve5 in a place where both inclined and horizontal compaction bands were observed (x=11.514 mm). The volumetric strains (compactant) inside compaction bands ranged from +1.4% to +3.5% and the shear strains were up to 2.9%. Note that the higher values of compactant volumetric strains were located in the central section of the specimen, while the higher shear strains were measured near the notches. Figure 6.18c shows the shear strain field superimposed on the volumetric strain field. The width of the compacted region is narrower than that of sheared inside these bands.

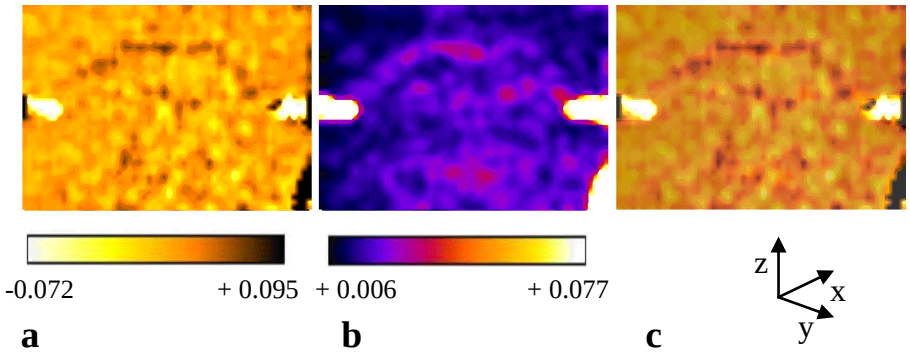

Fig. 6.18: Specimen Ve5: (a) Vertical projection from the volumetric strain field derived from pre-and post-mortem HR x-ray images (~ 30 µm resolution); (b) Vertical projection from the shear strain field derived from HR x-ray pre-and post-mortem images; (c) Superposition of the volumetric and shear strain field (x= 11.514 mm). Calculations have been made over sub-volumes of 20x20x20voxels^3 at spacing of 20 voxels in each direction.

Figures 6.19 show the standard deviation of the grey-scale values from HR x-ray images together with the volumetric and the shear strain fields from different vertical projections throughout the width of specimen Ve7.

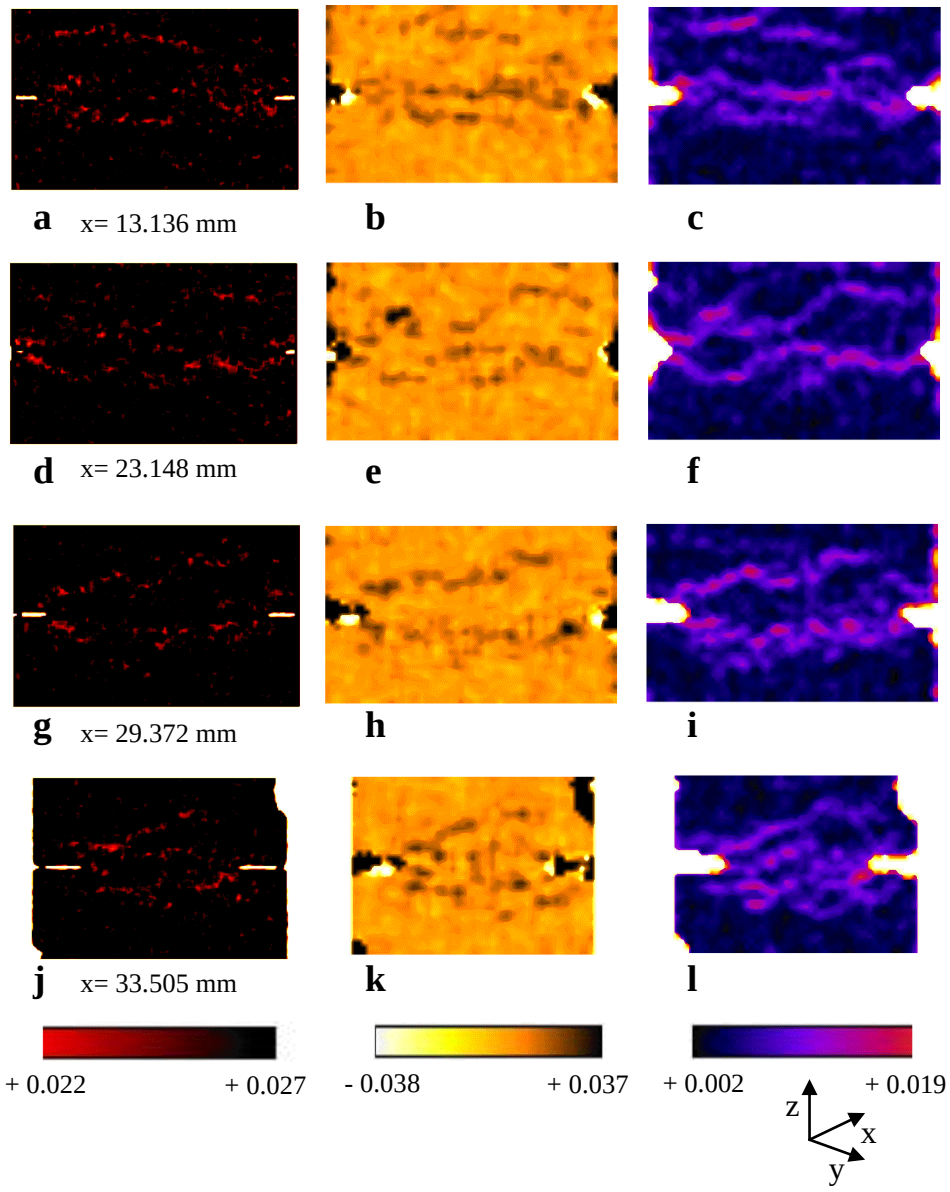

Fig. 6.19: (a), (d), (g), (j) Standard deviation of the grey-scale values from HR x-ray tomography images. Calculations were made over sub-volumes of 20x20x20 voxels^3 at spacing of 5 voxels in each direction. The threshold level is set to 0.027. Standard deviation values higher than the threshold level are visualised in black. (b), (e), (h), (k) Volumetric strain fields; (c), (f), (i), (l) Shear strain fields. Calculations were made over sub-volumes of 20x20x20 voxels^3 at spacing of 20 voxels in each direction.

Calculations of the standard deviation values were made throughout the image volume over sub-volumes of 600x600x600 μm^3 at a spacing of 150 μm in each direction (*i.e.*, the sub-volumes were equivalent to two undeformed grain-sizes and the spacing was equivalent to

half grain-size). Compaction bands appeared as regions of reduced values of standard deviation, positive volumetric strains (compaction) and higher values of shear strain (compared to regions outside the bands). Although the geometry of the compaction band network changed in space, the standard deviation and the volumetric and shear strain fields resolved almost similar geometries of deformation bands. The shear strain inside the compaction band ranged from 0.9% to 1.9% and the volumetric strain was always compactant with values of up to +4.0%.

To highlight the complex geometry of the network of compaction bands that developed in specimen Ve7, Figures 6.20 shows further vertical projections of the volumetric and shear strain fields in different positions, together with an image of the superposition of both strain fields. The inclination angle of these deformation bands, measured from the strain field images, ranged from 62° to 82°, with a mean value of 68° towards the major imposed principal stress (dip of 22°). Recall that the inclination angle measured from the standard deviation of the x-ray images was 70° (dip of 20°). Lower inclination angles of around 45°-53° were measured in some regions close to the notches. Furthermore, bands almost normal to the major imposed principal stress direction (*i.e.*, horizontal) were measured mainly in regions far from the notch. Therefore, it can be speculated that the notch controlled the orientation angle of the compaction bands; in places far from the notches, the bands tended to have an inclination angle controlled mainly by the confining pressure or/and the local textural heterogeneities of the region.

The standard deviation of the grey-scale values from x-ray images and the strain fields show that the geometry of compaction bands that developed in the Vosges sandstone specimens was not simple. This might be attributed to the mineralogy or/and to possible pore-network heterogeneities of the rock. It was observed that multiple bands developed in almost all specimens. Furthermore, the values of the volumetric and shear strains varied in space. It appears to be rather difficult to compare the volumetric and shear strains of all specimens based on single vertical projections. Therefore, to figure out the impact of the confining pressure on the geometry of the compaction bands, the median vertical projection throughout the whole volume of the specimens is considered to be more representative for such comparison.

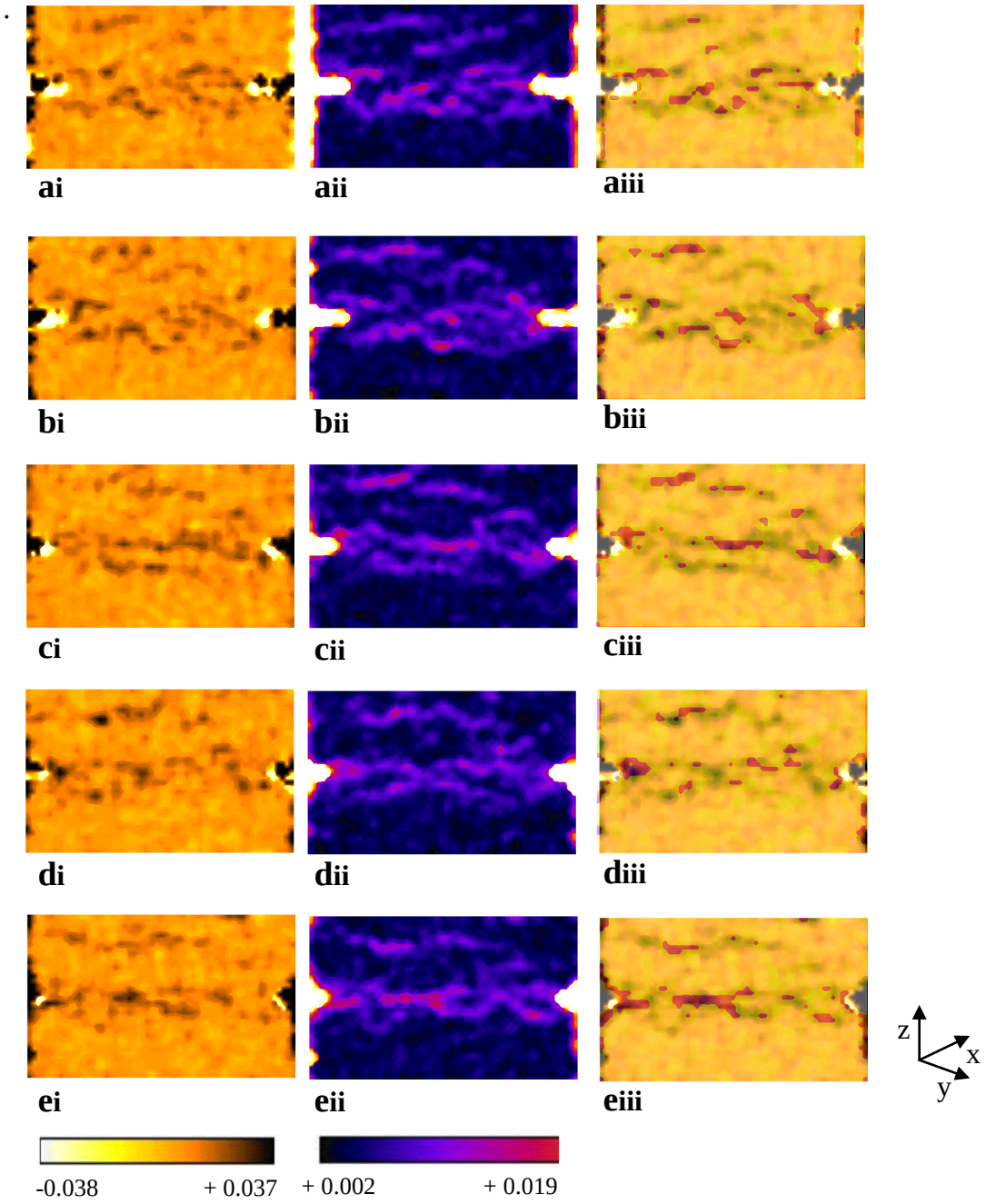

Fig. 6.20: Specimen Ve7: (ai)-(ki) Volumetric strain field derived from HR x-ray pre-and post-mortem images (~ 30 μm resolution); (aii)-(kii) Shear strain field derived from HR x-ray pre-and post-mortem images; (aiii)-(kiii) Superposition of the volumetric and shear strain field. Calculations have been made over sub-volumes of 20x20x20 voxels^3 at spacing of 20 voxels in each direction.

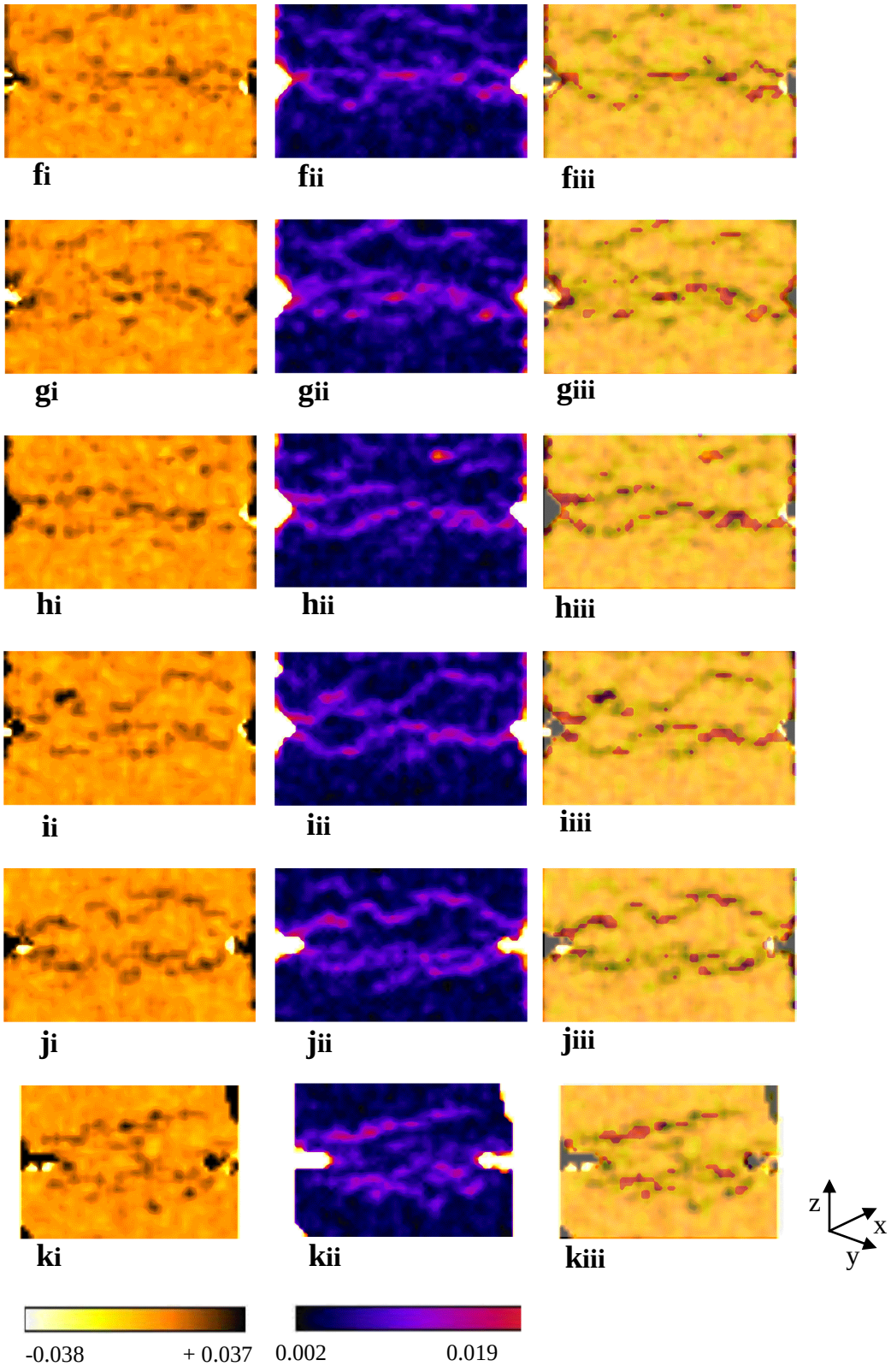

Fig. 6.20: Continued.

Figures 6.21, 6.24 show the median vertical projections from the volumetric and shear strain fields of specimens Ve4 (in blue), Ve5 (in red), and Ve7 (in green). Specimen Ve6 (in purple) is also shown in order to investigate the impact of different axial strain levels

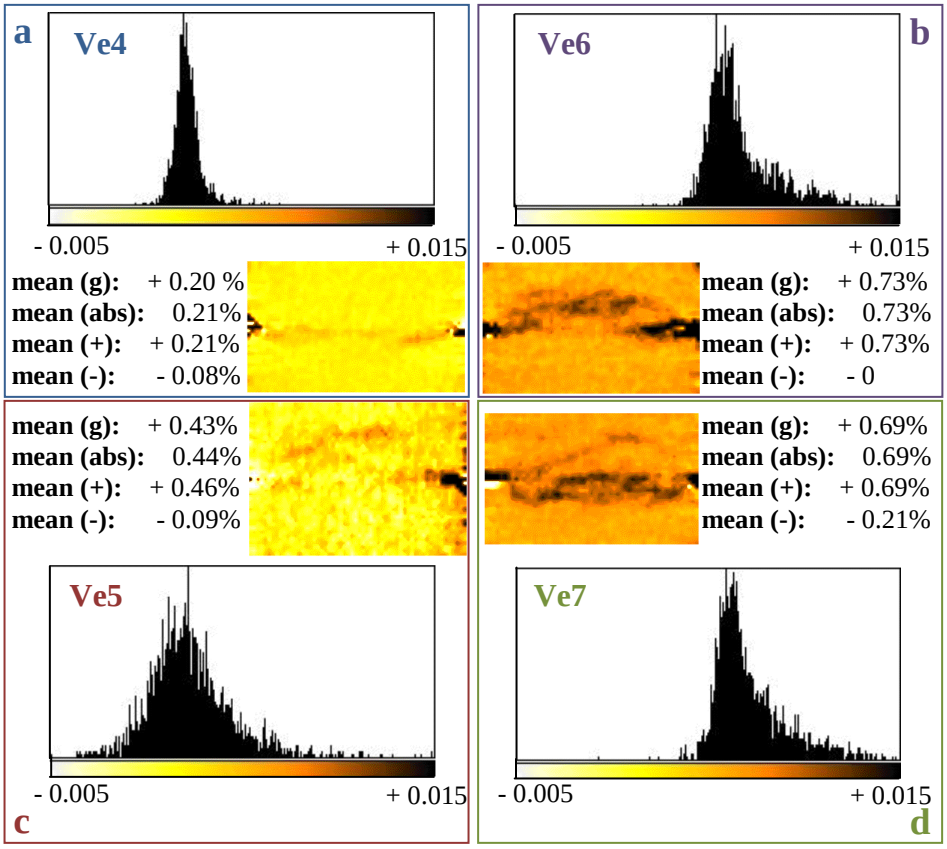

Fig. 6.21: Grey-scale values and volumetric strain values of the median vertical projections form specimens Ve4 (in blue), Ve6 (in purple), Ve5 (in red), and Ve7 (in green) together with the median vertical projections of the strain fields. The mean values were calculated for a thresholded range from -0.005 (dilation) to +0.015 (compaction). Strains calculations were made over sub-volumes of 20x20x20 voxels^3 at spacing of 20 voxels in each direction.

In addition, Figure 6.21 presents the histograms of grey-scale values and the mean volumetric strain values from these median vertical projections. Since there were both positive and negative volumetric strains, four different mean values were calculated: the mean and mean absolute volumetric strains (mean (g) and mean (abs), respectively), and the

mean compactant (mean (+)) and mean dilatant (mean (-)) volumetric strains. The mean absolute volumetric strain values increased with increasing axial strain and increasing confining pressure, since both parameters lead to further compaction of the specimen (*e.g.*, specimens Ve6 and Ve7). While the mean compactant volumetric strains followed the same trend, the mean dilatant volumetric strains decreased with increasing axial strain. Note that there were no dilatant volumetric strains in the median vertical projection of specimen Ve6. Furthermore, higher mean volumetric strains were measured in specimen Ve6 compared to those in specimen Ve7, which was loaded under the highest applied confining pressure. In general, the mean dilatant volumetric strains were relatively small compared to the compactant strains (with the exception of specimen Ve7, in which the absolute difference between the compactant and dilatant strains was smaller).

Table 6.1 summarises the ***S2*** parameter calculated from the median vertical projection of the volumetric strain field, the absolute values of these strains as well as the compactant and dilatant volumetric strains, separately, for the four specimens. ***S2*** parameter was discussed in detail for the case of the shear bands (see section 5.3). Recall that this parameter provides a global understanding of the volumetric strain distribution (similar to the mean values).

Table 6.1: S2 parameter calculated from the volumetric strain fields of the median vertical projections from specimen Ve4, Ve5, Ve6 and Ve7.

Specimen	S2: all volumetric strains	S2: absolute volumetric strains	S2: compactant volumetric strains	S2: dilatant volumetric strains
Ve4	0.80	0.81	0.82	0.56
Ve6	0.94	0.94	0.94	---
Ve5	0.68	0.71	0.73	0.45
Ve7	0.94	0.94	0.94	0.72

Given that the volumetric strains had either positive (compactant) or negative (dilatant) values, the ***S2*** parameter calculated from the absolute volumetric strain values was supposed to be more representative for further comparison to the ***S2*** derived from the shear strains (recall that shear strains are positive by definition, see Table 6.3). ***S2*** values, presented in Table 6.1, increased with increasing axial strain and confining pressure values (with the exception of specimen Ve5). Recall that ***S2*** represents the fraction of the system which had undergone considerable deformation. When the ***S2*** value is high, either no deformation or diffused deformation has occurred, while a small value of ***S2*** indicates the occurrence of localised deformation. Given that specimen Ve4 showed less localised deformation than specimens Ve6 and Ve7, one should expect a higher ***S2*** value for the former specimen. However, one should also keep in mind that the HR x-ray tomography images (which were used for the DIC from which the ***S2*** was calculated) were focused on the region near the notch, where the compaction bands were located, and not on the whole length of the specimen. Furthermore, in both Ve6 and Ve7 specimens, multiple compaction bands were formed, which had a broader width compared to the compaction band in specimen Ve4; therefore, more voxels were characterised by higher values of compactant volumetric strain (bigger population). In addition, the increased axial strain (Ve6) and confining pressure (Ve7) resulted in relatively higher mean volumetric strains. All these arguments may better explain why the ***S2*** values indicated a more homogeneous (less localised) volumetric strain field in specimens Ve6 and Ve7 compared to specimen Ve4.

To better understand the meaning of the ***S2*** values, a group analysis on the strain field was performed for all specimens, to focus on the compactant volumetric strain distributions inside the compaction bands. Compactant volumetric strains were divided into four equal population groups. Figure 6.22 shows the 25% of the highest compactant volumetric strains (median vertical projection) measured in each of the specimen (using the HR pre- and post-mortem x-ray images, which focused on the mid-height of the specimens). These values increased with increasing confining pressure (Ve4, Ve5, and Ve7) and increasing axial strain values (Ve4, Ve6). It is interesting to underline that the compactant volumetric strains from specimens Ve7 and Ve6 showed, for this strain group, similar distributions (up to almost +1%), but different distributions for strain values higher than +1%. In specimen Ve4, most

of the voxels (characterised by strains values belonging to the 25% of the highest compactant volumetric strains) had relatively low compactant volumetric strain values (*e.g.*, ~ 0.2%), whistle only few voxels had relatively higher values (*e.g.*, 0.5%-1.4%). Such plot explains further the ***S2*** values in Table 6.1.

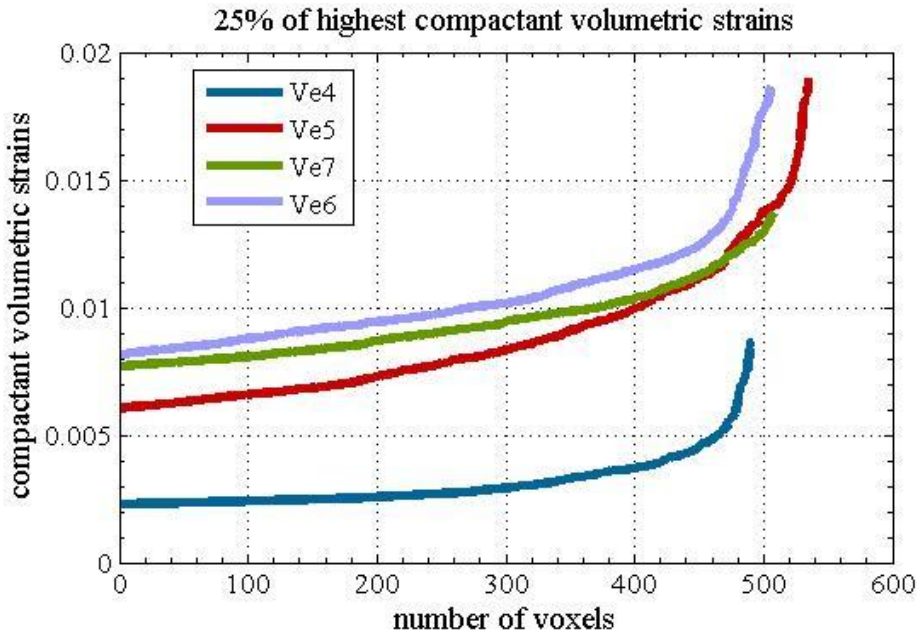

Fig. 6.22: Compactant volumetric strains, which correspond to the 25% of the highest compactant strains measured in the median vertical projections of specimens Ve4 (in blue), Ve6 (in purple), Ve5 (in red), and Ve7 (in green). Volumetric strain calculations were performed over sub-volumes of 20x20x20 voxels^3 at a spacing of 20 voxels in each direction.

The compactant volumetric strain values, which were measured inside compaction bands, belonged to the group of the 25% of the highest compactant volumetric strains. Table 6.2 shows the maximum and minimum compactant volumetric strains inside the bands (median vertical projections). These strain values increased with increasing confining pressure and increasing axial strain. Note for instance that the minimum compactant volumetric strains inside the compaction bands from specimen Ve6 were almost three times bigger than those from specimen Ve4. In addition, the compactant volumetric strain range inside the compaction bands of specimen Ve6 was much wider compared to that of specimen Ve4 and

Ve7 (0.99% compared to 0.61% for specimen Ve4 and 0.54% for specimen Ve7). Moreover, specimen Ve6 presented the highest compactant volumetric strain values compared to specimens Ve4 and Ve7. This indicates that the increased axial strain lead to higher compactant strain values and wider distribution of volumetric strains to a larger extent than the increase in confining pressures (Table 5.2). Note that specimen Ve6 was taken to a higher axial strain than the Ve7; the higher plastic axial strain (i.e., unrecovered strain before unloading to an isotropic compression stage, see Table 4.2) of the latter compared to the former could be explained by the more diffuse damage on its middle-top section.

Note that the volumetric strain values measured in specimen Ve5 appear to be rather inconsistent compared to those of the other specimens, since the conditions of this experiment (confining pressure and axial strain) as well as a possible textural heterogeneity (*e.g.*, bedding) could not explain such high strain values. This is more obvious in the shear strains (see Fig. 6.24 and Table 6.3). It is likely that a slight rotation of the position of this specimen during the post-mortem x-ray scanning might have biased the strain calculations..

Table 6.2: Minimum and maximum compactant volumetric strain values measured inside the compaction bands for specimen Ve4, Ve5, Ve6, and Ve7 (median vertical projections).

Specimen	Min volumetric strains inside the band [%]	Max volumetric strains inside the band [%]
Ve4	0.26	0.87
Ve6	0.87	1.86
Ve5	0.91	1.89
Ve7	0.82	1.36

In Figure 6.23 the normalised compactant volumetric strain population is plotted as a function of the compactant volumetric strains, inside the compaction bands, for the four different specimens. Strains were grouped in increments of 0.1 % (*i.e.*, strains with values ranging from 0.20% to 0.29% were grouped together; group analysis). The strain value range

was defined by the compactant strains presented in Table 6.2, which belonged to the 25% of the highest compactant volumetric strains of each specimen.

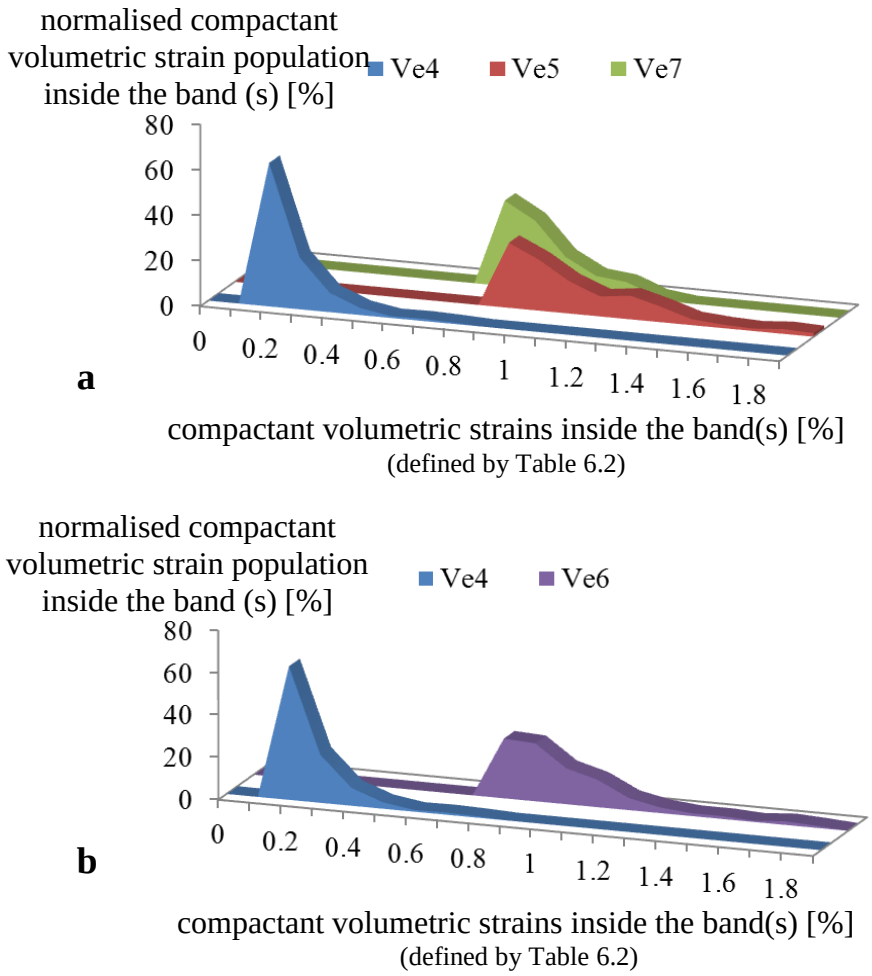

Fig. 6.23: Compactant volumetric strains inside the compaction bands of specimens Ve4 (in blue), Ve5 (in red), Ve7 (in green), and Ve6 (in purple): (a) Confining pressure comparison; (b) Axial strain comparison. The horizontal axis refers to the compactant volumetric strains grouped in increments of 0.1%, while the vertical axis shows the percentage of voxels inside the compaction bands. All strain values belong to the 25% of the highest compactant strains measured in specimens Ve4, Ve6, Ve5 and Ve7.

Figure 6.24a compares the results for different confining pressures (Ve4, Ve5, and Ve7) and Figure 6.24b compares the results for different axial strain values (Ve4, Ve6). The majority

of voxels with compactant volumetric strain values inside the range of compaction bands was characterised by the smaller compactant volumetric values. For instance, 85% of voxels in specimen Ve4 had volumetric strains from +0.2% to +0.4%, 68% of voxels in specimen Ve7 had volumetric strains from +0.8% to +1%, and 55% of voxels in specimen Ve6 had volumetric strains from +0.8% to +1% (compactant). Therefore, the highest volumetric strain values were located in less voxels. Furthermore, an increase in the confining pressure and axial strain values resulted not only in higher compactant strains inside the band(s) but also in a wider range of strains (Ve4 versus Ve7 and Ve6).

Figure 6.24 shows the median vertical projections from the shear strain field for the four different specimens (Ve4, Ve5, Ve7, and Ve6). The shear strain histogram from specimen Ve5 looks different from the three others. It is plausible that the positions of the pre-and post mortem HR x-ray scans, for this particular specimen, had not been identical (*i.e.*, slight rotation of the specimen); thus a non-realistic calculation of the Ve5 shear strains might explain the abnormally higher shear strain fields inside this specimen. Such possible mispositioning of the specimen it appears that it did not affect that much the volumetric strain fields or many of the individual vertical projections (see Fig. 6.19). Therefore, specimen Ve5 was left aside from the shear strain discussion.

The mean shear strains (median vertical projections, in Fig. 6.24) increased with increasing confining pressure and increasing axial strain values, similarly to what was observed for the compactant volumetric strains (Fig. 6.21). The mean shear strains from specimen Ve6 appear to be almost similar to those from specimen Ve7 (Fig. 6.24), while the mean global volumetric strain difference was relatively higher (Fig. 6.21). Given the fact that Ve6 was taken to a higher axial strain than Ve7, such observation likely indicates that for the case of compaction bands, one the one hand the increased axial strain resulted in higher compactant volumetric strain, and on the other hand that the increased confining pressure did not increased the mean shear strains.

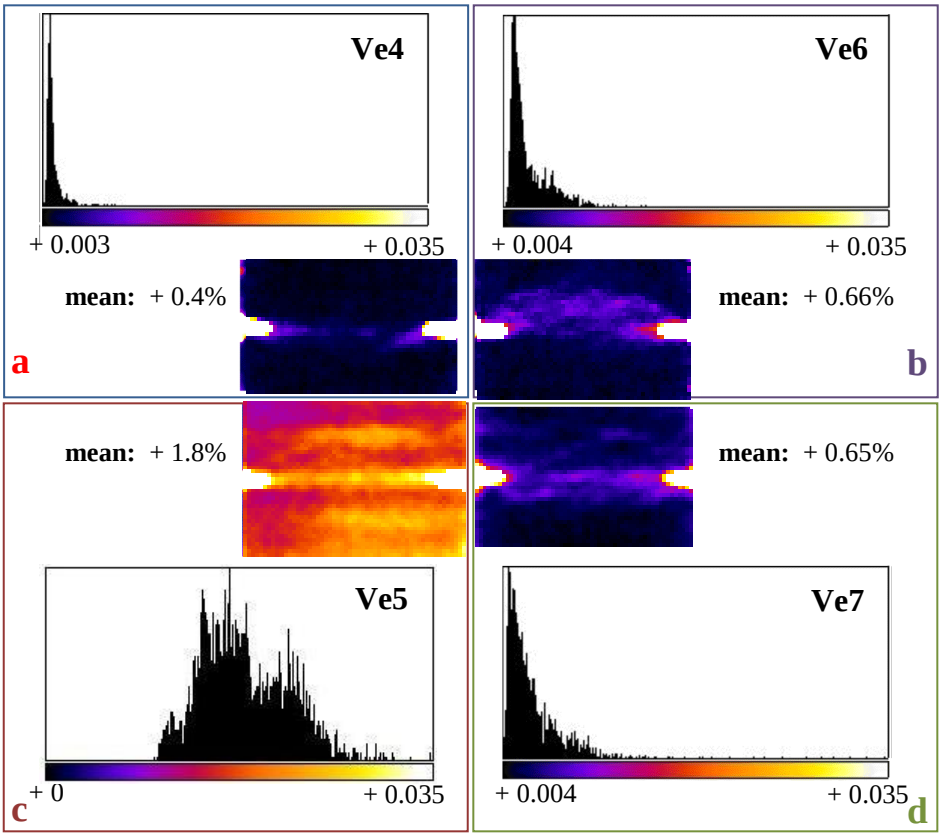

Fig. 6.24: Grey-scale values and shear strain values of the median vertical projections form specimens Ve4, Ve6, Ve5 and Ve7 together with the median vertical projections. The mean values were calculated from a thresholded range of shear strains from 0 to 0.0035. Strains calculations were made over sub-volumes of 20x20x20 voxels^3 at spacing of 20 voxels in each direction.

Table 6.3: S2 parameter calculated from the median vertical projections of the shear strain fields from specimen Ve4, Ve6, and Ve7.

Specimen	S2: values of the shear strains
Ve4	0.82
Ve6	0.91
Ve7	0.83

Table 6.3 presents the S_2 parameters, calculated from the shear strain median vertical projections, for specimens Ve4, Ve6, and Ve7. The S_2 values increased with increasing confining pressure and increasing axial strain. However, the S_2 shear strain for specimen Ve7 was similar to that for specimen Ve4. Recall that the absolute S_2 volumetric strain for specimen Ve7 was similar to that for specimen Ve6.

A comparison of the S_2 values for the absolute mean volumetric strains (Table 6.1) and the mean shear strains (Table 6.3) indicates that the volumetric strain field (median vertical projection) in specimen Ve4 was slightly more localised compared to the corresponding shear strain field, unlike what happened in specimen Ve6 (higher axial strain) and Ve7 (higher confining pressure). In particular, in specimen Ve7 the difference in the S_2 values for the shear and volumetric strains was more pronounced. From the comparison of the S_2 values, it might be suggested that during the early stages of the compaction band formation the degree of homogeneity of the volumetric and shear strain fields was similar, with the latter being a slightly more homogeneous. An increase in the axial strain level or the confining pressure value resulted in a more heterogeneous shear strain field compared to the corresponding volumetric strain field.

The minimum and the maximum shear strains inside the compaction bands, as well as the shear strains outside the bands followed the same trend as that of the mean shear strains (Table 6.4, Fig. 6.24). The highest of shear strain values, in all specimens, were measured near the notches.

Table 6.4: Minimum and maximum shear strain values measured inside the compaction bands and an average value of the strains outside the bands for specimens Ve4, Ve5, Ve6, and Ve7 (median vertical projections).

Specimen	Min shear strains inside the bands [%]	Max shear strains inside the bands	Indicative shear strains outside the bands
Ve4	0.6	0.9, 1.2 (notch)	~0.3
Ve6	0.8	1.9 (notch)	~0.5
Ve7	0.8	1.5, 2.1 (notch)	~0.4-0.6

Figure 6.25 shows the 25% of the highest shear strains measured in specimens Ve4, Ve7, and Ve6. Only specimen Ve4 followed a different shear strain trend, showing a smaller and less wide shear strain range. Specimens Ve7 and Ve6 presented similar shear strain distributions in the group of the 25% of the highest shear strains.

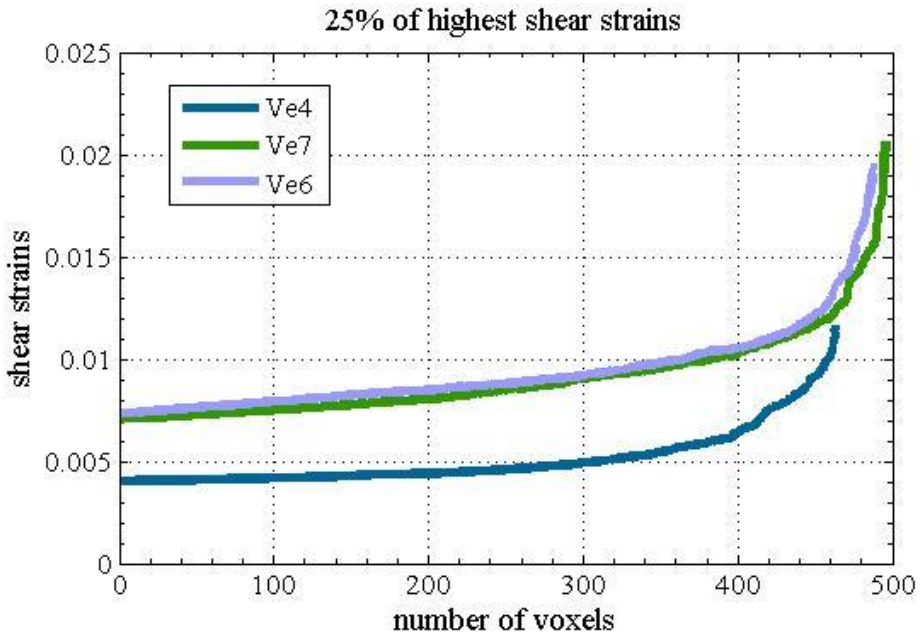

Fig. 6.25: Shear strains corresponding to the 25% of the highest shear strains measured in the median vertical projections of specimens Ve4 (in blue), Ve6 (in purple), and Ve7 (in green). Shear strain calculations were performed over sub-volumes of 20x20x20 voxels^3 at a spacing of 20 voxels in each direction.

Figure 6.26 plots the normalised shear strain population versus the shear strain range inside compaction bands for the three different specimens (Ve4, Ve7, and Ve6). Strains were grouped in strain increments of 0.1% (as in Fig. 6.23). The plotted shear strain range was defined by the strain values presented in Table 6.4, which belonged to the 25% of the highest shear strains inside each specimen.

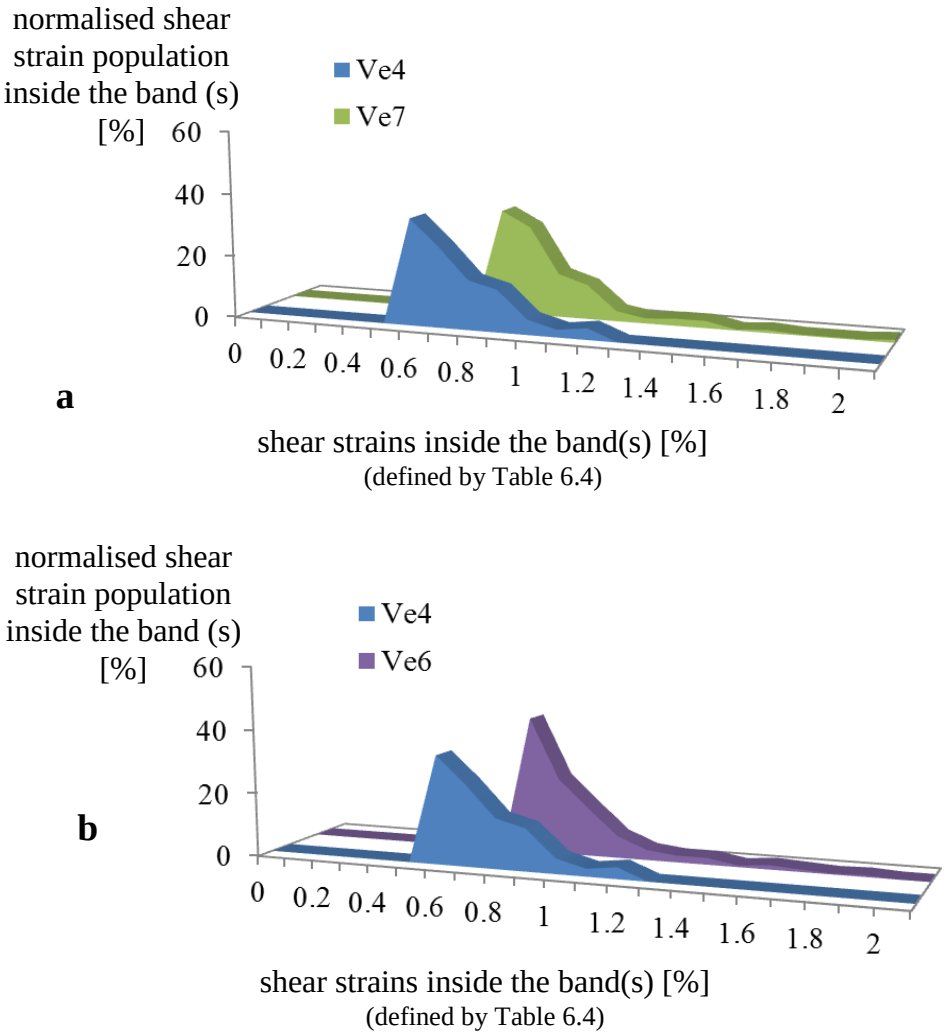

Fig. 6.26: Shear strains inside the compaction bands of specimens Ve4 (in blue), Ve7 (in green), and Ve6 (in purple): (a) Confining pressure comparison; (b) Axial strain comparison. The horizontal axis refers to the compactant volumetric strains grouped in increments of 0.1%, while the vertical axis shows the percentage of voxels inside the compaction bands. All strain values belong to the 25% of the highest shear strains measured in specimens Ve4, Ve7, and Ve6.

Figure 6.26a compares the results obtained for all different confining pressure levels. Almost the 1/3 of the voxel population, inside the compaction bands, was concentrated at the minimum shear strains for both specimens Ve4 and Ve7 (Table 6.4). However, these minimum strain values were higher for specimen Ve7 than for specimen Ve4. The maximum

shear strains, measured in specimen Ve7, were populated only by few voxels; however, the overall shear strain range was wider compared to that of specimen Ve4, suggesting that the increase in confining pressure resulted in a more distributed shear strain field inside the compaction bands.

Figure 6.26b illustrates the effect of different axial strain values. In that case, specimen Ve6, apart from presenting higher minimum shear strains inside the compaction band than the Ve4, presents also a higher percentage of voxel population concentrated on these minimum shear strains. Furthermore, the wider shear strain range resulted in a smoother distribution of the strains within this range. However, this might be also attributed to the fact that more bands were developed in this specimen compared to specimen Ve4. In addition, a comparison between specimens Ve6 and Ve7 showed that the former presented a slightly higher percentage of shear strain population concentrated on the minimum shear strain values than the latter, although the shear strain range inside the compaction bands was wider in specimen Ve7.

6.5 Influence of the notch

In this section, results from two specimens loaded at 160 MPa confining pressure, without and with a circumferential notch at their mid-height (Ve1 and Ve5, respectively), are presented (Table 4.2). Both specimens had experienced compaction bands. This section discusses the influence of a structural heterogeneity, *i.e.*, the notch, on the onset and evolution of the compaction bands. Herein, results from LR 3D-DIC from specimen Ve5 (with notch) are presented. In addition, AE results from specimen Ve1 are presented together with the 3D-DIC on LR x-ray images and the standard deviation analysis on LR and HR x-ray images. A comparison of AE maps and 3D-DIC LR images between the two specimens follows. Note that apart from the notch, these two specimens were subjected to different axial strain values (Table 4.2).

The pre- and post-mortem LR x-ray scans were carried out throughout the whole height of the specimens. Figures 6.27a and 6.27b present the volumetric and the shear strains,

respectively, for specimen Ve5, for the same vertical projection presented in Figure 6.19 (HR 3D-DIC). Calculations here were performed throughout the image volume over sub-volumes of 900x900x900 μm^3 at a spacing of 450 µm in each direction (*i.e.*, sub-volume equivalent to three undeformed grain sizes and spacing equivalent to one and a half grain sizes, respectively). Figure 6.27c is a superposition of both strain fields. Both LR and HR 3D-DIC resolved almost a similar geometry of compaction band networks (Fig. 6.27, 6.19). The maximum volumetric and shear strains measured in Figures 6.27 were +8.2% (compaction) and 3.9%, respectively (LR 3D-DIC). Recall that the maximum volumetric and shear strains measured, from the HR 3D-DIC, in Figures 6.19, were +3.5% (compaction) and 2.9%, respectively.

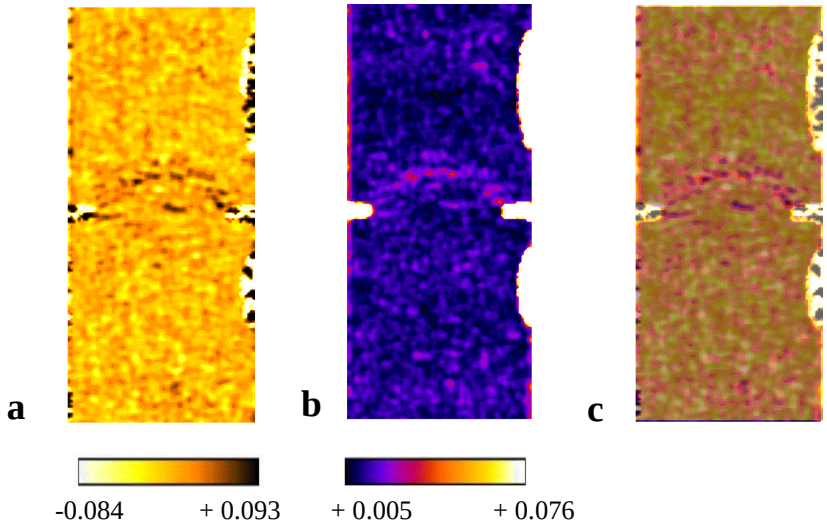

Fig. 6.27: Specimen Ve5: (a) Volumetric strain field derived from pre-and post-mortem LR x- ray images (resolution of ~ 90 µm); (b) Shear strain field derived from pre-and post-mortem LR x-ray images; (c) Superposition of the volumetric and shear strain fields. Strain calculations were made over sub-volumes of 10x10x10 $voxel^3$ at a spacing of 5 voxel in each direction.

To better understand the different strain values observed from the LR and HR DIC for specimen Ve5, Figure 6.28 compares the volumetric and shear strain fields, derived from the HR and LR x-ray images, presented in Figures 6.19 and 6.27, as well as their histograms. The strain range in the LR histogram was wider than that in the HR histogram. The higher

resolved values from the LR strain fields might be explained by the fact that although the calculations were performed over a bigger sub-volume size (in the case of LR 3D-DIC), the spacing size of the used gauge, in each direction, was smaller than that used for the HR 3D-DIC (recall that calculations of the former were made over sub-volumes of 900x900x900 μm^3 at a spacing of 450 μm in each direction, while those of the latter were made over sub-volumes of 600x600x600 μm^3 at a spacing of 600 μm). Furthermore, there are many concerns about the HR 3D-DIC strain fields for this particular specimen (see section 6.4.3).

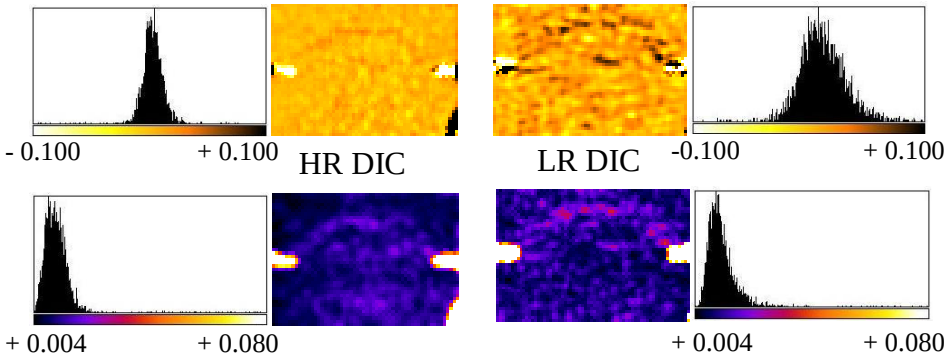

Fig. 6.28: Specimen Ve5: HR and LR volumetric and shear strain fields for the same vertical projection. Strain calculations were made over sub-volumes of 20x20x20 $voxel^3$ and 10x10x10 $voxel^3$, at a spacing of 20 and 5 voxels in each direction for the case of the pre- and post-mortem HR and LR x-ray tomography images, respectively (resolution of 30 and 90 μm).

Figures 6.29a-6.29c present three more vertical projections from specimen Ve5 (LR 3D-DIC), illustrating the volumetric and shear strain fields and their superposition, in which compaction bands were visualised in details. Dilatant volumetric strains between two compaction bands are shown in Figure 6.29a (in circle). Relatively low shear strains were measured at the same place, which possibly indicates that dilation developed close to the compaction bands accompanied by a small amount of shear, since the highest shear values were located inside the band. A quite similar situation is presented in Figure 6.29b. Compactant volumetric strains were measured in the region between two compaction bands with smaller values compared to those inside the bands (Fig. 6.29b). The shear strain field revealed also lower shear strains at this region. Dilation near the left notch of the Ve5 is

presented on Figure 6.29c. No increase in shear strains could be seen in this region. In such case, it is likely that dilation represented an open-crack initiating from the notch.

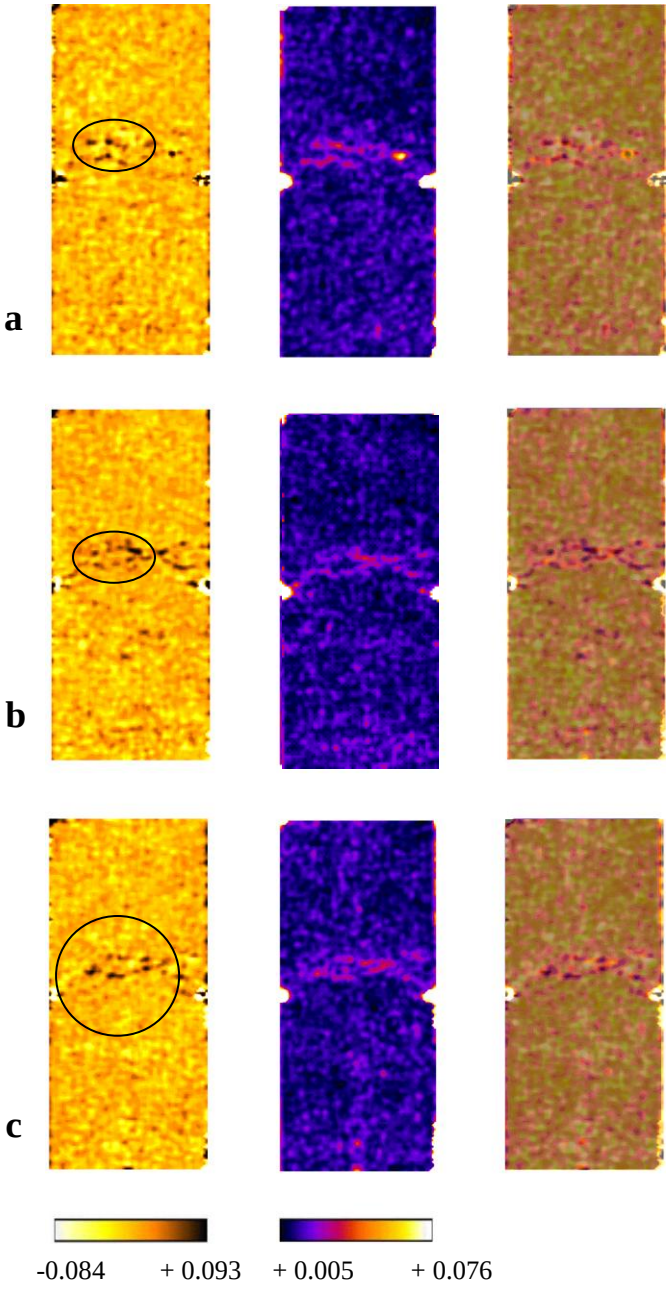

Fig. 6.29: Specimen Ve5: (a) Volumetric strain field derived from pre-and post-mortem LR x-ray images (~ 90 μm); (b) Shear strain field derived from pre-and post-mortem LR x-ray images; (c) Superposition of the volumetric on the shear strain field. Strain calculations were made over sub-volumes of 10x10x10 voxels^3 at a spacing of 5 voxels in each direction.

The AE analysis from specimen Ve5 was presented in section 6.4. Figure 6.30a presents the time history (in seconds) of the stress deviator and the cumulative AE number for specimen Ve1; the three 2D vertical projections of 3D distributions of AE event locations (one perpendicular and two parallel to the specimen axis) are shown in Figures 6.30b, 6.30c, 6.30d. Colours change to highlight most recent events. Only AE event amplitudes higher than 2 Volts were used for the cumulative number of AE events in Figure 6.30a and amplitudes higher than 1 Volt were used for the 2D projections in Figures 6.30b-6.30d. The perpendicular 2D projection of the 3D distribution of AE locations overprints AE events from the mid-height of the specimen (*i.e.*, from 20 mm to 60 mm from the bottom edge of specimen Ve1). The z-x and z-y perpendicular projection overprint AE events recorded in a central section of the specimen (i.e., +/- 2 mm of the central plane that is parallel and normal to the cutoff plane).

Specimen Ve1 had no notches. An intensive AE activity was recorded near the top edge of the specimen; AE events were also located near the mid-height of the top section of specimen Ve1 in horizontal bands. Once the bands propagated thought the width of the specimen, new bands developed. The number of the bands increased with increasing axial strain. Before the unloading, another band was developed at the bottom and near the mid-height of the specimen. These bands were inferred to be compaction bands. Note that these bands initiated near the boundaries of the specimen (top edge boundary and vertical boundaries). A spatial change of these bands was observed (Fig. 6.30c, 6.30d). Furthermore, these localised features developed mainly at the top edge and the middle section of the specimen; no AE activity was recorded elsewhere. Most likely, this is associated with local heterogeneities (*e.g.*, higher density bedding planes in these regions). Recall that the cumulative number of AE events in specimen Ve5 was higher at the early stages of the experiment, since the notches encouraged localisation to occur earlier (Fig. 6.15), while in specimen Ve1, the cumulative number of AE events was raised later. However, before the unloading, there was around 27500 events, which was much higher compared to that in specimen Ve5 (~ 16500 events), which seems to confirm that more damage occurred in specimen Ve1 (multiple bands) due to the higher axial strain.

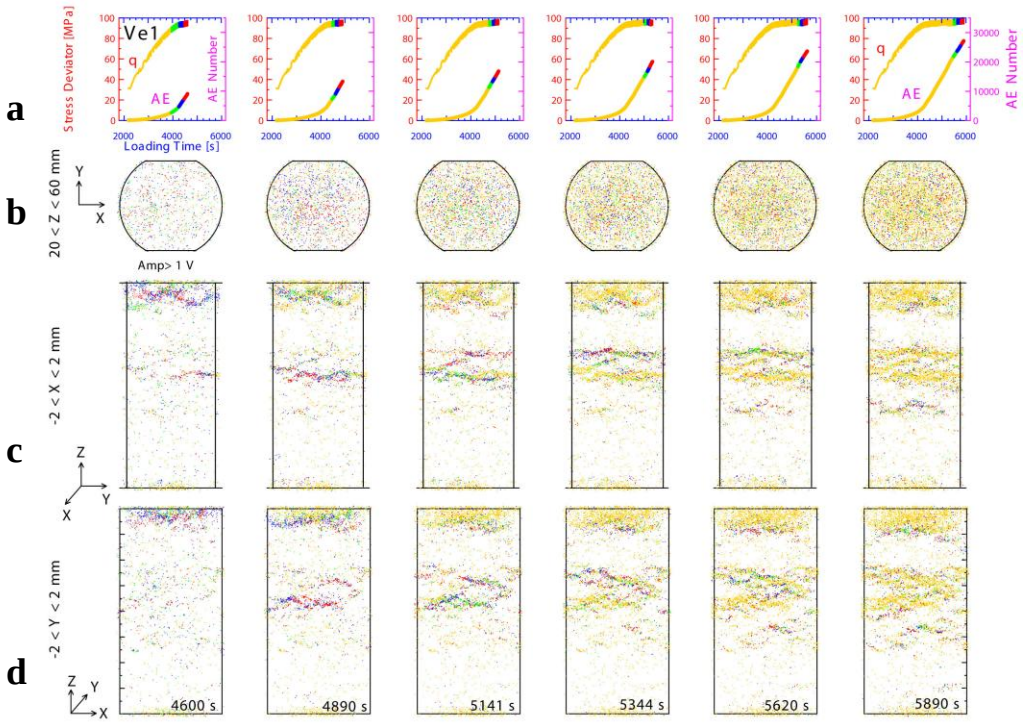

Fig. 6.30: AE results from Ve1: (a) Axial load as a function of the number of AE events in different time intervals; colours change to highlight most recent events; (b)-(d) Maps of AE event locations for the same time intervals viewed perpendicular to the specimen's height, parallel to the specimen's height in a projection perpendicular to the flattened surfaces projections and parallel to the specimen's height in a projection parallel to the flattened surfaces projections.

Pre- and post-mortem LR x-ray scans were carried out through the whole height of specimen Ve1, while post-mortem HR x-ray scans were focusing only at the part where the compaction bands developed. Figures 6.31a-6.31h illustrate two different vertical projections of the standard deviation values from post-mortem LR x-ray images (resolution of~ 90 μm) together with projections of the volumetric and shear strain fields, from pre- and post-mortem LR x-ray images. Calculations were made through the image volume, over sub-volumes of 900x900x900 μm^3 at a spacing of 450 μm in each direction (*i.e.*, sub-volumes equal to three undeformed grains at a spacing of one and a half grain-size).

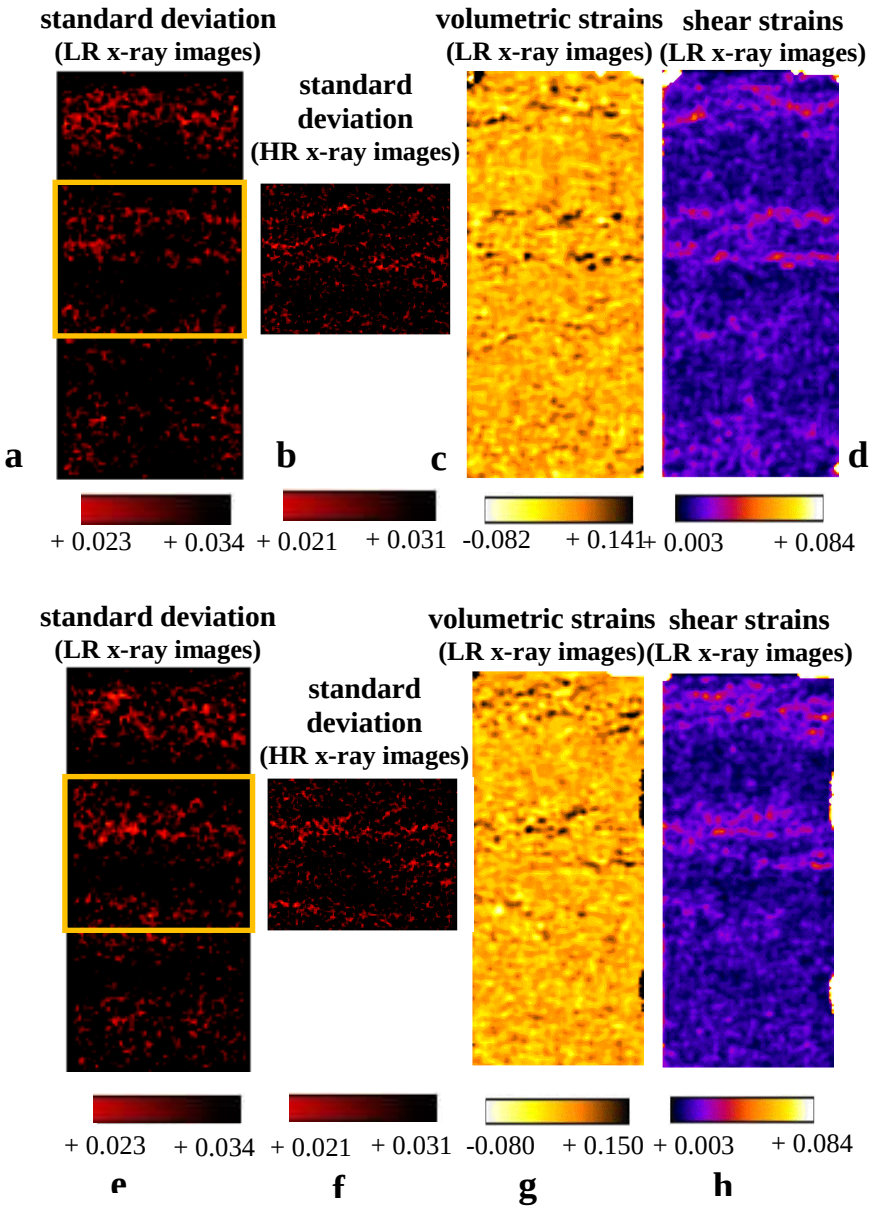

Fig. 6.31: Vertical projections of two different regions from specimen Ve1: (a), (e) Standard deviation of the grey-scale values from LR x-ray images (resolution of ~ 90 μm). Calculations were made over sub-volumes of 10x10x10 voxel^3 at a spacing of 5 voxel in each direction. Standard deviation values higher to 0.034 are depicted in black; (b), (f) Standard deviation of the grey-scale values from HR x-ray images (resolution of ~ 30 μm) focusing on the localised deformation region. Calculations were made over sub-volumes of 20x20x20 voxel^3 at a spacing of 5 voxels in each direction. Standard deviation values higher to 0.031 are depicted in black; (c), (g) Volumetric strain maps (LR x-ray images). Calculations were made over sub-volumes of 10x10x10 voxel^3 at a spacing of 5 voxels in each direction; (d), (h) Shear strain maps (LR x-ray images). Calculations were made over sub-volumes of 10x10x10 voxel^3 at a spacing of 5 voxels in each direction.

All images are compared to the standard deviation fields of the grey-scale values from the HR x-ray images (resolution of ~30 μm), which focused on the region of interest. For the HR x-ray images, calculations were carried out through the image volume, over sub-volumes of 600x600x600 μm^3, at a spacing of 150 μm in each direction (*i.e.*, sub-volumes equal to two undeformed grains at a spacing of half grain-size).

A network of compaction bands was developed near the top edge at the mid-height of specimen Ve1. Most of these bands were almost normal to the major imposed principal stress direction (*i.e.*, they were horizontal) , although locally, they had an inclination angle ranging from 60° to 75° (dip of 30° to 15°). Both volumetric (compactant) and shear strain was measured inside these bands of localised deformation. Outside the bands, the volumetric and shear strain values were decreased.

The standard deviation of the grey-scale values from the LR x-ray images revealed similar structures to those depicted by the volumetric and shear strain fields (Fig. 6.31). The lower standard deviation values, shown in red in Figures 6.31a, 6.31e, turn the image 'more homogeneous'. This is associated with grain breakage into smaller pieces such that the grain size becomes smaller than the size of the tomography image. The different grains and the porosity attenuations are averaged together over a voxel to give an average grey-scale, which can be similar over a region (as indicated by the standard deviation measure).

Compaction bands were depicted by the LR standard deviation analysis as wider structures compared to the LR volumetric and shear strain field representations (Figs. 6.31a, 6.31c-6.31e, and 6.31g-6.31h). Note that calculations were made over the same sub-volume gauge and spacing size, which indicates that the LR 3D-DIC is a more powerful tool in resolving the deformation features at this stress deviator and axial strain level compared to the standard deviation analysis of LR x-ray images if one assumes that the widths resolved by the latter method are somehow exaggerated. However, one should also keep in mind that both the LR DIC and standard deviation analysis are sensitive to different parameters (compaction, dilation and shear, and homogeneity of a region).

A comparison between the standard deviation values from HR and LR x-ray images showed that the former allow to resolve compaction bands as finer structures compared to the latter (Fig. 6.31b, 6.31f, 6.31a, 6.31e). In fact, the width of compaction bands in Figures

6.31b, 6.31f was approaching more that visualised by the LR 3D-DIC. Standard deviation values higher than 0.034 and 0.031, for the LR and HR x-ray analysis, respectively, are shown in black.

Figures 6.32, referring to the images presented in Figures 6.31, show the standard deviation of the grey-scale values from the HR x-ray images superimposed on the LR volumetric strain field (Fig. 6.32a, 6.32d) and LR shear strain field (presented in inverted colours, Fig. 6.32b, 6.32e). This superposition shows compaction bands as homogeneous zones, with low standard deviation values, in which both compactant and shear strains were identified.

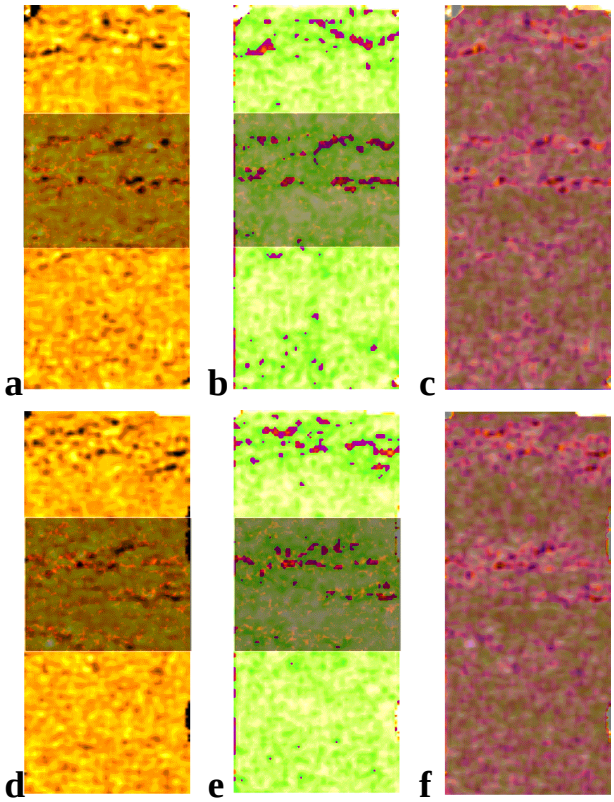

Fig. 6.32: Two different vertical projections from specimen Ve1, already shown in Figure 6.31: (a), (d) Superposition of HR x-ray images (standard deviation) on LR volumetric strain fields; (b), (e) Superposition of HR x-ray images (standard deviation) on LR shear strain fields; (c), (e) Superposition of LR shear strain fields on LR volumetric strain fields. Calculations of the LR DIC fields were made over sub-volumes of 10x10x10 voxel^3 at a spacing of 5 voxel in each direction, while those of the standard deviation of the HR x-ray images were made over sub-volumes of 20x20x20 µm^3 at a spacing of 5 µm in each direction.

In some regions near the compaction band, which appeared homogeneous (lower standard deviation values), no volumetric or shear strain was measured. Possibly the different resolutions (HR x-ray images superimposed on LR strain fields) and the different sub-volume and spacing sizes, used for the calculations, are responsible of such result. Therefore, it is likely that these particular regions refer to places where re-arrangement and damage of grains smaller than three undamaged grain-sizes took place. Recall that LR 3D-DIC calculations were made over sub-volumes equivalent to three undamaged grain sizes at a spacing equivalent to one and a half grains, while HR standard deviation was calculated over sub-volumes equivalent to two undamaged grain size at a spacing of a half grain in each direction.

Figures 6.32c and 6.32f show the LR shear strain field superimposed on the LR volumetric strain field. Dark colours, inside compaction bands, correspond to compactant volumetric strains, while lighter colours (pink) correspond to shear strains. Note that inside the compaction bands, regions where compaction and shear coincide were identified.

Figures 6.33a, 6.33b present the volumetric and shear strains from specimen Ve5 at same positions as those shown in Figures 6.31 for specimen Ve1. Figure 6.33c shows the shear strains superimposed on the volumetric strains for the same vertical projections.

Compaction bands were developed only in the middle section of specimen Ve5 (see section 6.4.3). In Figure 6.33, volumetric strains inside compaction bands reach up to +13.8% (compaction) and shear strains reach up to 4.8 %. However, lower values of both strains were identified in other vertical projections (see Fig. 6.27). Therefore, from the local maximum values of the strain fields, it is not straightforward to comment on neither the strain field inside a specimen nor the impact of the increased axial strain of specimen Ve1 nor the role of the notch in specimen Ve5.

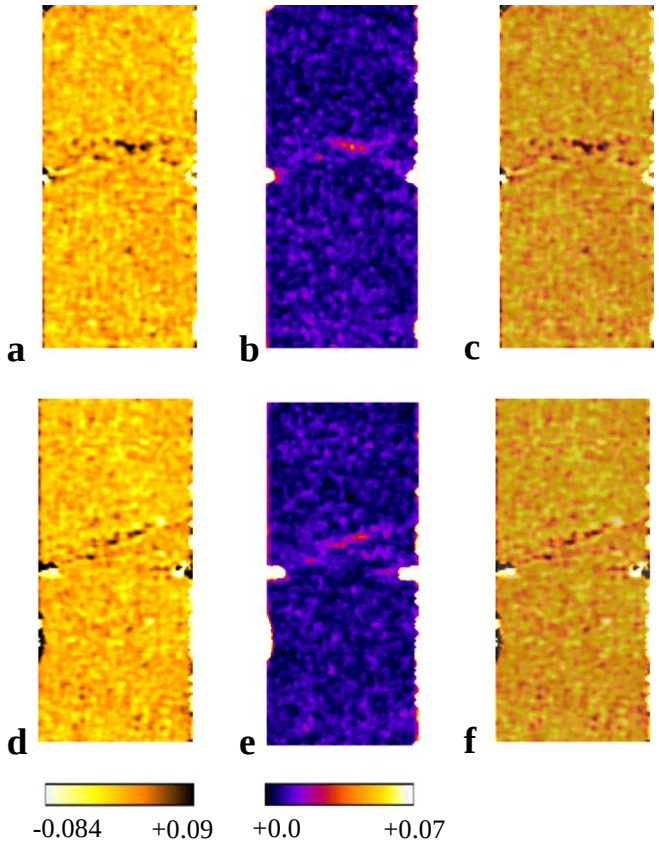

Fig. 6.33: Vertical projections of two different regions from specimen Ve5 at same places as those presented for specimen Ve1, in Figure 6.27: (a), (d) Volumetric strain fields (LR x-ray images, 90 μm voxel-size). Calculations were made over sub-volumes of 10x10x10 voxels^3 at a spacing of 5 voxels in each direction; (b), (e) Shear strain fields (LR x-ray images). Calculation were made similarly to the volumetric strain fields; (c), (f) Shear strain fields superimposed on volumetric strain fields.

Coming back to the comparison between specimens Ve5 and Ve1, Figure 6.34 shows the histogram of the median vertical projections from the strain fields of both specimens. The volumetric and shear strain range inside these projections was wider for specimen Ve1 than specimen Ve5 (Fig. 6.34). This might indicate that the increased axial strain resulted in higher strains inside Ve1, which in turn resulted in a wider strain range. However, since the strain values inside specimen Ve5 do not differ much from those in specimen Ve1, even if the latter had experienced a higher axial strain, it might also be argued that the notch, itself, should have increased the strains values in specimen Ve5.

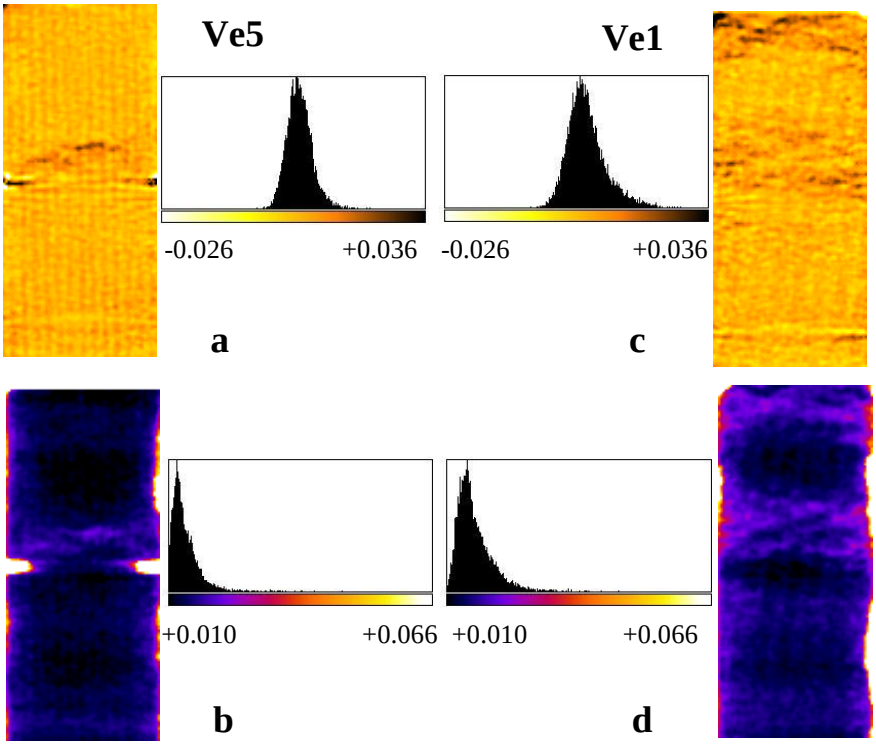

Fig. 6.34: Vertical median projections from specimens Ve5 and Ve1: (a) Volumetric strain field from specimen Ve5 together with the histogram of the strain values (median projection); (b) Shear strain field from specimen Ve5 together with the histogram of the strain values (median projection); (c) Volumetric strain field from specimen Ve1 together with the histogram of the strain values (median projection); (d) Shear strain field from specimen Ve1 together with the histogram of the strain values (median projection). LR x-ray images were used for the strain analysis (90 µm resolution). Calculations were made over sub-volumes of 10x10x10 voxels^3 at a spacing of 5 voxels in each direction.

6.6 X-ray tomography analysis and 3D-DIC: role of the parameters used for the analysis

Compaction bands in Vosges sandstone could not be detected solely by the raw HR x-ray tomography images (see previous sections). This is the reason why the standard deviation of the grey-scale values from the HR x-ray images was also calculated and used in this work.

Two parameters were important for this analysis: the sub-volume gauge in which the calculations were performed and the spacing size of this gauge in each direction. These parameters were important also for the calculation of the strain fields (3D-DIC, see section 3.5.3). Combinations of different spacing and sub-volume sizes were investigated. The optimal combination was defined as the one that allowed to best visualising compaction bands. In this section results from different combinations of these parameters are shown for both standard deviation values of HR x-ray images and volumetric and shear strain fields (for a single vertical projection from specimen Ve7).

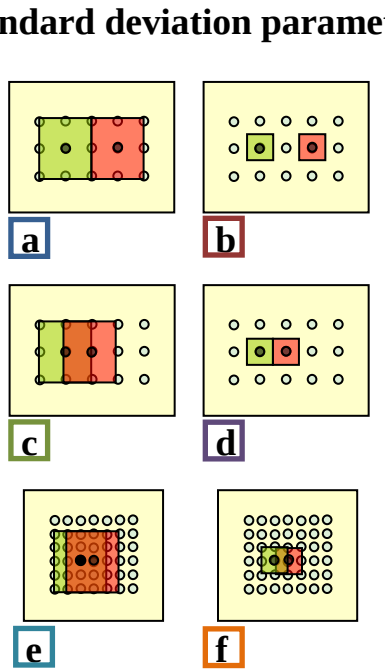

Fig. 6.35: 2D schematic representation of the combinations of sub-volumes and spacing sizes used for the calculation of the standard deviation of the grey-scale values from the HR x-ray images. The standard deviation calculations were made: (a)-(b) Over sub-volumes of 20x20x20 voxels^3 and 10x10x10 voxels^3, respectively at a spacing of 20 voxels in each direction (*i.e.*, sub-volumes equivalent to 2x2x2 and 1x1x1 intact grain-sizes, respectively at a spacing equivalent to 2 grain-sizes); (c)-(d) Over sub-volumes of 20x20x20 voxels^3 and 10x10x10 voxels^3, respectively at a spacing of 10 voxels in each direction (*i.e.*, sub-volumes equivalent to 2x2x2 and 1x1x1 intact grain-sizes, respectively at a spacing equivalent to 1 grain-size); (f) Over sub-volumes of 20x20x20 voxels^3 and 10x10x10 voxels^3, respectively at a spacing of 5 voxels in each direction (*i.e.*, sub-volumes equivalent to 2x2x2 and 1x1x1 intact grain-sizes, respectively at a spacing equivalent to 0.5 grain-sizes). The resolution of the x-ray images is of ~30 μm.

Six different combinations were used; a 2D schematic view is presented in Figures 6.35, 6.36. For the standard deviation of the grey-scale values from the HR x-ray images, calculations were made over sub-volumes of 600x600x600 μm^3 at a spacing of 600 µm (Fig. 6.35a), 300 µm (Fig. 6.35c), and 150 µm in each direction (Fig. 6.35e), and over sub-volumes of 300x300x300 μm^3 at a spacing of 600 µm (Fig. 6.35b), 300 µm (Fig. 6.35d), and 150 µm in each direction (Fig. 6.35f).

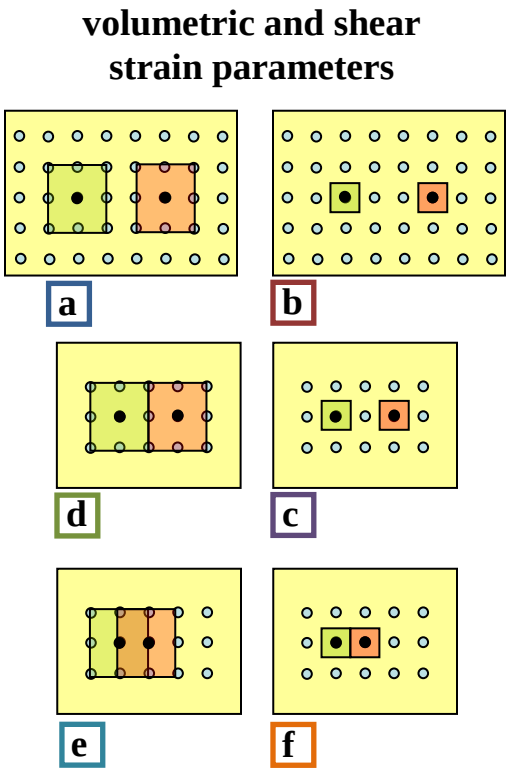

Fig. 6.36: 2D schematic representation the combinations of the sub-volumes and spacing sizes used for the calculation of the volumetric and shear strain fields. Strain calculations were made: (a)-(b) Over sub-volumes of 20x20x20 voxels^3 and 10x10x10 voxels^3, respectively at a spacing of 30 voxels in each direction (*i.e.*, sub-volumes equivalent to 2x2x2 and 1x1x1 intact grain-sizes, respectively at a spacing equivalent to 3 grain-sizes); (c)-(d) Over sub-volumes of 20x20x20 voxels^3 and 10x10x10 voxels^3, respectively at a spacing of 20 voxels in each direction (*i.e.*, sub-volumes equivalent to 2x2x2 and 1x1x1 intact grain-sizes, respectively at a spacing equivalent to 2 grain-sizes); (f) Over sub-volumes of 20x20x20 voxels^3 and 10x10x10 voxels^3, respectively at a spacing of 10 voxels in each direction (*i.e.*, sub-volumes equivalent to 2x2x2 and 1x1x1 intact grain-sizes, respectively at a spacing equivalent to 1 grain-size).

For the strain fields, calculations were made over sub-volumes of 600x600x600 μm^3 at a spacing of 900 µm (Fig. 6.36a), 600 µm (Fig. 6.36c), and 300 µm in each direction (Fig. 6.36e), and over sub-volumes of 300x300x300 μm^3 at a spacing of 900 µm (Fig. 6.36b), 600 µm (Fig. 6.36d), and 300 µm in each direction (Fig. 6.36f). Recall that the HR x-ray images used in this work had a resolution of 30 µm.

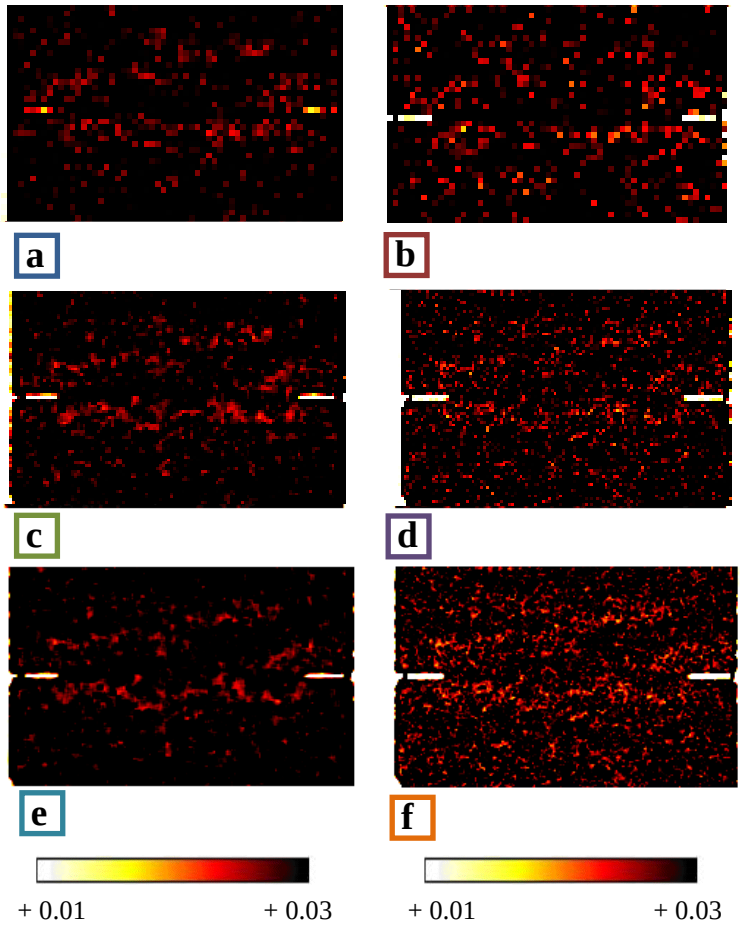

Fig. 6.37: Standard deviation fields from the same vertical projections of HR x-ray tomography images for specimen Ve7 (30 µm resolution). Calculations were performed at a spacing of 20 voxels in each direction and over sub-volumes of 20x20x20 $voxels^3$ (a), and over sub-volumes of 10x10x10 $voxels^3$ (b); At a spacing of 10 µm in each direction and over sub-volumes of 20x20x20 $voxels^3$ (c), and over sub-volumes of 10x10x10 $voxels^3$ (d); At a spacing of 5 µm in each direction and over sub-volumes of 20x20x20 $voxels^3$ €, and over sub-volumes of 10x10x10 $voxels^3$ (f). The threshold values range from 0.01 to 0.03. Higher values than 0.03 are visualised in black colours.

Figure 6.37 shows the standard deviation fields from a vertical projection of specimen Ve7, for different spacing size and sub-volume combinations, presented in Figure 6.35. Standard deviation fields, in Figures 6.37a, 6.37c, 6.37e, were calculated over sub-volumes of 600x600x600 μm^3 and spacing of 600 μm, 300 μm, and 150 μm in each direction, respectively, while those in Figures 6.37b, 6.37d, 5.37f were calculated over sub-volumes of 300x300x300 μm^3 and spacing of 600 μm, 300 μm, and 150 μm in each direction, respectively. The same standard deviation threshold was used in all images, from 0.01 to 0.03 (in red). Standard deviation values higher than 0.03 are shown in black. Using the latter threshold allowed to best visualised the compaction bands in specimens of Vosges sandstone.

Inside the compaction bands, lower values of standard deviation were measured. To get a better feeling of the standard deviation calculations, Figures 6.38a, 6.38b illustrate two BSE images coming from a region of a compaction band and from a region far from it, respectively. The red rectangle, in Figures 6.38 has a size of 600x600 μm^2, while the yellow one corresponds to 300x300 μm^2; size of the sub-volume over which the standard deviation calculations were performed can be directly compared in these images to the grain-size.

Standard deviation values, calculated in regions similar to the one shown in Figure 6.38b (*i.e.*, inside the compaction bands), are expected to be smaller compared to those calculated in regions similar to the one shown in Figure 6.38a. Inside compaction bands, pore space is reduced, grains are more compacted, and although grains contain many micro-cracks, the grey-scale values in such regions do not exhibit big variations (Fig. 6.38b). On the other hand, the pore space may introduce a higher heterogeneity in the grey-scale values and result in higher standard deviation value inside compaction band (Fig. 6.38b). However, note that a low standard deviation might be also attributed to a homogeneously dilated region (section 6.9).

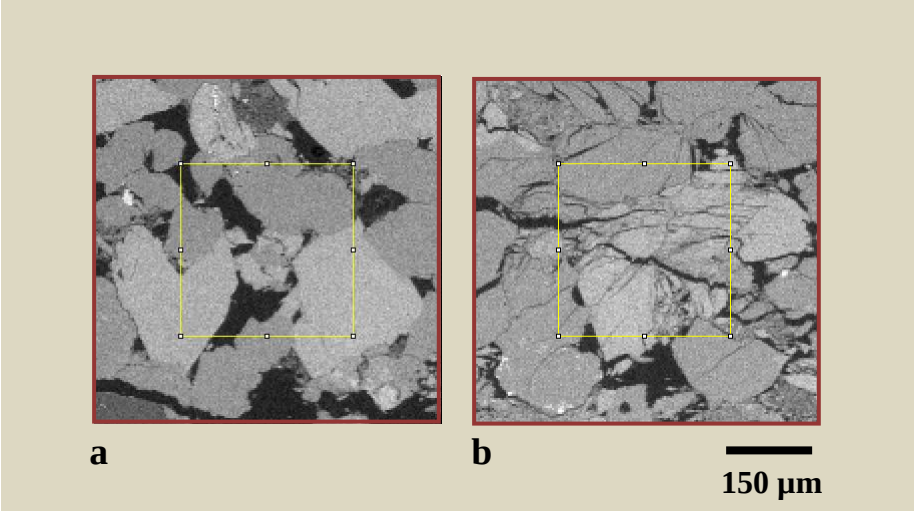

Fig. 6.38: Examples of BSE images coming from regions far from the compaction band (a) and inside the compaction band (b). Red rectangles represent a pixel of 600x600 µm^2 and yellow rectangles represent a pixel of 300x300 µm^2. The axis normal to the surface of these images gives the third dimensions of the voxel.

Figure 6.39 presents the thresholded standard deviation of the grey-scale values (*i.e.*, from 0.01 to 0.03) for the different spacing and sub-volume sizes, shown in Figure 6.37. Standard deviation values were divided in ten groups of an increment of 0.1% (inside the threshold range). The normalised voxel population corresponding to each of these standard deviation values was calculated. Figure 6.40 indicates that in all cases, the lower standard deviation values were obtained over smaller sub-volume sizes. However, it should be mentioned that the lower sub-volume size resulted in adding noise on the standard deviation fields (see Fig. 6.37). The decrease in the spacing size, on the other hand, resulted in a smoother transition from the lower to the higher standard deviation values, and thus in more clear images, for both the cases of 600x600x600 µm^3 and 300x300x300 µm^3 gauge (see also Fig. 6.37).

A similar analysis was performed on the strain calculations. Figure 6.40 shows the volumetric strain fields, for a single vertical section, determined using the six different spacing and sub-volume combinations presented in Figure 6.36. The histograms of the volumetric strain fields together with the mean volumetric strains are also shown. Similarly to section 6.4, four different mean values were calculated: the mean and the mean absolute

value of the whole volume (mean (g) and mean (abs), respectively), and the mean value of the compactant (mean (+)) and dilatant (mean (-)) volumetric strains.

Fig. 6.39: Comparison of the standard deviation fields calculated over sub-volumes of 20x20x20 voxel^3 and 10x10x10 voxel^3 and at a spacing of 20 voxel (a), of 10 voxel (b), and 5 voxel (c). The threshold level ranges from 0.01 to 0.03. The resolution was 30 µm. The horizontal axis refers to the standard deviation values within the threshold range, and the vertical axis shows the percentage of voxels inside each standard deviation increment.

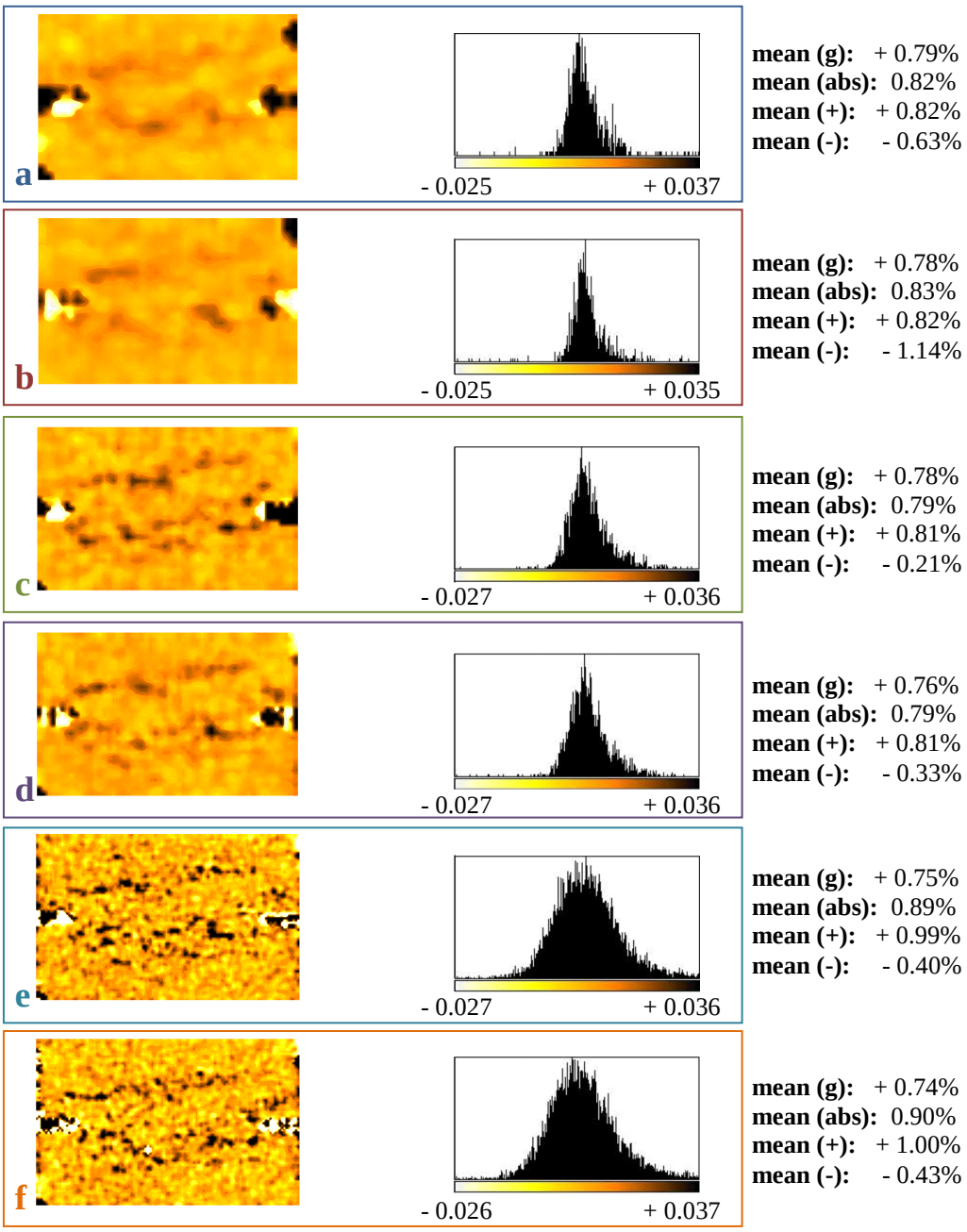

Fig. 6.40: Vertical projections and histograms of volumetric strain field calculations for a vertical projection from specimen Ve7. Calculations were performed over: (a)-(b) Over sub-volumes of 20x20x20 voxels^3 and 10x10x10 voxels^3, respectively at a spacing of 30 voxels in each direction; (c)-(d) Over sub-volumes of 20x20x20 voxels^3 and 10x10x10 voxels^3, respectively at a spacing of 20 voxels in each direction; €-(f) Over sub-volumes of 20x20x20 voxels^3 and 10x10x10 voxels^3, respectively at a spacing of 10 voxels in each direction. The resolution of the pre- and post-mortem HR x-ray images is of ~30 μm.

Note that the different spacing and sub-volume combinations result in a different strain ranges. In order to have a common strain-scale range in all images, for comparison reasons, the strain threshold was defined according to the combination which gave the maximum and minimum strain values. Figure 6.40 shows that the mean volumetric strain values decrease slightly with decreasing sub-volume and spacing size. However, the absolute, the compactant and the dilatant mean volumetric strains follow different trends with the different spacing and sub-volume combinations. Note, though, that these values do not change very much with the different combinations of parameters.

Table 6.5: S2 parameter of the volumetric strain fields calculated for the different spacing and sub-volume combinations (for the same vertical projection).

Different spacing and sub-volume size combinations	**S2: all volumetric strains**	**S2: absolute volumetric strains**	**S2: compactant volumetric strains**	**S2: dilatant volumetric strains**
900 μm spacing, 600x600x600 μm^3 sub-volume	0.68	0.72	0.73	0.43
900 μm spacing, 300x300x300 μm^3 sub-volume	0.70	0.787	0.78	0.69
600 μm spacing, 600x600x600 μm^3 sub-volume	0.67	0.69	0.71	0.40
600 μm spacing, 300x300x300 μm^3 sub-volume	0.65	0.69	0.71	0.312
300 μm spacing, 600x600x600 μm^3 sub-volume	0.44	0.62	0.67	0.53
300 μm spacing, 300x300x300 μm^3 sub-volume	0.4112	0.6120	0.6566	0.5261

The ***S2*** parameter for the same volumetric strain fields is presented in Table 6.5. In general, the volumetric strain field becomes more heterogeneous, in terms of the ***S2***, as the spacing

size reduces, for a constant sub-volume size (apart from the case of the dilatants volumetric strains). A reduction in the sub-volume size results in some cases in a more homogenous and in other cases in a more heterogeneous volumetric strain field.

Table 6.6 presents the maximum compactant strains inside the compaction bands of the vertical projections shown in Figure 6.41, for each of the combinations shown in Figure 6.36. A smaller sub-volume size results in slightly smaller maximum compactant volumetric strains. On the other hand, for this particular vertical projection, a smaller spacing size results in higher volumetric strain values.

Table 6.6: Maximum compactant volumetric strain values measured inside the compaction bands for the different spacing and sub-volume combinations (see Fig. 6.36).

Different spacing and sub-volume size combinations	**Max compactant volumetric strains inside the band [%]**
900 μm spacing, 600x600x600 μm^3 sub-volume	2.32
900 μm spacing, 300x300x300 μm^3 sub-volume	2.31
600 μm spacing, 600x600x600 μm^3 sub-volume	3.82
600 μm spacing, 300x300x300 μm^3 sub-volume	3.72
300 μm spacing, 600x600x600 μm^3 sub-volume	10.57
300 μm spacing, 300x300x300 μm^3 sub-volume	8.04

Figure 6.41 shows that the mean shear strain values increase with decreasing sub-volume and spacing sizes (unlike the absolute mean volumetric strain values shown in Fig. 6.40).

The values of the ***S2*** parameter for the shear strain fields, shown in Figure 6.41, are listed in Table 6.7. Note that the shear strain field becomes more homogeneous, in terms of the ***S2***, as the spacing size reduces for a given sub-volume size. Furthermore, the fraction of localised deformation represented in the shear strain field becomes smaller, and thus, the shear strain field appears to be more heterogeneous, as the sub-volume size decreases, for a given spacing size-apart from that of 900 μm.

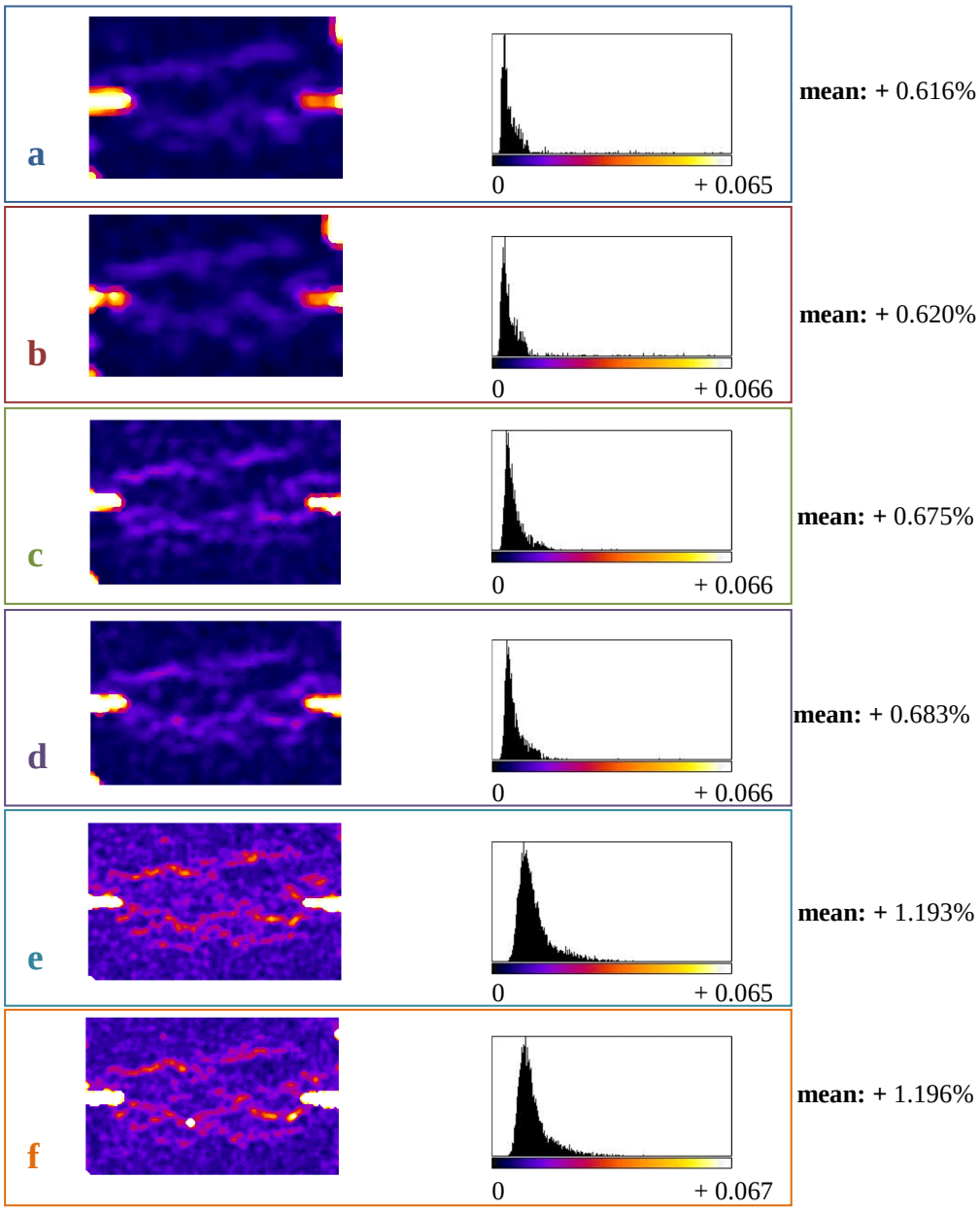

Fig. 6.41: Vertical projections and histograms of shear strain field calculations for a vertical projection from specimen Ve7. Calculations were performed over: (a)-(b) Over sub-volumes of 20x20x20 voxels^3 and 10x10x10 voxels^3, respectively at a spacing of 30 voxels in each direction; (c)-(d) Over sub-volumes of 20x20x20 voxels^3 and 10x10x10 voxels^3, respectively at a spacing of 20 voxels in each direction; €-(f) Over sub-volumes of 20x20x20 voxels^3 and 10x10x10 voxels^3, respectively at a spacing of 10 voxels in each direction. The resolution of the pre- and post-mortem HR x-ray images is of ~30 µm.

Table 6.7: S2 parameter of the shear strain fields calculated for the different spacing and sub-volume combinations (for the same vertical projection).

Different spacing and sub-volume size combinations	S2: values of the shear strains
900 μm spacing, 600x600x600 μm^3 sub-volume	0.4181
900 μm spacing, 300x300x300 μm^3 sub-volume	0.4215
600 μm spacing, 600x600x600 μm^3 sub-volume	0.6359
600 μm spacing, 300x300x300 μm^3 sub-volume	0.5873
300 μm spacing, 600x600x600 μm^3 sub-volume	0.7993
300 μm spacing, 300x300x300 μm^3 sub-volume	0.7905

The maximum shear strain values, measured inside compaction bands of the vertical projections shown in Figure 6.42, for each of the combinations in Figure 6.36 are shown in Table 6.8. These maximum measured shear strains increase with decreasing spacing size. They also appear to increase with decreasing sub-volume size (unlike the maximum compactant strains - Table 6.6), with the exception of those measured for a spacing size equal to 900 μm.

Table 6.8: Minimum shear strain values measured inside the compaction bands for the different spacing and sub-volume combinations.

Different spacing and sub-volume size combination	**Max shear strains inside the band [%]**
900 μm spacing, 600x600x600 μm^3 sub-volume	1.50
900 μm spacing, 300x300x300 μm^3 sub-volume	1.18
600 μm spacing, 600x600x600 μm^3 sub-volume	1.98
600 μm spacing, 300x300x300 μm^3 sub-volume	2.07
300 μm spacing, 600x600x600 μm^3 sub-volume	5.12
300 μm spacing, 300x300x300 μm^3 sub-volume	7.50

It should be underlined that when the mean strain and the ***S2*** values are calculated for the median vertical projections of the strain fields in specimens Ve4, Ve6, and Ve7 (see section 6.4) they can possibly provide a further understanding on the strain field values. However, it is suggested that these calculations on a single vertical projection do not contribute much to such an understanding.

6.7 Porosity calculations

This section discusses issues on porosity calculations (for a volume) performed on one small core taken from the deformed specimen Ve4, which had been previously impregnated in blue epoxy. The small deformed core of a diameter of 10 mm was x-ray scanned. Porosity

calculations were performed on a part of the core, close to the region of the circumferential notch. Figure 6.42 illustrates the place from which this small specimen had been cored, before the very HR x-ray scan (~ 6 μm voxel-size).

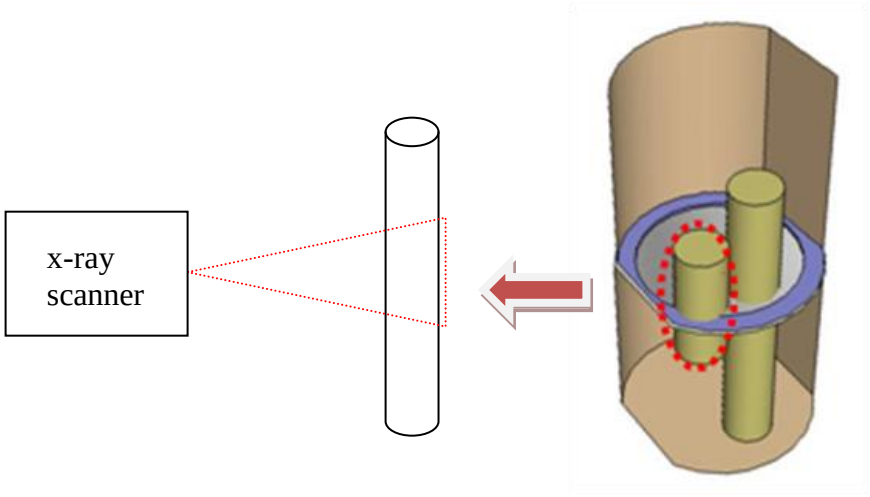

Fig. 6.42: The position from which the small specimen of 10 mm diameter had been cored. The deformed core was subsequently x-ray scanned. Porosity calculations were performed in a sub-region of the scanned specimen, close to the circumferential notch.

Figure 6.43 presents a very HR (6.76 μm resolution) slice normal to the major imposed principal stress direction and in the region of the circumferential notch (in black). The core material was highly deformed, since it comes from the region in which the compaction band developed. Several regions with a different degree of deformation could be observed in this particular slice. Porosity values seem to be reduced in certain regions, some grains having locally smaller grain-size (*i.e.*, 150-210 μm), while other grains appear to show inter- or intra-granular cracks. However, there are also certain regions which appear to have experienced less brittle deformation and in which the porosity seems to have relatively higher values when compred to the more compacted regions.

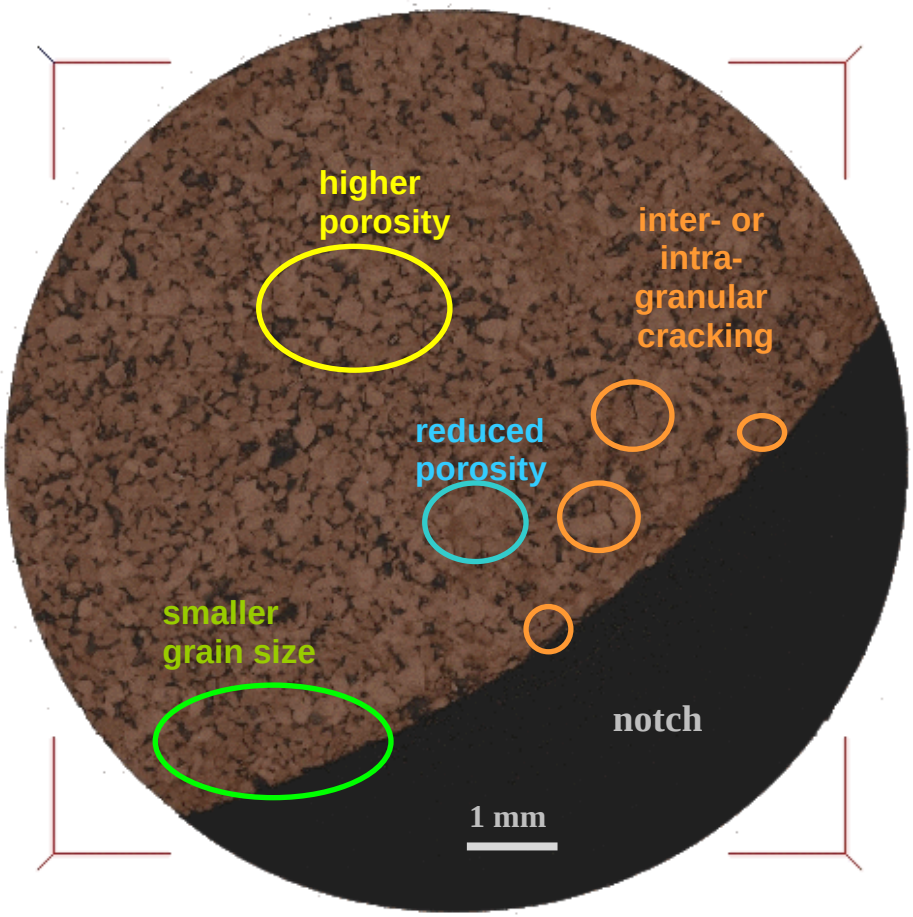

Fig. 6.43: HR x-ray tomography 2D slice vertical to the major imposed principal stress from a region close to the circumferential notch. Inter- and intra-granular cracking, reduction in the grain size, and regions of lower and relatively higher porosity values are illustrated.

A key issue difficulty, concerning the porosity calculations, was the selection of the appropriate threshold of the grey-scale histogram in order to separate the rock material to the void space. Such a task was not trivial in this particular rock since the grey-scale values corresponding to rock, void, rock debris, and Teflon ring, which covered the circumferential notch, had no distinct limits. Furthermore, the blue epoxy used to hold the material of the small core tight influenced the grey-scale values (*e.g.*, note that the histogram of the x-ray

tomography images of a small core coming from a laboratory undeformed specimen had different grey-scale values from those identified in the deformed rock).

The threshold investigation is described in Figures 6.44, 6.45. A sample region of an x-ray slice is used for such purpose.

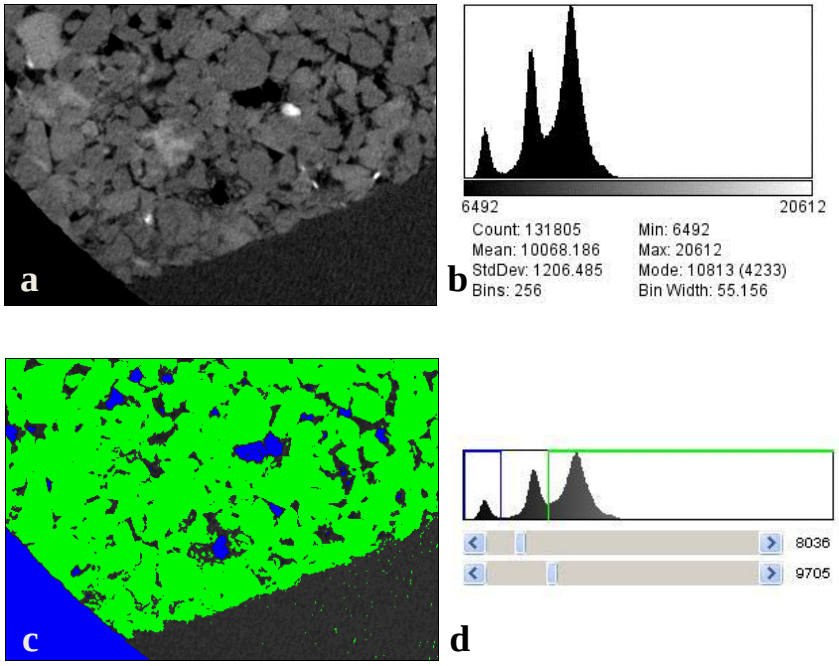

Fig. 6.44: Region of a very HR x-ray tomography 2D slice from the Ve4 deformed specimen, close to the notch. (a) X-ray image (2.96 mm x 2.075 mm); (b) Histogram of image (a); (c) Thresholded image of the same region 2.96 mm x 2.075 mm); (d) Thresholded histogram of image (c). Green colours correspond to the grains, blue colours correspond to the void, and dark colours correspond to the grain debris and the Teflon ring which covers the notch.

Three distinct grey-level regions were observed on the histogram of the very HR x-ray image, corresponding to void (Fig. 6.44c, 6.44d in blue), grains (Fig. 6.44c, 6.44d in green), and Teflon and grain fragments (Fig. 6.44c, 6.44d in dark colours), respectively. However, it was rather tough to determine the grey-scale values corresponding to the valleys of the histogram. Recall that these values are directly linked to the threshold values.

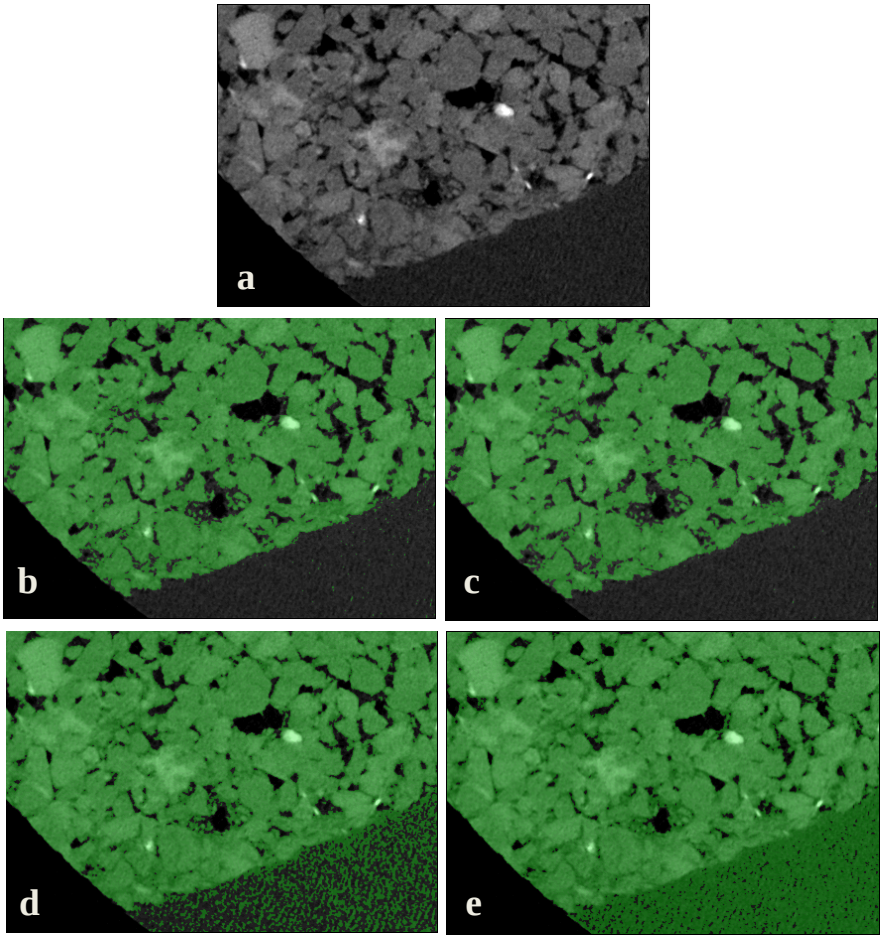

Fig. 6.45: Region of a very HR x-ray tomography 2D slice from the Ve4 deformed specimen, close to the notch. (a) X-ray image (2.96 mm x 2.075 mm); Superposition of Figure (a) on thresholded images corresponding to a threshold value of (b) 0.15; (c) 0.145, (d) 0.14; (e) 0.135.

Figure 6.45 illustrates four different threshold values used for the separation of the void space. Figure 5.45a shows the raw x-ray image, while Figures 6.45b-6.45e illustrate a superposition of the raw x-ray image on the thresholded grey-scale values, using a threshold of 0.15, 0.145, 0.14, and 0.135, respectively. Note that a threshold of 1 corresponds to 65536 grey-scale value, 16 bits image.

The obvious threshold choice, observing the grey-scale histogram, was that corresponding to the mid-distance of the second and the third peak of the histogram (see Fig. 6.44d). However, a threshold value equal to 0.15 did not follow the grain-void boundaries (Fig. 6.45b). A similar observation applied also to a 0.145 threshold value (Fig. 6.45c). A smaller

threshold value, equal to 0.140 (Fig. 6.45d) highlighted better the grain-void separation, while a smaller value equal to 0.135 underestimated the porosity, since such value also thresholded some grey-scale values corresponding to the voids.

For the following porosity calculations, which were performed throughout the image volume over sub-volumes of 100x100x100 voxels^3 at a spacing of 20 voxels in each direction (*i.e.*, 676x676x676 μm^3 and 135 μm, respectively), a threshold value equal to 0.14 was set. Figure 6.46 illustrates different vertical projections of porosity value calculations throughout the volume of the small deformed core. Only a small region above and below the notch is presented herein (images had 5.34 mm height). Figures 6.46a-6.46g show, thus, very local porosity variations around the region of the notch.

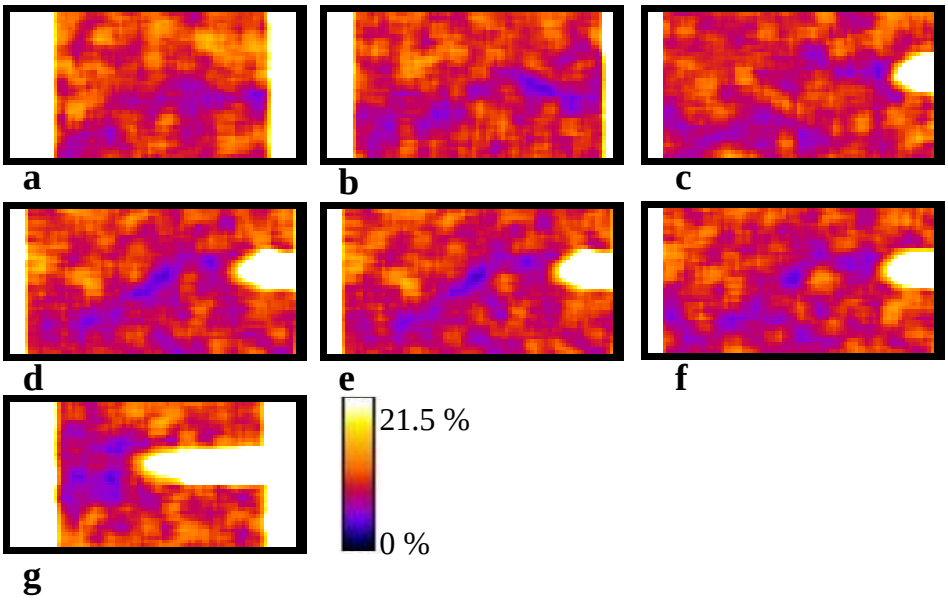

Fig. 6.46: Different vertical projections of porosity value calculations from the small core coming from specimen Ve4. The threshold used was 0.14, and the calculations were performed over sub-volumes of 100x100x100 voxels^3 at a spacing of 20 voxels in each direction. Recall that the resolution is 6.76μm.

The porosity fields, illustrated in Figure 6.46, showed highly compacted zones of 3% to 5% porosity values (dark purple) with a width of 284 μm to 622 μm. Regions of slightly higher porosity values, ranging from 7% to 8% (light purple), lay around the former zones or far from it and had a width of 310 μm to 852 μm. Regions of a bit higher porosity (from 9% to

14%), but relatively low compared to the porosity of the host rock, covered the rest of the volume. The above porosity field indicated that the heart of the compaction band had a much lower porosity, which increased moving far from it.

The mean inclination angle of the lower porosity features was around 49° towards the major imposed principal stress direction (dip of 41°). Given that the porosity variations, presented in Figure 6.46, came from a region very close to the notch (10 mm by 5.34 mm), it is argued that this mean inclination angle was not in serious conflict with the lower angles measured from the standard deviation of the HR x-ray images (recall that the lower inclination angles were measured in the proximity of the circumferential notch).

From a porosity calculation point of view, the threshold value is important since it determines the actual porosity values. Figures 6.47a-6.47f illustrate the porosity values from the median vertical and median horizontal projections of the small core (from specimen Ve4), using a threshold of 0.14 and 0.15.

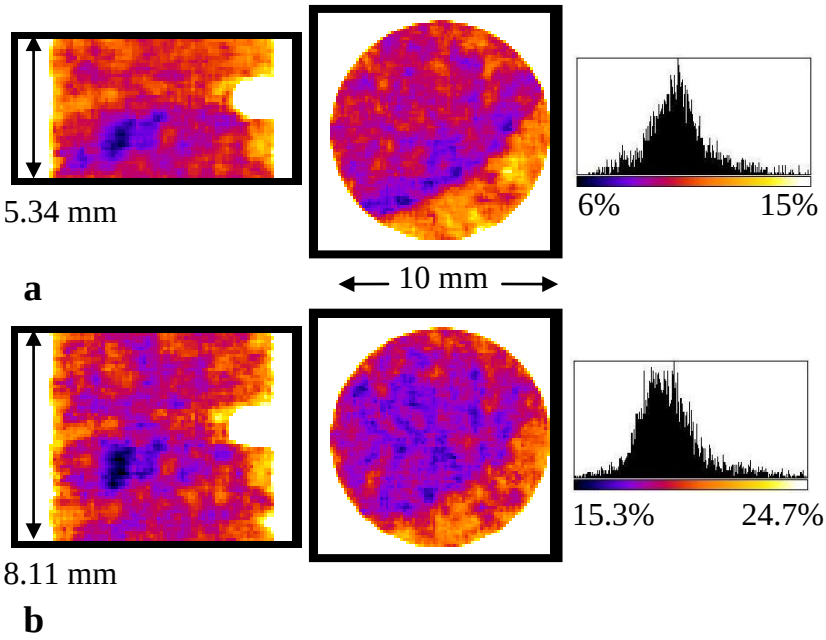

Fig. 6.47: Porosity calculations on the Ve4 small core using different threshold levels: (a) Median projection (vertical and horizontal) together with the porosity histogram for a threshold of 0.14 (dimensions of the projection: 5,34mm, 10mm); (b) Median projection (vertical and horizontal) together with the porosity histogram for a threshold of 0.15 (dimensions of the projection: 8,112mm, 10 mm).

Note that a difference of 1% on the threshold values (*i.e.*, a range of 655.36 grey-scale values out of 65536), bounds to estimate almost the double porosity values. The porosity calculations using a threshold of 0.15 were performed over a bigger x-ray images volume (Fig. 6.47b).

Baud et al., [2003], *Vadjova et al.*, [2004], and *Louis et al.*, [2006] calculated the porosity reduction inside discrete compaction bands of sandstones with an initial porosity of around 23%. These authors driven by micro-structural observations, which indicated intense grain damage almost only inside the bands, and assuming that the measured inelastic axial strain (neglecting any lateral strain) was only distributed inside these bands (and corresponded to pore collapse), suggested a porosity reduction inside discrete compaction bands of 14% - 15% (e.g. porosity of 8% - 9%). However, the porosity field in the Vosges sandstone is characterised by much lower values. Recall that 9% -14% is the calculated porosity in the vicinity of the band (small core), while porosities from 3% - 8/% are calculated inside the band. Given that the initial porosity of the host rock is 23% and the volumetric strains inside the band reach up to of 2% (see section 6.2), the presented porosity values of specimen Ve4 are quite small than the expected (if all volumetric strain corresponds to porosity reduction, then the expected porosity should be around 21% - 20%). This remains still an open issue. However one should keep in mind that the resolution of the porosity and the volumetric fields is not the same (the former has a spatial resolution of 140 μm and the latter of 600 μm). Further investigation of the threshold values is necessary (possibly in a more discrete range, e.g. 0.141, 0.142…, 1.149 etc, see differences in Fig.6.47). However, the qualitative interpretation of the porosity fields is considered to be valid.

6.8 Microscopy

This section comments on the microstructure revealed by the thin sections from some of the deformed specimens, which were subjected to triaxial compression at relatively high confining pressures (130 to 190 MPa). The scope of this section is to delve into the occurred micro-processes from the formation and propagation of compaction band. This understanding validated-in a sense-what was observed from the full-field methods in the previous sections. Light optical (planar light and cross-polarised) and scanning electron microscopy (SEM) were used.

After the post-mortem measurements, specimens Ve4, Ve6, and Ve1 were vacuum impregnated with low-viscosity blue epoxy; thin sections were prepared for optical microscopy and SEM (section 3.6). Vertical sections were taken near the mid-height of each specimen (*i.e.*, near the position where the notches had been machined, apart from the Ve1 specimen which had no notches). Observations on three different specimens are presented here.

6.8.1 Specimen Ve4

A region around the notch from specimen Ve4 (see Table 4.2, section 6.2) is presented in Figure 6.48. On the top row (Fig. 6.48a, 6.48b), optical images (plane-polarised and cross polarised light) are shown. The pale blue colour epoxy turned difficult the identification of the grain damage, since both grains and pore-space (covered by the epoxy) had almost similar pale colours. Close to the tip of the notch, Hertzian-like contact fractures between quartz grains were observed (more clearly in the cross-polarised image, Fig. 6.48b).

Figure 6.48c shows a SEM image, covering a somehow larger region around the notch, in which compaction band were illustrated in more details. Hertzian-like contact fractures and severe grain fracture and rearrangement of the fragments characterised the region close to the notch tip. The open fracture, seen in Figure 6.48, initiating from the notches and propagating inwards, plausibly had occurred due to the unloading of the specimen.

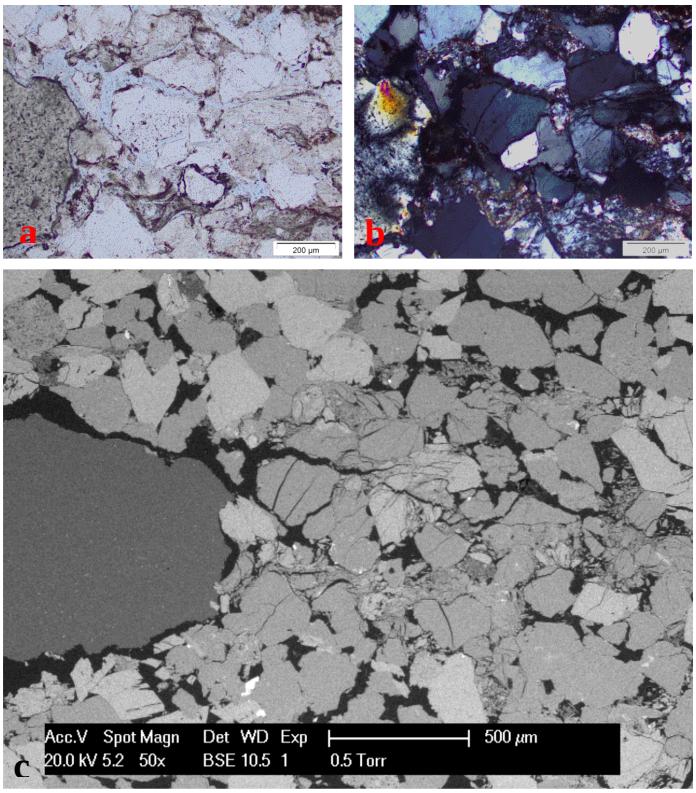

Fig. 6.48: (a) Plane-polarised light optical images of a region around the notch from the Ve4 specimen; (b) Cross-polarised optical image from the same region; (c) SEM image of a larger region around the notch. Hertzian-fractures, severe cracking in some grains, and grain fragment re-arrangement are seen in the region of compaction bands. The major imposed principal stress was normal to the direction of the longest dimension of the images.

6.8.2 Specimen Ve6

SEM images were also taken for a thin section coming from specimen Ve6 (Table 4.2, section 6.3). X-ray scan for Si, K, and Al was initially performed, in order to identify quartz grains, feldspars, clays and micas in a region around the notch. Figures 6.49a-6.49c show the Si, K, and Al x-ray scans, respectively, and Figure 6.49d illustrates a false colour image using the x-ray scans for the above mentioned minerals.

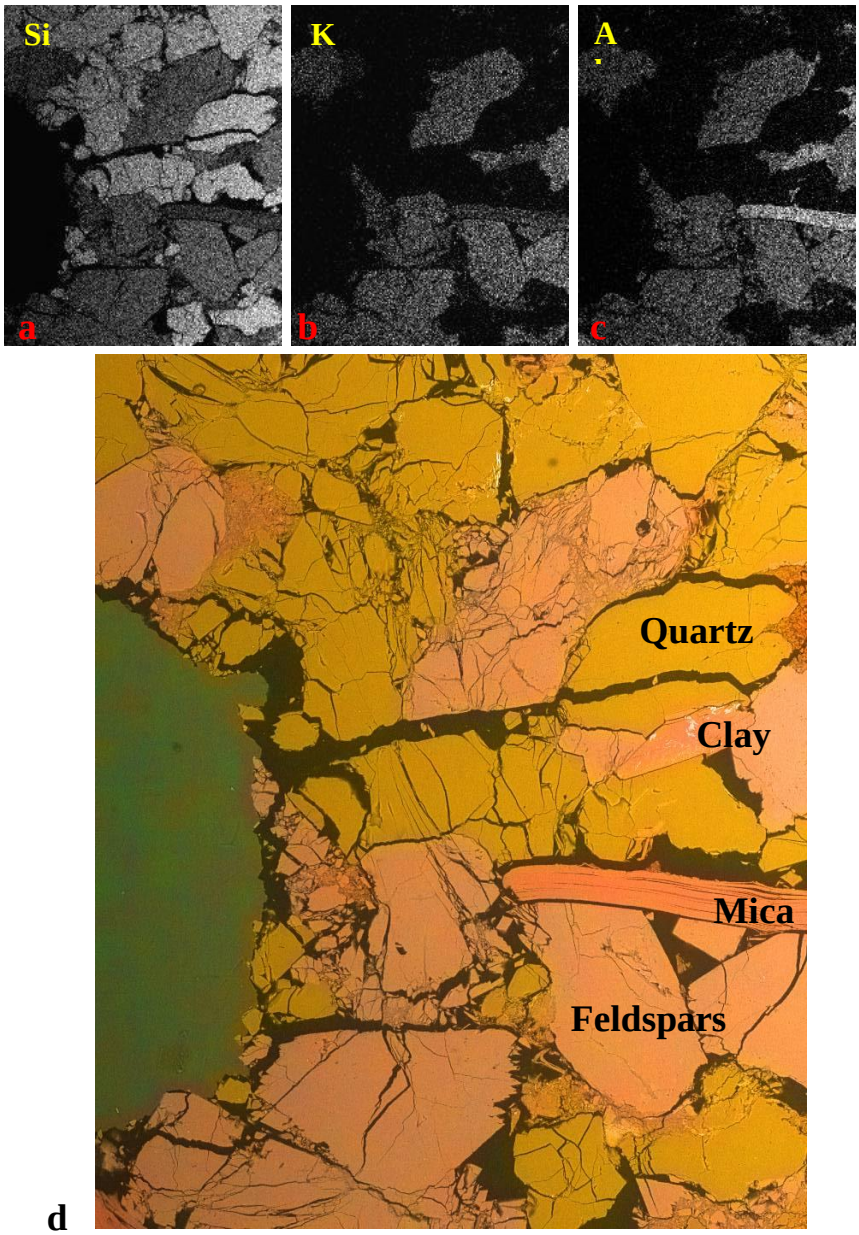

Fig. 6.49: (a-c) Si, K, Al x-ray image of a region around the notch from specimen Ve6; (d) False colour image using the Si, K, Al x-ray scans of the same region. Quartz, Feldspars, Clays and Micas were identified. Intense damage is observed in this region (grain fracturing, grain crushing). Shear and compaction resulted in a further re-arrangement of grains and fragments and in porosity reduction. The maximum compressive stress was vertical.

The silicate (Si) x-ray scan visualised quartz (SiO_2), feldspars (microcline $KalSi_3O_8$), clays (kaolinite $Al_2O_3.2SiO_2.2H_2O$), and micas (muscovite $KAl_2\ (OH)_2\ (AlSi_3O_{10})$) (Fig. 6.49a). Quartz grains were brighter than the rest of grain minerals (higher absorption). Note that the importance of the Si x-ray scan lays mainly on distinguishing quartz to feldspars, while the potassium (K) x-ray scan visualise solely feldspars and micas. The distinctive shape differences between these grains facilitated the identification of feldspars and micas (Fig. 6.49b). The aluminium x-ray scan provided further insights into the identification of feldspars, clays and micas (Fig. 6.49c).

Quartz grains (in yellow) and feldspars minerals (in pink), near the notch, were heavily damaged (Fig. 6.49d). An open fracture, initiating from the notch and propagating inwards, split in two a quartz grain. Hertzian-like fractures, initiating at the grain bonds, were obvious in both quartz grains and feldspars. In addition, in both quartz grains (more common) and feldspars (less common) crushing was observed, which resulted in further grain fragmentation; the fragments appeared to fill the adjacent pores. Hence, it is likely that the porosity values in places inside this highly damaged region were reduced. The mica (on the right part of the image) was regionally delaminated.

Figure 6.50a presents a SEM image from a wider region around the notch. Intense grain damage characterised the region around the notch and the compaction band. Pore collapse, intense grain crushing, and porosity reduction was observed in these regions. Less damaged grains were identified in regions far from the compaction band (regions of higher porosity). Figures 6.50b-6.50e are details from Figure 6.50a.

Figure 6.51a depicts a heavily damaged region of the compaction bands from specimen Ve6. Grains had impinged at a point contact and Hertzian fractures were generated. Clear Hertzian fractures could be seen in two feldspars on the left of the image, while in the central part and on the right of the image, both quartz (darker) and feldspars (lighter) were heavily crushed. The resulting grain fragments filled the adjacent pore-spaces and leaded to local reduction in porosity. Figure 6.51b is a zoom in Figure 6.51a (increasing magnification), focusing on a crushed feldspar. Intense grain crushing and fragmentation was located in a vertical zone along the feldspar, while several fractures covered the rest of the grain surface.

The fragments at the central zone had a very small size (smaller than 10 μm) and angular shapes.

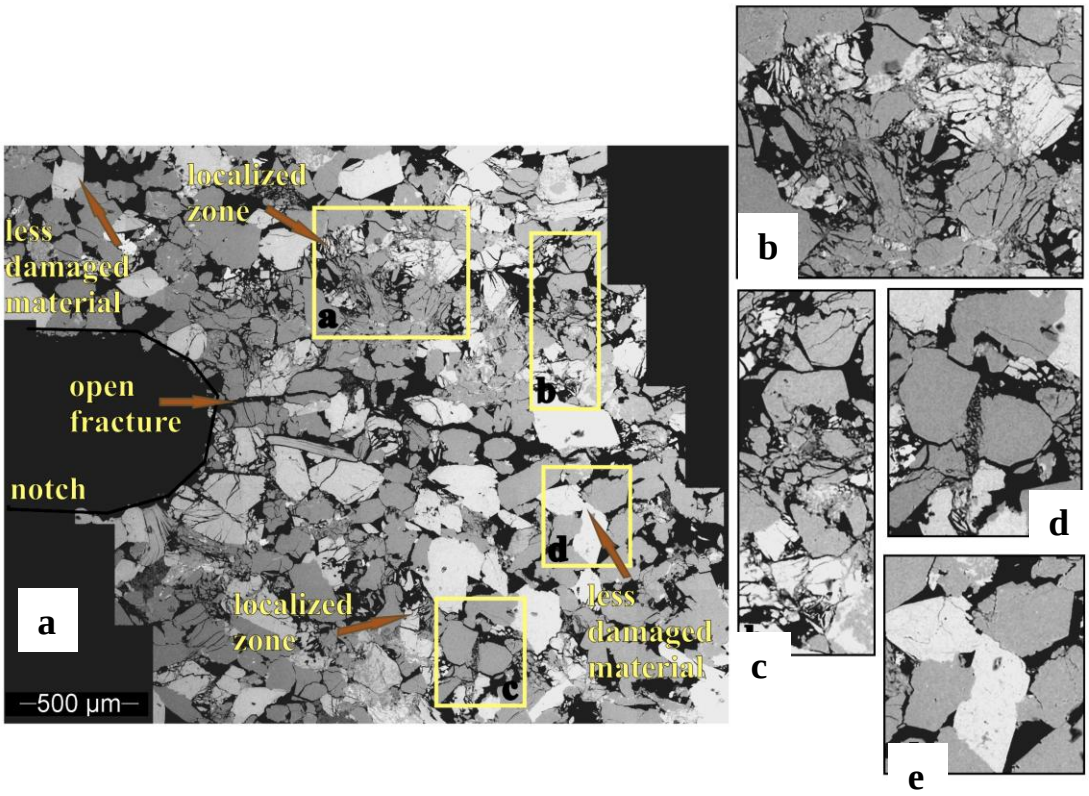

Fig. 6.50: (a) SEM image of a region near the notches from specimen Ve6. Localised zones (compaction bands) slightly inclined, an open fracture initiating from the notch and propagating inwards, and relatively undamaged material can be seen on the left image. The images on the right are zooms in several regions, which potentially show: (b) intra- granular fractures and grain crushing; (c) grain crushing and pore collapse; (d) grain damage; (e) relatively undamaged grains. The maximum compressive stress was vertical.

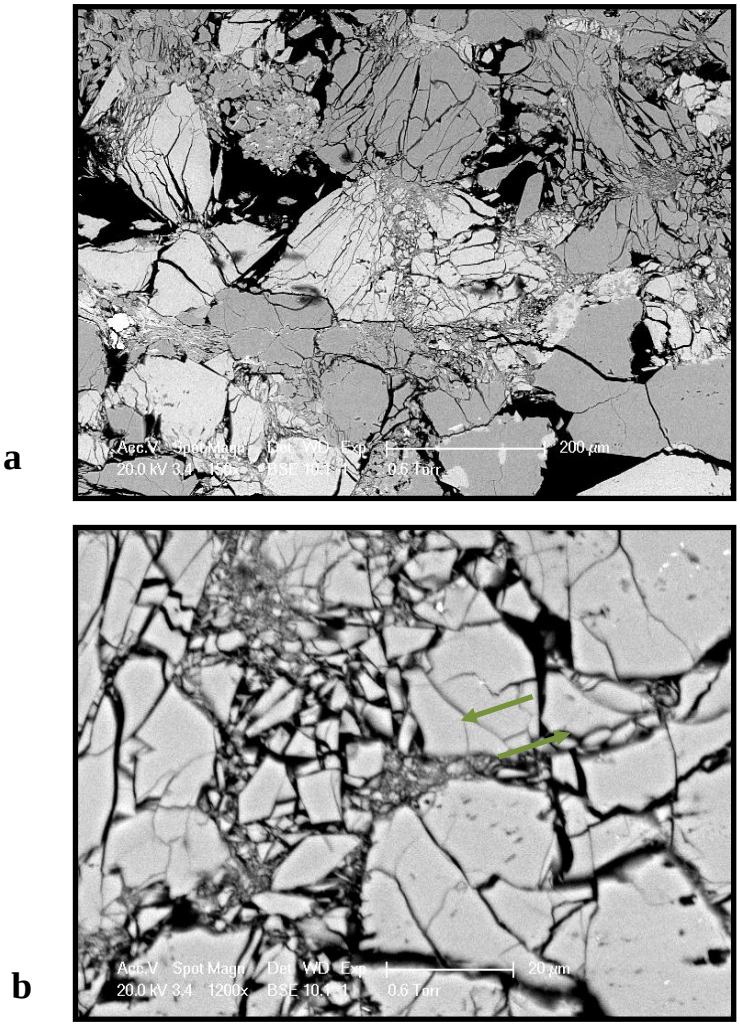

Fig. 6.51: Increasing magnification backscattered electron images (BSE) of heavily damaged quartz grains and feldspars from specimen Ve6. (a) BSE image of a wider region inside the compaction band showing Hertzian fractures and grain crushing. The scale-bar is of 200 µm; (b) BSE image zooming in a region of intense grain crushing. The grain fragments have angular shape and different sizes (smaller than 10 µm). Most of the grain fragments filled the grain micro-cracks. The positions of the detrital grains indicate that shearing possibly took place (in green arrows). The maximum compressive stress was vertical.

Another highly damaged region from specimen Ve6 is illustrated in Figure 6.52a. Hertzian fractures on quartz grains could quite clearly be seen. The severe damage on feldspars (in the

centre of the image) obscured most of the original grain boundaries and, therefore, this complicated the interpretation of the observed damage at this region. Figures 6.52b and 6.52c are magnified image of Figure 6.52a.

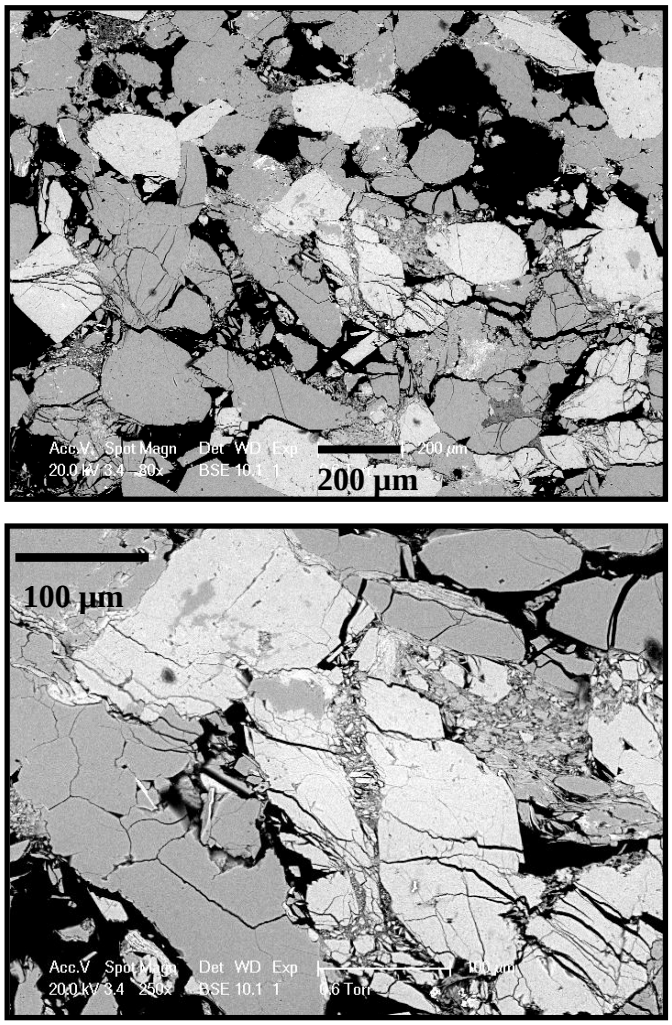

Fig. 6.52: Increasing magnification backscattered electron images (BSE) of heavily damaged feldspar from specimen Ve6. (a) BSE image of a wider region inside the compaction band showing Hertzian fractures and grain crushing;(b) BSE image zooming in crushed feldspars and fractured quartz grains; (c) BSE image showing further zoom in the zone of heavy grain crushing. The detrital grains have a very small size and different orientation. Such an observation might indicate that frictional shearing has also taken place inside this zone.

c

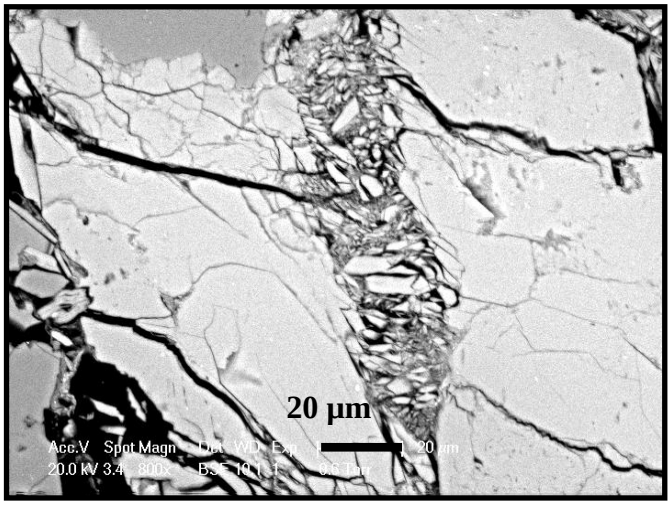

Fig. 6.52: Continued.

A possible scenario might be that the feldspar, shown in Figure 6.52b, was trapped due to pore collapse. A local stress re-distribution resulted in micro-cracks, which initiates at the point contacts of all grains (Fig. 6.52b) and propagated throughout the width of the grains. These micro-cracks along the feldspars possibly followed the cleavages. The zone of heavy grain fragmentation, being observed more clearly in Figure 6.52c, is possibly the result of intense crushing and sliding of the feldspar bigger pieces. Note that the fragments inside this gouge zone had a very small size and different orientations, which makes stronger the argument of the occurrence of rotation (local shearing). However, no obvious movement of the less damaged feldspar particles could be distinguished, since the intense local grain crushing obscured the original grain boundaries.

Figures 6.53 present similar deformation features to Figures 6.52, observed, this time, in quartz grains. A similar zone of intense crushing was distinguished between two quartz grains. Pore collapse should have taken place. For this case, a possible scenario might be the following. Potential fractures on grain bonds ‘liberated’ the quartz grains. Compaction and possible quartz rotation (see rotation angles in blue in Fig. 6.53b) increased the local stress concentration and plausibly resulted in frictional sliding and further crushing of the contact surfaces. The grain fragments inside the damaged zone had different orientations.

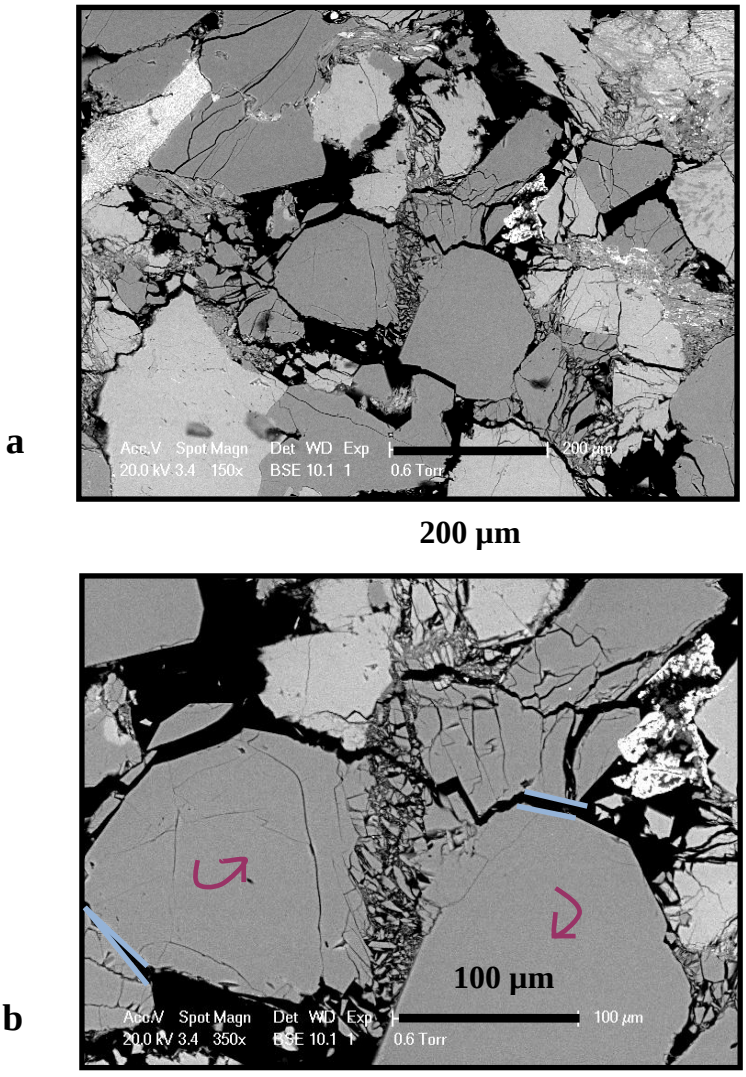

Fig. 6.53: Increasing magnification backscattered electron images (BSE) of heavily damaged quartz grain from specimen Ve6. (a) BSE image of a wider region inside the compaction band showing grains damaged by Hertzian fractures and intense grain crushing; (b) BSE image showing further zoom. A zone of crashed grains lies in between the quartz grains. Breakage of grain bonds and re-arrangement of grains due to pore collapse might have resulted in further rotation of the quartz grains. Local stress concentration and frictional sliding is likely to have resulted in further damage of the surface contacts. The positions of the detrital grains indicate that shear has also taken place. The fragments have different orientations and a size smaller than 10 µm. The maximum compressive stress was vertical.

6.8.3 Specimen Ve1

Figure 6.54 presents an example of severe deformed micas observed in specimen Ve1 (Table 4.2, section 6.5). Figure 6.54a is a plane-polarised light optical image, and Figures 6.54b-6.54d are cross-polarised optical images. In general, it could be argued that micas, which are easily identified in thin sections due to their distinctive shape, accommodate much of the deformation.

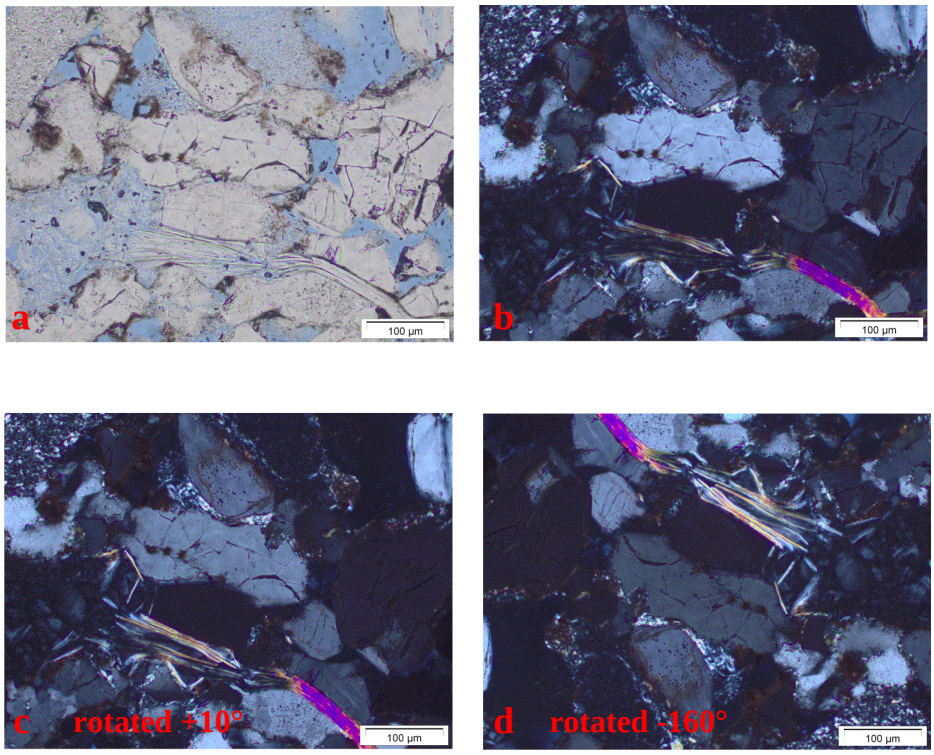

Fig. 6.54: (a) Plane-polarised light optical image from specimen Ve1 showing severely deformed micas, fractured feldspars and quartz grains; (b-d) Cross-polarised optical images from the same region, rotated at 0°, +10°, and -160°, respectively. The layers of the mica (left part of (b)) have been highly deformed. Some of them are twisted and others are torn apart. The maximum compressive stress was vertical (a-b).

The mica presented in Figures 6.54a-6.54d was slightly bent. The geometry of its left part could suggest that this region accommodated a big amount of deformation possibly due to the adjacent grain on the left, which appeared to be severely damaged. However, only few of these fragments had remained glued on the thin section (they had possibly removed during

the thin section preparation). The left part of the mica illustrates delaminated layers. In particular, some of them were twisted and others were torn apart. Near the deformed mica, fractured feldspars and Hertzian fractures on quartz were identified.

6.9 Different sandstones: the Bentheim

Additional results from the Bentheim sandstone are presented in this section as an initial comparison to the results presented on the Vosges sandstone (see also section 4.2). Bentheim sandstone specimen had a circumferential notch machined on the mid-height, similar to that of the Vosges specimens. The test was performed by *S. Stanchits* at GFZ (BE6 Bentheim specimen was tested at 185MPa under triaxial compression), and the x-ray scans and analysis were carried out at Laboratoire 3SR as a part of the present work. No stress-strain response from this specimen is presented here; only HR x-ray images (~ 30 μm resolution) from this Bentheim deformed specimen are shown.

As it has already been mentioned in sections 6.2-6.6, it is not always straightforward to depict compaction bands in Vosges specimens, using solely the raw x-ray data without applying an extra statistical analysis on them (*e.g.*, standard deviation analysis). However, this was not the case for the Bentheim sandstone. The localised bands can be partially visualised using the raw HR x-ray tomography data. The standard deviation analysis in this particular sandstone retrieved extra information.

Figures 6.55a-6.55c show post-mortem HR x-ray images from a vertical projection near the mid-height of the specimen, zooming in a region close to the notches, where localised deformation occurred. Figure 6.55a presents a raw x-ray image focusing on high (in white) and low (in black) density regions of the grey-scale histogram. A crack initiating from the right notch is apparent. In addition, denser regions (in white) can be identified around this crack and near the left notch. Figure 6.55b shows the local standard deviation of the grey-scale values from this HR x-ray tomography image. The lower values of standard deviation regions were illustrated in red. In fact, a low standard deviation grey-scale value might indicate either pore space or compacting material. Figure 6.55c presents the raw x-ray data

superimposed on the local standard deviation data. Compaction bands are more clearly defined in this case. Moreover, details on low or high density regions as well as on more or less homogeneous regions (as these are visualised by the image analysis) can be identified in such way. However, this kind of analysis requires that both raw and standard deviation x-ray images can partially or in full visualise the deformation features.

It is interesting to point out that in Bentheim sandstone, compaction bands appear to have curved trajectories (and not straight). Moreover, it is shown that although multiple compaction bands initiated at the notches, the propagation of some was halted not far from the notch. Further microstructural observations of thin sections can highlight why these bands did not further evolve.

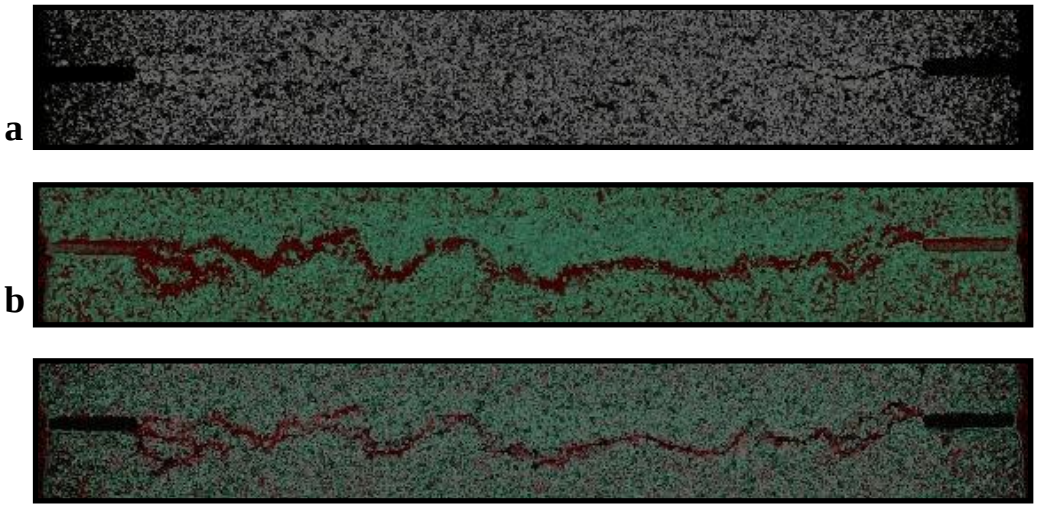

Fig. 6.55: Compaction band in BE6 specimen; (a) Raw data; (b) Local standard deviation; (c) Raw data and local standard deviation superimposed.

6.10 Conclusions

In this section, the main results from the compaction bands, which developed in Vosges sandstone are summarised:

- Full-field methods were able to depict compaction bands that formed in sandstone specimens tested at relatively high confining pressures (from 130 MPa to 190 MPa) and taken to different axial strain levels (Table 4.2). Thin section observations validated what was previously indicated by the full-filed experimental methods.
- AE hypocentre locations illustrated the onset and evolution of compaction bands, which initiated either at the tip of the notch (in notched specimens) or close to the specimen's surface (*e.g.,* Ve1). An increase in the stress deviator resulted in the full propagation of compaction bands as well as the creation of newer bands.
- The cumulative number of AE events increased with increasing stress deviator values, which indicated an increase in grain-scale activity (also visualised in the hypocentre locations). The AE rate was changing during all experiments; however, the onset of localised deformation in each band was not straightforwardly identified because damage had also occurred at the top and bottom boundaries of the specimens and new compaction bands developed while the older kept propagating. During the unloading of the deviatoric compression, further AE activity was identified, but the number of AEs was increasing with a much lower rate compared to the deviatoric loading stage.
- Initial source-mechanisms analysis for specimens Ve4 and Ve6 (Table 4.2) that had experienced compaction bands, demonstrated that pore collapse was the dominant mechanism, since the majority of the AE events was C-type. A relatively small number of S-type events and a much smaller number of T-type events were also identified. Recall that, although these two experiments were tested at the same confining pressure (130 MPa), they developed different number of compaction bands. The number of the S-type events for specimen Ve4 – in which one compaction band developed - was twice the number of specimen Ve6 –in which a network of bands developed - for the same axial strain (*i.e.,* 0.8%, Fig. 6.2, 6.10), This might indicate that the compaction band formation supressed S-type events.
- Compaction bands were identified as zones of low velocities (UT) which were linked to grain-scale damage.
- Compaction bands were visualised as features of decreased standard deviation values (calculated on the grey-scale values of the raw HR x-ray tomography images). Small

standard deviation values represented homogeneous regions in the images, but this is purely from an image analysis point of view (based on the x-ray tomography images at a given resolution). Low values of standard deviation are associated with grain fracturing and grain crushing, so that the grain size becomes smaller than the voxel size of the tomography image. The image becomes more homogeneous as the different grains and the porosity attenuations are averaged together over a voxel to give an average grey-scale, which might be similar over a region (as it is indicated by the standard deviation measure).

- Thin section observations revealed intense grain damage inside the regions of compaction bands. Grain fracturing of quartz and feldspars was identified. Some micas were also delaminated. Pore collapse and grain crushing were also obvious inside the compaction bands.
- Both volumetric (compactant) and shear strains were measured inside the compaction bands suggesting that these particular deformation features were not structures of pure compaction (see more in Chapter 7). The deformation features visualised by the shear strains were usually slightly wider than those by the volumetric strain, which might indicate that shearing was accumulated also around the centre of the band, in which both compactant and shear strains were identified.
- Porosity calculations showed that the porosity in the centre of the band was ranging from 3% to 5% and it was increasing moving beyond from the centre of the band.
- The inclination angle of the compaction bands was confining pressure dependant. The higher the confining pressure was, the more the deformation band was normal to the major principal imposed stress direction (*i.e.*, horizontal).
- The higher values of axial strain resulted in higher strain values and a wider damage (wider width of the compaction bands).

Chapter 7 - Discussion and Conclusions

7.1 Discussion and conclusions

In this work, the mechanical behaviour of the Vosges sandstone was investigated under a range of confining pressures in order to characterise the developed deformation features and better understand their mechanisms. Cylindrical dry specimens (80 mm in height and 40 mm in diameter) were subjected to triaxial compression and were taken to different axial strain levels (see Chapter 4, Table 4.2). From 20 to 50 MPa confining pressure, shear bands developed (Chapter 5), while from 130 to 190 MPa shear enhanced compaction bands developed (Chapter 6). A suite of full-field non-destructive methods (see Chapter 3) were used to investigate these deformation features (at the failure and post-failure stage), together with thin section and SEM observations (destructive). Each method has a different resolution and is sensitive to different properties or processes. Therefore, it has been possible to identify evidence of the mechanisms taking place in the localised deformation bands of this porous rock (Chapters 5 and 6). Similar mechanisms were observed in other porous sandstones in previous published studies (see Chapter 2).

This Chapter discusses the basic results of this thesis. The following topics are addressed:

- Experimental methods, full-field methods and multi-scale approaches
- Mechanical behaviour of the Vosges sandstone
- Deformation features: shear and compaction bands
- Role played by the introduced structural heterogeneities, particularly the notch
- Quantification of the results: width and orientation of the shear and compaction bands produced

✓ **Experimental methods, full-field methods, and multi-scale approaches**

The combined use of four non-destructive, full-field methods, presented in Chapter 3, described and quantified the formation and propagation of shear and compaction bands, from

laboratory tested Vosges sandstone specimens (Chapters 5 and 6). These deformation features were resolved by the full-field methods even when no direct evidence of deformation could be observed on the surface of the specimens (by visual inspections). The 3D (x-ray CT, 3D-DIC, AEs) and 2D (UT) structure of the resolved deformation bands permitted a richer interpretation and quantification of some of their characteristics, *e.g.*, volumetric and shear strain fields, porosity field and the identification of their width and orientation. Direct microstructural observations of thin sections and BSEM supported the interpreted inter- and intra-granular deformation inferred by the non-destructive, full-field methods.

Specimen-scale measurements (*e.g.*, mechanical data) and grain-scale observations (*e.g.*, thin sections) were performed in many previous experimental studies (see Chapter 3). Additionally, experimental results from AE hypocentre locations, x-ray tomography, and DIC were presented separately or in pairs (see Chapter 3). This thesis is the first attempt, to the author's knowledge, to present combined experimental results from five different experimental methods. The goal of such a combination was not the assessment of the best experimental method. On the contrary, the aim was to prove that the understanding of the deformation processes is much improved when multiple experimental methods are used, since the different methods are sensitive to different properties of the deformed material.

The experimental methods used in this work are presented according to their resolution in Figure 7.1, starting with the smallest (on the left side of the figure) and moving to the largest (on the right of the figure). Conventional force-displacement measurements (*e.g.*, specimen-scale, cm) describe only the global loading history (Chapter 4). Although the stress-strain curves provide insights into the sandstone's mechanical behaviour, which can be used to calibrate macroscopic constitutive models, this analysis does not take into account the sandstone's fabric developed during the experiments and its non-uniform distribution (*e.g.*, grain-scale deformation). On the other hand, microstructural observations on thin sections give a detailed description of the grain-scale damage (*e.g.*, μm), either from a qualitative or a quantitative point of view, and provide insights into the deformation mechanisms that developed in and around the bands (sections 5.6, 6.8). However, quantitative analysis from thin section observations is rather time consuming. Further insights into the deformation processes can be gained by the use of experimental methods with a resolution shifting from

specimen- to grain-scale, *e.g.*, ultrasonic velocity fields, with a resolution equal to the ultrasonic wavelength, x-ray tomography, with a resolution depending on the focal size and the positioning of the specimen towards the x-ray source, and DIC strain fields, with a resolution defined by the spacing distance (see Chapter 3). Such multi-scale approaches may enrich both constitutive modelling and numerical simulations.

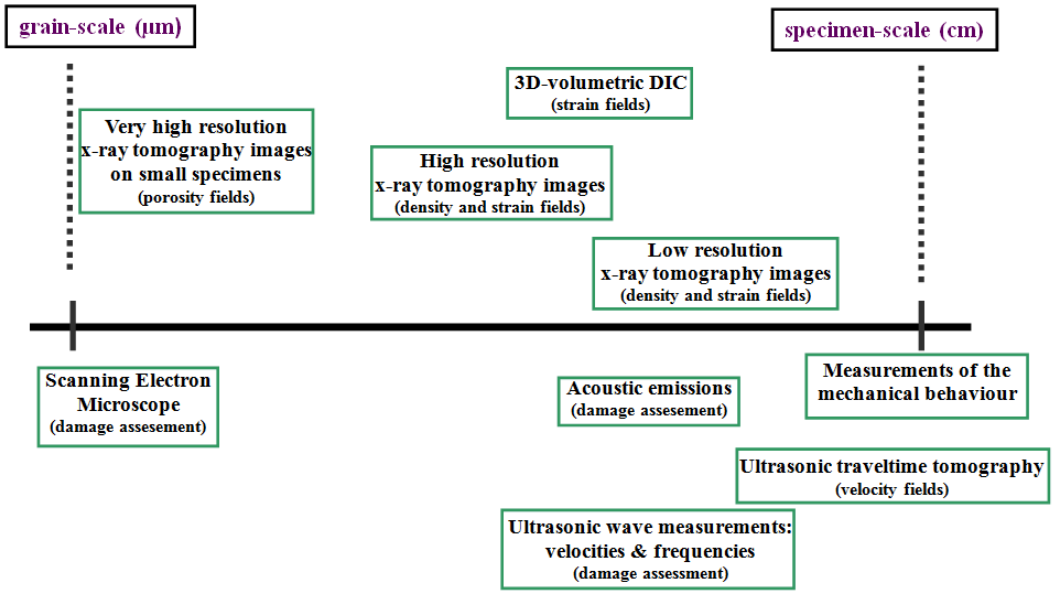

Fig. 7.1: Experimental methods used in the present study with a resolution ranging from cm (specimen scale) to some µm (grain-scale).

The challenge of using different experimental methods is to reasonably bind together all the multi-scale information, considering that each method has a restricted, and different, sensitivity and resolution. Quoting from *Rene Magritte*: 'No matter how closely, through realism-art, we come to depict an item accurately; we never do capture the item itself, but capture an image on the canvas'. If one compares the experimental methods to the *'realism-art'*, the visualisation of the deformation features is always a *capture of an image on the 'experimental' canvas,* which means that the resolved information is just a representation that might or might not describe the actual mechanism.

✓ **Mechanical behaviour of the Vosges sandstone**

The mechanical results from the triaxial compression experiments, in terms of stress-strain curves, were presented in Chapter 4. Figure 7.2 compares the peak stress values in the p-q plane from experiments subjected to relatively low confining pressures (up to 50 MPa) with those presented by *Bésuelle* [1999]. Although the results presented in the present thesis cannot be directly comparable with those by *Bésuelle* [1999], they are located in between the shear yield surfaces suggested by *Bésuelle* [1999]. Recall that the present specimens come from a block adjacent to those used by *Bésuelle* [1999] and also had notches machined in their offset flattened surfaces (unlike those in *Bésuelle's* study [1999]).

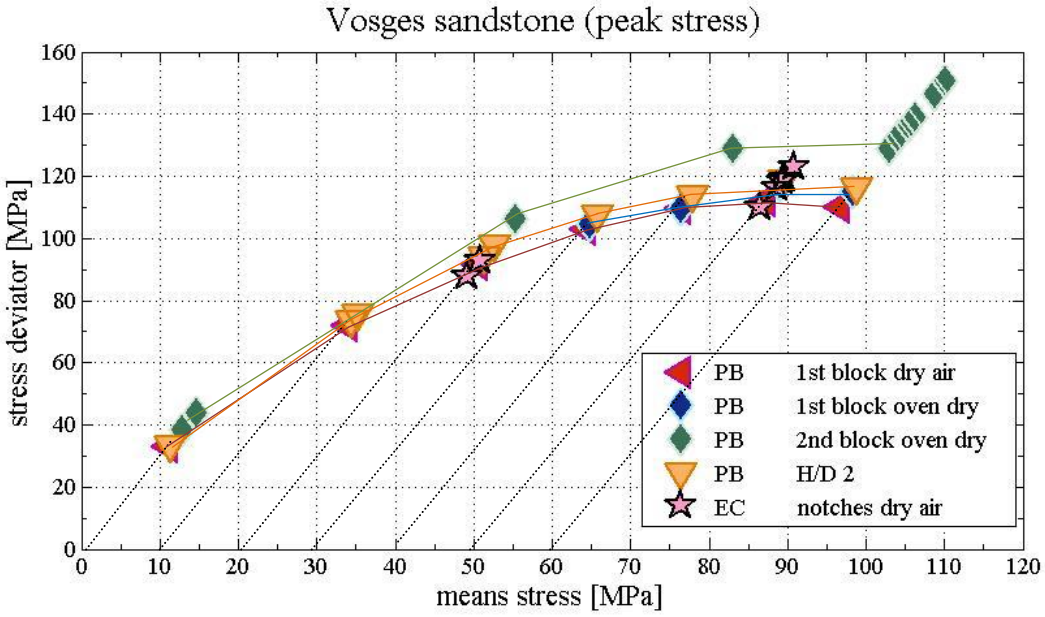

Fig. 7.2: Comparison of the peak stress values in the p-q plane for the triaxial compression experiments subjected to low to intermediate confining pressures (up to 60 MPa) presented by Bésuelle [1999] and those of the present study. Results from Bésuelle [1999] are presented as PB and results from the present work as EC.

For both the case of 20 MPa and of 50 MPa confining pressure, the notched specimens present p-q peak values lower than those from the unnotched specimens coming from the 2nd block used by *Bésuelle* [1999] and higher than those from the 1st block. Given that the notch facilitates the failure process acting as stress concentrator [*Tembe et al.*, 2006; *Vajdova et al.*,

2003a], it is assumed that the sandstone block used in the present study was very similar to the 2nd block from *Bésuelle*'s study.

Note that the p-q values for specimens loaded under 50 MPa confining pressure are relatively scattered (for both experiments performed at 3SR and GFZ laboratories). A scatter in the p-q values was also observed by *Bésuelle* [1999] for specimens loaded under 60 MPa (at 3SR). It is speculated that in terms of the peak p-q stresses and localised deformation features there is a degree of reproducibility, when different loading frames were used, but there is no repeatability in the post-localisation regime in terms of the place where the deformation bands developed (Chapter 4, Fig. 4.12). This can be attributed to the variations in microstructure of the sandstone.

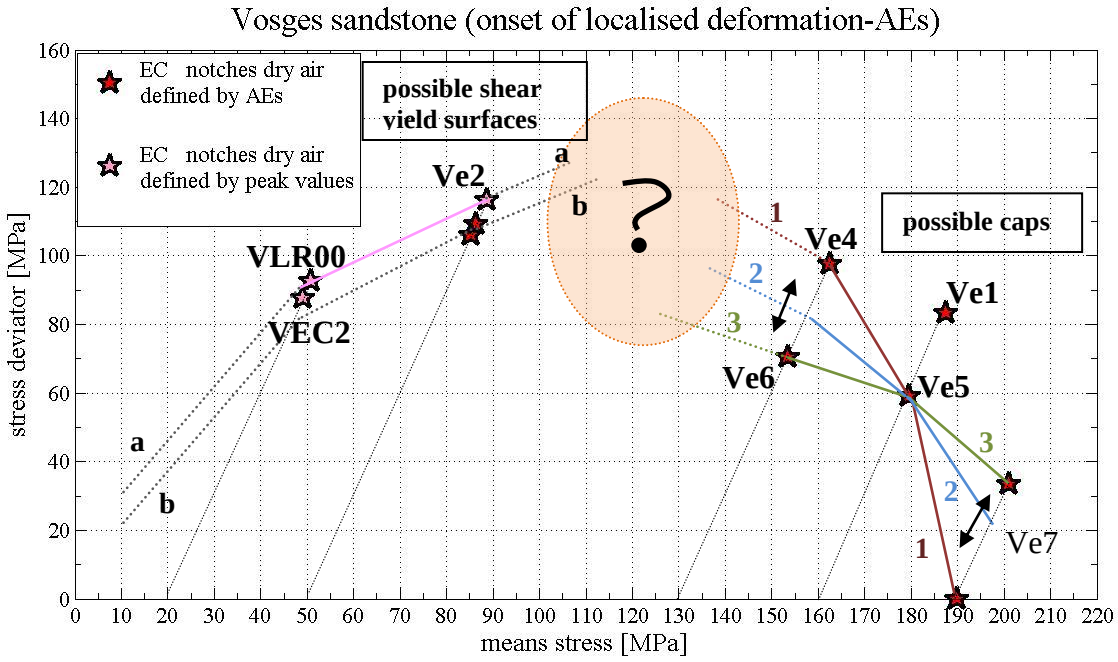

Fig. 7.3: Representation of possible shear yield surfaces and caps in the p-q planes from the triaxial compression experiments subjected to low to high confining pressures (from 50MPa to 190 MPa). The shear yield surface (line a) concerns peak values, while the shear yield surface (line b) and the three possible caps (1, 2, 3) refer to stress values defined by the AE hypocentre locations. Solid lines connect measured values and dashed lines connect measured values to expected values (through mean stress – stress deviator space that was not explored in this study).

Figure 7.3 presents the yield stresses (in the p-q plane) from Vosges specimens under confining pressure ranging from 50 MPa to 190 MPa. Red star values were defined by the AE hypocentre locations and pink star values by the peak stress (Chapter 4). The shear yield surface from the AE locations cannot be uniquely defined because only one experiment was performed with AE event recordings (*e.g.,* Ve2). A possible shear yield surface (line b) is shown in Figure 7.3 (on the left) assuming a shifting in the shear yield surface (line a) defined by the peak stress from specimens deformed at 20 MPa (VLR00, VEC2) and 50 MPa (Ve2) confining pressure. Yield stresses coming from both the AE locations and the peak stress are shown in Figure 7.3, for specimen Ve2. The latter are higher than the former, since the onset of localised deformation occurred before the peak stress (see also Chapter 4).

All sets of yield stresses, from specimens loaded from 130 to 190 MPa, map out yield surface caps with negative slopes in the stress space (p-q plane). A considerable difference in the yield stresses was observed for specimens Ve4 and Ve6 (Table 4.2), which is considered to be due to textural heterogeneities of the specimens. Recall that different number of deformation bands was developed in these two specimens for the same axial strain (Chapters 4 and 6). Furthermore, a range in the yield stresses was defined for specimen Ve7 (Fig. 4.31).

Three different possible caps are presented in Figure 7.3 (on the right side of the figure). Caps 1 and 3 describe the possible limit yield surfaces from experiments loaded under 130 to 190 MPa confining pressures (notched specimens). It is speculated that any yield surface placed between caps 1 and 3 might be possible. However, since cap 3 lays relatively low compared to the shear yield surface b, it could be argued that it is not a representative cap.

The yield stresses from specimen Ve1 (unnotched), corresponding to the onset of localised deformation, are relatively higher than these from the Ve5 (notched), which is like what it is observed in Figure 7.2, for the low to intermediate confining pressures (e.g., comparison of notched specimen from the present study to unnotched specimens coming from *Bésuelle's* work [1999]). For the case of high confining pressures (Fig. 7.3), the stress deviator difference between notched and unnotched specimens is 20 MPa. A relatively similar difference is also observed for the case of low to intermediate confining pressures between notched and unnotched specimens (*e.g.,* stress deviator difference of 20 MPa at 20 MPa

confining pressure and ranging from 10 MPa to 20 MPa at 50 MPa confining pressure, Fig. 7.2).

Figure 7.4 shows the yield stresses from notched and unnotched Bentheim sandstone specimens from *Tembe et al.* [2006]. The strength of the Bentheim sandstone (Fig. 7.4) is higher than that of the Vosges (Fig. 7.3). The stress deviator difference in notched and unnotched specimens is about 80 MPa, while this difference for the Vosges is about 20 MPa. Such differences can be probably attributed to the different grain shapes, the degree of cementation, or the feldspar removal from the Vosges sandstone (see Chapter 2, 4). Furthermore, recall that HR x-ray tomography images from the Bentheim and the Vosges sandstones (Fig. 4.4) have demonstrated that the former is denser and more homogeneous compared to the latter.

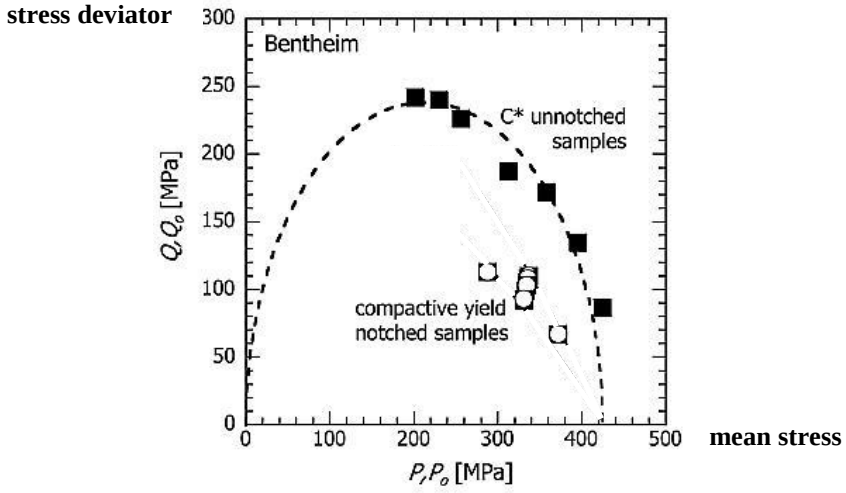

Fig. 7.4: Initial yield stresses for notched (solid squares) and unnotched (open squares) specimens of the Bentheim sandstone [*Tembe et al.*, 2006].

The experiments carried out in this work cannot indicate a unique shear yield surface and a unique cap. Some suggested yield surfaces were discussed in Figure 7.3. However, due to lack of experimental data, the connection between the shear yield surface and the cap remains still under consideration. From the given sets of yield stresses, it is likely that a vertex cap is more probable than a smooth transition; but this is still a speculation. Further

experiments are necessary to better describe the transition from shear faulting to shear enhanced compaction (and better define the region of the question mark shown in Fig. 7.3).

✓ **Deformation features: shear bands visualised by the experimental methods**

The common view of a shear band, which has already been reproduced at the laboratory scale by both biaxial and triaxial experiments (see Chapter 2), is of a band of deformed rock inclined to the major imposed principal stress direction by an angle that is mainly a function of material properties and the 'state' (*i.e.,* stress state and porosity). Typically, these inclination angles are observed to be 30 to 60 degrees (see Table 2.5). Furthermore, shear bands are characterised as zones of cracked and sheared grains, a few grains wide (see Table 2.5), in which the predominant displacement of grain pieces is parallel or sub-parallel to the band's long axis. Volumetric strain may be present and can be either dilatant or compactant [*Bésuelle et al.,* 2001].

In the present work, shear bands developed in cylindrical notched specimens of Vosges sandstone being subjected to triaxial compression under confining pressure ranging from 20 MPa to 50 MPa. The shear yield surface from notched specimens localised by shear bands was within the range of the yield surfaces from unnotched specimens observed by *Bésuelle* (1999 and Fig. 7.2). Non-destructive and destructive experimental methods (see Chapter 3) were used to capture the propagation and development of shear bands. These deformation bands were inclined to the major imposed principle stress in similar angles to those observed in the literature (see Table 2.5, Fig. 7.4).

AE hypocentre locations (syn-deformation) have suggested an *en-echelon* propagation of the AE clusters, which nucleated at the notches and in regions in between them (Fig. 4.15 and Fig. 5.1). Shear strain fields (DIC, pre-and post-mortem, Fig. 5.8 and Fig. 5.9) demonstrated higher shear strains in some parts of the shear band, which can be linked to both local temporal shearing, and cumulative shearing, which is to say that these regions might correspond to the initial shear bands clusters. HR post-mortem x-ray images have also resolved fractures along some shear bands (Fig. 5.29). It is speculated that propagation of shear bands should have been closely linked to textural heterogeneities of the host rock (local concentration of stresses), although this was not fully verified by the destructive techniques.

The 3D structure of shear bands (Chapter 5) suggested a non-planar structure, which can be attributed to propagation. Shears bands were typically characterised by higher shear strains; local compactant and dilatant strains were also identified inside their structure (Fig. 5.7). The interplay of compactant and dilatant volumetric strains inside the shear bands suggests more complex volumetric variations inside the same band and provides further insights into the grouping of dilatant and compactant shear bands suggested by [*Bésuelle et al.*, 2004, and also the x-ray images of the present study in Chapter 5].

Lower values of compactant or dilatant volumetric strains were observed in regions where particularly high shear strains were measured. Note that the volumetric strain fields for specimen Ve2 showed dilation near the notches and both dilation and compaction in the more central parts of the shear band (Fig. 5.7). When a single shear band was resolved by 3D-DIC, the compactant strains were located in the middle part, while dilatant strains were located near the notches. In places where two antithetic shear bands met, the compactant volumetric strains had higher values than the shear strains.

HR post-mortem x-ray tomography images indicated higher density (compacted) material inside the shear bands and captured some open fractures near the notches (Fig. 5.3, 5.21-5.27). Furthermore, the standard deviation of the grey-scale from x-ray images characterised the shear bands as zones of lower standard deviation values, which is linked to grain-scale deformation (grain fragmentation) and re-arrangement. Elastic wave methods (AEs and UT) indicated grain-scale activity (increased cumulative number of AEs either due to contact breakage or grain-breakage) and reduction in the elastic wave velocities, which is directly linked to damage mechanisms.

Finally, grain damage identified in thin sections in the shear bands takes the form of fractured quartz and feldspar grains together with delaminated micas.

✓ **Deformation features: compaction bands visualised by the experimental methods**

The common view of compaction bands, at the laboratory scale, is of a narrow zone-few grain wide-in which compaction takes place. Volume loss is taken to be a result of pore collapse, typically accomplished by grain breakage and movement of the grain fragments

into pores, so reducing porosity and also reducing total volume occupied by the compaction band.

Eichhubl et al. [2010] observed that naturally developed pure compaction bands, which formed normal to their major inferred principal stress direction, lack any shear component and have a non-planar wavy shape (in Aztec sandstone outcrops at the Valley of Fire, Nevada). The shear-enhanced compaction bands-observed at the same area- are oriented at 38 to 53 degrees to the major principal stress direction (oblique) and have developed a shear component. Both deformation bands present grain damage restricted to the grain contacts.

In the present work, the onset and propagation of deformation bands in cylindrical notched specimens of Vosges sandstone, which were subjected to triaxial compression under confining pressure from 130 MPa to 190 MPa, have been studied by means of non-destructive and destructive experimental methods (see Chapter 3). Specimens localised by these deformation bands had yield stresses on yield surface with negative slope (cap, Fig. 7.3). They were characterised by high inclination angle towards the major imposed principal stress (Table 7.1, Fig. 7.6); these values are consistent with those observed in the literature (see Table 2.5). Furthermore, these deformation bands were characterised by high compactant volumetric strains together with shear strains. The shear strain component is expected because of the oblique inclination angle of these bands. It can be argued that some of these deformation bands present common characteristics to the so-called shear-enhanced compaction bands in the Valley of Fire. However, the grain damage in the experiments reported here was not restricted solely to the grain contacts [like in *Eichhubl et al.*, 2010].

Multiple discrete shear-enhanced compaction bands developed under 130 MPa and 160 MPa, while rather diffuse compaction bands developed under 190 MPa. The latter were relatively longer (traversing a bigger part of the specimen). Both discrete and diffuse bands had a rather complex geometry. Their inclination angle varies with confining pressure (Fig. 7.6).

Compaction bands and shear-enhanced compaction bands were identified as zones of concentration of AE activity, which is linked to breakage of grain-cement bonds or of the grain itself. UT showed the localisation region as a zone of low velocity (and also low transmission amplitude, due to high attenuation), which suggests significant occurrence of

grain damage, as opposed to porosity reduction, which would give a velocity increase. In x-ray tomography, these deformation bands appear as zones of lower standard deviation values (calculated on the grey-scale of the HR raw x-ray tomography images), indicating a reduction in grain size via grain crushing to below the voxel size, and thus a homogenisation of the image. 3D-volumetric DIC measured compactant volumetric strains inside the shear enhanced compaction bands, which was taken as evidence of porosity reduction, together with shear strains. Lower volumetric and shear strains were measured outside the bands. Grain breakage of quartz and feldspars and delaminated micas were identified in thin sections inside these deformation bands together with pore collapse and local grain crushing. Porosity calculations indicated porosity values from 3% to 5% in the centre of the band (one to two grains) that increased when moving far from the centre of the band.

The locations of AE events recorded during the formation of compaction bands and shear-enhanced compaction bands showed a zone of localised intense AE activity, initiating near the notches and evolving toward the specimen centre. AE hypocentre locations indicated that existing bands could grow or deactivate and new deformation bands initiated (from possible textural heterogeneities inside the specimen). Higher values of shear strains and smaller compactant or dilatant strains were measured at the notches, while high compactant and smaller shear strains were measured at the propagating tip of these bands.

Increasing axial strain resulted in broader shear-enhanced compaction bands (*e.g.*, increase in damage) and higher compactant and shear strains. Furthermore, the difference in the ratio of volumetric to shear strains became more pronounced (*e.g.,* see the strains measured in specimens Ve4 and Ve6). Such observation indicates that both compaction and shearing are activated during the early stage of compaction band formation, with compaction being more pronounced. As the strain level increases, compaction becomes much more active when compared to shearing.

Compaction bands and shear-enhanced compaction bands in Vosges sandstone could not have been resolved by the post-mortem HR x-ray images without the calculation of the standard deviation of the grey-scale, while this was not the case for the deformation bands developed in Bentheim sandstone. This can be possibly attributed to the texture of grains, the mineralogy and the degree of cementation of the two sandstones. The detection of

compaction bands (by means of x-rays) in well sorted sandstones with round-shaped grains (*e.g.*, Bentheim) is easier compared to moderately sorted sandstones, with sub-angular shape grains, which are bound together with cement (*e.g.*, the Vosges). In the former case, compaction bands appear as a heterogeneous region inside a rather homogeneous matrix (compacted material), while in the latter case, the matrix is relatively less homogeneous, thus the heterogeneity of the compaction band is not easily distinguished.

- ✓ **Which the actual similarities and differences between the shear and compaction bands are**

Eichhubl et al. [2010] made a comparison at the field-scale between compactant shear bands and shear-enhanced compaction bands, showing that the former present a much larger macroscopic shear offset and a higher degree of cataclastic deformation. At the laboratory scale, shear and compaction bands appear to constitute different failure modes (*e.g.*, different stress states (see Chapter 2) that lead to different yield stress and macroscopic behaviour, and dipping angles). During this thesis, it was demonstrated that their formation involves similar micromechanical processes. In the grain-scale, both shear and shear-enhanced or compaction bands are characterised by grain bonds' fracturing (intense) and inter- and intra-granular cracking, which indicated brittle mechanisms that dissipate a significant amount of inelastic energy (*e.g.*, recorded by AEs). Shearing is related to grain sliding and grain fragmentation, which leads to further grain re-arrangement. Compaction is related to pore collapse and grain fracturing or grain crushing and movement of fractured grain particles, which potentially has a shearing component. With increasing axial strain values intense grain fracturing and grain-crushing leads to grain fragmentation, grain-size reduction, and comminution of the fragments, which are characteristics of cataclastic deformation (see for instance Chapter 5 and 6).

The quantification of strain fields (DIC), density changes (x-rays), and ultrasonic velocities (AEs, UT) provided evidence of both cracking and porosity decrease mechanisms taking place in both types of deformation bands. However, the use of full-field methods demonstrated that these similar mechanisms have differences in the order of occurrence and in their relative proportions with time.

3D-volumetric DIC have shown that inside shear bands, shear strain is more pronounced than is volume change. That is larger shear strains develop inside the compactant shear bands than in the shear enhanced-compaction band, while in shear enhanced-compaction bands volumetric strain magnitudes exceed shear strain magnitudes. More detailed analysis of the kinematics of the phenomena is required to better distinguish the deformation modes including analysis of locally-normal and-tangential components of displacements and displacement gradients, as suggested by *Bésuelle* [2001]. This 3D-DIC extension requires first defining the local trajectory of the localization features in 3D and then resolving the normal and tangential displacements and displacement gradient components (to be done in the future).

Fortin et al. [2009] carried out AE source analysis for the Bleurswiller sandstone and demonstrated that shear and compaction bands are characterised by different dominant grain-scale mechanisms (like what DIC has demonstrated in the present study, *i.e.*, different proportions of similar grain-scale mechanisms). In particular, *Fortin et al.* [2009] found that shear bands have a higher ratio of shear-type to pore-collapse events as compared to compaction bands (~1.25 versus ~0.4). However, a preliminary source-mechanisms analysis, based on the polarity method, for specimen Ve2 (Table 4.2), which developed shear bands, indicated pore collapse to be the dominant mechanism, since the great majority of the AE events were C-type. Initially, the number of S-type events was almost two times smaller than the C-type events, but this reduced much by the end of the experiment. Pore collapse was also the dominant mechanism in specimens Ve4 and Ve6 (Table 4.2), which developed shear-enhanced compaction bands. This inconsistency with what is reported in the literature could be possibly further elucidated by using a moment tensor analysis instead of the polarity method, or could be attributed to the different characteristics of the sandstones (mineralogy, cement, pore size, etc.), thought the latter seems less likely.

Both shear bands and shear enhanced-compaction bands in the Vosges sandstone were identified via their low values of standard deviation of the grey-scale values from HR x-ray images, which indicated similar grey-scale values inside the deformation bands and relatively variable values outside the bands. When only the raw x-ray tomography images were used shear bands were visualised as regions of higher material density (see Appendix B for the

visualisation range), but shear-enhanced compaction bands could not be visualised at all. Recall that the resolution of the x-ray images was of 30 μm voxel size, which possibly indicates that density variations in shear bands had size wider than 30 μm, and therefore could be resolved. However, density variations in shear enhanced compaction bands had a size lower that 30 μm, and thus could not be resolved. This could not be fully explained, since similar mechanisms were identified in these deformation features. A possible comparison of the grey-scale histograms from the same intact and deformed specimen at the same regions might further elucidate this issue, which for the time being remains an observation.

The 3D geometry of all deformation bands, as it was resolved by the full-field methods, was non-planar. Furthermore, the bands also varied in thickness.

- ✓ **The role of the notch (structural heterogeneity)**

In this work, notches with two different geometries were machined on the surface of the Vosges sandstone specimen (see Chapter 4). The notch was principally used to encourage the onset and propagation of the deformation bands in the central region of the specimens, so as to facilitate the use of the experimental methods.

The presence of a notch, which is an induced structural heterogeneity in the material, results in the enhancement of the local stresses and induces damage at lower stress values activating a number of failure modes (at different stress states) [*Tembe et al*., 2006]. Lower critical stresses in terms of the p-q plane were also observed by the present study (see Fig. 7.2, 7.3).

For the case of low to intermediate confining pressures, shear bands of different number and dip developed in the Vosges specimens. These dip angles were consistent with the observed and the theoretical values suggested by *Bésuelle* [2001]. Recall that the positioning of the notches was tuned to band dips for different confining pressures (Fig. 4.6). However, the 3D structure of the shear bands (resolved by the full-field methods) revealed a wider angle range, which changed with different axial strain achieved. Furthermore, shear bands were resolved as non-planar features.

Figure 7.5 illustrates the maximum and minimum dip angles from shear bands that developed at 50 MPa confining pressure visualised by post-mortem HR x-ray tomography images plotted against the maximum axial strain after the peak. These deformation bands, which initiated at the notches, propagated either towards the top and bottom edges of the specimens (*e.g.*, in specimen VLR0 and partially in VEC4) or between the notches (the remainders). The relative error of the mean dip angle compared with the theoretically predicted value ranges from 1.2% for specimen VEC4 to 15% for VEC5. Additionally the mean dip reaches the theoretical angle with increasing axial strain (with an exception of the VEC5). However, the range of the maximum and minimum dip values does not develop a trend with increasing axial (after the peak) strain. Therefore, it could be speculated that the dip could have been influenced also by other factors, such as possible local geometrical imperfection of notch or local textural heterogeneities, which might have slightly altered the local orientation of the deformation band. With increasing axial strain, the mean dip develops values closer to the values defined by the confining pressure (the theoretical values).

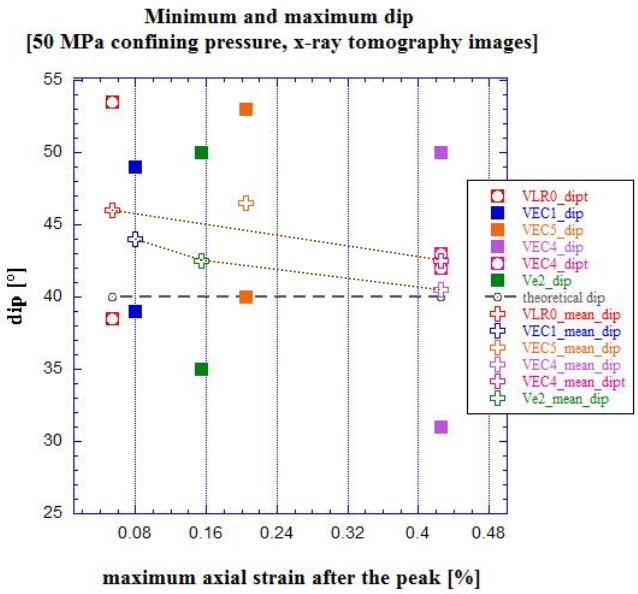

Fig. 7.5: Dip angles measured by post-mortem HR x-ray tomography images (30 µm voxel-size resolution) for notched specimens that were subjected to 50 MPa confining pressure and were taken to different axial strains. Solid squares illustrate the minimum and maximum dips from shear bands which propagated between the notches, while open squares illustrate those from bands which propagated towards the edges of the specimens. Crosses represent the mean values from each dip range.

Recall that the shear bands visualised from the AE hypocentre locations of specimen Ve2 had dips of 40° and 50° (Fig. 5.1). Additionally, mica flakes were dipping at 45° to 50° in a shear band shown in a single thin section from the VEC1 (Fig. 5.33c and 5.33d) and 45° from another thin section of the VEC4 (Fig. 5.37).

For the case of higher confining pressure (*e.g.*, from 130 to 190 MPa), it is argued that the notch controlled the inclination angle towards the major imposed principle stress of the shear enhanced compaction bands. In regions far from the notches the inclination was influenced by the applied confining pressure and possible local textural heterogeneities. For instance at 190 MPa confining pressure the deformation bands were almost normal to the major imposed principle stress. Table 7.1 illustrates the angle of the deformation bands, which developed under the higher confining pressures (see Table 4.2), measured by the different experimental methods, in regions close to and far from the notches.

Table 7.1: Inclination angles (and dip) from deformation bands that developed in specimens loaded under relatively high confining pressures (see Table 4.2), measured via different experimental methods.

specimen's name	inclination angle	mean inclination angle/dip far from the notch	mean inclination angle/dip at the notch	Experimental Method	Size of sub-volumes and spacing
Ve4	52°-84°		62°/28°	stand.deviation (x-rays)	600x600x600μm^3, 150μm
Ve4			66°/24°	DIC strain maps	600x600x600μm^3, 600μm
Ve4			49°/41°	porosity calculations	676x676x676μm^3, 135 μm
Ve6	53°-90°	67°/23°	63°/27°	stand.deviation (x-rays)	600x600x600μm^3, 150μm
Ve5	55°-83°	68°/22°	the lower	stand.deviation (x-rays)	600x600x600μm^3, 150μm
Ve7	58°-88°	70°/20° + many more horizontal		stand.deviation (x-rays)	600x600x600μm^3, 150μm
Ve7	62°-82°	68°/22° + many more horizontal	45°-53°/ 45°-37°	DIC strain maps	600x600x600μm^3, 600μm
Ve1	60°- 75°	60°- 75°/ 30°- 15°	No notch	stand.deviation (x-rays)	600x600x600μm^3, 150μm

Note that the angles measured by different methods are not alike (for the same specimen and the same position), since each method is sensitive to different parameters.

Figure 7.6 presents the range of the deformation bands' dip, shown in Table 7.1, versus the applied confining pressure. In general, with increasing confining pressure the dip decreases (with an exception of specimen Ve5), which is to say that the inclination angle towards the major imposed principle stress is confining pressure dependant (similar to what observed in other sandstones, see Chapter 2). Specimen Ve6, which has undergone high axial strain (Table 4.2), presents deformation bands that are almost horizontal (lower boundary). Furthermore, the range of the dipping angle is smaller in specimens with no notches compared to those with notches (specimens Ve1 and Ve5).

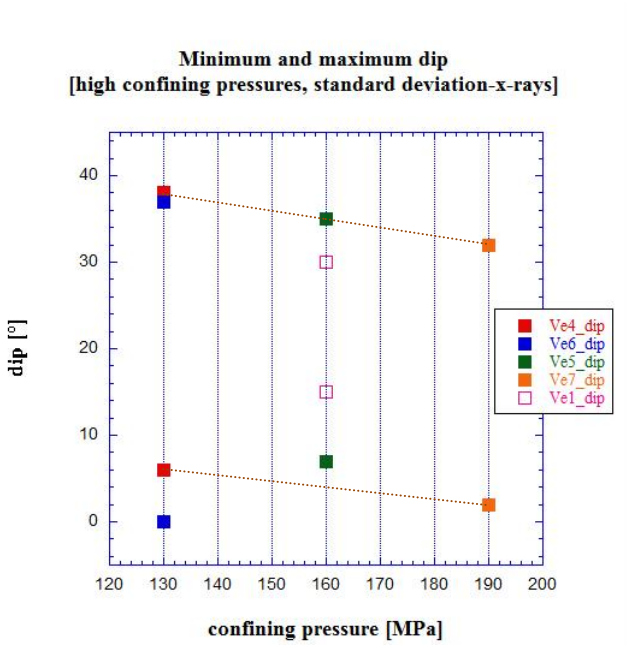

Fig. 7.6: Dip angles measured by standard deviation of the grey-scale values slices from post-mortem HR x-ray tomography images (30 µm voxel-size resolution) for notched and unnotched specimens that were subjected to 130 MPa to 190 MPa confining pressure and were taken to different axial strains. Solid squares illustrate the minimum and maximum dips from shear enhanced compaction bands in notched specimens, while open squares illustrate those from unnotched specimens.

Open fractures initiating from the tip of the notch were apparent in both HR post-mortem x-ray images and thin sections. These fractures were possibly caused during the unloading of the specimens. The width of the fractures was relatively small compared to the width of the

deformation band (thin sections and x-rays), and their length increased with increasing axial strain (thin sections). Recall for instance that more and longer cracks were identified at the tip of the notch of specimens VEC4 compared to those in the VEC5 (see Table 4.2).
Notches have also played a role in the number of the developed deformation bands. In particular, two shear bands –one from the top and the other from the bottom notch- were formed in specimens loaded under relatively low confining pressure, while a single shear band was resolved close to the surface of the specimens and far from the flattened surfaces (where the notches were machined).

✓ Characteristics of the deformation bands

The inclination angle towards the major imposed principle stress and the width of the deformation band are two important characteristics. The former was discussed in the section of the notch impact. Herein, some conclusions on the width of the deformation bands are drawn.

Table 2.7 (Chapter 2) presented the width of deformation bands, which developed in laboratory-deformed sandstone specimens, measured by different experimental methods. In general, the width of shear bands ranges between two to four grains, although wider band have also been observed (Table 2.7). For the case of compaction bands, the width range has similar values (Table 2.7). *Baud et al.* [2004] suggested a classification of the deformation bands based on their width (e.g., discrete and diffuse when the width is equal to three or more intact grain sizes, respectively).

This study presents the width of different deformation bands, as this was measured in images coming from different experimental methods. The width values are consistent with these reported in the literature (Table 2.7). However, it should be underlined that the measured width of the resolved deformation band is influenced by the resolution of the applied experimental method. Furthermore, the width is indicative of the observed physical parameter; therefore, slightly different widths might be measured from different representations of the same deformation band. Recall that the shear strain width from compaction bands was wider than the volumetric strain width (Fig. 6.11-6.12, 6.18, 6.27, 6.29, 6.32-6.33), which possibly suggests that shearing took also place close to the centre of

the band, which was highly compacted (and sheared). The higher shear strain values in the heart of the band might be linked to the grain fragment movements, which filled some of the pore space.

Table 7.2 presents the width of the observed deformation bands from this study. For instance, in specimen Ve4 very low porosity was measured on a width of one to two intact grain-sizes (3-5%) and slightly bigger on a width of one to four intact grain-sizes (7-8%), while relatively homogeneous regions inside the bands were identified in one to three grain-sizes. In both shear and shear enhanced compaction bands, the width of the deformation band increased with increasing axial strain values (see in Table 7.2 specimens VEC1 and VEC4-thin sections and specimens Ve4 and Ve6-standard deviation of the grey-scale values from post-mortem HR x-ray images), which indicates that the damage is broader. For the case of shear bands, this was also observed on the ultrasonic velocity fields (UT, Fig. 5.17) and post-mortem HR x-ray tomography images (Fig. 5.21-5.27).

Table 7.2: Widths deformation bands in different specimens measured by different experimental methods.

specimen's name	type of deformation bands	width of the deformation band	Experimental Method	size of sub-volumes and spacing
Ve2	shear band	300-810 μm	DIC	300x300x300μm³, 300 μm
VEC1	shear band	490-600 μm	thin sections	---
VEC4	shear band	1000 μm	thin sections	---
Ve4	shear enhanced compaction band	284-622 μm (n=3-5%) 310-852 μm (n=7-8%) rest of core (n=9-14%)	porosity calculations	676x676x676μm³, 135 μm,
Ve4	shear enhanced compaction band	300-900 μm	stand.deviation (x-rays)	600x600x600μm³, 150 μm
Ve6	shear enhanced compaction band	300-1500 μm	stand.deviation (x-rays)	600x600x600μm³, 150 μm

7.2 Perspectives and future work

In this work a combination of different methods was applied to study the localised deformation features in the Vosges sandstone, which developed under different stress and strain levels. Herein some perspectives are presented on the one hand, in terms of the experimental methods, and on the other hand in terms of further experiments.

UT:

- In both shear and compaction bands oriented cracks were observed by the microstrucutral observations, which indicate certain anisotropy of the laboratory deformed sandstone; this was also observed from the zero-offset velocity profile. However, an isotropic velocity model was assumed for the UT. The application of an anisotropic velocity model might ameliorate the resolution of the band.
- A regular grid was applied to the calculations of the ultrasonic velocity field. A refinement of the size of the grid or even the local use of a different geometry grid (*e.g.*, triangles) is suggested in places where the localised deformation bands occurred in order to ameliorate the resolution of such features.
- Straight rays were used as a ray path algorithm. This assumption is theoretically acceptable if the size of the anomaly is bigger than the wavelength and the velocity variations are smaller than 20-30% [*Santamarina and Fratta*, 2005]. This, to a certain extent was fine for the presented velocity fields. However, curved rays might fit better the physical reality.
- Ultrasonic velocity measurements, recorded together with the AE events during the experiments could be used for in-situ UT. A 3D ray-tracing algorithm has to be used; however, it is quite ambiguous if the ray-tracing is dense enough to resolve the deformation features.

AE:

- A multi-layer velocity model can be used as an initial velocity model, instead of the five-layer velocity model used here.
- Bent ray-paths can be incorporated in the AE location algorithm, instead of straight ray-tracing.
- Further understanding of the relation between the kinematics and strain fields with the source mechanisms has to be gained. The polarity analysis of the source mechanisms has not been very elucidating, for the time being; further investigation using moment tensor analysis is suggested.

X-ray tomography:

- A combined application of in situ measurements is suggested. For instance, x-ray CT may be well coupled with UT or AE recording. Such experiments demand also the use of appropriate experimental set-ups.
- Further investigation of the characteristics of the deformation bands on the micro-scale could be acquired by the analysis of the porosity fields from more small deformed cored coupled with the analysis of grain kinematics, grain contacts and preferential grain orientations.

3D-DIC:

- Definition of the local trajectory of the localization features in 3D and then resolving the normal and tangential displacements and displacement gradient components is

suggested, in order to get a more detailed analysis of the kinematics and better distinguish the deformation modes (including analysis of locally normal and tangential components of displacements and displacement gradients, as suggested by *Bésuelle* [2001]).

- Results from a 'continuum' DIC analysis can only provide part of the story. It is clear that the deformation behaviour of granular materials also involves significant rotations of individual grains.

Experiments:

- A relatively large number of data has been acquired, which demands possibly further elaboration. Additionally, more experiments should be carried out in order to better define the transition of brittle faulting to cataclastic flow.
- The orientation and the onset of localisation can calibrate constitutive models, however further elaboration of the mechanical data might be important.
- Further investigation of the role of other structural heterogeneities (*e.g.*, an inclusion) on the onset and propagation of the localised deformation bands is suggested.
- The same experimental set-ups can be expanded to different sandstone specimens.

List of References

A

Ando, E., Hall, S.A., Viggiani, G., Desrues, J., Besuelle, P., 2010. Analysing the evolution of grains and contacts in sand under load, Proceedings of the International Symposeum of Geomechanics and Geotechnics: From Micro to Macro, IS-Shanghai, Vol.1, 375-379.

Antonellini, M. & Aydin, A., 1994. Effects of faulting on fluid flow in porous sandstones: petrophysical properties: AAPG Bulletin, 78, 355-377.

Arns, J.-Y., Arns, C.H., Sheppard, A.P., Sok, R.M., Knackstedt, M.A., Pinczewski, W.V., 2003. Relative permeability from tomographic images; effect of correlated heterogeneity, Journal of Petroleum Science and Engineering, 39, 247-259.

Aydin, A., 1978. Small faults formed as deformation bands in sandstone, Pure and Applied Geophysics, 116, 913-930.

Aydin, A., Borja, R., Eichhubl, P., 2006. Geological and mathematical framework for failure modes in granular rocks, Journal of Strucutral Geology, 28, 83-93.

Aydin, A., Ahmadov, R., 2009. Bed-parallel compaction bands in Aeolian sandstone: Their identification, characterization and implications, Tectonophysics 479, 277-284.

B

Baud, P., Klein, E., Wong, T.-F., 2004. Compaction localisation in porous sandstones: spatial evolution of damage and acoustic emission activity, Journal of Structural Geology, 26, 603-624.

Baruchel, J., Buffiere, J.Y., Maire, E., Merle, P., Peix, G., 2000. X-ray tomography in material science, Hermes Science Publications, Paris, pp. 1-205.

Bay, B.K., Smith, T.S., Fyhrie, D.P., Saad, M., 1999. Digital Volume Correlation: Three-dimensional Strain Mapping Using X-ray Tomography, Experimental Mechanics, Vo. 39, pp. 217-226.

Berryman, J.G., 1990. Lecture Notes on Non-linear Inversion and Tomography, I Borehole Seismic Tomography, Earth Resource Laboratory of Technology, Massachusetts Institute of Technology.

Bésuelle, P., 1999. Déformation et Rupture dans les roches tenders et les sols indures: comportement homogène et localisation, Université Joseph Fourier, Grenoble, pp. 1-374.

Bésuelle, P., Desrues, J., Raynaud, S., 2000. Experimental characterisation of the localisation phenomenon inside a Vosges sandstone in a triaxial cell, International Journal of Rock Mechanics and Mining Science, 37, 1223-1237.

Bésuelle, P., 2001. Evolution of strain localisation with stress in a sandstone: brittle to semi-brittle regimes, Phys.Chem. Earth (A), Vol. 26, No. 1-2, pp.101-106.

Bésuelle, P., Baud, P., Wong, T.-F., 2003. Failure mode and spatial distribution of damage in Rothbach sandstone in the brittle-ductile transition, Pure and applied geophysics, 160, 851-868.

Bésuelle, P., 2004. X-ray CT observations of strain localization and failure in two porous sandstones, in: Proc. 1st Int. Workshop X-ray CT for Geomaterials, *Soils, Concrete, Rock*, GeoX 2003, Kumamoto, Japan, November 6-7 2003, Otani, J. and Obara Y. Eds., Balkema, pp. 287-292.

Bésuelle P. and Rudnicki J.W., 2004, Localization: Shear Bands and Compaction bands. In Mechanics of Fluid-Saturated Rocks. Guéguen Y. and Boutéca M. edts, pp. 219-321, Academic Press.

C

Challa, V. and Issen, K.A., 2004. Conditions for localised compaction of porous granular material, Journal of Engineering Mechanics, 130, pp. 1089-1097.

Chapman, C.H., and Pratt, R.G., 1992. Traveltime tomography in anisotropic media-I. Theory, Geophys. J. Int., 109, pp. 1-19.

Charalampidou, E.M., Combe, G., Viggiani, G., Lannier, J., 2009. Mechanical behaviour of mixtures of circular and rectangular 2D particles, AIP Conference Proceeding, POWDERS AND GRAINS 2009: PROCEEDINGS OF THE 6TH INTERNATIONAL CONFERENCE ON MICROMECHANICS OF GRANULAR MEDIA, Vol. 1145, pp. 821-824, doi:10.1063/1.3180054.

Charalampidou, E.-M., Hall, S.A., Stanchits, S., Lewis, H., Viggiani, G., 2010a. Characterization of shear and compaction bands in sandstone using X-ray tomography and digital image analysis. In: Alshibli, H.A., Reed, A. (Eds.), Proc. 3rd International Workshop on X-Ray CT for Geomaterials, GEOX 2010. ISTE Pub, Orleans, pp. 59–66.

Charalampidou, E.-M., Hall, S.A., Stanchits, S., Lewis, H., Viggiani, G., 2010b. Characterization of shear and compaction bands in a porous sandstone deformed under triaxial compression, Tectonophysics Special volume of the 8th Euroconference of Rock Physics and Rock mechanics, doi:10.1016/j.tecto.2010.09.032.

Charalampidou, E.M., Hall, S.A., Stanchits, S., Viggiani, g., Lewis, H., 2010c. Experimental characterisation of shear and compaction band mechanisms in porous sandstone by a combination of AE and 3D-DIC, EPJ Web of Conferences**,** Vol.6, ICEM 14 – 14th International Conference on Experimental Mechanics, DOI: 10.1051/epjconf/20100622009.

Chemenda, A.I., 2011. Origin of compaction bands: Anti-crack or constitutive instability? , Tectonophysics, 499, 156-164.

Coll, C., 2005. Endommagement des roches argileuses et perméabilité induite au voisinage d'ouvrages souterrains, Université Joseph Fourier, Grenoble, pp. 1-265.

D

Daigle, M., Fratta, D., Wang, L.B., 2005. Ultrasonic and x-ray tomographic imaging of highly contracting inclusions in concrete specimens, GeoFrontier Conference, Austin, Texas.

Dautriat, J., Bornert, M., Gland, N., Dimanov, A., Raphanel, J., 2010. Localised deformation induced by heterogeneities in porous carbonate analysed by multi-scale digital image correlation, Tectonophysics, doi : 10.1016/j.tecto.2010.09.025.

Debski, W., 2002. Imaging rock structures using acoustic waves: methods and algorithms, In: Seismogenic Process Monitoring, Ogasawara, H., Yanagidani, T, Ando, M. (eds), Balkema, pp.309-326.

Desrues J., Chambon R., Mokni M., Mazerolle F., 1996. Void ratio evolution inside shear bands in triaxial sand specimens studied by computed tomography, Géotechnique vol.46 No 3, pp. 529-46.

DiGiovanni, A.A., Fredrich, J.T., Holcomb, D.J., Olsson, W.A., 2000. Micromechanics of compaction in an analogue reservoir sandstone,

Du Bernard, X., Eichhubl, P., Aydin, A., 2002. Dilation bands, a new form of localised failure in granular media, Geophysical Research Letters, 29 (24), 2176, doi:10.1029/2002GL015966.

E

Eichhubl, P., Hooker, J.N., Laubach, S.E., 2010. Pure and shear-enhanced compaction bands in Aztec Sandstone, Journal of Structural Geology (article in press), doi: 10.1016/j.jsg.2010.02.004, v. 32, no. 12, p. 1873-1886.

El Bied, A., Sulem, J., Martineau, F., 2002. Microstructure of shear zones in Fontainebleau Sandstone, International Journal of Rock Mechanics and Mining Sciences, 39, 917-932.

F

Fortin, J., Schubnel, A., Guéguen, Y., 2005. Elastic wave velocities and permeability evolution during compaction of Bleurswiller sandstone, International Journal of Rock Mechanics and Mining Science, 42, 873-889.

Fortin, J., Stanchits, S., Dresen, G., Guéguen, Y., 2006. Acoustic emission and velocities associated with the formation of compaction bands in sandstones, Journal of Geophysical Research, Vol. 111, B10203, 16 pp, doi: 10.1029/2005JB003854.

Fortin, J., Guéguen, Y., Schubnel, A., 2007. Effects of pore collapse and grain crushing on ultrasonic velocities and Vp/Vs, Journal of Geophysical Research, Vol. 112, B08207, 16 pp, doi: 10.1029/2005JB004005.

Fortin, J., 2008---personal communication.

Fortin, J., Stanchits, S., Dresen, G., Gueguen, Y.. 2009, Acoustic Emissions monitoring during inelastic deformation of porous sandstones: Comparison of three modes of deformation, Pure and applied geophysics, 166, 823-841.

Fonseca, J., O`Sullivan, C., Coop, M.R., 2010. Quantitative Description of Grain Contacts in a Locked Sand, In: Alshibli, H.A., Reed, A. (Eds.), Proc. 3rd International Workshop on X-Ray CT for Geomaterials, GEOX 2010. ISTE Pub, Orleans, pp. 17-25.

Fossen, H., Schultz, R.A., Shipton, Z.K., Mair, K., 2007. Deformation bands in sandstone-a review. Journal of the Geological Society, Vol. 164, No. 4, p. 755-769.

Fredrich, J.T., Greaves, K.H., Martin, J.W., 1993. Pore geometry and transport properties of Fontainebleau Sandstone, International Journal of Rock Mechanics, Mining Science & Geomechanics Abstr., Vol. 20, No. 7, pp. 691-697.

G

Gibson, R.G., 1998. Physical character and fluid-flow properties of sandstone-derived fault zones, in: Coward, M. P., Daltaban, T.S. & Johnson, H., (eds) structural Geology in Reservoir Characterisation, Geological Society, London, special Publications, 127, 83-97.

Graham, C.C., Stanchits, S., Main, I.G., Dresen, G., 2010. Comparison of polarity and moment tensor inversion methods for source analysis of acoustic emission data, International Journal of Rock Mechanics and Mining Sciences, 47, 161-169.

Gubbins, D., 2004. Time Series Analysis and Inverse Theory for Geophysicists, Cambridge University Press, pp. 1-255.

Guéguen, Y., Sarout, J., Fortin, J., Schubnel, A., 2009. Cracks in porous rocks: Tiny defects, strong effects, The leading edge, Vol. 28, No. 1, pp. 40-47.

H

Haied, A. and Kondo, D., 1997. Strain localisation in Fontainebleau Sandstone: Macroscopic and Microscopic investigations, International Journal of Rock Mechanics and Mining Sciences, 34:3-4, Paper No 161.

Haimson, B. and Lee, H., 2004. Borehole breakouts and compaction bands in two high porosity sandstones, International Journal of Rock Mechanics and Mining Science, 41, pp. 287-301.

Hall, S.A., 2006. A methodology for 7D warping and deformation monitoring using Time-lapse seismic data, Geophysics 71, O21–O31.

Hall, S.A., Lenoir, N., Viggiani, G., Desrues, J., and Bésuelle P., 2009. Strain localisation in sand under triaxial loading: characterisation by x-ray micro tomography and 3D digital image correlation, Proceedings of the 1st International Symposium on Computational Geomechanics (ComGeo I), Juan-les-Pins, Cote d'Azur, France, April 29 – May 1st, 2009.

Hall, S.A., Muir Wood, D., Ibraim, E., Viggiani, G., 2010a. Localised deformation patterning in 2D granular materials revealed by digital image correlation, Granular Matter, 12:1-14, DOI: 10.1007/s10035-009-0155-1.

Hall, S.A., Bornert M., Desrues J., Pannier Y., Lenoir N., Viggiani, G., Bésuelle, P., 2010b. Discrete and Continuum analysis of localised deformation in sand using X-ray micro CT and Volumetric Digital Image Correlation, Géotechnique, 60, 315 –322.

Hall, S.A., Lenoir, N., Viggiani, G., Besuelle, P., Desrues, J., 2010c. Characterisation of the evolving grain-scale structure in a sand deforming under triaxial compression, In: Alshibli, H.A., Reed, A. (Eds.), Proc. 3rd International Workshop on X-Ray CT for Geomaterials, GEOX 2010. ISTE Pub, Orleans, pp. 34-42.

Hill, R. E., 1989. Analysis of deformation bands in the Aztec Sandstone, Valley of Fire State Park, Nevada, Master's thesis, Univ. of Nev., Las Vegas.

Holcomb, D., Rudnicki, J.W., Issen, K., Sternolf, K., 2007. Compaction localisation in the Earth and the laboratory: state of research and research directions, Acta Geotechnica, 2, 1-15.

Hormati, A., Jovanovic, I., Roz, O., Vetterli, M., 2010. Robust Ultrasound travel-time tomography using the bent ray model, Proceedings of the SPIE Medical Imaging, LCAV-CONF-2010-001.

I

Issen, K. A., & Rudnicki, J.W., 2000. Conditions of compaction bands in porous rocks, Journal of Geophysical Research, 105 (B9), 21529-21536.

Issen K.A., & Rudnicki, J.W., 2001. Theory of compaction Bands in Porous Rocks, Phys. Chem. Earth (A), Vol. 26, No. 1-2, pp. 95-100.

Issen, K.A., 2002. The influence of constitutive models on localization conditions for porous rocks, Engineering Fracture Mechanics, 69, 1891-1906.

J

Johnson, W.B., 2004. Design and Testing of a Laboratory Ultrasonic Data Acquisition System for Tomography, Master of Science Thesis in Mining and Minerals Engineering, Virginia Polytechnic Institute and State University, pp. 1-108.

K

Katsaga, T., Sherwood, E. G., Collins, M. P., Young, R. P., 2008. Acoustic emission imaging of shear failure in large reinforced concrete structures, International Journal of Fracture, 148(1): 29-45.

Katsman, R., Aharonov, E., 2006. A study of compaction bands originating from cracks, notches and compacted defects, Journal of Structural Geology, 28, 508-518.

Kerr, P.F., 1959. Optical mineralogy, 3rd edition, McGraw-Hill Book Company, INC, pp.1-442.

Ketcham, R.A. & Carlson, W.D., 2001. Acquisition and interpretation of X-ray computed tomography imagery: applications to the geosciences, Computers & Geosciences, 27, 381-400.

Klein, E., Baud, P., Reuschle, T., Wong, T.-F., 2001. Mechanical behaviour and failure mode of Bentheim Sandstone under triaxial compression, Phys. Chem. Earth (A), Vol. 26, No. 1-2, pp. 21-25.

Knackstedt, M.A., Lathan, S., Madadi, M., Sheppard, A., Varslot, T., 2009. Digital rock physics: 3D imaging of core material and correlations to acoustic and flow properties, The Leading Edge, Special section: Rock Physics, 28-33.

Kurz, J.K., Grosse, C.U., Reinhardt, H.-W., 2005. Strategies for reliable automatic onset time picking of acoustic emissions and ultrasonic signal in concrete, Ultrasonics, 43, 538-546.

L

Labuz, J. F., and Bridle, J. M., 1993. Reducing Frictional Constrain in Compression Testing through Lubrication, International Journal of Rock Mechanics and Mining Sciences, 20, 451-455.

Labuz, J. F., Cattaneo, S., Chen, L.-H., 2003. Acoustic emission at failure in quasi-brittle materials, Construction and Building Materials, 15, 225-233.

Lei, X., Kusunose, K., Rao, M., Nishizawa, O., Satoh, T., 2000. Quasi-static fault growth and cracking in homogeneous brittle rock under triaxial compression using acoustic emission monitoring, J. Geophysical Research, 105, (B3), 6127-6139.

Lenoir, N., Bornert, M., Desrues, J., Besuelle, P., Viggiani, G., 2007. Volumetric Digital Image Correlation applied to X-ray Microtomography images from Triaxial compression tests on Argillaceous rocks, Strain, 43, 193-205.

Leonard, M. and Kennett, B.L.N., 1999. Multi-component autoregressive techniques for the analysis of seismograms, Phys. Earth Planet. Int. 113 (1-4), 247.

Lin, Q., Fakhimi, A., Haggarty, M., Labuz, J.F., 2009. Initiation of tensile and mixed-mode fractures in sandstone, International Journal of Rock Mechanics and Mining Sciences, 46, 489-497.

Lockner, D., Byerlee, J., 1978. Development of Fracture Planes during Creep in Granite, Proceeding 2nd Conference on Acoustic Emissions/ Microseismic Activity in Geological Structures and Materials, Hardy, H.R., Leighton, F.W., (eds), Trans Tech Publications, The Pennsylvania State University, November 13-15, pp. 11-25.

Lockner, D.A., Byerlee, J.D., Kuksenko, V., Ponomarev, A., Sidorin, A., 1991. Quasi-static fault growth and shear fracture energy in granite, Nature, No. 6313, Vol. 350, pp. 39-42.

Lockner, D.A., Byerlee, J.D., Kuksenko, V., Ponomarev, A., Sidorin, A., 1992. Observation from quasi-static fault growth from acoustic emissions, In: Evans, B., Wong, T.-F., (Eds), Fault mechanics and transport properties in rocks, Academic Press, London, pp. 3-31.

Lockner, D., 1993. The role of Acoustic Emission in the Study of Rock Fracture, Int. J. Rock Mech. Min. Sci. & Geomech. Abstr. Vol.30, No.7, pp. 883-899.

Lokajicek, T., and Klima, K., 2006. A first arrival identification system of acoustic emission (AE) signals by means of a high-order statistics approach, Measurement Science and Technology, 17, 2461-2466.

Louis, L., David, C., Robion, P., 2003. Comparison of anisotropic behaviour of undeformed sandstones under dry and saturated conditions, Tectonophysics, 370, 193-212.

Louis, L., Wong, T.-F., Baud, P., Tembe, S., 2006. Imaging strain localisation by X-ray computed tomography: discrete compaction bands in Diemelstadt sandstone, Journal of Structural Geology, 28, 762-775.

Louis, L., Wong, T.-F., Baud, P., 2007a. Imaging strain localisation by X-ray radiography and digital image correlation: Deformation bands in Rothbach sandstone, Journal of Structural Geology, 29, 129-140.

Louis, L., Baud, P., Wong, T.-F., 2007b. Characterisation of pore-space heterogeneities in sandstone by X-ray computed tomography, in: David, C. & Le Ravalec-Dupin, M., (eds), Rock Physics and Geomechanics in the study of Reservoirs and Repositories, Geological Society, London, Special Publications, 284, 127-146.

M

MacKenzie, W.S. and Adams, A.E., 2009. Rocks and Minerals in Thin Sections, 6th edition, Wiley, pp. 1-192.

Mair, K., Main, I., Elphick, S., 2000. Sequential development of deformationbands in the laboratory, Journal of Structural Geology, 22, 25– 42.

Mair, K., Elphick, S., Main, I., 2002. Influence of confining pressure on the mechanical and structural evolution of laboratory deformation bands, Geophysical Research Letters, Vol. 29, No. 10, 1410, doi:10.1029/2001GL013964.

Marketos, G., Bolton, M.D., 2005. Compaction bands as observed in DEM simulations, Powders and Grains, Garcia-Rojo, Herrmann and McNamara (eds), Taylor and Francis Group, London, ISBN041538348., 1405-1408.

Marketos, g., Bolton, M.D., 2009. Compaction bands simulated in Discrete Elements Models, Journal of Structural Geology, 31, pp. 479-790.

Martin, J.L., Soares, J.A., Da Silva, J.C., 2007. Ultrasonic travel-time tomography in core plugs, Journal of Geophysics and Engineering, 4, 117-127.

Maxwell, S.C. & Young, R.P., 1993. A comparison between controlled source and passive source seismic velocity images, Bull. Seismic. Soc., Am. 83 (6): 1813-1834.

Mees, F., Swennen, R., Geet, M.V. & Jacobs, P., 2003. Applications of X-ray computed tomography in the geosciences, In: F. Mees, R. Swennen, M. Van Geet, & P. Jacobs (eds), Applications of X-ray Computed Tomography in the Geosciences, Geological Society Special Publications, vol. 215, pp. 1-6.

Menéndez, B., Zhu, W., Wong, T.-F., 1996. Micromechanics of brittle faulting and cataclastic flow in Berea sandstone, Journal of Structural Geology, Vol. 18, No. 1, pp.1-16.

Mollema, P.N. and Antonellini, M.A., 1996. Compaction bands: a structural analog for anti-mode I cracks in Aeolian sandstone, Tectonophysics, 267, 209-228.

Myers, R. and Aydin, A., 2004. The evolution of faults formed by shearing across joint zones in sandstone, Journal of Structural Geology, 26, 947-966.

N

Nelder, J. and Mead, R., 1965. A simplex method for function minimisation, Computer J., 7, 308-312.

Nguyen T.L., Hall S.A., Vacher P., Viggiani G., 2010. Fracture mechanisms in softrock: identification and quantification of evolving displacement discontinuities by digital image correlation, Tectonophysics, Special volume of the 8th Euroconference of Rock Physics and Rock mechanics, doi:10.1016/j.tecto.2010.09.024.

O

Olsson, W.A., 1999. Theoretical and experimental investigation of compaction bands in porous rocks, Journal of Geophysical Research, Col. 104, B4, 7219-7228.

Olsson, W.A. and Holcomb, D.J., 2000. Compaction localisation in porous rocks, Geophysical Research Letters, Vol. 27, No.21, pp. 3537-3540.

Olsson, W.A., 2001. Quasistatic propagation of compaction fronts in porous rocks, Mechanics of Materials, 33, pp. 659-668.

Olsson, W.A., Holcomb, D.J., Rudnicki, J.W., 2002. Compaction Localisation in Porous Sandstones: Implications for Reservoir Mechanics, Oil and Gas Science and Technology, Rev. IFP, Vol. 57, No. 5, pp.591-599.

Opielinski, K. J., Gudra, T., 1998. Main error sources in ultrasound transmission tomography imaging, The Journal of the Acoustical Society of America, Volume 103, Issue 5, p.2793.

Ord, A., Vardoulakis, I., Kajewski, R., 1991. Shear band formation in Gosford Sandstone, International Journal of Rock Mechanics and Mining Sciences & Geomechanics Abstracts, Volume 28, Issue 5, pp. 397-409.

Otani, J., Mukunoki, T., & Sugawara, K., 2005. Evaluation of particle crushing in soild using X-ray CT data, Soils and Foundations, 45, 99-108.

Ouyang, C., Landis, E., Shah, E.P., 1991. Damage Assessment in Concrete using quantitative Acoustic Emission, Journal of Engineering Mechanics, Vol. 117, No. 11, 2681-2698.

Oye, V., Roth, M., 2003. Automated seismic event location for hydrocarbon reservoirs, Computers and Geosciences, 29, 851-863.

P

Pan, B., Qian, K., Xie, H., Asundi, A., 2009. Two-dimensional digital image correlation for in-plane displacement and strain measurement: a review, Measurement Science and Technology, 20, doi:10.1088/0957-0233/20/6/062001, pp.16.

Passchier, C.W. & Trouw, R.A.J., 2005. Microtectonics, 2nd Edition, Springer, pp. 1-365.

Peng, Z., Ben-Zion, Y., Michael, A.J, Zhu, L., 2003. Quantitative analysis of seismic fault zone waves in the rupture zone of the 1992 Landers, California, earthquake: evidence for a shallow trapping structure.

Pratt, R.G., and Chapman, C.H., 1992. Traveltime tomography in anisotropic media-II. Application, Geophys. J. Int., 109, pp. 20-37.

Pratt, R.G., McGaughey, W.J., Chapman, C.H., 1993. Anisotropic velocity tomography: A case study in a near-surface rock mass, Geophysics, Vol. 58, No. 12, pp. 1748-1763.

Q

Quinta Da Fonseca, J., Mummery, P.M., Withers, P.J., 2005. Full-field strain mapping by optical correlation of micrographs acquired during deformation, Journal of Microscopy, Vol. 218, pp. 9-21.

R

Reches, Z., and Lockner, D.A., 1994. Nucleation and growth of faults in brittle rocks, Journal of Geological Research, Vol. 99, No. B9, pp. 18159-18173.

Remeysen, K. & Swnnen, R., 2008. Applications of microfocus computed tomography in carbonate reservoir characterisation: Possibilities and limitations, Marine and Petroleum Geology, 25, 489-499.

Restaino, F. L., 2008. Characterising strain localization in sandstones by full-field measurements, Master Thesis, Université Joseph Fourier, Grenoble , pp. 1-48.

Riedel, J.J., Labuz, J.F., 2007. Propagation of a shear band in sandstones, International Journal for Numerical and Analytical Methods in Geomechanics, Volume 31, Issue 11, pp. 1281-1299.

Rudnicki, J.W., and Rice, J.R., 1975. Conditions for the localisation of deformation in pressure-sensitive dilatants materials, J. Mech. Phys. Solids, 23, 371-394.

Rudnicki, J.W., 2004. Shear and compaction band formation on an elliptic yield cap, Journal of Geophysical Research, Vol. 109, BO3402, doi: 10.1029/2003JB002633.

Rudnicki, J.W., 2006. Models for compaction band propagation, in: David, D. (ed) Geomechanics and Rock Physics for reservoir and repository characterisation, Geological Society of London, Special Publication**s,** Vol. 284; p. 107-125.

Rudnicki, J.W., 2007. Models for compaction band propagation, Geoplogical Society, London, Special Publications, V. 284, pp. 107-125.

Russ, John C., Dehoff, Robert T. (2000). Practical Stereology, 2nd edition, New York: Kluwer Academic / Plenum Publishers, pp.1-307.

S

Santamarina, J.C., and Fratta, D., 2005. Discrete Signals and Inverse Problems: An introduction for Engineers and Scientists, John Wiley & Sons, pp.1-345.

Schultz, R.A. and Siddharthan, R., 2005. A general framework for the occurrence and faulting of deformation bands in porous granular rocks, Tectonophysics, 441, 1-18.

Scott, T.E., Abousleiman, Y., Zaman, M., 2002. Acoustical Imaging and Mechanical Properties of soft Rocks and Marine Sediments (Quarterly Technical Progress Report, 15302R06), PoroMechanics Institute, University of Oklahoma, pp. 1-22.

Sornette, A., Davy, P., Sornette, D., 1993. Fault Growth in Brittle-Ductile Experiments and the Mechanics of Continental Collisions, Journal of Geophysical Research, Vol. 98, No. B7, pp. 12111-12139.

Stanchits, S., Fortin, J., Guéguen, Y., Dresen, G., 2009. Initiation and Propagation of Compaction Bands in Dry and Wet Bentheim Sandstone, Pure and Applied Geophysics, 166, 843-868.

Stanchits, S., 2010a---personal communication.

Stanchits, S. & Fortin, J., 2010b---personal communication.

Stein, S., Wysession, M., 2003. An introduction to seismology, earthquakes and earth structure, Blackwell, pp. 1-498.

Sternlof, K., Chapin, J., Pollard, D.D., Durlofsky, L.J., 2004. Effective permeability in sandstone containing deformation band arrays, AAPG, Bull., 88, 1315–1329.

Sternlof, K., Rudnicki, J.W., Pollard, D.D., 2005. Anticrack-inclusions model for compaction bands in sandstone, Journoal of Geophysical Research, 110, pp. 1-16, B11403.

Sulem, J. and Ouffroukh, H., 2006. Shear banding in drained and undrained triaxial tests on a saturated sandstone: Porosity and Permeability evolution, International Journal of Rock Mechanics and Mining Sciences, 43, 292-310.

T

Tembe, S., Vajdova, V., Wong, T.-F., Zhu, W., 2006. Initiation and propagation of strain localisation in circumferentially notched samples of two porous rocks, Journal of Geophysical Research, Vol. 111, B02409, doi: 10.1029/2005JB003611.

Tembe, S., Baud, P., Wong, T.-F., 2008. Stress conditions for the propagation of discrete compaction bands in porous sandstone, Journal of Geophysical Research, Vol 113, BO9409, doi: 10.1029/2007JB005439.

Tucker, M.E., 2001. Sedimentary Petrology, 3rd Edition, Blackwell, pp. 1-262.

Tudisco, E., 2009. Ultrasonic and x-ray tomographies to study localised deformation in sandstones, Master Thesis, Université Joseph Fourier, Grenoble, pp. 1-62.

U

V

Vajdova, V. and Wong, T.-F., 2003a. Incremental propagation of discrete compaction bands: Acoustic emission and microstructural observations on circumferentially notched samples of Bentheim, Geophysical Research Letters, Vol. 30, No. 14, 1775, doi: 10.1029/2003GL017750.

Vajdova, V., Wong, T.-F., Farrell, D.E., Issen, K.A., Challa, V, 2003b. Experimental observation and numerical simulation of initiation and propagation of compaction bands in sandstone, 16th ASCE, Engineering Mechanics Conference Proceedings.

Vajdova, V., Baud, P., Wong, T.-F., 2004. Permeability evolution during localised deformation in Bentheim sandstone, Journal of Geophysical Research, Vol. 109, B10406, doi: 110.1029/2003JB002942.

Vernon, R.H., 2008. A practical guide to Rock Microstructure, 2nd edition, Cambridge University Press, pp. 1-594.

Viggiani, G. & Hall, S.A., 2008. Full-field measurements, a new tool for laboratory experimental geomechanics, deformation characteristics of geomaterials, 3–26. IOS Press, Atlanta, USA.

Viggiani, G., 2009. Mechanisms of localized deformation in geomaterials: an experimental insight using full-field measurement techniques. In: Mechanics of Natural Solids, D. Kolymbas & G. Viggiani (Eds), Springer-Verlag, 105-125.

W

Wang, B., Chen, Y., Wong, T.-F., 2008. A discrete element model for the development of compaction localization in granular rock, Journal of Geophysical Research, Vol. 113, BO3202, doi:10.1029/2006JB004501.

Wenk, H.-R. and Bulakh, A., 2008. Minerals: their constitution and origin, 3rd edition, Cambridge University Press, pp. 1-646.

Wibberley, C.A., Petit, J.-P., Rives, T., 2007. The mechanics of fault distribution and localization in high-porosity sands, Provence, France, in: Lewis, H. & Couples, G., D., (eds), the relationship between Damage and Localisation, Geological Society, London, Special Publications, 289, 19-46.

Wibberley, C.A., Yielding, G., Di Toro, G., 2008. Recent advances in the understanding of fault zone internal structure: a review, from Wibberley, C.A.J., Kurz, W., Imber, J., Holdsworth, R.E &Collettini, C. (eds) The internal Structure of Fault Zones: Implications for Mechanical and Fluid-Flow Properties, 299, 5-33.

Wong, T.-F., 1990. Mechanical compaction and the brittle-ductile transition in porous sandstones, Geological Society, London, Special Publications, Vol. 54, pp. 111-122.

Wong, T.-F., Szeto, H., Zhang, J., 1992. Effect of loading path and porosity on the failure mode of porous rocks, Appl. Mech. Rev., 45, 281-293.

Wong, T.-F. and Wu, L.-C., 1995. Tensile stress concentration and compressive failure in cemented granular materials, Geophysical Research Letters, 22: 1649-1652.

Wong, T.-F., David, C., Zhu, W., 1997. The transition from brittle faulting to cataclastic flow in porous sandstones: Mechanical deformation, Journal of Geophysical Research, Vol. 102, No. B2, pp. 3009-3025.

Wong, T.-F., Baud, P., Klein, E., 2001. Localised failure modes in a compactant porous rock, Geophysical Research Letters, vol. 28, No. 13, pp. 2521-2524.

Wong, T.-F., David, C., Menendez, B., 2004. Mechanical compaction, In: Mechanics of Fluid-saturated rocks, Guéguen, Y., Bouteca, M., (eds.), International Geophysics Series, Vol. 89, Elsevier Academic Press, pp. 55-115.

Wu, X.Y., Baud, P., Wong, T.-F., 2000. Micromechanics of compressive failure and spatial evolution of anisotropic damage in Darley Dale sandstone, International Journal of Rock Mechanics and Mining Science, 37, 143-160.

X

Y

Yordkayhun, S., Tryggvason, A., Juhlin, C., 2007. A 3D seismic traveltime tomography study of the shallow subsurface at the CO2SINK project site, Ketzin, Germany, EAGE 69th Conference and Exhibition-London, UK.

Z

Zang, A., Wagner, F.C., Stanchits, S., Dresen, G., Andresen, R., Haidekker, M.A., 1998. Source analysis of acoustic emissions in Aue granite cores under symmetric and asymmetric compressive loads, Goephys. J., Int., 135, 1113-1130.

Zhang, J., Wong, T.-F., Davis, D.M., 1990. Micromechanics of pressure induced grain crushing in porous rocks. J. Geophys. Res., 95, 341-352.

Zhao, D., 2009. Multiscale seismic tomography and mantle dynamics, Gondwana Research, 15, 297-323.

Zhu, W., Wong, T.-F., 1997. Shear-enhanced compaction in sandstones under nominally dry and water-saturated conditions, International Journal of Rock Mechanics and Mining Science, 34: 3-4, paper No. 364.

Zietlow, W.K., Labuz, J.F., 1998. Measurement of the Intrinsic Process Zone in Rock Using Acoustic Emission, Int. J. Rock Mech. Min. Sci., Vol. 35, No. 3, pp 291-299.

Ultrasonic Sensors

Appendix A

A.1 Introduction

Ultrasonic sensors convert electrical to mechanical energy, in the form of sound, and vice versa. For the field measurements, usually these sensors are produced by industrial manufacturers. However, in the laboratory scale, the use of industrial sensors is limited due to the rather small dimensions of the tested specimens. A drawback of the in-home sensors is that they have to be calibrated in order give trustworthy measurements.

Six small P-wave sensors were constructed, during this work, for the measurement of P-waves in rock specimens. The principal idea behind these sensors was based on previous works among which those by *Lockner et al.*, [1992], *Stanchits, 2010, Fortin, 2008.*

Each sensor consists of three main components: the active element, the backing and the housing. The transducers are linked to the connectors via coaxial cables (Fig.A.1).

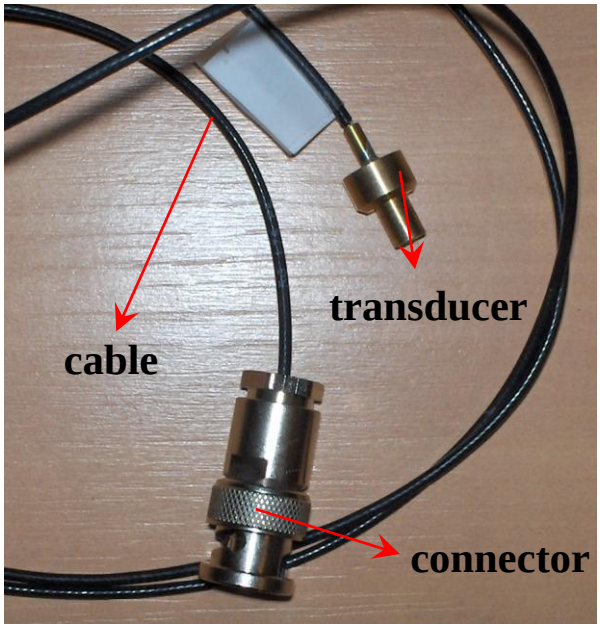

Fig. A. 1: Photograph of the transducer-cable-connector.

A.2 Cable

A cable 180-314 RG 178 was used to link the transducer (active element, Fig. A.3) to the connector (Fig. A.4). A schematic representation of the cable is illustrated in Figure A.2, where the conductor (1), the dielectric (2), the shied (or braid) (3) and the outer jacket (4) are shown. The conductor acts as the positive connection of the cable, while the shied acts as a ground. The dielectric isolates the conductor from the shied. These three components are surrounded by an outer protective jacket.

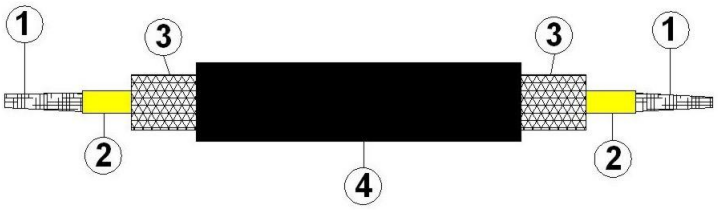

1	**conductor**
2	**dielectric**
3	**shied**
4	**outer jacket**

Fig. A.2: Cross-sectional view of a typical cable. (1) Conductor; (2) Dielectric; (3) Shied; (4) Outer jacket.

A.3 Main components of the transducer

In this section, the main component of the P-wave transducers will be described shortly. The active element, which consists of a piezoelectric material, converts the electrical energy (transmitted through the cables) to ultrasonic energy. Piezoelectric materials, such as piezo-polymers and composites or polarised ceramics, are used for this purpose. In the present version, piezo-ceramics crystals were applied (lead zirconat titaninate). These ceramics had a resonant frequency of 1MHz.

A schematic view of the active element of the transducer is presented in Figure A.3.

Appendix A

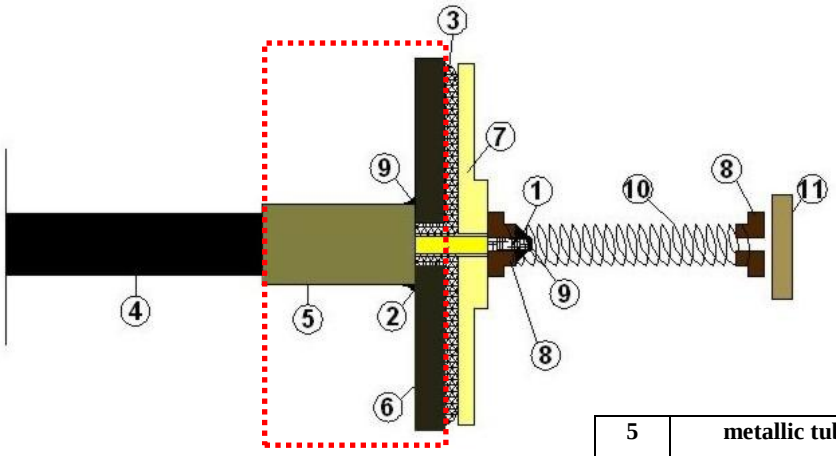

1	conductor	cable
2	dielectric	
3	shied	
4	outer jacket	

5	metallic tube
6	metallic plate
7	insulation
8	metallic end-stop
9	soldering
10	spring
11	ceramic

Fig. A. 3: Schematic representation of the transducer. (1) Conductor; (2) Dielectric; (3) Shied; (4) Outer jacket; (5) Metallic tube; (6) Metallic plate; (7) Insulation; (8) Metallic end-stop; (9) Soldering; (10) Spring; (11) Piezo-ceramic.

The connections of the sensor's components should be mechanically stable and well electrically protected. A metallic tube is suggested to be soldered on the metallic plate in order to ensure a stable mechanical connection (shown in the red rectangle, Fig. A.3). This particular part is very fragile since the frequent use of the sensor might cause local breakage of the conductor at this place.

The spring transfers the electrical pulse to the ceramic (active member). The one end of the former is connected to the main body of the transducer, while the other touches the piezo-ceramic. The spring gets in direct contact with the ceramic through a metallic end-stop, which provides a good electrical coupling (the spring force helps this coupling). The piezoelectric material vibrates when an oscillating electrical signal is applied (*i.e.*, electrical energy is converted to mechanical energy).

The transducer's housing protects the piezo-crystal from the testing environment. Usually, a metallic cylinder is screwed on the metallic plate (female-male). To ameliorate the transmission of the ultrasonic signal, a drop of oil is used as couplant between the ceramic and the wear plate. The transducer's housing is in contact with the specimen through a viscous couplant *i.e.*, oil, grease, washing-up liquid, or molasses (depending on the tested material).

The backing of the transducer is usually a highly attenuated, high density material that is used to control the vibration of the transducer by absorbing the energy radiating from the back face of the active element. In these transducers, the backing is absent due to technical difficulties.

A.4. Connector

The connector is the part of the sensor that is connected to the ultrasonic source-receiver system. Figure A.4 presents a schematic view of the main part of the connector. The whole system is screwed into a casing.

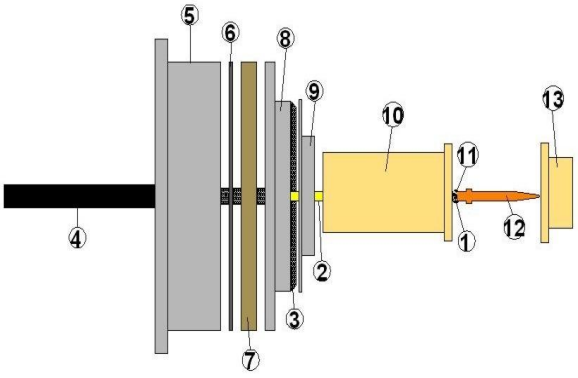

1	**conductor**	**8**	**locking system**
2	**dielectric**	**9**	**bush**
3	**shied**	**10**	**insulator**
4	**outer jacket**	**11**	**soldering**
5	**nut**	**12**	**contact pin**
6	**washer**	**13**	**insulator**
7	**gasket**		

Fig. A.4: Schematic representation of the connector. (1) Conductor; (2) Dielectric; (3) Shied; (4) Outer-jacket; (5) Nut; (6) Washer; (7) Gasket; (8) Locking system; (9) Bush; (10, 13) Insulator; (11) Soldering; (12) Contact pin; (13) Insulator.

A.5. Ultrasonic tomography application

These sensors were initially used to take wave measurements (ultrasonic transmission) in Vosges specimens. Multiple wave measurements were acquired by shifting these sensors in different positions along the flatten surfaces of the specimens (see Fig. 4.5). The recorded P-waves were later elaborated and UT velocity fields were produced (see section 3.2). Figure A.5 presents velocity maps from an undeformed Vosges sandstone specimen (VEC1, Table 4.2). Recall that notches were machined at the flattened surfaces of this specimen (Fig. 4.6). Figure A.5 illustrates the trade-off curve of the misfit (of the time residuals) and the roughness (of the slowness) together with different ultrasonic velocity field solutions. Discretisation was made on square cells of 5^2 mm^2 size. The higher the misfit of the time-residuals is, the smoother the images appear. A solution close to the 'knee-point' has to be chosen (see section 3.2).

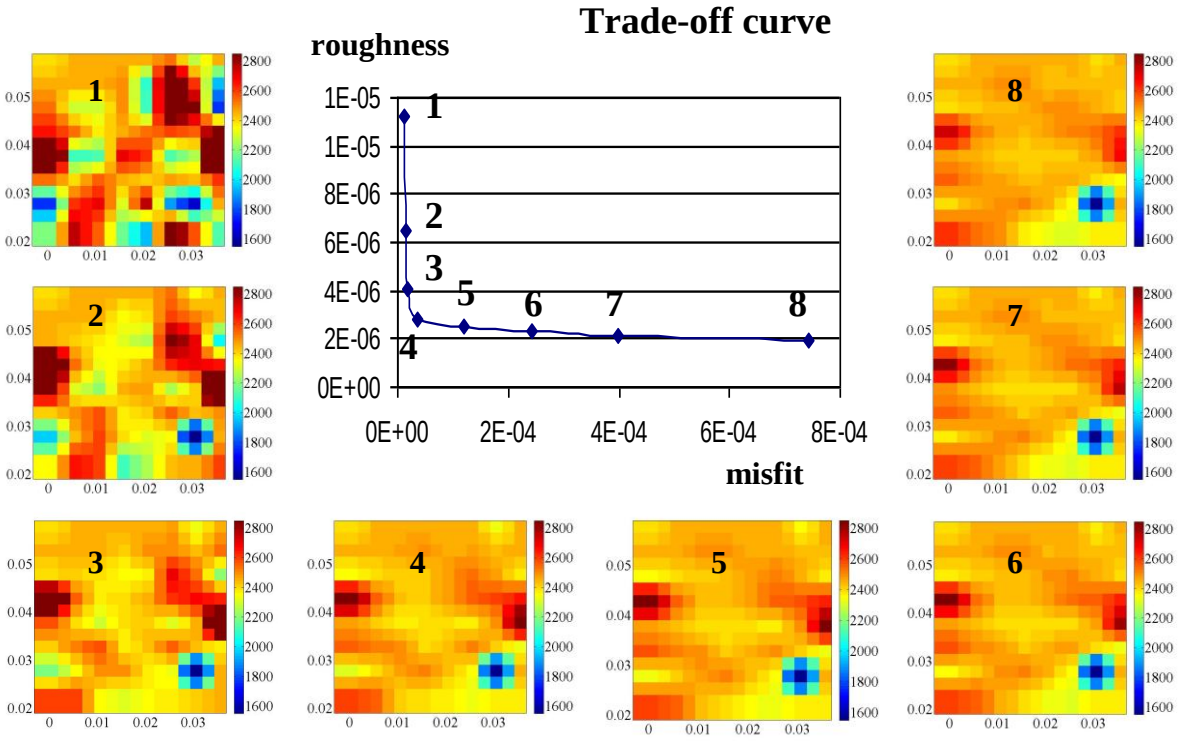

Fig. A.5: (1-8) Solutions of velocity fields from specimen VEC1 (notched), using different ε parameters (in terms of the misfit-roughness curve). The best solution is this for ε=5E-07 (4).

Figure A.6a illustrates the suggested solution for ε=5E-07 (see Fig. A.5) and Figure A.6b shows the equivalent ray-coverage from this UT field. Note that no measurements were taken in regions close to the notches (in black rectangles, Fig. A.6a) since the size of the sensors was mainly covering the void at this region (notch). The ray-coverage was less dense than that acquired by the barrettes (see Fig. 3.9). Furthermore, there were cells which were not covered by any rays (ghosts). Also at the top and bottom of the specimen the ray-coverage was relatively poor. Note that there were cells which were covered only by one ray (Fig. A.6b). Therefore, some artefacts observed on the velocity field could be attributed to the ray-coverage issues. Any attempt to acquire a denser ray-coverage was rather time-consuming. It could be, therefore, speculated, that measurements coming from the small sensors could be used for the reproduction of adequate velocity field; however, such measurements could not reproduce the velocity fields obtained by the barrettes.

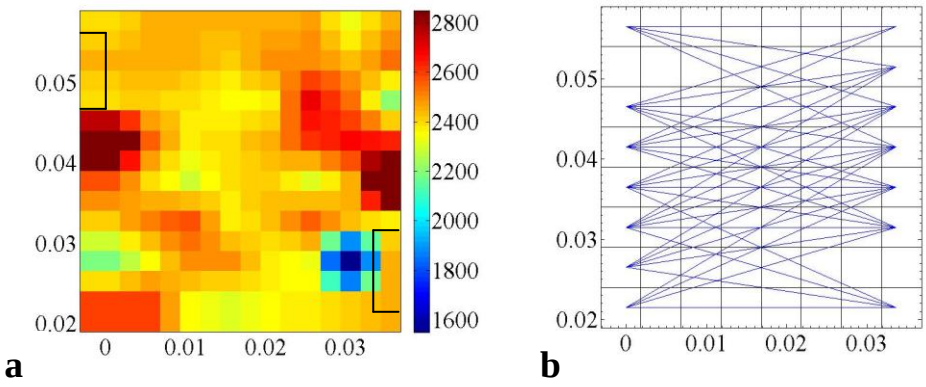

Fig. A.6: (a) The best solution from Fig. A.5; (b) Ray-coverage from (a).

Appendix B

Procedures to validate the DIC and x-ray tomography measurements

Appendix B

B.1 Introduction

The present Appendix presents a comparison between the displacements coming from the DIC (full-field method), the piston and the LVDTs (point-wise measurements). Although, shear and volumetric strain fields were presented in Chapters 5 and 6, instead of displacement fields, such comparison is necessary to evaluate the accuracy of the local displacement measurements. Furthermore, this Appendix describes the threshold criteria applied to the measurement of the width of the shear and compaction bands. Recall that the width of shear bands was defined by the raw x-ray tomography images, while that of compaction bands was defined based on the standard deviation of the grey-scale values.

B.2 Local and global displacement comparison

The correlation between the pre- and post-mortem x-ray images aimed at the calculation of the displacement fields, and the subsequent strain fields, of these two different deformation stages (see also section 3.5). HR and LR x-ray images were used for such reason (~30 μm and ~90 μm, respectively). Recall that the former were focused on the part of the specimen where the actual deformation took place (and in most cases covered about 20 mm around the mid-height of the specimen), while the latter were performed throughout the whole height of the specimen. However, it should be underlined that due to some reconstruction restrictions, the actual reconstructed LR x-ray images did not cover in most of the cases the last 3.5 mm at the top and bottom of the specimen; in other words the reconstructed volume had a height of 73-72 mm instead of 80 mm, which was the height of the specimens. In this section, a comparison of the local displacements (derived by the DIC) and the global displacement of the piston is presented together with a comparison of the former displacements and the local displacements measured by the LVDTs, which were attached on the specimen between +10 mm and +70 mm from its lower edge. Displacement fields from LR x-ray images are used herein for such comparison, since they covered almost the whole height of the specimen (unlike HR x-ray images, which covered only the central part). Figure B1 illustrates the

various parts of the specimen in which the different displacements were measured (or calculated).

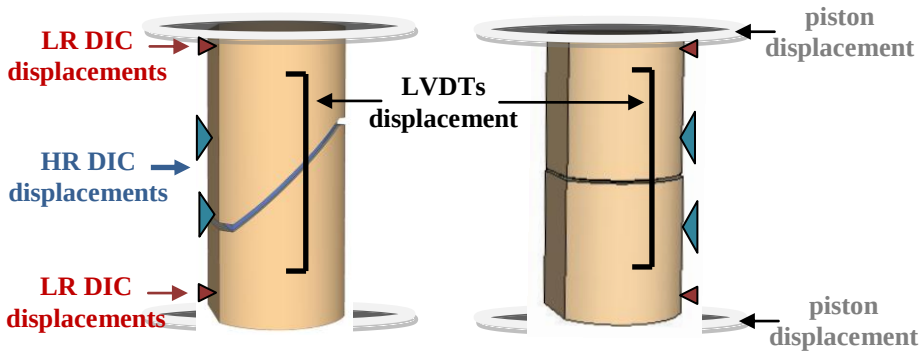

Fig. B.1: Schematic configuration of specimens localised by shear and compaction bands presenting the different heights in which the different displacement measurements were made. Displacements of the piston covered the whole height of the specimen. DIC displacements calculated by LR DIC covered a height from 3.5 mm to 76.5 mm from the bottom of the specimen. LVDT displacements were measured from 10 mm to 70 mm from the bottom of the specimen. DIC displacements calculated by HR DIC covered 20 – 30 mm from the mid-height of the specimen (in total).

Examples of two specimens are presented; one deformed by a shear band (specimen Ve2) and one by a compaction band (specimen Ve4).

- Specimen Ve2: Global displacements compared to DIC displacement field

Figure B.2a presents the stress deviator as a function of the global axial displacement (displacement of the piston) for specimen Ve2 (Fig. B.2b). After the unloading of the deviatoric compression stage, the non-recoverable displacement, measured by the displacement of the piston is about 437 µm. Figures B.2c and B.2d show two 2D projections of the vertical displacement field (at a plane normal to the height of the specimen) calculated at the lower and upper edges of specimen Ve2 (using the LR x-ray tomography images).

Appendix B

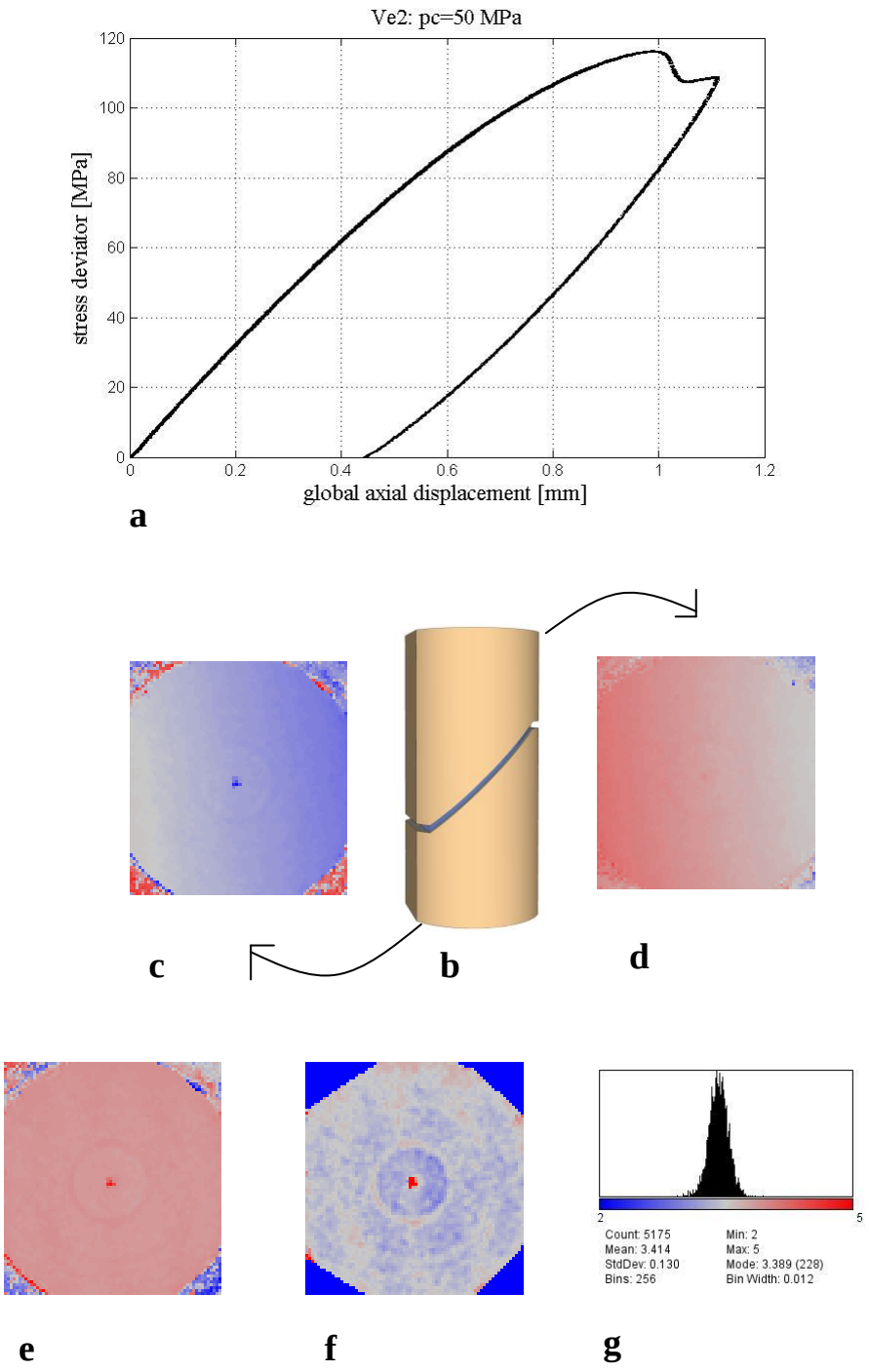

Fig. B.2: Specimen Ve2: (a) Stress deviator versus axial displacement (piston); (b) Schematic representation of specimen; (c) Vertical displacement field of the bottom slice (lower boundary); (d) Vertical displacement field of the top slice (upper boundary); (e) Vertical displacement field difference between the top and the bottom slice; (f) Masked (e); (g) Histogram of the displacement field difference.

Figures B.2e-B.2g show the vertical displacement field difference between the bottom and the top 2D projections, the masked displacement difference image and the thresholded histogram of the masked displacement field difference. The mean relative vertical displacement of the 2D slice in Figure B.2f is equal to 3.39 pixels (relative displacement between the top and the bottom axial displacement field). Recall that the pre- and post-mortem LR x-ray tomography images had a pixel resolution of around 90 μm. Therefore, the mean relative vertical displacement measured in specimen Ve2, using the LR-DIC is equal to 305 μm (3.39x90 μm). Ring artefact at the central part of the core is evident in Figures B.2c-B.2f. The displacement values in places where the ring artefact is present were not taken into account for the calculation of the mean relative vertical displacement.

By comparing the vertical displacements calculated from the axial displacement of the piston and the LR 3D-DIC, it could be argued that they are of the same range; though the former appears to be slightly higher. However, recall that no lubricant was placed at the top and bottom of this specimen, so these places were more prone to intense damage (which is not shown in Fig. 5.1 due to restricted AE plotted coordinates at the z-axis). Furthermore, the displacement from the LR 3D-DIC is linked to a relatively shorter height of the specimen compared to that of the piston. Finally, it is worth to mention that the displacement of the piston is measured before the unloading of the hydrostatic loading, while the displacement derived from the LR 3D-DIC is after the unloading of the hydrostatic loading.

- <u>Specimen Ve2: Local displacements compared to DIC displacement field</u>

Figure B.3 shows the vertical displacement fields calculated by the LR 3D-DIC for the upper (Fig. B.3b) and the lower (Fig. B.3c) 2D slices, located at the place where the LVDTs were attached (e.g. +10 mm and +70 mm from the lower boundary of the Ve2 specimen, Fig. B.3a). The vertical displacement field difference between these two 2D projections, the thresholded vertical displacement field difference of the masked image and its histogram are shown in Fig. B.3d-e, respectively. The mean relative vertical displacement of the 2D slice in Figure B.3e is equal to 2.957 pixels (relative displacement between the top and the bottom axial displacement field, at the level of the LVDTs). Thus, the mean relative vertical displacement at this height measured in specimen Ve2, using the LR 3D-DIC is equal to

266.13 µm (2.957x90 µm). The displacement values in places where the ring artefact is present were not taken into account for the calculation of the mean relative vertical displacement (like in Fig. B.2).

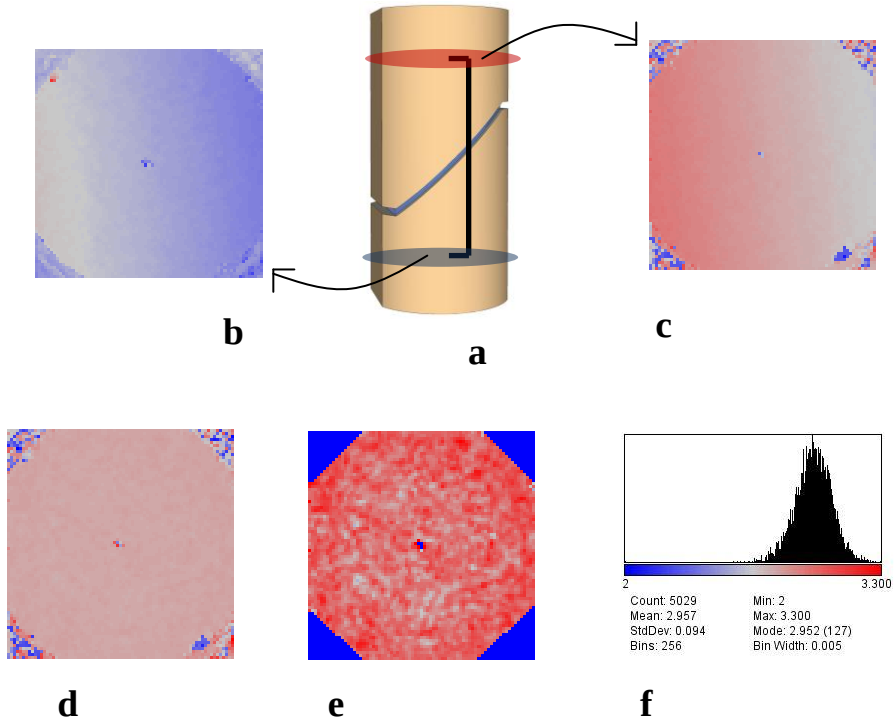

Fig. B.3: Specimen Ve2: (a) Schematic representation of specimen, showing the position of the LVDTs (in black); (b) Vertical displacement field of the bottom slice at the level of the lower boundary of the LVDT; (c) Vertical displacement field of the top slice at the level of the upper boundary of the LVDT; (d) Vertical displacement field difference between the top and the bottom slice; (e) Thresholded displacement field for the calculation of the mean displacement from the masked (d); (f) Histogram of the displacement field difference (e).

The non-recoverable displacement, measured by the LVDTs, for specimen Ve2 is about 297.48 µm (0.4958% x 6 cm, the former being the non-recoverable axial strain shown in Fig. 4.14a and the latter being the length of the LVDT). The vertical displacements measured by the LVDTs and the LR 3D-DIC are of same magnitude. Note the slight difference may be explained by the fact that the former is measured before the unloading of the hydrostatic

loading, while the displacement derived from the LR 3D-DIC is after the unloading of the hydrostatic loading.

- Specimen Ve4: Local displacements compared to DIC displacement field

Figure B.4 shows the vertical displacement fields calculated by the LR 3D-DIC for the upper (Fig. B.4b) and the lower (Fig. B.4c) 2D slices, located at the place where the LVDTs were attached (e.g. +10 mm and +70 mm from the lower boundary of the Ve4 specimen, Fig. B.4a). The vertical displacement field difference between these two 2D projections, the thresholded vertical displacement field difference of the masked image and its histogram are shown in Fig. B.4d-e, respectively.

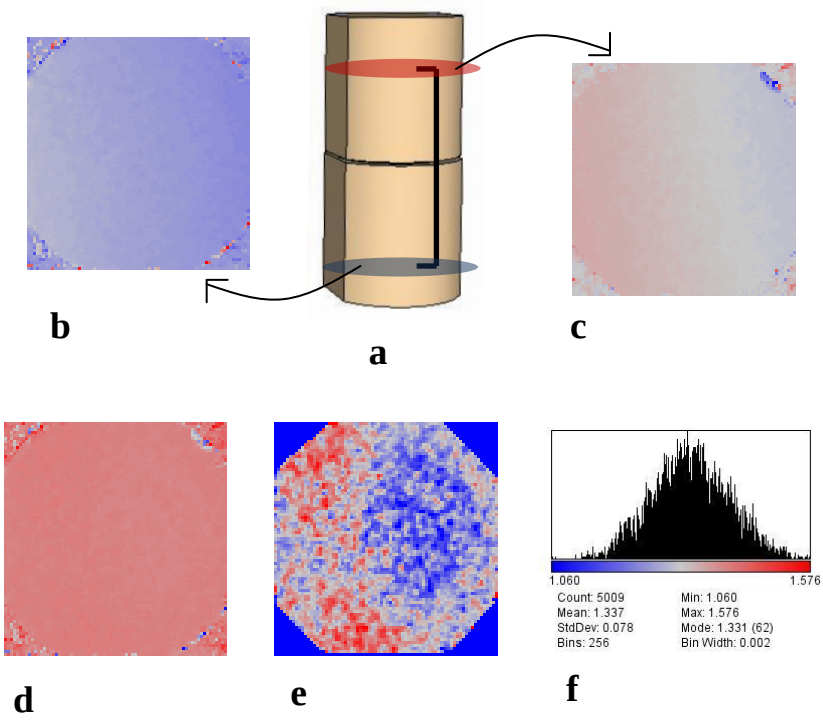

Fig. B.4: Specimen Ve4: (a) Schematic representation of specimen, showing the position of the LVDTs (in black); (b) Vertical displacement field of the bottom slice at the level of the lower boundary of the LVDT; (c) Vertical displacement field of the top slice at the level of the upper boundary of the LVDT; (d) Vertical displacement field difference between the top and the bottom slice; (e) Thresholded displacement field for the calculation of the mean displacement from the masked (d); (f) Histogram of the displacement field difference (e).

The mean relative vertical displacement of the 2D slice in Figure B.4e is equal to 1.337 pixels (relative displacement between the top and the bottom, at the level of the LVDTs). Thus, the mean relative vertical displacement at this height measured in specimen Ve4, using the LR 3D-DIC is equal to 120.33 μm (1.337x90 μm).

The non-recoverable displacement measured by the LVDTs for specimen Ve4 is about 179.46 μm (0.2991% x 6 cm, the former being the average non-recoverable axial strain shown in Fig. 4.17a and the latter being the length of the LVDT). The vertical displacements measured by the LVDTs and the LR 3D-DIC are of same magnitude. However, it could be claimed that the difference in displacement is much more pronounced in this case compared to that of specimen Ve2 (shear band). Although this difference may be explained by the fact that the LVDT displacement was measured before the unloading of the hydrostatic loading, while the displacement derived from the LR 3D-DIC was after the unloading of the hydrostatic loading, it could be argued that the LVDT readings in this case might have been erroneous (*e.g.*, not proper calibration) since they also differ considerably from the global displacement values (see Fig. 4.17). As already mentioned in Chapter 4, although in such cases the absolute values of the displacements from LVDTs might not be trustworthy, they are considered valuable from a qualitative point of view (*e.g.,* p-q plane description, see Chapter 4).

B.3 Definition of the width of the deformation bands

Table 2.5 (section 2.7.8) presents measured deformation band widths from different sandstones, applying different experimental methods (mainly thin section observations). In this work, the width of the deformation bands in the Vosges Sandstone was mainly defined by post-deformation HR x-ray images (Chapters 5 and 6, and section 7.4). In this particular sandstone, shear bands were visualised using solely the raw x-ray tomography images (post-mortem HR images); however, this was not the case for compaction bands, which were visualised by the standard deviation of the grey-scale values instead of the raw data (Chapter

5 and 6). In both cases, a threshold on the grey-scale data (raw or standard deviation) was applied in order to visualise the deformation features.

Figure B.3 illustrates the threshold values of the grey-scale values (histogram) from the HR x-ray tomography images of specimen Ve2 (raw data, Fig. 5.3, section 5.2), which was deformed by a shear band. Vg-max software (3SR, Grenoble) was used for the visualization of these images. The visualized grey-scale range was initially defined by trial and error aiming at this range of the histogram that turns shear bands visible. The optimum grey-scale range of the visualised pixels shown in Figure 5.3 (section 5.2) was chosen to be between the low density (lower grey-scale values of the histogram) and the middle density (peak grey-scale value of the histogram) grey-scale values (Fig. B.5). The threshold range was further distinguished in two different parts, which were visualised in different colours, *e.g.*, yellow and red. The limit grey-scale value between the two parts (Interval 2 and Interval 3) was defined as the projection of the linear part of the histogram curve (starting from the peak value) to the grey-scale value axis (red dashed line, Fig. B.3). In these particular image, yellow colours represented relatively lower density values, while and red colour represented higher density values.

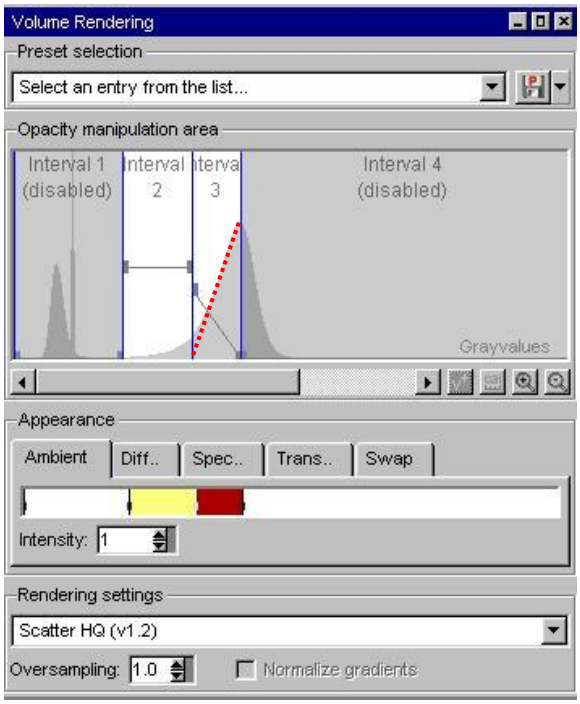

Fig. B.5: Thresholded histogram of the grey-scale values from HR x-ray tomography images, for the visualisation of the shear bands in specimen Ve2 (Fig. 5.2).

Figures B.6 present the same vertical projection of the standard deviation field from specimen Ve4 (Fig. 6.7, section 6.2), using a different threshold of the standard deviation grey-scale values. In particular, Figure B.6a contains the whole grey-scale range (histogram on the left); however, the standard deviation field does not reveal any particular distinct feature. For a narrower grey-scale range (Fig. B.6b), compaction bands appear to be visible close to the notches (yellow colours). Note that in Figure B.6a, yellow was visualising a wider grey-scale range, therefore, the values corresponding to the compaction bands could not be seen.

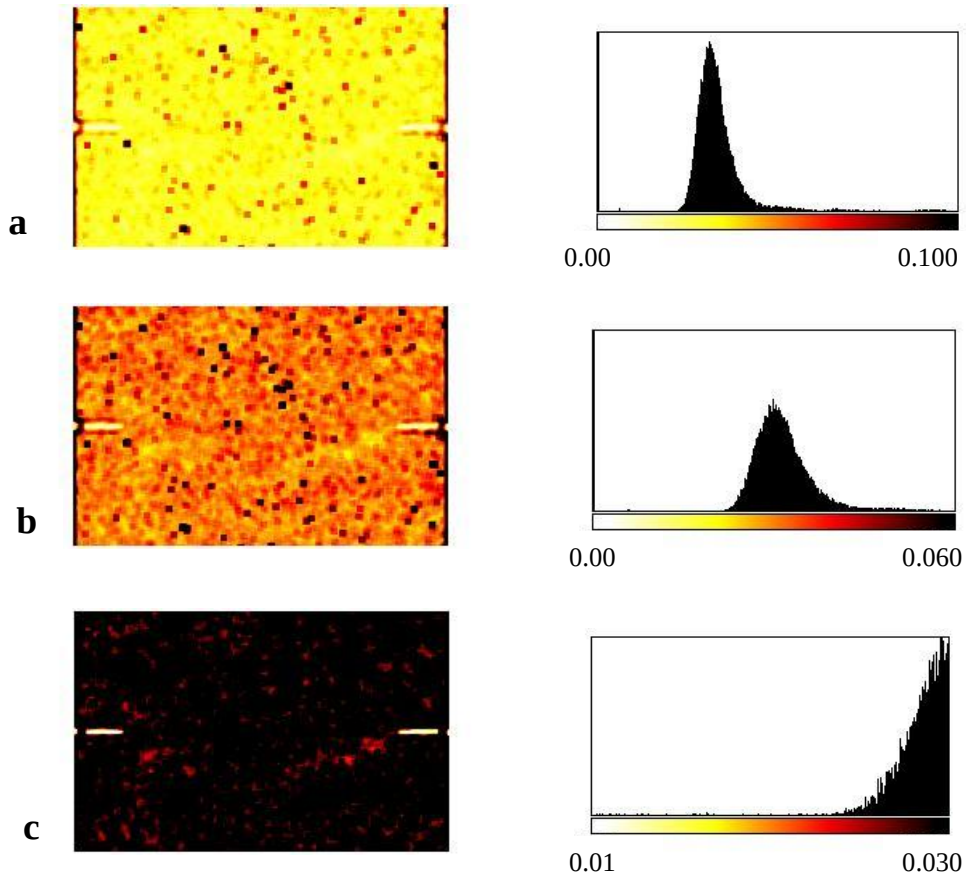

Fig. B.6: Thresholded standard deviation grey-scale fields and equivalent histograms from HR x-ray tomography images (specimen Ve4, Fig. 6.7, section 6.2). (a) Threshold value from 0 to 0.1; (b) Threshold value from 0 to 0.06; (c) Threshold value from 0.01 to 0.03.

From both Figures B.6a and B.6b, it is shown that low standard deviation values are located inside compaction bands. A smaller grey-scale threshold was chosen in Figure B.6c. In such case, compaction bands are shown in red, while standard deviation values higher than 0.030 are shown in black. Most of the standard deviation x-ray images (HR), presented in Chapters 4 and 5, have a threshold range from 0.01 to 0.03.